THE GEOTECHNICAL CHARACTERISATION
AND
STABILITY ANALYSIS OF BHP BILLITON'S CANNINGTON MINE PASTE FILL

Thesis submitted by

Rudd McAuslan RANKINE BEng(Hons) *Qld*

in April 2004

for the degree of Doctor of Philosophy
in the School of Engineering
James Cook University

STATEMENT OF ACCESS

I, the undersigned, the author of this thesis, understand that James Cook University will make it available for use within the University Library and, by microfilm or other means, allow access to users in other approved libraries.

All users consulting this thesis will have to sign the following statement:

> **In consulting this thesis, I agree not to copy or closely paraphrase it in whole or in part without the written consent of the author; and to make proper public written acknowledgement for any assistance which I have obtained from it.**

Beyond this, I do not wish to place any restriction on access to this thesis.

Signature Date

STATEMENT OF SOURCES

DECLARATION

I declare that this thesis is my own work and has not been submitted in any form for another degree or diploma at any university or other institution of tertiary education. Information derived from the published or unpublished work of others has been acknowledged in the text and a list of references is given.

Signature Date

DIGITAL STATEMENT OF SOURCES

DECLARATION

I, the undersigned, the author of this work, declare that the electronic copy of this thesis provided to the James Cook University Library is an accurate copy of the print thesis submitted, within the limit of the technology available.

Signature Date

Acknowledgements

The author wishes to thank

Dr. Nagaratnam Sivakugan – for your guidance, friendship and good humour throughout. Rohini – thanks for the parties, good memories and friendship.

Mum, Dad and the Family, – Love, caring and support and chats around the table.

BHP Billiton and in particular Dr. Martyn Bloss, for their support

Nan and Grandad – Ongoing support and encouragement throughout all studies.

Muz and Sharon: - Mum's beautiful sisters

The Engineering Technical Staff – Warren O'Donnell, Stuart Petersen and Don Braddick and last but certainly not least, the staff and students of St Marks College, James Cook University.

Dedication

This work is dedicated my family: - John & Glenda, Tegan, Shauna, Briony, Kirralee, Kelda and Lachlan, for their unconditional love and support - Always.

Thank you.

Abstract

BHP Billiton's Cannington mine is a silver-lead-zinc mine located in North West Queensland, which utilizes post-placed backfill technology in tailings disposal. The backfill is known as paste fill. Paste fill is simply mine tailings, with typical effective grain size of 5 μm, mixed with a small percentage of cement binder. As mine stopes are removed, the paste fill is used to backfill the empty space. Paste fill provides substantial benefits to mining operations including an effective means of tailings disposal, improvement of local and regional rock stability, greater ore recovery and greatly reduced environmental impacts.

The studies undertaken as part of this dissertation has included extensive laboratory testing to study the geotechnical behaviour of paste fill. The testing programme included direct shear, triaxial, UCS in addition to the index property tests. These were prepared and cast in the laboratory and cured over different times to include short, medium and long term properties. The study period ranged from less than 24 hours to one year. Additional in-situ testing was conducted at Cannington mine with James Cook Universities' dynamic cone penetrometer to identify the variation of strength with depth. Additional in-situ samples were taken and tested, with the results compared to the laboratory prepared samples.

FLAC3D was used to study the stress development in paste, taking into account the geometric properties of the stope and material properties of the paste fill. A sensitivity analysis was done on the geometry and material properties of the paste to measure the effect on stress development.

Artificial neural networks were used as a predictive tool to tie all the outputs from the geotechnical characterisation phase and stress modelling phases. By combining the two phases of the study an integrated model for the prediction and optimisation of the cement content in the backfill masses was achieved. The results of which have been presented within the findings.

The stability of fill barricades was also investigated and a relationship between the horizontal stress and the stope geometry, drive location and fill rate developed.

Contents

APPENDICES

List of Figures

List of Tables

Chapter 1

Introduction

1.1 General

The mining industry worldwide has typically not conducted the development of mines with the overall design objective of a safe, environmentally sound and aesthetically satisfactory post-operational mine-site. Mine waste has typically not been engineered to any large degree but has rather been disposed of in the easiest or most cost effective manner with little (if any) regards for the social and/or environmental consequences. Mines such as the Ok Tedi Mine (P.N.G.), Marcopper Mine (Phillipines) are testament to this. Experience gained from these failures underlines the need to dispose of mine waste in a safe, stable and economically attractive manner. This has highlighted the requirement to be able to accurately predict backfill behaviour and performance. The empirical relationships and operator experience used in yesteryear needs to be replaced by the specific engineering of mine waste.

Australia, by any standards, is extremely well endowed with most minerals even though it has barely scratched the surface of its mineral resources. The nation holds the world's largest known economic resources of bauxite, iron ore, lead, zinc, silver, uranium, industrial diamonds and mineral sands. The need to ensure the longevity of the nation’s economic wealth through the proper and efficient mining operation of mines is then obvious. The backfilling of mines is an integral part of the mining process and requires the same level of attention generally afforded to the more commonly recognised “profit-producing” parts of the operation. The change in perception of backfilling from an additional cost to mining operations to one of a pre-profit activity will aid the required advancement in technology required for backfills.

Backfilling is required for the continuance and efficiency of mining operations. Additional benefits include: - improved regional and local rock stability though support, reduced costs of building significant tailings disposal structures on the surface and the reduced environmental impacts by the underground containment of waste material. All these focus the operation towards the overall design objective of a “safe, environmentally sound and aesthetically satisfactory post-operational mine-site.”

1.2 Overview

Backfilling has occurred in many forms, from coarse loose rock through aggregates and sand to the highly processed hydraulic and paste fills. The advancement of processing technology has resulted in the reduction of the effective grain size of the tailings as the grind size reduces to maximise the retrieval of valuable minerals from the ore. Mining techniques, such as the open stope mining method have also required backfill technology to advance. Fills have to be engineered to ensure the stability of large vertical faces (exposures) when stopes adjacent to the backfill are being mined. Cement has been added in relatively small quantities (2%-10%) to backfill mixes to give it this freestanding ability. Paste fill is in essence the culmination of these two. It is comprised of full mill tailings, cement and water. Where full mill tailings refers to the tailings which are obtained from the processing of the ore, including the fines (-20 μm), where as in previous backfills the fines have been stored on the surface in large tailings dams.

To optimise the mining process the cost of the placed backfill must be minimised. The major cost component in paste fill is the binder cost, which is increased substantially in remote mines. The reduction of the cement content in paste is thus the critical factor in the reduction of the paste costs. Care must be taken to determine the minimum cement content required to ensure the static stability of the paste filled stopes when exposed through the mining sequence, without additional cement, which results in additional expense for no benefit.

In addition to the static stability of the paste fill stopes, the stability of the barricade walls, which are used as an underground retaining wall during filling, must be ensured to provide a safe working environment. Failure of these barricade walls results in significant economic loss and potentially the loss of life, such as the one that occurred at Bronzewing Mine, Western Australia in 2000. Very little is known about the lateral stress development of paste against barricade walls during filling. Subsequently, the design and construction of these barricades has remained largely based on operator experience, without the input of engineering design.

1.3 Problem Statement

The large underground voids created in the process of mining are generally backfilled by the waste materials left after processing. Backfills can take the form of rocks, sand, aggregate, hydraulic fill, paste etc. This dissertation deals with paste fill in particular, with special reference to Cannington Mine in North-West Queensland, Australia. Backfilling constitutes approximately 20% of the total mining cost, with the cost of cement being the single largest expense in the backfilling operation. Any reduction in the cement content will lead to substantial economies and will be well received by the mining industry. This can only be done in the context of a thorough understanding of the paste fill properties and the effects of reducing the cement content on those properties.

The stability of underground barricades is critical to the provision of a safe working environment within the mine. Therefore, reducing the cement content has also to be studied on the context of stress developments within the mine stope and especially on the barricades within the drives.

1.4 Objectives

The objectives of this research are as follows.

1. To determine the geotechnical properties of the paste fill used at Cannington mine, and to study the effects of various factors contributing to the strength and deformation characteristics of the paste fill.

2. To develop a numerical model to study the stress developments within the mine stope and adjoining drives, enabling a realistic assessment of the lateral thrusts on barricades and the stability of the stopes during the mining cycle.
3. To develop a procedure to determine the minimum cement content for each backfilled stope.

1.5 Relevance of the Research

Paste fill is a relatively new backfill in the Australian mines. Cannington was the first mine to be able to use paste as an economic alternative to the more common cemented hydraulic fill (CHF). Although the use of paste fill is now growing, there is still very limited literature available on the geotechnical characteristics of paste fills.

The higher the cement content, the higher the strength of the paste and the more stable the fill is during the sequential exposure of the vertical faces of the backfill as the stopes around it are progressively mined out also. As cement is the major cost component in paste, there have been a number of reductions made in the cement addition, from the original 8% to the current average 3.5% cement (by dry weight). The reductions in the cement content have often been based on analytical methods, trial and error and a healthy portion of empiricism. The question then remains “how low can the cement content go?” The potential cost saving associated with the reduction in cement content, without jeapordising the safety within the mine, can improve mining economies substantially. For example, if the cement content was able to be reduced from 3.5% to 3.0 %, the saving would be in the order of a *million* dollars!

The primary motivation for this research is to explore the possibility of reducing the cement content in the paste fill. This can only be done through a thourough analysis of the stress developments within the stopes and drives, and fully understading the geotechnical characteristics of the paste fill with the reduced cement content. The extensive laboratory test program coupled with in situ testing and the numerical modeling work addressed the above issues very well.

1.6 Thesis Overview

This chapter introduced the research problem, objectives and has identified the relevance of the research. Chapter 2 reviews previous research that has been conducted into paste fill. The review also covers the development of paste fill and the various factors involved with the static analysis of cemented backfills. Empirical, analytical, numerical modeling research and techniques have all been reviewed. Chapter 3 describes the geotechnical characterization of Cannington paste using a thorough laboratory testing program. The results of which have been compared to and validated against in-situ test results. A brief review of the liquefaction potential of placed paste fill is presented to asses the long term strength requirements of the fill barricades. Chapter 4 covers the geotechnical characterization of the rock types associated with the Cannington deposit. This dissertation is part of a larger project looking into the static and dynamic stability of paste filled stopes and will form the basis for additional ongoing research. The findings from the experimental investigations of the various rock types would be more useful in the determination of dynamic stability, with wave propagation characteristics through rock masses etc. A review of the theory and application of artificial neural networks is presented in Chapter 5.Chapter 6 reviews the development, verification and application of a three dimensional finite difference numerical model for the sequential extraction and filling of stopes in an idealised nine - stope grid arrangement. In addition to this, the development and application of an integrated approach to backfill design is presented and discussed also. Chapter 7 describes the development and application of a numerical model for underground fill barricades. The factors that contribute to the stress development are identified through a sensitivity analysis of input parameters. Chapter 8 provides a summary and conclusions of the research and some recommendations for future research.

Chapter 2

Literature Review

"…we are aware of the fact that a great deal of mining operations take place below the ground and that most of the best men in the industry are employed there. It is there that the coal is won and in that direction that the attention of those who are employed in the industry is naturally turned. Rubbish tips are a necessary and inevitable adjunct to a coal mine, even as a dust bin is to a house, but it is plain to see that miners devote no more attention to rubbish tips than householders do to dust bins…"

The "Report of the Tribunal appointed to inquire into the Disaster at Aberfan, (Wales) on October 21st, 1966" detailed the events leading up to and causes of the massive tailings slip from the Merthyr Vale Colliery onto the small mining village of Aberafan, killing 144 people, 116 of whom were schoolchildren. The Tribunal was scathing in its appraisal of the competency of those responsible for the stability of the colliery likening them to "moles being asked about the habits of birds". Since then the disposal of mine waste has had a great deal more attention paid to the design and placement of tailings, resulting in a highly engineered "designer waste" (Jones 2000).

2.1 General

In mining engineering backfill refers to any waste material that is placed into voids mined underground for the purposes of either disposal or to perform some engineering function. Waste materials are often placed with a very lean content of some form of pozzolanic binders to improve the soil strength properties. Backfills that are used only to fill the voids created by mining need only to have sufficient strength to prevent any form of remobilisation through liquefaction – typically caused by dynamic loading, however, where backfills are used as an engineering material, sufficient strength is required to ensure stability during exposure during ore pillar mining in tall vertical faces or undercuts. Generally the binders are added to produce backfills with an unconfined compressive strengths ranging between 0.5 to 4 MPa (Grice 1998 b).

Backfills can be divided into two categories, i) uncemented backfills (mainly **A**ggregate **F**ills (**AF**) and **S**and **F**ills (**SF**)) and ii) cemented backfills (which include:- **C**emented **R**ock **F**ill (**CRF**), **C**emented **A**ggregate **F**ill (**CAF**), **C**ement **H**ydraulic **F**ills (**CHF**) and Paste Fill (**PF**).

Uncemented backfills, as the name suggests, do not use any binding agents mixed in with the filling material. The behavior and performance of uncemented backfills can thus be studied using soil mechanics theory. Cemented backfills incorporate the use of a small amount of binder material, normally Portland cement, or a blend of Portland cement with another pozzolan such as fly-ash, gypsum or blast furnace slag to the parent backfill material to produce a binding agent for the fill. Cement Hydraulic Fill (CHF) is the most common type of cemented backfill. CHF is produced by the addition of cement to deslimed mill tailings. The process of desliming tailings is simply the removal of the very fine fraction of particles (i.e. any particle finer than 10 μm). CHF is the most similar form of backfill to paste fill with the most significant difference being the larger grain size distribution of CHF when compared to paste. Typically in CHF all tailings particles are less than 420 μm and have been deslimed (i.e. no particles less than 10 μm) (Bloss 1992), whereas paste utilizes the full compliment of tailings – without dewatering. The grain size distribution of paste fills is typically significantly finer than CHF and contains a minimum of 15% of particles smaller than 20 μm. This fine fraction provides a significantly increased surface area for water particles to attach to and is the basis for many of the rheological characteristics specific to paste. These are covered in more detail in Section 2.4.1.

Rock Fills (RF) are produced by crushing rock such that the particle sizes are between 25 – 300 mm. The material is then transported to the stope being filled and mixed with CHF at ratios of between 1:1 and 3:1, RF:CHF, by weight. This combined fill is termed Cemented Rock Fill (CRF). The properties of this fill vary significantly within the stope as the two fills segregate during placement. The ratio of RF:CHF at any location is the dominant factor of the fills behavior at that point (Bloss 1992). Materials finer than 25 mm that has been rejected from RF production is described as Aggregate Fill (AF). As with CRF, AF are mixed with CHF at a ratio of approximately 1:3 AF:CHF by weight. The resulting fill is termed Cemented Aggregate Fill (CAF). CAF typically suffer from segregation during placement, and thus properties at any location within a stope are dependent on the ratio of AF:CHF at that point as in the case of CRF (Bloss 1992).

Paste Fill is the newest form of mining backfill. It is produced from the full mill tailings and has a much finer grain size distribution than any other form of backfill. Typically it has a minimum of 15% of the material smaller than 20 μm. Typically the maximum size of particles in paste is between 350-400 μm. The origin and definition of paste is covered in greater detail in Section 2.4.

2.1.1 Mining Methods Used with Backfills

There are two distinct types of mining methods: stable stope and caving, with a complete spectrum of methods available between these two extremes. The three stable stope methods which use backfill are the open stoping, room and pillar, and cut and fill mining methods. Caving is an unstable form of mining where ore is allowed to collapse under it's own weight through prolific natural cracking and failures. In caving the ore will fail where undermined and will continue to fail while there is a void fill and sufficient cracking of the ore body. Hamrin (1982), Budavari (1983) and Brady and Brown (1985) have given a comprehensive description of each various mining methods. BHP Billton's Cannington Mine, one of the largest paste backfilling operations in Australia, and worldwide, uses the open stoping mining method in conjunction with post placed paste backfill

2.2 Purpose of Backfill

Backfill is used in a mine to: -

- Provide local and regional stability to the ore body,

  (Note: The increased stability in the mine is not due the direct transfer of rock stresses into the fill mass but rather the reduced level of relaxation of the rock mass. This ensures the integrity of the load carrying capacity of the rock).
- Reduced need for large tailings dams,
- Lessens the environmental impacts of the mining operations, and
- Provides higher rates of ore recovery.

Items above are not just ameliorative measures, but provide significant cost savings to the mine through the increase mining ability and longevity of the mine. Paste fill in particular has gained favor over alternative fill materials when considering the final three points. Indeed the governmental regulations on mines and their respective impact on the environment have become ever more vigilant over the last decade. Nantel (1998) refers to the trend in Canadian mines where future environmental permitting will require the maximum quantity of mine wastes to be returned to the underground workings. The obvious limit was reached when the Australian Federal Government recommended approving an option for the proposed Jabiluka Mine (JMA alternative) where *all* milling wastes were required to be placed underground.

Superficially, this may seem like a reasonable requirement based on a desire to preserve environmental integrity, however, such an approach may limit the financial viability of a significant number of mines. A recent study was conducted by Grice (1998 b), which compared the options of placing all paste fill underground compared to surface disposal. It was shown that a 46% increase in mined volume would need to be realized, to compensate of the expanded volume of the fill, to achieve this aim. Capital expenditure for such a venture would be very hard to justify.

2.3 Backfill Performance Requirements

Any backfill placed underground should satisfy three major criteria, namely static, dynamic and drainage requirements. Each of the requirements has been discussed separately in the following sections.

2.3.1 Static Requirements

Grice (2001) summarises the key requirements as: -

- Stand open in vertical faces when exposed by adjacent pillar mining
- Support the weight of loading equipment when used as a mucking (trafficked) floor
- Confine the rock mass surrounding the stope in order to maintain local and regional stability within mining areas
- Permit mining underneath fill by production blasting for undercut ore extraction
- Permit mining through in development sized headings for the purposes of access or ventilation
- A requirement to achieve a high early strength in order to minimize loading on stope barricade structures

2.3.2 Dynamic Requirements

The key requirement for stability during dynamic loadings are to: -

- Withstand the effects of close proximity blasting from production or development sized excavations.
- Withstand the effects of regional seismic events

(viz Grice 2001)

The dynamic loading requirements and performance of paste fill are currently under investigation at BHP Billiton’s Cannington Mine and James Cook University. It will thus not be considered in any further detail within this thesis. The design methods used to ensure static stability are covered further in Section 2.6.

2.3.3 Drainage Requirements:

- Permit drainage of excess water from backfilled stope to reduce liquefaction potential.

Excess water may come from either groundwater, service water or water used in the placement of fill. Generally the majority of the water to be drained through the fill mass comes from the water used to transport the fill to the site of deposition. (i.e. the water used to suspend the particles as a hydraulic fill). Once placed, the solid particles tend to consolidate, leaving the water on top of the solidified material to percolate through the fill mass. To reduce the obvious risk of liquefaction, the design permeability of fills is typically considered adequate when above k=100mm/hr. A general range for the design of permeability for hydraulically placed backfills is between 20 –100 mm/hr. Paste, by definition, retains the water that is used in the transport of the material. This eliminates any drainage requirements for paste.

Backfill barricades are also typically designed to allow for the drainage water from stopes. Barricades are designed to be typically ten times more permeable than the fill mass (Cowling 2002, personal communication) to avoid any restriction to the flow of water from the stope and consequential pore pressure buildup.

2.4 History of Paste Backfill

Paste fill falls into the broad category of thickened tailings, a concept which was introduced by Dr. Eli Robinsky in the mid 1970’s while describing surface disposal of concentrated tailings using pipeline reticulation (Robinsky 1975, 1976, 1978). However the first true “paste” backfill was produced at the Bad Grund Mine in Germany in 1979. The backfill was a 50:50 mix of medium to fine mill reject aggregate and medium to fine silt filtered tailings. The Helca Mining Company in their Lucky Friday Mine (U.S.A.), developed a similar system using filtered full plant tailings in the mid 1980’s (Brackebusch 1994). Initially both systems were only referred to as “high density backfills” until the introduction of the term “paste backfill” in the late 1980’s. Acceptance of paste backfill, as a viable alternative to hydraulic slurry and rock fill, did not truly occur until the mid 1990's with the construction and successful operation of several paste backfill systems in Canada and Cannington Mine in Australia in the late 1990's. The establishment of an "Underground Paste Backfill Research Centre" in Sudbury, Canada (Landriault 1995) resulted in a 32% saving by the conversion of cemented hydraulic fill to paste backfill for INCO's Coleman mine. The savings were primarily realised from the reduction in the binder content.

In April 2000 there were 22 paste backfill systems operating in mines throughout the world, of which, three were in Australia (Landriault 2000) Figure 2.1 shows the location of paste fill plants worldwide and Figure 2.2 the paste fill plants specifically in Australia). Australia's first paste backfill system was in Elura Mine in NSW in the mid 1980's, however it was not successful. The five paste fill systems shown in Figure 2.2 are the major established paste filling sytems in Australia. Additional paste fill plants were being constructed at Leinster and Plutonic Mines, but had not been commissioned at the time of writing.

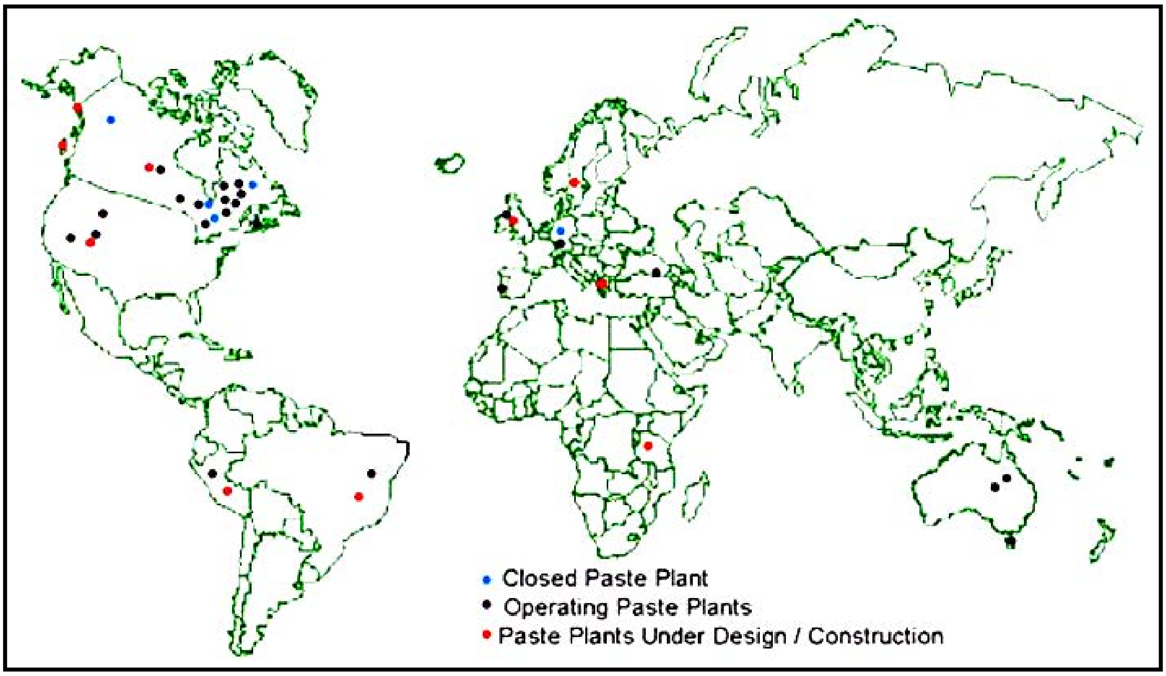

Figure 2. 1 Location of Worldwide Paste Fill Plants, (Landriault 2000)

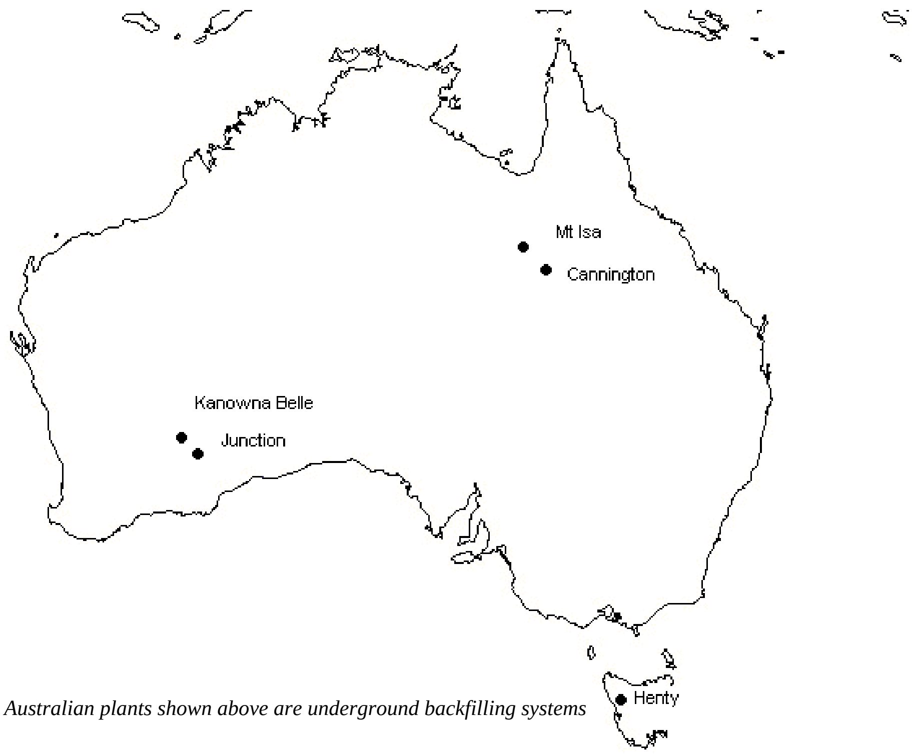

Note: The Australian plants shown above are underground backfilling systems

Figure 2. 2:- **Location of Australian Paste Fill Plants**

.

2.4.1 Definition of “Paste Fill”

The definition of “paste backfill” has been one of great debate since it’s inception in the late 1980’s. Primarily because a number of different industries have been involved in the evolution of paste and the definition which is adopted by each industry reflects their respective needs and experiences. Process equipment manufacturers define “paste” in terms of their dewatering equipment capabilities, just as pump manufacturers define it in terms of the design limitations of their pumps. The actual origin of the “paste” terminology is in the concrete industry where cement and water are added together to produce a cement paste that is similar in consistency and size distribution to the paste backfills made from full plant tailings. Currently most definitions of paste are in terms of its rheological and pumping characteristics. This has resulted from the need for the delivery of tailings underground, at high pulp densities, using existing pipeline reticulation technology and infrastructure. Most of the research was therefore concentrated in this area, which resulted in many of the definitions for paste fill used today.

In an attempt to unify the various definitions of "paste", Figure 2.3 was devised and formally recognised by a number of industry experts and academics (Jewell 2001). It should be noted that the boundaries between the mediums are not defined at specific levels or concentrations; rather they depend on a number of physical and material characteristics of the tailings materials. The shaded area represents the backfills that are commonly referred to as "thickened tailings". Thickened tailings are a special case of slurry tailings and tend to show many similar characteristics to paste. The similarity of thickened tailings and paste, while moving, is the basis for thickened tailings being commonly confused with or wrongly identified as paste. The primary difference between thickened tailings and paste is that thickened tailings will segregate or settle out once a minimum velocity is reached. A more detailed description of the characteristics which define the difference between slurry, thickened tailings and paste is give in Table 2.1. Figure 2.3 identifies the full tailings continuum and does not include binder.

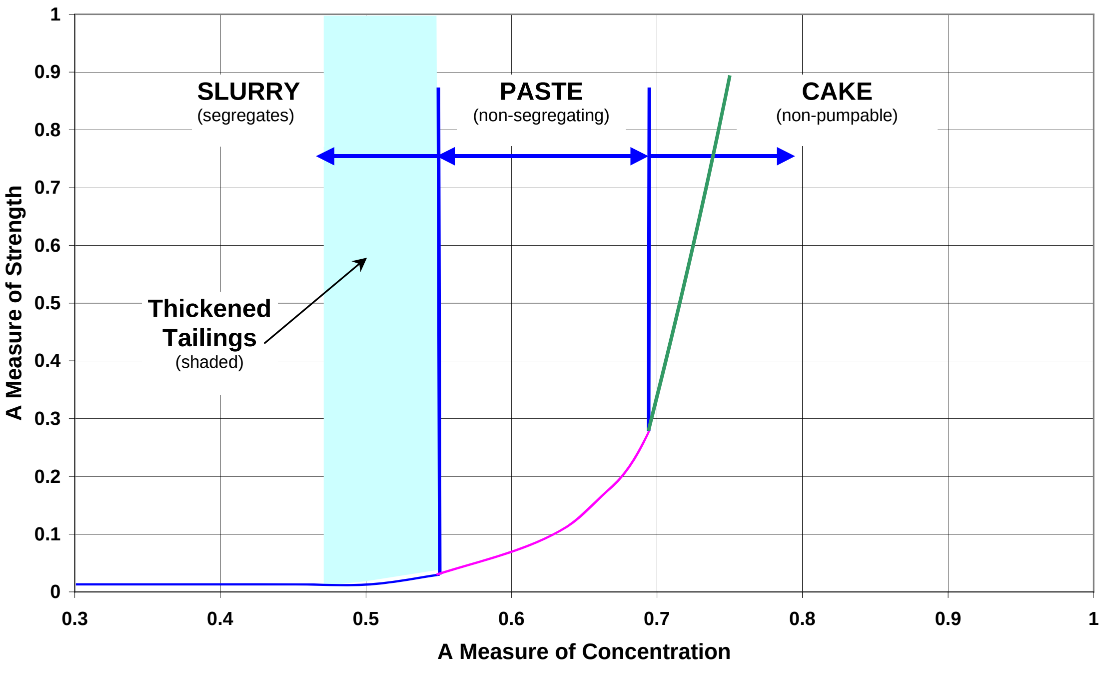

Figure 2. 3 Concept of Thickened Tailings Continuum (Jewell 2001)

Although the above graph implies that tailings may be prepared as any type of backfill, from slurry through to a cake, by simply reducing the water content, this is not the case. Not all tailings may be used to make paste fill. Landriault (1995) described paste as "a granular material, which is mixed with sufficient water to fill the interstices between the particles so that the material behaves as a fluid". This is not entirely correct. In order for a material to form, and be considered a paste, water must be retained between the particles and not be released back into the mix under static or dynamic loading conditions. In true "paste fills" this is achieved by the charges of the colloidal particles attracting, and holding, the water particles. The amount of colloidal charge of a material is strongly governed by particle size and shape. Finer particles have more surface area and thus colloidal charge to bond with water. It is this characteristic which makes the fines content such an important part of paste formation. It is also this characteristic of the finer particles to retain water that has lead to the general paste guideline of a minimum 15 % by weight of particles to be finer than 20 microns. Landriault later recognized this and re-defined paste as:-

> "a single phase water/soil mixture which, by virtue of a high proportion of fine material (minimum of 15% finer than 20 μm) within it's matrix, is able to remain non-segregating when bought to rest".

Characteristics specific to paste have been complied and are shown in Table 2.1 where the differences between slurry, thickened tailings and paste have been listed. When referring to Figure 2.3 "thickened tailings" is typically referring to the shaded portion of the graph.

Table 2. 1 Material properties for thickened tailings continuum (Jones 2000, Barret 2000)

Material Property	Slurry	Thickened Tailings	Paste
Particle Size	Coarse fraction only. No particles less than 20 μm. Segregation during transportation and or placement is dependent only on the coarse fraction	Some Fines included (typically <15%), Fines content tends to modify behaviour from slurry – i.e. rheological characteristics more similar to paste, however does segregate when bought to rest. Segregation during transportation and or placement is dependent only on the coarse fraction	Additional / most fines (typically 15%(min)>20 μm
Pulp Density	60%-72%	70%-78%	78%-82%
Flow Regimes/ Line Velocities	Critical Flow Velocity. To maintain flow must have Turbulent Flow (vel>2m/s). If vel<2m/s settling occurs Newtonian Flow	Critical Flow Velocity. To maintain flow must have Turbulent Flow (vel>2m/s). If vel<2m/s partial settling occurs Newtonian Flow	No critical pipeline flow velocity. i.e. no settling in pipe Laminar/ plug flow
Yield Stress	No minimum yield stress	No minimum yield stress	Minimum yield Stress
Preparation	Cyclone	Cyclone end elutriation	Filter/ centrifuge
Segregation in stope	Yes / High	Slight/ Partial	None
Drainage from Stope	Yes	Partial/ Limited	None/ Insignificant
Final Density	Low	Medium/ High	High
Supernatant water	High	Some	None
Post placement Shrinkage	High	Insignificant	Insignificant
Rehabilitation	Delayed	Immediate	Immediate
Permeability	Medium/ Low	Low	Very Low
Application	Above ground	Above ground	Above ground and underground
Water consumption	High	Medium	Low
Reagent Recovery	Low	Medium	High

2.5 Laboratory Testing

The focus of the literature review will be laboratory testing of paste fills for: -

- Permeability
- Compressibility and Consolidation
- Strength
    - Total Stress Analysis
    - Effective Stress Analysis
- Liquefaction potential

The permeability of the fills govern the drainage requirements and the strength compressibility and liquefaction potential govern the static and dynamic stability of the system.

Information regarding the laboratory testing of paste fills is limited. Where it is available it is typically site specific or is retained "in-house" by the mining companies for personal reference. References to other forms of backfill, cemented soils etc. will be made in an attempt to relate to paste fill behavior where actual testing has not been carried out.

2.5.1 Permeability Testing

Permeability is the measure of the ability of a fluid to percolate through a porous media. Traditionally it has been a primary consideration in the design of backfills. It describes the drainage of backfills under various loading conditions. The permeability of a fill mass becomes important when one considers the potential of liquefaction. Liquefaction describes the transition of saturated soil from a solid to liquid state, by means of increased pore pressure. Pore pressures are increased by additional loading being applied to the soil mass. Typically when considering the liquefaction potential of backfills, only cyclic loading (i.e seismic or blasting activity) was considered because the permeability of fills were high, in the order of 100 mm/hr. Liquefaction through monotonic loading, such as in the case of wall closures was never considered. By definition, paste fill retains the water used for transport and placement, resulting in high levels of saturation for extended periods of time. The liquefaction potential of paste fills through undrained monotonic loading is therefore considered a genuine concern.

Permeability of a porous media is described by Darcy's Law:-

$$k = \frac{qL}{\Delta h A} \qquad \text{…(2.1)}$$

Where

k = permeability of porous medium, m/s

q = rate of flow through porous medium, m^3/sec

L = length of porous medium, m

Δh = static pressure differential across the porous medium, m

A = cross sectional area of porous medium, normal to the direction of flow, m^2

The coefficient of permeability, k, (hereafter referred to as permeability) is affected by the effective grain size (or more accurately the effective pore size and shape), void ratio, effective flow paths through the soil pores (tortuosity), plasticity, degree of saturation and fluid properties. Hansbo (1960) and Holtz and Broms (1972) found that there was a deviation from Darcy's Law for low permeability clays at a very low hydraulic gradient. This is in contrast to Mitchell's (1976) observations, who after reviewing a number of investigations regarding the applicability of Darcy's Law and stated that "with all else held equal, Darcy's Law is valid, even for fine grained soils at low hydraulic gradients". Mitchell (1976) cited the difficulties associated with obtaining accurate results with material of materials of very low permeability, using laboratory test methods as the main source of deviation.

An attempt to relate the permeability of a porous media to its physical properties was made by Hazen (1911) and Taylor (1948). Both related the flow of water to the effective flow paths of the water through the soil. Hazen (1911) related the effective flow paths to the effective grain size and, Taylor (1948) to the void ratio. Equations 2.2 and 2.3 show the form of the equations derived by Hazen (1911) and Taylor (1948) respectively.

$$k = CD_{10}^2 \qquad \ldots(2.2)$$

Where

k = permeability, cm/s

D_{10} = grain size in millimetres for which 10% of the particles pass by weight

C = constant, varies between 0.4 – 1.2, (Av = 1.0)

$$k_1 : k_2 = \frac{C_1 e_1^3}{1+e_1} : \frac{C_2 e_2^3}{1+e_2} \qquad \ldots(2.3)$$

In the case of clean sands C_1 and C_2 are roughly equivalent, thus simplifying equation 2.3 to: -

$$k\alpha \frac{e^3}{1+e^3} \qquad \ldots(2.3\ b)$$

These equations have been used to predict the permeability of sand fills and some coarse hydraulic fills (Vick 1983, Mittal and Morgenstern 1975). This is considered appropriate and reasonable when considering the equations were developed for clean sands with a grain size distribution of between 0.1mm and 3mm, with less than 5% passing the 75 μm sieve. The use of the equations with paste fill is questionable as neither of the proposed relationships works well with silts or clays. Permeability for paste is therefore best predicted using Darcy's Law in conjunction with some very finely controlled laboratory or field measurements.

Table 2.2 shows the range of permeability values for uncemented tailings proposed by Vick (1983). More recent research (Clark 1986, Noranda Technology Center 1991, Rankine 2003) undertaken on the permeability of backfill tailings, shown in Table 2.3, also agrees with the guidelines proposed by Vick (1983). The value of permeability of the tailings used to make paste will be similar to that of non-plastic or low plasticity slimes.

Table 2. 2 Typical tailings permeability ranges (Vick 1983)

Type of Tailings	**Average Permeability (cm/s)**
Clean coarse or cycloned sands with less than 15% fines	$10^{-2} – 10^{-3}$
Peripheral discharged beach sands with up to 30% fines	$10^{-3} – 5 \times 10^{-4}$
Non-plastic or low plasticity slimes	$10^{-5} – 5 \times 10^{-7}$
High Plasticity Slimes	$10^{-4} – 10^{-8}$

Table 2. 3 Laboratory results of permeability testing of various mine tailings

Tailings	**k (cm/s)**	**Reference**
Hydraulic uncemented cycloned tailings de-watered	5.0 x 10^{-5}	Clark (1986)
Unclassified tailings uncompacted (Golden Giant Mine - Canada)	4.2 x 10^{-5}	Noranda Technology Centre (1991)
Total Tailings (Niobec Mine – Quebec)	3.0 x 10^{-6}	Anon (1994)
Total Tailings (Mobrun Mine – Quebec)	8.5 x 10^{-5}	Anon (1994)
Classified Tailings (Australian Mine A)	2.3 x10^{-5}	Rankine K (2003 -unpublished)
Total Tailings (Australian Mine B)	1.4 x 10^{-6}	Rankine K (2003 -unpublished)
Classified Tailings (Australian Mine C)	8.5 x 10^{-5}	Rankine K (2003 -unpublished)
Classified Tailings (Australian Mine D)	5.7 x 10^{-5}	Rankine K (2003 -unpublished)

* Australian Mine testing results provided on the provision of anonymity

The effect of cementation is reduced porosity. The cement bonds filling the voids and thus blocking drainage paths. The reduced permeability of a fill mass was quantified for hydraulic fills by Thomas et al. (1979). The permeability of cemented fill is shown to decrease rapidly with an increase in the level of cementation (Figure 2.4). It should be noted that finer materials experience a greater percentage decrease in the permeability with the increase in cement addition (Mitchell and Smith 1979).

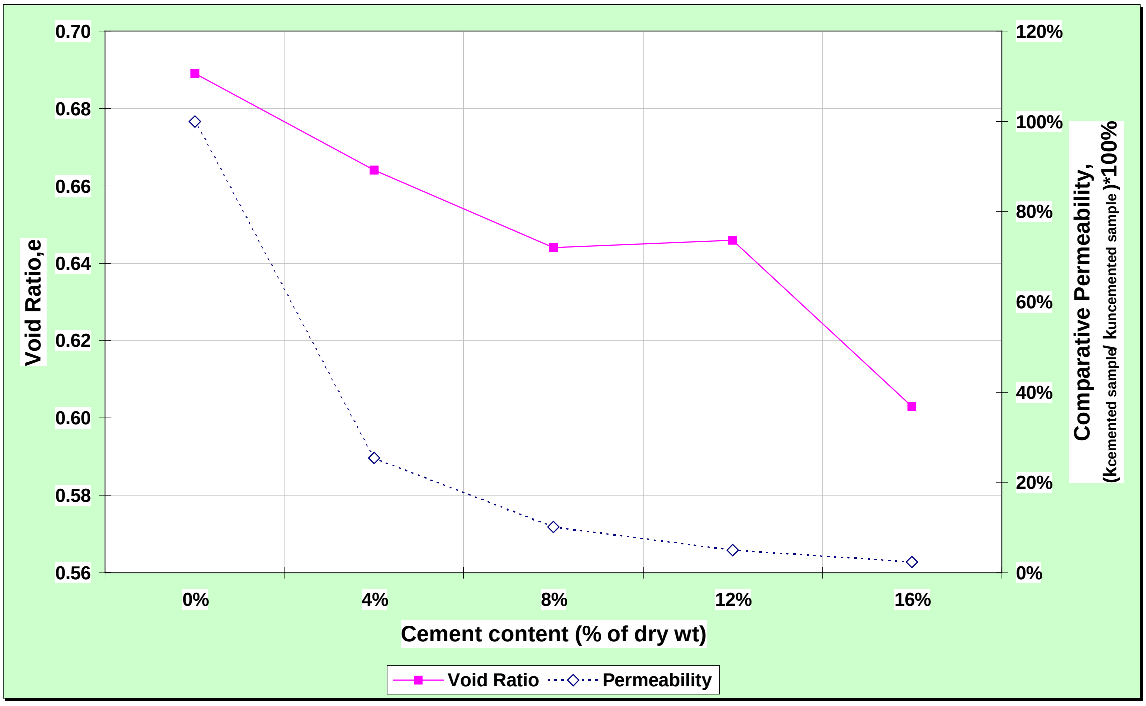

Figure 2. 4 Effect of cementation on fill permeability (Thomas et al. 1979)

Pierce (1997) investigated the permeability of paste fill for the Golden Giant Mine as a function of binder content applied stress and curing time. The binder contents were:- 3 wt%, 5 wt% and 7 wt% curing time:- 28, 56 and 112 days and applied stress between 110 to 880 kPa in 110 kPa increments. The solids content was held constant at 75% solids. Figure 2.5 shows the results for the calculated permeability results of Golden Giant mine’s paste fill for 28, 56 and 112 days respectively.

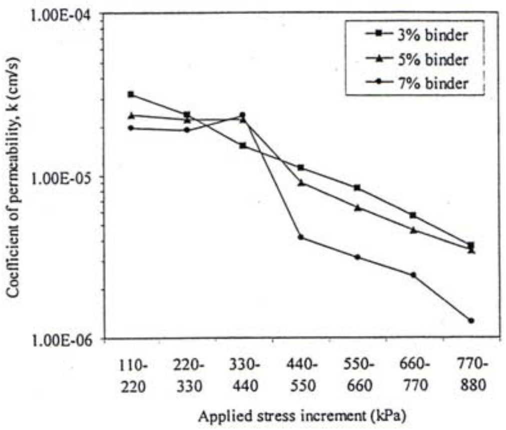

(a)

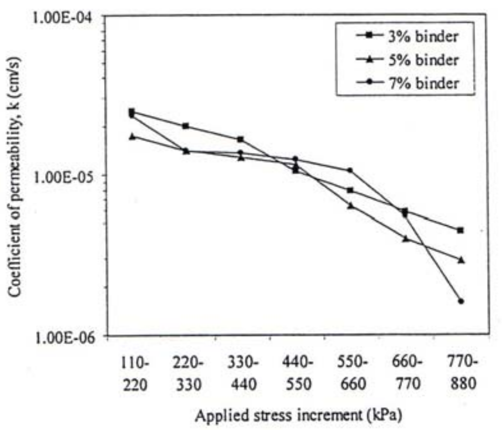

(b)

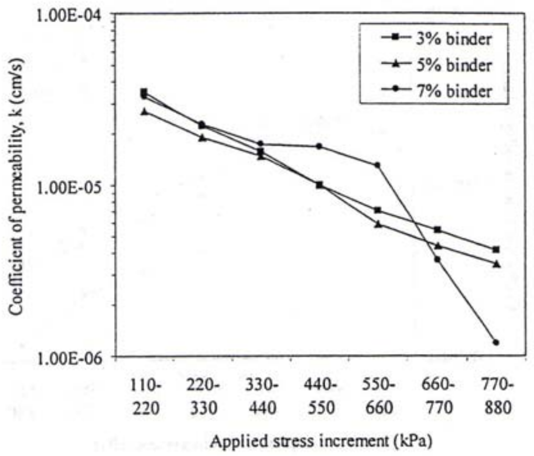

(c)

Figure 2. 5 Calculated permeability results of Golden Giant mine’s paste fill for (a) 28 (b) 56 and (c) 112 days respectively (Pierce 1997)

The permeability of the paste decreased with the increase in vertical stress and binder content until 28 days of curing had occurred. The permeability values were typically in the range of 5.0 x 10^{-5} to 1.0 x 10^{-6} cm/s. These values seem slightly higher than would be typically expected when compared to the values of tailings given in Table

2.3. These permeability values correlate well with the Hazen's approximation for permeability even though it was developed for clean sands and has been identified as having poor predictive abilities for permeability of silts and clays (Holtz and Kovacs 1981) and does not account for the reduction in permeability due to cementation. Pierce (1997) did not directly measure the permeability directly, but instead indirectly calculated the values using the coefficient of consolidation and coefficient of volume compressibility using equation 2.4.

$$k = c_v \gamma_w m_v \qquad \ldots(2.4)$$

where

k = coefficient of permeability m/s

γ_w = unit weight of water kN/m^3

c_v = coefficient of consolidation m^2/s and

m_v = 1/ constrained modulus = coefficient of volume compressibility 1/kPa

The slightly higher values of k are considered to be related to the indirect calculation of the permeability and the testing difficulties associated with testing of low permeability substances, as noted by Mitchell (1976).

2.5.2 Compressibility and Consolidation Testing

The compressibility can be used as an indirect measure of the resistance to compression (through closure or subsistence) of a soil. In soil mechanics terms consolidation describes the densification of a soil matrix under an applied load through the dissipation of excess pore pressure i.e. A saturated soil must undergo "consolidation" to be "compressed". Both the consolidation and compression characteristics of a specimen are generally found using one – dimensional compression (odeometer) test. The coefficient of volume compressibility (m_v) is found by determining the constrained modulus (D) from the effective stress versus axial strain plot obtained then finding the reciprocal (m_v = 1/D). The constrained modulus may be calculated using Young's Modulus and Poisson's ratio using equation 2.5.

$$D = \frac{E(1-\nu)}{(1+\nu)(1-2\nu)} \qquad \ldots(2.5)$$

The coefficient of volume compressibility is defined as the volumetric strain per unit increase in effective stress,

$$m_v = \frac{\left(\dfrac{\Delta V}{V}\right)}{\Delta\sigma} \qquad \ldots(2.6)$$

In an odeometer the volumetric strain will be equivalent to the axial strain in because there is no lateral strain in the sample during testing.

Figure 2.6 shows the response of classified tailings, both cemented and uncemented, in confined compression. Mitchell and Smith (1979) showed the response of cemented tailings to be linear followed by a non-linear response after the cement bonds had yielded at approximately 1.5 MPa. The uncemented tailings show a highly non-linear response throughout, similar to that of granular soils. Tests by Stewart et al. (1986) on classified tailings, also confirmed that cementation governs backfill response until the cement bonds break, after which, backfill response was frictional. The strength at which the cement bonds yielded depends on the level of cementation and the frictional response on the frictional properties of the parent material. Under higher confining stresses the behaviour of the cemented and uncemented samples converge, again supporting the trend of parent materials governing behaviour.

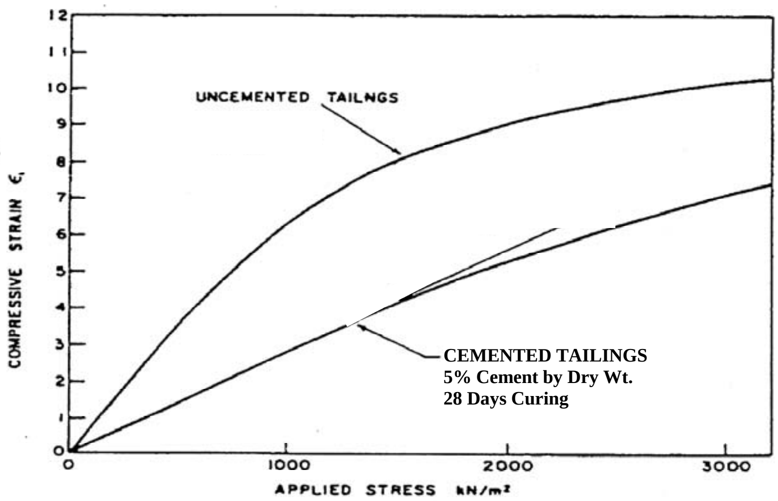

Figure 2. 6 Compressibility curves in the low stress region for cemented and uncemented tailings prepared at the same porosity (Mitchell and Smith 1979)

Pierce (1997) undertook a series of one-dimensional compression tests on Golden Giant Mine paste fill to determine the response of the constrained modulus to confined compression. Test results for paste fill after 28 days of curing are shown in are shown in Figure 2.7.

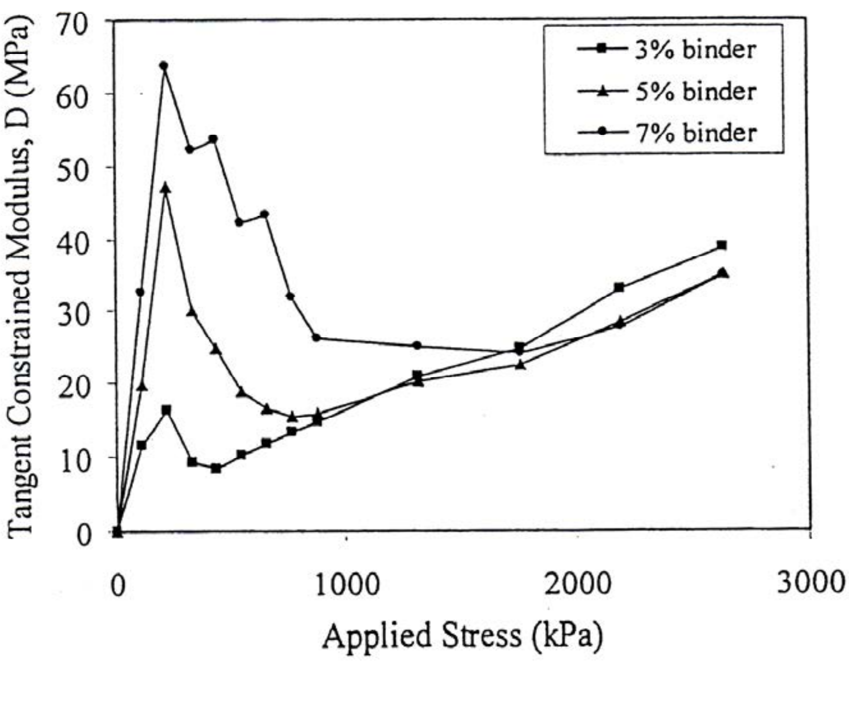

Figure 2. 7 Tangent constrained modulus behaviour of 28 day Golden Giant Paste fill in confined compression (Pierce 1997)

The constrained modulus increased rapidly to a peak value at low stress with higher peak values resulting from higher strength fills. After the initial peak (cement bond failure) the soil particles re-arrange themselves to a more tightly packed structure. During this rearrangement of particles the constrained modulus (D) drops to a minimum value. Once the densest state is achieved D then again starts to increase. This behavior is observed in cemented backfills regardless of binder content when at higher strain levels (i.e. after the cement bonds have broken). D was also found to increase with the applied level of stress. This is similar the to the behavior of cemented sands observed by Mitchell and Smith (1979) at low stress levels. Pierce (1997) also found that the cement bond strength in confined compression is equal to 1.6*UCS. The aforementioned behavioral characteristics were observed for paste fills after 56 and 112 days curing also.

Consolidation testing of fills in general and paste fills in particular is limited. This is probably due to the popular perception that "backfills" consolidate almost instantaneously upon placement Thomas et al. (1979). This perception was founded when considering hydraulic and other more coarsely graded fills and indeed backfills did tend to consolidate very rapidly. The high permeability of earlier backfill types is testament to this. Paste fill has a low permeability and challenges this perception.

The coefficient of consolidation, (c_v) may be found by rearranging equation 2.4 to:-

$$c_v = \frac{k}{\gamma_w m_v}$$

Work by the U.S. Navy (1971) relates c_v to the liquid limit of the fine soils using Figure 2.8. The value of c_v for in-situ samples is bounded by the samples which have been completely remoulded (lowest c_v) and samples which are in the recompression range on a fine grained soil (highest c_v)

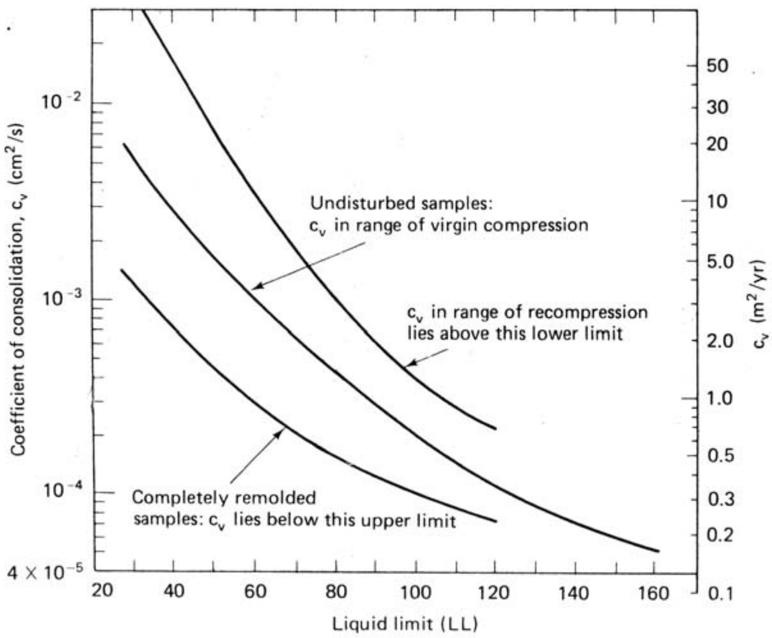

Figure 2. 8 Correlations between c_v and LL (US Navy 1982)

For backfills, which are not specifically limited to fine grained soils, and contain a binder fraction, Vick (1983) suggests that c_v for classified sands is between 0.5 to 100 cm^2 /s. Pierce (1997) found c_v for the Golden Giant Mine paste fill ranged from 0.2 to 9 cm^2/s for vertical stresses between 880 to 0 kPa (refer Table 2.4). The c_v increased significantly with binder content. This resulted from:-

- Increased rigidity and decreased compressibility of the fill
- Maintenance of the structural integrity of the soil associated with lower vertical stresses (by virtue of the curing of cement)
- As water is used in the hydration of water – additional void space occurs commensurate with the usage in hydration of cement and the subsequent drying of the cemented backfill induces a negative pore pressure

The effect of a higher c_v is faster dissipation of pore water pressure and resulting consolidation. Table 2.4 summarises the results of testing for c_v by Pierce (1997)

Table 2. 4 Summary of c_v values for Golden Giant Mine (Pierce 1997)

	Coefficient of consolidation cv (cm^2/s)			
	Curing	**28 Days**	**56 Days**	**112 Days**
Binder content (%wt) 50:50 NPC:FA	3% Cement	1.6	2.7	2.1
	5% Cement	2.0	2.9	3.3
	7% Cement	2.9	4.8	4.8

NPC = Normal Portland Cement, FA= Fly Ash

Further analysis of Pierce's (1997) results reveals a relationship between permeability and vertical stress in the form: -

$$k = -3E^{-8}\sigma_v + 3E^{-5} \qquad \ldots(2.5)$$

where

σ_v = average vertical stress (kPa)

k = permeability (cm/s)

Pierce's (1997) values were used to investigate the effect of consolidation on the backfill in a stope of the dimensions 25m x 25m x 50m. An average of $c_v = 3.0$ cm^2/s was used and the stope was considered to be double draining. Upper and lower bounds of c_v were investigated using $c_v = 0.2$ and 10 cm^2/s respectively. These values correlate to the values obtained by Pierce (1997) during testing. Figure 2.9 shows the calculated values of the time of consolidation for various levels of consolidation

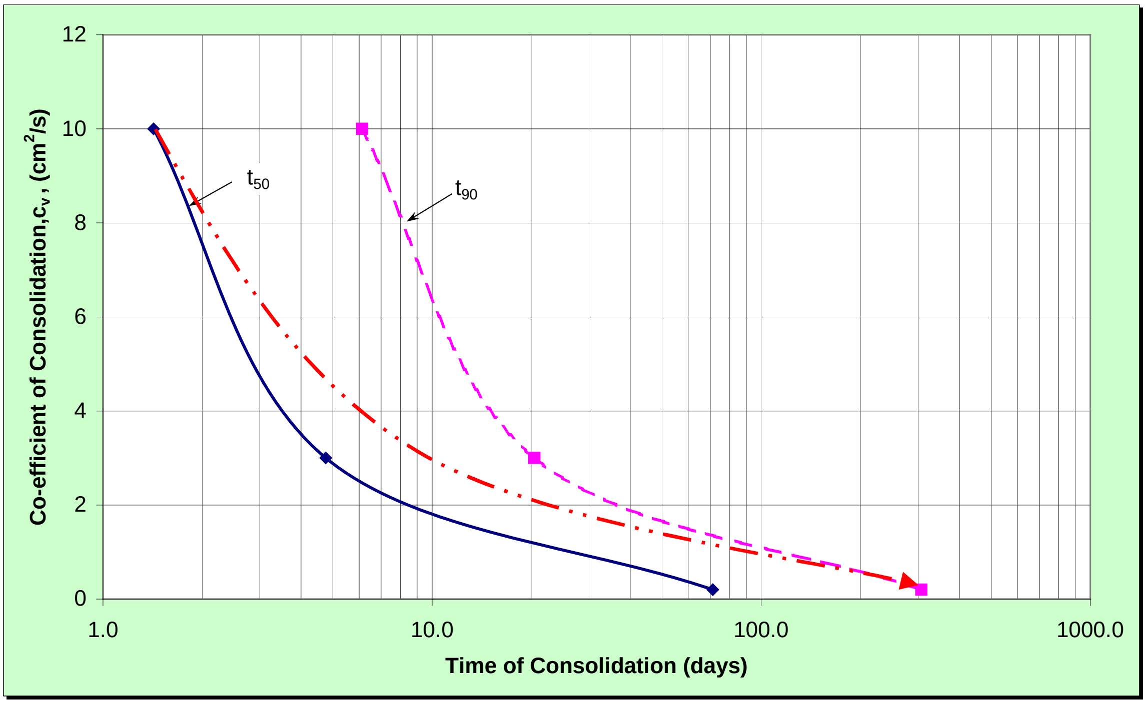

Figure 2. 9 Co-efficient of consolidation vs. time of consolidation for t_{50} and t_{90} (Pierce 1997)

The issue of consolidation in backfills is a complex area of study. As the stope is filled the verticals stress increases, which in turn increases consolidation, decreases permeability and the co-efficient of consolidation and results in the rate of consolidation dropping as filling continues. If one were to consider an element in a backfilled stope the path followed would be closest to that of the red dashed line. With the filling continuing, the vertical stress would increase and decrease k and c_v, thereby slowing the rate of consolidation. The concept of a critical state soils mechanics approach to the consolidation of a fluid backfill mass is intriguing, but unfortunately falls outside of the scope of this thesis. A complex coupled mechanical / fluid flow model for back fills is being investigation by K. Rankine at James Cook University using FLAC^{3D} and is keenly awaited.

2.5.3 Strength Testing

Soil strength can be found using either total or effective stress analysis techniques. In a "total" stress analysis the stresses on soil and water are not separated. The "effective" stress analysis technique separates the component stresses into pore water pressure and effective soil stresses. It measures and describes how loads are passed through the soil and what proportions are taken by the soil matrix and water respectively. Loading conditions are then applied to determine the soil and behaviours observed, analysed and the material properties determined. Soil behaviour for any loading conditions may then be described.

Typically mines have relied on the use of total stress analysis. This is probably a result of a number of factors including: - a simpler evaluation technique, the expense and difficulties involved with the determination of effective stress parameters and previous laxity of financial constraints regarding backfilling practices. With an increased commercial pressure to make the mining process more efficient, there is a requirement to understand the material and processes more. Both analysis techniques have been described in this thesis to ensure a thorough review of available literature.

2.5.3.1 Total Stress Analysis

Under the total stress regime, loading occurs rapidly, thereby reducing drainage from the sample, generating excess pore pressure. Laboratory tests such as the unconfined compressive strength (UCS), unconsolidated - undrained triaxial (UU) and undrained direct shear tests all return the undrained shear strength at failure (τ_f). It should be noted that the shear strength at failure, is equivalent whether an effective or total stress analysis is considered.

Unconfined Compression Strength Tests

The UCS test is the most common tool for comparison of the relative strengths of cemented backfills. The UCS of samples are strongly dependent on a number of material physical and environmental factors. Bloss (1992) gives a good review of these factors and provides a rationale for the standardisation of UCS test results.

Through a number of research programs Lamos and Clark (1989), Mitchell and Wong (1982) and Berry (1981) have tried to develop relationships between strength and material properties. Most are site specific and are considered to lose relevance applicability on other materials. Examples of such relationships include: -

Lamos and Clark (1989) developed a relationship for the prediction of strength based on the material properties of the deep South African Gold mines. The relationship is: -

$$UCS\alpha \exp\left\langle P_1 + \left[P_2\left(\frac{OPC}{W} + P_3 * \frac{PFA}{W} + P_4 * \frac{PBFC}{W} \right)\right] * \left[1 + P_5 * \frac{CT}{NCS} + P_6 * \frac{CW}{NCS} \right] + P_7 * \frac{NCS}{W} \right\rangle \quad \ldots(2.7)$$

where

UCS = Uniaxial Compressive Strength	(MPa)
OPC = Ordinary Portland Cement	(g)
PFA = Pulverised Fuel Ash	(g)
PBFC = Portland Blast Furnace Slag	(g)
W = water	(g)
CT = classified tailings	(g)
CW = comminuted waste	(g)
NCS = non-cement solids	(g)

P_1-P_7 = Experimentally derived constants

It is difficult to ascertain from this relationship the physical relevance of the exponential function or any of the various terms are. The complex relation suggests little about the most important parameter affecting the UCS and is therefore of limited relevance. Mitchell and Wong (1982) made a definite attempt to show the affect on strength by each of the material properties. The relationship was derived using a single particle grading (sand tailings) thus restricting its general proven applicability.

$$(\sigma_1)_F = K_1 c_c^b \left(n^{-6} w^{-n} + K_2\right) \qquad \ldots(2.8)$$

where

n = porosity

w = water content (%)

c_c = cement content (%)

b, K_1 and K_2 = constants determined experimentally

Berry (1981) related the cement content and porosity to the unconfined compression strength as: -

$$UCS = 9.4\left(\frac{n}{24}\right)^{-1.48} * \left(\frac{c}{11}\right)^{1.61} \qquad \ldots(2.9)$$

where

c = cement content (%)

p = porosity

The correlation coefficient for the analysis was 0.95 over a range of UCS values from 5 MPa to 20 MPa for backfills from Gavorrano Mine (Italy). The relationship is significant, however it can only be confidently used for a particular grading (CHF) for a single mine. The typical UCS of paste fills are significantly less than this and generally lie in the range 0.5 MPa to 1 MPa. The applicability of Berry's formula must still be investigated.

To generalise the approach to strength prediction, Swan (1985) developed the "binder number" concept. The theory was based on the concept of the "mean free inter particle distance" proposed by Fagerlund (1977). Swan (1985) proposed that the size distribution of any fill material could be described by a dimensionless factor (i.e. “binder number”) of the form:

$$UCS\alpha(BN)^k \qquad \ldots(2.10)$$

Where

$$Binder\ Number(BN) = \frac{c}{(d\alpha_p)^n}$$

c = cement content (%)

d = mean free inter-particle distance of the aggregate particles (mm)

α_p = specific surface area of the aggregate particles (mm^2/mm^3)

n = constant (1.0<n<1.7, typically 1.3<n<1.5, viz Bloss 1992)

k = power factor (typically in the range of 2-3, values of 2.36 quoted by Swan,1985 and 2.12 by Bloss 1992 for MIM back fills)

Swan (1985) analysed backfills from more than 30 mines with a very wide variety of backfills, from very lightly cemented tailings to concrete and developed a relationship between the unconfined compressive strength and binder number shown in Figure 2.10 and described by equation 2.11.

$$UCS = 0.283 * BN^{2.36} \qquad \ldots(2.11)$$

Saliba (1996) applied the binder number concept to a number of cemented hydraulic fills and paste fills with the fill strengths being predicted moderately well by equation 2.11. Saliba’s (1996) UCS values were typically lower than predicted by the binder number. Saliba (1996) cured samples for 11 days at 40^{o}C, while Swan (1985) used samples that had been cured for a period of 28 days at 20^{o}C for all samples tested. The lower obtained strengths are likely to be attributable to this incongruity.

It should be noted that the binder number does not include the effects of moisture content or scale effects. Also the apparent correlation of the binder number to the UCS strength is assisted by the use of logarithmic scales on both axes. The full derivation of the binder number may be obtained from either Bloss (1992) or Fagerlund (1977).

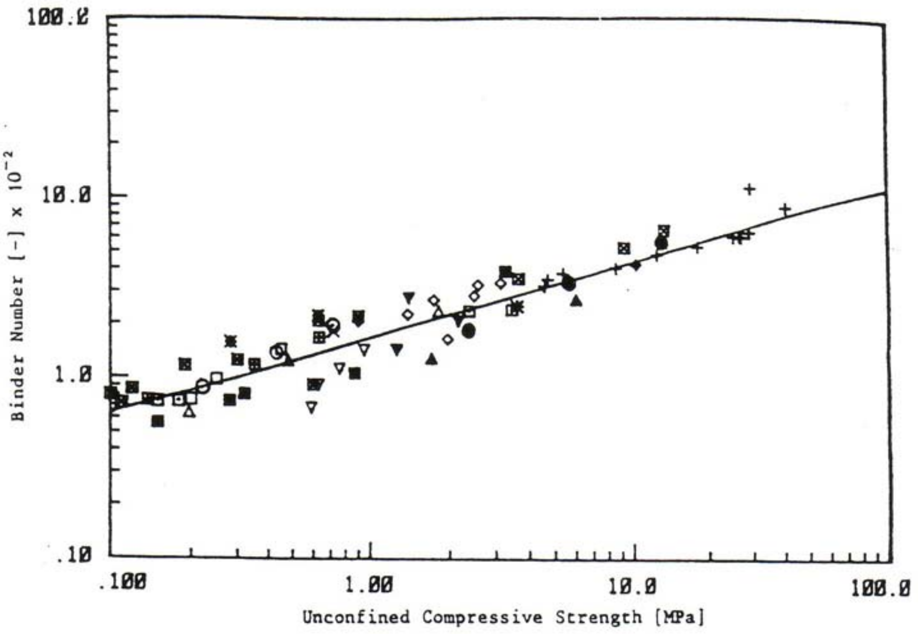

Figure 2. 10 Relationship between binder number and Compressive Strength for numerous backfills from around the world (Swan 1985)

Most of the research on paste fills to date has focussed on the UCS as a function of solids content, grain size distribution, binder content and curing time. Landriault (1995) studied the effect of particle sizing and grading on the solids density and UCS of paste fill. The results are compared to a cemented hydraulic fill and shown in Figure 2.11.

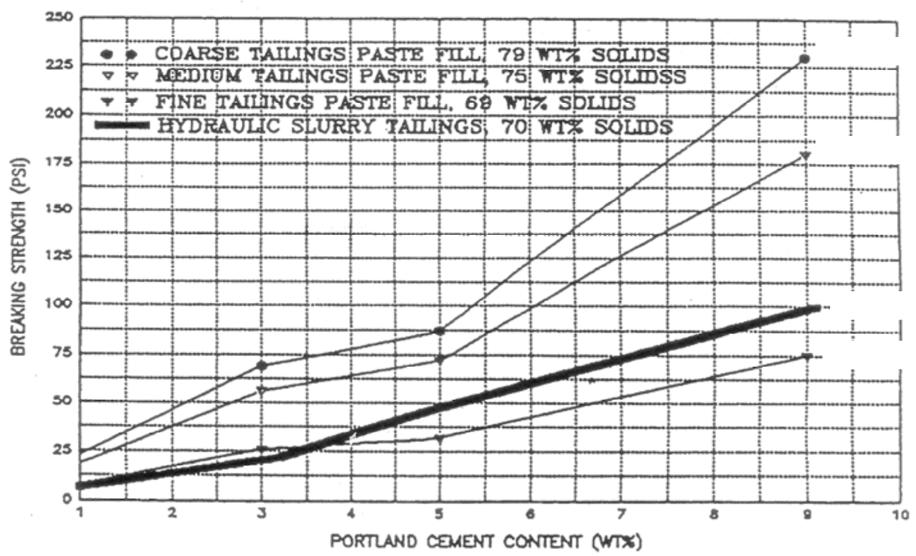

Figure 2. 11 28-day UCS of paste fills prepared from tailings of varying paste blends, compared to conventional hydraulic slurry fill (Landriault 1995). 1psi =6.895 kPa

Landriault (1995) used the various blends of paste fills from Macassa mine and the cemented hydraulic fill from Inco Mine to give a comparison of the strengths of various types and blends of fills. Macassa's "coarse" paste fill is a blend of full mill tailings and alluvial sand in the ratio of 25:75. The medium and fine paste fills represent mix proportions of 50:50 and 100:0 respectively. Inco's hydraulic fill is made from 100% classified tailings. Each of the backfill types were mixed with enough solids content to give a slump of 7 inches (~175 mm). An increase in solids content is associated with the increase in the coarseness of the blend.

Figure 2.11 shows the Macassa full plant tailings paste fill, produces strengths that are equivalent or less than those of Inco hydraulic slurry tailings fill. This would be expected given the closeness of the relative solids contents. The 50:50 and 2:75 blended paste fills are shown to be two to four times stronger than the full plant tailings paste fill at all binder concentrations. This is primarily due to the lower water to binder ratios of the blended paste mixes. The improved gradation of the blended paste also contributes to the increase in strength generation for the same binder concentration.

Aref and Hassani (1988) testwork showed an increase in strength was proportional to the increase in moisture content, which is shown in Figure 2.12. They stated that the higher UCS values were obtained by the provision of additional water for use in the hydration of cement. This contradicts the well-established fact that there is ample water in both paste and hydraulic fills to allow for the full hydration of cement. A lower water cement ratio tends to give higher cement bond strengths (Thomas et al. 1979).

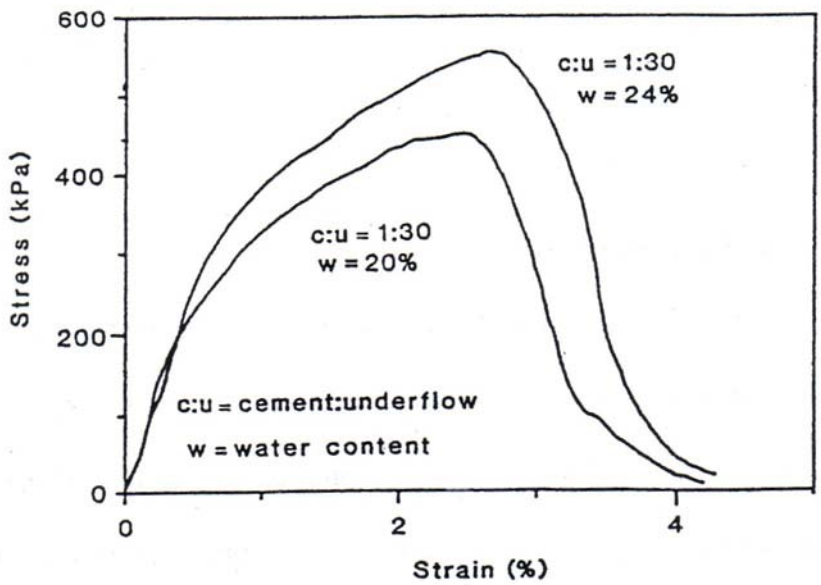

**Underflow = coarser fraction of the tailings with any of the finer (<10 m) material being removed during cyclone sizing*

Figure 2. 12 UCS of Placer Dome Mine paste backfill at two different moisture contents. (Aref and Hassani 1988)

The cement to underflow ratio (c:u) was kept constant at 1:30, indicating a cement content of 3.33%. The solids content was 80% for the sample with a water cotent of 20%, and 76% for the sample with 24% moisture. Considering the time of the testing, the use of underflow material only and the only very recent definition of "paste fills" it is likely that the material tested by the aforementioned authors was more likely to be a thickened hydraulic slurry fill, rather than a true paste. The increase in strength with an increase in water content is not considered to be attributable to the increase in water available to the hydration process, but to the additional percolation of the fine cement particles through the sample. With the removal of the fines, the cement used in the sample preparation would be the finest fraction of the soil and would likely be the last to settle when deposited using a hydraulic fill. The additional water in the fill mixes would make give a greater opportunity for the fine cement particles to be transported through the fill, with the water.

Unconsolidated Undrained Triaxial Tests

Oullete et al. (1998) carried out a series of unconfined compression tests and unconsolidated undrained triaxial tests, to derive unique failure criterion for paste fill, shown in Figure 2.13. As expected the shear strength of the paste increased with cement content and curing time. Oullete et al. (1998) suggests that there should be two failure envelopes, one prior to cement bond yielding and one post bond yield. This is very similar to concept applied to determine the peak and residual friction angles from direct shear testing. The failure surfaces tend to indicate that at the higher confining pressure the bonds are crushed and the difference in behaviour is again dictated by the parent material properties. The results of Thomas (1969), Mitchell and Smith, (1979), Stewart et al., (1986) and this current research work support this also.

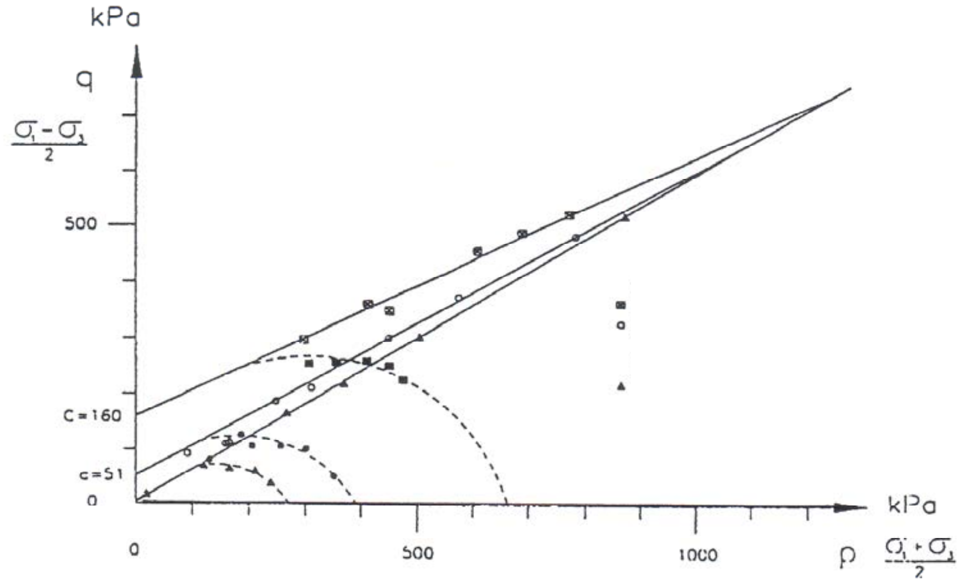

Where

p = mean stress

q = deviator stress

Figure 2. 13 A proposed failure envelope for paste back fill (Ouellet 1998)

Winch (1999) completed a series of unconsolidated undrained (UU) tests on BHP Billiton Cannington’s paste fill. The samples used had cement contents varying from 3% to 5% and solid content between 74% and 78%. Curing times of 7, 14 and 28 days were used to determine the progressive strength gain. The reported results showed the friction angle for the samples lied between 1.6° and 8.4° indicating the fill underwent limited consolidation and had a very high level of saturation. The cohesion and friction angle had linear relationships with the cement, solids content. These strength parameters were also found to increase with time.

A comparison was made relating the UCS to the undrained friction angle and cohesion. The relationship took the form :-

$$UCS = 2c_u\left(\frac{\cos\phi_u}{1-\sin\phi_u}\right) \qquad \ldots(2.12)$$

As expected, with the low undrained friction angles obtained from testing, the UCS was predicted by doubling the cohesion, c_u, as there was negligible increase due to the undrained friction angle.

2.5.3.2 Effective Stress Analysis

By definition the water in the soil matrix is unable to support any shear stress at all. Thus any resistance to shear must be through the soil matrix. The effective stress and pore pressure of a soil a related by equation 2.13.

$$\sigma = \sigma' + u \qquad \ldots(2.13)$$

Where

σ = Total Stress, kPa

σ' = Effective Stress, kPa

u = Pore Pressure, kPa

Effective stress parameters are typically found using either the Consolidated Undrained (CU) or Consolidated Drained (CD) triaxial compression tests. The specimen is consolidated under a predetermined confining pressure, which is set to represent the likely insitu stress conditions. Even though the insitu stress conditions are anisotropic CU and CD tests are often carried out on isotropically consolidated samples, where the consolidation pressure is equal to the effective insitu vertical stress. Drainage is allowed to continue throughout the consolidation phase. Loading occurs in either drained or undrained conditions. Undrained loading conditions represent rapid loading of the soil. Under these conditions the water is unable to escape quickly enough resulting in pore pressure build up. In an effective stress analysis the pore pressures must be measured so that the analysis can be carried out in terms of effective stresses. The loading in the consolidated drained (CD) test occurs very slowly as to allow pore water to drain through the applied loading with negligible pore pressure build up. The effective parameters of friction angle and cohesion are found by conducting a series of tests under increasing consolidation pressures. The failure surface is then described using Mohr's circle and the effective parameters obtained, as shown in Figure2.14.

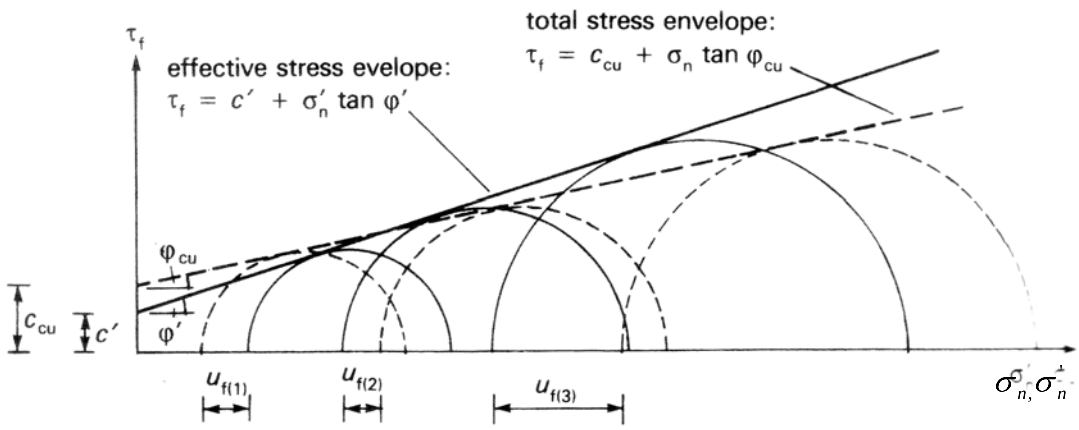

Figure 2. 14 Determination of Effective stress parameters using Mohr circles (viz Whitlow 1990)

Consolidated Undrained Tests

The change in pore pressure due to a change in the total stress under undrained conditions is determined using Skempton's (1954) pore pressure parameters, A and B. The pore pressure coefficient B is used to estimate the change in pore pressure resulting from an increase in isotropic stress using the equation.

$$\Delta u = B\Delta\sigma_3 \qquad \ldots(2.14)$$

In a fully saturated sample, B approaches 1. In partially saturated soils the compressibility of the pore fluid is high due to the presence of air resulting in B decreasing rapidly with decreasing saturation level. According to Skempton (1954), a soil sample must have a B value of 0.95 or above to be confident that the sample is saturated and allow the calculation of the drained parameters from an undrained test. The B value of any sample is a function of the saturation level and soil skeleton compressibility $B = \int(\textit{saturation}, \textit{compressibility of soil skeleton})$. It may not therefore provide an accurate indication of the saturation level in the stiffer cemented soil samples – such as that of paste fills. Wissa (1969) found B to be lower than 0.95 for cemented soils, even when backpressure had been applied and were under high confining stresses and fully saturated. Krizek et al.(1982) found that for grouted sand samples the maximum value of B for 28 day cured samples was 0.85 even with the application of back pressure to saturate the samples. Pierce et al. (1998) suggests that a B value of 0.85 is considered reasonable for paste fills also. In conventional triaxial tests where the confining pressure remains constant, the pore pressure coefficient A is used to estimate the pore pressure resulting from an increase in the major principal stress and is written in the general form:

$$\Delta u = AB\Delta\sigma_1 \qquad \ldots(2.15)$$

In saturated sands 0<A<1 for loose samples. Positive pore pressures are developed because the sample contracts during shearing. In dense sands A<0 as negative pore pressures develop as the sample dilates. For a very loose sand A>1 as the sample will collapse under the application of pressure (Skempton 1954).

Aref et al. (1989) presented stress-strain and pore pressure-strain curves from CU tests prepared on backfill produced from the total tailings. Typical results for a cement:tailings ratio of 1:30 and a solids content of 74% are shown in Figure 2.15. The samples were cured in 100% humidity at ambient temperatures, for a period of 28 days. The confining pressures are denoted in the figures at the end of the stress strain curves. The magnitude of backpressures applied to the samples is unknown.

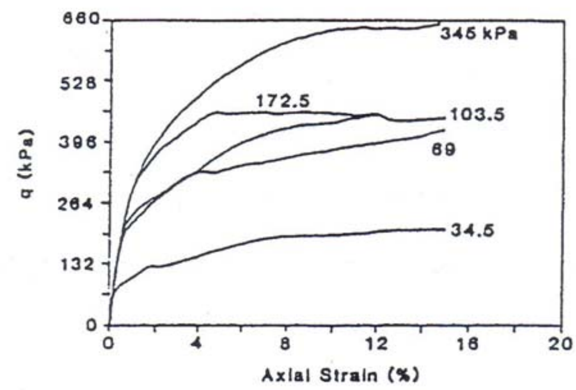

(a)

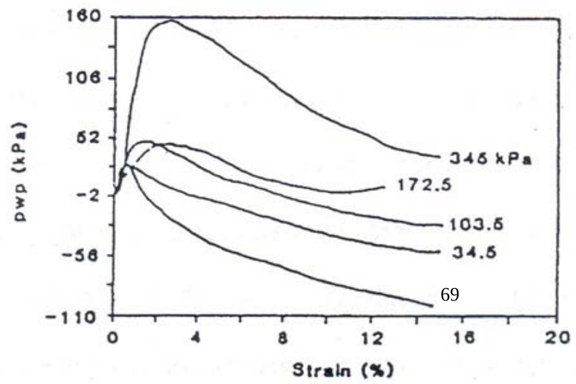

(b)

Where

pwp = pore water pressure (kPa)

q = deviator stress $=\left(\frac{\sigma_1-\sigma_3}{2}\right)$ (kPa)

Figure 2. 15 (a) Stress -strain and (b) pore pressure strain curves for CU tests performed on Dome Mine paste backfill (Aref et al. 1989).

At high confining pressures samples behave like normally consolidated sands, generating positive pore pressures. At low levels of confinement, they behave like over consolidated sands, generating negative pore pressures. After the sample start to dilate, between 1% and 3% axial strain, the pore pressure drops and the effective stress increases. As expected, the higher confining pressures result in higher pore pressures. The effective deviator stress increased until strains reached approximately 15%. All samples tended towards negative pore pressure at high strain levels, and increased sample dilation. Samples with higher cement content samples showed a stiffer response and higher peak strength, as expected. A summary of the effective parameters from testing are collated and shown in Table 2.5.

Table 2. 5 Shear Strength Parameters from Consolidated-undrained triaxial compression tests on Dome Mine paste backfill (Aref et al. 1989)

Cement:Tailings	**1:30**	**1:40**	**1:50**
Friction Angle, ϕ', (degrees)	31	33	33
Cohesion, c' (kPa)	53	20	20

With the increasing cement content, friction angle increases and cohesion decreases. This phenomena has been reported in literature for cemented slurry fill by a number of other researchers (Mitchell and Wong (1982), Williams (1994), Ouellet (1995)). Pierce (1997) also reported a similar response for tests on paste fill tests from the Golden Giant Mine, which is shown in Figure 2.16. This is in stark contrast to the results reported within this body of research, which show friction angle increasing with UCS. Pierce (1997) attributes the reduction in friction angle to the yielding of cement bonds during isotropic compression. Which during unconfined compression strength (UCS) tests is not applicable. It is considered likely that the results of the CU tests may have been used for interpretation and the deviator stress, instead of the UCS, was used to plot against the friction angle. The low values of the cohesion intercept, from Table 2.5, would support this interpretation. The values of the cohesion and friction angle reported by Pierce (1997) indicate that the results of the CU testing fall somewhere between the drained and undrained parameters of the fill. This highlights the difficulties of testing of low permeability, cemented samples in conventional triaxial testing equipment.

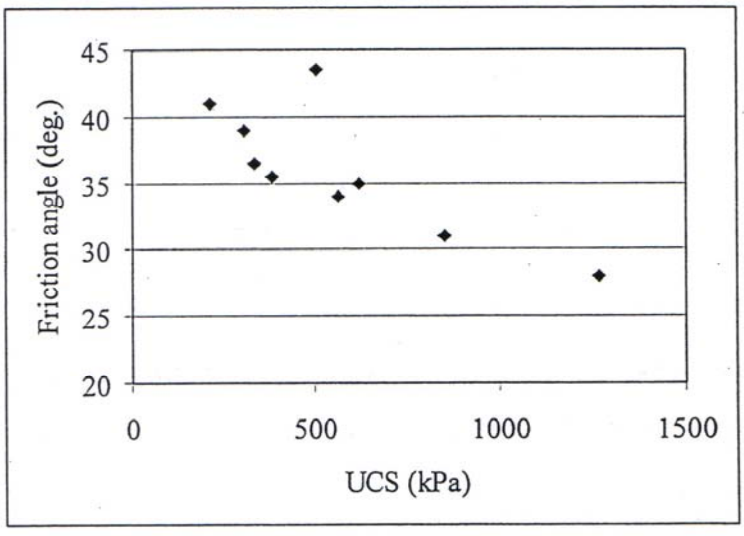

Figure 2. 16 Friction angle vs. UCS for Golden Giant Paste Fill (Pierce 1997)

Pierce (1997) undertook a series of CU tests on Golden Giant Paste fill to determine the general stress-strain and pore pressure behaviour of paste fill in undrained triaxial shear and determine the effective stress parameters c' and ϕ' in terms of binder content and cure time. Figure 2.17 shows the response of Golden Giant Mine paste fill with 3% binder and cured for 28 days.

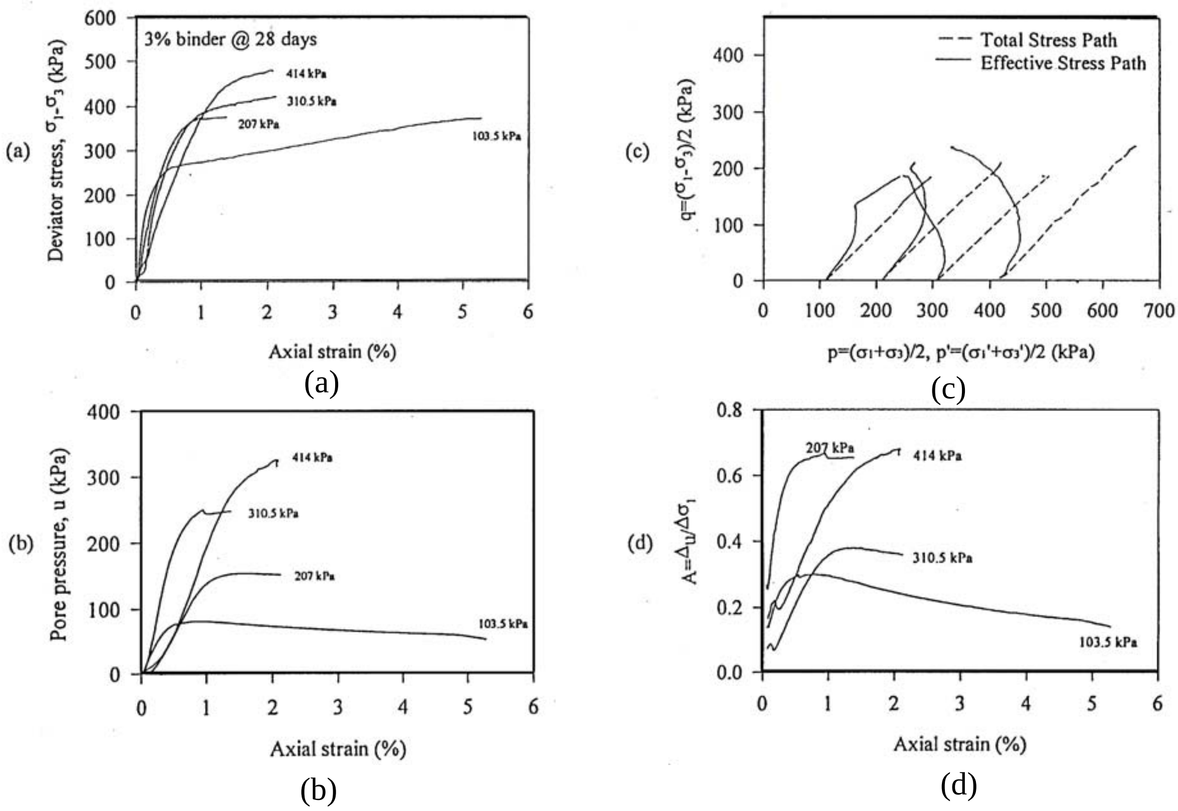

Figure 2. 17 CU Behaviour of Golden Giant Mine paste fill with 3% binder after curing for 28 days in CU triaxial compression. (a) Deviator Stress (b) Pore pressure (c) Stress path and (d) Pore pressure parameter A (Pierce 1997).

Pierce (1997) found that the response of paste to loading in a CU test behaved similarly to that of loose sands with the pore pressure increasing rapidly to a peak value and then decreasing with strain until the peak deviator stress is reached. All samples were 75% solids (by weight) and underwent initial yielding at 0.5 to 1% axial strains. As expected, deviator stress at failure and initial stiffness increase with binder content and cure time. Table 2.6 shows the effective strength parameters determined from the CU testing. With increasing binder content and curing time, while the cohesion increased, the friction angle decreased significantly. This re-enforces the trends observed by Aref et al. (1988, 1989).

Table 2. 6 Effective shear strength parameters for Golden Giant Paste Fill (Pierce 1997)

		Cure time (days)					
		28		56		112	
		c' (kPa)	ϕ' (deg.)	c' (kPa)	ϕ' (deg.)	c' (kPa)	ϕ' (deg.)
Binder content (wt%) (50:50 NPC:FA)	3	40	41	64	37.5	101	35.5
	5	75	39	108	34	147	35
	7	89	43.5	251	31	331	28

NPC = Normal Portland Cement, FA= Fly Ash

Consolidated Drained Triaxial Testing

Drained triaxial loading occurs very slowly, to allow drainage and avoid pore pressure build up. Ouellet et al. (1995) carried out a series of consolidated drained triaxial tests to determine the stress-strain characteristics of paste fill used in four Canadian mines. During shearing it was found the specimens underwent volume contractions and the cohesion observed appeared to be a function of cement content. It was reported that the cement bonds progressively broke during shearing until the paste acted as a granular material with no apparent cohesion. Assuming that loading can destroy the cement bonds, the cohesion of the backfill is thus dependent on the load history. This behaviour is consistent with that observed by Mitchell and Wong (1982) with cemented hydraulic tailings.

Drained Direct Shear Testing

The majority of published work on the shear strength of paste fills has been done by Aref and Hassani (1988) and Aref et al. (1989) on Dome Mine paste backfill. The average effective shear strength parameters were obtained from a drained direct shear test and are shown in Table 2.7. The friction angles for the paste backfills are all reasonably low, which is thought to be a resultant of the low normal stresses (<100 kPa) used to determine the parameters. At the lower levels of normal stress, behaviour is dominated by cohesion.

Table 2. 7 Shear Strength Parameters from direct shear tests on Dome Mine paste backfill (Aref and Hassani 1988).

Moisture content	**20 %**			**24%**		
Cement:Tailings	1:30	1:40	1:50	1:30	1:40	1:50
Drained Friction Angle, ϕ' (degrees)	18	19	23	14	10	7
Cohesion c (kPa)	94.7	78	39.5	74.2	65	49.4

The friction angles of the samples with moisture content of 24% are contradictory to the well-documented trend of an increasing friction angle with reduced cement content (Mitchell and Wong (1982), Williams (1994), Ouellet (1995), Pierce (1997)). The results of the samples with the cement: tailings ratio of 1:40 (cement content = 2.5%) and 1:50 (cement content =2%) have very low drained friction angles of 10 and 7 respectively. The low friction angles are not likely to be representative of the true "effective" friction angle. Instead, it is considered likely that the shearing rate of the direct shear test was set too high, resulting in excess pore pressure build-up and premature failure of the specimens. Indeed the friction angles of the samples with moisture content of 20% are considered reasonably low as well. When the results are considered in parallel to the results obtained from consolidated undrained triaxial tests on the same backfill (Dome Mine paste backfill), conducted by the same author (Aref et al. 1989) this assumption is even further validated. The results of the CU testing are shown in Table 2.5 and indicate a constant effective friction angle of between 31-33 degrees. The slightly lower value of 31 for the cement:tailings ratio of 1:30 (cement content of 3.33%) is due to increased cohesion of the material. The increase in cohesion results in a lower friction angle through the fitting of a line of best fit using linear regression. Confining pressures used to determine the friction angles were significantly higher (up to 345 kPa) than those used to determine those same properties as the direct shear apparatus.

2.5.4 Liquefaction Potential

The primary hazard of slurry-based backfills is the potential for the materials to remobilise, or liquefy after placement. In a cohesionless granular fill mass, fill particles are kept in place by intergranular forces. When cement is added, true cohesion then exists between particles. When loading is applied rapidly, pore pressure builds up until such time as the pore pressure equals or exceeds the total stress in the soil. This reduces the effective stress in the soil and thus the shear strength to zero (refer Equation 2.13). The soil then liquefies. The soil particles are forced apart by the excess pore pressure, and become loosely suspended in a soil /water slurry, unable to be held in position by the forces applied by the surrounding particles. Figure 2.18 shows the progression of a saturated cohesionless soil towards liquefaction, as the water pressure increases. The white arrows indicate the contact forces between the particles, with the magnitude of the forces being shown by the length. The blue column to the right hand side of each of the pictures shows the relative water pressure.

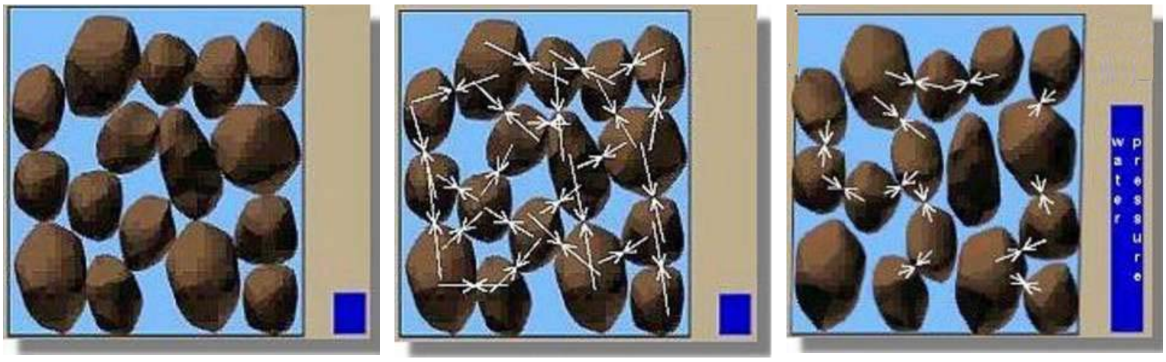

Soil grains in a soil deposit. The height of the blue column to the right represents the level of pore water pressure in the soil.

The length of the arrows represents the size of the contact forces between individual soil grains. The contact forces are large when the pore water pressure is low.

Observe how small the contact forces are reduced because of the high water pressure.

Figure 2. 18 Behaviour of Fill Under Increasing Porewater Pressure (www.ce.washington.edu/~liquefaction/html/main.html)

In uncemented hydraulic fills, the pore pressure is kept low by desliming the fine fractions and ensuring that the fill is relatively free draining ($k = 10^{-5} - 10^{-6}$ m/s). Under a wide range of fill placement conditions, uncemented hydraulic fill remains unsaturated and is not susceptible to liquefaction. However, Grice (1998) and Bloss and Chen (1998), have shown that saturated hydraulic fill can still be remobilised through the “piping” phenomena in fill masses.

By contrast, paste fill requires the presence of the finest size fractions in order to achieve the paste like flow behaviour and water retentive nature of the pulp with a typical permeability in the order of $k = 10^{-6}$ cm/s. Paste also remains fully saturated. To minimise the risk of liquefaction and increase stability, cement is added to generate inter particle cohesion. Grice (1998) noted that in cemented hydraulic fills the quantity of fill that can be mobilised is typically limited to that material which has not yet undergone an initial set.

A number of investigations into the liquefaction potential of paste fill have been undertaken by several including Been, Brown and Hepworth (2002), Aref et al. (1989), Ouellet et al. (1998) and Pierce et al. (1998). Ouellet et al. (1998) notes that the following three conditions are relevant to liquefaction potential;

- the paste fill has a contractant behaviour under loading,
- the paste fill is saturated, and
- there is a loss of, or no cohesion

In triaxial testing, paste fill generally contracts under load thereby meeting the first criterion. Paste fill maintains a state of near saturation since it is by nature a non-draining material, thereby meeting the second criteria. For saturated materials under undrained loadings, the friction angle tends towards zero and thus the shear strength of the material is governed by the cohesion that results from cementation alone.

Clough et al. (1989) tested weakly cemented sands with a range of cementation levels and unit weights in a cyclic triaxial shear device. For the sands under investigation a UCS of 100 kPa was enough to prevent liquefaction under cyclic loads typical of a very large earthquake (M=7.5). This level of cementation has been adopted worldwide to address the question of potential liquefaction of backfill masses. Additional levels of cement are sometimes added to account for any long-term decay of strength associated with sulphate attack or self-desiccation.

2.6 Static Stability of Cemented Backfills

Studies into the static stability of backfilled stopes have been divided into three subsections: -

1. Analytical solutions
2. Numerical Modeling
3. Physical (Scale) Modeling

2.6.1 Analytical Methods

Under the category of analytical methods, there are currently five commonly used backfill stability prediction methods. These are:-

1. Free Standing Vertical Face (viz Grice 2001),
2. Vertical Slope (viz Grice 2001)
3. 3-D Sliding Wedge Failure (Mitchell 1982) and
4. Simple Arching (Marston, 1930, Aubertin, 2003, Li et al., 2003)
5. Modified Simple Arching (Winch 1999)

All of the analytical methods describe the fill mix in terms of a required unconfined compressive strength to ensure stable exposures. The level of cementation required is found be either experimental data of predictive equations comparing the UCS vs. the fill mix (%Cement, % Solids).

2.6.1.1 Free Standing Vertical Face

When designing the exposed face as a freestanding wall the required UCS of the fill at any given depth was defined as:-

$$UCS \geq \gamma z \qquad \ldots(2.16)$$

where

γ = bulk unit weight of backfill =(ρg) and
z = depth from the free surface (top of the fill).

The effect of lateral confinement and the strength increase due to confinement is completely ignored, which is conservative. According to Equation 2.16 the required UCS increases linearly with depth. This is shown in Figure 2.19.

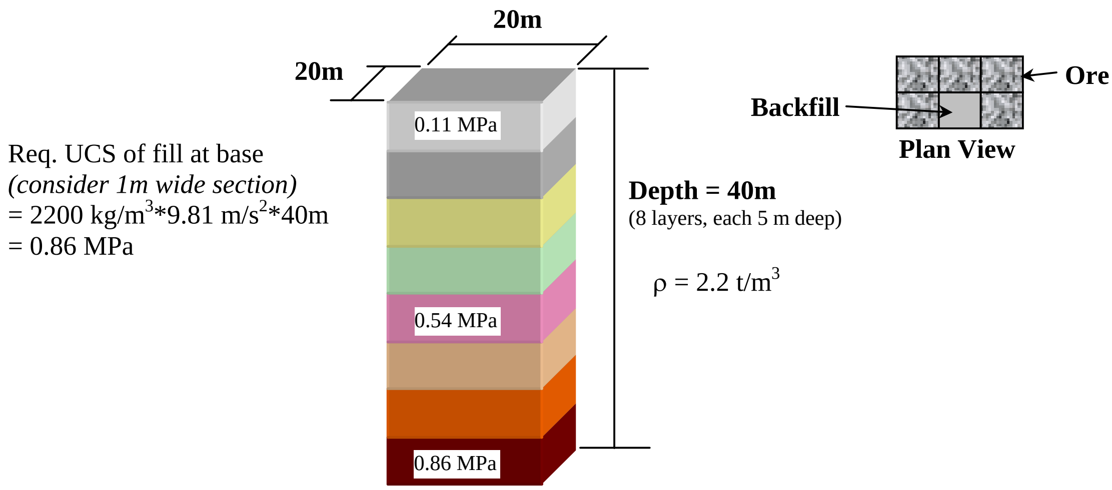

Figure 2. 19 Design of backfill as a freestanding wall (viz Grice 2001)

This approach is very conservative. There is no account taken of the reduction in stress in a backfilled mass due to arching or cementation. Indeed this would be the worst case: - instantaneous filling, prior to consolidation and curing, with fully hydrostatic pressures being developed. The analysis is only two-dimensional and does not take account of the three dimensional geometry of backfilled stopes.

2.6.1.2 Vertical Slope

When designing fill strength assuming the exposure to be a vertical slope with constant strength fill and $\phi = 0$, the required UCS of the fill must satisfy the condition that: -

$$UCS \geq \gamma H / 2 \qquad \ldots(2.17)$$

where

H = overall height of the exposed fill.

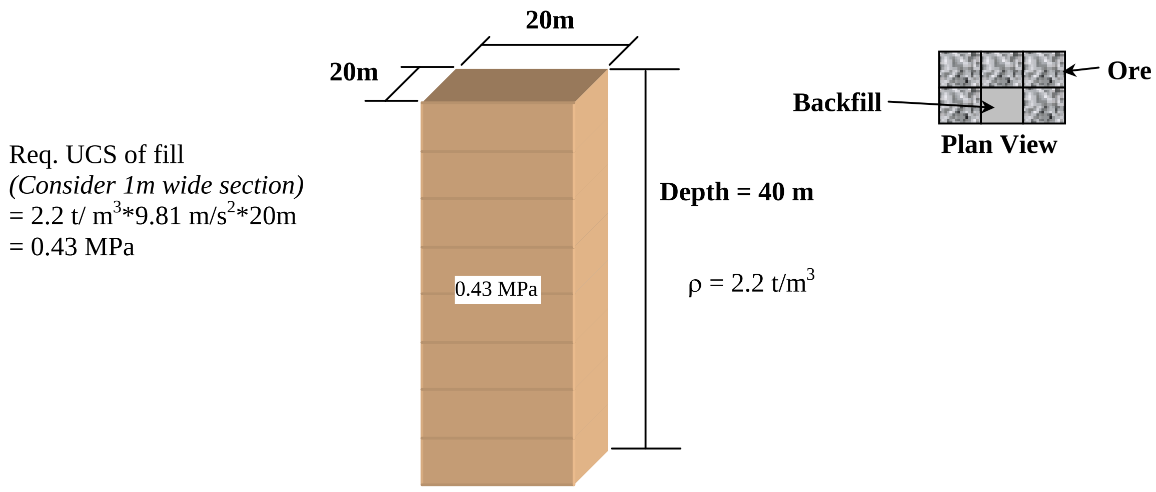

Figure 2. 20 Design of backfill as a vertical slope (viz Grice 2001)

This approach is a somewhat quizzical as it assumes that the level of cementation to resist the in-situ stresses is independent of spatial position within the stope. This is obviously incorrect as the in-situ stresses at the base of the exposed stope will be significantly larger than those at the top. It is interesting to note that a large number of stopes in the early days of cemented backfilling were designed and constructed like this, and when exposed, remained stable. This indirectly inferring that there was another mechanism in the fill mass which significantly reduced the vertical stresses in the fill mass. The arching mechanism, which is responsible for the reduction in vertical stresses, is discussed in greater detail in the following subsection on simple arching.

Both the “vertical slope” and “free standing wall” methods give approximately the same overall result for cement usage, but neither account for the true three-dimensional geometry of the cemented fill block. An attempt was made by Mitchell (1982) to incorporate the actual three-dimensional nature of backfills, when he proposed the “Limit Equilibrium Wedge” model.

2.6.1.3 Limit Equilibrium Wedge

Mitchell (1982) modeled the failure of a single exposure, 3-D fill mass as shown in Figure 2.21. A shear plane for sliding failure was defined within the ‘block’. Arching was assumed in the model by assuming a constant shear wall stress equal to the cement bond shear strength.

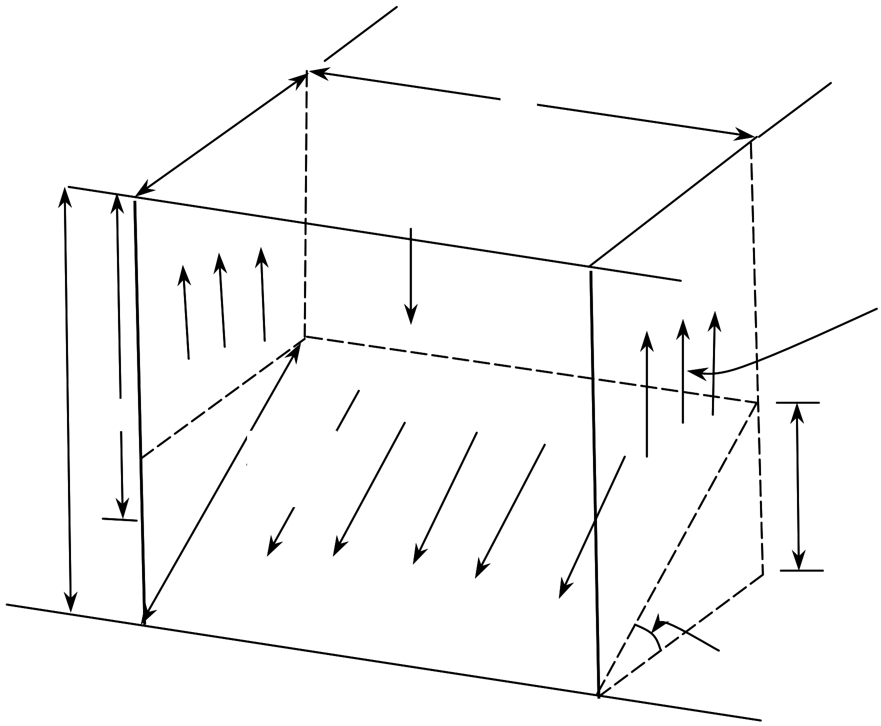

Figure 2. 21 Confined block mechanism (Mitchell et al. 1982)

where

W_n = net weight of block

α = angle of failure plane from horizontal (= 45°+ϕ/2)

ϕ = friction angle of fill

Cb = cement bond strength of fill

l = length of block

w = width of block

h = height of the block

h^* = height of block from top to the centroid of the triangular section of the sliding wedge.

The required strength (UCS) of fill is given by:-

$$UCS = \frac{\gamma H}{\left(1 + \frac{H}{L}\right)} \qquad \ldots(2.18)$$

The assumptions made in this model are:-

- Mobilised wall shear is equal to the material cohesion
- Material Friction angle equals zero
- The fill height is much greater than the fill maximum width of (or length) of fill.
- Stresses are evenly distributed within the fill mass

The use of a zero friction angle, was supported by initial analysis suggesting that the breaking of the cement bonds did not occur and therefore, cement bond shearing resistance was stabilised at small strains. Further calculations concluded that although conservative, the assumption of constant shear along the walls, made in Equation 2.18, was satisfactory. The major criticism of limit equilibrium approach is it is valid only for a single exposure on a fill mass. In general stopes are typically exposed on a minimum of two sides. Stone (1993) and Moss (unpublished) present methodologies for backfill design based on the use of this formula also, and have published charts from which a UCS strength may be determined for a give stope exposure geometry (refer Figure 2.22).

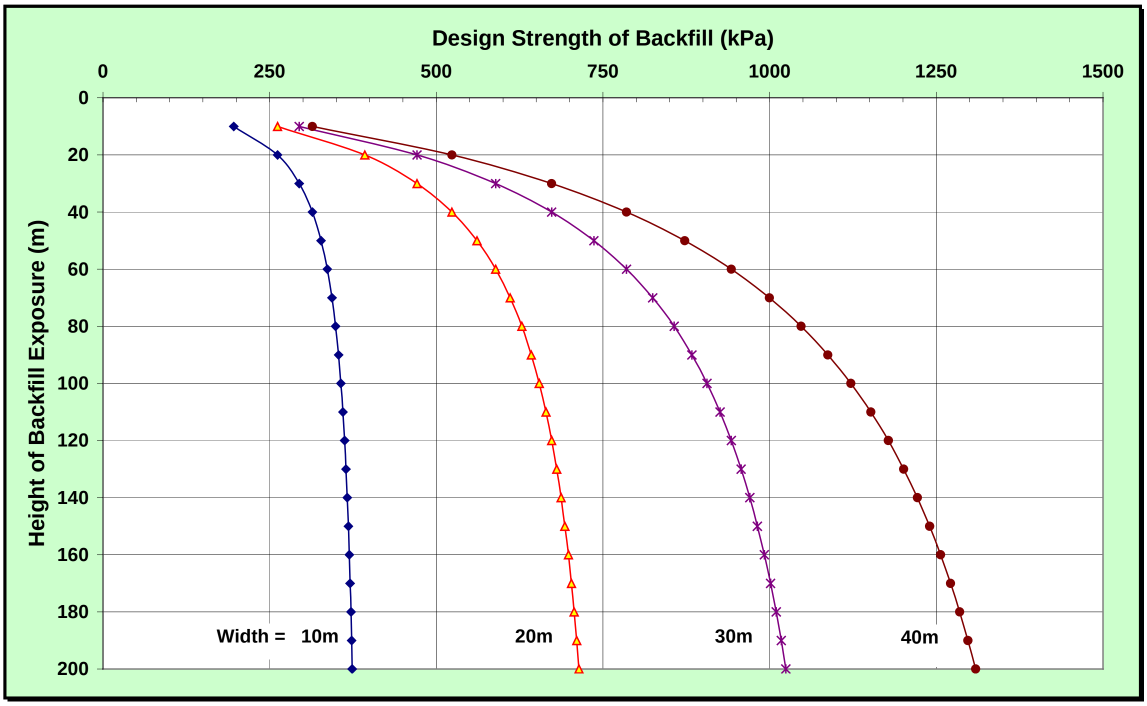

Figure 2. 22 Backfill Stability Design Chart (Moss, unpublished)

2.6.1.4 Simple Arching

The effects of arching have been best described by Li et al. (2003). “Arching occurs when differential stresses mobilise shear strength while transferring part of the overburden stress to stiffer structural components. This typically occurs when portions of a frictional material yields while the neighbouring material doesn’t. As the yielding material tends to move beside the stable region, shear resistance in the stable zone is generated along the interface. The shear stress generated on the contact area tends to retain the yielding material in its original position. This is accompanied by a pressure reduction in the yielding mass and a pressure increase in the adjacent stiffer material. Above the position of the main arch, the greatest fraction of the overburden weight in the yielding mass is transferred by unyielding ground on both sides”.

Since the early pioneering work of Jannsen (1895) and Terzaghi (1943), there have been a number of researchers who have investigated the effect of arching in granular masses. Arching in granular medium has been investigated by:- Richards (1966), Cowin (1977) and Blight (1986) - in grain silos and bins, Spangler and Handy (1984) - in ditches, and Hunt (1986), Take and Valsangkar (2001) with the effect of arching behind retaining walls.

Marston (1930) proposed a theory on arching which was later expanded and investigated further by Aubertin et al. (2003) and Li (2003) in relation to the development of stresses in narrow, backfilled stopes.

Figure 2.23 shows the free body diagram of the forces acting on an isolated layer within a vertical stope. In this diagram, H is the backfill height, B the stope width, dh the size of the layer element; W is the weight of the backfill in the unit thickness layer. At the position h, the horizontal layer element is subjected to a lateral compressive force C, a shearing force S, and vertical forces V and V + dV.

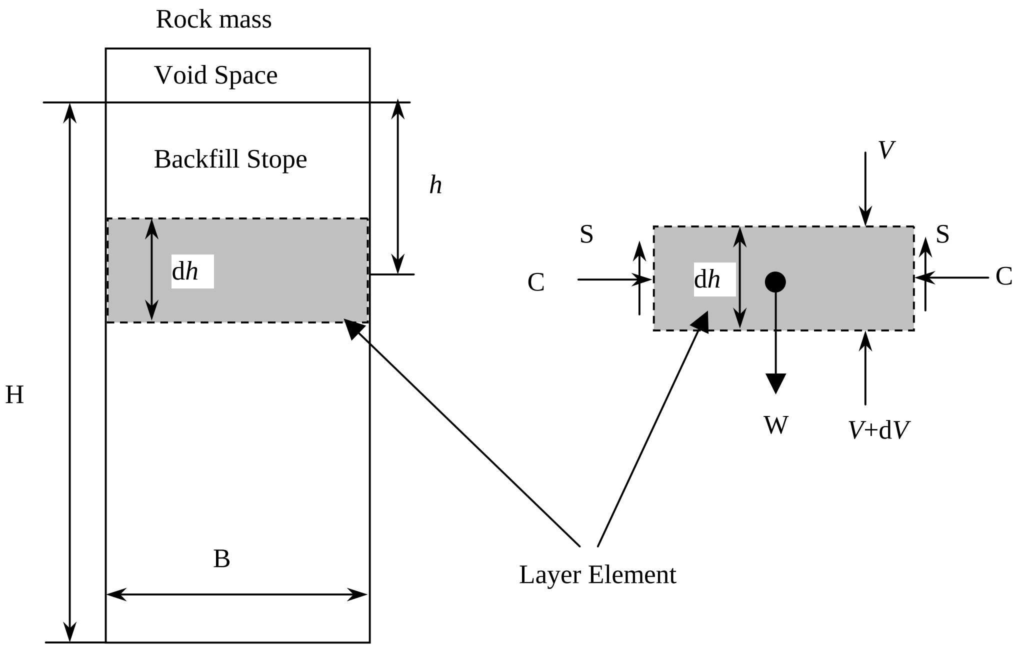

Figure 2. 23 Free body diagram of forces acting on an isolated layer in a stope (Viz Aubertin et al., 2003)

By using the force equilibrium equations on the layer element, Aubertin et al. (2003) provided an approximation to the vertical stresses acting across the bottom of the stope in the form of Equation 2.19:

$$\sigma_{vh} = \frac{\gamma B}{K}\left(\frac{1-\exp(-2Kh/B\tan\delta')}{2\tan\delta'}\right) \qquad \ldots(2.19)$$

Where

σ_{vh}	= vertical stress at depth h
γ	= Unit weight of fill
δ'	= effective friction angle between the wall and the backfill
K	= lateral earth pressure co-efficient.

The lateral earth pressure co-efficient used depended on wall movement with closure and material properties. If there was no relative movement of the walls once the fill was placed $K = K_0$. If the convergence of the walls occurred, K would tend towards K_p and conversely, if the walls were to relax or $K=K_a$. If the assumption is made that convergence of the wall will occur prior to filling, $K=K_0$ is considered a reasonable approximation.

There are two major limitations with Marston's (1930) theory which should be considered. The shear stress along the interface beween the rock and the fill is deduced from the Coloumb criterion (Aubertin et al. 2003). The value of which corresponds to the maximum stress sustained by the fill material as postulated by the limit analysis approach. Through numerical modelling (Li et al. 2003) this is shown not to be the case, with the maximum stress being reached only near the bottom part of the stope. Also, the vertical and horizontal stresses are assumed to be uniform across the dimension of the stope plan. The approximations for horizintal stresses may be reasonable (Li et al., 2003), however the vertical stress variation is significant (Rankine, K, 2000). Marston's theory (1930) would predict a uniform K value for any plan dimension of a stope, which is obviously incorrect if the vertical stress values vary. The true lateral earth pressure co-efficient is a function of location and material properties within the stope.

2.6.1.5 Modified Simple Arching

Winch (1999) developed the basis for an analytical model based on the Terzaghi (1943) theory of arching to study the failure of fill masses. If the backfill mass is considered to be a rectangular prism as shown in Figure 2.24. Figure 2.2.5 shows a three dimensional element of backfill with the associated free body forces acting on it.

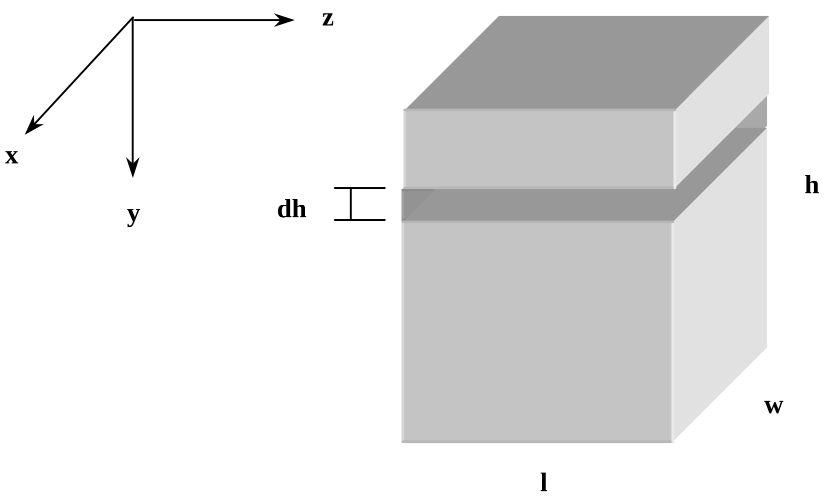

Figure 2. 24 Three dimensional element of backfill

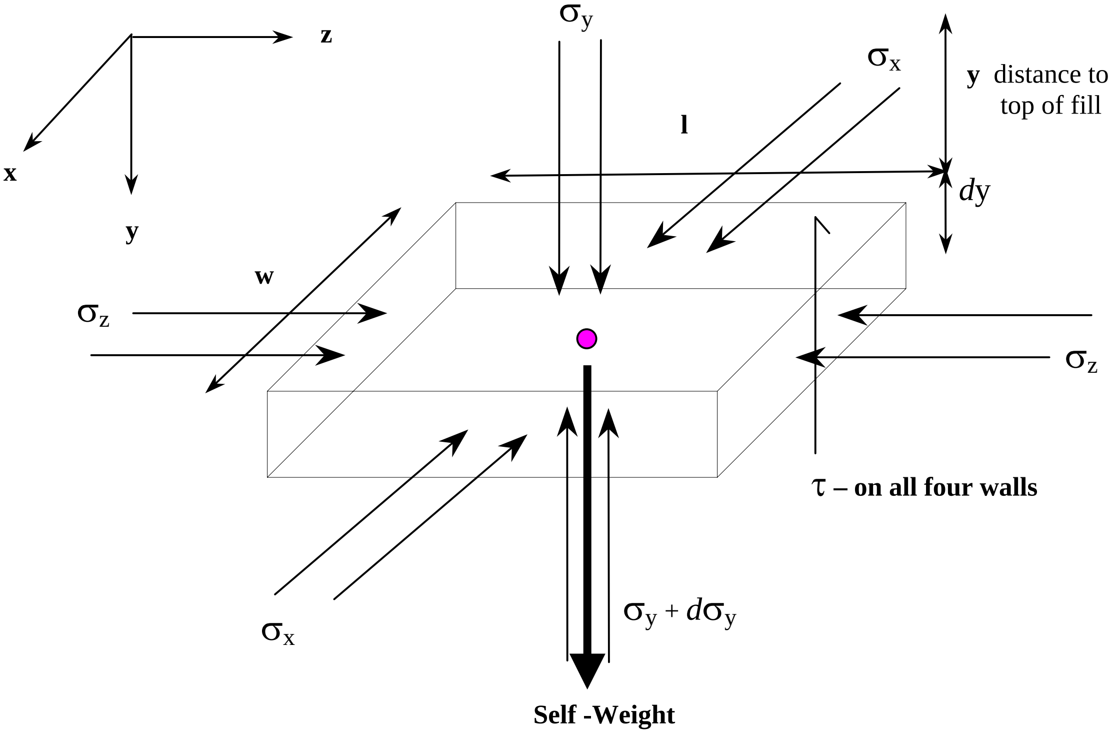

Figure 2. 25 Forces on a differential element

where

y	=	distance to the top of the overlying fill (metres)
l	=	length of fill mass (metres)
w	=	width of fill mass (metres)
dy	=	vertical thickness of differential element (metres)
ρ	=	fill density (t/m^3)
g	=	gravitational constant (m/s^2)
σ_x	=	stress in horizontal x-direction (kPa)
σ_z	=	stress in horizontal z-direction (kPa)
σ_y	=	vertical stress at top of element (kPa)
$d\sigma_y$	=	increase in vertical stress over distance dy (kPa)
τ	=	constant shear stress between paste fill mass and confining wall (kPa)

Winch (1999) notes that arching does not develop until paste is sufficiently cured. This is not entirely true. Arching develops in the fill mass as shear stress can be generated and transferred between particles. In the case of hydraulic fills this will be after it has settled after being in the slurry suspension. In paste fills, arching occurs after the cement bonds cure and provide sufficient cohesion between the particles. Winch (1999) referrers to the stresses developed within the fill before it has cured are referred to as the "initial stress condition".

The total vertical stress is made up of two components: - the initial stress plus the incremental stress. The incremental stress results from the additional load of uncured paste. When cured, the paste fill does arch and transfers some of the overburden weight to the walls of the stopes. This reduces the vertical load to less than would be experienced by the the self-weight of the overlying fill. Winch (1999) proposed that not all contact surfaces contribute equally to arching. Winch (1999) suggests that fill to fill contacts are able to transfer only one quarter as much shear stress, as rock to fill contacts. The figure of one quarter is empirical in nature and was made as an initial approximation, to be refined with time and additional experience. The concept of effective wall area has been introduced to modify the effective contact area against which arching takes place.

From the equilibrium considerations for the differential element shown in Figure 2.25. the following relationship can be obtained.

$$W_1W_2\rho g dy + \sigma_{yT}W_1W_2 - (\sigma_{yT} + d\sigma_y)\, W_1W_2 - \tau(\text{EffectiveAreaFor}\tau)=0 \qquad \ldots(2.20)$$

Rearranging , the stress at any elevation in the fill can be calculated from

$$\sigma_y = \sigma_{y0} + \frac{\frac{W_1W_2\rho g}{2R(W_1+W_2)} - \left(c + K\sigma_{y0}\tan\phi\right)}{K\tan\phi}\left[1 - e^{\frac{-2R(W_1+W_2)}{W_1W_2}K\tan\phi(y-y_0)}\right] \qquad \ldots(2.21)$$

where

σ_{y0} = horizontal direction in stope (metres)

c = cohesion (kPa)

y_0 = height of fill at which arching starts to develop (~fill height/day) and valid for $y \geq y_o$ (meters)

ϕ = friction angle (degrees)

K = ratio of horizontal to vertical stress

R = Ratio of active wall length to total wall length

$$= \frac{\Sigma A_i}{\Sigma W_i} = \frac{\Sigma F_i W_i}{\Sigma W_i}$$

where W_i = wall length for side I

F = arching potential factor.

= 0 for exposed side

= 1 for adjacent rock

= 0.25 for adjacent paste

The ratio of horizontal stresses, K, can be directly related to Poisson's ratio. When there is no lateral strain and the fill is in a rest or "K_o" condition, the ratio of horizontal to vertical stresses is given by: -

$$K_o = \frac{\nu}{1-\nu} = 1 - \sin\phi' \qquad \text{…(2.22)}$$

With the exposure of one and later more faces of a stope, K_o tends towards the K_A condition, where failure occurs. The value of K_A may be calculated using: -

$$K_A = \frac{1-\sin\phi'}{1+\sin\phi'} = \tan^2\left(45 - \frac{\phi'}{2}\right) \qquad \text{…(2.23)}$$

Winch (1999), suggested decreasing values for K of 0.25 for first exposure, 0.20 for second exposure and 0.15 for the third exposure. The model calculates vertical stress at a specified distance from the top of the fill. The calculated value is based on the mobilisation of the full shear strength at the sides of the fill mass, which occurs when arching is fully developed. When the fill is stable, the full shear strength will not be mobilised and arching will not be fully developed. In this case, vertical stresses are underestimated. This condition is of little concern as stresses are only underestimated when the fill mass is stable. The model improves in accuracy as the shear strength of the fill reaches approaches its limit. On the exposed fill surface, horizontal confining stresses are low and therefore the vertical stress can be compared with the uniaxial compressive strength (UCS). If the maximum vertical stress exceeds the UCS, then the fill mass can be rated as potentially unstable. Equation 2.20 may also be re-arranged to rate the potential stability of the stopes based on the geometry of the stope (width, depth and height). By re-arranging the vertical stress equation and letting the vertical stress equal the in-situ compressive strength (failure condition) then Equation 2.20 can expressed as: -

$$\sigma_y - \sigma_{y0} = \frac{\frac{W_1 W_2 \rho g}{2R(W_1+W_2)} - \left(c + K\sigma_{y0}\tan\phi\right)}{K\tan\phi}\left[1 - e^{\frac{-2R(W_1+W_2)}{W_1W_2}K\tan\phi(y-y_0)}\right] \qquad \ldots(2.24)$$

Which when re-arranged using the following steps may be expressed finally as Equation 2.25.

$$\frac{\left(\sigma_y - \sigma_{y0}\right)K\tan\phi}{\frac{W_1W_2\rho g}{2R(W_1+W_2)} - \left(c + K\sigma_{y0}\tan\phi\right)} = 1 - e^{\frac{-2R(W_1+W_2)}{W_1W_2}K\tan\phi(y-y_0)}$$

$$1 - \frac{\left(\sigma_y - \sigma_{y0}\right)K\tan\phi}{\frac{W_1W_2\rho g}{2R(W_1+W_2)} - \left(c + K\sigma_{y0}\tan\phi\right)} = e^{\frac{-2R(W_1+W_2)}{W_1W_2}K\tan\phi(y-y_0)}$$

$$\ln\left[1 - \frac{\left(\sigma_y - \sigma_{y0}\right)K\tan\phi}{\frac{W_1W_2\rho g}{2R(W_1+W_2)} - \left(c + K\sigma_{y0}\tan\phi\right)}\right] = \frac{-2R(W_1+W_2)}{W_1W_2}K\tan\phi\left(y - y_0\right)$$

$$\frac{-W_1W_2}{2R\left(W_1+W_2\right)K\tan\phi}\ln\left[1 - \frac{\left(\sigma_y - \sigma_{y0}\right)K\tan\phi}{\frac{W_1W_2\rho g}{2R(W_1+W_2)} - \left(c + K\sigma_{y0}\tan\phi\right)}\right] = y - y_0$$

$$y = y_0 - \frac{W_1W_2}{2R\left(W_1+W_2\right)K\tan\phi}\ln\left[1 - \frac{\left(\sigma_y - \sigma_{y0}\right)K\tan\phi}{\frac{W_1W_2\rho g}{2R(W_1+W_2)} - \left(c + K\sigma_{y0}\tan\phi\right)}\right] \qquad \ldots(2.25)$$

Plotting equation 2.25 forms a hyperbolic graph, with three distinct regions, as shown in Figure 2.26 below.

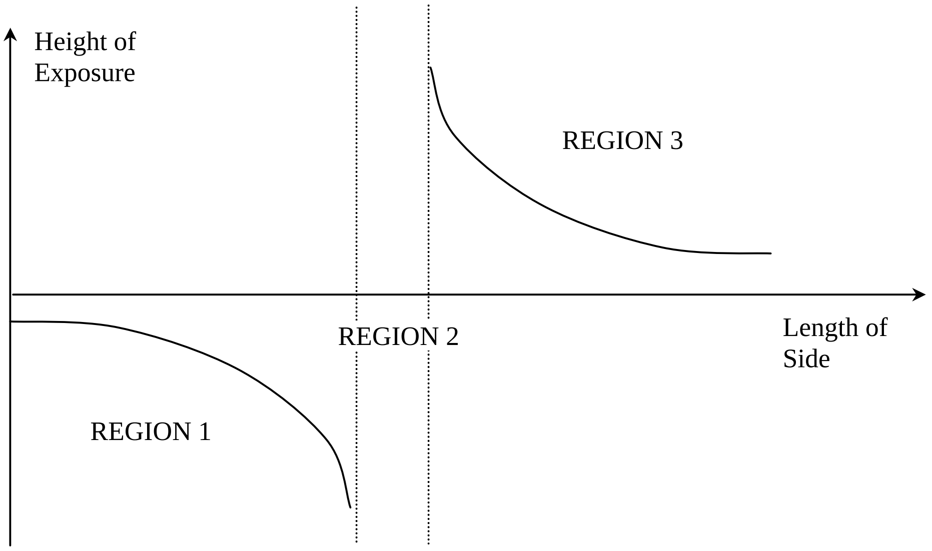

Figure 2. 26 Generic hyperbolic solution to Winch (1999) fill stability equation

The dependant variable (height of exposure) is negative in the first region approaching a vertical asymptote, undefined in the second region and positive in the third region, also approaching a vertical asymptote. This form is due to the presence of the natural logarithm in the equation. A natural logarithm, when plotted has three defined regions, as shown in Figure 2.27. Values that are less than zero are undefined, numbers between zero and one are negative and numbers greater than one are positive.

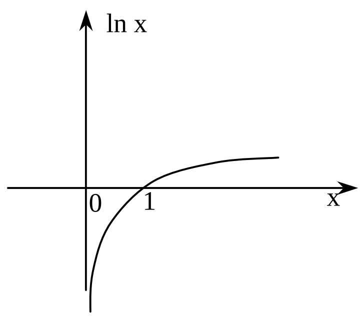

Figure 2. 27 Generic form of the natural logarithm function

The side lengths of the stope are which these asymptotes occur can then be calculated. However as the only region on Figure 2.26 that returns a realistic answer is region three. In this case the stope height is greater than y_o, therefore:-

$$\ln\left[1-\frac{(\sigma_y-\sigma_{y0})K\tan\phi}{\frac{W_1W_2\rho g}{2R(W_1+W_2)}-(c+K\sigma_{y0}\tan\phi)}\right]$$ has to be negative.

For this to occur, $0<\left[1-\frac{(\sigma_y-\sigma_{y0})K\tan\phi}{\frac{W_1W_2\rho g}{2R(W_1+W_2)}-(c+K\sigma_{y0}\tan\phi)}\right]\leq 1$, since the natural logarithm of a number between 0 and 1 will result in a negative answer.

$$0\leq\left[\frac{(\sigma_y-\sigma_{y0})K\tan\phi}{\frac{W_1W_2\rho g}{2R(W_1+W_2)}-(c+K\sigma_{y0}\tan\phi)}\right]<1$$

$$\frac{W_1W_2\rho g}{2R(W_1+W_2)}-(c+K\sigma_{y0}\tan\phi)>(\sigma_y-\sigma_{y0})K\tan\phi$$

$$\frac{W_1W_2\rho g}{2R(W_1+W_2)}>(\sigma_y-\sigma_{y0})K\tan\phi+(c+K\sigma_{y0}\tan\phi)$$

Now if we assumed that the stop is square in plan $W_1=W_2$

$$\frac{W^2\rho g}{2R(2W)}>(\sigma_y-\sigma_{y0})K\tan\phi+(c+K\sigma_{y0}\tan\phi)$$

$$\frac{W\rho g}{4R}>(\sigma_y-\sigma_{y0})K\tan\phi+(c+K\sigma_{y0}\tan\phi)$$

$$W>\frac{4R}{\rho g}\left[(\sigma_y-\sigma_{y0})K\tan\phi+(c+K\sigma_{y0}\tan\phi)\right]$$

This gives us the position of the asymptote between the undefined and positive region. Similarly, the position of the asymptote between the negative and undefined region can be calculated. Similarly for the negative region, the stope failure height would be less than y_o, so the term

$$\ln\left[1-\frac{(\sigma_y-\sigma_{y0})K\tan\phi}{\frac{W_1W_2\rho g}{2R(W_1+W_2)}-(c+K\sigma_{y0}\tan\phi)}\right]$$ would be positive.

The limit at which the stope failure height becomes positive is of interest. This asymptote is the critical height of the stope for arching. Below this height, full arching is developed and the stope is completely stable. After this point, the effects of arching reduces causing a decrease in failure height. Therefore, if the length of the side and height of stope are plotted on the graph, then an indication as to the stability of the stope can be made. If the point is in the negative or undefined region of the graph, then failure will not occur, regardless of stope height. If the point is in the positive region, and below the plotted line, the stope is stable. If the point plots above the line, the vertical stress in the fill mass is above the UCS of the paste and the stope is classified as unstable, and in danger of failing.

If the model proposed by Winch (1999) is extended to analysis of rectangular stopes, one side must be held constant and the other side varied at a time. The proportion of the active wall length will vary according to the length of that side. It is of most interest when the length of side that is varied, causes the failure of the stope to be dependent on the height. Graphically, this is the region on Figure 2.26 as the region of the graph that is between the undefined and positive region of the graph.

If we let:-
W_1 = length of side held constant
W_2 = length of side varied

$$y = y_0 - \frac{W_1 W_2}{2R(W_1 + W_2)K\tan\phi}\ln\left[1 - \frac{(\sigma_y - \sigma_{y0})K\tan\phi}{\frac{W_1 W_2 \rho g}{2R(W_1+W_2)} - (c + K\sigma_{y0}\tan\phi)}\right]$$

For y to be greater than y_o,

$$0 < \left[1 - \frac{(\sigma_y - \sigma_{y0})K\tan\phi}{\frac{W_1 W_2 \rho g}{2R(W_1+W_2)} - (c + K\sigma_{y0}\tan\phi)}\right] \leq 1$$

$$0 \leq \left[1 - \frac{(\sigma_y - \sigma_{y0})K\tan\phi}{\frac{W_1 W_2 \rho g}{2R(W_1+W_2)} - (c + K\sigma_{y0}\tan\phi)}\right] < 1$$

$$\left(\sigma_y - \sigma_{y0}\right)K\tan\phi < \tfrac{W_1 W_2 \rho g}{2R(W_1 + W_2)} - \left(c + K\sigma_{y0}\tan\phi\right)$$

$$\tfrac{W_1 W_2 \rho g}{2R(W_1 + W_2)} > \left(\sigma_y - \sigma_{y0}\right)K\tan\phi + \left(c + K\sigma_{y0}\tan\phi\right)$$

Now $R = \dfrac{Effective\ \ Length}{Total\ \ Length}$

$$R = \frac{EL}{2(W_1 + W_2)}$$

$$\frac{W_1 W_2 \rho g}{2\frac{EL}{2(W_1 + W_2)}(W_1 + W_2)} > \left(\sigma_y - \sigma_{y0}\right)K\tan\phi + \left(c + K\sigma_{y0}\tan\phi\right)$$

$$\tfrac{W_1 W_2 \rho g}{EL} > \left(\sigma_y - \sigma_{y0}\right)K\tan\phi + \left(c + K\sigma_{y0}\tan\phi\right)$$

$$\tfrac{EL}{W_1 W_2} < \frac{\rho g}{\left(\sigma_y - \sigma_{y0}\right)K\tan\phi + \left(c + K\sigma_{y0}\tan\phi\right)}$$

Now if the effective length was expressed as:-

$$EL = \alpha W_1 + \beta W_2$$

$$\tfrac{\alpha W_1 + \beta W_2}{W_1 W_2} < \frac{\rho g}{\left(\sigma_y - \sigma_{y0}\right)K\tan\phi + \left(c + K\sigma_{y0}\tan\phi\right)}$$

$$\frac{\alpha}{W_2} + \frac{\beta}{W_1} < \frac{\rho g}{\left(\sigma_y - \sigma_{y0}\right)K\tan\phi + \left(c + K\sigma_{y0}\tan\phi\right)}$$

$$\frac{\alpha}{W_2} < \frac{\rho g}{\left(\sigma_y - \sigma_{y0}\right)K\tan\phi + \left(c + K\sigma_{y0}\tan\phi\right)} - \frac{\beta}{W_1}$$

$$\frac{\alpha}{W_2} < \frac{W_1 \rho g - \beta\left[\left(\sigma_y - \sigma_{y0}\right)K\tan\phi + \left(c + K\sigma_{y0}\tan\phi\right)\right]}{W_1\left[\left(\sigma_y - \sigma_{y0}\right)K\tan\phi + \left(c + K\sigma_{y0}\tan\phi\right)\right]}$$

$$W_2 > \frac{\alpha W_1 \left[\left(\sigma_y - \sigma_{y0} \right) K \tan\phi + \left(c + K\sigma_{y0} \tan\phi \right) \right]}{W_1 \rho g - \beta \left[\left(\sigma_y - \sigma_{y0} \right) K \tan\phi + \left(c + K\sigma_{y0} \tan\phi \right) \right]} \qquad \ldots(2.26)$$

Equation 2.26 is a general solution and may be applied to any exposure combination. Appendix 2 shows the solutions for the various cases.

2.6.2 Numerical Modelling

With the development of higher powered and more affordable computers, numerical methods have been increasingly utilised in backfill design to identify areas of potential instability. Zones of induced stress were first modelled using simple two dimensional programs such as FLAC, PCBEM, and more recently three-dimensional software such as FLAC^{3D}, ABAQUS and ELFEN codes are being used. The output of these models being subsequently validated by comparison with in-situ measurement using extensometers, stress meter, pressure cells etc.

The stability of cemented hydraulic fill at Mount Isa Mines was modeled using the finite element program TVIS, by Bloss (1992). The stress distribution and stability of the fill mass due to exposure were predicted during the sequential phases of the backfilling cycle (i.e. filling, exposing and re-support). This was successfully achieved by activating and de-activating discrete rows of elements through the stope. To model excavation all the nodes were deactivated, conversely to model filling nodes were systematically activated upwards through the stope. Curing of the fill was modeled by the manipulation of boundary conditions and fill modulus values of individual elements. Rigid nodes were used to characterize the fully cured paste in contact with rock boundaries, and free nodes along the wall represented wall exposure.

Stresses throughout the entire filling and extraction process were predicted using this program. The modelled stope was 40m x 40m x 200m tall. The stress history central to the plan of the stope and 40 meters from the base of the stope is shown in Figure 2.28. A simple comparison between the depth stress function ($\sigma_v = \rho gh$) and the vertical stress within the stope, shows the development of and extent of the effects of arching down almost the entire length of the stope. For example, at the end of lift 7, the stress, if calculated using the depth stress function, $\sigma_v = \rho gh$, would be equal to 1.8*t/m ^{3} *9.81 m/s^2 *(7 lifts* 14 m thick/ lift) = 1730 kPa, as shown in Figure 2.28. Whereas, including the effects of arching the vertical stress predicted was 750 kPa. Arching reduced the vertical stress to one, which equates to an equivalent stope with only three overlying lifts.

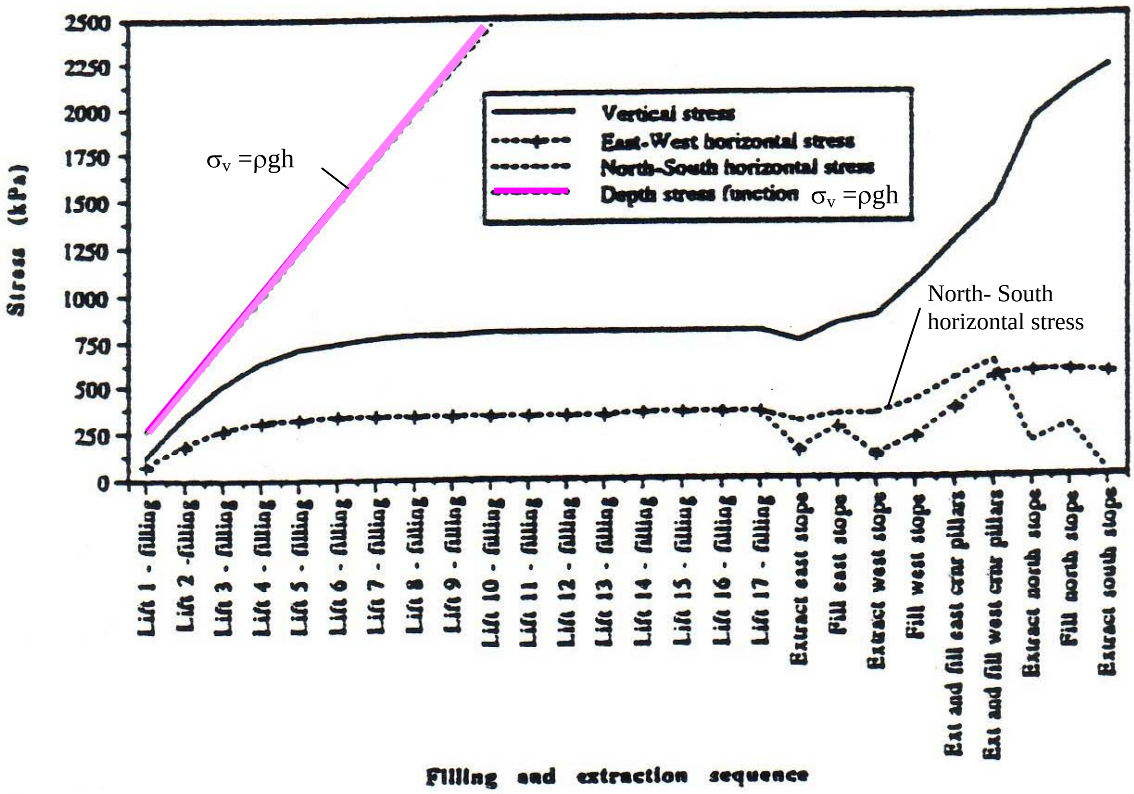

Figure 2. 28 Stress versus filling and extraction sequence (Bloss 1992)

The results included the following observations:

(a) Increased binder content resulted in increased stability

(b) Stability of exposures with a constant height is decreased with an increase in exposure width

(c) As more faces get exposed, the less stable the fill mass becomes, and

(d) The onset of surface failure occurs prior to major failure.

A later version of the TVIS program was used by Bloss and Greenwood (1998) to model stresses during a sequence of two extractions. It was found that an overestimate of the vertical stress had resulted from an underestimate of the degree of horizontal confinement acting upon the primary fill mass. From the analysis, it was shown that arching was still evident within the fill mass even after the progressive exposure of all four sides. It is thus regarded as the dominating factor with respect to fill stability.

Winch (1999) developed a spreadsheet to describe the stability of paste fill based Terzaghi's arching theory discussed previously. Stability was expressed as a function of the stope geometry, geotechnical properties and the exposure history of the fill mass. Baldwin and Grice (2000) has reported a similar model based on earlier work by Bloss (1992).

Pierce (1997) investigated the effects of stability for exposure and various closure strains and the potential for liquefaction of backfilled stopes in undrained loading. He used the following primary parameters in his analysis:- stope widths:- 5, 10, 20 and 30 m; cement contents of 3% wt, 5% wt, 7% wt (50:50 NPC:FA); and cure times of 28, 56, and 112 days. Stope closure strains were investigated for values of 0.33% to 2%.

Pierce (1997) compared the results for stability of an exposure backfill face from an analytical solution (vertical fill face) to those obtained by using a three-dimensional FLAC ^{3D} numerical model. Both models compare favourably with each other in predicting the onset of failure, however only the FLAC^{3D} model was able to predict the depth of failure and the failure mechanism. Pierce (1997) found that the depth of failure was reasonably insensitive to the degrees of binder content and that paste failed according to the "sliding block mechanism" proposed by Mitchell et al. (1982).

Pierce (1997) also investigated the response of the paste filled stopes to various degrees of closure, with closure strains ranging from 0.33% to 2%. To model the closure strains, Pierce (1997) fixed the floor of the stope and one of the sets of opposing walls. The other set of opposing walls were moved inwards as rigid plates. The walls were moved a specified distance towards each other within the fill. Displacements cannot be directly modelled by FLAC^{3D}, so, a very slow inward velocity was applied to the walls for a specified number of steps was used. The specified displacement for each wall was 5 cm, implying 10 cm total closure applied to the stope. This level of displacement was held constant over the various stope widths to investigate the effect of the degree of closure on stability. Closure strains ranged from 0.33% for a 30 m wide stope to 2.0% for a 5 m wide stope. The effect of inducing closure on a stope is to increase the stress perpendicular to strike at the face of the fill. At smaller closure strains the major principal stress remains vertical and the increase in horizontal stress improves stability of the fill mass. However, once the major principal stresses are rotated to horizontal the fill face is compressed in an unconfined compressive state thus reducing stability. Application of 2% closure strain caused unconfined failure on the free face in all cases. The increase in binder content, and thus stiffness, also resulted in an increased level of induced stress.

The liquefaction potential of the stopes due to undrained loading conditions was also investigated using $FLAC^{3D}$. Pierce (1997) who cited numerous difficulties that opposed accurate numerical modelling questioned the assumption of an “undrained” condition. Some of these included the uncertain rates of closure, unclear drainage path lengths and a reasonably ambiguous value of c_v for the Golden Giant Mine paste backfill. From the analysis it was found that the liquefaction potential for a fill mass with at least 3% binder at cure times of greater than 28 days is very low.

2.6.3 Physical Modelling

Very limited scale modelling on cemented backfill has been done. Mitchell (1982) conducted 26 small-scale model tests to verify his proposed 3-dimensional analytical solution given by equation 2.18. Mitchell (1982) formulated dimensionless factors comprising of the cement bond shear strength, specific weight, friction angle, and height, width and depth of the stope. The reported results confirmed the 3-D analytical solution. They also suggested that arching contributes significantly to the stability of the backfill.

In the authors opinion the use of scale model testing is important, but should be used for the observation of general trends or qualitative analysis only. This is considered important, as there are a number of limitations associated with scaled laboratory including: -

- Modelling of cohesion. There are no reported instances of investigators being able to accurately model cohesive forces, as per those caused by cementation of a backfill mass in a static scale model. Mitchell (1982) assumed that the capillary attraction of a scale model approximated the cohesive forces of cement in the field
- Similitude of gravitational forces. Small, laboratory scale models of geotechnical structures, under gravity loads, lacks the proper similitude to generate the induced stresses within a fill mass. Modelling the structures in an increased gravitational field, has addressed this problem. Centrifuge testing has become a more frequently used tool in the last 50 years. Studies on the static stability of cemented backfills using centrifuge modelling have been reported in literature (De Souza et al. 2002, Dirige et al. 2002, and Mitchell 1998).

2.7 Artificial Neural Networks

Numerous investigations have been conducted in recent years to predict the strength and behaviour of mine backfills (Pierce 1997, Bloss 1992, Berry 1981). The mechanisms are not yet clearly understood nether are the contribution of attributes (binder content, solids content, grain size etc). To overcome the complexities of this issue, correlations have been made with the UCS of cast fill samples. Although the UCS tests may reflect to some degree the actual in-situ behaviour of the fills, it does not take into account the compressibility of soil or the effect of confinement, but limited by location specificity and simplifying assumptions. It was therefore necessary to develop an alternative method that is capable of resolving the non-linear response of soils and the subtle interrelationships between the large numbers of variables.

The application of artificial neural networks in geotechnical applications is increasing and includes the prediction of:- liquefaction potential (Goh 1994, 1995, 1996) pile capacities (Teh et al. 1997), settlement of shallow foundations in sands (Arnold and Sivakugan 1997, Sivakugan et al. 1998) and compressibility characteristics in clays (Arnold 1999)

Neural networks are problem-solving program, based on the structure and function of the human brain. They use a large number of simple processors called neurons. Both the brain and neural networks use acquired knowledge and data to make decisions for new problems or situations. Artificial Neural Networks (ANN's) provide a powerful and dynamic solution package for complex, multivariate problems easily and expediently.

In the case of paste fills, where geotechnical characteristics and strengths are governed by several variables, such as the cement content, solids content, curing time and particle sizing, ANN appears to offer good potential for the prediction of the fill characteristics and strengths based on the definition of input variables (%C, %S etc.). ANN's outperforms traditional regression analysis undertaken, providing an accurate and convenient solution mechanism for multivariate problems.

2.8 Summary

There has been a growing trend towards the engineering of backfills worldwide to provide a more economical solution to tailings disposal and longevity of mines. The "art" of backfills is becoming a very precise and highly engineered "science". Paste backfill provides the newest innovation in the family of backfills. The original concept of thickened tailings was proposed by Dr Eli Robinsky in the mid 1970's with the first true paste backfill system being developed at the Bad Grund Mine in Germany in 1979. Acceptance of paste backfill as a viable alternative to hydraulic slurry and rock fill, did not truly occur until the mid 1990's with the construction and successful operation of several paste backfill systems in Canada and Cannington Mine in Australia in the late 1990's. In mining circles, paste technology is still in its infancy.

A thorough review of literature on paste backfill has been provided and investigates the properties of paste using the total and effective stress analysis techniques. These analysis techniques allow for the meaningful prediction of the strength and behaviour of paste when placed underground and when under different loading conditions. A review of the static stability modelling of backfilled stopes covered:- empirical correlations, analytical solutions and more recently complex numerical models. The liquefaction potential of paste was reviewed and a very brief introduction to the use of artificial neural networks was also presented.

Chapter 3

Geotechnical Characterisation – I: Paste Fill

3.1 General

Paste Fill is a new back fill technology, with little about the geotechnical characteristics or behaviour being known. Laboratory testing was used to determine the mineralogical, chemical and physical characteristics of the paste. In-situ test results were then obtained and compared to validate the laboratory test data and provide additional information on cured paste in stopes. This chapter reports the in-depth investigations into the geotechnical characterisation of Cannington Mine's paste fill.

BHP Billiton's Cannington Mine was used as the basis for the research work, due to its proximity to James Cook University and suitability of the tailings. Cannington was the only mine on the Australian mainland using paste at the commencement of research. Henty Gold Mine in Tasmania (an additional 7000 km away) used paste backfill, however the logistics, practicality and prohibitive costs involved with the transport of tailings over any significant distances excluded any other mine as a potential source of tailings for the research. Forthwith, any reference made to "paste fill" will imply Cannington Mine paste fill.

3.2 Overview of Cannington Mine

Cannington mine is located in northwest Queensland, 200 km southeast of Mount Isa, near the township of McKinlay (refer Figure 3.1).

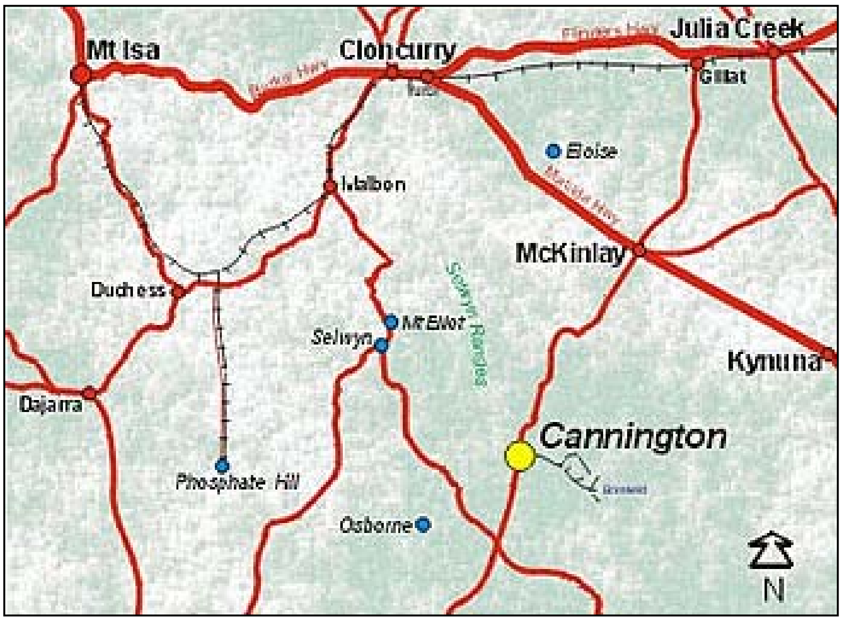

Figure 3. 1 Location of Cannington mine (BHP Billiton web page 2000)

Cannington Mine is owned and operated by BHP Billiton and is the world's largest, and lowest cost, single mine producer of silver and lead. The mine is expected to have a life of 20 years, and to have an average annual production of 750 t silver, 265,000 t lead and 111,000 t zinc.

Cannington lies in the southeast corner of the Proterozoic Mount Isa Block, within the metamorphics of the lower middle Proterozoic eastern succession and overlain by 60 meters of younger sediments. It is divided by faulting into a shallow, low-grade Northern Zone and a deeper, higher grade Southern Zone. Cannington’s major economic sulphides are galena and sphalerite. The silver occurs mainly as freibergite but is also present in solid solution within galena. A detailed description of the Cannington ore body is contained within Chapter 4, and the material data sheets for galena and sphalerite are contained with Appendix 4.2.

Mine production is approximately 6,500 tonnes per day (tpd) and is achieved by using the open stope mining method in conjunction with the post-placement of paste backfill. Paste fill is consists simply of mine tailings, with an effective grain size (D_{10}) less than 5 μm, mixed with a small percentage of binder (typically Portland cement) and water. The effective grain size of Cannington tailings range between 2 μm and 10 μm, with a weighted average of approximately 5 μm.

Open stope mining is a systematic mining method where the ore body is divided into fundamental volumetric units called "stopes" which can be approximated as rectangular prisms. The stopes at Cannington have a typical base dimension of 20 to 40 m square and height of 25 to 75 m (see Figure 3.2). The physical size of any given stope will vary depending on various factors including geometry of the local ore body, strength of the surrounding rock, residual stress conditions within the local rock and the stopes place in the removal sequence.

During the mining sequence, as ore is extracted from a stope, one or more walls may remain unsupported until all of the ore has been removed. Paste fill is then placed to fill the void and allowed to cure for a minimum period of between 14 to 28 days. The entire procedure is then repeated for the adjacent stopes. Figure 3.3 shows the plan view of the 9-stope grid arrangement. The numbers indicate the sequence in which the stopes will be systematically mined and subsequently backfilled.

Cannington initially chose to use paste as the backfill as it provided a rapid filling system, which minimised surface disposal of the tailings and reduced the environmental impact associated with mining.

Preliminary research has typically focussed on the preparation and transportation of paste rather than it's cured geotechnical properties. In the absence of any detailed information on the development of paste fill's strength and deformation characteristics, initial backfill designs are likely to be conservative. To optimise fill mixes and to ensure safe engineering practices at Cannington, a more detailed laboratory testing program was undertaken.

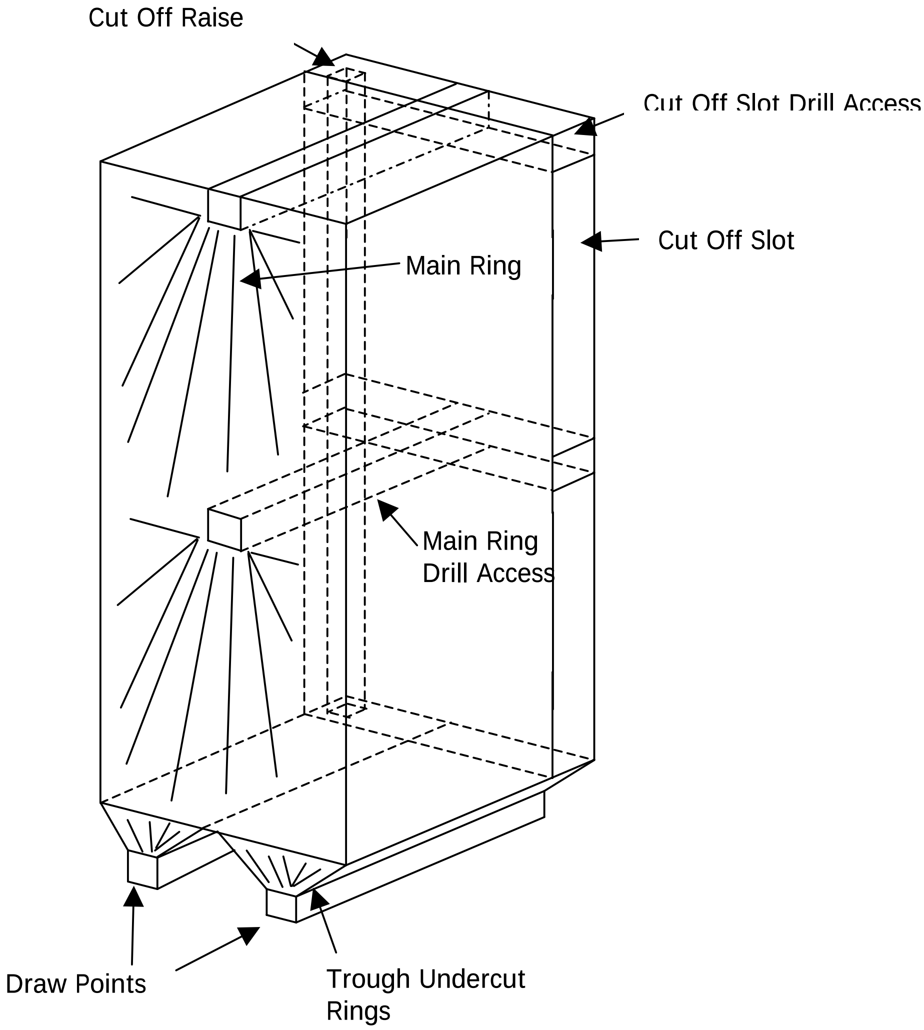

Figure 3. 2: Idealized stope arrangement (Bloss and Morland 1995)

Tertiary **6**	Secondary **5**	Tertiary **4**
Secondary **3**	Primary **1**	Secondary **2**
Tertiary **9**	Secondary **8**	Tertiary **7**

Figure 3. 3 Plan view of an ore body showing a typical stope extraction sequence in a nine-stope grid arrangement

3.3 General

To understand the behavior of paste fill it was considered pertinent to investigate the behavior of its base components (tailings and cement) separately. Cement, is typically used as the binding agent in paste. There are two processes affecting strength gain (hardening of cement and curing conditions) and two that affect the loss of strength over time (sulphate attack and self-desiccation). These processes have been simplified and discussed briefly.

3.3.1 Hardening of Portland Cement

Portland cement is basically a mixture of calcium silicates, consisting mainly of tricalcium silicates (C_3S) and dicalcium silicates (C_2S). Tri calcium aluminate (C_3A) and alumino ferrites (C_4AF) are also present to a lesser degree.[1]

In cement there are two main reactions which dominate the strength attainment of the fill, they are the:

1. Aluminate hydration (short and immediate strength gain)
2. Silicate hydration (long and on-going strength gains)

The setting of portland cement is predominantly related to the hydration of the silicate compounds.

Aluminate Hydration

The aluminate hydration reaction occurs in the very early stages of the hardening process (minutes to hours) and is responsible for the setting properties of the cement during this time. The aluminate hydration process is greatly affected by the presence of gypsum. In the absence of gypsum, C_3A reacts violently with water to cause immediate setting of the paste (i.e. “flash set”). When gypsum is present, it reacts with C_3A to form calcium trisulpahte aluminate hydrate or “ettringite” (refer equation 3.1),

[1] *For matters of simplicity the oxides of calcium, silicon, aluminium and iron will be represented by C, S, A and F respectively. Water is represented by as H also. This convention will be held consistently throughout.*

which after all the gypsum is used reacts with more C_3A to form mono sulphate hydrate (refer equation 3.2). A flow diagram showing the two step reaction for Aluminate hydration is shown in Figure 3.4.

CALCIUM ALUMINIATES + **GYPSUM** + **WATER** → **ETTRINGITE**

$C_3A + 3(CaSO_4.2H_2O) + 32H \longrightarrow C_3.A.3(CaSO_4.2H_2O).H_{32}$ …(3.1)

ETTRINGITE + **CALCIUM ALUMINIATES** + **WATER** → **MONO-SULPHATE HYDRATE**

$C_3.A.3(CaSO_4.2H_2O).H_{32} + 2C_3A{+}4H \longrightarrow C_3.A.(CaSO_4.2H_2O).H_{12}$ …(3.2)

Figure 3. 4 Flow diagram for the Aluminate Hydration Reaction

Silicate Hydration

The silicate hydration reactions occur over the medium to long term (hours to months). In the hydration of silicates the calcium silicates combine with water to form a calcium silicate hydrate gel (cement gel) and calcium hydroxide. Figure 3.5 shows the flow diagram associated with the silicate hydration reaction.

CALCIUM SILICATES + **WATER** → **CSH* GEL** + **CALCIUM HYDROXIDE**

* CSH = Calcium-Silicate-Hydrate = $C_3 S_2 H_3$

$2C_3S + 6H \rightarrow C_3S_2H_3 + 3CH, \Delta H = 120$ cal/g …(3.3)

$C_2S + 4H \rightarrow C_3S_2H_3 + CH, \Delta H = 62$ cal/g …(3.4)

Figure 3. 5 Flow diagram of silicate hydration in cement

The tricalcium silicate (alite) is hydrated to produce calcium silicate hydrates, lime and heat: The CSH has a short-networked fibre structure, which contributes to the hardening of the cement in the early to medium stages (i.e. hours onwards).

Tricalcium silicate + water → calcium silicate hydrate + lime + heat

$2C_3S + 6H \rightarrow C_3S_2H_3 + 3CH, \Delta H = 120$ cal/g …(3.5)

The belite (dicalcium silicate) also hydrates to form calcium silicate hydrates and heat.

Dicalcium silicates + water → calcium silicate hydrate + lime

$C_2S + 4H \rightarrow C_3S_2H_3 + CH, \Delta H = 62\ cal/g$ …(3.6)

As in the alite reaction, generates less heat and proceeds at a slower rate than the belite reaction, meaning that the contribution to the strength is slower. However it is this reaction which is responsible for the long-term strength of portland cement (days to months).

Hardening of cement results in the production of heat and a reduction in overall volume. This reduction in volume is known as "chemical shrinkage" and results from the water taking up a smaller volume once chemically assimilated into the cement gel, than was originally occupied as "free water". This chemical shrinkage typically results in a reduction of volume of approximately 10%. The hydration of cement is an exothermic reaction and is summarized in Figure 3.7 and Table 3.1.

3.3.2 Curing of cement

The curing of cement typically refers to the environment under which the hardening of cement has taken place (temperature and humidity). Slightly elevated temperatures and high levels of humidity are the preferred curing environment for cement. Paste fill cures underground, in stopes at approximately 38 C and 95% -100% relative humidity, which provides the preferred curing conditions.

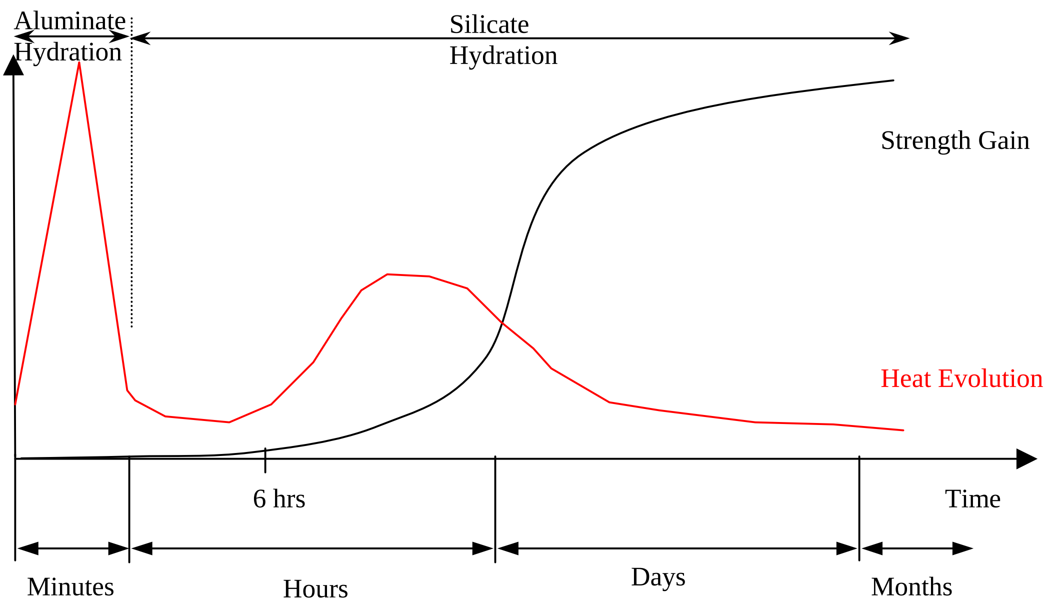

Figure 3. 6 Representation of the strength gains and heat evolution typical during the hardening of cement.

Table 3. 1 Summary - Physical Processes of the Hardening of Cement

	Physical Process	
Timeframe	**Strength Gain**	**Heat Generation**
Minutes	Ettringite Formation	Rapid exothermic reaction of Ettringite formation
Hours	**<2 hrs** Gelatinous envelopes of hydrate material form around cement particles. Cement can be broken and will reform, gain strength as cement grains re-coagulate **3-5 hrs** Irreversible hardening of paste occurs. Gel of hydrate material around cement particles start to form tubular fibrils of hydrated calcium silicate	Cement particles are coated in gel, reducing heat evolution until CSH and CH form (increased heat produced – second peak)
Days	Continued hardening of cement through fibril formation	Reduced heat generation – slowing down of hydration process
Months	Continued, but slowed, strength gain through fibril formation	Reduced heat generation –hydration process well advanced

All samples used in laboratory testing were cured at 38 C and at 100% relative humidity to match the in-situ conditions. The procedure for the preparation of tailings and curing of samples has been summarised and outlined in Appendix 3.1.

3.3.3 Sulphate Attack

The chemical degradation of the paste occurs due to the presence of fine-grained reactive solids such as sphalerite and pyrrhotite, which makes it susceptible to degradation by oxidation. The process of sulphide oxidation is commonly known as "sulphate attack" and is an acid producing reaction in the presence of water and oxygen. Oxidized mineral grains lose some of their mechanical strength by conversion to microcrystalline or amphorous oxides, and the acid produced in the reaction attacks the Portland cement. This process will reduce overall strength, cohesion, and friction angle by the reduction of the effective binder content. The chemical reactions involved in sulphate attack are described below.

Sulphide oxidation:

$ZnS+2O_2+H_2O \rightarrow ZnO + 2H^+ + SO_4^{2-}$ (Acid formation) …(3.7)

Cement dissolution[2]*:*

$6H^+ + 3CaO.SiO_2 \rightarrow 3Ca^{2+} + 3H_20 + SiO_2$ …(3.8)

3.3.4 Self Desiccation

As desiccation is associated with a lack of available moisture for hydration (such as in the production of high-performance concrete with low initial water cement ratios, <0.38). This results from the water contained in the capillary pores to be reduced through the formation of cement gel and internal stresses to be generated. When these internal stresses are greater than the strength of the soil structure – self desiccation occurs. Paste fill is considered a very low risk to degrade from self-desiccation.

3.4 Mineralogy

The mineralogy of the paste fills was studied using scanning electron microscope (SEM), and X-Ray Fluorescence (XRF) techniques. The SEM was used to identify

[2] *$3CaO.SiO_2 = C_3S$ = tricalcium silicate, which is a major component in cement*

features of the microfabric of the paste and the XRF was used to identify the mineralogical composition.

3.4.1 Microfabric Studies

The microfabric of the paste was investigated using a SEM and observations were made of the physical changes that occurred in different fill mixes over time. These included the grain shape, size, presence and magnitude of voids. Two cement contents were used (2% and 6%) to identify the changes in the microfabric structure associated with the cement content. Only qualitative trends could be observed, as individual samples could not be re-used to investigate qualitative trends as the electron beam that is used to investigate the samples and the continuous exposure to air dry out the paste significantly, modifying the curing conditions of the paste. Table 3.2 shows the qualitative trends observed for the paste fills over time.

Table 3. 2 Qualitative trends observed for paste fill samples using the SEM.

Factor	Description	Time dependent
Particle		
Size	Particles remained well graded for all samples. Av. Size 40 – 50 μm. Some large localised grains which appeared to be heavy minerals	No
Shape	Sub-angular, Flakes in some instances.	No
Voids		
Size	Varied significantly. Appeared to be reasonably well packed – no marco size air voids observed, typically voids on micro scale.	No
Quantity	Appeared reasonably consistent over observation time. Slight decrease in observable void space with cement fibrils covering voids.	Yes - indirectly
Cement Bond Development	Small fibrils/ protuberances identified after 1-3 days. Appeared to occur earlier for high cement contents – although may have just been abundance of fibrils Protrude like fingers between particles, when developing, many fibrils together appear to have the texture of cotton wool.	Yes

Figure 3.7 shows a scanning electron microscope image of the tailings (a) and cemented backfill (b). The lighter portions in the photo (a) indicate heavier ionic compounds (heavy metals). The filamentous cement bonds can be seen in the cracks shown in photo (b). The specific gravity of the tailings was measured as 3.20, reflecting high content of heavy metal in the tailings.

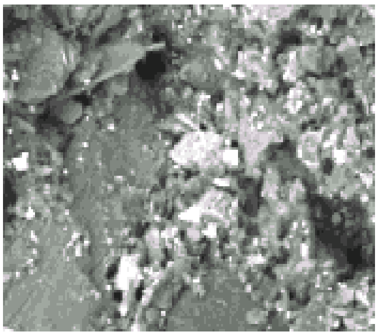

(a)

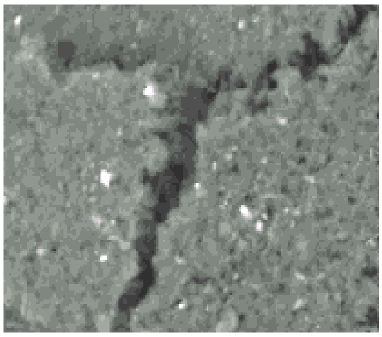

(b)

Figure 3. 7. Scanning electron microscope images (a) tailings only (b) paste fill mix (6% cement, 76% solids)

3.4.2 X- Ray Fluorescence Analysis

The mineralogical properties of the tailings were identified using X-ray fluorescence (XRF) analysis technique. The analysis was performed periodically over 10 months to identify any variations in the mineralogical compositions. The mineralogical composition of the tailings was observed to be very consistent. Tables 3.3 show the mineral elements of the tailings. Empirical correlations, developed on-site, were used to generate the proportions of parent materials shown in Table 3.4

Table 3. 3 Mineral Elements of Cannington tailings (XRF analysis)

	% Composition for Month						
Element	**Jul-00**	**Sep-00**	**Nov-00**	**Jan-01**	**Mar-01**	**May-01**	**Average**
Ag	0	0	0	0	0	0	0
Pb	2.110	2.140	2.060	2.070	2.100	2.150	2.105
Zn	0.772	0.777	0.744	0.747	0.769	0.759	0.761
Fe	17.300	17.300	17.100	17.200	17.200	17.300	17.233
S	2.650	2.670	2.590	2.580	2.690	2.720	2.650
Cu	0.015	0.013	0.014	0.019	0.012	0.011	0.014
Sb	0.029	0.036	0.031	0.029	0.027	0.030	0.030
As	0.188	0.180	0.193	0.194	0.180	0.182	0.186
SiO_2	47.400	47.100	46.900	46.800	46.400	46.600	46.867
CaO	N/ A	N/A	8.630	8.660	8.670	8.770	8.683
MgO	2.420	2.440	2.410	2.400	2.450	2.510	2.438
Al_2O_3	3.080	3.020	3.100	3.040	3.020	3.070	3.055

Table 3. 4 Typical mineralogical composition of Cannington Tailings

Minerals	% Mineral composition of tailings for the Month						
	Jul-00	**Sep-00**	**Nov-00**	**Jan-01**	**Mar-01**	**May-01**	**Average**
Silver Minerals	0.0	0.0	0.0	0.0	0.0	0.0	**0**
Galena	2.4	2.5	2.4	2.4	2.4	2.5	**2.4**
Sphalerite	1.3	1.3	1.3	1.3	1.3	1.3	**1.3**
Iron Sulphides	39.7	39.6	39.2	39.4	39.4	39.5	**39.5**
Talc	11.0	11.1	11.0	10.9	11.1	11.4	**11.1**
Other silicates	41.2	40.9	40.8	40.7	40.2	40.2	**40.7**

The predominant waste products are the silicates (mostly quartz), together with magnetite and minor pyrrhotite (both of which are types of iron sulphide). Paste fill is slightly magnetic. The 5% deficit in the total composition is thought to consist primarily of oxides (Al_2O_3) such as Chalcopyrite etc. and the errors associated with the empirical relations.

3.5 Physical Properties

Paste fill consists of a bonded soil skeleton, air and water. The added binder causes significant changes in the nature and behaviour of the soil skeleton over time. It was considered important to investigate these changes and the reasons for them. The determination and analysis of the physical and index properties was used to provide the basis for the changes.

3.5.1 Grain Size Distribution

The grain size distribution (GSD) plot is a basic geotechnical property and indicator of a soils engineering performance. It should be noted the grain size distribution is used predominantly for coarse grained soils and very rarely for fines. It has been included so that a basis for comparison to other tailings grinds and fill mixes can be made. Figure 3.7 shows the grain size distribution curve of the tailings, and granulated cement used in the manufacture of paste. The combined GSD curves for the cemented paste samples has not been included on the diagram, as it is not considered likely to deviate discernibly from the sizing curve for the tailings.

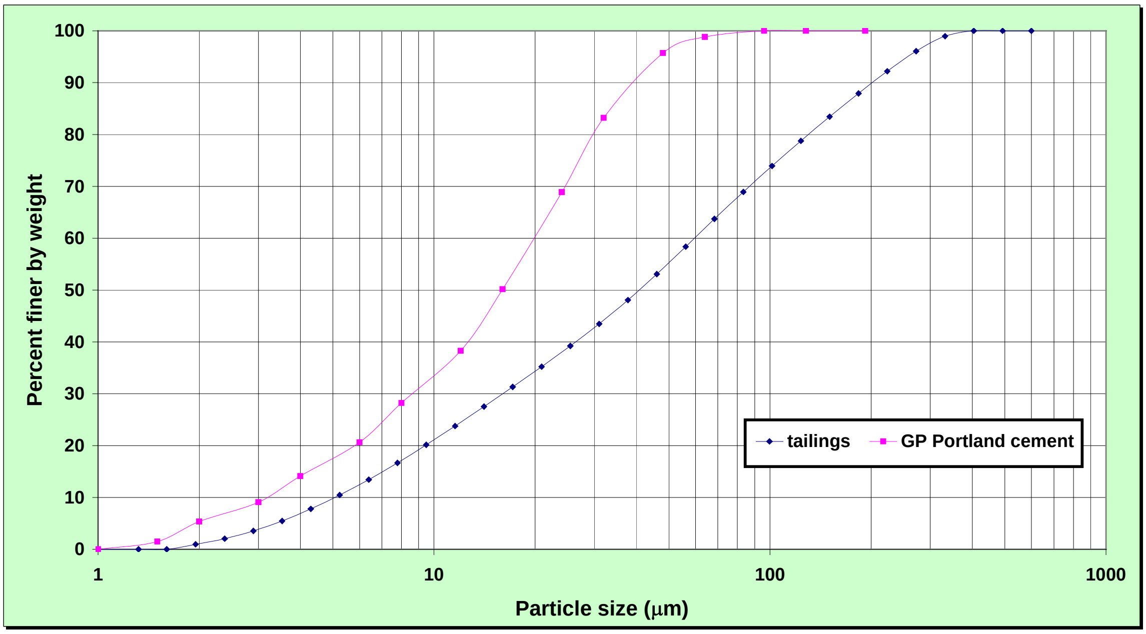

Figure 3. 8 Grain size distribution plots for Cannington tailings and QCL type GP Portland cement

The determination of the grain size distribution of the tailings was done using laser diffraction, as it was found to provide superior results to sieve and hydrometer analysis. This is consistent with the findings of Wen. et al. (2002) who suggested that the sieve and hydrometer analysis suffers from inconsistencies in sizing when changing from the sieves to hydrometer.

To test the variation of the grind size[3] of the tailings, a review of the P80 grind size, as produced by the mill, was conducted. Figure 3.10 shows the variation of the P80 grind size for the mill, over two years. "P80" is the grind size at which 80% of the material is finer and is equivalent to the D_{80} of a soil in geotechincal terms.

The line of best fit for the P80 grind size shows has slowly reduced from a P80 of 108 μm (Oct-2000) to the current 104 μm (Oct-2002). The moving average moves between a maximum of 132 μm to a minimum of 75 μm. A statistical analysis was performed to identify the likelihood of such grain size fluctuations. The results are shown in Table 3.6.

[3] The variations in ore type, hardness, mill throughput and grind time will all affect the average size of the tailings grind.

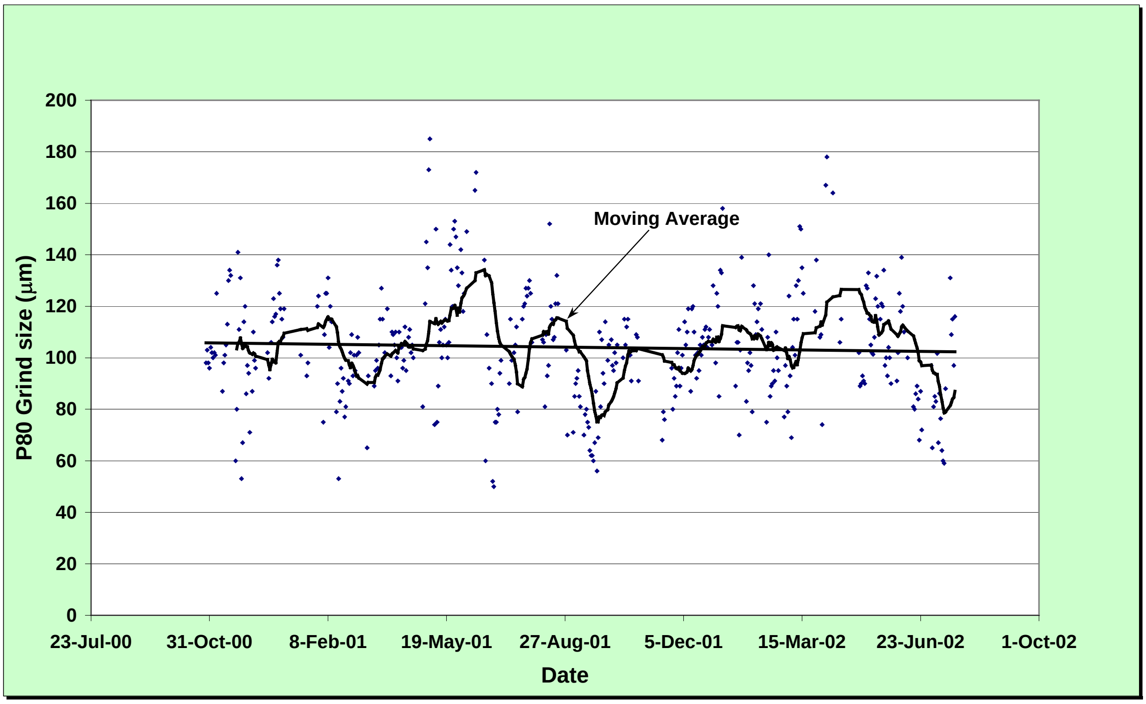

Figure 3. 9 Variation of P80 grind size time for Cannington Tailings

Table 3. 5 Confidence intervals for the P80 grain size at BHP Cannington Mine (mean =104.04 µm, Std. Deviation = 21.88 µm).

Confidence Level	Min Particle Size (µm)	Max Particle Size (µm)
95%	101.71	106.37
90%	102.08	105.99
85%	102.33	105.75
80%	102.51	105.56

The variation of only 5 µm for a confidence level of 95% was shows the consistency of the produced tailings. The fluctuations observed in Figure 3.9 are thought to represent the extremes of the grain sizes recoded and were plotted automatically by Microsoft Excel to provide the greatest contrast to the data set.

The variation of only 5 µm for a confidence level of 95% suggests that a “representative” tailings grading would have a P80 of 105 µm +/- 5 µm. Indeed the tailings tested as part of this research project are consistent with the “representative case” with a P80 of approximately 105 µm (see Figure 3.9).

3.5.2 Specific Gravity

The specific gravity (SG) of the tailings was found in accordance with the current Australian Standard (AS 1289.3.5.1-1995) and the MSDS for the supplied cement. A SG of 3.20 was considered representative of the tailings and 3.10 for the Portland cement. The results from SG testing on the tailings has been included as part of Appendix 3.3.

3.5.3 Particle Shape

The shapes of particles can also significantly affect the engineering response of a granular soil. Using the SEM photograph of the tailings only (refer Figure 3.7 (a)) and can be identified as *flaky and angular.*

The identification of particle shape is commonly defined only for coarse grained soils. Although tailings are fine grained soils, it was considered pertinent to identify the shape of the particles as part of the micro-fabric study.

3.5.4 Index Properties

The index properties of a soil include the Atterberg limit tests as well as the phase relations. A summary test findings have been reported and additional information included as part of Appendix 3.5.

3.5.5 Atterberg Limits

The Atterberg limits tests are soil classification tests that are used to classify the fine fraction of the grain size distribution. Standardised tests, developed by A.Atterberg (1911) and further refined by K.Terzaghi & A.Casagrande (1932) include the determination of the liquid, plastic and shrinkage limits of the soil. Average values for the LL and PL were: -

Liquid Limit (LL): 21
Plastic Limit (PL): 14

Plasticity Index[4] (PI): 7

Using Casagrande's (1948) plasticity chart the tailings are classified as:-
CL-ML, low plasticity, clayey silt.

The *shrinkage limit* (SL) for the paste fill mixes was not determined in accordance with the Australian Standards, which requires samples to be oven dried at 105 C. Testing was carried out under curing conditions of 38 C and 100% relative humidity so as to identify likely shrinkages to be experienced in the field. Table 3.6 and Figure 3.10 summarise the results from linear shrinkage testing.

Table 3. 6 Progressive linear shrinkage of different paste samples

	Linear Shrinkage (%) after x days of curing				
Mix	**1**	**3**	**7**	**14**	**18**
0%, 74%	0.0%	3.6%	6.8%	6.8%	6.8%
0%, 78%	1.6%	5.2%	5.5%	5.6%	5.6%
2%, 74%	2.2%	2.6%	2.6%	2.6%	2.6%
2%, 78%	1.8%	2.4%	2.4%	2.4%	2.4%
4%, 74%	1.6%	2.0%	2.2%	2.2%	2.2%
4%, 78%	0.4%	0.8%	0.8%	0.8%	0.8%
6%, 74%	0.8%	1.2%	1.2%	1.2%	1.2%
6%, 78%	0.6%	1.0%	1.2%	1.2%	1.2%

From Table 3.6, it is shown that shrinkage within paste is complete in the cemented samples after 7 days and in all samples after 14 days. Cement and solids content restrict the degree of shrinkage that occurs. The cement content has the most immediate and profound effect on the reduction of shrinkage. The reduction in shrinkage with the addition of cement is due to the formation of a rigid, bound soil matrix which resists shrinkage. Unbound tailings show an average LS of approximately 6%. LS in paste is also limited by the curing time of the cement. From Figure 3.10, paste with cement levels above 4% resists shrinkage, limiting it to just over 1%. Anything under this requires longer periods of curing to provide sufficient resistance, resulting in larger levels of shrinkage. The expected trend line is shown as a dashed line in Figure 3.10. The slight anomaly between the mixtures for the 4% cement blends is not considered to be representative of actual behaviour.

[4] *The "Plasticity Index" (PI) is the difference between the LL and PL.*

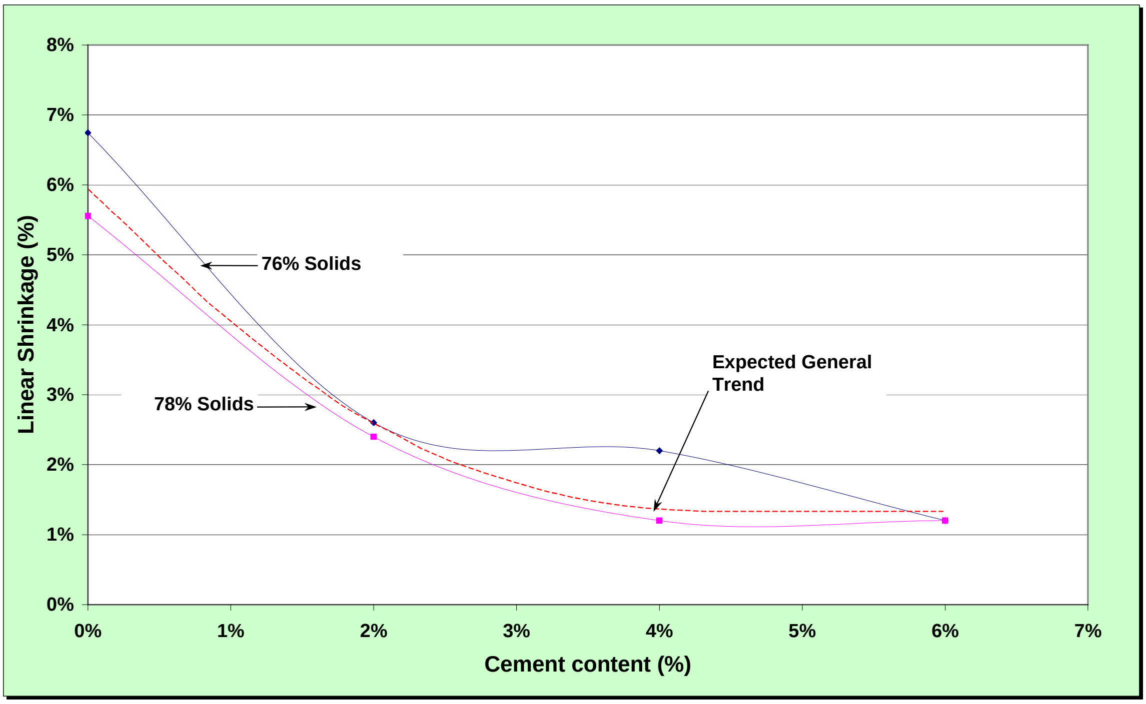

Figure 3. 10 Effect of mix proportions on linear shrinkage of paste samples (14 days curing)

The occurrence of linear shrinkage in a paste fill mass has significant effects on the stability of the backfilled stopes. This occurs in three ways.

1) When the paste has developed a rigid soil skeleton, so as to oppose the shrinkage forces, internal stresses develop which induces an internal confining stress on the fill mass, which increases the shear strength.
2) Paste fill has very low permeability. When initially, exposed a pressure differential exists between the atmosphere and the gas entrapped in the paste. This provides an effective confinement of equal to atmospheric pressure. As the gas permeates into the fill the pressure differential reduces, as does the effective confinement provided.
3) The development of the arching mechanism relies on solid wall to paste contacts so that transfer of vertical loads through shear stress to the walls may be achieved. If the integrity of the supports is violated the backfill may loose it's ability to support the vertical loads through arching. Consequently the vertical stresses within the paste fill increases significantly as to does the likelihood of failure.

In the field the effects of LS is significantly mitigated by the time taken to fill each of stope. As linear shrinkage occurs in a fill mass in the early hour of curing (<6 hrs) the paste compresses and expands laterally with the applied weight of overlying fill. The paste which is a liquid when placed is also able to flow into any openings, thus reducing the potential for "gaps" or shrinkage cracking to occur.

3.5.6 Zeta potential

The Zeta potential is a measure of the net (usually negative) electrostatic potential of a molecule or particle. It is concentrated at the surface of the particle, as shown in Figure 3.11 and reduces with distance from the charged surface. The magnitude of the Zeta potential correlates to the magnitude of the repulsive forces between particles, and as such, it influences the rheological characteristics significantly. A high negative zeta potential results in the particles flowing over each other more freely, reducing material yield stress and viscosity.

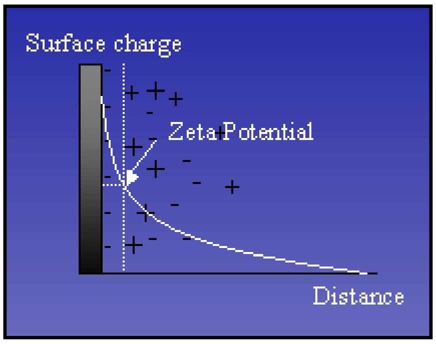

Figure 3. 11 Zeta potential profile for a charged particle

Figure 3.12 shows the effect on the zeta potential of materials varying the concentration of additives or material pH. The zeta potential of the Cannington tailings is approximately 17mV at a pH of 8 and is shown in Figure 3.12 (a) (Huynh 2003). In Geomechanics it is typically only the clay fraction that is tested for zeta potential as it is the only fraction with ionic bonding on a molecular level. Inert materials, such as quartz or gravels, have a zeta potential of 0. In mining, samples of 38 mm or less are tested for the zeta potential using an Acoustosizer.

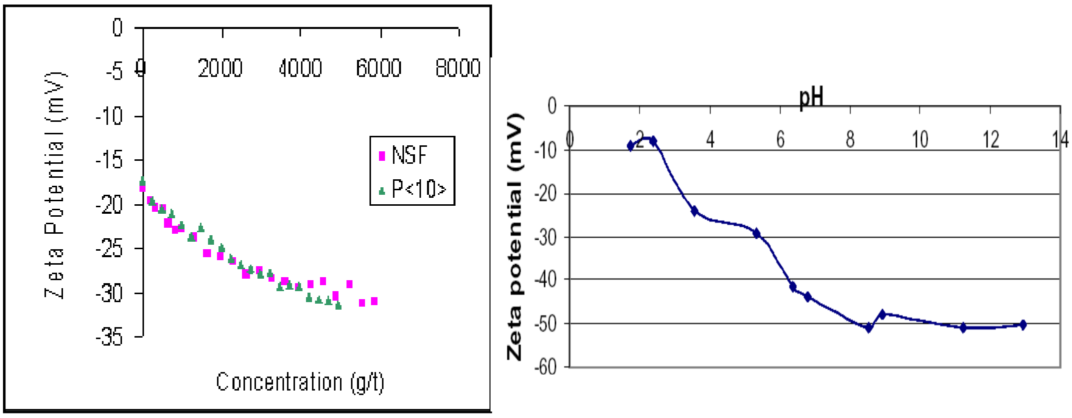

(a) (b)

Figure 3. 12 Variation of zeta potential with (a) concentration of additives (Huynh 2003) and (b) pH (Fourie 2003)

3.5.7 Phase relations

The phase relations the paste were determined and used as a basis for the explanation of the engineering behaviour. The average properties were calculated from a minimum of three samples for each mix (*x* % cement, *y* % solids) and curing time. Properties were determined for cement contents of 2% and 6% and 74% and 78%, for curing times of between seven days to 12 months. Table 3.7 shows the maximum and minimum values for each of the properties and a general trend through time. Additional summary tables of the index properties have been included in Appendix 3.3.

Table 3. 7 Trends and Range of the physical properties of paste over a 12 month period

Physical Property	Trend With Time	2%, 74%		2%, 78%		6%, 74%		6%, 78%	
		min	max	min	Max	min	max	Min	max
e	Increase	1.050	1.247	0.862	0.982	0.924	1.193	0.856	0.940
n (%)	Increase	51.2%	55.5%	46.3%	49.5%	48.0%	54.3%	46.0%	48.5%
w (%)	Decrease	26.8%	32.8%	20.0%	28.4%	6.7%	32.1%	6.7%	26.1%
S (%)	Decrease	72.8%	96.2%	66.1%	95.8%	23.3%	91.2%	23.3%	94.4%
ρ_m {t/m^3}	Decrease	1.881	2.071	1.968	2.180	1.790	2.046	1.790	2.172
ρ_d {t/m^3}	Decrease *(slightly)*	1.436	1.574	1.628	1.733	1.475	1.677	1.663	1.742
ρ_{sat} {t/m^3}	Constant	1.997	2.091	2.129	2.201	2.023	2.162	2.152	2.207
γ_m {kN/m^3}	Decrease	18.46	20.32	19.31	21.38	17.56	20.07	17.56	21.30
γ_d {kN/m^3}	Decrease *(slightly)*	14.09	15.44	15.98	17.00	14.47	16.45	16.31	17.09
γ_{sat} {kN/m^3}	Constant	19.59	20.52	20.88	21.59	19.85	21.21	21.12	21.65

The trends general trends are: -

- Void ratio and porosity increase as curing continues.
- Moisture content and saturation levels are reasonably constant for 9 months at which time they start to decrease. Higher the cement content, higher the level of moisture loss.
- The bulk modulus of the fills decreases over time but only slightly.

These general trends may all me attributed to the hydration of cement within the paste. Specifically, the increase in void ratio and porosity over time (especially after six to nine months) are due to chemical shrinkage, oxidation of the paste or simply a reduced level of free water in the fill mass after percolation and evaporation of any free water has taken place.

Related to the reduction in water content and saturation levels is the increase in air voids and void ratio. Thus as the void ratio is increased, the water content and saturation levels decrease. Figure 3.13 and additional plots A3.3.10 – A3.3.13 show a significant drop in water content after a period of nine months. This timeframe is considered to be a laboratory specific phenomenon and is likely to be associated with the oxidation, or “drying out” of the paste samples through evaporation. When the initial curing of samples commenced, each of the sample containers was sealed in three garbage bags with 250 ml of free water and an airtight seal maintained. It was observed that after 12-months a significant proportion, if not all, of the water had been completely used inside the garbage bags suggesting that the hydration of the paste used more than was in the fill alone. Field evidence suggests that this is not the case. To date, anecdotal evidence suggests that paste dries out or oxidise in the outer 300 mm on exposed faces, but has not been identified as occurring at levels any further into the fill mass than this.

The bulk density of the fill decreases slightly over time as the additional air voids decrease the overall mass of the fill. The dry density remains relatively constant throughout curing, as would be expected. Summaries of the physical properties for the fill mixes over time have been included in Appendix 3.3 in Tables A3.3.2 to A3.3.5 as well as additional plots, Figures A3.3.9 to A3.3.14, which summarise the aforementioned trends.

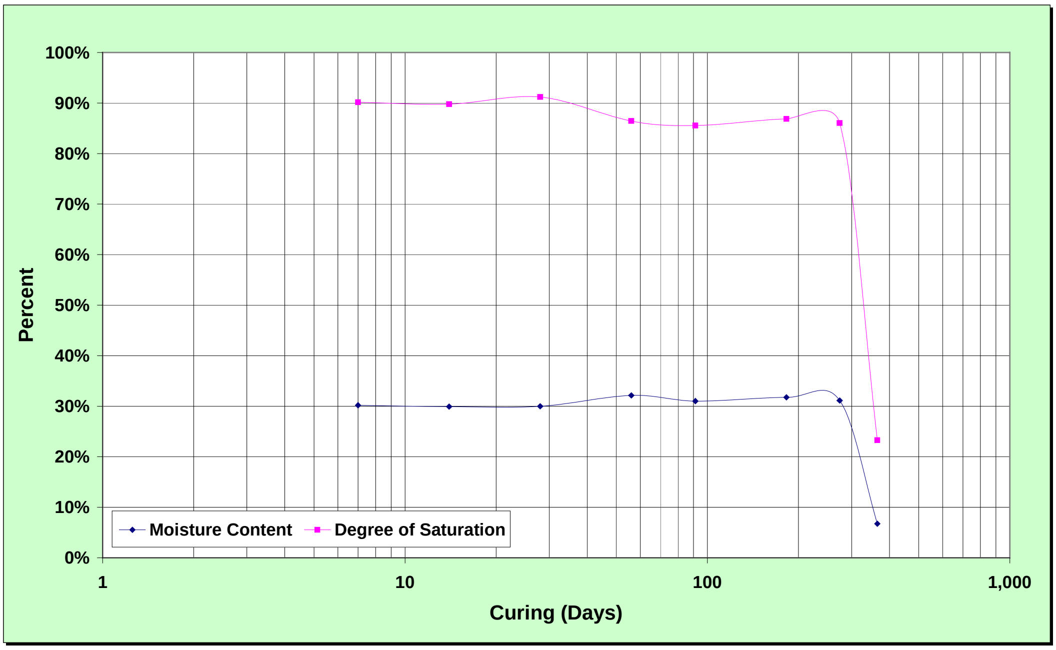

Figure 3. 13 Variation of moisture content and saturation levels of paste over time (6%, 74%)

3.6 Strength Testing

The correct determinations of strength and deformation characteristics of paste are critical to the safe and effective usage of paste as an engineered backfill material. Determinations of these characteristics were identified over three time domains (short, medium and long term) to fully characterise the progressive strength. Table 3.8 summarises the test methods and analysis techniques used for each.

Table 3. 8 Definition of timeframes and laboratory test methods used to determine the progressive strength of paste fill

Timeframe	**Short-term** (0 – 7 days)	**Medium-term** (7 – 28 days)	**Long-term** (1 –12 months)
Laboratory Testing Method	Viscometer, Shear vane Modified Pocket Penetrometer UCS	*Total Stress Analysis* Triaxial (UCS, UU) *Effective Stress Analysis* Triaxial (CD)	Triaxial (UU)
Analysis Technique	Total Stress	Total and Effective Stress	Total Stress

To date paste has been considered to be non-draining material, and thus total stress tests were initially considered most appropriate. To investigate this assumption a series of effective stress tests were also undertaken.

An effective stress analysis would typically be used to assess the long-term or drained behaviour of paste. During this testing phase it was conducted only in the medium term. This was primarily to preserve time. The CD triaxial tests give effective stress parameters which do not fluctuate with water content and are not expected to fluctuate significantly over time. A (very) slight reduction in the effective friction angle, caused by the increased effective cohesion (i.e. level of cementation) may be observed over longer curing times.

The UU triaxial testing method provided a simple and quick testing procedure, to be used to provide base line data over the 12 month period from which the behaviour of paste may be investigated.

3.7 Total Stress Analysis

3.7.1 Short Term: Early Strength of Paste Fill

Currently, there is no documented knowledge of the strength gain in paste fills during the first 24 hours of curing, yet it is critical to the understanding of the development of stresses in the fill mass. Barricade design, filling rate and early stability of the paste fill mass are all dictated by the early strength of the paste backfills. To understand how the strength of paste fill is measured whilst in the uncured form, it is pertinent to briefly review the rheology of paste.

Paste fill rheology closely conforms to the Bingham plastic flow model, which is strongly non-Newtonian in its behaviour. Figure 3.14 shows a number of fluid models and plots the change in shear stress that is experienced as a function of the shear rate. Fluids which exhibit Newtonian flow characteristics have no “yield stress” to be overcome to initiate movement and have a constant viscosity. Viscosity is defined as the rate of rise of shear stress with the increase in shear rate. Water is an example of a Newtonian fluid. Fluids exhibiting non-Newtonian characteristics are the Power Law (pseudo plastic and dilatant) flow and Bingham plastic flow regimes. Pseudo plastic fluids are characterised by the reduction of the viscosity with an increased shear rate (shear thinning), whereas the viscosity for dilatant fluids increases with an increased shear rate (shear thickening).

Bingham plastics exhibit a significant shear stress that must be overcome before movement (shearing) commences. This value of shear stress is commonly referred to as “yield stress”. Once shearing has commenced, the viscosity remains approximately linear.

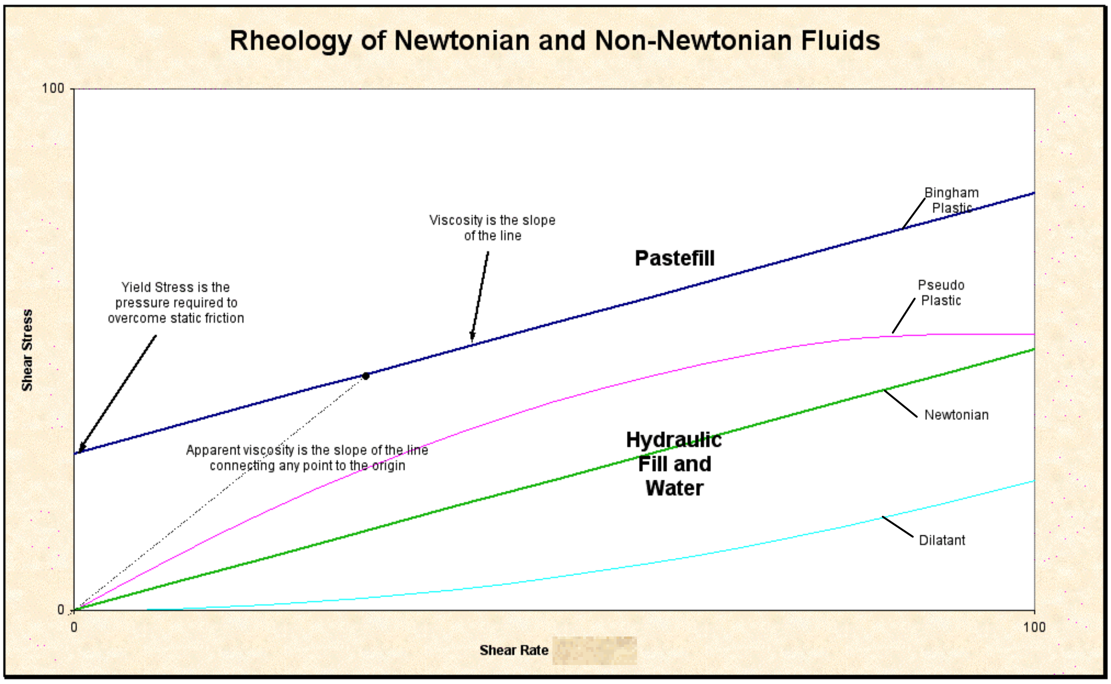

Figure 3. 14 Rheological curves for particulate fluids (Grice and Bloss 2002)

The key determinant of the rheological properties of paste fill is the yield stress. Clayton (2000), shows the yield stress to be exponentially proportional to the solids density of the mix (see Figure 3.15). The suggested relationship is defined as:-

$$\tau_o = 10^{-11} e^{39.694x} \qquad \ldots(3.9)$$

where

τ_0	=	yield stress (Pa)
x	=	% solids (expressed as a decimal)

equation 3.9 does not take the time dependant nature of paste into account, nor does it take into account the effective grind size of the parent tailings. Clayton’s (2002)

doctoral research was restricted to the determination of pipe flow characteristics of Cannington's paste, in which case, the time dependent characterisation of cemented paste fill would not needed to have been considered as the time between batching and placement is less than the time taken for the initial setting of cement to occur.

Smith (2002) addressed the effect of the cement addition and grind size on rheological behaviour of paste , but did not consider the time dependant behaviour of paste either. Smith (2002) found the yield stress and viscosity of the paste increased with cement addition and reduced particle grind size. The increase of the both parameters with cement is attributable to fine grading of the cement particles – rather than any bonding properties as all tests were conducted within 15 mins of cement being added. (Any significant bonding properties are only observed after 60 to 90 minutes). Predictably the yield stress and viscosity of the paste increased with a decreased nominal grain size**.**

The consistency of concrete is defined in terms of its slump, using the standard test procedure AS1012.3.1-1998. This was initially adopted for the determination of paste consistency on-site also. Clayton (2000) suggested that the consistency might be determined more accurately by using a 200 mm diameter cylinder. Both tests can be used to indirectly measure the yield stress, by the establishment of a suitable correlation. Figures 3.15 shows the correlation between the yield stress, paste density and cylinder slump values. Figure 3.16 shows the direct correlation between the yield stress and the cylinder slump values of the paste. The correlations shown are independent of cement content and were conducted immediately following batching.

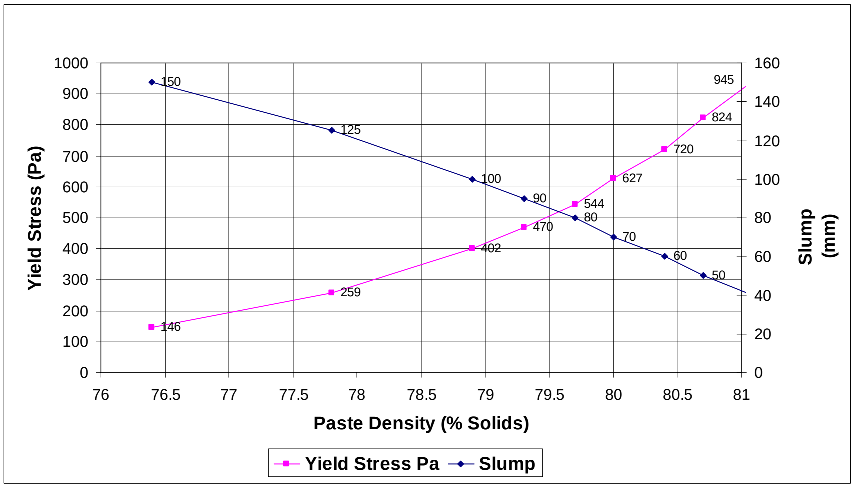

Figure 3. 15 Correlation between yield stress paste density and slump - based on a 200mm diameter x 200mm tall slump cylinder (Clayton 2000).

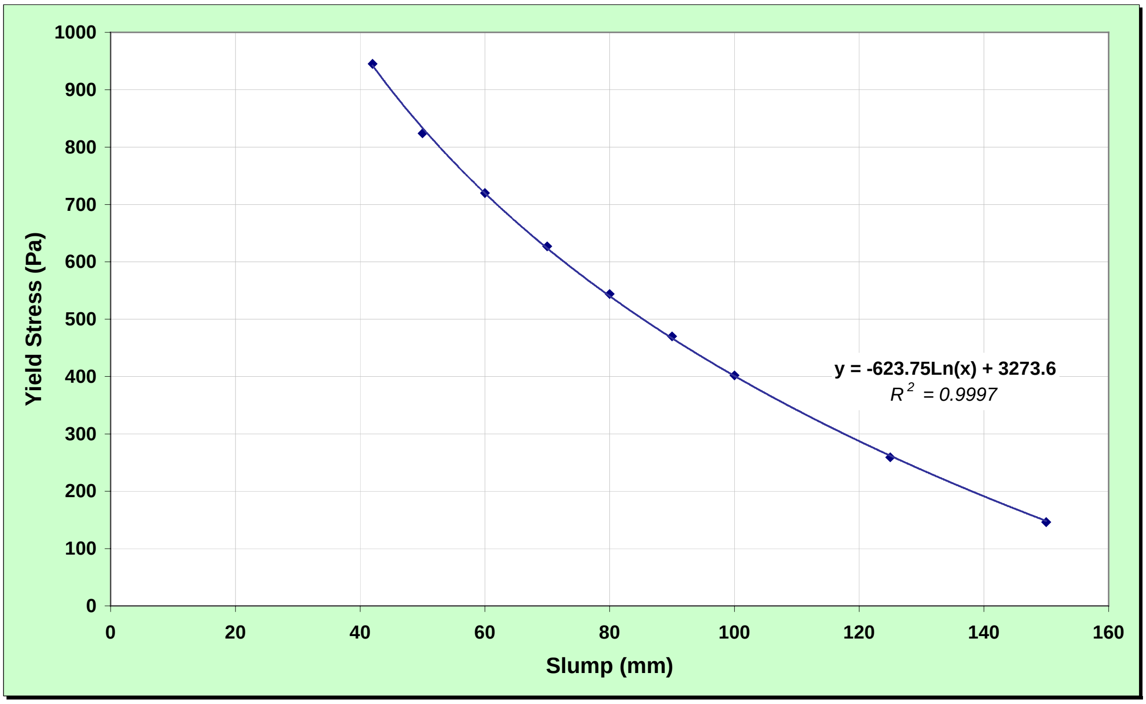

Figure 3. 16 Correlation between yield stress and 200mm diameter x 200mm tall slump cylinder

An experimental programme involving various tests was conducted to find the progressive strength of paste. Figure 3.17 shows a schematic timeline and associated test methods for paste.

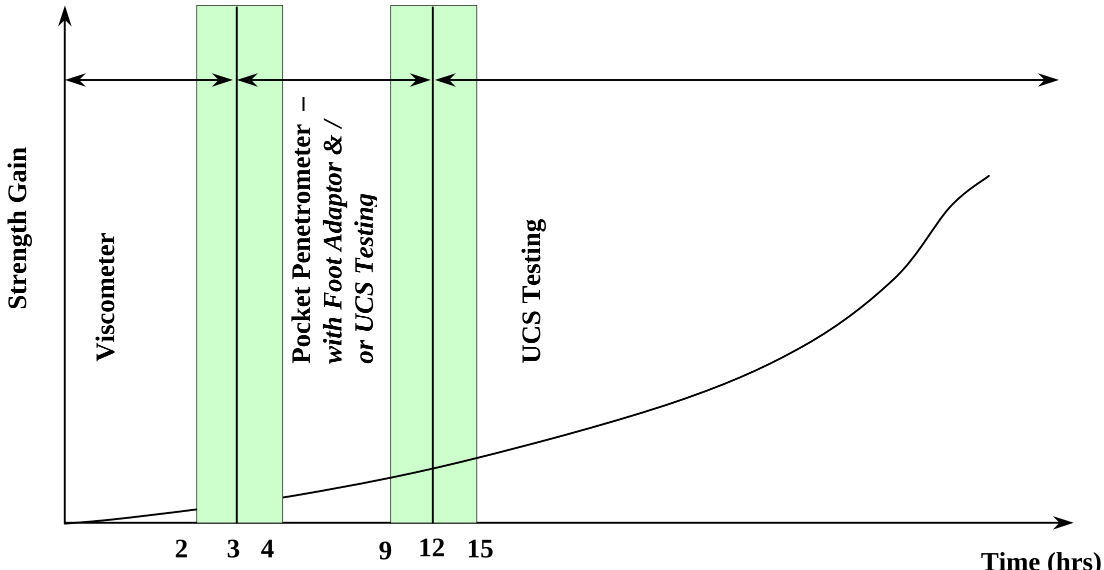

Figure 3. 17 Schematic Representation of early strength gains measurement for paste.

Testing was nominally broken into three sections, each with equipment available on-site to measure the fill strength. The shaded areas represent times at which both test methods (on either side of the line) were used to calibrate and validate the results from the other. The experimental studies on the early strength f paste were carried out to define the early strength gain curves for various fill mixes. This enabled the development of an empirical procedure to determine the final strength.

3.7.1.1 Shear Vane Testing

A mechanical shear vane was used to determine the strength gain for the paste fill based on a 3.5%, 79% solids mix. A minimum of three tests for each mix (*x*% cement, *y*% solids) and curing time were conducted and the average plotted (refer Figure 3.18). The shear stress has been plotted in log scale on the vertical axis, to allow a comparison of strengths between the various cement contents, assuming a constant solids content of 79%.

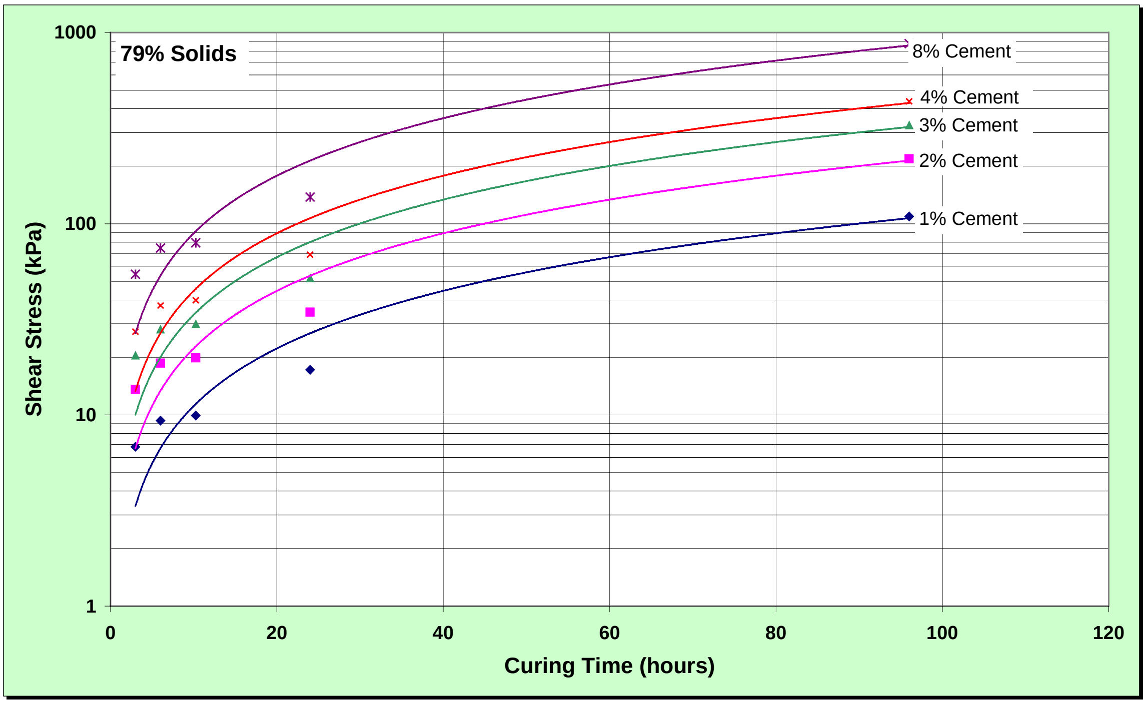

Figure 3. 18 Early Strength Gain of paste (assuming constant 79% solids content)

From the reproducibility of the strength gain trends, normalised for cement content (refer Figure 3.29) it was considered reasonable to extrapolate the results the testing on samples with a cement content of 3.5 % to other cement contents. The trends observed, although not obvious with the vertical axis being logarithmic, are strongly linear with a correlation co-efficient of r^2=0.985. The “yield stress” (i.e. shear stress at t=0) of each of the mixes can be calculated using equation 3.9. The full spreadsheet of results has been included in Appendix 3.4.

There was need to develop an intermediate stress measurement tool, to provide a means of assessing the paste strengths above the capacity of the viscometer (~1kPa) to a strength which can be readily and accurately identified by a triaxial testing machine ~ (60kPa). This was done using the Modified pocket penetrometer.

3.7.1.2 Modified Pocket Penetrometer Testing

The "modification" was an adaptor foot which is attached to the end of the pocket to effectively increase the cross sectional area of the applied load and thus increase the resolution of the penetrometer. Figure 3. 19 shows the foot attachment for the penetrometer – used to obtain the undrained shear strength of paste which lay in between the bounds of the on-site viscometer and triaxial compression testing machine.

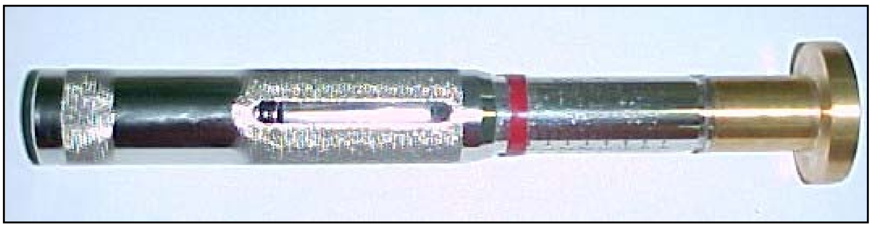

Figure 3. 19 Pocket Penetrometer and adaptor foot.

The relationship between the modified pocket penetrometer and the results from the shear vane are shown in Figure 3.20. The relationship only shows a moderate correlation between the relative strengths of the measured values (r^2=0.74) but very poor correlation between the actual magnitudes of the measured values, with the pocket penetrometer over predicting the undrained shear stress by 3.7 times. Additional work will be required in to refine and develop an adequate relationship. Possible test methods may include a larger diameter foot – to provide a finer resolution to the test work, or the correlation of undrained yield stress to penetration depth of the cone penetrometer (as is used in the determination of the liquid limits of soils).

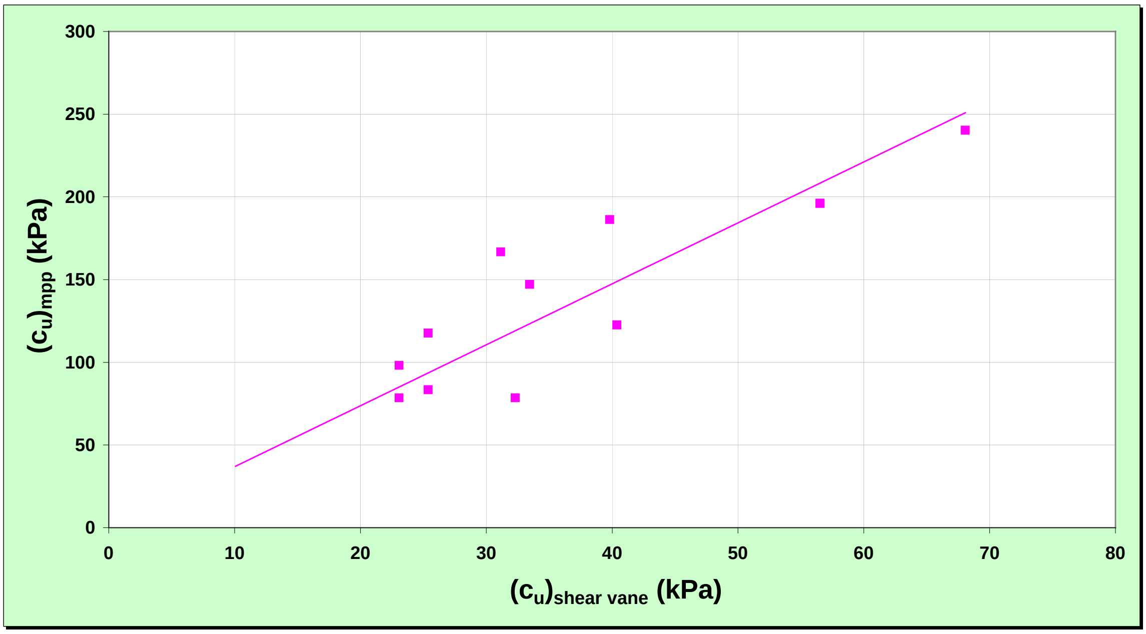

Figure 3. 20 Pocket Penetrometer with adaptor foot attachment versus mechanical shear vane readings of undrained shear strength resistance

The lower bound of approximately 25 kPa results from the initial readings being taken after three hours. Readings lower than this are expected to show the linear trend, however a larger foot may be required to ensure the resolution of the pocket penetrometer is fine enough. Readings above 60 kPa can be determined by using UCS tests.

3.7.1.3 Unconfined Compressive Strength Testing

To calibrate the modified pocket penetrometer a small number of UCS tests were conducted on paste fills cured under the same conditions and for the same length of time. Three samples were tested after one, three and five days. The results from testing are shown in Figure 3.21.

It is not possible to relate the yield stress of the initial paste mix with a final unconfined compressive strength, as there is no continuity of a mechanism "governing" strength development. In the very short term – up to periods of about two hours, the solids content of paste governs behaviour and strength of the mix. After which cement content typically governs. It is reasonable to begin the relationships back to the final UCS after the "initial set" has occurred, which is typically seen to occur in paste after approximately three to four hours.

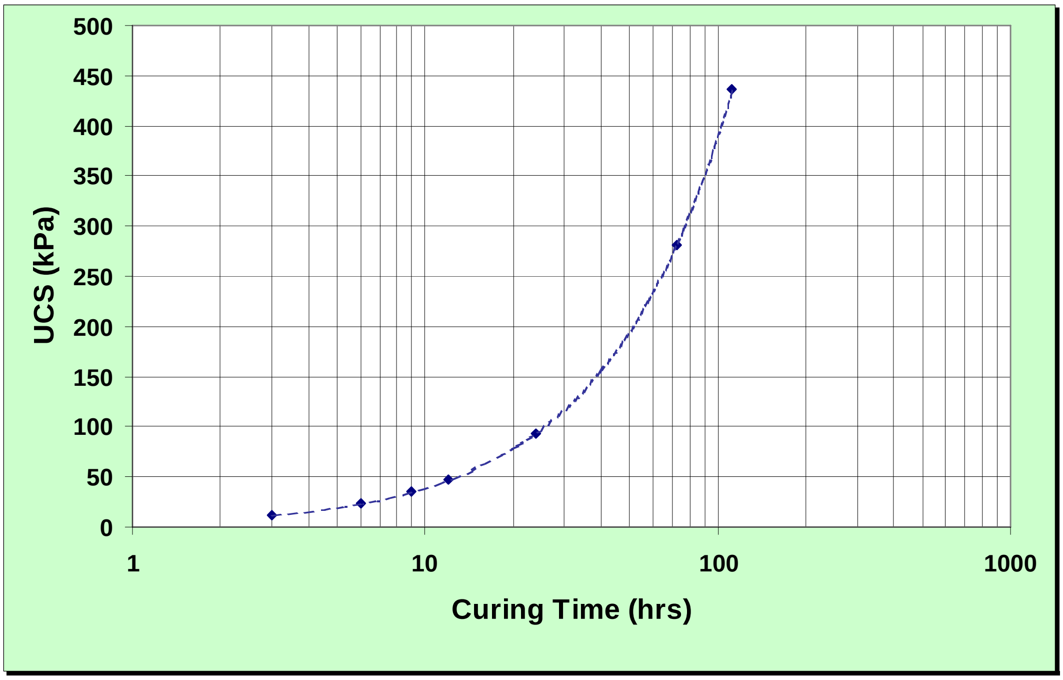

Figure 3. 21 UCS testing results of early strength of paste (3.5% cement, 79% Solids).

The variation of early strength of the paste, with curing time and cement content has been identified for a 79% solids mix and has been included in the PASTEC program (refer Chapter 5).

3.7.2 Mid-term Strength Gain of Paste Fill

Backfill designs have traditionally been based on the 28 day UCS of fill samples. This reference originated in the cement industry where the 28 day cured strength is used as a reference for cement strengths. The UCS test is simple and easy to conducts on site with very basic equipment and is used as a reference test as the fill at the base of an exposed face is considered to be in a predominantly unconfined state. Hence once the UCS of the material is reached, failure is deemed to have occurred. Paste, has historically been assumed to remain fully saturated and provided a constant level of shearing resistance when sheared undrained, regardless of confinement. This is shown in Figure 3.22 by the flat failure envelope. Thus the UCS has been assumed to provide a simple and valid assessment of the undrained shear stress regardless for all levels of confinement. A series of total stress tests (refer Table 3.9) were conducted to investigate the assumption of paste saturation levels. The testing conclusively showed that paste does indeed lose saturation through hydration of cement over time, which induces a definite friction angle.

Table 3. 9 Summary of medium term undrained tests

Test Method	Parameters obtained	Justification
UCS	UCS, E, ε_f, ν, Effect of Time	Gives direct basis for comparison to existing data Simple and expedient testing Wide range of mix samples done to identify strength gain curves.
Unconsolidated Undrained Triaxial	c_u, ϕ_u	Identify total stress parameters for Mohr-Coulomb plot

A minimum of three specimens was tested for each mix, confining pressure and curing time for the UCS and triaxial tests. For direct shear testing one test specimen was used for each mix, confining pressure and testing interval. This was as result of the difficulties associated with the casting and preparation of the direct shear samples.

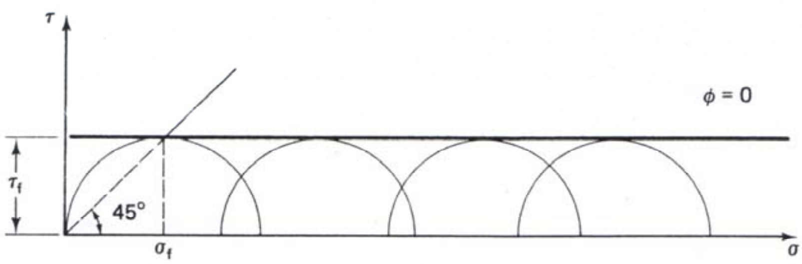

where

τ_f = Shear stress at failure (kPa)

ϕ = Total (undrained) friction angle = ϕ_u

Figure 3. 22 Mohr-Coulomb failure envelope for a fully saturated undrained material.

A friction angle of zero, as shown above, is indicative of a fully saturated soil under fast loading conditions. The pore water absorbs 100% of the applied loading, reducing the effective stress. However, if the sample is not fully saturated, an increase in confinement pressure will result in the consolidation or densification of the soil structure, and an increase in the shear strength of the soil will occur, resulting in a friction angle, as is shown in Figure 3.23.

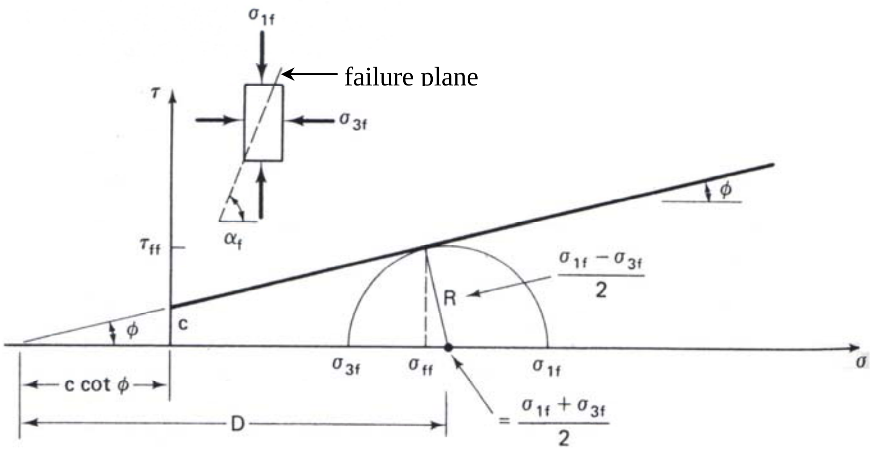

where

τ_{ff} = Shear strength at failure (kPa)

ϕ = Friction angle in terms of total stress

α_f = $45 + \phi/2$

σ_{3f} = Minor principal stress (confining pressure) at failure

σ_{1f} = Major principal stress at failure

c = cohesion

Figure 3. 23 Generic Mohr Coulomb failure envelope, with a soil specimen at failure.

Theoretically, if paste remains fully saturated, it should have a friction angle of zero. This has been shown not to be true, as has be shown in the following sections (UU triaxial and Direct shear testing).

3.7.2.1 Unconfined Compressive Strength Testing

The investigations into the strength and deformation of paste samples during UCS testing have been divided into two separate sections: -

1. The effect of mix proportions (% cement and % solids) on strength
2. The effect of grain size on strength

The stresses and strains at failure, deformation characteristics (E and ν), and effect of time were considered as part of the investigation into each section.

3.7.2.1.1 Effect of mix proportion variation on UCS

Initially the variation of mix proportions were focussed on the blend used at Cannington Mine at the time (4% cement, 76% solids). Cement contents between 2% and 6% and solids contents of between 74% and 80% provided a reasonable spread around the existing parameters. Table 3.10 summarises the results obtained from testing. The shaded cells are for the 80% solids samples after 56 days, where testing was not conducted.

Table 3. 10 Unconfined compression strengths (kPa) for different fill mixes over time

		Curing Time (days)			
%Cement	**% Solid**	**7**	**14**	**28**	**56**
2%	74%	61	58	78	65
2%	76%	85	97	90	89
2%	78%	138	174	134	133
2%	80%	204	264	215	
4%	74%	142	166	193	186
4%	76%	244	233	237	237
4%	78%	386	391	406	335
4%	80%	384	509	624	
6%	74%	369	474	489	371
6%	76%	588	623	614	594
6%	78%	822	875	856	828
6%	80%	725	918	1361	

Stresses and Strains at Failure

Generic stress – strain plots for different paste blends (%C, %S) are shown in Figures 3.24 and 3.25, for 28 days of curing. Paste shows an increasingly brittle response as either the cement or solids content increases. Low cement content samples showing the most ductile response (with strains up to 9.8% and show slight strain hardening. As the cement content increases so the brittleness of the response and reduced failure strains. Strain softening after a period of strain hardening is observed with the higher cement contents as well. The variation in the stress strain response at the lower strain levels (for some samples) is indicative of the load testing machine – levelling out any minor inconsistencies in the surface of the prepared specimen, or the absorption of any residual “slack” in the loading system. Such affects will not be discussed any further.

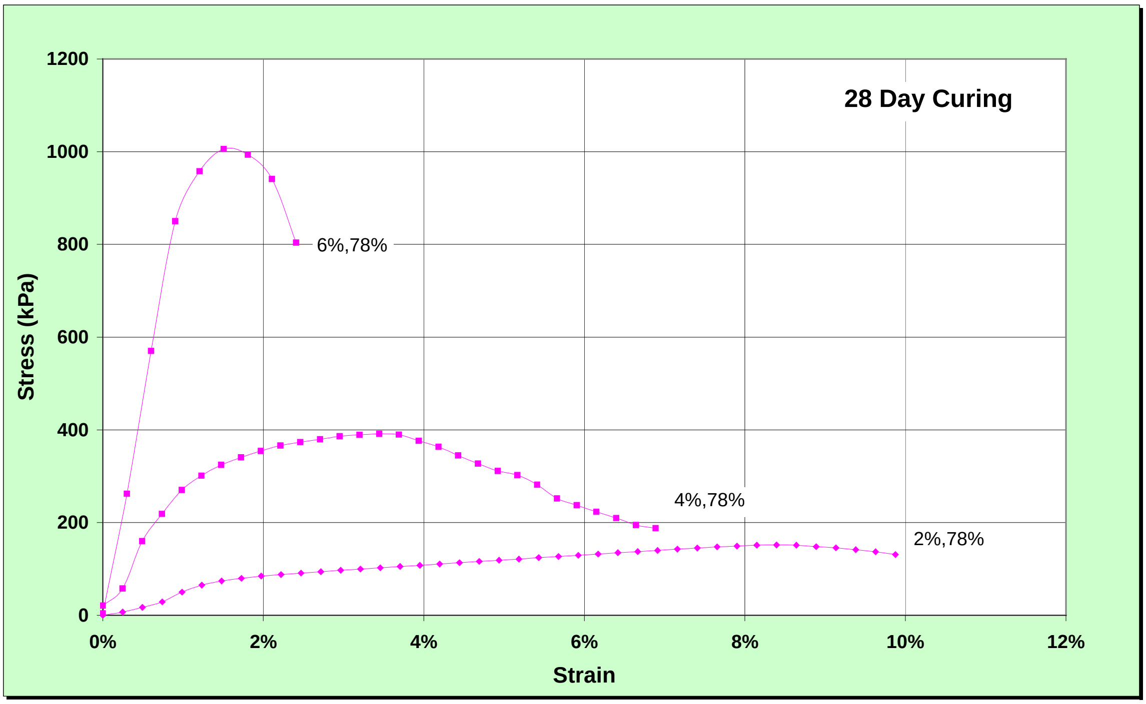

Figure 3. 24 Stress - strain response of paste fill mixes for varying cement contents (28 day curing)

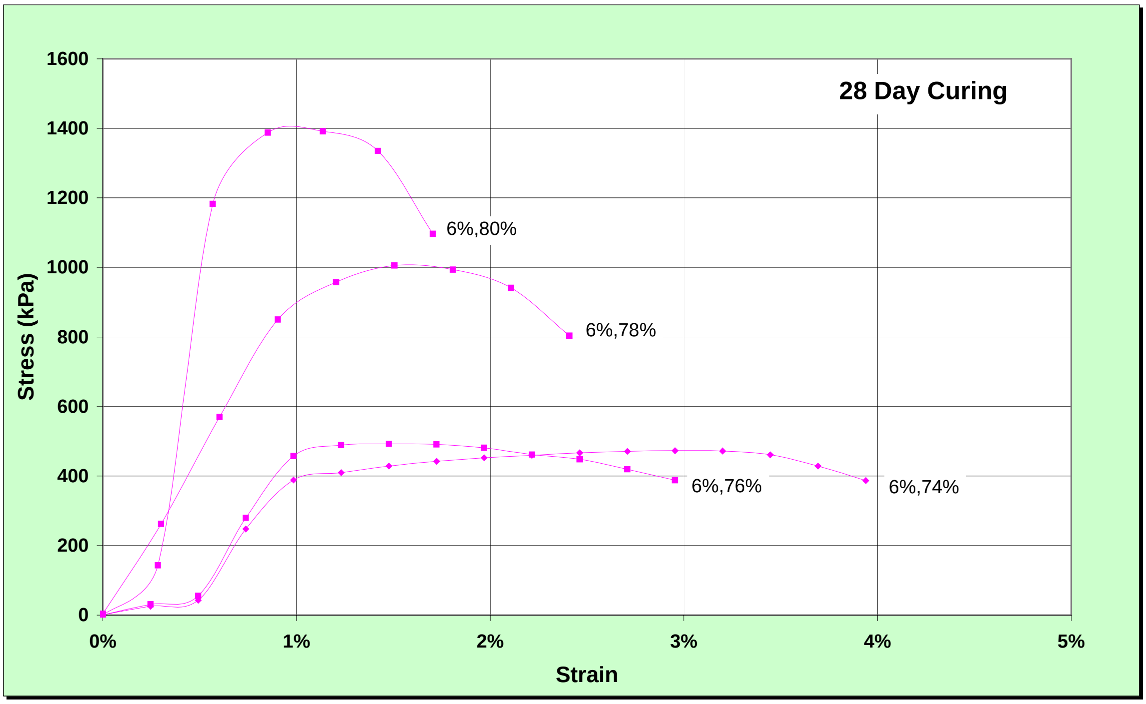

Figure 3. 25 Stress-strain response of paste fill mixes for varying solids contents (28 day curing)

The increase of strength associated with an increase in cement and solids content is shown in Figure 3.26.

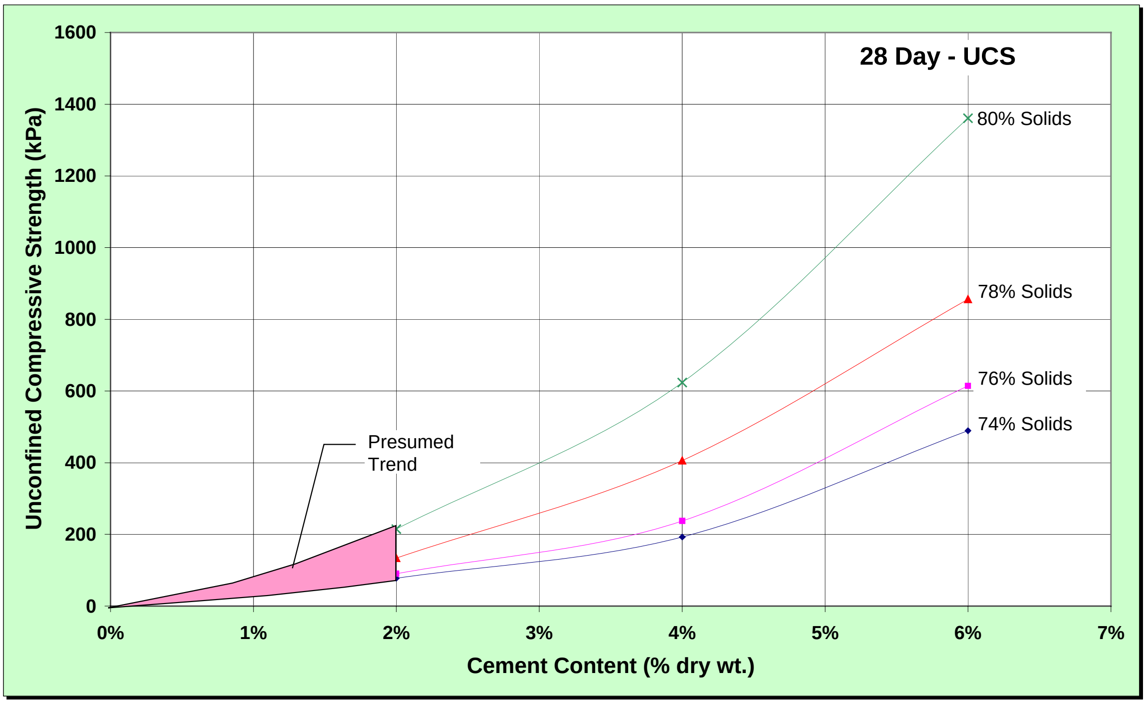

Figure 3. 26 Increase of strength associated with cement and solids content

An increase in either cement content or solids content results in an increase in the UCS of the paste. An obvious implication of this is to maximise the solids content with paste to minimise the required cement, and by doing so reduced the cement content (and cost) of the paste.

UCS values of paste were normalised with respect to a sample with 2% cement and the same solids content to identify the contribution to UCS of additional cement. The value of which is that if a “standardised response is observed, as “standardised” testing procedure for paste may be defined also. This would significantly improve the testing efficiency. The thin band of normalised UCS for the paste samples shown in Figure 3.27 suggests that such a “standardised” testing procedure is achievable and justified.

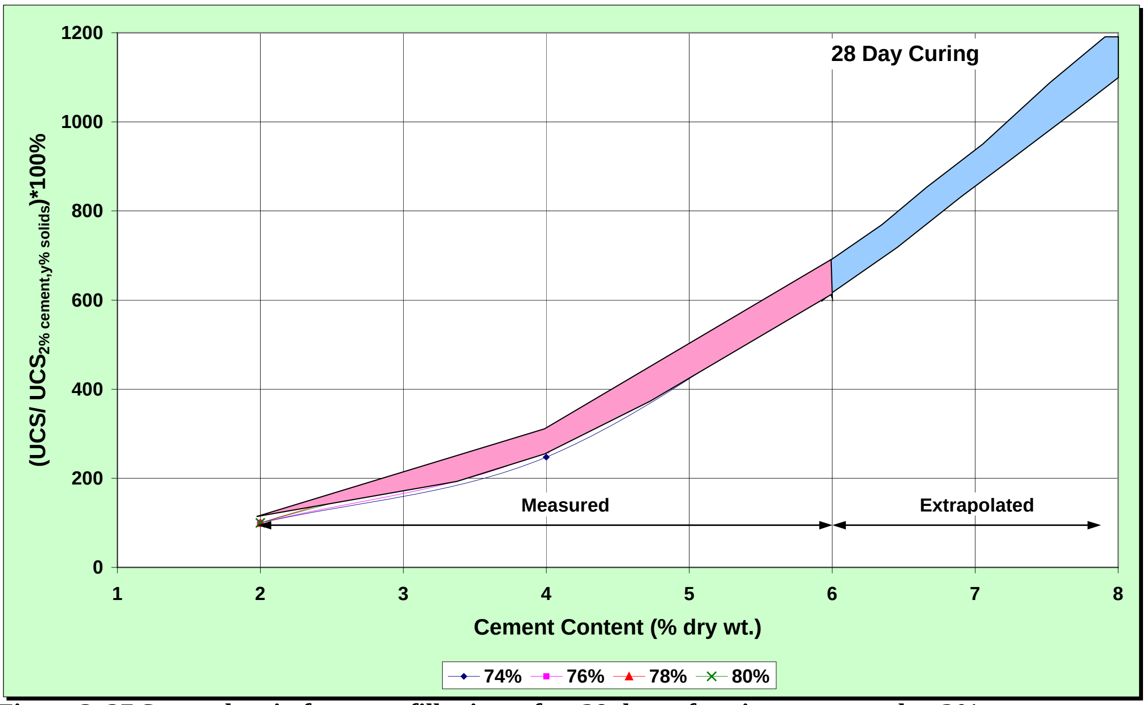

Figure 3. 27 Strength gain for paste fill mixes after 28 days of curing, compared to 2% cement samples

A similar methodology was applied to identify the contribution to strength of the solids content. Samples were normalised to samples with 74% solids and the results summarised in Figure 3.28. By compares both Figures the relative contribution of cement and solids content may be observed.

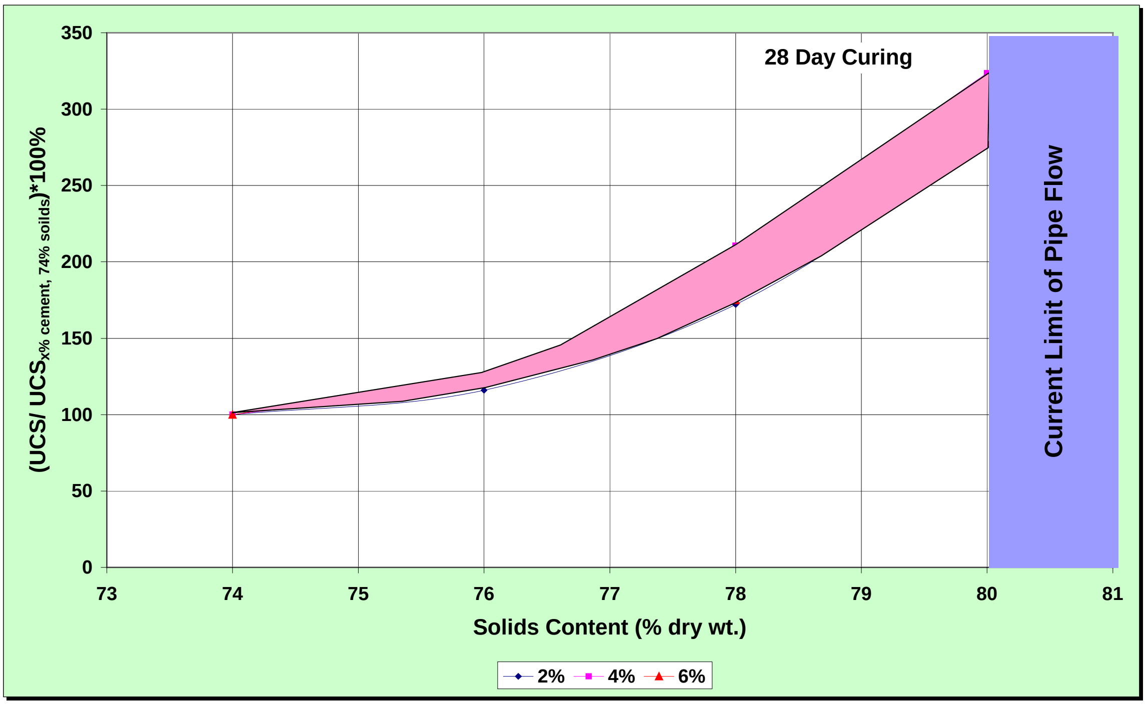

Figure 3. 28 Strength gain for paste fill mixes after 28 days of curing, normalised by 74% solids samples

From this a number of conclusions can be made: -

- Strength gain is directly related cement content, solids content and time
- Cement hydration is not affected by the reduced water levels at solids contents of between 74%-80% solids. *The restriction of the hydration of cement is never expected to occur in paste fill as the minimum recognised Water to Cement ratio to affect complete hydration is only 0.4. Putting this in context, for a 4% cement sample to not reach the complete hydration, through lack of water which would mean that the water content would be less than 1.6%*.
- Cement content contributes more to the development of strength than does an increase in solids content.

The trends observed in Figure 3.29 were measured extrapolated to a cement content o 8%, which is the maximum cement addition rate at Cannington's paste fill plant. 8% cement samples, were not included in the general body of work as they are only used for high strength plugs. The vast majority of filling (>99%) falls within the band of cement contents considered.

Figure 3.27 shows the axial failure strains for the samples tested for UCS. At solids contents less than 76%, the cement content tends to dominate the failure response of the fill. Over 76% solids however this affect is reduced, suggesting that frictional response in failure contributes more or dictates failure.

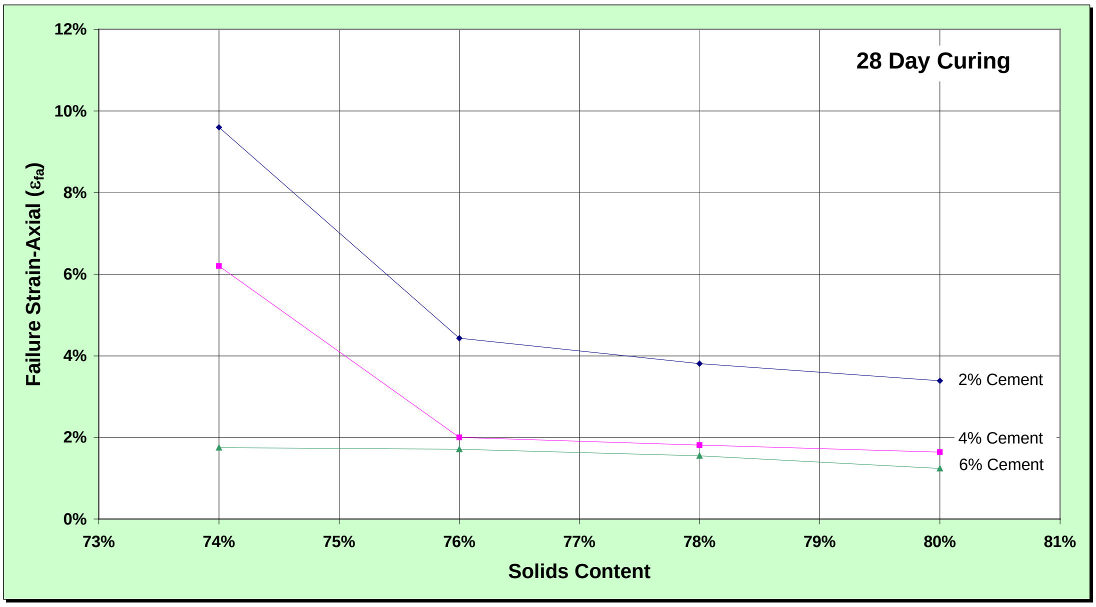

Figure 3. 29 Failure Strain responses of paste fills after 28 days of Curing

Deformation Characteristics

The deformation characteristics of UCS tests on paste fill included the determination of Young's Modulus (E) and Poisson's Ratio (ν). The variation of Young's modulus with cement and solids content is illustrated in Figure 3.28. Poisson's ratio, however, could not be obtained accurately over time, although testing was undertaken to try and obtain this (refer to Note:).

Note:

As part of this research into the characteristics of BHP Billiton's paste fill, Singh-Samra (2001) investigated the determination of a constitutive model (including the determination of Poisson's ratio) using digital imaging technology (i.e. Particle Image Velocimetry – "PIV"). Results from this indicated paste fill to have a very low Poisson's Ratio typically between 0.01 and 0.09 (Singh-Samra, unpublished data), regardless of cement content. The published ratios are not considered representative. Through approximate measurement of the fill during UCS testing using digital vernier callipers, a Poisson's ratio of between 0.10 – 0.25 was identified. The higher cement contents (6%) showed a lower Poisson's ratio (~0.10)before fracture/ failure.

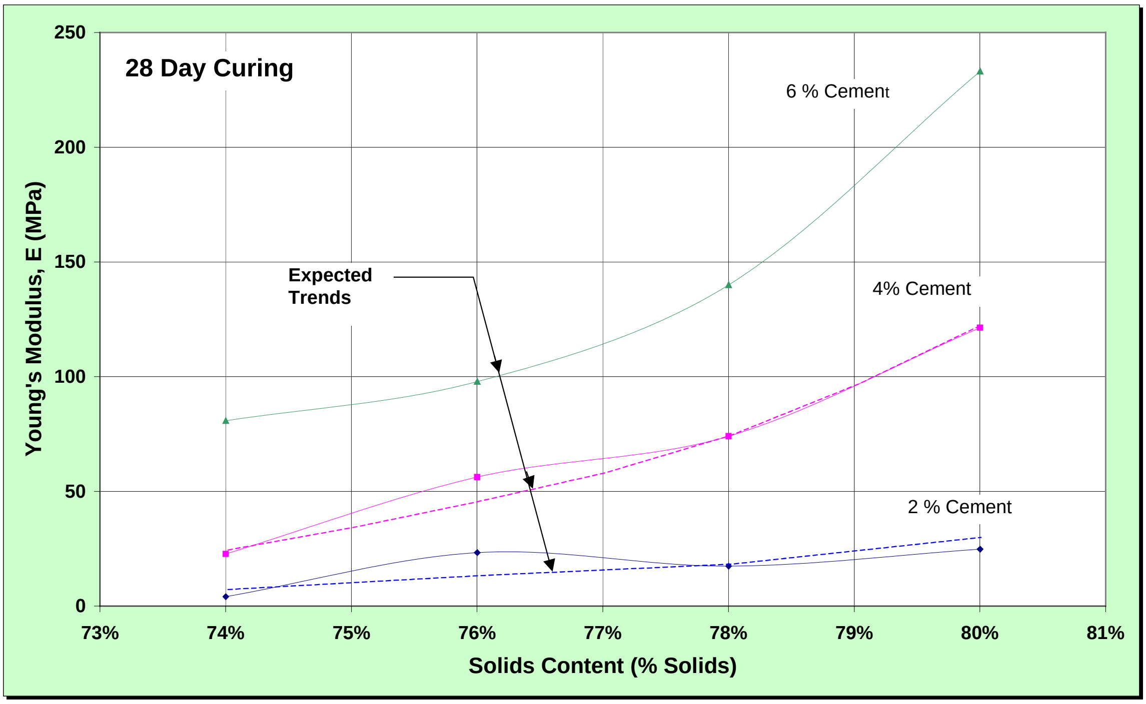

Figure 3. 30 Young's Modulus for 28 Day UCS Samples

Effect of Time

The effect of time on paste fill samples may be summarised as: -

- An increase UCS associated with the curing.
- A decrease in average failure strains, and increase in tendency towards brittle failure of paste.
- An increase in Young's modulus.

The UCS of paste tends to increase rapidly up to a period of 7 days after which the gain of strength is more gradual (refer Table 3.10).

The variation of the failure strain with time is summarised in Table 3.11. As expected as curing continues and the material gains rigidity, the strains at which failure occurs- reduce. This trend is less obvious at the lower cement contents.

Table 3. 11 Effect of time on axial failure strains, ε_f

		Curing Time (Days)		
%C	**%S**	**7**	**14**	**28**
2%	74%	11.0%	10.3%	9.5%
	76%	5.7%	3.8%	4.4%
	78%	4.2%	3.3%	3.8%
	80%	3.1%	3.4%	3.4%
4%	74%	4.5%	4.5%	3.0%
	76%	2.4%	2.1%	2.0%
	78%	3.5%	2.5%	1.8%
	80%	2.8%	2.4%	1.6%
6%	74%	2.0%	1.8%	1.8%
	76%	2.2%	1.8%	1.7%
	78%	2.3%	2.2%	1.6%
	80%	1.9%	1.7%	1.2%

The effects of cement content and solids content on failure strain were investigated by normalising the axial failure strains with respect to mixes with 2% cement contents and varying solids contents, as per previous UCS testing The results are shown in Figure 3.31.

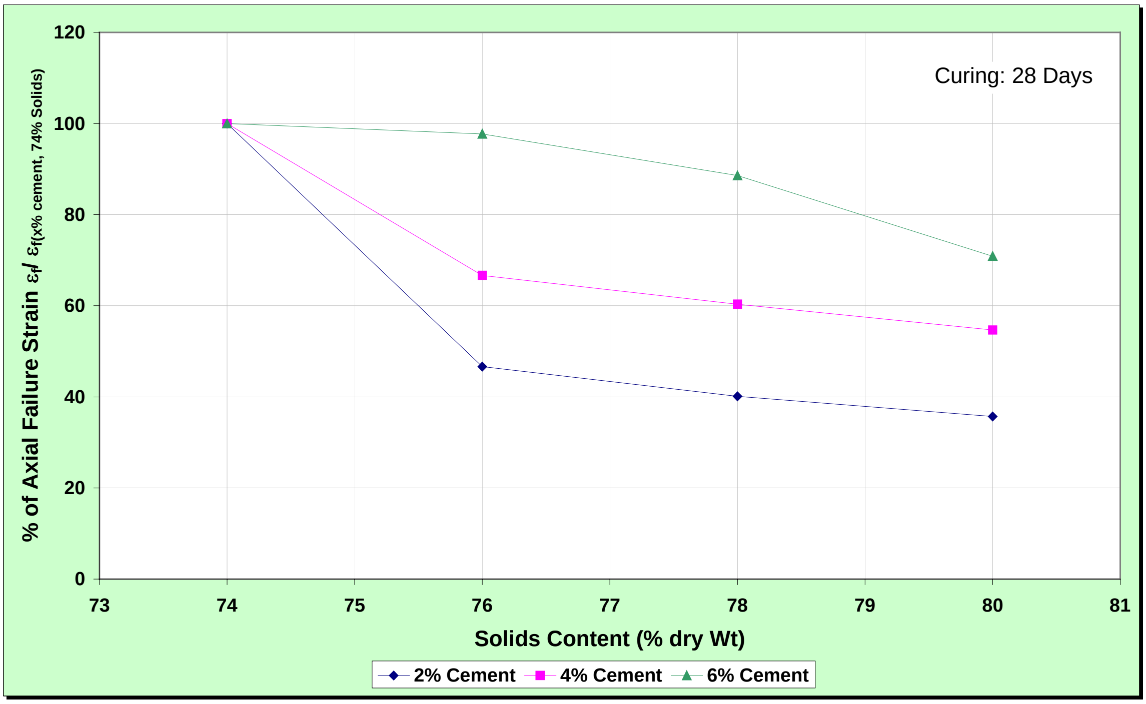

Figure 3. 31 Failure Strains in Paste normalised by 74% solids paste samples

Comparing Table 3.11 and Figure 3.31 the following conclusions can be made: -

- Failure strains reduce with an increase in cement content, solids content and time.
- Solids content has a more pronounced effect on the magnitude of failure strains at lower levels of cementation.
- Samples with higher cement contents have a more brittle response during loading, and fail at lower levels of strain.
- Ductility of paste in unconfined compression reduces with cement content, time and solids content.

Additional testing and analysis has been completed and the results collated within Appendix 3.4

The effect of curing time Young's Modulus was investigated and the results collated in Table 3.13. As expected the values increase with cement content, solids content and time.

Poisson's Ratio was measured at 28 days only using the PIV technology. Although generally regarded as a material constant, it is believed that the ratio would decrease to the levels outlined previous as curing continues. It is considered reasonable to assume a Poisson's Ratio of ν=0.35 to 0.25, for lower cement contents and 0.2 to 0.1 for the higher cement contents. Poisson's ratio would decrease with an increased time of curing.

Table 3. 12 Effect of time on Young's Modulus (E) values of paste

		Young's Modulus (MPa)		
%C	**%S**	**7 Days**	**14 Days**	**28 Days**
2%	74	2	2	4
	76	17	23	23
	78	27	25	17
	80	19	36	25
4%	74	19	12	23
	76	37	55	56
	78	34	52	74
	80	69	60	121
6%	74	88	41	81
	76	54	108	98
	78	82	109	140
	80	91	140	233

3.7.2.1.2 Effect of Grain Size Distribution on UCS

The effect of the grain size distribution on strength of paste was investigated using three tailings grind sizes. These were nominally referred to as "fine", "medium" and "coarse" blends. The grain size distribution curves for each are shown in Figure 3.32 and the principal grain size distribution parameters of grind sizes are shown in Table 3.13. The "fine" and "coarse" grinds represent the likely bounds of grind sizes at Cannington.

Table 3. 13 Grading indicators for the various grind sizes.

Tailings Grind	**P80** (μm)	D_{60} (μm)	D_{30} (μm)	D_{10} (μm)	C_c	C_u
Fine	37	11.49	5.62	2.19	5.26	1.26
Medium	107	96.15	25.65	4.08	23.55	1.68
Coarse	290	232.38	122.41	21.88	10.62	2.95

The medium grind size corresponds to the grain size distribution of the tailings used in the paste at Cannington during the time of testing (P80=107.5 μm) and correlates well to the historical "average" grind size, as discussed in Section 3.5.1. The UCS testing was used as a basis for comparison of strength. The results of which are shown in

Table 3.14 and Figures 3.33 and 3.34. Additional data from testing has been summarised in Table A3.4.3 in Appendix 3.4.

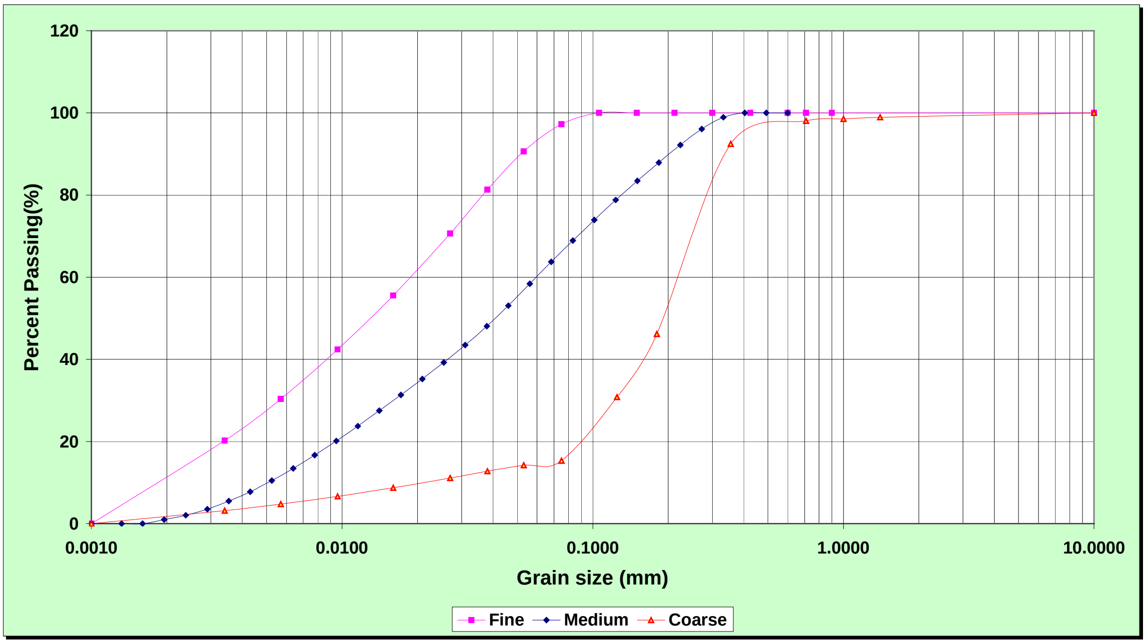

Figure 3. 32 Grain size distribution curves for "fine", "medium" and "coarse" grind sizes

Table 3. 14 Unconfined compression testing results for grains side distribution variation

			Average UCS (kPa) after *(x)* Days of Curing		
%Cement	**% Solid**	**Grind**	**7 Days**	**14 Days**	**28 Days**
2	76	Fine	69	174	200
		Med	46	117	144
		Coarse	85	117	110
	80	Fine	137	389	423
		Med	161	325	361
		Coarse	166	198	208
6	76	Fine	612	1024	1146
		Med	536	826	899
		Coarse	465	584	722
	80	Fine	1107	1570	2280
		Med	1065	1489	1640
		Coarse	806	1030	1258

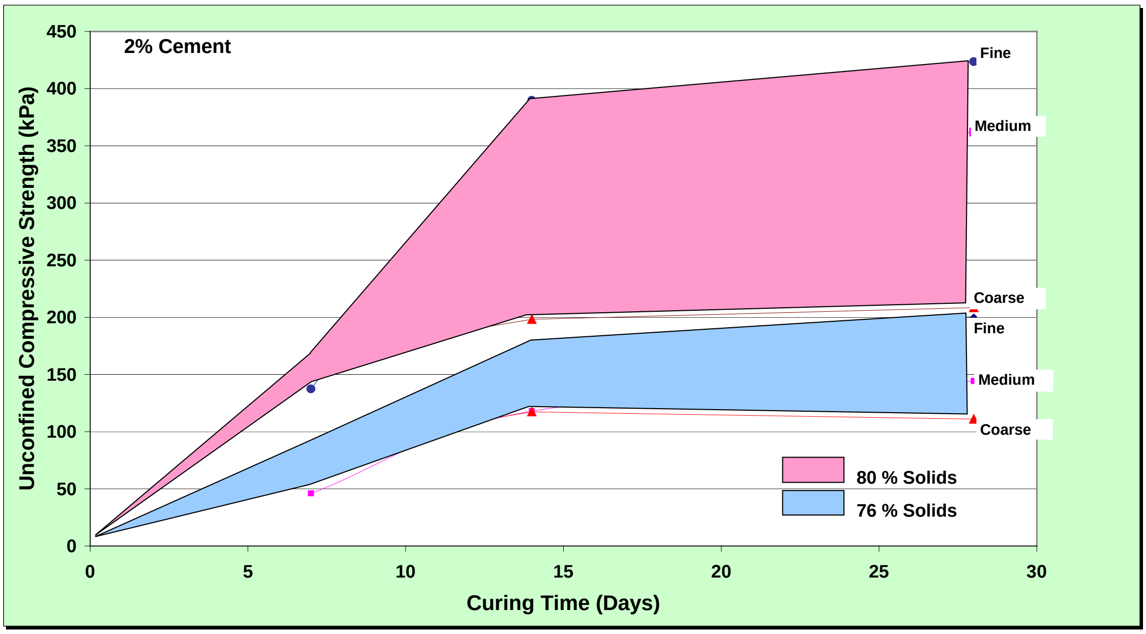

Figure 3. 33 Progressive UCS strengths for various grain size distributions – (2% cement)

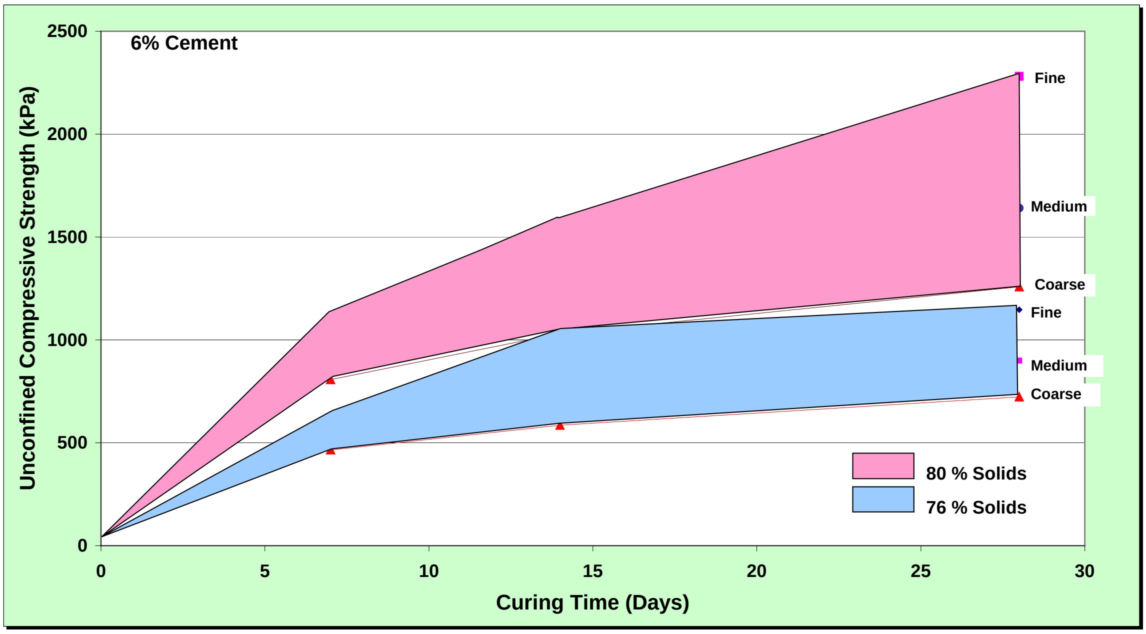

Figure 3. 34 Progressive UCS strengths for various grain size distributions – (6% cement)

The strength of the paste is decreases with the increasing grain size of the tailings. The reasons behind that are attributed to: -

- Capillary forces and surface tension. The finer grain size results in finer pore spacing with a substantially larger surface area, thus significantly increasing the surface tension forces binding the paste together.

- The "fine" blend contains 10% of the fines under 2 μm (which in geotechnical terms are classified as clays). Clay particles generate genuine cohesion through the ionic bonds, which occur between the charged surfaces. This contributes to the shear strength in the "fine" blend.
- The "coarse" grind size lacks the requirement that at least 15% of particles be less than 20 μm, to be considered a "paste" fill. The lack of fines, results in a significantly reduced surface area of the soil mass, and lacks ability to hold water. Consequently, the fines and cement within the paste get washed out through the coarse soil matrix upon placement, reducing cementation level of the fill.

The Young's Modulus and failure strains of the fill mixes were investigate and the results have been summarised in Figures 3.35 and 3.36. Supplementary plots for UCS, E and ε_f over time for both 2% cement and 6% cement samples have been included in Appendix 3.4.

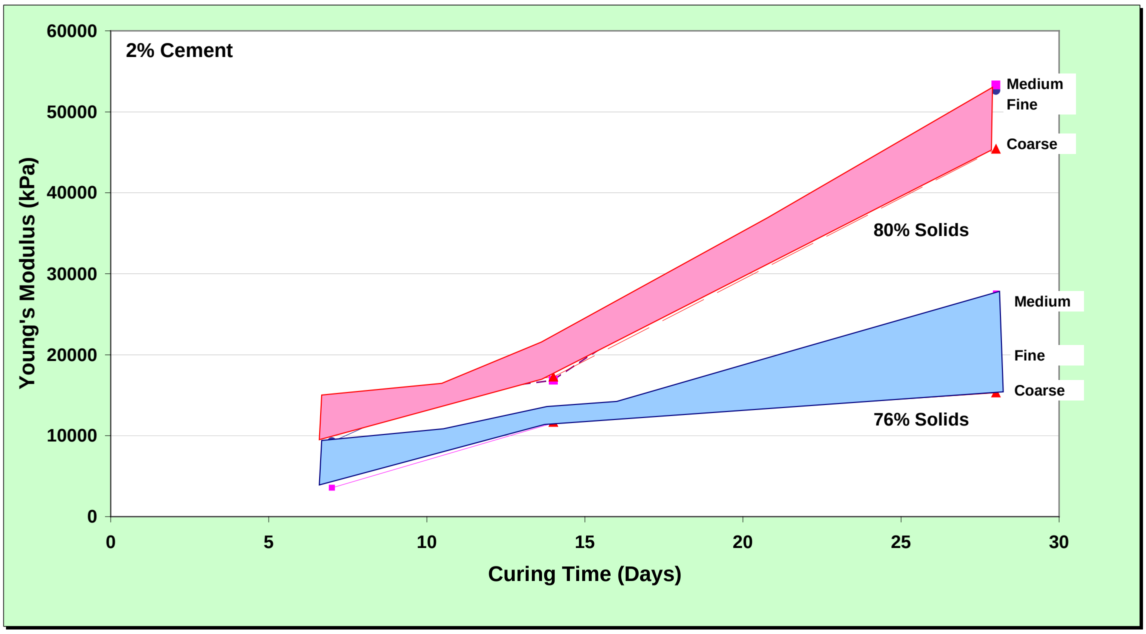

Figure 3. 35 Variation of Young's Modulus with time and GSD of paste

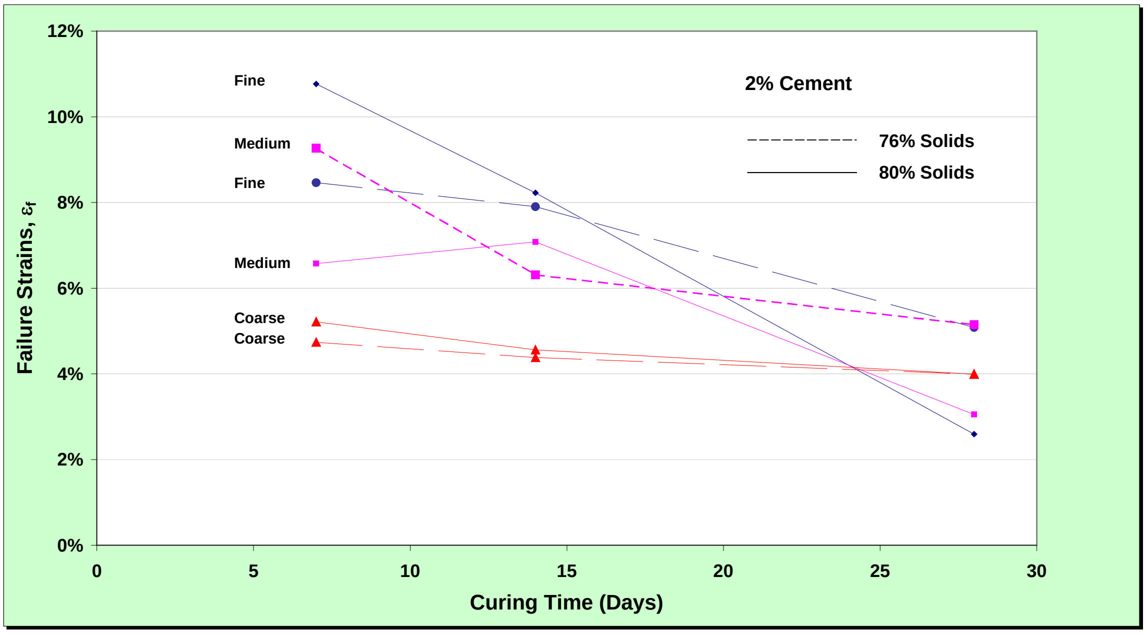

Figure 3. 36 Variation of failure strains with time and GSD of paste

From the analysis of the effect of grain size distribution on the properties and behaviour of the paste, the following *general* conclusions can be drawn: -

- The UCS of paste increases with cement content, solids content, time and the fineness of the grind of the tailings
- The Young's Modulus of the paste increases with cement content, solids content and time. The Young's Modulus of the paste decreases with the increase in coarseness of the grind size of the tailings. The effect of the grind size on E is less than the effect of cement content, solids content or time.
- Failure strains decrease with time and grind size. The effect of increasing the cement content decreases the observed trends with grind size (refer Figure A3.4.17) as the failure strain is dictated by the cement content alone. This theory is supported with the thin band of failure strains encompassing all samples between 1 % and 2 %. Figure 3.36 also shows that the paste is less ductile as curing time increases – as expected.

3.7.2.2 Unconsolidated Undrained Triaxial Testing

The unconsolidated undrained triaxial (UU Txl) test is a total stress test method used to represent in-situ field conditions where loading occurs rapidly, and pore water is unable to escape. The material properties such as Young's modulus (E), Poisson's ratio (ν), UCS, failure strain, (ε_f) etc. should theoretically remain constant if the sample is fully saturated also. During this investigation paste has been shown to be partially saturated (albeit typically higher than 90%). The strength of the paste fill sample will change with the variation in each of these properties. The quantification of this falls outside the scope of this dissertation.

The determination of the undrained cohesion (C_u), and undrained friction angle (ϕ_u), were the primary focus for UU triaxial testing and have been summarised in Table 3.15.

Table 3. 15 Average UU Triaxial testing results for medium term testing of paste fills

Curing Time	7 Days		14 Days		28 Days		56 Days	
Mix	ϕ_u (deg)	c_u (kPa)	ϕ_u (deg)	c_u (kPa)	ϕ_u (deg)	c_u (kPa)	ϕ_u (deg)	c_u (kPa)
2%C, 74%S	2.3	50	4.0	55	1.3	47	3.7	61
2%C, 78%S	4.3	143	7.1	136	5.0	168	3.5	154
6%C, 74%S	14.3	139	16.2	157	12.8	174	14.4	178
6%C, 78%S	15.9	259	16.0	247	16.4	255	17.0	269

Both ϕ_u and c_u increase significantly with cement and solids content at all stages of curing. The substantial increase in ϕ_u when the cement content was increased from 2% to 6%, at all stages of curing, may be attributed to the air voids produced as a result of hydration, thus making the paste consolidate only under higher confining pressures. The undrained friction angle, ϕ_u, is influenced more by the cement content than by the solids content. The influence of cement content and solid content on c_u appear to be in similar levels. For example 2% cement, 78% solids (2%C, 78%S) had similar values of c_u at all times of curing. Here increasing the cement content by 2% and reducing the solids content by 4% had little effect on c_u but resulted in a significant increase in $\phi_{u.}$

Figure 3.37 show the relation between the undrained friction angle, ϕ_u, and UCS – which may be correlated to undrained cohesion, c_u suing equation 3.10. The plot shows that the undrained friction angle increases as UCS increases. ϕ_u increases more rapidly with an increase in cement content than with solids content.

The relationship between ϕ_u, c_u and UCS is :-

$$UCS = 2c_u\left(\frac{\cos\phi_u}{1-\sin\phi_u}\right) \quad \ldots (3.10)$$

If paste remains unsaturated, then UCS, ϕ_u = 0 and UCS = 2*c_u, however, if paste is *not* fully saturated and increases in shear strength when confined, a friction angle results (ϕ_u > 0). Current mine practise is to determine the UCS of a sample and use a friction angle of zero, to predicts the strength of paste, which is conservative. Figure 3.37 shows the relationship, which may be used to identify the undrained friction angle with a determined UCS.

The horizontal lines show the effect of increasing cement content on the friction angle. Similarly, when moving from left to right the vertically angled lines show the effect of increasing solids content on ϕ_u. The cement content is the dominant consideration in the development of a friction angle, with an increase in solids content, resulting in minor increase in friction angle. Higher levels of cementation are considered to aid the hydration reaction by slightly elevating the latent heat in the curing environment.

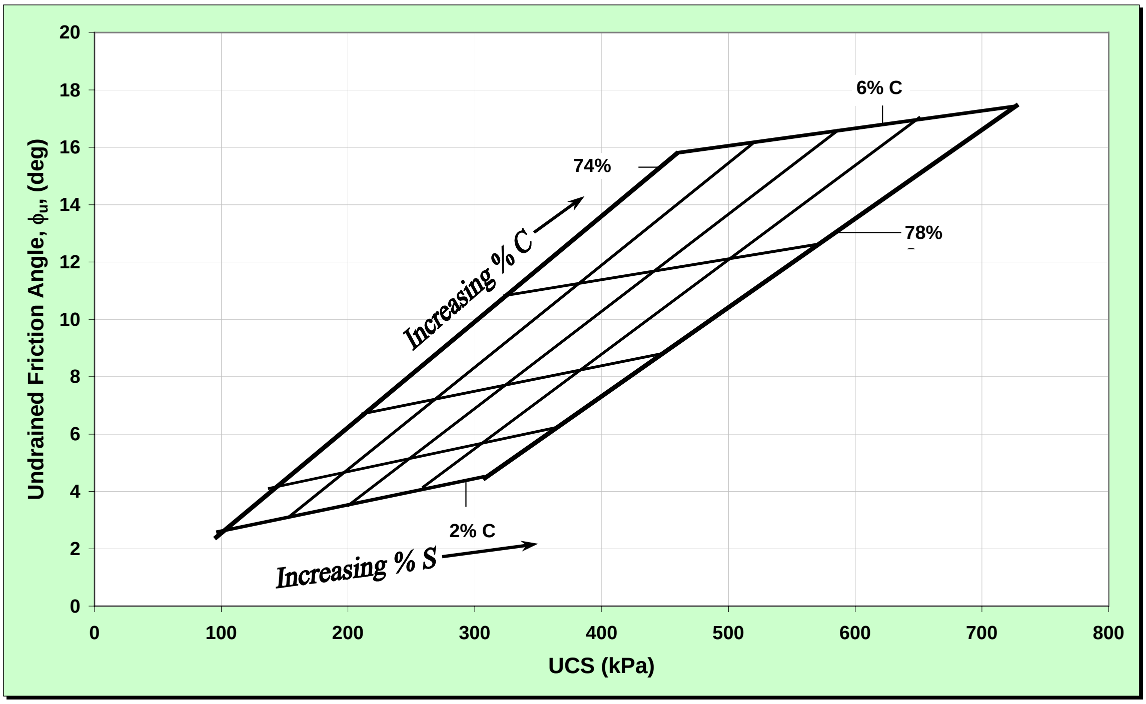

Figure 3. 37 Undrained friction angle vs. UCS (7-56 Days curing)

Polygons were found for the remainder of UCS values (from Table 3.10) to show the effect of time, cement and solids content on strength development also. The combined strength polygon was form and is shown in Figure 3.38. By inspection of Table 3.10, time after seven days curing was not expected to influence the size or shape of the polygon significantly, which is shown to be the case. The consistency of the cement content lines indicates that paste gains effectively its full strength after little more than seven days. As in Figure 3.37 the trends are major increase in the strength with the addition of cement and minor increases with the increase in solids content. The implication of this is that stope turn around time may be significantly reduced resulting in increasing stoping ability and production capacity.

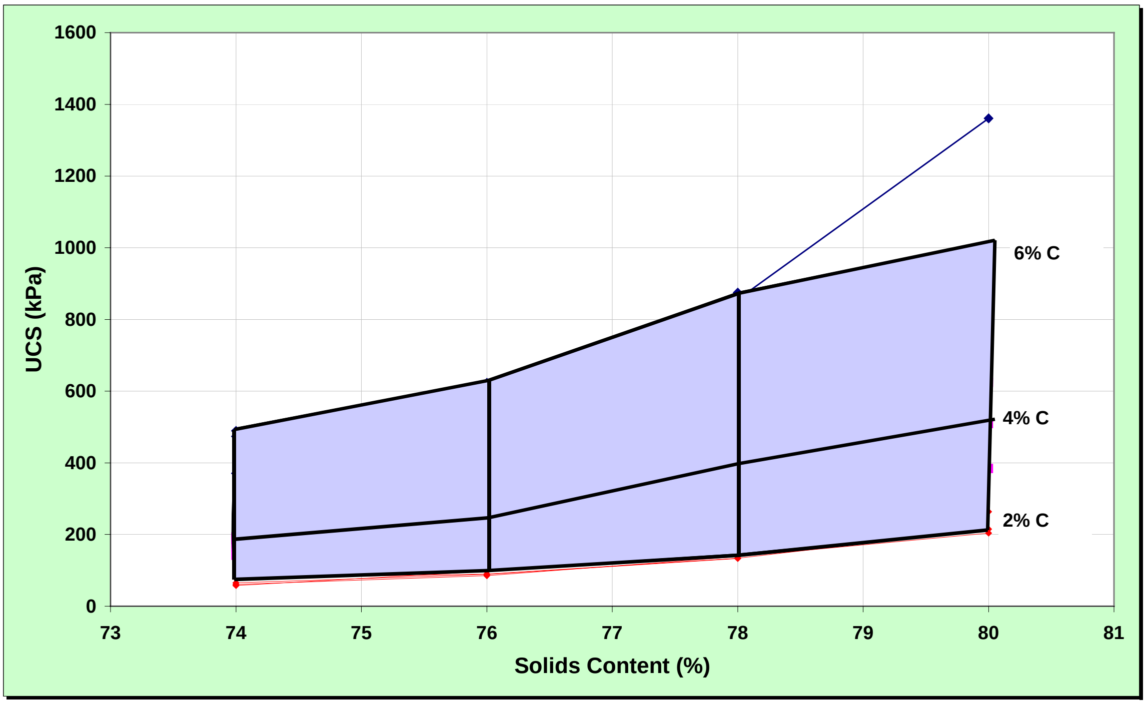

Figure 3. 38 Combined Strength Polygon (7-56 days curing)

The theoretical line for saturated paste, where ϕ_u = 0 and UCS=2*c_u, is shown in Figure 3.39 by the dashed line. The solid line represents testing results. The deviation from the theoretical line represents the presence of a friction angle in the paste. The deviation of the line in a non- linear fashion indicates that the development of the friction angle increases with UCS, which further supports the trends observed in Table 3.15 and Figures 3.37 and 3.38.

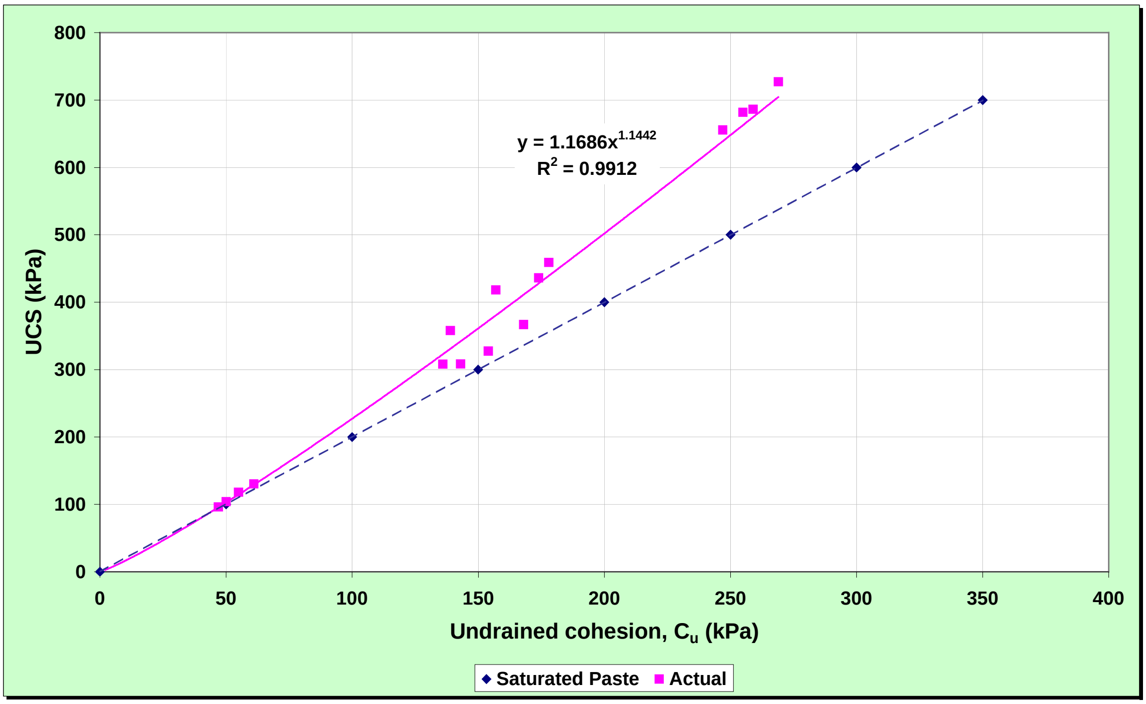

Figure 3. 39 Relationship between UCS and C_u for paste

Figures 3.37 and 3.39 can be used in conjunction with each other to fully characterise the Mohr-Coulomb parameters, C_u and ϕ_u, for paste in terms of total stress. These parameters are then easily determined from a single UCS test. Alternatively Figure 3.26 may be used to estimate the UCS of the sample based on mix proportions after 28 days and then Figures 3.37 and 3.39 used to relate UCS to ϕ_u and c_u respectively. PASTEC, a program developed in a Microsoft EXCEL working environment, using artificial neural networks (ANN) also has the ability to predict the undrained friction angle and cohesion from simple user defined inputs (Refer Chapter 5).

3.7.3 Long Term Strength of Paste

UU Triaxial tests were used to identify the time dependent behaviour of the total stress parameters (c_u and ϕ_u) of paste over a period of one month to one year. Table 3.16 summarises the results from testing. Figure 3. 40 was generated from the results of UU triaxial testing in conjunction with equation 3.10, to show the expected UCS results of paste over a one year period.

Table 3. 16 UU Triaxial test results

	Shear Strength parameters									
	1		3		6		9		12	
Mix	ϕ_u (deg)	c_u (kPa)	ϕ_u (deg)	c_u (kPa)	ϕ_u (deg)	c_u (kPa)	ϕ_u (deg)	c_u (kPa)	ϕ_u (deg)	c_u (kPa)
2%C, 74%S	5.7	49.4	4.8	48.9	2.5	54.9	4.9	95.0	15.2	113.9
2%C, 78%S	6.0	95.0	2.9	105.4	3.9	118.6	10.1	157.5	31.5	141.2
6%C, 74%S	12.7	157.6	14.7	173.1	17.9	326.9	20.7	383.7	28.4	318.8
6%C, 78%S	15.8	264.2	12.6	337.8	24.7	445.0	30.4	309.0	31.1	309.5

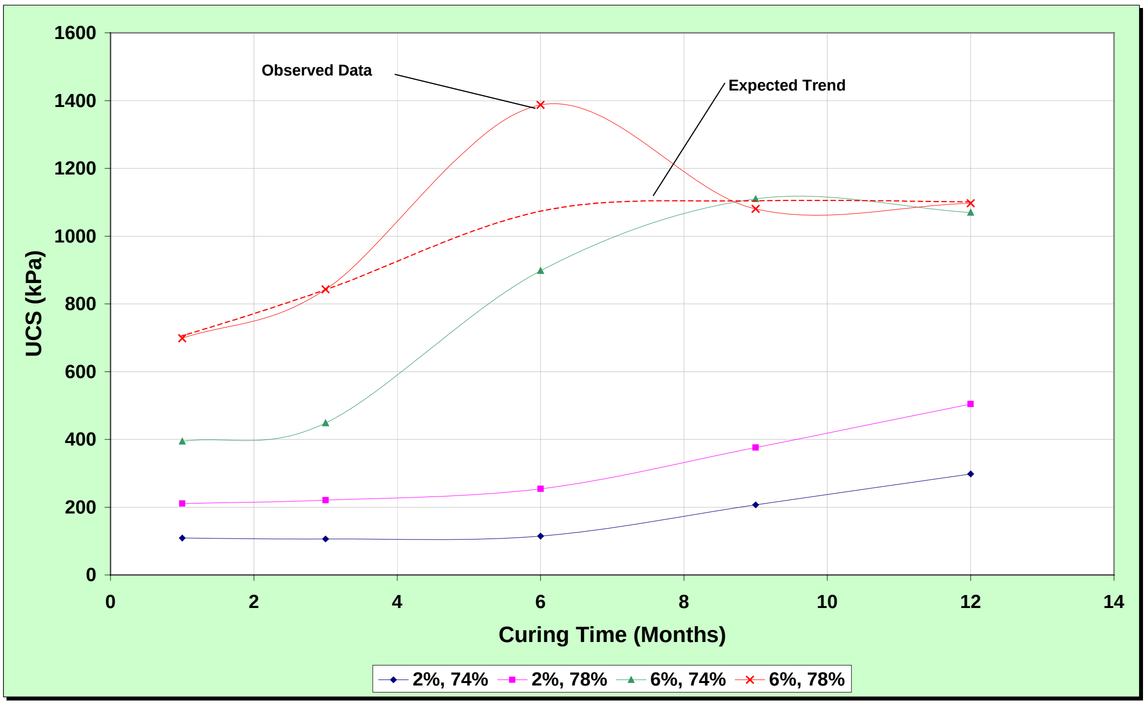

Figure 3. 40 Calculated UCS of paste fill

Using Table 3.16 and Figure 3.40 it can be seen that paste increases strength after 28 days of curing. The more dramatic increase in strength after six months, however, can be related to the increase in ϕ_u, as shown in Table 3.16. This results from the paste "drying out" as a result of the progression of the hydration process. The 6% cement content samples appear to increase in shear strength most rapidly between three to six months, with the 6%C, 78% solids mix reaching a peak after 6 months and then reducing to a plateau of constant strength between nine and 12 months. The peak strength for the 6%C, 78%S mix, after six months, is questionable. The expected trends has been plotted in Figure 3.40 also. The 6%C, 74%S mix increased rapidly in strength after three months and again reached a constant strength after approximately nine months. Long term degradation of fill by sulphate attack or self desiccation are not considered to have occurred. To date, anecdotal evidence suggests that paste fill may oxidise in the outer 300 mm on exposed surfaces, however, oxidation and reduction of fill strengths at depths any greater than this, has not been observed.

The reason for the increase of strength was observed for two distinct regions, before and after six months. The boundary of six months was chosen as all paste fill samples trended in the same fashion prior to this point and changed significantly after it (Refer Figure 3.40). The relationship between the undrained friction angle and undrained cohesion was developed and is shown in Figure 3.41.

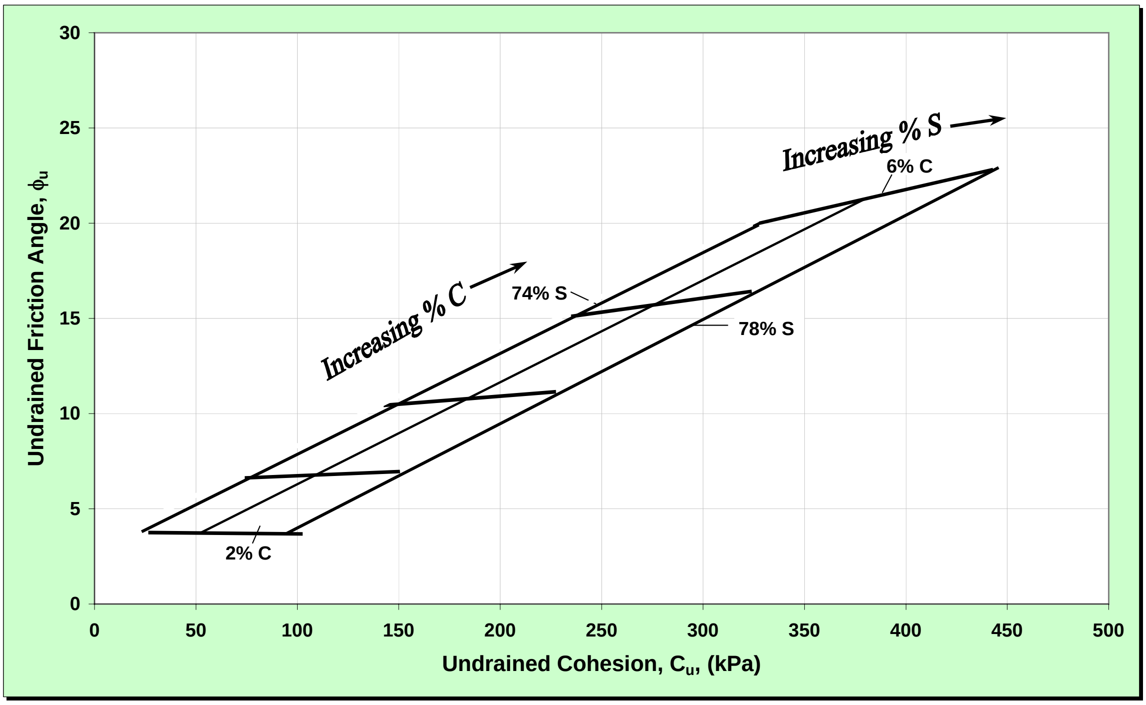

Figure 3. 41 Undrained friction angle vs. Cu (1-6 months curing)

The undrained cohesion is heavily dependant on the cement content and moderately dependant on the solids content. This trend is independent of the cement content. The undrained friction angle is predominantly governed by the cement content.

A comparison of the predicted UCS for the UU triaxial samples, calculated from equation 3.10, was made against a theoretically saturated paste (ϕ_u = 0) and is shown in Figure 3.42. The trend of deviation from the theoretical “saturated paste” line indicates that as the UCS of the paste increases, so to does the deviation. The magnitude of deviation is attributable to the increase in ϕ_u This indirectly confirms that an increase in cement content will result in an increase in ϕ_u (as shown in Figure 3.41).

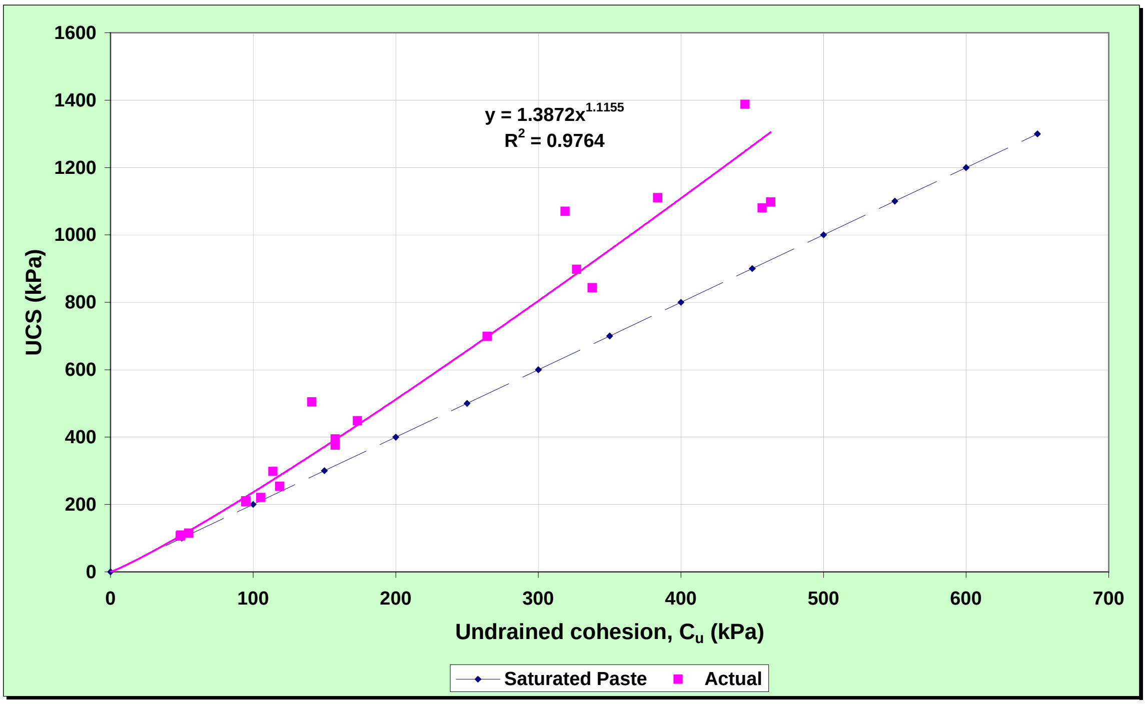

Figure 3. 42 UCS vs. Cu (1-6 months curing)

To identify the reasons for the behaviour of the paste after six months, additional investigations were undertaken. A significant and distinct increase in the air voids and decrease in moisture contents was identified at the same time as the increase in strength was observed. Figure 3.43 shows the variation of undrained friction angle and air void content against curing time. Air content is defined as the percentage of the total volume of the sample, which is occupied by air.

$$Air\ Content\ (a) = \frac{V_a}{V_t} * 100\% \qquad \ldots(3.11)$$

The piece-wise straight line fit was plotted from the data points, however the smooth trend lines, as show by the dashed lines above, are the expected trends. Additional piece-wise, straight line plots for other paste fill mixes have been included in Appendix 3.4. With the rationale that the undrained friction angle is induced by the air voids, all air content –undrained friction angle data points, irrespective of the curing time and mix, were plotted in Figure 3.44.

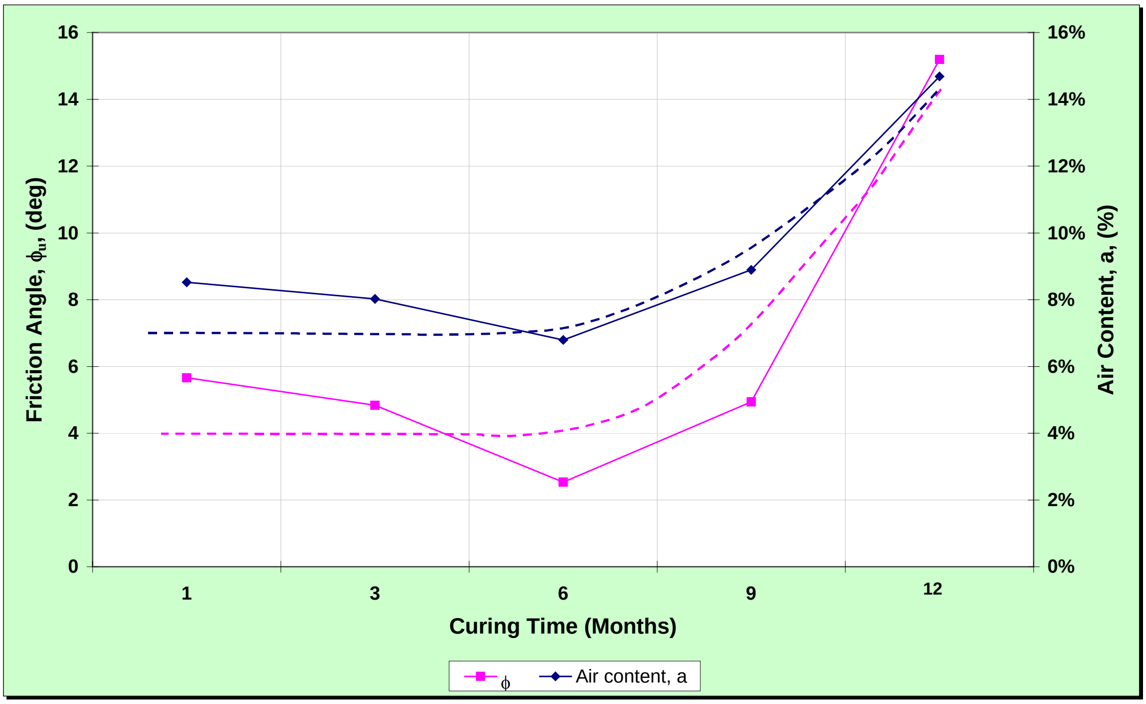

Figure 3. 43 Relationship between undrained friction angle, curing time and air void content (2% Cement, 74% Solids)

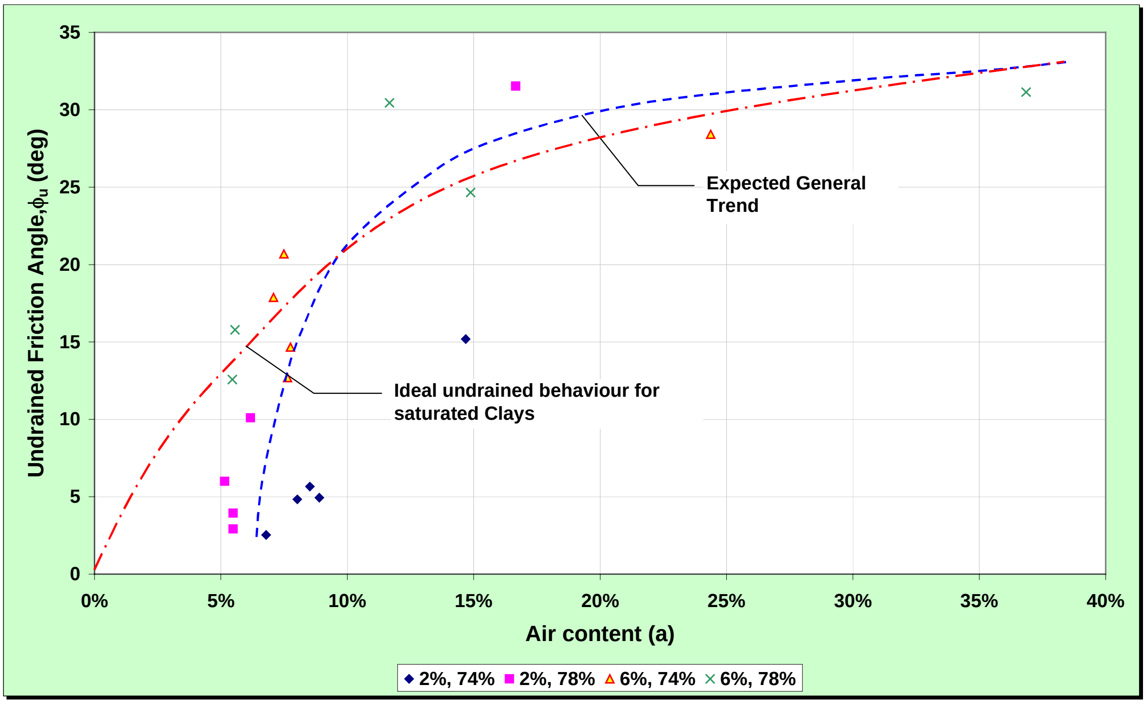

Figure 3. 44 Undrained friction angle vs. air voids (%) in paste.

Even at 2% cement content the hydration process leads to an air void content of about 7%. At cement contents of 6% the extent of hydration was so great that air contents in the order of 30% to 40% were achieved, with a resulting undrained friction angle of near 30 . The "ideal" undrained behaviour for saturated clays has also been plotted on Figure 3. 44 so that a comparison between them can be made.

3.7.4 Direct Tensile Testing

The direct tensile strength of the paste fill samples was found using the standard procedure for the testing of rock cores in tension, D2936-95 (2001). Direct tensile testing involves the sample being glued to two end caps with a high strength epoxy resin and then pulled apart using a constant strain rate (1.00 mm/min). Figure 3.45 shows the test set-up for the direct tensile tests undertaken for the paste fill samples.

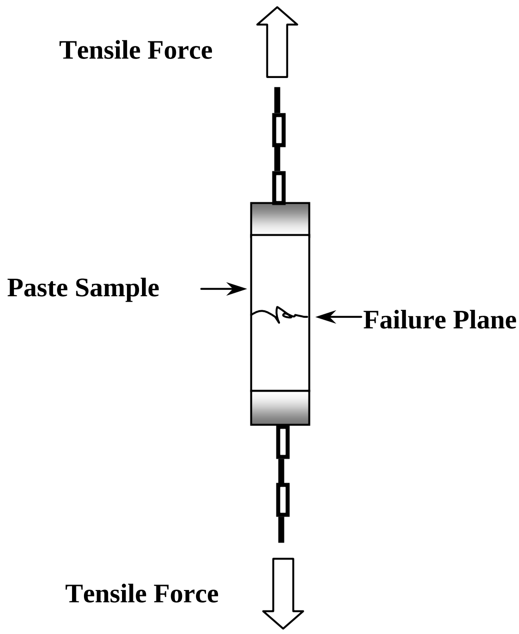

Figure 3. 45 Experimental set up for direct tensile testing of paste

The progressive gain in tensile strength is shown in Figure 3.46. With the exception of the 6% cement, 78% solids sample the tensile strength remained low and reasonably constant after seven days of curing. In the 6% cement, 78% solids mix, the tensile strength increased steadily up to 56 days. A significant increase in the strength is observed for the increase in cement content and solids content. In general the tensile strengths of paste are in the order of 10%-15% of the measured UCS. Additional calculations have been included in Table A3.4.8 in Appendix 3.4.

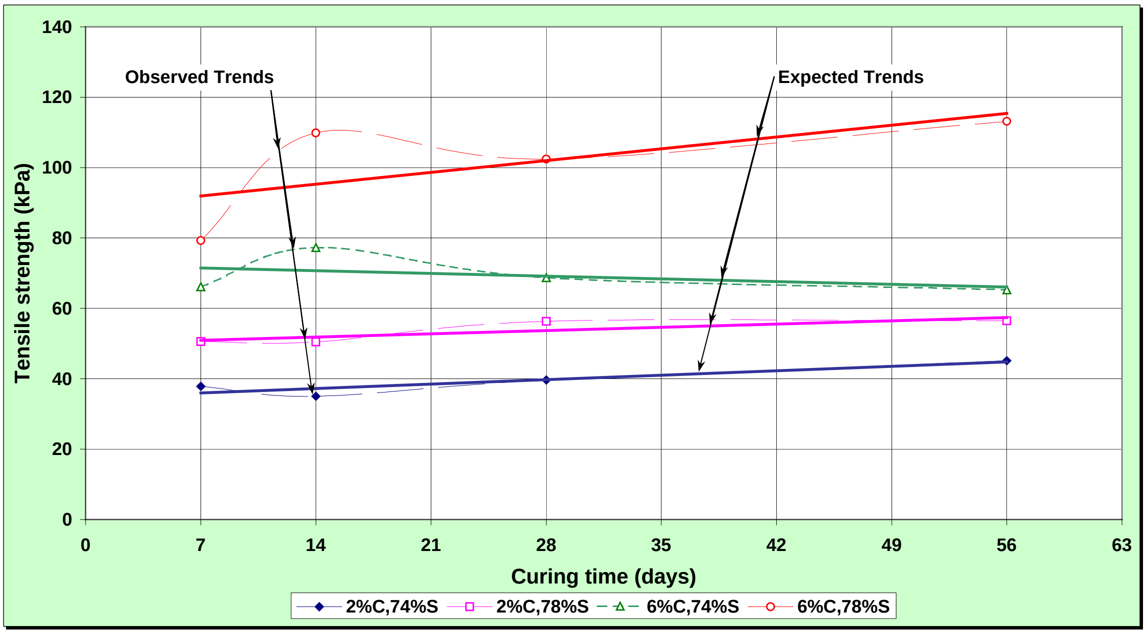

Figure 3. 46 Progressive tensile strength development of paste.

3.8 Effective Stress Analysis

An effective stress analysis of the paste was undertaken to identify the material characteristics of the paste. The effective stress analysis of paste was conducted using consolidated drained, triaxial and direct shear tests.

3.8.1 Consolidated Drained Triaxial Testing

In the effective stress analysis the stress-strain response at failure and deformation characteristics (E and ν) were investigated. The effect of time on each of these was considered also.

Stress-strain response at failure

The stress strain response was studied for different mix proportions and confining pressures. Figure 3.47 shows the response of varied mix proportions in unconfined compression, and varied mix proportions, whereas Figure 3.48 shows the response of a specific paste fill mix under varied levels of confinement. Additional plots have been included in Appendix 3.5.

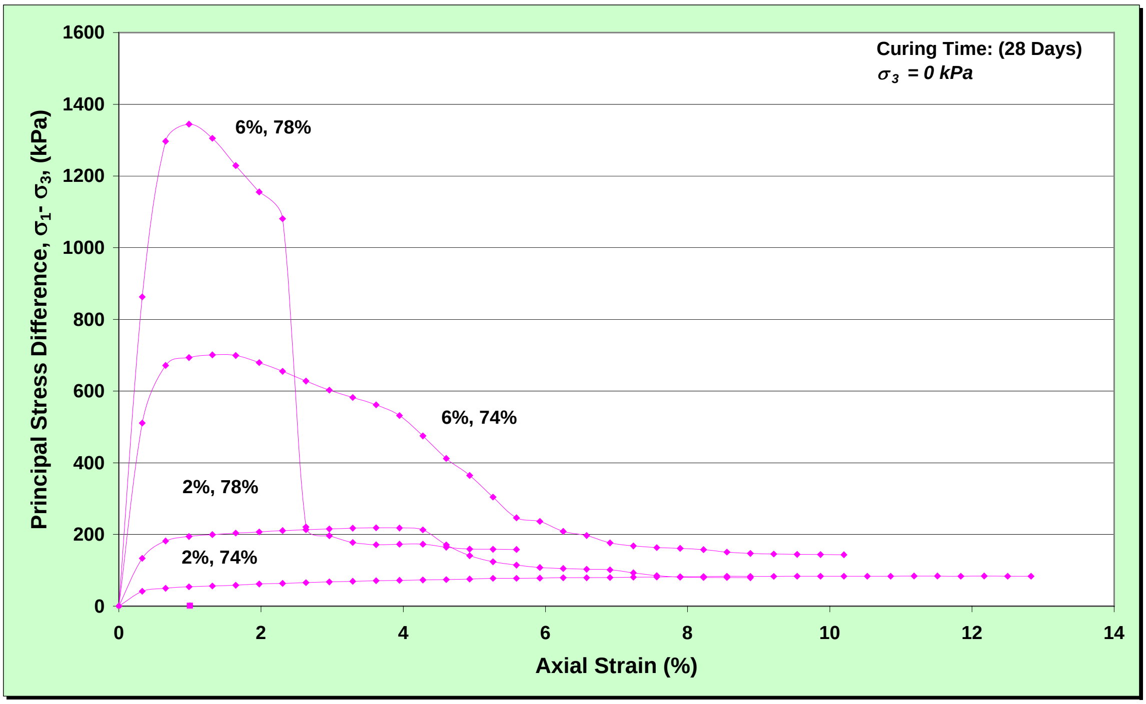

Figure 3. 47 General Stress strain behaviour of paste for different mix proportions

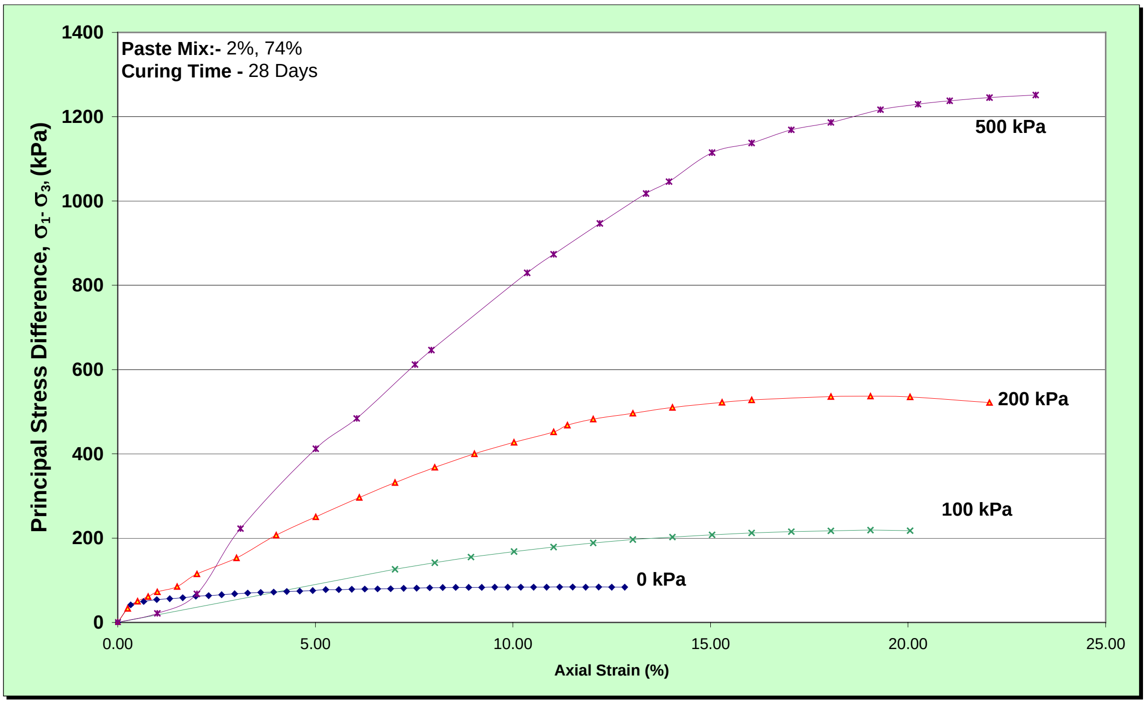

Figure 3. 48 General Stress strain behaviour of paste for different confining pressures

As expected an increase in either the cement or solids content resulted in a stiffer mix and an increasingly brittle response from the paste. The increase in the confining pressure, results in a more significantly more ductile response from the paste. Many of the samples tested showed signs of the onset of failure only after exceeding axial strains well in excess of 20%. The mechanical limit of 25% axial strain was imposed by the travel of the load rod in the triaxial cell. Therefore the true extend of the axial strains before failure may be underestimated. The axial strain at failure was plotted against the minor principal stress and is shown in Figure 3.49. An additional figure showing the failure strains for the fill mixes after 14 days has been included in as Figure A3.5.1 in Appendix 3.5 also.

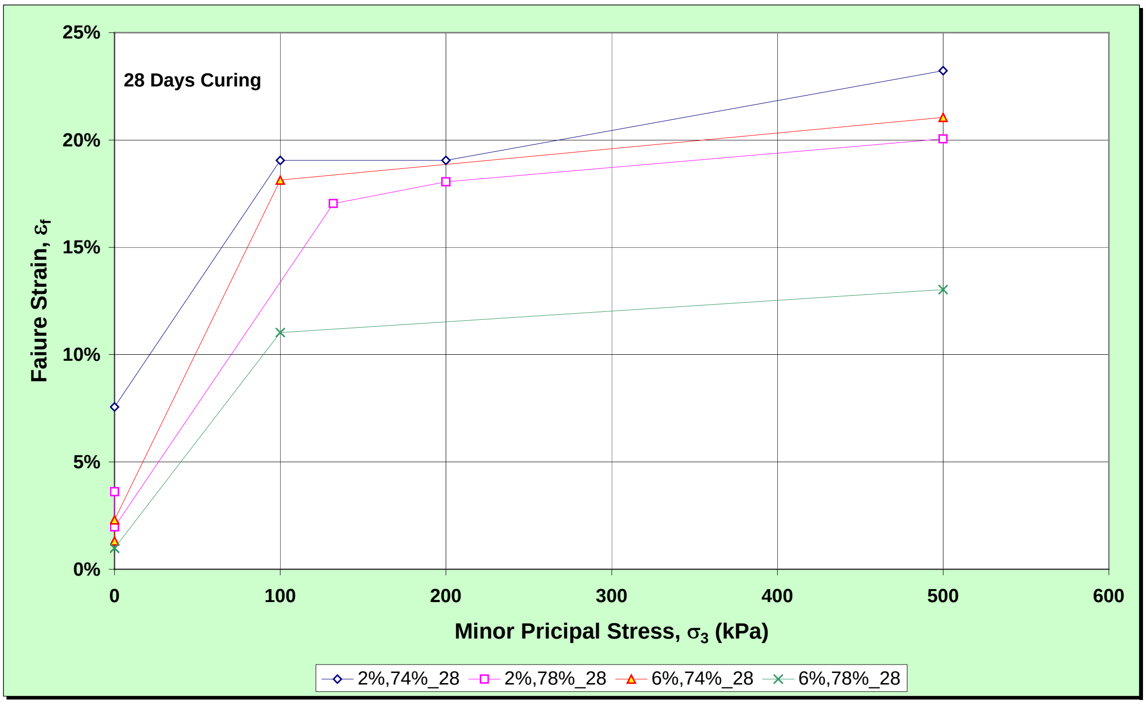

Figure 3. 49 Failure strains vs. confining pressure for 28 days curing for various paste mixes

The two interesting points to note on this graph is that the failure strains are high and do not increase substantially after 100 kPa of confining pressure has been applied. The high failure strain rates are related to the fine grain size distribution in the tailings and the clay fraction in particular. The highly ductile behaviour of clays typically exhibit ε_f of 15% and above. The increase of ε_f after σ_3 = 100 kPa similar for all mixes. In both instances the indication is that paste has reverted to the behaviour of the parent material. The small and consistent increases in failure strains after σ_3 = 100 kPa for all mixes results from the increased frictional resistance of samples under higher levels of confinement. The failure strains for the 6% cement, 78% solids samples are significantly lower than for other paste mixes. The higher density fill, coupled with the high cement contents were shown to resist the fracturing/ crumbling effect along the failure planes, to a greater degree than any other samples during testing, resulting in the lower failure strains.

A confining pressure 100 kPa is considered low. All paste in situ is considered likely to be subjected to confining stresses greater than this, which from testing would indicate that all the cementitious bonds would be broken and only the frictional resistance of the fill would be effective. This is not the case, as failures during exposure would result in all cases. The 100 kPa is an incremental increase in the effective confining pressure, after the formation of the permanent and rigid CSH (calcium silicate hydrate) bonds. The formation of the CSH bonds from the alite reaction occurs after approximately twenty four hours and continues until curing is complete. These bonds are most commonly associated with the long term strength of cement. It is there for assumed that no yielding of cement bonds occur until after isotropic compression of the specimens has occurred fully.

To identify the effect of cementation and initial mean effective stress on the deviator stress at failure Figure 3.50 was plotted. The unconfined compressive strength indirectly takes into account the affect of strength of the increases in cement or solids content and provides a simple and effective reference tool.

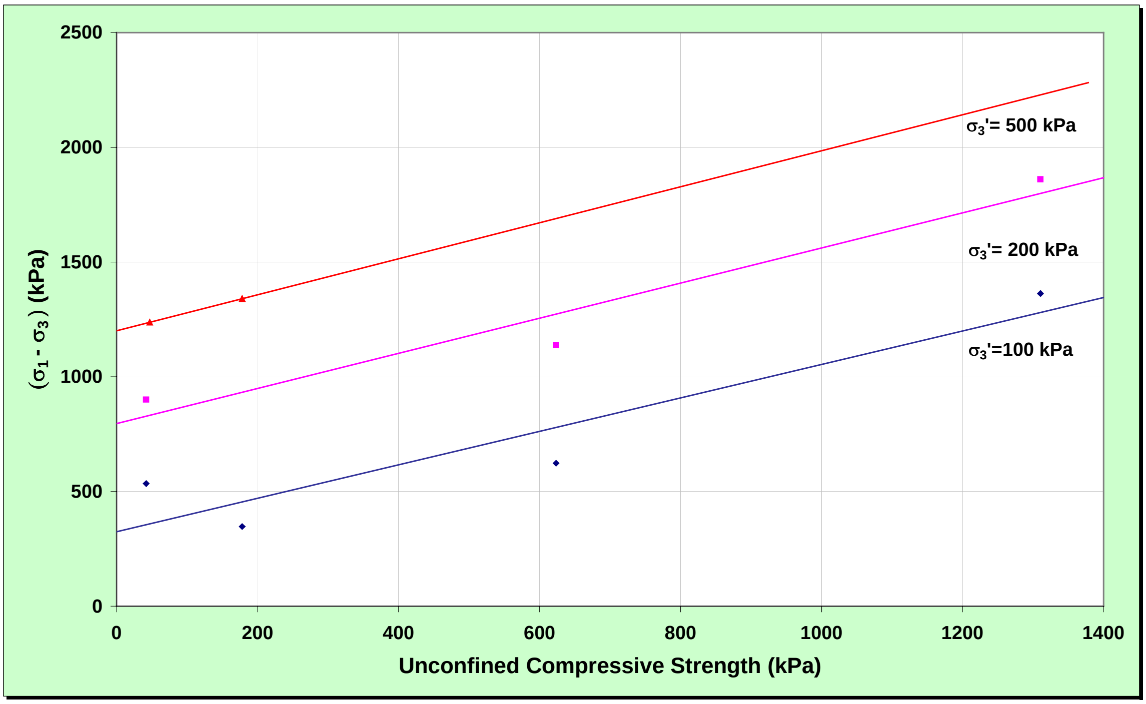

Figure 3. 50 Effect of cementation and mean effective stress on deviator stress at failure (14 days Curing)

Each of the lines in Figure 3.50 may be expressed in general terms by the equation: -

$$q_f = a\sigma_{3i}^{'} + bq_u \quad \text{… (3.12)}$$

where

q_f = deviator stress at failure (kPa)

$\sigma_{3i}^{'}$ = initial mean effective stress (kPa)

q_u = unconfined compressive strength (kPa)

a = constant

b = constant – relating the gradient of the slope with the increase in unconfined compressive strength, which is dominated by cement content.

The deviator stress at failure for a cohesive soil described in terms of the initial mean effective stress and effective friction angle by:-

$$a\sigma'_{3i} = \sigma'_{3i} * \tan^2\left(45 + \frac{\phi^{'}}{2}\right) + 2 * c' * \tan\left(45 + \frac{\phi^{'}}{2}\right) \quad \text{…(3.13)}$$

Assuming that the tailings are not cohesive, equation 3.13 reduces to:-

$$a\sigma'_{3i} = \sigma'_{3i} * \tan^2\left(45 + \frac{\phi^{'}}{2}\right) \quad \text{…(3.14)}$$

From Figure 3.50 the constant b can be determined to be approximately 0.75. The deviator stress at failure may then be determined using the form:-

$$q_f = \sigma_{3i}^{'} * \tan^2\left(45 + \frac{\phi^{'}}{2}\right) + 0.75q_u \quad \text{…(3.15)}$$

The frictional and cohesive component of the total strength may then be identified by each of the separate terms in equation 3.15. The effect of dilation on the shear strength is inherently taken into account if the peak effective friction angle is used.

To identify the pre-failure behaviour of the paste was observed by observing the secant deformation modulus (E_s). Jardine et al. (1984, 1986) and Tasuoka et al. (1993,

1997) noted the difficulties associated with the interpretation of the modulus, with its interdependence on the shear strain amplitude and mean effective stress. Additional, recent work by Kim et al. 1994, has identified modulus degradation of granular materials with increasing shear strains. Schnaid et al. (2001) identified a constant modulus for cemented sand samples at low confining pressures, until such time as the cement bonds yielded and a distinct degradation of the deformation modulus was observed. To date there has been no investigations undertaken into the effect of higher confining pressures on cemented triaxial samples. Figure 3.51 is typical of the responses observed for paste fills with lower levels of cementation in triaxial compression.

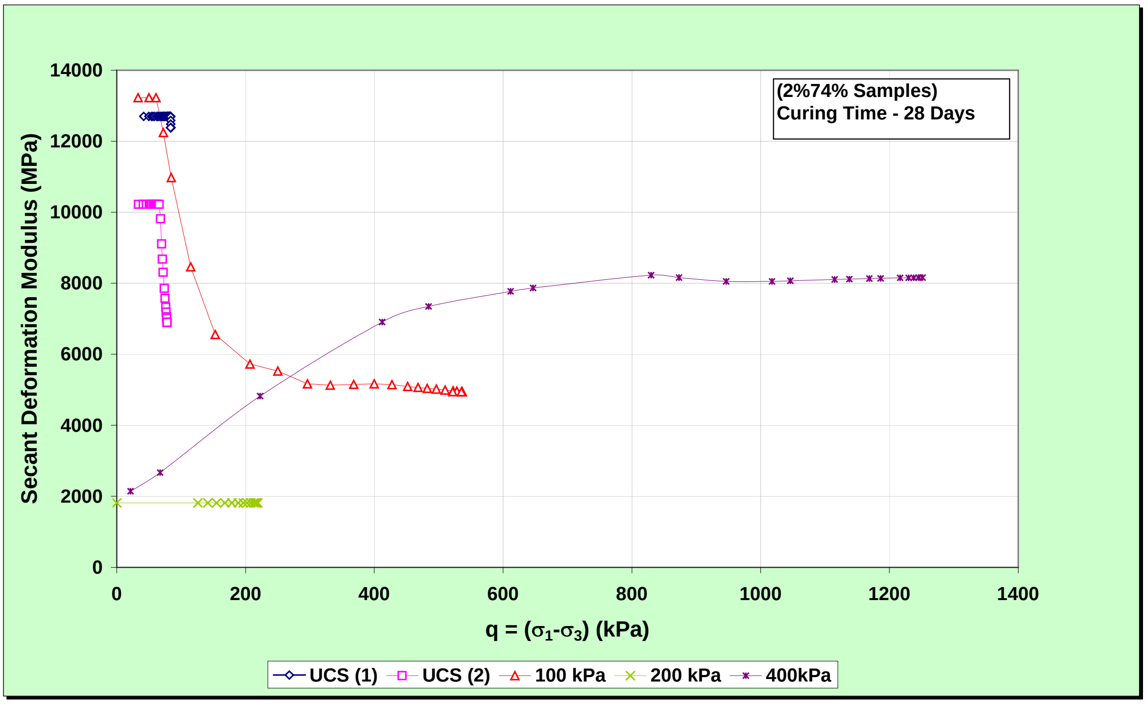

Figure 3. 51 Response of the secant deformation modulus for paste in triaxial shear under different levels of confinement.

Lower levels of cementation with the paste shows the distinct pattern observed for cemented sands by Schnaid et al. (2001), of modulus remaining constant to the point of cement bond yielding followed by a significant decrease to asymptote to a lower value. The sample confined under 200 kPa shows a constant modulus, significantly lower than the UCS samples, but equivalent to the initial E_s value of the sample confined at 500 kPa. This consistency in the value suggests that the effective confinement placed on the samples initially, reduces the effect of the cement bonds, resulting in the frictional response dominating behaviour. Under the highest levels of confinement, E_s increases steadily until failure. This form of strain hardening is associated with the particles collapsing to fill any available voids, thus increasing the density of the samples, as is observed with loose sands in direct shear. The peak values for E_S, found from the average UCS tests, were plotted against the "residual" values, obtained from the samples effected by higher confining stresses, for all of the paste mixes to identify whether there existed any correlation. Figure 3.52 shows a strongly linear relationship between the peak and residual stiffness of a fill mix.

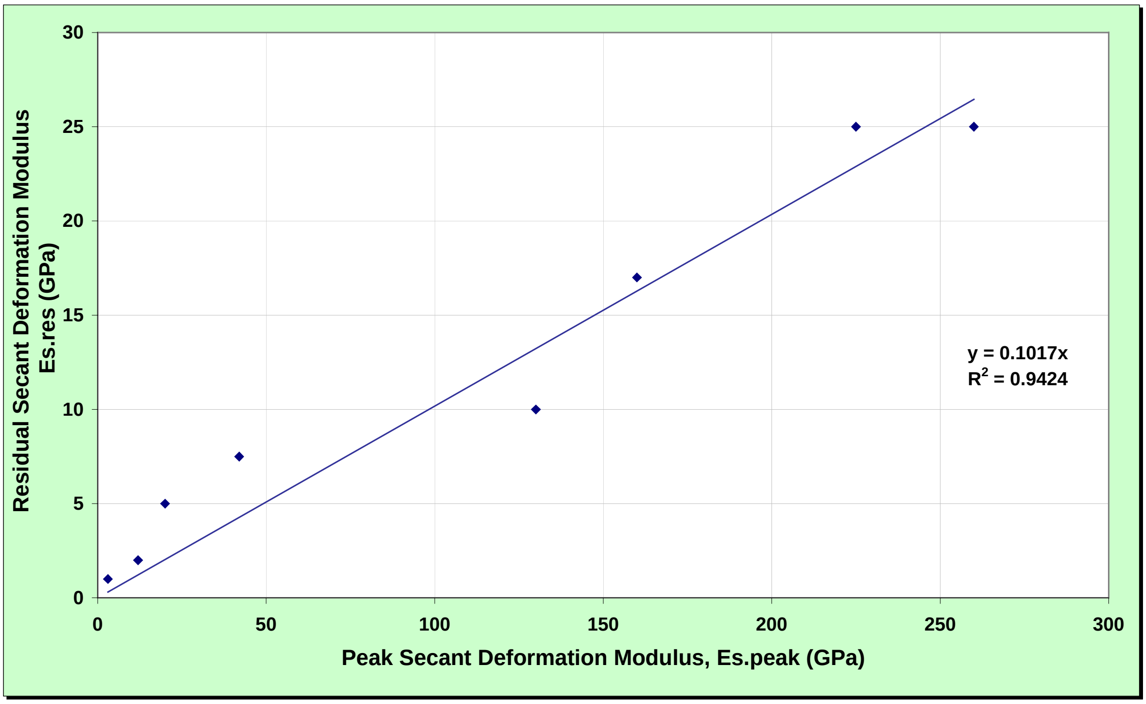

Figure 3. 52 Peak versus residual secant deformation modulus (E_s) for paste fills.

The dependence of the residual stiffness on the peak E_s shows that the effect of cementation is simply reduced under higher confining pressures and frictional factors may dominate the response. This would indicate that cement provides additional stiffness in the vicinity of 10 times that which is provided by the friction of the tailings. This finding contradicts those of previous researchers including Schnaid et al. (2001), who suggested that the secant deformation modulus of cemented sands revert to a stiffness equivalent to that of the equivalent unbound material.

When comparing the additional plots for E_s against the deviator stress for the remaining paste samples and curing times (refer Figures A3.5.2 to A3.5.9) the following trends are observed.

- Stiffness increases with cement and curing time
- Brittle failure occurs with 6% cemented samples and no decrease in E_s was observed.
- Cement content provides approximately 10 times the stiffness to the paste than the frictional component of the tailings
- Confinement of 100kPa or greater tends to cause the yielding of cement bonds and a reduction of E_s to a residual stiffness of the fill.
- The effect of confinement on samples is related to the strength of the sample. Higher levels of confinement are required to affect or yield the cohesive bonds the of higher strength samples
- Work hardening of samples is only observed in the 2% cement 74% solids samples (i.e. weakest and lowest solids density samples).

The effective strength parameters of the effective friction angle, ϕ' and effective cohesion, c' were found from CD triaxial testing and have been summarised in Table 3.17

Table 3. 17 CD Triaxial Summary – effective friction angle and cohesion

Mix	Curing Time (Days)	Effective cohesion, c' (kPa)	Effective friction angle, ϕ' (Deg)
2%, 74%	14	11.3	43.3
2%, 78%		43.4	32.7
6%, 74%		141.0	35.4
6%, 78%		317.6	36.0
2%, 74%	28	17.2	44.1
2%, 78%		70.3	31.7
6%, 74%		170.5	32.5
6%, 78%		474.4	33.0

A gain in the effective cohesion for the paste was observed for all samples and is associated with an increase in solids or cement content and time. The effective friction angles vary significantly but maintain similar trends to those reported by Pierce (1997) and Aref et al. (1988, 1989). Pierce reported that c' increased with binder content and curing time and ϕ' decreased significantly (refer Table 2.6). Trends of which are observed with Cannington paste also. The effective friction angle range of 28 to 41 reported by Pierce for CU testing of the Giant Golden mine paste is very similar to those for Cannington paste also.

The applicability and validity of the Mohr- Coulomb failure criteria to paste, was investigated using s-t plots. A typical response is shown in Figure 3.53, additional plots are contained within Appendix 3.5.

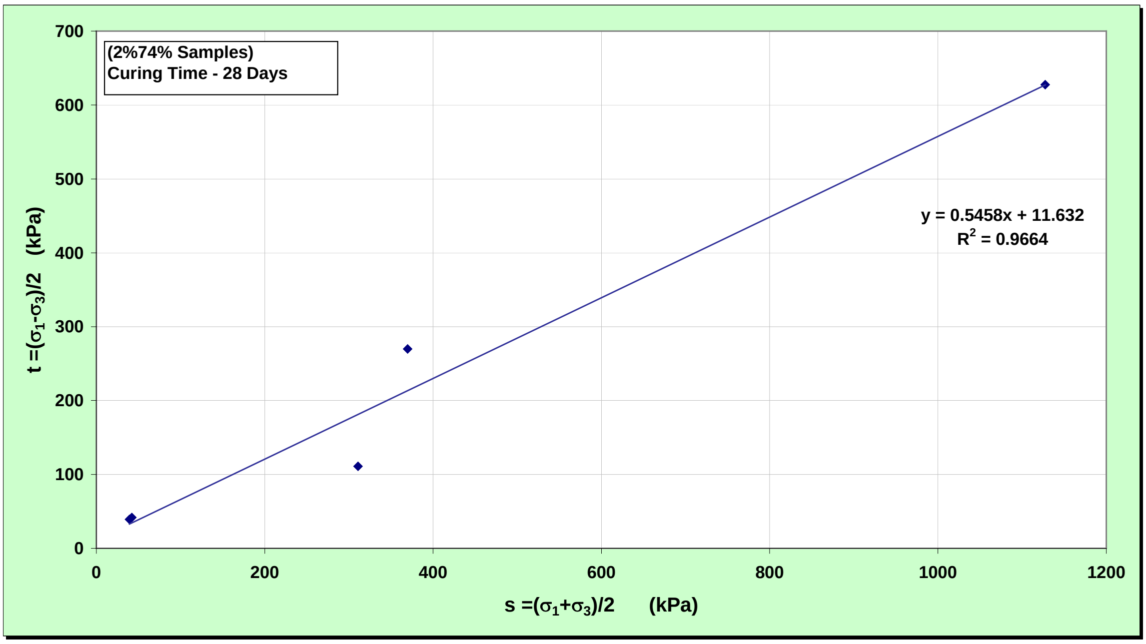

Figure 3. 53 s-t plot for 2% cement, 74% solids after 28 days curing

All plots returned correlation coefficients of greater than 0.9, indicating a very strong relationship to the Mohr-Coulomb failure criterion. It is considered valid and applicable to paste. A quick reference chart has been developed and is included as Figure A3.5.10 in Appendix 3.5 to determine the effective cohesion of paste, c' from mix proportions.

Deformation Characteristics (E and ν)

The Poisson ratio of the paste is expected to remain within the 0.1 to 0.25 range previously defined. Samples with a higher cement contents are expected to have a lower Poisson's Ratio.

Effect of Time

The curing time each one of the material properties associated with the strength and deformation of the paste. The bonds of hydrated cement continue to form and solidify, causing a rigid soil matrix to form. The most rapid change is from the initial placement to 14 days cured strength, after which the relative strength and stiffness of the mix are not significantly affected by curing time. Neither are the deformation characteristics of E or ν.

3.9 Consolidation Testing

Odeometer testing was undertaken to identify the of consolidation parameters of paste fills. The constitutive model used to model the fill was the Mohr-Coulomb model and thus does not require the identification of any material properties from consolidation testing. However, more advance constitutive models, such as the Cam-Clay model does use state parameters, which are derived from oedometer tests. To satisfy the need for future modeling requirements the full results from testing have been included in Appendix 3.7. The procedures for the preparation of the tailings, test samples and the test procedure have been included in Appendix 3.1 along with the testing schedule.

Preliminary investigations have focussed on identifying three parameters; the coefficient of consolidation, c_v, and the coefficients of primary, C_c, and secondary compression, C_{α}.
c_v, describes the rate of settlement during primary consolidation, C_c the variation of the void ratio with effective stress and C_{α} the settlement rate during secondary consolidation. The test results for:- c_v, C_c, and C_{α}, have been summarized in Tables 3.18 to 3.20 respectively.

Table 3. 18 c_v for different mixes under different loadings

MIX		c_v (m^2/yr) for X kPa normal pressure				Average
% Cement	**% Tailings**	**12.5k Pa**	**25 kPa**	**50 kPa**	**100 kPa**	c_v (m^2/yr)
2	74	4.89	1.82	4.88	0.94	3.13
2	78	7.64	4.04	3.63	6.03	5.34
6	74	4.52	2.50	1.73	1.22	2.49
6	78	4.90	5.78	8.47	6.93	6.52

The general trends are: -

- c_v increases with solids contents
- c_v is independent of cement content
- c_v reduces with the increased stress levels in samples with lower solids content
- c_v remains reasonably constant with samples with higher solids content

It can be deduced that solids content dictates the rate at which consolidation occurs. The c_v for paste with a lower solids content, tend to reduce under higher loads whereas they remain reasonably constant, and significantly higher, in samples with a higher solids density. This can be explained if one considers a volumetric unit of saturated paste under compression. In a higher density sample the volume of water available in the volumetric unit to resist any immediately applied load, is less. The pore pressure will therefore be accordingly higher than it would be in the lower density samples. The higher pressure increases the rate of consolidation by forcing the pore water out of the sample under greater pressure.

The compression index, C_c, relates the change in void ratio to the change in effective stress. From oedometer testing a step change between the C_c values were observed at after the 25 kPa loadings had occurred, especially with the higher cement content samples. This value was chosen to represent the yielding of cement bond and the averages of C_c prior and post bond yield calculated. The results are shown below.

Table 3. 19 C_c for different mixes under different loadings

MIX		C_c				Average C_c	
% Cement	% Tailings	12.5k Pa loading	25 kPa loading	50 kPa loading	100 kPa loading	Prior to cement bond failure	Post cement bond failure
2	74	0.3571	0.3811	0.4335	0.5320	0.3691	0.4828
2	78	0.2218	0.2873	0.3453	0.3716	0.2546	0.3585
6	74	0.1088	0.2543	0.4714	0.6294	0.1816	0.5504
6	78	0.0627	0.1024	0.2083	0.3729	0.0825	0.2906

Solids content governs the deformation (C_c) of the paste fill matrix prior to cement bond yielding, and solids content after yielding has occurred, as expected. This is shown by the significant changes in C_c for the higher cement content samples. A significantly lower C_c value for higher solids content samples (after yielding) can be seen when compared to lower solids content samples. The variation for the compression index, is expected as until cement bond yielding occurs the rigidity provided by the cement, governs and limits the deformation, once broken, the lower solids content samples are able to compress further through the additional re-alignment of the soil matrix structure into the available void space.

The coefficient of secondary compression, C_α refers to the rate re-alignment of the particles in a soil matrix under a defined normal load, after primary consolidation has occurred. The test results on the paste mixes have been summarized in Table 3.20 and show that the samples with lower solids density tend to undergo larger secondary compression settlement than those with a higher solids density.

There are several factors that may affect the magnitude of secondary consolidation, however some of them are not very clearly understood. The ratio of secondary to primary consolidation for a given thickness of soil layer is dependent on the stress increment, ($\Delta\sigma'$) and the initial effective stress (σ_{3i}') (Mesri 1973). The smaller the ratio ($\Delta\sigma'/\sigma_{3i}'$), the larger the ratio of secondary- to-primary compression.

Table 3. 20 C_α for different mixes under different loadings

MIX		C_α				Average C_α
% Cement	**% Tailings**	12.5k Pa loading	25 kPa loading	50 kPa loading	100 kPa loading	
2	74	0.0232	0.0233	0.0242	0.0247	0.0239
2	78	0.0132	0.0132	0.0253	0.0226	0.0186
6	74	0.0063	0.0200	0.0300	0.0306	0.0217
6	78	0.0053	0.0105	0.0137	0.0369	0.0166

Ladd (1971) suggested that the ratio of C_α/C_c is a constant (approximately 0.05) for natural soils during secondary compression. Mesri and Godlewski (1977) confirmed the validity, of this assumption for a range of soils. The validity of this assumption was tested for the paste fills using C_c before and after cement bond yielding. A summary of the results is reported in Table 3.21.

Table 3. 21 C_α / C_c for different mixes prior to and after cement bond yielding

MIX		$C_{\alpha\ (av.)}$	Prior cement bond yielding		Post cement bond yielding	
% Cement	**% Tailings**		C_{c_prior}	C_α/ C_{c_prior}	C_{c_post}	C_α/ C_{c_post}
2	74	0.020	0.369	0.054	0.483	0.041
2	78	0.019	0.255	0.073	0.359	0.052
6	74	0.022	0.182	0.120	0.550	0.039
6	78	0.017	0.083	0.201	0.291	0.057

The ratio of C_α/ C_c for paste after cement bond yielding, correlate well to the values suggested by Mesri and Godlewski (1977). Samples with higher solids contents had slightly higher ratios, resulting from the decrease in C_c. The lower cement content samples yielded ratio which agree also with those proposed by Mesri et al. (1977). However the samples with higher cement contents had ratios well in excess of the 0.05 average that was an “assumed” constant. The structural integrity of the cement bonds had not been violated, therefore restricting C_c and increasing the ratios. As the confinement increased, the cement bonds yielded and the paste fill reverts to the behavior of the parent materials, dependent only on the packing solids density of the fill.

Appendix 3.7 contains the summary plots from consolidation testing.

UCS Tests on samples cured under surcharge

Some preliminary testing was conducted on samples with surcharge during the curing phase. Paste samples were cast into cylinders with top and bottom caps, which had a number of drainage holes drilled into them to allow free drainage. Filter paper was cut to size and placed over the end of the end caps to stop the migration of the fines. Surcharges were applied to the curing specimens via buckets that were filled with various amounts of water to provide a range of applied pressures as would be expected in the field. The paste samples were then left to cure for 28 days and then tested in unconfined compression.

The trends show an increase in the strength of the paste under increased consolidation pressure. The increase in the measured tangential Young's modulus and decrease in measured failure strain all indicate the densification of the solid matrix in the paste structure. Results from the *preliminary* testing have been included in Appendix 3.7. The curing of samples under surcharge is thought to be more indicative of actual in-situ conditions, as curing occurs under the load applied from the continuous filling of stopes. The results are not considered to be absolutely conclusive but do provide a basis for justification for further research.

3.10 In-Situ Testing

A series of Dynamic Cone Penetrometer Tests (DCPT) were carried out on in-situ paste fill. Also, undisturbed samples were recovered from various paste fill stopes and UCS tests were performed on these.

3.10.1 Dynamic Cone Penetrometer Testing

The dynamic cone penetrometer (DCP) is one of a series of dynamic penetrometers that correlate the strength and stiffness of the material to the penetration resistance of the tip. The penetration resistance is measured in number of blows per penetration interval. The Standard Penetration Test (SPT) is the best known and most widely used. DCP test (DCPT) was preferred in the underground environment, as there were very tight physical restraints provided by the narrow excavations, headings etc. The size and superior manoeuvrability of the DCP rig precluded the use of any other type of in-situ testing equipment (i.e. SPT of CPT). Table 3.22 compares the specifications of four of the most popular dynamic penetration techniques. The specifications outlined for the DCPT are accurate for the rig used for testing the in-situ paste at Cannington.

Table 3. 22 Dynamic penetrometer Specifications (after Foruria 1984)

Dynamic Penetration Method	Mass of Hammer (kg)	Height of fall (m)	Dimensions of Probe				Penetration Interval (mm)	Relevant Standard
			Diameter		Shaft Length (mm)	Apex Angle ( )		
			Outer (mm)	Inner (mm)				
HDP/ DCPT	50	0.5	43.7	-	43.7	90	100	DIN 4094 Part 1 and 2 (German Std.)
SPT	63.5	0.75	50.8	35	~800	60	300	ASTM D 1566-67

The in-situ appraisal of the strength of paste was done on stope 42..61 HL in the experimental drive, 59XC. Stope 42..61 HL was backfilled with waste rock (mullock) and paste from a fill winze that was approximately central to the plan of the stope. The resulting fill contained a rock core with paste fill surrounding it, as shown in Figure 3.54

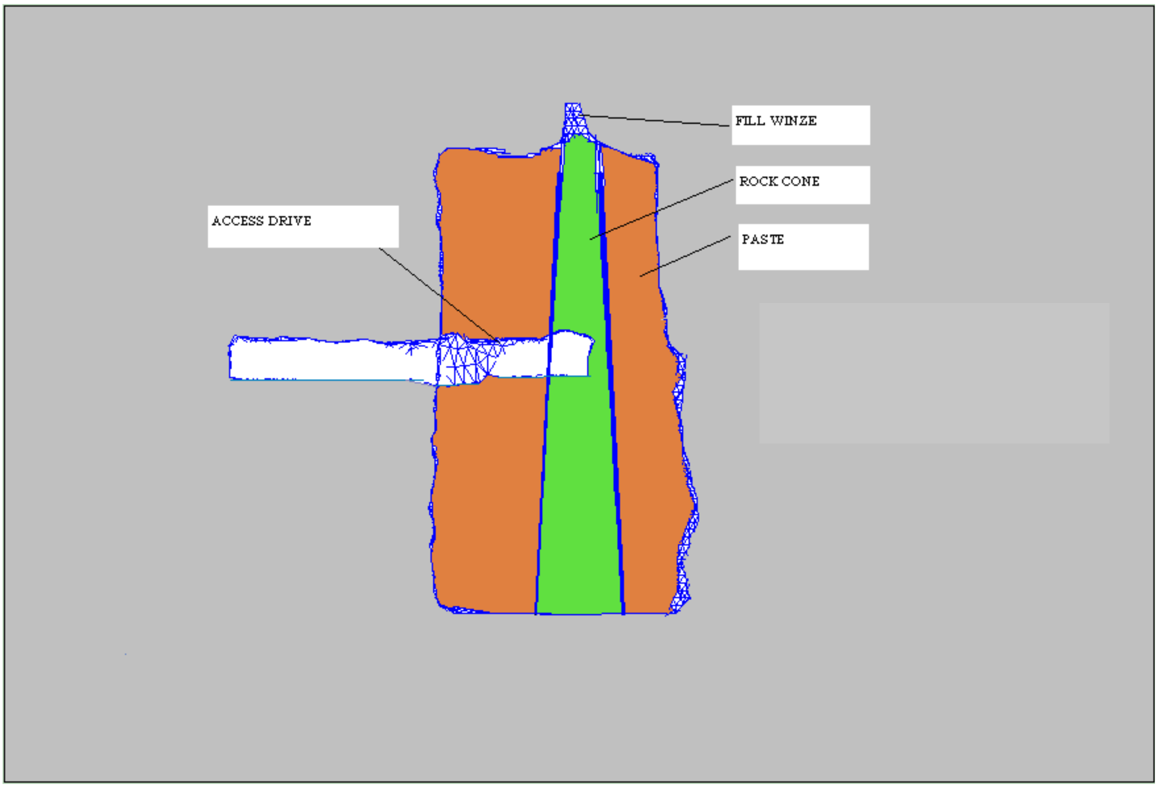

Figure 3. 54 Cross sectional elevation of stope 42_61 HL

Six evenly spaced holes were then drilled into the floor, as shown in Figure 3.55 and cleaned out using compressed air. The holes were prepared to a depth of approximately 1.5 m, to ensure that the broken and fractured paste and road base[5] had been passed and the testing would be indicative of the actual paste. Figure 3.55shows the plan view locations of the DCPT holes in relation to the rock cone within the stope.

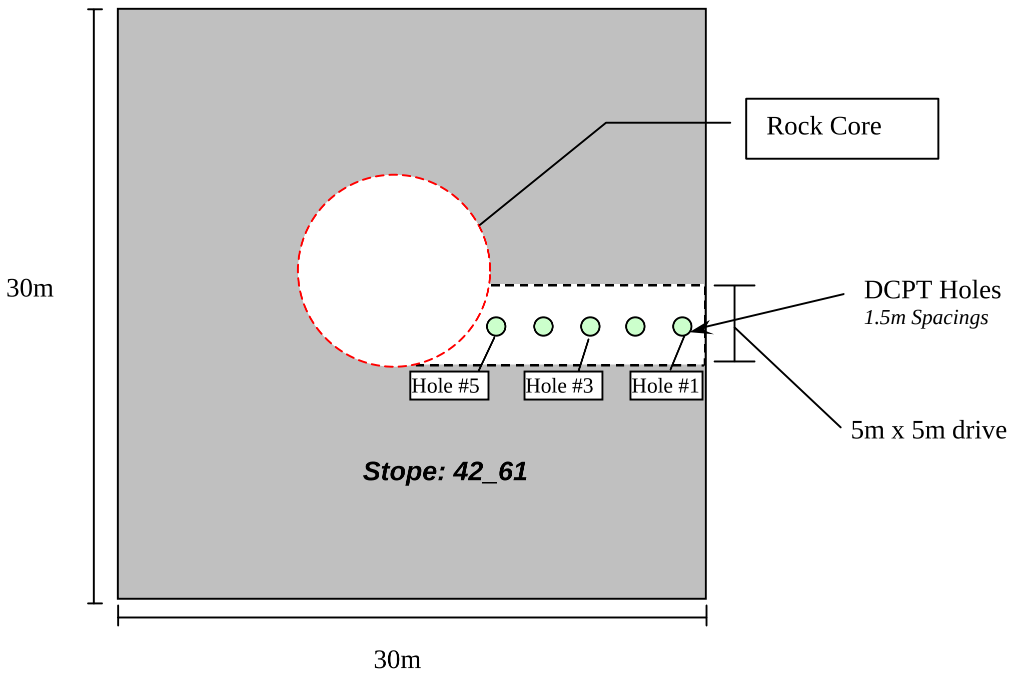

Figure 3. 55 Location of DCP Testing Holes

Figure 3.56 hows the DCPT operational, underground at Cannington mine. The confinement provided by the drive, and applicability of the DCPT rig to such tightly confined situations is obvious.

To date the SPT is the most widely used in-situ testing equipment world wide. A number of correlations with strength and deformation characteristics to blow count have been determined for the SPT (Meyerhof 1957, Teng 1962, Skempton 1986, Ishihara 1993, and Cubrinovski, M. & Ishihara, K., 1999, 2000, 2001).

---

[5] Road base is typically placed on access roads where trafficking occurs to provide

Figure 3. 56 Operational DCPT rig, underground at Cannington Mine

The dynamic probing mechanism is very similar to that of pile driving, from which the theory has been applied. To relate the DCPT blow count to an SPT "N-value" the data was converted using a specific energy equivalence ratio (S_e). Specific energy is defined as the energy required to displace a unit volume of material, and was calculated in accordance with equation 3.16 (Poulos and Davies 1980).

$$S_e = \left(\frac{m + n^2 m'}{m + m'}\right)\left(\frac{mgh}{e}\right)e_f \qquad \ldots(3.16)$$

where

m = mass of hammer

m' = mass of rods

n = coefficient of restitution

g = gravitational constant

h = fall of hammer

e = average penetration per blow in meters

e_f = hammer efficiency

traction and stability to vehicles and reduce the associated erosion.

Previously the value of the coefficient of restitution, n , has been used as either 0 or 1 (Bock 1984; Weisner, 1982). Assuming n = 0 is considered unreasonably conservative as it will overestimate the impact losses and thus over reduce the values of the penetration resistance. Polous and Davies (1980) suggest that n = 0.5 is a more realistic assumption.

A relationship between the DCPT and SPT results was found by determining the ratio of the specific energies of the DCP to the SPT. To incorporate the different geometries of the tips for the SPT and DCP rigs, the specific energy was divided by the respective cross sectional areas.

$$S_{DCP} = \left(\frac{m + n^2 m'}{m + m'}\right)\left(\frac{mghN_{DCP}}{0.1A_b}\right) \qquad \text{…(3.17)}$$

where

N_{DCP} = blows per 10cm interval in DCPT

=0.1 / e

and from Table 3.22,

m = 50 kg

h = 0.5m

A_b = 1500 mm^2

m’ = 6 kg/ length

and for the SPT

$$S_{SPT} = \left(\frac{m + n^2 m'}{m + m'}\right)\left(\frac{mghN_{SPT}}{0.3A_b}\right) \qquad \text{…(3.18)}$$

where

N_{SPT} = blows per 30cm interval

=0.3/ e

and from Table 3.22

m =63.5 kg

h = 0.75 m

A_b = 2027 mm^2 – solid/ plugged SPT Tip

= 1065 mm^2 – unplugged sampler

m' = 8 kg/ length

In both equations the $\left(\frac{m + n^2 m'}{m + m'}\right)$ terms are approximately equal at any given depth. Thus they may be ignored when considering the ratio of equations 3.17 and 3.18, resulting in equation 3.19

$$\frac{S_{DCP}}{S_{SPT}} = r.\left(\frac{N_{DCP}}{N_{SPT}}\right) \quad \ldots(3.19)$$

Where

r =2.13 (for plugged or solid SPT tip)

=1.12 (unplugged SPT split spoon sampler)

Assuming tests are in the same medium and similar friction losses, then

$$\frac{S_{DCP}}{S_{SPT}} = 1 \quad \ldots(3.20)$$

Therefore a ratio of,

$$\frac{N_{SPT}}{N_{DCP}} = 1.12 \quad or \quad 2.13 \quad \ldots(3.21)$$

depending on whether the tip is plugged or unplugged. This is in agreement with the relationship published in DIN 4094 Part 2 (refer Table 3.23). A factor of 1.2 was assumed for the correlation of the DCPT results to the SPT N value and was considered reasonable for the application to paste fill. Most correlations discussed in literature are based on the unplugged split spoon sampler.

Table 3. 23 Relationship between blow count for SPT and DCPT in non-cohesive soils

Relationship	$\frac{N_{SPT}}{N_{DCP}}$ **Ratio**
Theory	1.12 - 2.13
DIN 4064 (Part 2) – German Standard	1.2 - 1.7

Results

In general, more than one empirical correlation is available to derive each particular soil property (refer Appendix 3.8, Table A3.8.5), and the accuracy of estimations is highly dependent on selection of the appropriate correlations for the respective material. Use of available laboratory soil test results, as well as any other available collateral information to select the right correlation for each soil material can increase significantly the confidence in the estimated parameters. A basic outline of the procedure used to identify the the soil parameters is shown the flow diagram in Appendix 3.8.

The initial blow counts obtained from the DCP rig were corrected using a specific energy equivalence ratio of 1.2 to obtain an equivalent SPT blow count. Corrections were then applied for overburden stress and efficiency of the energy transference of the rods. When correlating the results to an equivalent CPT tip resistance, $q_{c,}$ a correlation between the grain size distribution and (q_c/N) ratio for the material. The corrected blow count for overburden $(N_1)_{60}$, or equivalent tip resistance (q_c), were then used to correlate the penetration resistance of the paste to physical properties and liquefaction potential using various empirical charts.

SPT Corrections

The equivalent SPT blow count, N, was corrected for hammering efficiency and overburden stress. The hammering efficiency was calculated and standardized to $(N_1)_{60}$ by using equation 3.22 and the factors summarised in Table 3.24.

$$(N_{60})_1 = C_N * N * \eta_1 * \eta_2 * \eta_3 * \eta_4 \qquad \ldots(3.22)$$

where

η_i = adjustment factors

$(N_{60})_1$ = adjusted N using adjusted to a efficiency of 60

C_N = adjustment for effective overburden pressure,

Table 3. 24 Corrections for Hammer Efficiency (source: Foundation and Design, Bowles 1995)

Hammer for η_1					Remarks
	Average energy ratio E_r				
	Donut		Safety		
Country	R-P	Trip	R-P	Trip/Auto	R-P = Rope-pulley or cathead $\eta_1 = E_r/E_{rb} = E_r/70$ For U.S. trip/auto $w/E_r = 80$ $\eta_1 = 80/70 = 1.14$
United States/ North America	45	—	70–80	80–100	
Japan	67	78	—	—	
United Kingdom	—	—	50	60	
China	50	60	—	—	
Rod length correction η_2					
	Length	> 10 m		η_2 = 1.00	N is too high for $L < 10$ m
		6–10		= 0.95	
		4–6		= 0.85	
		0–4		= 0.75	
Sampler correction η_3					
		Without liner		η_3 = 1.00	Base value
	With liner:	Dense sand, clay		= 0.80	N is too high with liner
		Loose sand		= 0.90	
Borehole diameter correction η_4					
	Hole diameter:†	60–120 mm		η_4 = 1.00	Base value; N is too small when there is an oversize hole
		150 mm		= 1.05	
		200 mm		= 1.15	

Corrections for overburden pressure have been developed by a number of researchers, Seed et al. (1975), Peck and Bazaraa (1969), Peck et al. (1974) and Liao and Whitman (1986). The correction by Liao and Whitman (1986) takes the form of equation 3.23 is the most widely used and accepted in industry and was used in the calculation of the correction for overburden pressure for this research.

$$C_N = \sqrt{\frac{95.76}{\sigma'_{vo}}} \qquad \ldots (3.23)$$

where

σ'_{vo} = overburden pressure (kPa)

The calculation of the overburden pressure is made difficult by the inclusion of the curing of cement in the fill mass. The development of overburden pressure is limited by the time taken for the paste to "set" (i.e. gain enough strength to resist consolidation via additional overburden pressure). Once the initial set of paste had occurred the additional weight is transferred to the walls via shear. Preliminary investigations and discussions with underground personnel suggest that a period of five hours is sufficient to allow the initial set to occur. The effective overburden pressure is thus calculated from the depth of paste before initial set has occurred. This is a function of the cross-sectional area of the stope, filling rate and paste density. A initial set time of five hours was assumed to allow initial set. This approximation was based on field observations which suggest paste gains sufficient cured strength to support additional weight after a period of four to six hours. The effect of the curing of cement is to maintain the correction for overburden at a constant level, with the exception of the portion of the stope which is filled in the final five hours. The correction was applied to all depths of the fill as the experimental drive was developed into paste at approximately mid-height of the stope.

The corrections used for the the determination of an equvalent SPT $(N_{60})_1$ were:-

η_1 = 0.85
η_2 = 0.75
η_3 = 1.00
η_4 = 1.00
C_N = 1.75 (based on a cross-sectional area of 400 m^2, a filling rate of 250 t/hr and a paste density of 2.2 t/m^3)

SPT Correlations - Relative Density, D_r

Relationships between the relative density and the SPT blow count (N) have been proposed by Meyerhof (1957), Teng (1962), Skempton (1986) and more recently by Ishihara (1993) and Cubrinovski & Ishihara, (1999, 2000, 2001). The earlier attempts (Meyerhof 1957 and Teng 1962) to relate the relative density to N_1 the corrected blow count for overburden. Initially Meyerhof (1957) suggested that the penetration resistance of the soil was assumed to increase with the square of the relative density and in direct proportion to the overburden pressure of the sands in the form of equation 3.24.

$$N = \left(17 + 24\frac{\sigma_v'}{98}\right)D_r^2 \qquad \ldots(3.24)$$

where

N = SPT blow count

σ_v' = effective overburden pressure (kPa)

D_r = relative density expressed as a decimal

Skempton (1986) generalised the equation, by setting the values of 17 and 24 nominally to "a" and "b", and then normalized it to an overburden pressure of 98 kPa to reduce the expression to: -

$$\frac{N_1}{D_r^2} = a + b \qquad \ldots(3.25)$$

where

N_1 is the normalised penetration resistance to an overburden pressure of 98 kPa.

Meyerhof (1957), indirectly suggests that the penetration resistance of the soil is independent of the grading or type of soil by maintaining that (a+b) = 41 is a constant. Subsequent work by Tatsuoka et al. (1978), Skempton (1986) and Ishihara (1993) suggest that the parameter a+b tends to decrease with decreasing mean grain size distribution. Meaning that a well-graded fine material will be at a significantly higher relative density to a poorly graded coarse material at the same blow count. A method of the quantification of the grading and indicative size of the soil particles was required.

Cubrinovski & Ishihara (1999, 2000, 2001) proposed the void ratio range (e_{max}-e_{min}) as an indirect measure of the soil gradation, especially for sandy soils. They then related (e_{max}-e_{min}) to D_{50} as shown in Figure 3.57 where they suggested the equation:

$$e_{\max} - e_{\min} = 0.23 + \frac{0.06}{D_{50}} \qquad \ldots(3.26)$$

where

D_{50} is measured in mm.

The relationship between $\frac{N_1}{D_r^2}$ and the void ratio range, e_{max}-e_{min}, was then related by the same authors (refer Figure 3.58) and takes the form:-

$$\frac{N_1}{D_r^2} = \frac{9}{(e_{\max} - e_{\min})^{1.7}} \qquad \ldots(3.27)$$

By substituting equation 3.26 into 3.27, a function relating mean grain size and the corrected blow count may be established.

$$\frac{N_1}{D_r^2} = 9\left(0.23 + \frac{0.06}{D_{50}}\right)^{1.7} \qquad \ldots(3.28)$$

Therefore, once the mean grain size D_{50} and N_1 are known, D_r can be estimated from the following graphs.

From this – it is a simple manipulation of the above result to obtain the relative density of the soil. The concept of increased relative density for finer grained soils is considered a notable aspect of this design approach.

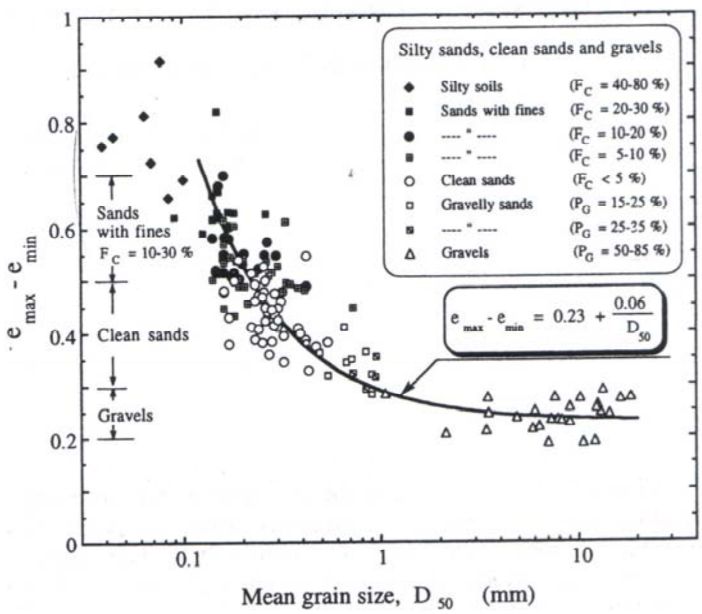

Figure 3. 57 Variation of Void Ratio Range with Mean grain size distribution (Cubrinovski & Ishihara 2001)

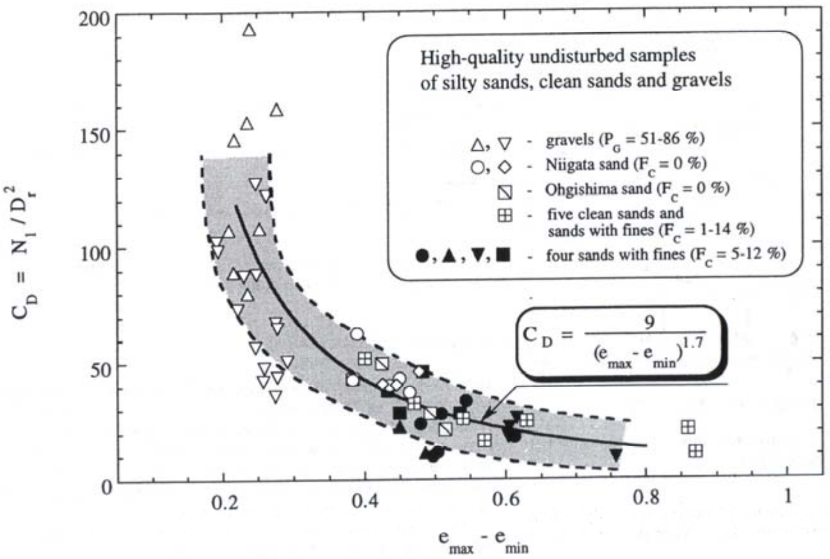

Figure 3. 58 Relationship between the N_1 / D_r^2 and void ratio range

When comparing equation 3.28 to other well established relationships between the corrected blow count and relative density such as:-

$$\frac{(N_1)_{60}}{D_r^2} \cong 60 \text{ (Kulhawy and Mayne 1990)} \qquad \ldots(3.29)$$

$$\frac{(N_1)_{60}}{D_r^2} \cong 70 \text{ (Skempton 1986)} \qquad \ldots(3.30)$$

The corrected blow count $(N_1)_{60}$ to relative density ratio is only consistent with the previously determined relationships when D_{50} is approximately 15 microns, which implies that it is only valid for a very small range of values. A decrease in grain size results in a decrease in the relative density of the material for a constant blow count. A small variation in the mean grain size also results in a significant variation to the ratio also. It may then be inferred that the variation of stiffness, blow count, void ratio range caused by the addition of cement to a backfill may cause the results to be unrepresentative and unreliable, using the void ratio range as an indicator. When using the relationship proposed by Meyerhof (1957), (refer equation 3.24), and using an effective overburden pressure of 30 kPa (refer to calculations and explanations for C_N = 1.75 for overburden in the previous section). The ratio of blow count, N (uncorrected) to relative density results in (a+b) = 24.4 as opposed to the 41 suggested by Meyerhof (1957). This implies a lower relative density for a given blow count. This results from the solidification of the fill through the hydration of cement. The increased stiffness and self-supporting ability of the paste after the initial set has occurred hours enables the transfer the vertical load, through shear, to the supporting walls. This reduces the densification of the fill through consolidation, by limiting the applied vertical pressure

Table 3. 25 SPT blow count vs. relative density (after Teng 1962)

Compactness	SPT Blow Count, $(N_1)_{60}$		Relative Density D_r	
Very Loose	0	4	0%	15%
Loose	5	10	16%	35%
Medium	11	30	36%	65%
Dense	31	50	66%	85%
Very Dense	51	100	86%	100%

Teng (1962) suggested the correlations between SPT blow count, N, and relative density of geomaterials that are shown in Table 3.25.The ranges have been used to give indicative ranges of the relative density of the paste. Teng (1962) was chosen on the basis that the results used to derive the correlations were on lightly to heavily compacted sands and silts, with some inclusion of cement sands. The average corrected $(N_1)_{60}$ blow count of paste ranged from 29 to 34, which suggests that the insitu relative density of the fill lies somewhere between D_r of 60% to 70%.

SPT Correlations – Drained Friction Angle

A number of researchers have attempted to relate the SPT-N value corrected for overburden to the effective friction angle (Meyerhof 1956, Bowles 1982, Peck et al. 1974, Schmertmann 1975 and Das 1984) (refer Figure 3.59).

Of these relationships, Peck et al. (1974) is the most widely used and will provide the basis for the determination of the friction angle from the test results in this research. Using Peck et al. (1974) correlation, the paste fill tested returned a drained friction angle of between 35 and 36 degrees, which is in reasonable agreement with the drained friction angles found during CD triaxial testing.

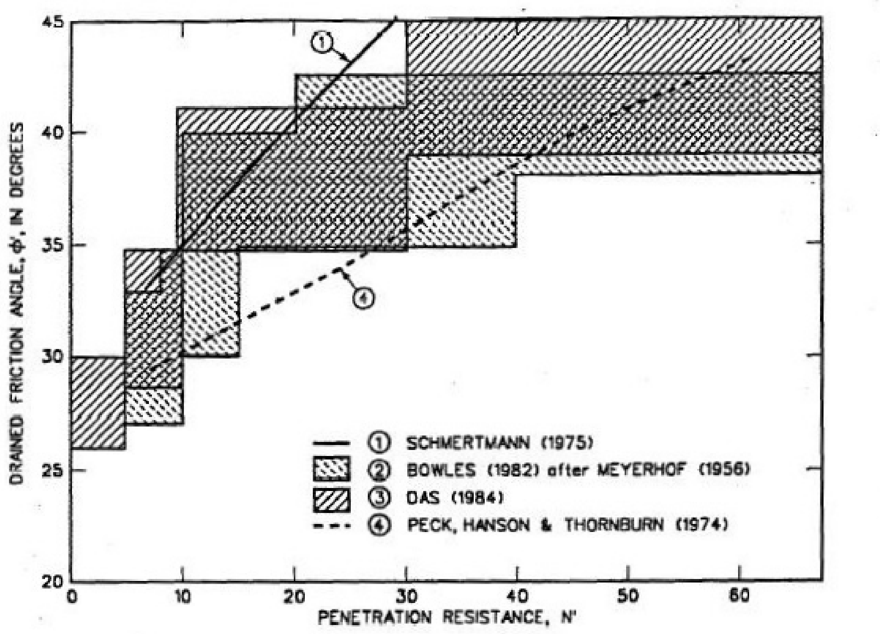

Figure 3. 59 Correlations between drained friction angle and corrected SPT results.

SPT Correlations – Youngs Modulus

Leonards (1986), suggests a correlations between the SPT blow count, $(N_1)_{60}$, and Young's Modulus (E) for normally consolidated sands of $8*(N_1)_{60}$, when E is expressed in terms of kg/cm^2. The equivalent SPT blow count from the DCPT testing is shown in Figure 3.60 for holes one, three and five located as shown in Figure 3.55.

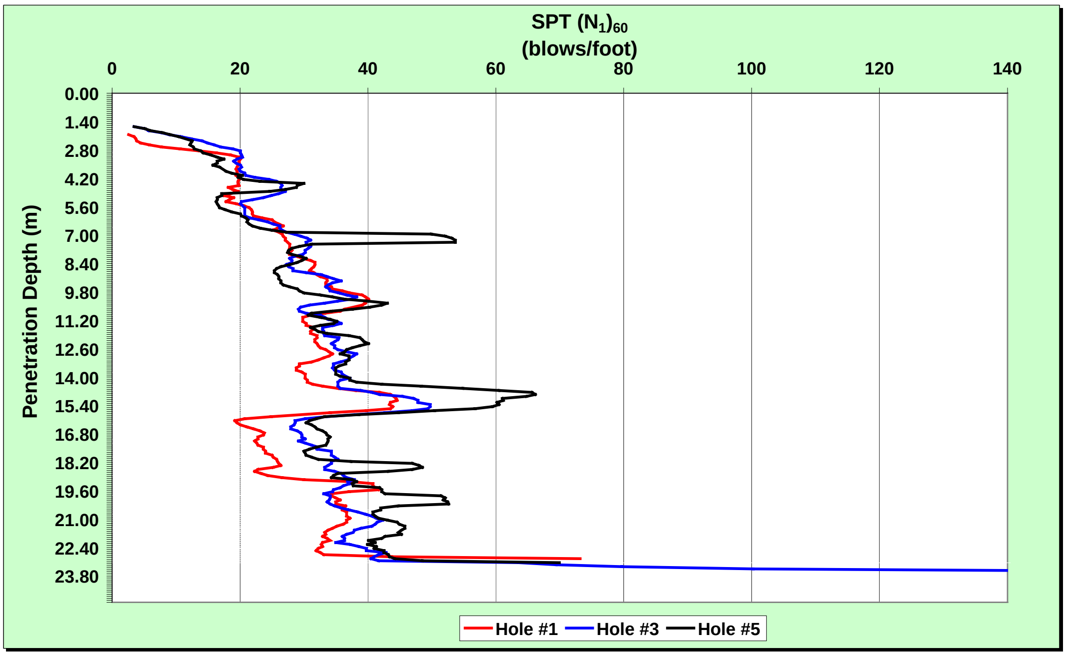

Figure 3. 60 Equivalent SPT blow count, $(N_1)_{60}$ vs. depth

The Young's modulus for in-situ paste samples taken adjacent to where the testing occurred was approximately 45 MPa or 458.9 kg/cm^2. Average multiplication factors of 20.1, 19.5 and 19.7 were found for holes 1, 3 and 5 respectively. The effects of hydration, would contribute significantly to the increase in the stiffness of the material. The consistency of the factors indicate the uniformity of the placed paste. A line of best fit was inserted for each of the DCPT test holes and the trends of the blow counts observed. Figure 3.61 shows the increasing trend of the corrected penetration resistance, N_1, with the depth and movement towards the centre of the stope. This is consistent with the effects of consolidation with the highest vertical loads and hence consolidation occurring towards the centre of the stope. Additional loads with the increasing depth would have contributed to the consolidation of fill also. Currently there is an assumption that consolidation of fill does not occur, as paste remains fully saturated. These in-situ results are in opposition to this theory, and support the idea of an increased research potential to define the consolidated strength of paste. As was briefly discussed in Section 3.9 *"UCS Tests ion samples cured under surcharge"*

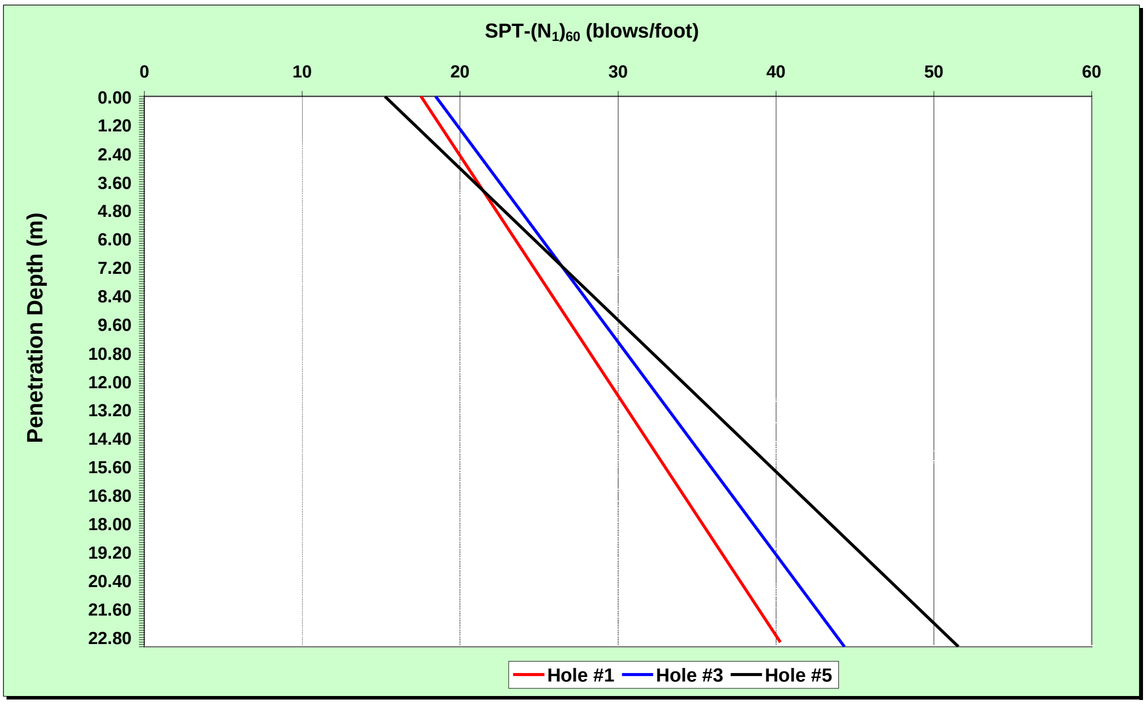

Figure 3. 61 Trend of corrected blow count vs. depth

SPT Correlations and Liquefaction Potential

The liquefaction potential of paste fill has been assessed by a number of researchers including, Been et al. (2002), Aref et al. (1989), Ouellet et al. (1998) and Pierce et al. (1997). The identified conditions conducive to the liquefaction of a fill mass are: - contractant behaviour under loading, high saturation levels and the absence of cohesion. The determination of the liquefaction potential of soils has been simplified by the evaluation of liquefaction potential with field-based tools such as the DCPT, SPT and CPT rigs.

Seed et al. (1985) developed a procedure using the equivalent cyclic stress ratio ($CSR_{eq} = \frac{\tau_h}{\sigma'_{vo}}$) and SPT blow count N to estimate the liquefaction potential of sandy soils. The CSR_{eq} relates an earthquake magnitude to an equivalent number of laboratory loading cycles. The CSR is considered to have been induced in the middle of the critical layer normalises the shear stress, induced by the seismic activity by dividing it by the initial overburden stress. Stark and Olsen (1995) refer to the CSR_{eq} as the seismic shear stress ratio or SSR. Citing the basis of field data to evaluate liquefaction for the more appropriate name. The SSR may be calculated using the simplified method proposed by Seed and Idriss (1971).

$$SSR = 0.65 * \frac{a_{\max}}{g} * \frac{\sigma_{vo}}{\sigma'_{vo}} * r_d \qquad \ldots(3.31)$$

where

a_{max} = peak acceleration measured or estimated at the ground surface of the site

g = acceleration of gravity (9.81m/s^2)

σ_{vo} = vertical total overburden stress

σ'_{vo} = vertical effective overburden stress

r_d = depth reduction factor, where in the top 10 m of soil, it may be estimated by $r_d = 1 - (0.012 * z)$. No depth reduction factor is applied in the top 10m (r_d=1.0)

z = depth in meters

The SSR is then standardised with respect to an earthquake of magnitude 7.5, using the magnitude correction factor c_m, proposed by Seed et al. (1985) and plotted on Figure 3.62 to indicate the liquefaction potential. Seed et al. (1985) and Seed & De Alba (1986) proposed boundary lines that separate regions of with significant liquefaction potential from those with limited potential. The solid lines plotted on Figure 3.62 show the delineation between the areas of high and low potential for liquefaction with various percentages of fines. The solid lines were developed for clean and silty sands, and therefore contain a significantly coarser size grading of material. The dashed line indicates the expected behaviour of fills with higher proportions of fines. Because the undrained yield strength of the soil controls the triggering of liquefaction, Stark and Mesri (1992) concluded that the SSR at the boundary line is equal to the undrained yield-strength ratio of the soil mobilized in the field for a given corrected blow count.

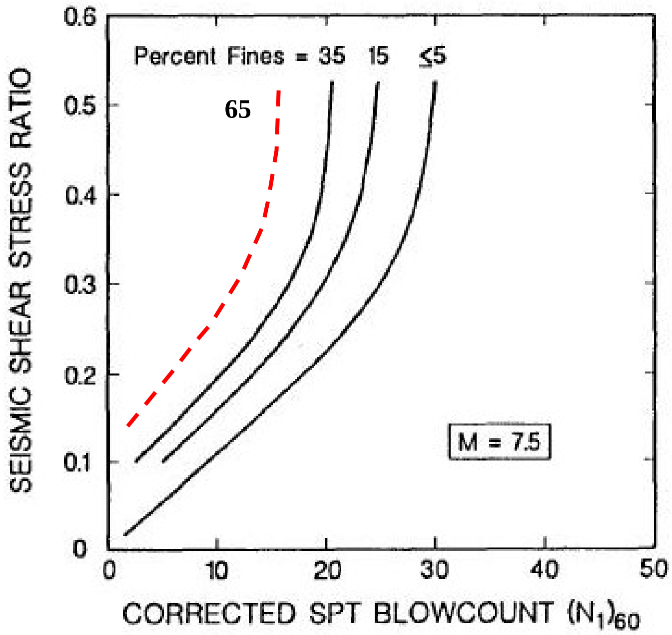

Figure 3. 62 Relationship between seismic shear-stress ratio triggering liquefaction and $(N_1)_{60}$ - values for clean and silty sand for M=7.5 Earthquakes (After Seed and De Alba 1986)

It should be noted that Figure 3.62 does not account for the effect of cementation. Lewis et al (1999) suggests dividing the blow count by a factor of 2.2-3.0 for old sand deposits that had undergone natural cementation. The average corrected SPT $(N_1)_{60}$ values for the paste fill tested (3.5%, 76% solids) are 30, 32 and 35 for Holes 1,3, and 5 respectively. If a correction of 3.0 is applied to account for the cementation of the paste, the SPT $(N_1)_{60}$ values become 10, 10 and 11 respectively. There is approximately 65% < 75 μm in the Cannington paste. If the trends from Seed & De Alba's (1986) graph are extrapolated, as indicated by the dashed line, it which would suggest the tailings themselves would have a moderate to high susceptibility liquefaction.

CPT Correlations

To further investigate the indicative properties of the soil from the in-situ testing, correlations using an equivalent CPT tip resistance, q_c, were used. To obtain an equivalent tip resistance q_c, Figure 3.63 was used.

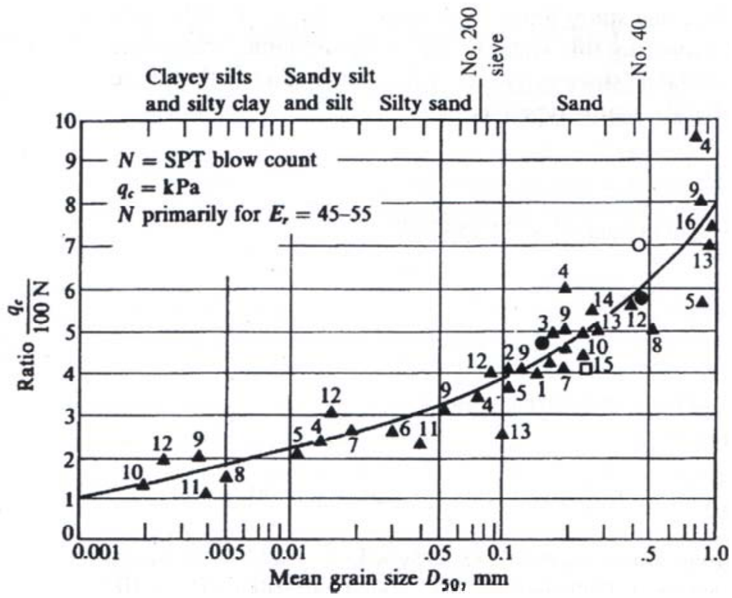

Figure 3. 63 Relationship between mean grain size (D_{50}) and qc/N ratio (After Robertson and Campanella 1983)

It is important to note that the relationship shown in Figure 3.63 is based on an energy ratio of 55% i.e. N=N_{55}. To convert N_{60} to an equivalent N_{55} value, multiply the SPT-N value by the ratio of 55/60.

CPT Correlations – Liquefaction Potential

Empirical charts relating the liquefaction potential of various types of soil, to the corrected CPT results have been presented by Stark and Olson (1995), after the back analysis of 180 liquefaction case histories of sandy and silty sandy soils (Figure 3.64).

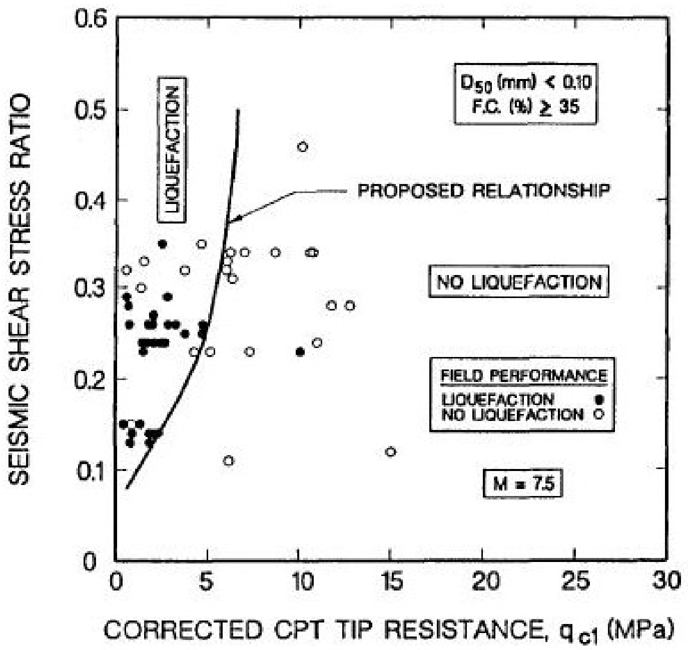

Figure 3. 64 Relationship between seismic shear stress ratio triggering liquefaction and qc1 values for silty sand to sandy silt and M=7.5 Earthquakes (After Stark and Olson 1995)

An increase to the resistance to liquefaction resistance is observed with the increased fines content. The effect of fines on the liquefaction resistance is clearly identified in Figure 3.65. The liquefaction potential reduces with the increased level of fines. Paste fill is considered to be a lightly cemented sandy clayey silt, which would plot to the left of the sandy silt line (Approximately 65% fines content).

DCPT being a dynamic test like SPT, and having the blow counts in both tests well related, the liquefaction potential charts based on SPT results are recommended when DCPT data are used.

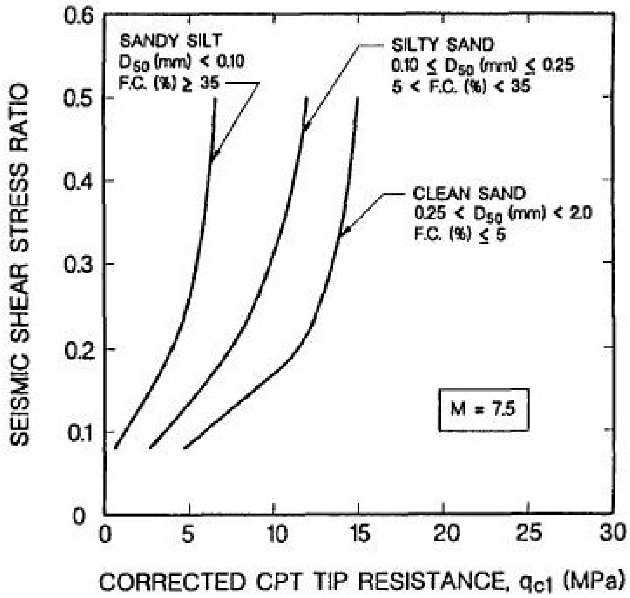

Figure 3. 65 CPT-Based Liquefaction- Potential Relationships for Sandy Soils and M=7.5 Earthquakes, (After Stark and Olson 1995)

Summary of DCPT Testing Results

Table 3.26 summarises the results from the analysis of the in-situ field testing done on the paste / rock fill in stope 42_61.

Table 3. 26 Summary of in-situ field measurements obtained from DCPT testing

Hole Number	$(N_1)_{60}$	Av. D_r Range Teng (1962)	Av. ϕ'(Deg) Peck et al. (1974)	E /$(N_1)_{60}$ (MPa)
1	29	36%-65%	36	1.9
3	32	66%-85%	36	1.5
5	34	66%-85%	37	1.5

From this it would appear that the paste is becoming denser towards the middle of the stope. The increasing average corrected blow count shows an increased resistance towards the centre of the stope, which is consistent with an increased level of consolidation due to the higher vertical loads, resulting from the reduced effect of arching towards the centre of the stope. Although the relative densities of the fill fall within the same range, the increasing corrected blow count indicates that the paste towards the centre of the fill mass (hole #5) would at a higher relative density in-situ than the paste towards the edges (hole #1). The average relative density of the in-situ samples was found to be 60% which correlates reasonably well to the predicted values from Teng (1962), albeit on the lower end of the spectrum.

The variation between the holes is found to increase only slightly towards the centre of the stope. Increased friction angles have been associated with a decrease in void ratio which equates to an increase in relative density (Holtz & Kovacs 1981, US Navy 1971). The predicted values of 36 to 37 correlate well to the drained friction angles from the CD triaxial testing (32 - 44), which show a greater degree of scatter and a bias towards drained friction angles approximately 32 –34 . An increase in the friction angle may be expected with the increased confining pressure of insitu paste, as compared to laboratory cast sample, however, it should be noted that the relationships are empirical correlations based on sand and silty sand based materials.

The decrease of the ratio of $E/(N_1)_{70}$ as the holes tend towards the centre of the also suggest a definite densification of the paste. Figure 3.61 confirms this with the average corrected blow count to increasing as movement is made from hole #1 to hole #5. A similar and more distinct trend is observed with the increase in depth, which suggest that consolidation of paste increases with depth also. The effect of which is to cause the backfill to be the strongest and stiffest in the areas of highest stress.

3.10.2 In-situ Unconfined Compressive Strength Testing

A series of uniaxial compressive strength samples were formed from the blocks of in-situ paste recovered from underground stopes. Two blocks from different stopes were tested for strength and the physical properties quantified. Table 3.27 summarises the two test series.

Table 3. 27 Summary of UCS test smples

Block	Location	Paste Mix	Sample Identification
1	Stope: - 47_73 77 XC–475 mLv	8% C,77% S	4773.1
			4773.2
			4773.3
			4773.4
2	Stope: - 42_61 59 XC–400 mLv	3.5% C, 76%S	4261.1
			4261.2
			4261.3
			4261.4

Samples were formed by skilfully cutting back the original block to a shape, which approximated the correct dimensions for the samples. The sample tubes (38 mm ID) previously used for the casting of the laboratory samples were used as a guide and a finishing tool to provide very accurate and well-formed samples. The samples were then cut to size using conventional soil sample formers.

The UCS test results of the in-situ cores are summarised in Table 3.28 and Figures 3.66 and 3.67. The full summary of results is contained within Appendix 3.8.

Table 3. 28 In-situ UCS core testing

Block	Sample No.	UCS (kPa)	Moisture Content	Bulk Density (t/m^3)	Dry Density (t/m^3)	Porosity
1	4773.1	874	32.23%	2.09	1.58	0.51
	4773.2	1311	26.94%	2.04	1.61	0.50
	4773.3	2262	15.35%	1.84	1.60	0.50
	4773.4	1374	25.80%	2.23	1.77	0.46
2	4261.1	478	5.50%	1.79	1.70	0.47
	4261.2	244	24.05%	2.02	1.63	0.50
	4261.3	250	24.48%	1.98	1.59	0.51
	4261.4	337	10.58%	1.87	1.69	0.48

A strong trend emerged with the paste samples relating the water content of the samples of the same fill mix with strength. The phenomena is not to be confused with the samples of varying solids content and complementary water contents showing variation in strength. As each of the sets of samples were formed from the same block of material, it is reasonable to assume that the solids and cement content for each of the samples were equivalent. The variation of water contents was achieved by the saturation of samples over various times (from minutes to days).

This result has previously been observed for saturated clays by Rutledge (1940), but would seem to be applicable to unsaturated paste fills also.

The reduction of strength with the increased water content would indicate that the premature failure was being caused by the inclusion of water into the soil matrix, and or pore pressure development. The variation of strength between the samples will be explained as a combination of the factors contributing to the strength gain and those detracting from it.

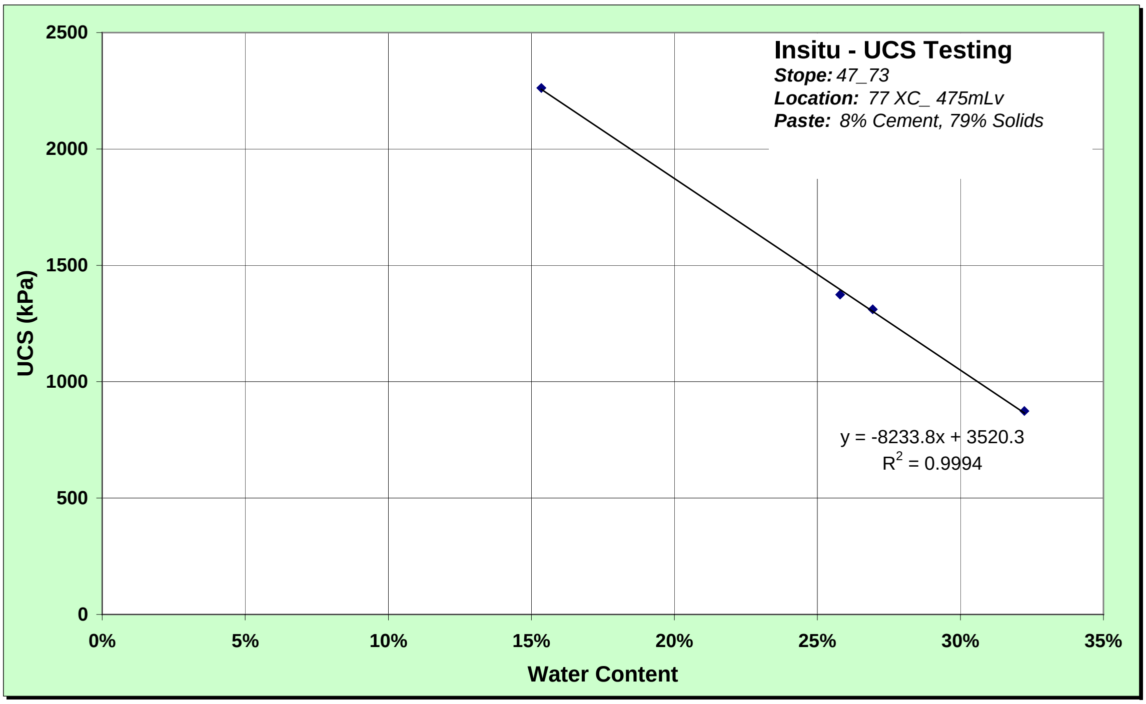

Figure 3. 66 UCS vs. Water content for paste (47..73 Stope)

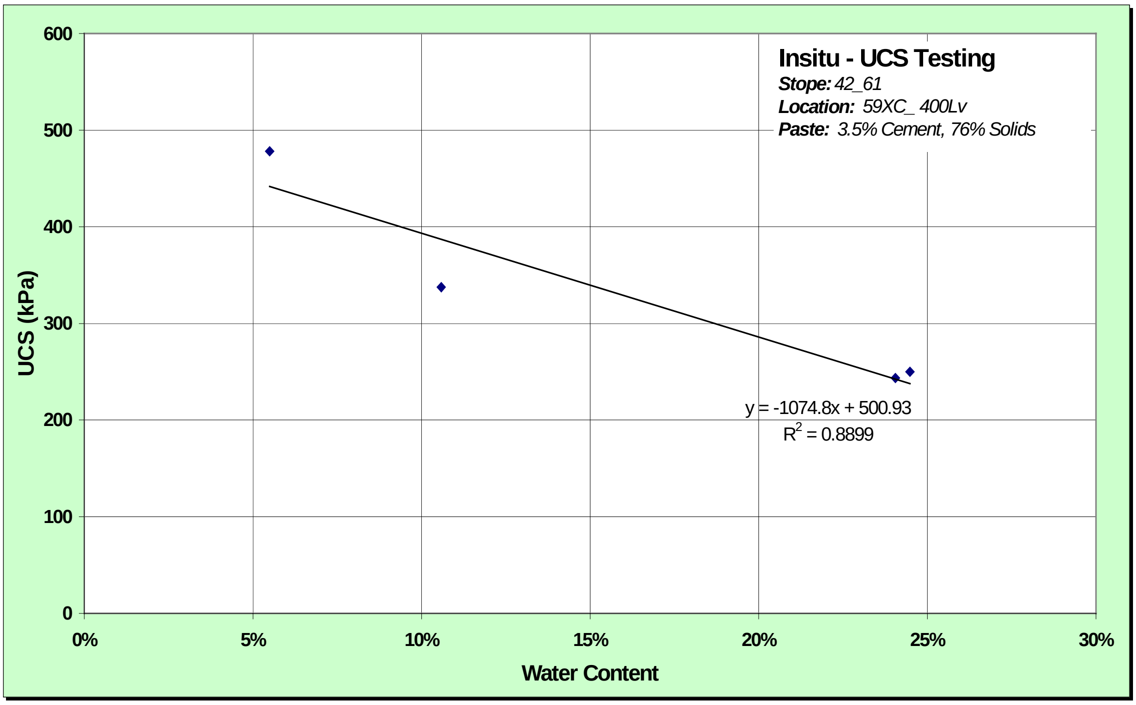

Figure 3. 67 UCS vs. Water content for paste (42..61 Stope)

As the "drying out" of the paste occurs it is postulated that a significant capillary force is generated which effectively provides a form of effective confinement by inducing internal stresses through the capillary effects. It is thought to be significantly stronger in paste than would be expected in other backfills due to the increased surface area and finer capillary pores.

The reduced strength of the samples with the higher water contents is due to the increase in excess pore water pressure. As the sample is loaded in unconfined compression, the additional loads are transferred into the paste matrix. If the voids are fully saturated the pore pressure will increase by the amount of the applied load, which will decrease the effective strength of the paste matrix and cause an internal failure through excess pore pressure build up. With the reduced levels of saturation, the proportion of the load transferred to the pore water reduces and effective strength at failure increases.

The determination of the strength variation with saturation levels fell outside the scope of the thesis. The strength of fill increases with the drying out of the paste, and hence analysis which was performed on paste with very high levels of saturation and will provide neglect any increases in strength of the paste due to this phenomena.

An artificial neural network (refer Chapter 5) using the long-term strength data for training was used to predict the strength of the samples listed in Table 3.29. It used the cement content, solids content and curing time to predict UCS. Figure 3.68 shows the performance of the neural network. The two horizontal lines on the graph result from the ANN predicting the strength of the samples using cement content, solids content and curing time as the principal criteria. The lateral spread of data shows the significant effect that moisture content has on sample strength – as described above. The shaded cells on the right hand side of Table 3.29 show the decrease in strength associated with the increase in moisture content, which causes the ANN to over predict sample strength.

Table 3. 29 ANN predicted strength vs. actual tested values of in-situ UCS cores

Sample ID	% Cement	% Solids	Curing Time (months)	Actual UCS (kPa)	ANN Predicted UCS (kPa)	**Moisture Content (%)**
4773.1	8	77	36	874	1777	32.2
4773.2				1311		26.9
4773.3				2262		15.4
4773.4				1374		25.8
4261.1	3.5	76	3	478	344	5.5
4261.2				244		24.0
4261.3				250		24.5
4261.4				337		10.6

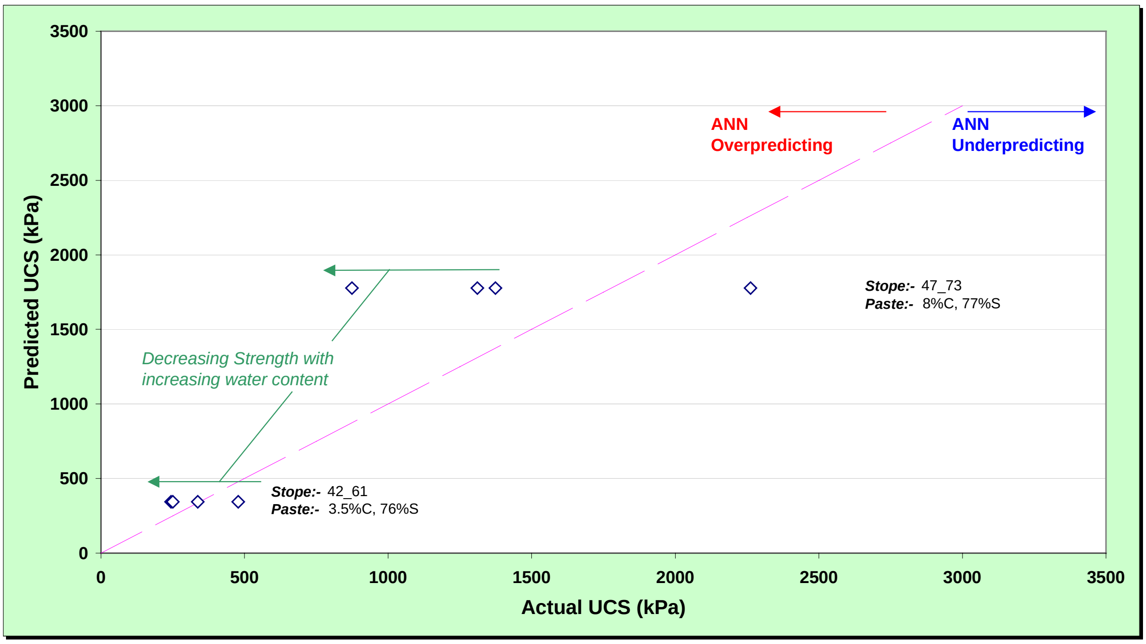

Figure 3. 68 ANN predicted UCS vs. Actual UCS for in-situ samples

3.11 Conclusions

Paste fill composes of full mill mine tailings, with a typical effective grain size of 5 μm, water and a small percentage of binder. In order to provide stability, paste fill must remain stable during the extraction of neighbouring stopes. If the paste becomes unstable, the adjacent faces may relax and displace into the open stope.

A qualitative assessment of tailings mineralogy using x-ray diffraction (XRD) coupled with a semi-quantitative x-ray fluorescence analysis indicated the presence of: - silver minerals (<1%), galena (2.4%), spalerite (1.3%), iron sulphides (39.5%), talc (11.1%)

and other silicates (40.7%). The silicates are mostly quartz as well as a small amount of chalcopyrite. The iron sulphides (39.5%) include pyrite, pyrrhotite and arsenopyrite. The remaining 5% consists of aluminium oxides (Chalcopyrite).

The specific gravity of the tailings was measured as 3.18, reflecting high content of heavy metal. The grain size distribution is shown in Figure 3.68

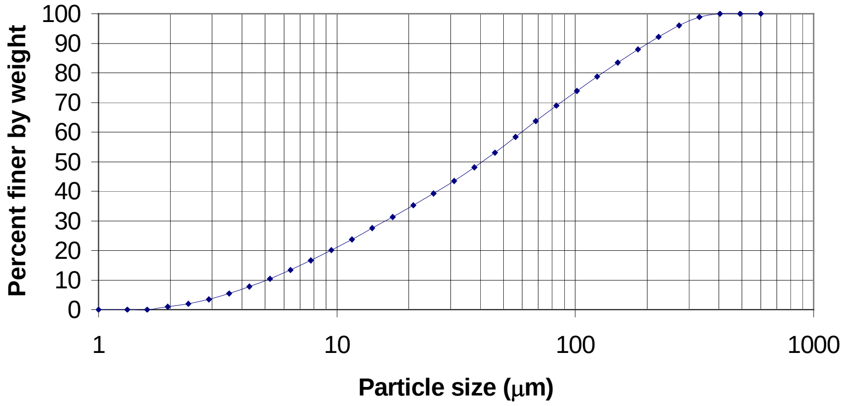

Figure 3. 69 Grain size distribution curve for Cannington Tailings

Distribution	2% clay, 8% Sand, 90% Silt
USCS Classification	Low plasticity clayey silt (CL-ML)
Coefficient of uniformity	0.82
Coefficient of curvature	11.2
%<20 μm	35.2%

Permeability (Hazen approximation) 2.6 – 3.9 x 10^{-7} m/s

Table 3.30 summarises the range and general trend of physical properties for paste for various fill mixes over a 12-month period. The variation in the properties associated with the water content and void ratios were observed to vary over time, as a result of the hydration of the cement within the fill mass. The ongoing hydration of cement caused the reduction in the water content and increased the entrained air voids within the paste.

Strength Testing

The investigation of strength and deformation characteristics of fill was conducted using both total and effective stress analysis. The progressive strength gain profile was investigated over the short medium and long term. Tables 3.31 and 3.32 summarises the tests and briefly describe the outcomes of testing, for the total and effective stress analysis techniques respectively.

Total Stress Analysis

Table 3. 30 Summary of testing and general outcomes from total stress analysis

TOTAL STRESS ANALYSIS		
TESTS	**DESCRIPTIONS**	**OUTCOMES**
Short Term (Batching – 7 Days)		
Viscometer Modified Pocket Penetrometer Mechanical shear vane UCS	Test program used to identify the early gains of strength for paste. test methods were calibrated against each other to ensure accuracy of predictions and determine relationships for practical on, site use.	Yield stress of paste dictated by solids content. Cement content provides additional strength after the “initial set” has occurred (1-3 hours) Linear strength gain of paste Modified pocket penetrometer correlations reasonable for a general trend, poor predictor of c_u values.
Medium Term (7 Days – 1 Month)		
UCS UU triaxial	Compressive strength testing undertaken to determine strength and deformation characteristics of paste. Used to identify the effect of mix proportions (%cement and % solids), time and grain size distribution on:- UCS, E, ε_f,	Paste shows increased brittle behaviour with cement and solids content. Ductile behaviour is observed with increasing levels of confinement. Cement and solids content increase the strength of the paste. In fills with a solids content of between 74% - 78% cement is the primary contributor to strength. In higher density fills, solids content contributes more significantly to strength. The reduction in effective grain size increase the UCS of the paste fill. The undrained cohesion was found to vary with cement and solids content. So too did the undrained friction angle. Paste fill is unsaturated with air being entrained into the cemented soil skeleton. Relationships to correlate UCS to ϕ_u have been developed. Mohr-Coulomb failure criteria applicable to undrained paste fills up to σ_3 = 600 kPa

Table 3. 30 (cont'd)

TOTAL STRESS ANALYSIS		
TESTS	**DESCRIPTIONS**	**OUTCOMES**
Short Term (Batching – 7 Days)		
Tensile Testing	Direct tensile testing was undertaken using a modified rock core test procedure. Quantification of the tensile strength, effect of time and relationship to the unconfined compressive strength were found.	Tensile strength of paste is approximately one order of magnitude less than that of the compressive strength. Strength development is rapid, remaining constant after the first 7-14 days.
Long Term (1 – 12 Months)		
UU triaxial	UU triaxial testing was used to identify the undrained strength characteristics of fill including ϕ_u . Indication as to whether Cannington paste is effected by sulphate attack or self desiccation also investigate.	Paste tended to increase in strength well after the 28 days standard. Progressive drying out of the sample was observed through the monitoring of the levels of saturation, which was accompanied by a significant increase in the undrained friction angle. The effects of sulphate attack or self desiccation were not evident after 12 months

The very early strength of paste, within the first 30 mins of mixing, is dependent on solids content only, as the cement has not started to set, and can be calculated from equation 3.6. After initial set had occurred, a mechanical shear vane was used to determine the strength in undrained shear of the paste. The shear vane was checked and calibrated against UCS tests conducted in a triaxial test machine. All trends showed a linear gain in strength for the early strength of paste. Figures 3.18 and 3.21 show the strength gains for paste over the short term. The scales on the axis should be noted as log scales distort the profiled trends, which are in fact linear.

The strength of paste in the medium term (7- 28 days) was found using UCS and UU triaxial tests. UCS tests were used to identify the progressive strength of paste with various mix proportions and grain size distributions. The UU triaxial tests were used to provide additional information as to the development of an undrained friction angle, ϕ_u. The progressive strength gains of paste for various mix proportions and grain sizes are shown in Figures 3.70 and 3.34 respectively.

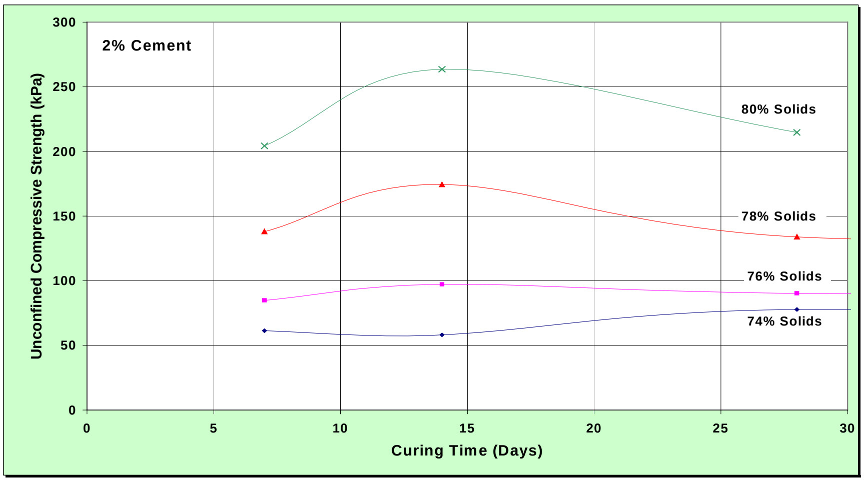

Figure 3. 70 Progressive strength of paste, 2% cement , varied % solids, 28 days curing

In both cases the paste fill gains strength to a reasonably constant value at between 7 and 14 days. Strength increases with cement and solids content as well as a decrease in effective grain size. The failure strains, ε_f, decreased and stiffness, E increase with cement content, solids content and curing time. Figures 3.33 to 3.36 show this in quantitatively in conjunction with Tables 3.10 to 3.15.

The undrained friction angle, ϕ_u and undrained cohesion c_u, were found using the UU triaxial test. If fully saturated, paste would return a flat failure envelope, ($\phi_u = 0$). From the series of UU triaxial tests that were performed, a definite friction angle was observed for all paste fill mixes. It increased with cement content and time, primarily, and to a lesser extent the solids content. The increase in ϕ_u, was shown to be related to the increase in air voids, through the hydration of cement. The level of hydration and cementation was related to the UCS of the paste and Figure 3.37 was developed.

The effect of cement and solids content on the development of the friction angle may then be identified by the gradient and spacing of the dividing lines. A similar trend was found for the long-term samples up to 6 months. After a period of approximately 6 months the samples were observed to "dry out" significantly, resulting in a significant increase in ϕ_u. This is shown clearly in Figure 3.43. The "drying out" of paste fill was observed in the laboratory and in the outer layers of paste fill, but have not been definitively proven to occur within the centre of the paste fill mass.

Direct tensile tests identified the tensile strength for various times and mix proportions. Figure 3.46 shows the progressive tensile strength development of paste. By normalising the UCS strength of paste by the tensile strength, strength ratio of approximately 10:1 was observed.

Effective Stress Analysis

The effective stress analysis involved the investigation of the strength and deformation characteristics of the paste, as well as the effect of confining pressure on the strength and behavior of paste. Tables 3.31 and 3.17 summarize the CD triaxial test method and effective strength parameters found from testing respectively.

Table 3. 31 Summary of testing and general outcomes from effective stress analysis

EFFECTIVE STRESS ANALYSIS		
TESTS	**DESCRIPTIONS**	**OUTCOMES**
CD Triaxial	Test program used to identify deviator stress q_f at failure $(\sigma_1' - \sigma_3')_f$, ϕ', c' and the effect of confinement on strength and deformation behaviours for various paste mixes, after 14 and 28 days.	Varying effective strength parameters. c' range: 11 – 474 kPa ϕ' range: 33.7 – 44.1 Paste showed increasing levels of ductility (ε_f>15%) with increasing levels of confinement Mohr-Coulomb failure criteria applicable to paste fill

The variation in effective friction angles is similar to that observed by Pierce (1997), when investigating the response of the Golden Giant mine paste fill using CU triaxial tests. In general, the effective cohesion increases with cement and solids content and curing time. The effective friction angle tends to reduce with the increase in strength. The exception to the general trend is the 2% cement, 74% solids samples, which act as uncemented tailings. The increased effective friction angle of 43 is consistent with additional direct shear tests done on Cannington tailings, reported by Sing-Samra (2001). It is expected that the effective confinement may have crushed the internal cement bonds, causing the paste to act as an unbound material.

The behaviour of tailings under various levels of effective confinement were investigated and related to the UCS to provide a quick and easy reference. This is shown in Figure 3.50. Previously it has been assumed that once the cement bonds yield, that the material under consideration reverts to the behaviour of the unbound material. By investigating the peak and residual secant deformation modulus, this was found to be untrue, and a linear relationship found. This shows that paste maintains stiffness above that of the parent material as the UCS (refer to Figure 3.53).

Consolidation Testing

Oedometer testing was testing was carried out on paste fills of various mix proportions. Table 3.32 summarises the findings. It was found that solids content tend to dictate the rate at which consolidation occurs. Samples with higher solids contents, have higher coefficients of consolidation. The magnitude of c_v ranged from 2.49 m^2/yr to 3.13 m^2/yr for the samples with 74% solids and between 5.34 m^2/yr to 6.52 m^2/yr for samples with 78% solids. This is attributable to the build up of excess pore pressure in samples of higher density and increased rigidity of flow paths for pore water.

Table 3. 32 Summary of consolidation parameters

MIX		Average			
% Cement	**% Cement**	**c_v (m^2/ yr)**	**C_α**	**C_c** After bond failure	**C_c/C_α** After bond failure
2	74	3.13	0.0239	0.4828	0.041
2	78	5.34	0.0186	0.3585	0.052
6	74	2.49	0.0217	0.5504	0.039
6	78	6.52	0.0166	0.2906	0.057

The co-efficient of secondary compression, C_α, refers to the re-alignment of the soil particles under a defined normal load, which occurs after primary consolidation has finished. Higher settlements due to secondary compression result in samples with a lower solids density, as the particles rearrange into the densest state.

The coefficient of compression, C_c, showed a step change in response, depending on whether the cement bonds had yielded or not. Prior to yielding C_c was appreciably lower, with the compression of the soil structure (and voids) being restricted by cement bond strength. Once yielding had occurred, the changes in C_c were dependent primarily on solids content and to a lesser degree, cement content. The values of C_c

ranged from between 0.483 to 0.550 for the 74% solids samples and 0.291 to 0.3585 for the 78% solids samples. C_c is considerably lower for the higher solids content samples, as the soil matrix is already at a higher relative density, thereby reducing the extent to which soil particles may re-align under the given pressures.

The co-efficient of secondary compression, C_α and ranged between 0.0217 and 0.0239 for the 74% solids samples and 0.0166 to 0.0186 for the 78% samples. C_α was also dependent on the solids content of the mix, and less on the cement content. The ratio of C_α/C_c was compared to $C_\alpha/ C_c = 0.05$ (Mesri and Godlewski 1977). Results were consistent with this proposed ratio, only after the cement bonds had yielded. Before yielding occurred, the ratio was significantly higher because of the strength of the cemented fill matrix.

UCS Tests on samples cured under surcharge.

Preliminary testing was conducted on samples under various levels of surcharge, to simulate the expected in-situ conditions. The trends show an increase in the strength of the paste under increased consolidation pressure. The increase in the measured tangential Young's modulus and decrease in measured failure strain all indicate the densification of the solid matrix in the paste structure. Preliminary results from testing have been included as part of Appendix 3.7, and are considered a basis for further research.

In-Situ Testing

Testing of in-situ paste was achieved in was achieved using a series of DCP tests and UCS tests on undisturbed samples recovered from various paste filled stopes. DCP test results were collated and related to an equivalent SPT blow count, N, using the ratios of specific energies between the DCP and SPT rigs. The correlations developed for the SPT were then used to predict various properties of the fill, including the relative density, D_r, drained friction angle, ϕ', and Young's Modulus, E. DCP tests were conducted in three places from the edges to the centre of stope 42_61 HL (refer Figure 3.55). The UCS tests on undisturbed samples taken from adjacent to the DCP testing were used to provide a basis for comparison of the predicted properties. Table 3.33 shows the summary of predicted parameters from in-situ testing.

The results reported from the UCS testing of undisturbed cores from in-situ testing, correlate reasonably well with equivalent laboratory UCS test specimens. Section 3.7.2.1 reports the full results for laboratory cast specimens.

Table 3. 33 Empirical correlations vs. in situ strength for paste fill

Empirical Correlations		From Testing		Comments
Relative Density, D_r	Teng (1962) (Table3.25) $31<(N_1)_{60}<50$	DCP (=> SPT) D_r= 60%-70%	UCS D_r = 60%	Teng (1962) provides good correlation for D_r
Drained Friction Angle ϕ'	Peck et al. (1974)	DCP (=> SPT) $35 < \phi' <36$	CD Triaxial $32 < \phi' <36$ (typ.)	Very consistent ϕ' from Peck et al. (1974), Correlations relate better to ϕ' of paste after 14 days than 28 days.
Young's Modulus, E	Leonards (1986) $E = 8(N_1)_{60}$ (kg/cm^2) $E=784.5(N_1)_{60}$ (kPa)	DCP (=> SPT) $E=20(N_1)_{60}$ (kg/cm^2) $E=1960(N_1)_{60}$ (kPa)	UCS E = 45 MPa *(measured)*	E significantly higher for cemented paste than for normally consolidated sands. Additional stiffness provided by cement and compaction upon placement

The laboratory cast samples provide a reasonable indication as to the likely in-situ paste performance. The relative increase in strength with the in-situ strength is attributable to the longer curing time and gives increased confidence of paste to the resistance of sulphate attack. Some factors that should be noted with the in-situ samples is that disturbances as a result of the blasting or mining operations associated with development may have caused micro-cracking and weakening of the fill structure. The indirect tensile loads applied to the paste from the fill mass as it relaxed into the void after mining, may also have caused the paste to be weaker than absolutely "undisturbed" samples. The DCP testing indicated as tendency of the paste to consolidate and increase in strength with increased vertical loads, as did the preliminary testing performed on sample cured under surcharge. Further investigation and research into this aspect of paste is required. From the DCP test results the liquefaction potential of the paste (3.5% cement, 76% solids in 42..61 HL) was found to be negligible.

Paste has been misunderstood since its inception. It is hoped that the geotechnical characterisation of the paste, provided as part of this research has increased the level of knowledge, and available resources to those involved with the design of suitable backfilling systems. Simple graphs and relationships have been identified and presented to aid in this endeavour. A user-friendly program, PASTEC, has also been developed with the use of Artificial Neural Networks (ANN's) and is reported in Chapter 5.

The stability of fill is significantly affected by the strength and properties of the surrounding mineralogy. Chapter 4 provides a geotechnical characterisation of some of the most common mineralogy's identified at Cannington. The results from the laboratory testing program, detailed in Chapter 4 were incorporated into the PASTEC program and used as inputs to the numerical model described in Chapter 6.

3.12 Summary

Paste backfill is a new technology within the mining industry, with very little understood about the geotechnical characteristics or behaviour under different loading conditions. Previously held assumptions regarding the saturation levels of paste, consolidation of paste and in-situ behaviour of fill has been investigated, as part of this research, with results that challenge existing views. Quick reference guides to for the determination of fill strength characteristics from the basic UCS test have been developed and presented for both total and effective stress analysis. Laboratory testing results have been presented and supported by testing of in-situ paste. PASTEC - a program to identify the geotechnical characteristics of fill, based on simple input parameters such as the cement and solids content, grains size and curing time has been developed and discussed further in Chapter 5.

Chapter 4

Geotechnical Characterisation – II: Cannington Deposit

"All things by immortal power,
Near or far,
Hiddenly
To each other linked are,
That thou canst not stir a flower
Without troubling of a star."

Francis Thompson,
English Victorian Poet,
(1859-1907)

4.1 General

The fact that there has there are interactions between all things has long been recognised, and is illustrated by Francis Thompson's poem. The interaction between the backfill material and the host rock is obvious. To determine the strength and deformation characteristics of the host rock provides additional information into the potential local and regional stability of the rock mass.

The investigations have been limited to the strength and deformation characteristics of the typical rock types at Cannington. In particular, rock types that occur in the "Northern Zone" of the mine. Currently it is currently being developed and the informational requirements were coincident with the testing procedures for the determination of the strength and deformation characteristics for any new mine. It is the test program that provides the focus for this chapter.

4.2 Cannington Mine

Cannington is a Broken Hill type mineral deposit, containing lead, silver and zinc and is similar in nature to the other Broken Hill type mineral deposits shown in Figure 4.1.

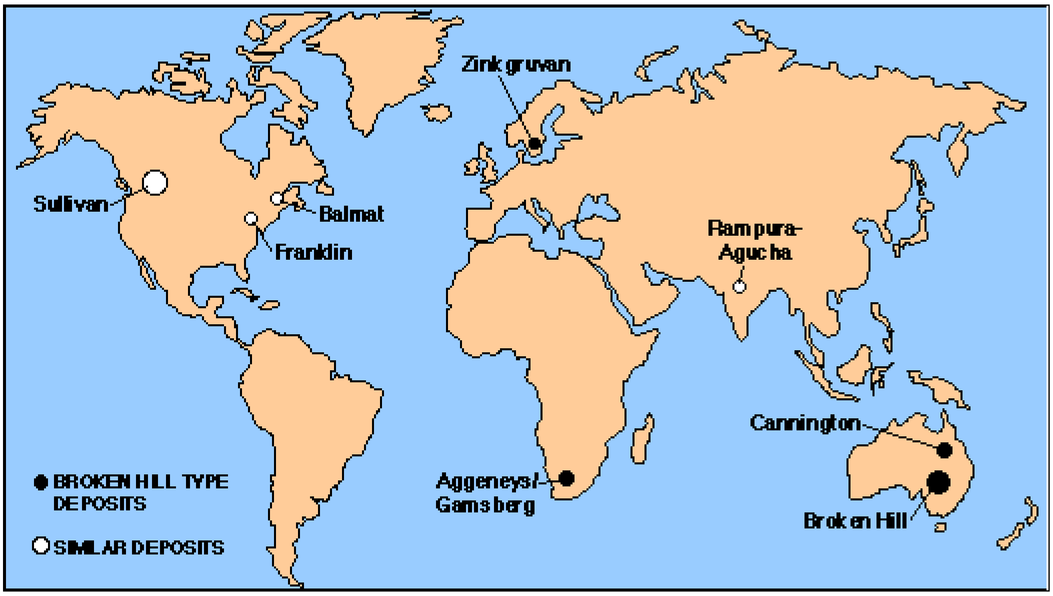

Figure 4. 1 International Broken Hill type mineral deposits

The mineralisation types of commercial importance at Cannington are Sphalerite ((Zn,Fe)S) and Galena (PbS), which are the primary source of zinc and lead respectively. Silver is also contained in the mineral structure of Galena. At Cannington, the concentration of silver is high at approximately 570 ppm and is the third economic mineral mined at Cannington. Mineral Data Sheets for Sphalerite and Galena have been included in Appendix 4.1.

The mine lies in the southeast corner of the Proterozoic Mount Isa Block and is divided by faulting into a shallow, low grade, “Northern Zone” and a deeper, high grade, “Southern Zone.” The ore body was discovered using magnetic resonance imaging. The results of which is shown in Figure 4.2. This identified the presence of iron type minerals, specifically magnetite, which has subsequently associated with some of the richer ore types found at Cannington.

The Northern and Southern Zones are divided by the northwest trending, steeply northeast dipping, Trepell Fault. The Southern Zone is also bounded by the Hamilton Fault, which runs approximately parallel to the Trepell Fault. Figure 4.3 shows a simplified plan view of the structural elements and geologies of the two zones.

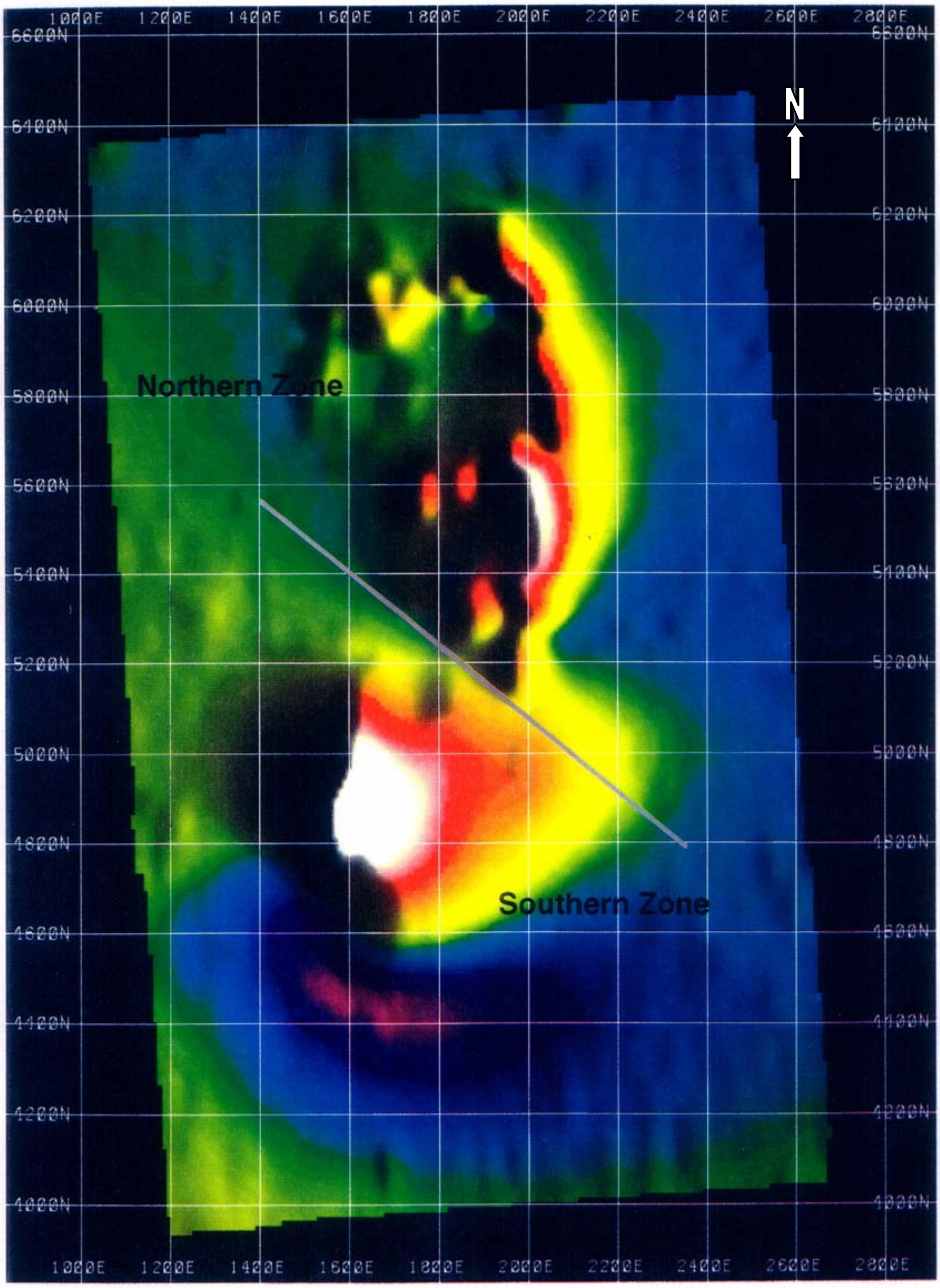

Figure 4. 2 Cannington Ground Magnetics. Total magnetic intensity colours draped on E-W gradient filter (Walters 1994).

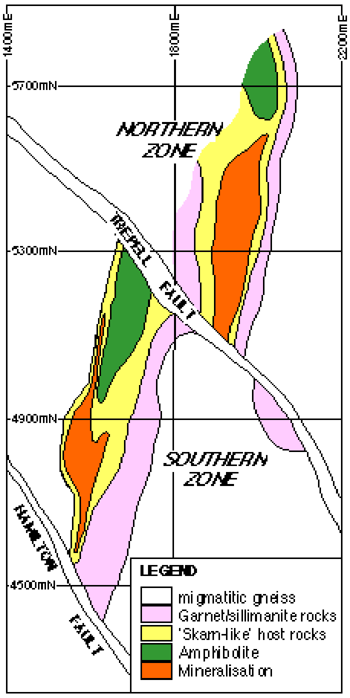

Figure 4. 3 Simplified plan view of the geometry of the Cannington ore-body deposit (www.virtualexplorer.com.au/VEexploration/VEorebodies/Cannington/)

The Southern zone contains the bulk of the defined reserve and has been the focus of development to date (Walters and Bailey 1998). The Southern zone mineralisation dips at approximately 50 toward the East reaching a maximum depth of about 600 m (refer to Figure 4.4). Lying at the heart of the deposit is a body of amphibolite, up to 200m thick, known as the "core amphibolite". Mineralisation lying structurally above and below the amphibolite is referred to as hanging wall and footwall respectively. This mineralisation has been divided into a number of specific ore types, which define a stacked sequence of chemically and mineralogically distinct sheets. (Walters 1994).

In the Northern zone the geometry and the distinction between specific ore types is less clear (Bodon 1998). The majority of mineralisation occurs above the core amphibolite in a sub-vertical to steeply west dipping zone up to 200m wide, which is terminated by the Trepell Fault. Table 4.1 defines the main mineralisation (ore) types at Cannington (Walters 1994).

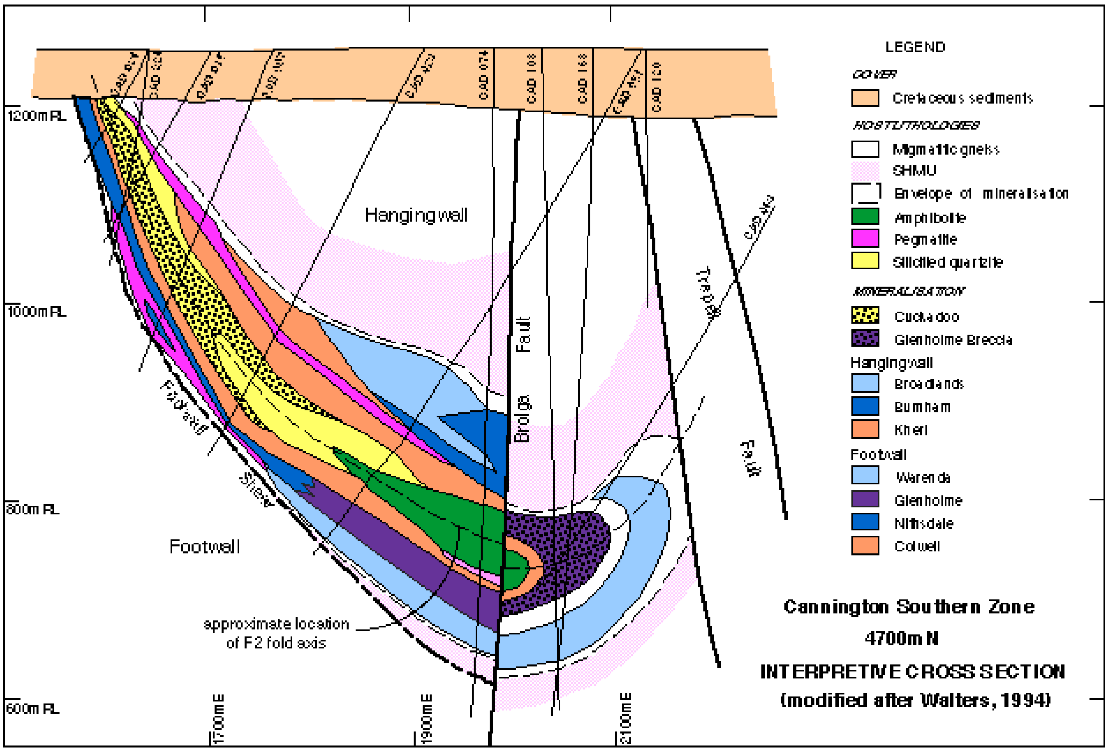

Figure 4. 4 Simplified geometry and distribution of mineralisation and lode types at 4700N in the Southern Zone of the Cannington Ore deposit (Walters 1994)

Table 4. 1 Summary of the lode horizon and mineralisation (Ore) types at Cannington (Walters 1994)

Lode Horizon	Mineralisation	Log Type	Fe: Si	Pb:Zn	Ag: Pb%	Ore Grade	Gangue*
Hangingwall Lead	Broadlands, BL	PQ, QZ	Mafic-siliceous bands	Pb>>Zn	21-50	Med-Low	qtz-pxm-gn
	Burnham, BM	PA, PT	Mafic	Pb>>Zn	41-56	High	mag-fl-pxm-px-qtz
Hangingwall Zinc	Kheri, KH	PA	Mafic	Zn>Pb	29-63	Low	px-qtz-mag-fl
	Kheri/ Colwell, KC	PA, PT	Mafic	Zn>Pb	110	Low	mag-fl-px-qtz
Footwall Zinc	Colwell, CW	PA, PT	Mafic	Zn>Pb	28-74	Low-Med	mag-fl-px-qtz
	Cuckadoo, CK	QZ, QT	Siliceous	Zn>>Pb	23-38	Med	qtz-(chl-gn)
	Glenholme, GH	QZ	Siliceous	Pb<>Zn	33-41	High	qtz-carb
Footwall Lead	Nithsdale, NS	PT, PA	Mafic	Pb>>Zn	N/A	Med	mag-fl-pxm-px-qtz
	Warenda, WA	PQ,QZ	Mafic-siliceous bands	Pb>Zn	N/A	Low	qtz-pxm-gn
Brolga Fault	Glenholme GH	QZ	Siliceous	Pb<>Zn	33-41	Very High	qtz-(carb)

* Where: mag-magnetite, fl-fluorite, px-pyroxenes, qtz-quartz, gn-garnet, carb-carbonates, pxm-pyroxmangite, chl-chlorite

The complex structural nature of Cannington Mine is shown more clearly in Figure 4.5. The top 60 – 70 m of overlying soil on the Cannington deposit consists mainly of mudstones.

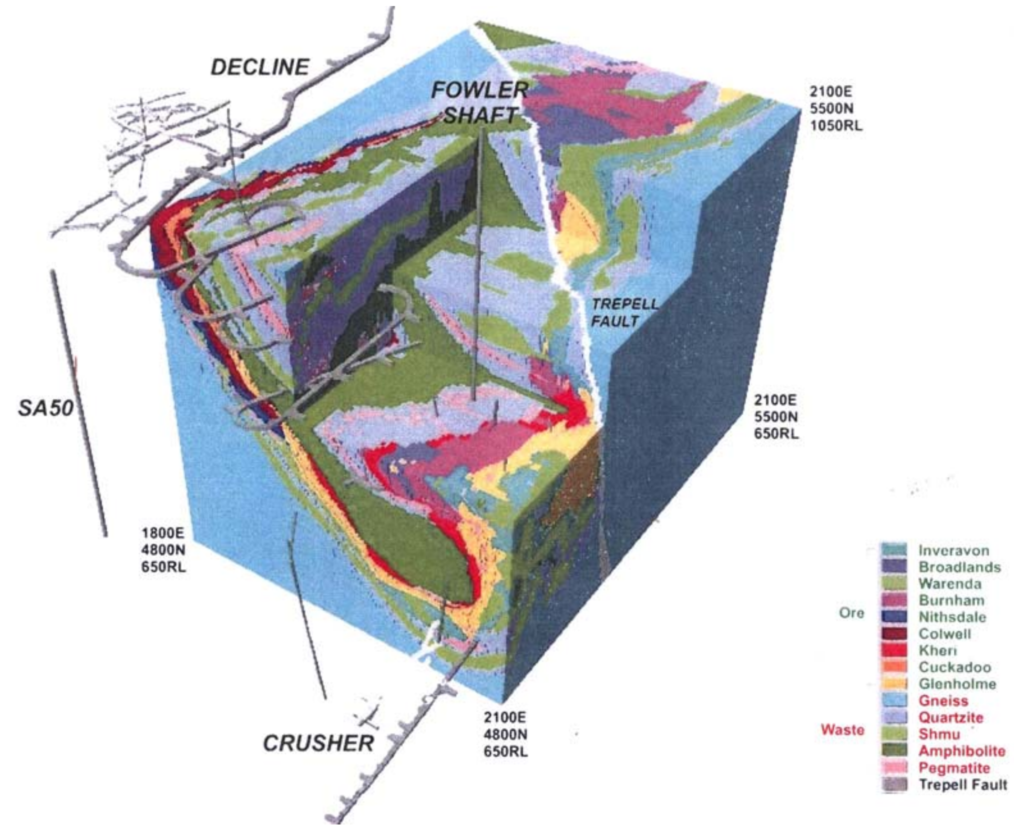

Figure 4. 5 Three Dimensional view of the Cannington deposit

As mining through the ore body continues, stresses are re-distributed from the stoped out areas to vertical pillars surrounding the mined areas. When the pillar's load capacity is exceeded, failure of the pillars may occur. This may lead to catastrophic failure of local or regional areas which may resulting in significant economic loss, and the potential loss of lives. To minimise the risk of this occurring, strength and deformation characteristics of the different rock types are determined and used to predict the loading and capacity of the pillars. This was achieved by a thorough laboratory testing program the results of which have been reported in the following section.

4.3 Laboratory Testing

4.3.1 General

The laboratory tests focussed on the strength and deformation characteristics of the different mineralogical types, which have been summarised in Table 4.2. Table 4.3 outlines the test methods and standards used.

Table 4. 2 Rock types tested

Rock Type	Name	Ore/ Waste
AMPH	Amphibolite	Waste
BL	Broadlands	Ore
BM	Burnham	Ore
GH	Glenholme	Ore
GNES	Quartzo-felspathic gneiss	Waste
HDMT	Magnetite bearing Hedenbergite rock	Possible Ore **
PEGM	Pegmatite	Waste
PXAM	Pyrobole Rock	Possible Ore **
QZGA/ IT	QZGA – garnetiferous quartzite/ arkose QZIT - meta quartzite/ arkose	Possible Ore **
QZHD	Hedenbergite Quartzite rock	Possible Ore **
SHMU	Muscovite sillimanite schist	Waste

** Depends on grade of Pb, Zn , Ag, and designated cut off grade. Typically found in ore bearing rocks and zones

Table 4. 3 Testing standards

Item	Tests - Description	Standard
Rocks	Rock strength tests - Determination of point load strength index Geotechnical site investigations	AS 4133.4.1-1993 AS 1726-1993
	Rock strength tests – Determination of uniaxial compressive strength, 3pp	AS 4133.4.2-1993
	Rock strength tests - Determination of deformability of rock materials in uniaxial compression, 7 pp.	AS 4133.4.3-1993
	Determination of indirect tensile strength of concrete cylinders ("Brazil" or splitting test), 5 pp.	AS 1012.10-2000* (modified)

A brief description of the sample preparation for the testing standards and has been given in Appendix 4.2.

The locations from which the rock samples were cored, is shown in Figure 4.6 (over page) From each borehole a minimum of four samples were taken for each type of mineralisation.

Figure 4. 6 Plan view – Borehole locations from which cored rock samples were taken

The laboratory testing was broken categorised into: -

1. Physical Property Testing
    a. Porosity
    b. Bulk density
    c. Specific gravity

2. Strength and Deformation Testing
    a. Unconfined compressive strength
    b. Brazilian indirect tensile strength
    c. Point load
    d. Poisson's ratio

4.3.2 Physical Property Testing

The physical properties were determined to provide some base line data and identify any trends between the mineralisation types based on the physical properties.

4.3.2.1 Porosity

Porosity testing is typically conducted when a significant void fraction exists within a sample. Igneous and metamorphic rocks have a typical porosity range of 0-2% (Franklin and Dusseault 1989). The reduction in strength due to increase in porosity within this range was considered negligible and unable to be determined accurately using current technologies. (Kelsall et al. 1986). Cannington mineralisations fall into the metamorphic and igneous categories and were therefore not tested for porosity.

4.3.2.2 Dry Density

Indicative bulk density of each of the mineralisation types has been shown in Table 4.4. The recorded values were averaged from a minimum of four samples. A minimum of three measurements of the length and diameter for each sample were taken to identify the volume of the sample. All testing was completed in accordance with the appropriate Australian Standards.

Table 4. 4 Average dry densities

Rock Type	ρ_d **(t/m^3)**
SHMU	2.76
AMPH	2.94
PEGM	2.58
GNES	2.65
BM	4.44
BL	3.95
GH	3.84
QZGA/IT	2.93
QZHD	2.87
HDMT	4.06
PXAM	3.67
Mudstone	2.85

4.3.2.3 Specific Gravity

The specific gravity of the various ore types vary significantly within the variation of composition, granulation within the samples tested. In mineralisation with a very low void volume, the specific gravity may be considered to be slightly higher than their respective bulk density.

Additional data pertaining to the physical properties of the rock cores tested are contained with Appendix 4.3.

4.3.3 Strength and Deformation Testing

The strength and deformation characteristics of intact rock specimens can be used to predict the intact strength of a rock mass and used in conjunction with the joint wall roughness to determine the shear strength of the rough joint surfaces. The strength of the samples was determined using the *unconfined* or *uniaxial compressive strength* (UCS) test. A number of additional strength index tests, in the form of the point index test and Brazilian test, were also done to provide a test method which could be used to quickly and easily approximate the compressive or tensile strength respectively. Rocks are considered to behave elastically prior to failure. This requires the determination of the elastic Young's Modulus and the Poisson's Ratio of the rock types to be determined. The elastic Young's Modulus is defined in the elastic region of the stress strain curve during the UCS test (refer Figure 4.8). Poisson's ratio requires additional testing, which is described further in Section 4.3.4.

4.3.3.1 Unconfined Compressive Strength

The *unconfined* or *uniaxial* compressive strength (UCS) test (ISRM 1981) is the most common strength index test for the characterisation of the intact strength of rock materials (Hawkes and Mellor 1970).

To carry out a UCS test, a right circular cylinder with a length to diameter aspect ratio of 2.5-3.0 is compressed between platens on a loading machine. The UCS is then calculated by dividing the peak load by the cross-sectional area. There is negligible increase in the cross sectional area if rupture is reached before 2-3% strain (Franklin and Dusseault 1986). The problem of frictional end restraint is addressed by using low friction platens – graphite lubrication on spherical seats or similar, in conjunction with the specimens of the designated 2.5-3.0 aspect ratio. In this case the central third in a "true" uniaxial state of stress. The degree of flatness of the ends of the specimen become more critical when testing stronger, stiffer rocks, because even small irregularities can cause concentrations of high local tensile stresses and premature rupture (Pells and Ferry 1983). The strain rate is typically matched as close as practically possible to the protype to be analysed. Typical UCS testing takes 10 minutes or less. Very fast strain rates during loading cause the strength to be overestimated, while very slow loading (over days) can reduce the UCS by up to 30% (Franklin and Dusseault 1986). The influence of specimen size on the UCS has also been investigated (Hoek and Bray 1981). The UCS of an intact specimen increases with a decrease in sample diameter. To standardise the reporting of UCS, a sample diameter of 50mm is considered "standard" and corrections are applied in accordance with Figure 4.7.

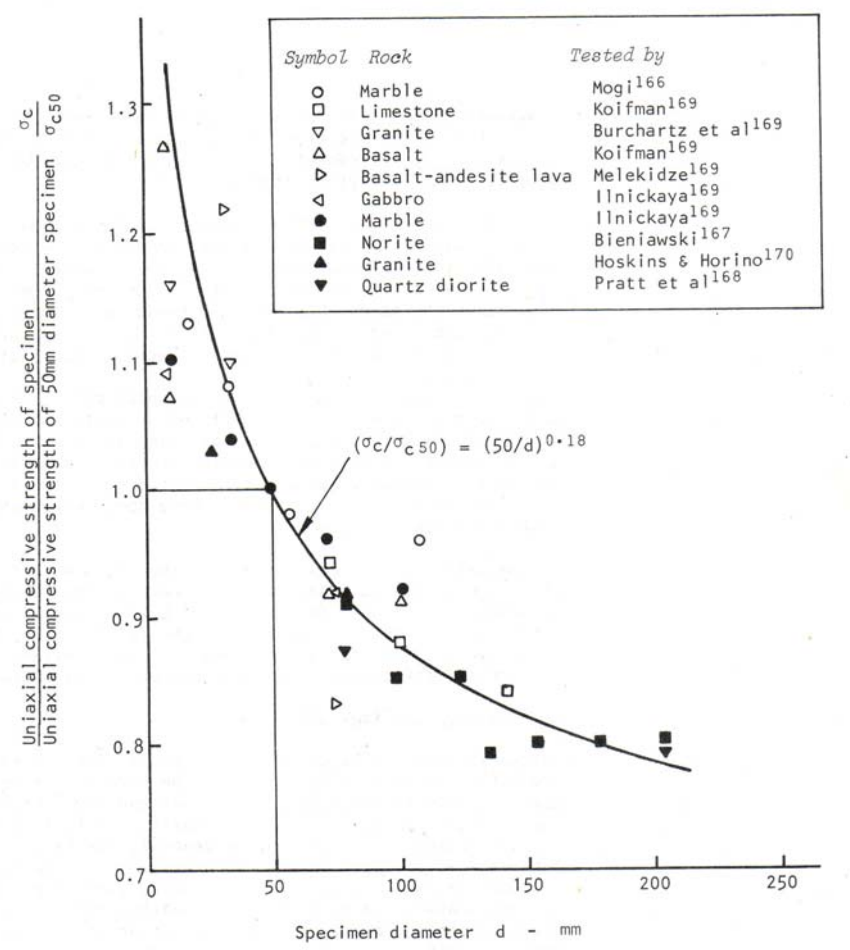

Figure 4. 7 Influence of specimen size upon the strength of intact rock (Hoek and Bray 1981)

All samples were testing using James Cook University's fully automated, 1000 kN MTS machine. All samples were loaded at a rate of 0.5mm/min. The force and displacement measurements were logged at a frequency of 10 Hz, which typically resulted in several thousands of data points from which to plot the graphs (Refer Appendix 4.4). The parameters obtained from the unconfined compressive strength testing of most interest were:-

1. E_{s50}: – Secant Young's Modulus, (GPa) a tangent measured at when the axial stress = 50% of the maximum value. It is considered to be the elastic Young's Modulus for the rock materials
2. UCS: – The maximum unconfined compressive strength of each sample (MPa) and
3. ε_f: - The failure strain, of each of the samples.

All are shown schematically in Figure 4.8

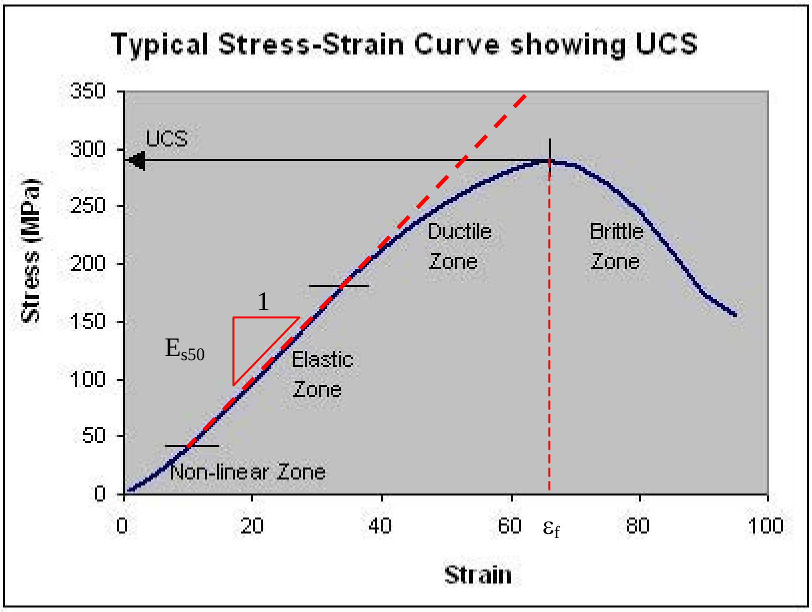

Figure 4. 8 Parameters obtained from UCS testing

The UCS and ε_f have been included in Table 4.5, and the Young's Modulus in Table 4.6. The plots used to obtain the data have been included as part of Appendix 4.4.

Table 4. 5 Uniaxial compression strengths and failure strains of various rock types

	Uniaxial Compressive Strength (MPa)			Failure Strain, ε_f (%)		
Rock Type	**Min.**	**Max.**	**Av.**	**Min.**	**Max.**	**Av.**
SHMU	23.2	60.8	41.2	0.2	0.5	0.4
AMPH	182.3	182.3	182.3	0.6	0.6	0.6
PEGM	76.6	147.2	120.0	0.5	0.7	0.6
GNES	0.0	49.2	25.5	0.1	0.3	0.3
BM	1.5	231.7	220.0	0.0	0.9	0.8
BL	157.9	296.3	216.8	0.7	1.1	0.8
GH	41.6	47.0	44.3	0.3	0.4	0.3
QZGA/IT	69.3	276.5	189.3	0.8	1.3	0.9
QZHD	73.8	322.2	222.1	0.3	1.1	0.8
HDMT	118.6	166.8	142.7	0.7	0.7	0.7
PXAM	27.0	297.1	162.0	0.6	1.0	0.8

Table 4. 6 Elastic Young's Modulus for various rock types

Rock Type	E_{s50} (GPa)		
	Min.	Max	Av.
SHMU	3.5	11.0	7.0
AMPH	19.7	19.7	19.7
PEGM	8.8	19.6	13.8
GNES	0.0	10.4	4.2
BM	0.9	24.5	20.9
BL	19.1	19.5	19.3
GH	7.8	12.7	10.3
QZGA/IT	5.2	24.5	16.0
QZHD	8.1	26.9	18.9
HDMT	9.9	13.4	11.7
PXAM	2.1	22.1	12.1

A number of relationships were found to exist for the rock samples. The two that were of most use and importance were: -

- UCS and failure Strain (refer to Figure 4.9)
- UCS and Young Modulus (refer to Figure 4.10)

From Figure 4.9, the relationship between the UCS and the failure strain of the rocks was found, and is expressed in the form of Equation 4.1.

UCS = 317.9ε_f – 60.86 (for 0.3% < ε_f < 0.9%) …(4.1)

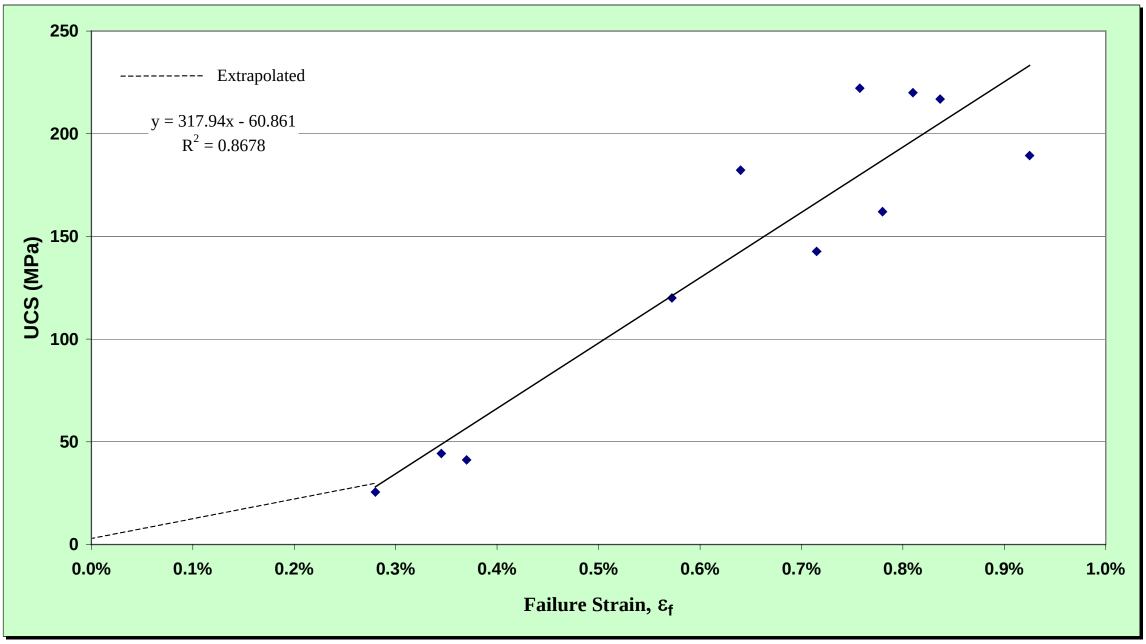

Figure 4. 9 Unconfined Compressive Strength vs. Failure Strain

There are two distinct data groups. The first (GNES, SHMU and GH) all failed at lower strain levels and UCS than the mineralisation in the second group. Both GNES and SHMU are non-economic ore and are considered as "waste" materials. GH is a very high-grade brecciated[1] ore with low uniaxial compressive strength. The other data group consists of the "ore" or "potential ore." The higher UCS values are complemented with higher failure strains in an approximately linear relationship over the range of tested values.

The author is not aware of any published global relationships between UCS and ε_f. This is likely to be attributable to the site-specific nature of these relationships. The formation, geology and degree of geomorphology that the rock formations have undergone, significantly influence the ultimate strength. Global relationships for specific relationships for intact rocks masses are therefore difficult to identify and validate.

It should be noted that the values derived for the GNES and BM rock types were based on the exclusion of samples GM58380 and GM58388 respectively. The results obtained for both specimens were dubious and were not considered representative of their respective rock types, and were thus excluded from the analysis.

Similarly, a relationship between the UCS and the elastic Young's Modulus was found (refer to Figure 4.10) and takes the form: -

$UCS = 8.343E_{s50}-79.33$ (for $13GPa< E_t < 36GPa$) …(4.2)

[1] Brecciated: *Consisting of angular fragments cemented together. The cementitious bond may be formed by clay, sands etc.*

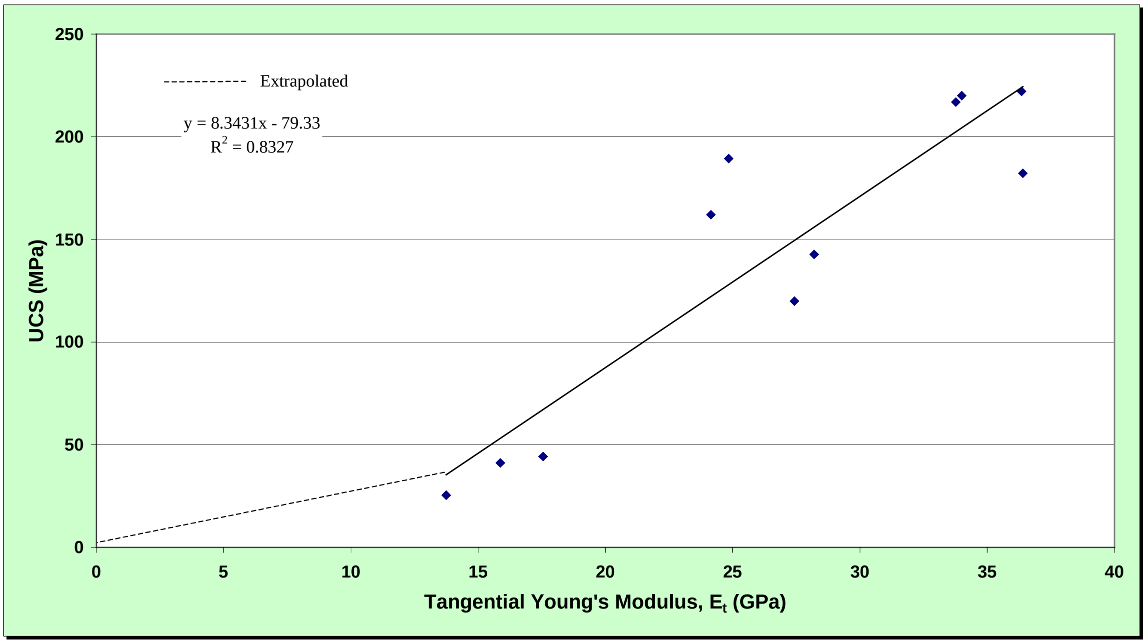

Figure 4. 10 Unconfined Compressive Strength vs. elastic Young's Modulus (E_{s50})

The increases in stiffness of the materials associated with an increase in the unconfined compressive strength are attributable to the finer grain size and higher densities of the rock types (Deere et al. 1966)

Relationships between Young's modulus and unconfined compressive strength have been investigated by a number of researchers (Tatsuoka and Shibuya 1992, Brady and Brown 1983, Deere et al. 1966). Brady and Brown (1985) suggests that:

$$E_{(typically)}=(300\text{-}1000) \times UCS \qquad \ldots(4.3)$$

The results from testing show that the typical results from Cannington are well below the lower bound of E=300UCS. Table 4.7 shows the multiplication factors ranging from 75 to 235, with an average of 118. The average multiplication factor drops to 108 if GH is excluded from the analysis.

Table 4. 7 Multiplication factors relating UCS to E_{s50}

Rock Type	Multiplication Factor (E_{s50}/ UCS)
SHMU	169
AMPH	108
PEGM	115
GNES	165
BM	95
BL	89
GH	231
QZGA/IT	84
QZHD	85
HDMT	82
PXAM	75

The lower results are attributed to the complex geological structure involved in the Cannington ore body, which is highly foliated and sheared.

Figure 4.11 shows the widely accepted nomenclature published by Deere et al. (1966). Tatsuoka and Shibuya (1992) used the same basic format as Deere et al. and applied additional points, which re-aligned some boundaries slightly. Deere et al. (1966) is still more commonly recognised and used in industry and will be referred to here.

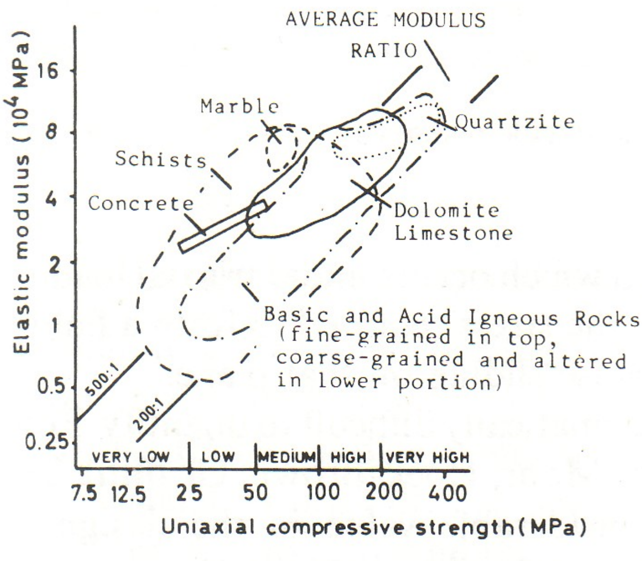

Figure 4. 11 Typical strength and modulus values for rock materials (Deere et al. 1966)

When comparing the testing results in Figure 4.12 to Figure 4.11, a number of facts may be observed. As expected the sample two groups as was identified in the UCS testing are present again. The group of samples at the base of the graph, which includes GH, GNES and SHMU, are categorised according to Deere et al. (1966) as a Schist type rock of low to medium uniaxial compressive strength, with a medium to high modulus ratio. Both GNES and SHMU are waste materials and GH is a high grade ore. The brecciated nature ore tends to reduce the UCS of the material and return a higher E/UCS ratio. Similarly the other group of samples would be described as a medium to fine grained igneous rock, with a high to very high uniaxial compressive strength, and a low to medium modulus ratio (Deere et al. 1966).

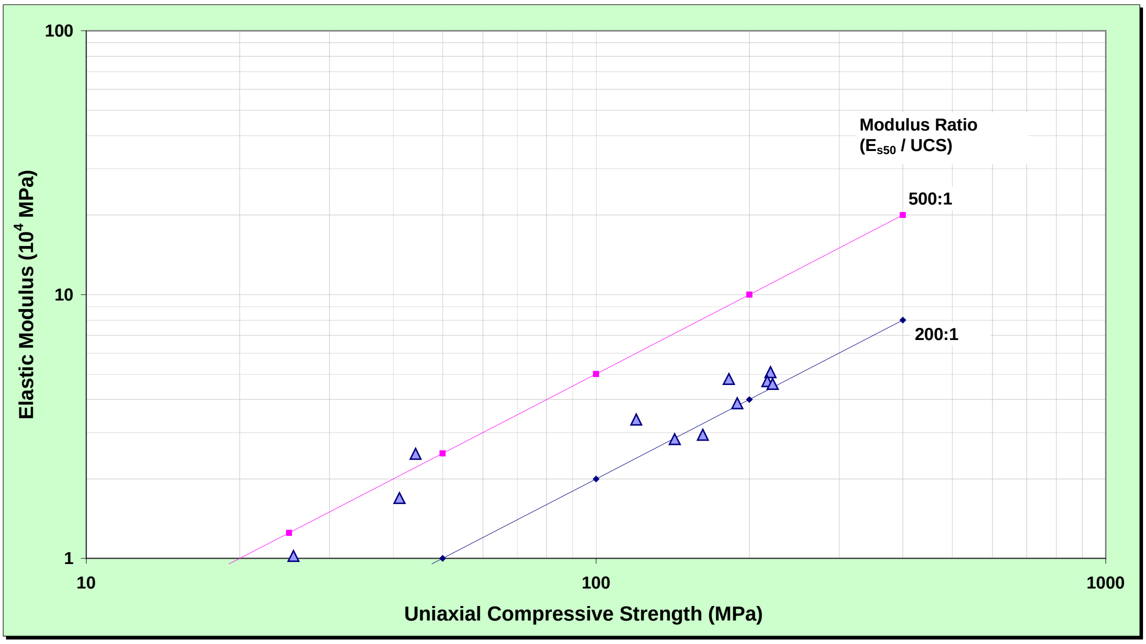

Figure 4. 12 Modulus ratios of Cannington Mineralisation types compared to Deere et al. (1966) profiles

There was no specific trend observable with between E_{s50} and ε_f. However, the general response was for the failure strain to increase with stiffness, which is opposite to what would be expected.

4.3.3.2 Point Load Strength

Point load strength testing was carried out to provide a strength index (I_{s50}) for the rock types, which could easily be determined on site. The results from the point load index testing were also correlated with the UCS and Brazilian testing to give indicative values for the compressive and tensile strengths for the rock types respectively. The results for I_{s50} testing have been summarised in Table 4.8.

Table 4. 8 Point load strength index (I_{s50}) test results

Rock Type	Point Load Strength Index, I_{s50} (MPa)			Interpreted Rock Strength*
	Min.	Max.	Av.	
SHMU	3.0	6.7	4.3	**VH**
AMPH	4.1	9.7	6.0	**VH**
PEGM	1.0	6.6	4.3	**VH**
GNES	0.5	4.1	2.7	**H**
BM	1.1	9.1	5.7	**VH**
BL	2.7	13.1	8.0	**VH**
GH	3.2	6.5	4.9	**VH**
QZGA/IT	3.8	7.2	5.5	**VH**
QZHD	3.2	13.5	8.4	**VH**
HDMT	2.4	8.6	6.5	**VH**
PXAM	6.4	27.3	15.6	**EH**

* **H**-High, **VH**-Very High, **EH**-Extremely High,. Rock Strength Classes have been identified using Table 8, AS 1726-1993.

Rock strength is usually defined in terms of unconfined compressive strength (UCS). UCS and I_{s50} have an approximately linear relationship, as shown in Figure 4. 13. The UCS is used to determine the stability of open spans, pillars, stopes and stress modeling for local and regional stability (Potvin 1988).

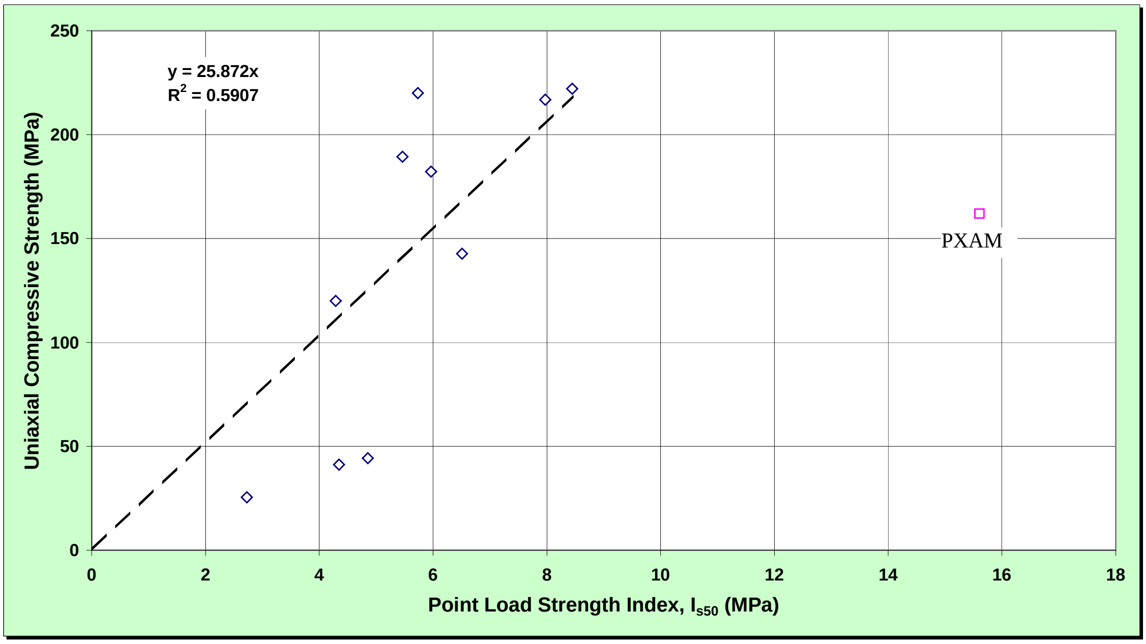

Figure 4. 13 Determined linear relationship between UCS and I_{s50}

The data for the PXAM samples were excluded from the analysis due to the exaggerated eccentricity of the data point.

Several attempts have been made to relate the I_{s50} to the UCS (Pettifer and Fookes 1994, Rosengren 1994, Brady 2001, Hawkins 1986). A value of I_{s50} = 0.5 MPa is considered the lower bound for the reliable and consistent determination of I_{s50} (Hawkins 1986).

A conversion factor of between 18 and 24 is normally used to correlate UCS and Is_{50}. (Quigley and McSwiney 1996). A widely accepted chart (Bieniawsiki 1974) defined the correlation between UCS and Is50 to be linear and constant at UCS = $24I_{s50}$, regardless of the mineralization type, as shown in Figure 4.14.

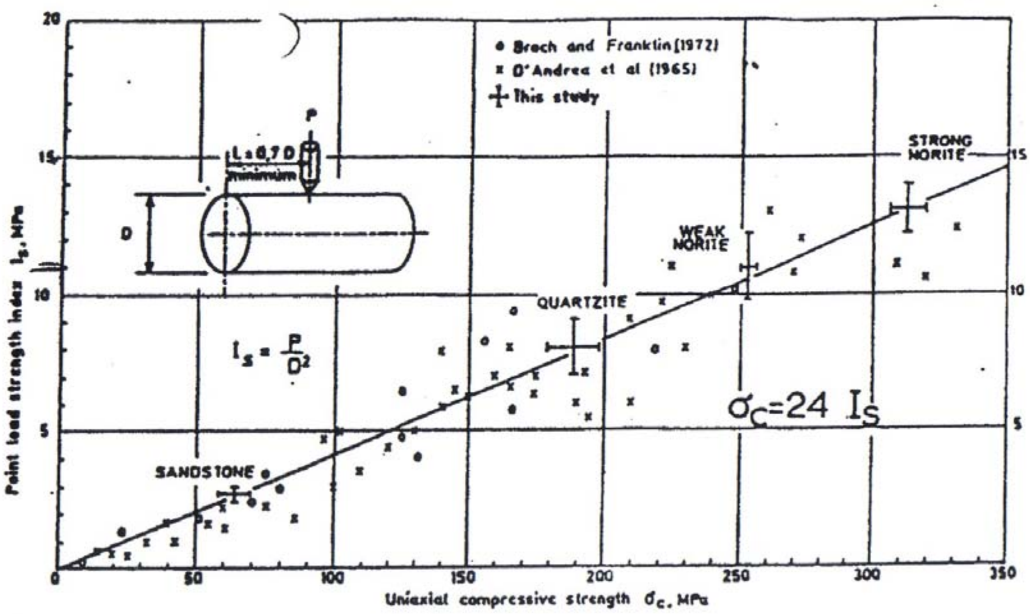

Figure 4. 14 Relationship between point load index I_{s50} and UCS (Bieniawski 1974)

Testing done by Rosengren (1994) and Brady (2001) oppose this theory, with different mineralization types returning very different correlations between UCS and I_{s50}. Due to the large scale of operations, and the remoteness geological formations of Cannington Mine, it was considered appropriate to determine the applicability of Bieniawsiki's (1974) global conversion factor or whether individual factors were required for each mineralization type. Results have been summarized in Table 4.9.

Table 4. 9 UCS to I_{s50} Ratios

Rock Type	I_{s50} (MPa)	UCS (MPa)	UCS/I_{s50}
	Av.	Av.	Av.
SHMU	4.3	41.2	9.5
AMPH	6.0	182.3	30.6
PEGM	4.3	120.0	28.0
GNES	2.7	25.5	9.4
BM	5.7	220.0	38.4
BL	8.0	216.8	27.2
GH	4.9	44.3	9.1
QZGA/IT	5.5	189.3	34.7
QZHD	8.4	222.1	26.3
HDMT	6.5	142.7	21.9
PXAM	15.6	162.0	10.4
		Average	***22.30***

Collating the rock types with similar UCS to I_{s50} ratios was done to simplify the results and reduce the number of multiplication factors. The results for which have been shown in Table 4.10.

Table 4. 10 Suggested I_{s50} to UCS multiplication factors for Cannington Rock types

Rock Type	Multiplication Factor
GH, GNES, SHMU, PXAM	9
HDMT	20
QZHD, PEGM, BL	25
AMPH	30
QZGA/ IT, BM	35

The "average" UCS to I_{s50} ratio of 22 found from testing does fall within the 18-24 band (Quigley and McSwiney 1996, Bieniawski 1974) but is considered inappropriate as a global conversion factor for all mineralisation types. The range of 9-35 shows the I_{s50} to UCS conversion ratios to be highly dependent on mineralisation type. This finding is supported by previous work done by Brady (2001) and Rosengren (1994).

Additional data pertaining to the determination of I_{s50} is included in Appendix 4.5.

4.3.3.3 Indirect Tensile Strength

The indirect tensile strength of the rock cores was found using the "Brazilian" or "Splitting Test". Where the samples were laid on their side and loaded along the diametrical axis until the specimen is failed in tension. The tensile strength is found using equation 4.4: -

$$\sigma_t = \frac{2Q_f}{\pi DL} \qquad \ldots(4.4)$$

Where

σ_t	= tensile strength as determined by the indirect tensile method
Q_f	= failure load
D	= diameter of the specimen and
L	= specimen length

The theoretical stress distributions across the diameters (in line and perpendicular to the direction of loading can be obtained using the theory of elasticity. Figures 4.15 (a) and (b) show the induced stresses distributions in the indirect tensile test.

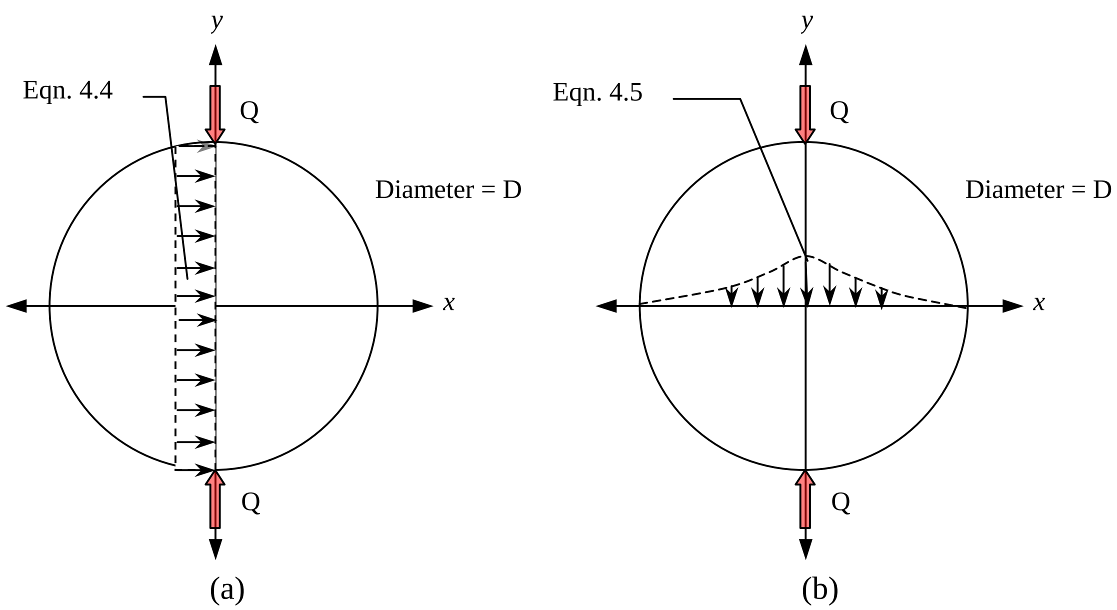

Figure 4. 15 Theoretical stress distribution of tensile stress in indirect tensile strength tests

The stress along the axis perpendicular to loading (Figure 4.15 (b)) may be calculated using equation 4.5.

$$\left(\sigma_{t-B}\right)_f = \frac{2Q}{\pi DL}\left(\frac{D^2 - 4x^2}{D^2 + 4x^2}\right) \qquad \ldots(4.5)$$

The results have been summarised in Table 4.11 and shown in Figure 4.16. All other data pertaining to the tests have been included in Appendix 4.6. The minimum and maximum values give the range of results for each mineralisation. The averaged value for the specimens tested is reported and are considered to represent a reasonable approximation of the indirect tensile strength for each type of mineralisation. A very conservative approach may adopt the minimum value of the indirect tensile strength. This is highlighted by the GNES (Gneiss) and BL (Broadlands) rocks types, which show a reasonably consistent indirect tensile strength, with a single aberration (low value) in the data set. Exceptional results of this nature are typically attributable to an inhomogeneity (eg. microcracking, plane of weakness etc) in the rock matrix prior to testing.

Table 4. 11 Brazilian indirect tensile strength testing results

Rock Type	Indirect Tensile Strength (MPa)		
	Min.	Max	Average
SHMU	7.4	10.8	8.7
AMPH	6.4	20.5	14.9
PEGM	9.3	25.1	12.9
GNES	0.9	6.8	5.6
BM	12.4	20.4	16.2
BL	8.7	15.3	13.1
GH	7.0	11.2	8.9
QZGA/IT	7.5	19.1	12.8
QZHD	11.3	16.1	14.7
HDMT	13.9	16.2	15.3
PXAM	18.5	28.8	22.5

Figure 4.16 shows the indirect tensile strength compared to the density of the specimen. The ores and potential ores form one group and the waste materials another. The division into two groups based on density is not surprising as Sphalerite and Galena, which the economic mineralisations (“ore”) contain, have average densities of 4.05 and 7.4 g/cm^3. Mineralisation types containing these minerals thus

tend to have higher densities. The coloured dots in each of the groupings represent the centroid of the figure and can be used as an average point of reference. The higher indirect tensile strengths seen associated with the group of ores and potential ores related to the density and fine grain structure of the ores.

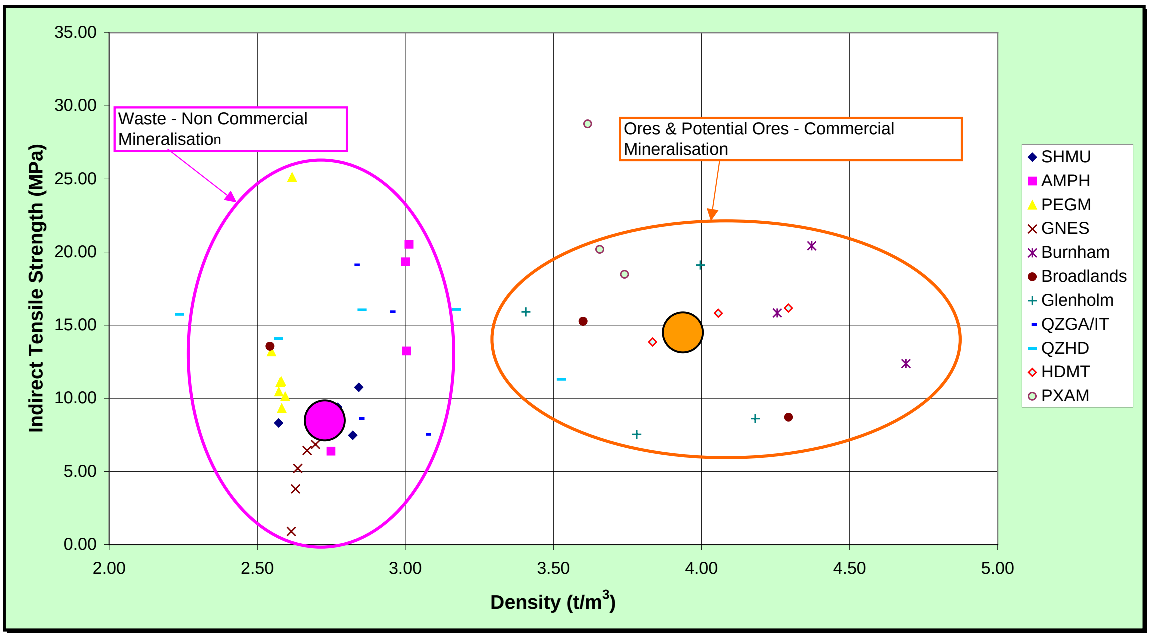

Figure 4. 16 Indirect Tensile Strength vs. Density

The ratio of the tensile strength to the unconfined compressive strength has been investigated by a number of researchers (Griffith 1921, McClintock and Walsh 1962 and Jaeger et al. 1969). Experimental results (Griffith 1921) provided a range of $\frac{UCS}{\sigma_t} = \frac{1}{9}\ to\ \frac{1}{17}$ which compared only moderately with the theoretical results of $\frac{UCS}{\sigma_t} = \frac{1}{8}$ (Griffith 1921) or $\frac{UCS}{\sigma_t} = \frac{1}{12}$ (Jaeger et al. 1969). The results from current testing range from $\frac{UCS}{\sigma_t} = \frac{1}{5}\ to\ \frac{1}{17}$ which is in reasonable approximation to the early experimental results of Griffith (1921). The lower ratio of $\frac{UCS}{\sigma_t} = \frac{1}{5}$ correlates to the waste materials and GH – which have been previously described. The lower UCS for these samples are responsible for the elevated ratios. Testing results have been summarised in Table 4.12 and additional data reported in Appendix 4.6.

Table 4. 12 Tensile to compressive strength ratios for Cannington rock types

Rock Type	Ratio σ_t/ UCS	Multiplication Factor σ_t=> UCS
GNES	0.22	4.5
SHMU	0.21	4.8
GH	0.20	5.0
PXAM	0.14	7.1
PEGM, HDMT	0.11	9.1
AMPH	0.08	12.5
BM, QZGA/IT, QZHD	0.07	14.3
BL	0.06	16.7

From a processing viewpoint, a lower UCS and σ_t/UCS ratio are more attractive. The energy required to grind the mineral down to a fine power is low, especially in comparison to other harder mineral ores. GH (Glenholm) matches this description and indeed provides Cannington with a very rich source of ore with very high levels of recovery.

When comparing the compressive strength to the tensile strength directly the relationship was approximately linear. The results for the testing of the PXAM mineralisation were removed from the analysis, on the basis that they provide an exceptional ore when considering the very large tensile strength (See Table 4.11). Figure 4.17 shows the relationship between the Brazilian indirect tensile strength and the unconfined compressive strength of the rocks tested, which can be described by Equation 4.6.

$$UCS = 20.024\sigma_t - 105.99 \quad (\text{for } 7\text{ MPa} < \sigma_t < 16\text{MPa}) \qquad \ldots(4.6)$$

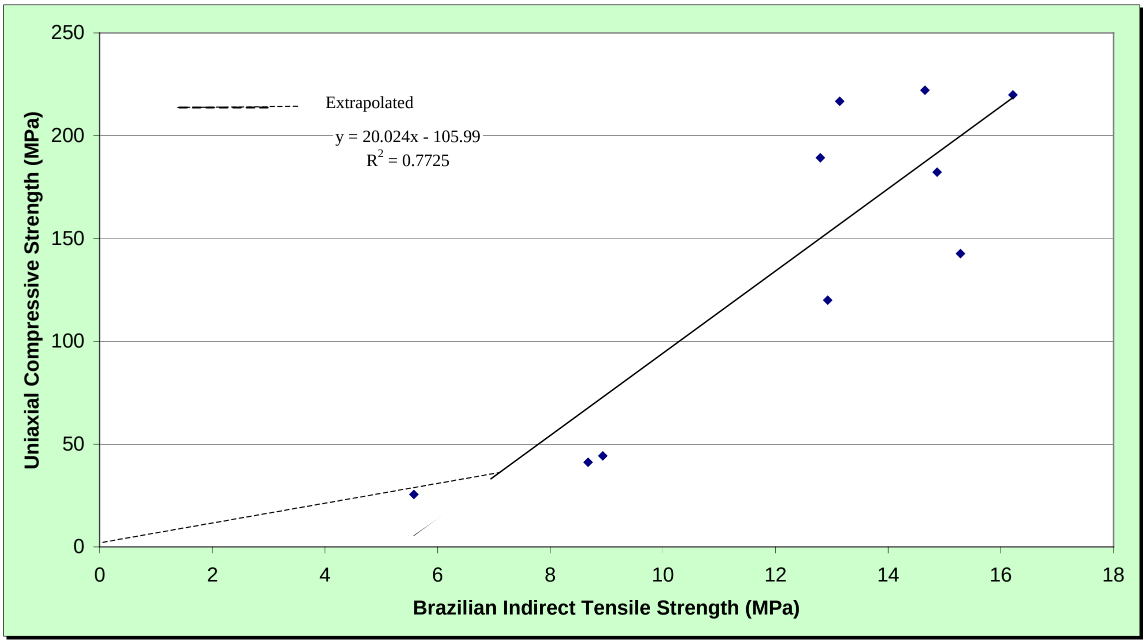

Figure 4. 17 Uniaxial Compressive Strength vs Brazilian Indirect Tensile Strength

It should be noted that an increase in temperature significantly affects the physical properties and strength of the rocks (Lee et al. 1996; Brown and Heuze 1979; Heuze 1983; and Homand-Eitienne and Houpert 1989). Specifically the indirect tensile strength reduces slightly with increasing temperature. The loss of strength with temperatures up to 100°C is typically negligible and can thus be ignored in consideration of normal mining circumstances.

4.3.3.4 Poisson's Ratio

Poisson's ratio, ν, is the ratio of change of the lateral strain to longitudinal strain and is defined by Equation 4.7. Tensile deformation is considered positive and compressive deformation is considered negative.

$\nu = - \varepsilon_{trans} / \varepsilon_{longitudinal}$ …(4.7)

where

$\varepsilon = \Delta L/L$

A number of methods have been proposed for the measurement of Poisson's ratio including ultrasonic testing (Pollchik et al. 1992), particle image velocimetry (Singh-Samra 2001), lasers (Zhu 1996), back calculation involving numerical modelling (Luo et al. 2003), and the traditional methods of strain gauges or measured deflections

(AS4133.4.3-1993). At stresses up to approximately 50-60% of the UCS, a Poisson's ratio in the order of 0.1 – 0.25 is typical (Franklin and Dusseault 1989). At higher stress levels approaching rupture, micro-cracking occurs, resulting in additional lateral deformations. This results in a reading of Poisson's ratio, which includes elastic deformation, and well as cracking. Poisson's ratio is a measure of elastic deformation. Therefore when the rock behaves inelastically, through cracking, the measured value of ν may be much greater than 0.5, which is the theoretical maximum for a purely elastic material.

The value for ν found in this range was reported as the Poisson's ratio for each of the samples. Results have been summarised in Table 4.13 with the full complement of data being included in Appendix 4.7. Typical values for the Poisson's ratio and Young's Modulus for various common rocks types are included in Appendix 4.7 also.

Table 4. 13 Poisson's Ratios for Cannington Rock types

Rock Type	$\nu_{(min)}$.	$\nu_{(max)}$.	$\nu_{(average)}$.
SHMU	0.04	0.21	0.11
AMPH	0.05	0.16	0.09
PEGM	0.09	0.36	0.22
GNES	0.15	0.35	0.23
BM	0.10	0.29	0.21
BL	0.11	0.21	0.17
GH	0.05	0.19	0.11
QZGA/IT	0.06	0.27	0.17
QZHD	0.07	0.19	0.13
HDMT	0.10	0.18	0.13
PXAM	0.06	0.27	0.17

In all cases there was a significant amount of scatter with results ranging from the very low ν=0.04 (SHMU) to very high ν=0.36 (PEGM, GNES). The low, ν=0.04, results for SHMU are thought to have been a result of the difficulties associated with the minimal lateral deflections with a low UCS. Lateral deformations involved when loading the sample to very low levels of stress are minimal and small variations in the recorded value may result in significant variations in the calculation of ν. The elevated result of ν~0.36 (PEGM, GNES)is considered attributable to micro cracking within the sample. This may have been pre-existing or caused by loading. In general, the $\nu_{(average)}$ results for the Poisson's Ratio are thought to be a reasonable estimates for each of the various rock types.

4.4 Conclusions

Chapter 4 has reviewed the need for testing of the rock materials surrounding the backfill material and has given the testing methods and procedures used within the investigation. Testing was divided into physical property and strength and deformation tests.

The results from the investigations can be summarised as: -

Physical Property testing

- The density of the mineralisation types were used to identify two clear groups – "ore and potential ore" and "waste" materials.
- Two groups were again identified using classifications published by Deere et al. (1966). The classification were also used to categorise and describe the groups as: -
    - "Ore and Potential Ore": - medium to fine grained igneous rock, with a high to very high uniaxial compressive strength, and a low to medium modulus ratio.
    - "Waste Materials": - A Schist type rock of low to medium uniaxial compressive strength, with a medium to high modulus ratio.

It should be noted that Glenholm (GH) did provide an abhorrent result when classified using the Deere et al. (1966) classifications, because of its heavily brecciated nature. This reduces peak UCS of the sample and results in an incorrect classification.

The strength testing focussed on the determination of the unconfined compressive strength of the sample and developing site based correlations with other strength index tests such as the point load test and Brazilian test. Deformation characteristics of the samples were determined using the Poisson's Ratio test.

- The average UCS for the mineralisation types ranged from 25 MPa to 222 MPa. Two distinct groups were identified with using the UCS. Group 1 had lower UCS strengths and was composed of the non-economic mineralisations

(SHMU and GNES) and GH – a very high grade brecciated ore. The economic mineralisation types tended to have higher UCS strengths.

- Linear correlations were found for UCS and Young's Modulus (Et) values, failure strains (ε_f). The relationships took the form:-

  - UCS = 317.9ε_f – 60.86 (for 0.3% <ε_f < 0.9%) …(4.1)
  - UCS = 8.343E_{s50}-79.33 (for 13GPa< E_t < 36GPa) …(4.2)

- Point Load testing was performed to provide a strength index (Is50) to which the UCS could be correlated. The global conversion factor of UCS=24 x Is50 (Bieniawski 1974) was found to be inappropriate to describe the different mineralisation types found at Cannington Mine. Individual factors were found and ranged between 9 to 35 (refer to Table 4.10).

- The Brazilian test was used to investigate the indirect tensile strength of the mineralisations. Ratios of $\frac{UCS}{\sigma_t} = \frac{1}{5}\ to\ \frac{1}{17}$ were found during testing which was in reasonable agreement with earlier experimental results by Griffith (1921).

- The average Poisson's Ratios found from testing ranged between 0.09 (AMPH) to 0.26 (GNES). The overall average for all mineralization types was ν = 0.16. The results from testing correlate well with previously published data and indicate Cannington rock types, have a comparatively low Poisson's ratio.

4.5 Summary

The interactions between various aspects of the underground mining environment are complex and difficult to quantify. By investigating individual components within the system, fundamental understandings of behavior are gained and slightly more accurate or informed decisions can be made. In this way, the behavior of a highly jointed rock masses may be interpreted with the understanding of the intact rock strengths.

The investigations and laboratory testing program outlined in this chapter, and used to determine the physical properties and strength and deformation characteristics for Cannington rock types, is generic and applicable to any mine. By employing the laboratory-testing program, more efficient mining practices are expected to result through an increased level of knowledge of material properties and confidence in design.

Chapter 5

Artificial Neural Networks

5.1 Introduction

Numerous investigations have been conducted in recent years to predict the strength and behaviour of mine backfills (Pierce 1997, Bloss 1992, Berry 1981). The mechanisms are not yet clearly understood neither are the contribution of attributes such as binder content, solids content, grain size etc. Correlations have been made for the UCS of cast fill samples in terms of these attributes. Although the UCS tests may reflect to some degree the actual in-situ strength of the fills, it is typically bound by paste fill mix and site specificity and lacks applicability to the "general" case. It was therefore necessary to develop an alternative method that is capable of resolving the response of soils and the subtle interrelationships between the large number of variables which effect the fill strength.

The application of artificial neural networks in geotechnical applications is increasing and includes the prediction of:- liquefaction potential (Goh 1994, 1995, 1996), pile capacities (Teh et al. 1997), settlement of shallow foundations in sands (Arnold and Sivakugan 1997, Sivakugan et al. 1998) and compressibility characteristics in clays (Arnold 1999).

Neural networks are problem-solving programs, based on the structure and function of the human brain. They use a large number of simple processors called neurons. Both the brain and neural networks use acquired knowledge and data to make decisions for new problems or situations. Artificial Neural Networks (ANN's) provide a powerful and dynamic solution package for complex, multivariate problems easily and expediently.

In the case of paste fills, where geotechnical characteristics and strengths are governed by several variables, such as the cement content (%C), solids content (%S), curing time (t) and particle sizing (P_{80}), ANN appears to offer good potential for the prediction of the fill characteristics and strengths based on these input variables. ANN's outperforms traditional regression analysis undertaken, providing an accurate and convenient solution mechanism for multivariate problems.

5.2 Overview Of Artificial Neural Networks

5.2.1 General

ANN's are powerful, computer based models, which use and analyse historical data to develop solutions to complex, multivariate problems. Neural networks are comprised of a series of interconnected nodes or "neurons", which perform the same function as their biological namesakes. They manipulate data using mathematical models. The model instructs the neuron to multiply the inputs by their respective weightings and then passes the summed result through a non-linear transform function. Typically, the transform function takes the form of the S shaped sigmoid function (refer to Section 5.2.3.1). The weighted, transformed result is the output of the neuron. Figure 5.1 shows an artificial neuron.

Neurons are interlinked by a series of connectors to form a series of layers, as shown in Figure 5.2. All networks will have at least two layers, the input and output layers. Intermediate layers of neurons are not visible to users of neural networks and are referred to as hidden layers. There can be any number of hidden layers, which may be interconnected in a variety of ways or "architectures". A number of references for the basic architecture of an ANN may be found in publications by Rumelhart and McClelland (1986), Lippman (1987) and Flood and Kartman (1994).

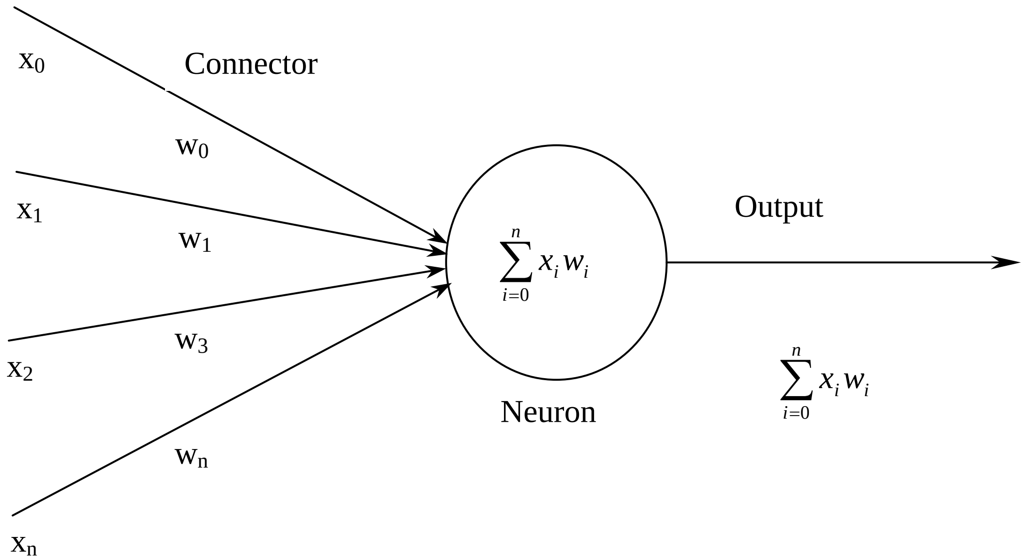

where

x_i	=	Input
w_i	=	Input weight

Figure 5. 1 Artificial neuron (Aleksander and Morton 1990)

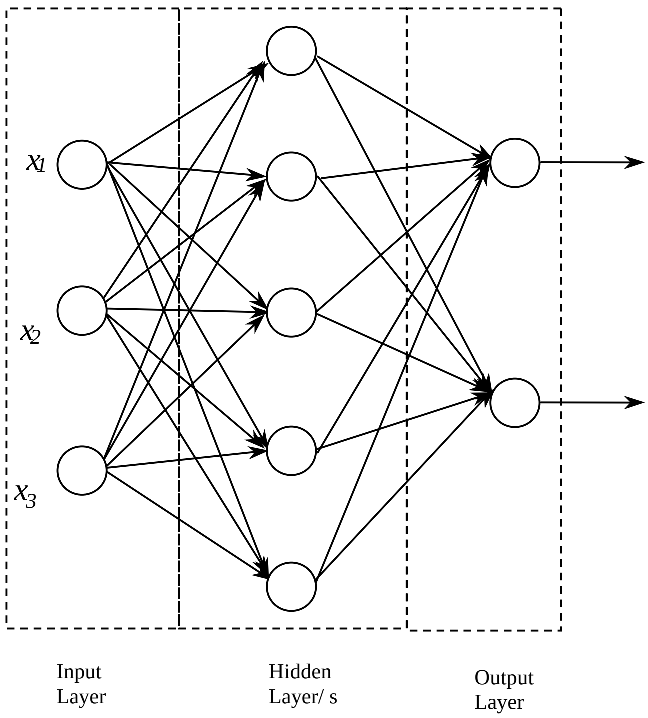

Figure 5. 2 Example artificial neural network

The configurations of the layers of the ANN will affect the interpretation of the input data and relationships with the resultant outputs. The increased complexity of the interconnection of the layers and neurons also affect the ANN's ability to generalise. With more complex ANN's number of nodes and connections increase, which give the network an increased ability to identify increased levels of detail, however if the input data doesn't contain the specified traits or distinctions used by each neuron, the ANN predictive ability is reduced. This is roughly equivalent to the memorising of information by humans, who if asked about an item, which lies slightly outside the tightly defined fields of the network, will be unable to apply the knowledge (network) and make an accurate prediction. An example of which would be that an ANN was trained to identify black or white, and was handed a grey sample. Unable to be categorised into either "black" or "white" it would erroneously predict it as either one. Conversely, very simple networks are able to generalise better and lose specificity or of the solution. Simple ANN's are able to predict the solution "approximately", but typically produce less accurate predictions than the more complex networks.

There are two main features in developing an artificial neural network; the architecture and learning algorithm. The "architecture" dictates the structural configuration of the networks, which is the interconnection of neurons and layers. Neural network architectures are discussed in Section 5.2.2. The "learning algorithm" defines the method in which the networks are able to learn from the data to minimise the output error. Learning may occur in either a supervised or unsupervised environment, which are discussed Section 5.2.3.

5.2.2 Neural Network Architecture

There are two main neural network types; feedforward networks and recurrent networks. Feedforward networks use connectors to link the neurons sequentially between layers, but not within the same layer. Outputs are related to the inputs at any given time. Information is not recirculated back into the network or between neurons in the same layer. Data is manipulated sequentially in a pre-determined and consistent manner. They are most effectively used in the interpretation of a continuous feed of information. A typical application may be a quality control measure on a production line. When the product is faulty, or does not meet the designated specifications, the network would order a series of events to occur. Decisions would be consistent and the margin of error minimal.

Recurrent networks use the outputs of some neurons as inputs to neurons within the same layer. Recurrent networks have a dynamic memory, which means they are able to use the current inputs as well as previous inputs and outputs to make decisions – effectively “learning” from previous experiences. An example of which may be the prediction of trends in the stock market, based on previous information.

5.2.3 Learning Algorithms

The learning algorithms for neural networks are either supervised or unsupervised. Supervised learning algorithms (SLA) compare measured results to the outputs of the ANN and adjust the weights of the interconnections to reduce the difference between the two. This is continued until the difference between the predicted and actual outputs reaches a minimum value. The two most popular learning algorithms are back-propagation and the cascade correlation algorithms. These are covered in Sections 5.2.3.1 and 5.2.3.2 respectively.

Unsupervised learning algorithms (ULA) are most effective as classification tools, using the similarity of input parameters to identify and classify data into groups. Unsupervised networks are trained without any output values, whereas supervised networks are trained with the outputs which are target answers (Dayhoff 1990). Supervised networks are far more common. Unsupervised networks are used mainly for classification of pattens into similar groups. An example of which is the classification of various forms and species of bacteria.

5.2.3.1 Back-Propagation Learning Algorithm

Developed by Werbos in 1974, the back propagation learning algorithm remained largely unused until widely publicised by Rumelhart et al. (1986), and represents one of the most significant milestones in the development of artificial neural networks (Dayhoff 1990).

Initially arbitrary weights are assigned to the connectors between neurons and the data is fed forward through the network, with the output recorded for each data point. The mean error between the network output and the training data is then calculated. Starting at the output side of the network, the connection weights between previous neurons and layers are adjusted using the gradient of steepest descent method, which basically examines the variation of error with connection weight and chooses in which direction to alter weights so as to minimise error (Dayhoff 1990). The outputs are fed back through the network until the root mean square of the error has reached a predefined limit, or a minimum value. The process of adjusting the weights from the output back to the input layers is where name of the network is derived. Yeh et al. (1993) discussed the mathematical model describing the back propagation process. Figure 5.3 shows the basic structure of the back propagation network with an input layer (N), output layer (O) and hidden layer (H). The connector weights between the N and H layers and the H and O layers are denoted by V and W respectively.

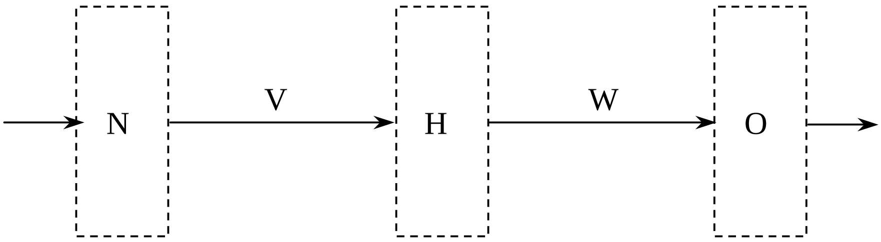

Figure 5. 3 Back-propagation neural network

The output from each node is determined using a transfer function, which multiplies the neuron input by the connector weighting and transfers it into a value within the required numeric range. The most commonly used transfer function is the sigmoid transfer function, which takes the form

$$y = \frac{1}{1+e^{x}} \qquad \dots (5.1)$$

where

y = output

x = input (= connector weighting * input value)

Therefore the input for neuron k in the hidden layer is given by:-

$$H_k = \frac{1}{1 + e^{\left(-\sum_i V_{ik} N_i\right)}} \qquad \text{… (5.2)}$$

where

V_{ik} = weight of connector from input neuron i to hidden neuron k.

N_i = input value to neuron i

A similar expression may then be derived for any output neuron (O_m)

$$O_m = \frac{1}{1 + e^{\left(-\sum_i W_{kj} H_k\right)}} \qquad \text{… (5.3)}$$

The network is then evaluated by comparing the network output (O_m) with the measured value (T_m). The error term (E) is then found using the average of the sum of square errors, as shown in equation 5.4.

$$E = \frac{1}{2}\sum_m (T_m - O_m)^2 \qquad \text{… (5.4)}$$

The error, E, varies with connection weights. To minimise the error, the gradient of steepest descent method is used. For a given weight W_{kj} (hidden to output) the partial derivative is given by equation 5.5 (Rumelhart et al. 1986).

$$\frac{\partial E}{\partial W_{kj}} = -O_j(1 - O_j)(T_j - O_j)H_k = d_j H_k \qquad \text{…(5.5)}$$

where d_j is the adjusted output of the output neurons, expressed as:

$$d_j = -O_j(1 - O_j)(T_j - O_j) \qquad \text{… (5.6)}$$

The weight W_{jk} is then adjusted by ΔW_{kj} given by amount using equation 5.6.

$$\Delta W_{kj} = \eta\left(-\frac{\partial E}{\partial W_{kj}}\right) = \eta d_j H_k \qquad \text{…(5.7)}$$

where η is termed the "learning rate", which is the step size for the error correction (minimisation). The learning rate may be stipulated by the user or left at the default value.

To improve the learning efficiency of the learning process a "momentum term", α, has been included. The nth increment of the weighting, ΔW_{jk} is ΔW_{kj}^{n}, which can be calculated using equation 5.8.

$$\Delta W_{kj}^{n} = \eta d_j H_k + \alpha \Delta W_{kj}^{n-1} \qquad \ldots(5.8)$$

The output of each of the hidden neurons must then be adjusted using by equation 5.9.

$$d_k^{*} = H_k (1 - H_k) \sum_j (d_j W_{kj}) \qquad \ldots(5.9)$$

where d_k^{*} is the adjusted output of the hidden neurons, d_j the adjusted output of the output neurons, W_{kj} are the weights from the hidden neuron (k) to be adjusted to the output neurons and H_k is the previous output from hidden neuron k.

In a similar fashion, the connector weights from the input layer to the hidden layer are then adjusted by equation 5.10.

$$\Delta V_{kj}^{n} = \eta d_k^{*} N_i + \alpha \Delta V_{ik}^{n-1} \qquad \ldots (5.10)$$

where V_{ik} is the connection weight from input neuron i to hidden neuron k and ΔV_{ik}^{n} is the nth incremental adjustment for that weight. Once the weights have been set for all the connectors from the output layer back to the input layer, (back propagation), the network is then presented with the input data again, which is subsequently passed through the network and additional corrections made to minimise the error. This process is repeated until the network has minimised the error within the system.

5.2.3.2 Cascade Correlation Learning Algorithm

The cascade correlation algorithm was developed and presented by Scott Fahlman in 1990. The networks are dynamically constructed using hidden nodes (neurons) as part of the learning architecture, removing the need for the user to experiment in order to identify the optimal network architecture. Cascade correlation is comprised of two concepts, namely the correlation architecture and learning algorithm. The architecture dynamically adds hidden nodes as required to identify a certain feature of the problem. Each additional layer attempts to eliminate error between the network output and the measured (known) results. The first layer unlocks a major feature of the problem, with additional layers progressively refining the problem until an appropriate level of accuracy has been reached. An analogy to this may be to blindfold someone and give them an Australian coin to identify. To decide which coin it was, the subject may initially categorise on the basis of shape, then size, circumference, thickness and finally the feeling of the pictures.

The cascade architecture is that every input node is connected to every output node and every hidden node (as shown in Figure 5.4). There are no hidden nodes in the initial architecture and as such, there is no need to back-propagate to train the network. Instead the network is trained using Fahlman's "quickprop" algorithm. Once the weights of the network connections have been trained, they are fixed and do not change. If performance is to be improved, additional neurons are dynamically added to the network. When the training process stops improving the entire training set is passed through the network to ascertain the magnitude of the error between predicted and measured output. A patience factor is also applied, so that if training occurs for a designated number of cycles without an appreciable reduction in error, training is stopped and the network saved.

5.2.4 Power of Artificial Neural Networks

The true power of ANN's lies in their applicability to a wide range of problems. In essence one may consider the use of ANN's as a solution process, searching for a problem. ANN also uses parallel solution processing, capable of analysing non-linear problems, with a multivariate data input without limiting assumptions.

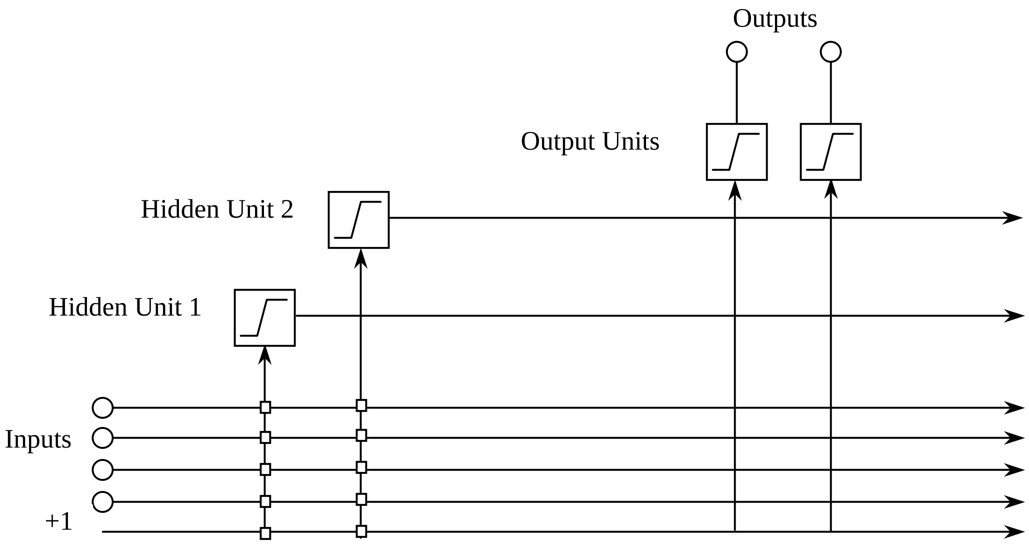

Figure 5. 4 Cascade architecture (Fahlman 1990)

5.2.5 Limitations of Artificial Neural Networks

The main limitations of neural networks are:-

- The training of networks requires significant amounts of historical data and the predictive ability of the neural nets outside of the data provided is very poor.
- The solution process is not made explicit to the user. The application of ANN has been limited as it has been seen as a “black box” solution, with a lack of quantifying logic.

5.3 Neural Network Software

Software development of neural networks has typically been associated with the fields in which large amounts of historical data are available, such as in stock market analysis, marketing and more recently in medical and engineering fields. Geotechnical engineering in particular lends itself to the use of ANN’s. Typically the solutions for the real world problems encountered in geotechnical engineering will rely heavily on the individual engineer’s interpretation of the various factors influencing their decision and their own experience of similar types of problems, which make each solution specific to the individual engineer. This was shown explicitly at the Texas 94’ settlement prediction summit where 37 internationally recognised geotechnical engineers (both from academia and industry) were asked to predict the loads required to cause 25mm and 150mm settlement on five different footings (Berardi and Lancellotta 1994). Presented with identical information, the predictions returned quite different results.

ANN's objectively collate and analyse historical data. In supervised systems they learn specifically about the prescribed inputs affect on the outputs, using both raw input data, and the corrected or learning data. This provides a simple and rational tool for design that includes gained or learned experience. Indeed the application of ANN's in geotechnical engineering is consistently growing (Arnold and Sivakugan 1997, Arnold 1999, Sivakugan et al. 1996, 1997; Abu Kiefa 1998; Goh 1994, 1995, 1996; Ellis et al. 1995; Ghaboussi 1995).

The range of software available to undertake neural network analysis is ever increasing. The website ftp://ftp.sas.com/pub/neural/FAQ6.html provides a good reference to some of the commercially available neural network software. Neuroshell 2©, developed by Ward Systems, was used as the software package for the analysis undertaken as part of this research. Of the packages reviewed, Neuroshell 2©, was deemed to be the most suitable package available for the current application.

5.3.1 Neuroshell 2©

Neuroshell 2©, is a neural network package which provides for both the beginners and more advanced users. The beginner's module uses a three layer back-propagation network while the advanced module offers five different neural networks. Each has its own network architecture and learning algorithms.

1. Back-propagation Learning
2. Kohonen Learning
3. General Regression Neural Network (GRNN) Learning
4. Probabilistic Neural Network (PNN) Learning
5. Group Method of Data Handling (GMDH) Learning

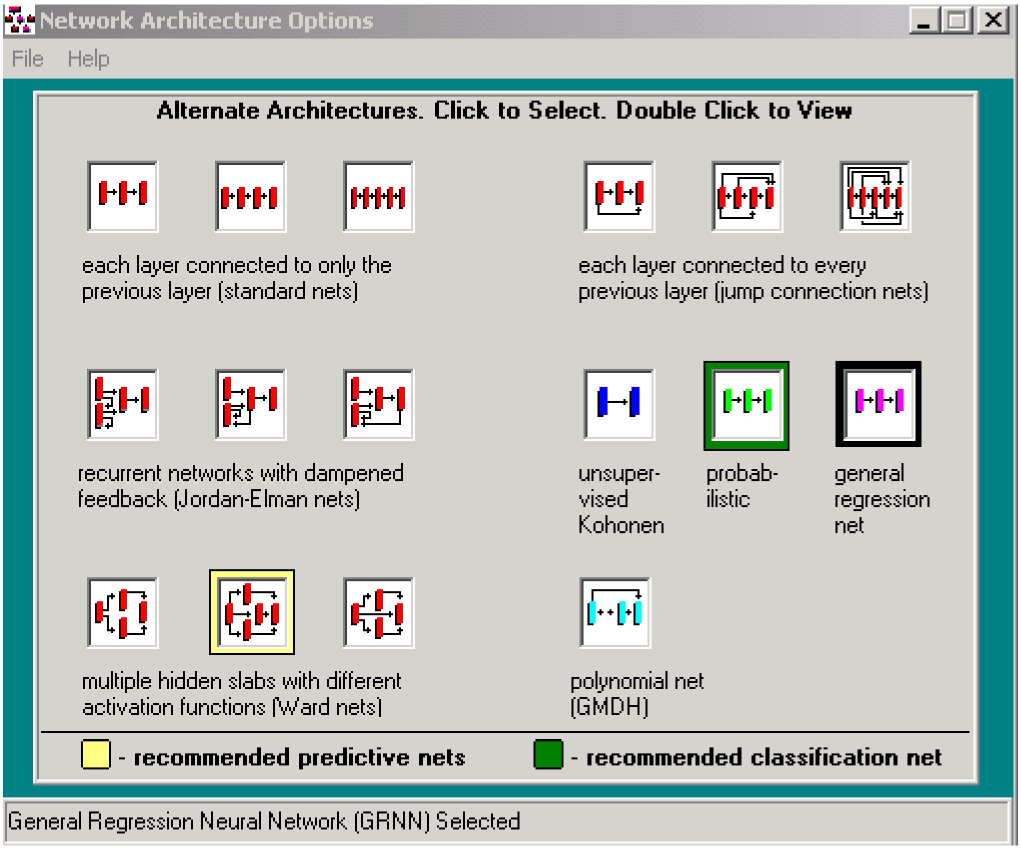

Figure 5. 5 Neuroshell 2©, advanced neural network options

Figure 5.5 shows the various architectures available from the advanced module of Neuroshell 2© (NS2). The networks on the left half of the screen are back propagation networks as are the networks on the top row of the right side. Variations of the back-propagation networks available in NS2 include:- standard, Jordan-Elman, jump connection and Ward nets. Of the other networks available, Kohonen is the only network that uses unsupervised learning. The Probabilistic and Kohenen networks are both used as classification networks, as opposed to predictive networks. PASTEC required the use of a predictive network, reducing the list of applicable architecture types to three; back-propagation, GRNN and GMDH. A brief review of each type of network is covered below.

5.3.1.1 Back-Propagation Networks

The back-propagation network uses a back-propagation learning algorithm, and has been covered in Section 5.2.3.1.

5.3.1.2 Group Method of Handling Data (GMHD)

This network is often referred to as the "polynomial" network, and is essentially a regression technique that uses the optimum polynomial or combination of polynomial terms for the modelling. This is in stark contrast to traditional regression methods, which require the polynomial to be stated prior to the analysis. All possible pairs of input variables are selected and combined to produce set of polynomial terms. For each set, all the possible polynomial models are then tested to determine output variable prediction performance. The model with the best performance is then saved. The optimum polynomial models for each set are then compared and a pre-set number of the best performing pair kept. These become the terms for the second layer in the network. Each layer in the network represents a polynomial. The second layer polynomial terms and the input variables are then used to create a third layer, in the same fashion as the first. This process is repeated until the polynomial performs satisfactorily (Arnold 1999).

5.3.1.3 General Regression Neural Network (GRNN)

The final network covered is the GRNN and is considered to be the most powerful of the networks available (Ward Systems 1996). There are three layers in a GRNN, the input, hidden and output layer. The number of neurons in each layer corresponds to the number of input variables, training sets (data points) and output variables respectively. The GRNN compares the input data with the training data, in the hidden layer, measuring the difference. The input variable contributing most to the magnitude of error is then adjusted. This provides the GRNN with a very high degree of sensitivity. A useful feature of the GRNN is the smoothing factors which can be applied to the data. These factors are indirect measures of the importance of the input variables on the predicted outputs. They range from 0-3, with 0 indicating maximum smoothing, limited sensitivity and therefore limited importance. Conversely, a smoothing factor of 3 indicates, minimum smoothing, maximum sensitivity and therefore maximum importance.

The publication of information regarding mine backfills in general and paste fills in particular is rare. It was therefore required to identify the network which performed well on limited data. GRNN's are known for their ability to train quickly on sparse data sets (Specht 1991) and was therefore chosen for application in this research. Abu Kiefa (1998) used Neuroshell 2© and GRNN's to predict load carrying capacities of piles.

5.4 Artificial Neural Networks Applied to the Prediction of Mine Backfill Strengths

5.4.1 Mine Backfill Data

Data was collated from various sources including the tests conducted on Cannington paste fill as part of this research, results of strength testing of paste fills reported in literature, and from results of worldwide backfills collated by Bloss (1992). As the testing of backfills strength is not a standardised procedure world-wide, the testing methods and parameters reported vary immensely. Table 5.1 summarises the data sets used for modelling with ANN's and the parameters used for each analysis.

Table 5. 1 Data set delineations

Data Set	Back Fill	Testing Parameters Available	Source
1	Paste Fills – Cannington Model Name: "**PFCAN**"	**Inputs:** %C, %S, P80, Curing time **Outputs:** ε_f, E, UCS	Rankine, 2003, (refer Chapter 3)
2	Paste Fills – World wide Model Name: "**PFVAR**"	**Inputs:** %C, %S, P80, Curing time **Outputs:** UCS	Various Authors (refer Table 5.2)
3	Various Fills – World wide Model Name: "**BFVAR**"	**Inputs:** %C, P80, Curing Time **Outputs:** UCS	Bloss (1992) (refer Tables 5.3 and 5.4)

Tables 5.2 to 5.4 summarise the reported results for paste and other backfills from worldwide sources. They also summarise the training data used for the modelling with the ANN's. A significantly larger body of research was consulted to construct the tables, however, only the backfills that reported the full complement of desired inputs, as shown in Table 5.1, were used. All other data was discarded from the analysis.

Three separate models were developed, one for each of the groups of backfills considered in Table 5.1, to predict the unconfined compressive strength from the input parameters. For the ANN developed for Cannington paste (PFCAN), the effect of the inputs on the compressive failure strain (ε_f) and stiffness (E) were also studied. Figure 5.6 (a) through (c) shows the layout of these three ANN's using GRNN architecture.

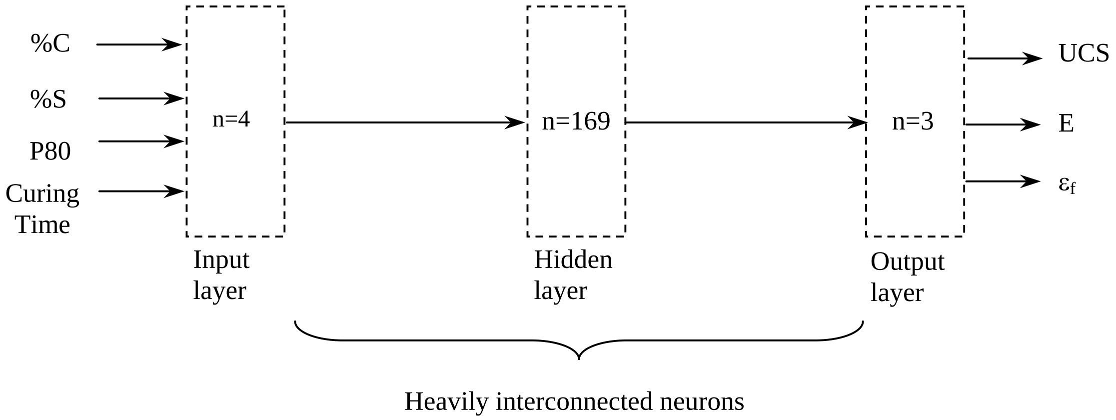

Figure 5. 6 (a) Artificial Neural Network 1:- Name: PFCAN, Type GRNN

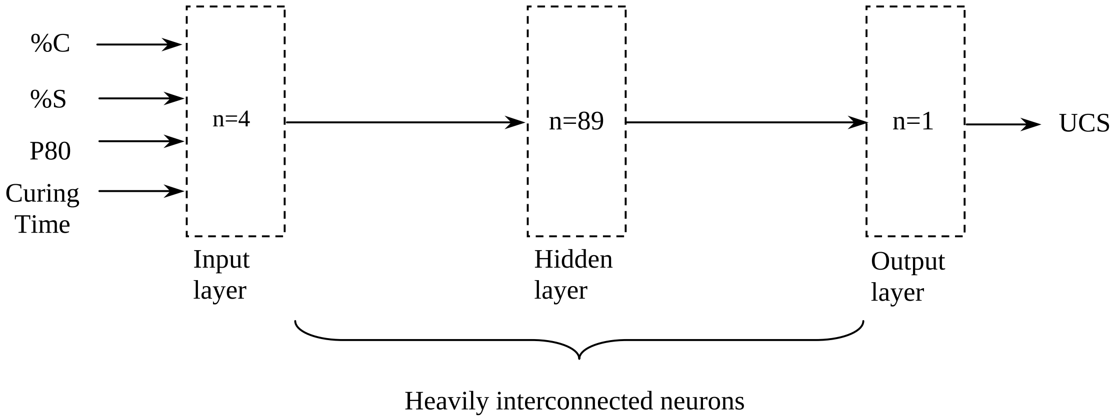

Figure 5. 6 (b) Artificial Neural Network 1:- Name: PFVAR, Type GRNN

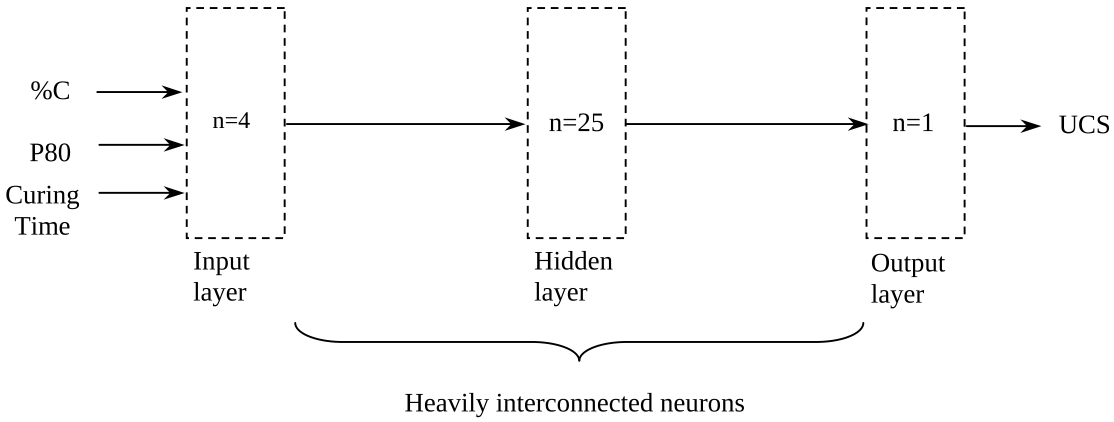

Figure 5. 6 (c) Artificial Neural Network 1:- Name: BFVAR, Type GRNN

The first step to developing an ANN model is to define the output parameters and then to intuitively identify the parameters which may influence the output. In the case of the Cannington paste fill, UCS, E and ε_f, were deemed to be useful in the stability analysis of paste filled stopes, and were thus defined as outputs. The other two models were limited by what was reported in literature.

To increase the predictive ability of the neural networks, it would be advantageous for the testing of fills to be standardised. The physical properties that would be of most interest to the determination of backfill strengths would be:-

- Backfill type
- Test method used and including strain rate
- Curing environment (temperature & humidity)
- Strength parameters (UCS, ϕ_u, ϕ', c_u, c') and
- Deformation characteristics (E_{s50}, and ε_f)

Table 5. 2 Training data for worldwide paste fills (PFVAR)

Backfill Source	Reference	Type of Fill					Equivalent Binder Content (% dry wt.)	Solids Content (% wt.)	P80 (μm)	Curing Time (Days)	UCS (kPa)
		PF	HF	SF	AF	RF					
Golden Giant Mine	Pierce (1997)	x					3	75	100	28	213
		x					3	75	100	56	332
		x					3	75	100	112	384
		x					5	75	100	28	307
		x					5	75	100	56	562
		x					5	75	100	112	620
		x					7	75	100	28	502
		x					7	75	100	56	852
		x					7	75	100	112	1267
Typical Canadian unclassified fill	Hunt (1989)	x					5.88	79	50	28	1260

Table 5. 2 (cont'd 1)

Backfill Source	Reference	Type of Fill: PF	HF	SF	AF	RF	Equivalent Binder Content (% dry wt.)	Solids Content (% wt.)	P80 (μm)	Curing Time (Days)	UCS (kPa)
Placer Dome Mine	Perry and Churcher (1990)	x					2.4	76	40	28	380
	Lamos and Clark (1989)	x					3	61	40	3	170
		x					3	61	40	10	250
		x					3	61	40	30	330
		x					3	61	40	50	450
		x					3	61	40	90	500
		x					6	61	40	3	300
		x					6	61	40	10	425
		x					6	61	40	30	700
		x					6	61	40	50	880
		x					6	61	40	90	1200
		x					10	61	40	3	520
		x					10	61	40	10	750
		x					10	61	40	30	1250
		x					10	61	40	50	1720
		x					10	61	40	90	2000
	Aref and Hassani (1988)	x					3.33	80	40	28	440
		x					3.33	76	40	28	555

Table 5. 2 (cont'd 2)

Backfill Source	Reference	Type of Fill: PF	HF	SF	AF	RF	Equivalent Binder Content (% dry wt.)	Solids Content (% wt.)	P80 (μm)	Curing Time (Days)	UCS (kPa)
Macassa Mine-tailings	American Barrick Resources Inc. (1995)	x					3	69	20	1	90
		x					3	69	20	3	117
		x					3	69	20	7	159
		x					3	69	20	28	172
		x					5	69	20	1	76
		x					5	69	20	3	131
		x					5	69	20	7	172
		x					5	69	20	28	207
		x					9	69	20	1	110
		x					9	69	20	3	303
		x					9	69	20	7	331
		x					9	69	20	28	517
Macassa Mine-Tailings:sand (50:50)	American Barrick Resources Inc. (1995)	x		x			3	82	1700	1	179
		x		x			3	82	1700	3	228
		x		x			3	82	1700	7	303
		x		x			3	82	1700	28	379
		x		x			5	82	1700	1	186
		x		x			5	82	1700	3	372
		x		x			5	82	1700	7	421
		x		x			5	82	1700	28	689
		x		x			9	82	1700	1	421
		x		x			9	82	1700	3	896
		x		x			9	82	1700	7	1365
		x		x			9	82	1700	28	2386

Table 5. 2 (cont'd 3)

Backfill Source	Reference	Type of Fill: PF	HF	SF	AF	RF	Equivalent Binder Content (% dry wt.)	Solids Content (% wt.)	P80 (μm)	Curing Time (Days)	UCS (kPa)
Macassa Mine-Tailings:sand (25:75)	American Barrick Resources Inc. (1995)	x		x			3	86	3700	1	221
		x		x			3	86	3700	3	303
		x		x			3	86	3700	7	414
		x		x			3	86	3700	28	538
		x		x			5	86	3700	1	269
		x		x			5	86	3700	3	545
		x		x			5	86	3700	7	689
		x		x			5	86	3700	28	1069
		x		x			9	86	3700	1	669
		x		x			9	86	3700	3	1517
		x		x			9	86	3700	7	2068
		x		x			9	86	3700	28	3275
Louvicourt Mine	American Barrick Resources Inc. (1995)	x					3	76	50	28	475
		x					5	76	50	28	505
		x					7	76	50	28	775
	Landriult (1995) *Paste:- Fine*	x					3	79	20	28	200
		x					5	79	20	28	235
		x					7	79	20	28	300
	Landriult (1995) *Paste:- Medium*	x					3	75	135	28	475
		x					5	75	135	28	505
		x					7	75	135	28	775
	Landriult (1995) *Paste:- Coarse*	x					3	70	200	28	500
		x					5	70	200	28	630
		x					7	70	200	28	1150

Table 5. 2 (cont'd 4)

Backfill Source	Reference	Type of Fill					Equivalent Binder Content (% dry wt.)	Solids Content (% wt.)	P80 (μm)	Curing Time (Days)	UCS (kPa)
		PF	HF	SF	AF	RF					
Inco Mine	Landriult and Lidkea (1993)	x					3.25	70	180	1	14
		x					3.25	70	180	3	55
		x					3.25	70	180	7	90
		x					3.25	70	180	28	165
		x					4.8	70	180	1	34
		x					4.8	70	180	3	103
		x					4.8	70	180	7	248
		x					4.8	70	180	28	324
		x					9.2	70	180	1	172
		x					9.2	70	180	3	345
		x					9.2	70	180	7	827
		x					9.2	70	180	28	1034
	Lidkea and Landriult (1993)	x					3	84	210	3	756
		x					3	84	210	7	910
		x					3	84	210	28	1500

Table 5. 3 Training data for worldwide back fills (BFVAR) (Bloss 1992)

Country	Backfill Source	Reference Source	PF	HF	SF	AF	RF
Canada	Quebec Area Mine (unknown)-classified	Weaver and Luka (1970)		x			
	Quebec Area Mine (unknown)-unclassified	Weaver and Luka (1970)		x			
	Ontario Area Mine (unknown)	Barsotti (1978)		x			
	Falconbridge Mine	McGuire (1978), Singh and Hedley (1981)		x			
	Chadbourne Mine	Nantel and Lecuyer (1983)		x			
	Kidd Creek Mine	Yu and Counter (1983, 1988)					x
	Dome Mine	Perry and Churcher (1990)	x				
Australia	Warrego Mine	Ingles et al. (1973)				x	
	Que River Mine	Barrett et al. (1983)				x	
	Olympic Dam Mine	Thomas (1983)					
	Broken Hill Mine - Tails	Askew et al. (1978)		x			
	Broken Hill Mine - Sand	Lun (1985)			x		
	Mount Isa Mine - CHF	Bloss (1992)		x			
	Mount Isa Mine - CAF	Bloss (1992)		x		x	
	Mount Isa Mine - CRF	Bloss (1992)		x			x
	Cannington Mine	Rankine et al. 2001	x				
South Africa	S.A. gold mines-CT	Lamos and Clark (1989)		x			
	S.A. gold mines-FT	Lamos and Clark (1989)		x			
	S.A. gold mines-CW	Lamos and Clark (1989)			x	x	
Finland	Vammala Mine	Koselka (1983)		x			
	Vihanti Mine	Koselka (1983)		x			
	Keretti Mine	Koselka (1983)				x	
Italy	Gavorrano Mine	Berry (1981)				x	
	Sardinian Mine	Manca et al (1984)			x		
Turkey	Uldag Mine	Arioglu (1983)		x		x	

where PF= Paste Fill, HF = Hydraulic Fill, SF=Sand Fill, AF= Aggregate Fill, RF = Rock Fill. “x” in more than one box indicates a blended fill.

Table 5. 4 Material Properties for the various mine backfills (Bloss 1992)

Backfill Source	Binder Content (%)	Curing Time (Days)	P80 (μm)	UCS (kPa)
Quebec Area Mine (unknown)-classified	6.30	90	108	780
Quebec Area Mine (unknown)-unclassified	6.30	90	100	650
Ontario Area Mine (unknown)	12.00	112	108	3100
Falconbridge Mine	6.00	112	108	600
Chadbourne Mine	5.00	112	108	200
Kidd Creek Mine	7.30	84	29000	10300
Dome Mine	2.40	28	40	380
Warrego Mine	4.00	14	10000	1400
Que River Mine	6.70	56	24000	4600
Olympic Dam Mine	6.00	28	40	800
Broken Hill Mine – Tails	6.00	112	200	840
Broken Hill Mine – Sand	6.00	28	280	4200
Mount Isa Mine – CHF	7.00	112	102	840
Mount Isa Mine – CAF	2.25	250	10000	1300
Mount Isa Mine – CRF	2.10	365	50000	1600
Cannington Mine	3.50	28	105	600
S.A. gold mines-CT	10.00	90	180	1300
S.A. gold mines-FT	10.00	90	95	1800
S.A. gold mines-CW	10.00	90	1500	5200
Vammala Mine	5.88	224	105	1500
Vihanti Mine	8.33	365	105	1050
Keretti Mine	6.37	28	13000	2100
Gavorrano Mine	10.90	90	27000	10200
Sardinian Mine	9.00	28	1800	2000
Uldag Mine	2.40	28	20000	880

5.4.2 Modelling Procedure

The two objectives to be achieved from ANN modelling were:-

- To construct and validate a neural network capable of predicting fill strengths for each of the three data sets as outlined in Table 5.1
- To identify the factors that contribute most significantly to the development of strength for the fills reported.

5.4.3 ANN Modelling

Neuroshell 2© was used to build three separate ANN models. The models describe the data delineated in Table 5.1 and presented in Tables 5.2 to 5.4. The models take the generic form of those outlined in Figure 5.6 (a) through (c). The contribution of each of the input variables to the outputs were assessed by means of the effective weightings which are provided by Neuroshell 2© during the training phase for the GRNNs.

5.4.3.1 Modelling Parameters

All models use the most comprehensive data available and were assumed to be very “noisy”. The data was assumed to have a high degree of scatter and variability, which is considered reasonable, especially when considering the various fill types, test methods, and mix proportion of the back fills studied.

The data sets for each of the ANN model were subdivided into “modelling” and “validation” data. The modelling data was then further subdivided into a test set and training set (refer Figure 5.7). The difference between validation and test data is that the validation data is used to assess the predictive ability of the network on “unseen” data, whereas the “training set” is “seen” data used to calibrate the network during training. In each case the division of data was conducted randomly, using a seed to generate a random number and selection criteria. Arnold (1999) observed that networks that were trained with a minimal test set tend to outperform those with larger test sets. Negligible differences were observed in the variation of the predictions of networks that used tests sets comprising of between 0%-10% of the input modelling data. Figure 5.7 shows the proportional division of the data into the various subsets used in the present exercise.

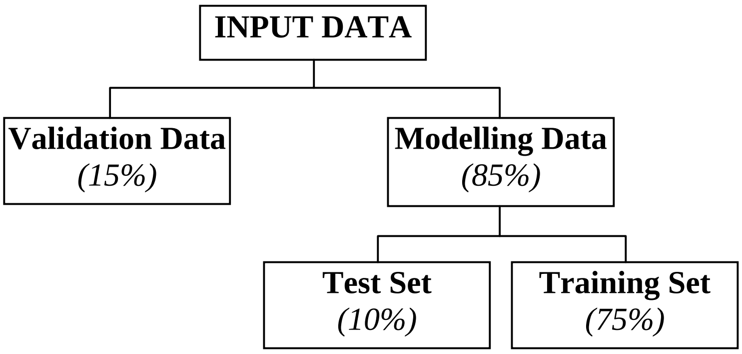

Figure 5. 7 Division of data for ANN

5.4.3.2 Results

Once each of the models had been constructed, their individual performances were assessed using the coefficient of correlation, r, and the coefficient of determination, r^2. The precision of the model was assessed using the coefficient of determination between the predicted and measured data. The validation data was used to provide an indication of the predictive ability of the trained networks on unseen data. The weighting for each of the input parameters provided by the NS 2 package was used to assess the effective contribution of the various inputs to strength. As the validation data and test set data were randomly chosen within the framework of NS 2, five models for each data set were developed for prediction. The results from the tests are reported in Table 5.5. The shaded rows (PFCAN_3, PFVAR_5, BFVAR_3) are the models with the highest predictive quality for each data set. The smoothing factor (SF) for each network was also recorded in the last column to provide an indication as to the likely generality (or specificity) of the solutions. Smoothing factors (SF) range between 0 and 3. A SF of close to 0 indicates that the information in the ANN has undergone a significant amount of smoothing and will likely provide a more generalised solution, whereas a SF of 3 indicates very limited smoothing and a highly specific solution. The results show a high degree of smoothing occurring for all of the models tested, inferring all of the models would provide generalised solutions.

Table 5. 5 Neural network modelling results

<table>
<tr><th rowspan="2">Data Set</th><th rowspan="2">Model Name</th><th colspan="4">Input parameter Importance
Most ⟶ Least</th><th rowspan="2">Model Output</th><th colspan="2">Model Performance</th><th rowspan="2">Smoothing Factor</th></tr>
<tr><th>1</th><th>2</th><th>3</th><th>4</th><th>r</th><th>r^2</th></tr>
<tr><td rowspan="15">Paste Fills (Cannington)</td><td rowspan="3">PFCAN_1</td><td rowspan="3">%C</td><td rowspan="3">%S</td><td rowspan="3">Curing Time</td><td rowspan="3">P80</td><td>UCS</td><td>0.993</td><td>0.986</td><td rowspan="3">0.149</td></tr>
<tr><td>E</td><td>0.928</td><td>0.862</td></tr>
<tr><td>ε_f</td><td>0.973</td><td>0.946</td></tr>
<tr><td rowspan="3">PFCAN_2</td><td rowspan="3">%C</td><td rowspan="3">%S</td><td rowspan="3">Curing Time</td><td rowspan="3">P80</td><td>UCS</td><td>0.981</td><td>0.963</td><td rowspan="3">0.134</td></tr>
<tr><td>E</td><td>0.893</td><td>0.798</td></tr>
<tr><td>ε_f</td><td>0.957</td><td>0.915</td></tr>
<tr><td rowspan="3">PFCAN_3</td><td rowspan="3">%C</td><td rowspan="3">%S</td><td rowspan="3">P80</td><td rowspan="3">Curing Time</td><td>UCS</td><td>0.996</td><td>0.991</td><td rowspan="3">0.014</td></tr>
<tr><td>E</td><td>0.935</td><td>0.875</td></tr>
<tr><td>ε_f</td><td>0.974</td><td>0.949</td></tr>
<tr><td rowspan="3">PFCAN_4</td><td rowspan="3">%C</td><td rowspan="3">P80</td><td rowspan="3">Curing Time</td><td rowspan="3">%S</td><td>UCS</td><td>0.995</td><td>0.990</td><td rowspan="3">0.095</td></tr>
<tr><td>E</td><td>0.929</td><td>0.863</td></tr>
<tr><td>ε_f</td><td>0.976</td><td>0.953</td></tr>
<tr><td rowspan="3">PFCAN_5</td><td rowspan="3">Curing Time</td><td rowspan="3">%S</td><td rowspan="3">P80</td><td rowspan="3">%C</td><td>UCS</td><td>0.983</td><td>0.966</td><td rowspan="3">0.158</td></tr>
<tr><td>E</td><td>0.915</td><td>0.837</td></tr>
<tr><td>ε_f</td><td>0.949</td><td>0.901</td></tr>
<tr><td rowspan="5">Paste Fills (World Wide)</td><td>PFVAR_1</td><td>P80</td><td>%S</td><td>%C</td><td>Curing Time</td><td>UCS</td><td>0.681</td><td>0.464</td><td>0.507</td></tr>
<tr><td>PFVAR_2</td><td>%C</td><td>P80</td><td>%S</td><td>Curing Time</td><td>UCS</td><td>0.895</td><td>0.802</td><td>0.134</td></tr>
<tr><td>PFVAR_3</td><td>%S</td><td>P80</td><td>Curing Time</td><td>%C</td><td>UCS</td><td>0.918</td><td>0.843</td><td>0.072</td></tr>
<tr><td>PFVAR_4</td><td>P80</td><td>%C</td><td>%S</td><td>Curing Time</td><td>UCS</td><td>0.748</td><td>0.560</td><td>0.259</td></tr>
<tr><td>PFVAR_5</td><td>%C</td><td>Curing Time</td><td>%S</td><td>P80</td><td>UCS</td><td>0.949</td><td>0.901</td><td>0.070</td></tr>
<tr><td rowspan="5">Various Back Fills (World Wide)</td><td>BFVAR_1</td><td>P80</td><td>%C</td><td>Curing Time</td><td rowspan="5">No Solids Content reported for fills</td><td>UCS</td><td>0.927</td><td>0.859</td><td>0.363</td></tr>
<tr><td>BFVAR_2</td><td>%C</td><td>P80</td><td>Curing Time</td><td>UCS</td><td>0.942</td><td>0.887</td><td>0.259</td></tr>
<tr><td>BFVAR_3</td><td>Curing Time</td><td>%C</td><td>P80</td><td>UCS</td><td>0.948</td><td>0.898</td><td>0.134</td></tr>
<tr><td>BFVAR_4</td><td>Curing Time</td><td>P80</td><td>%C</td><td>UCS</td><td>0.943</td><td>0.888</td><td>0.445</td></tr>
<tr><td>BFVAR_5</td><td>%C</td><td>P80</td><td>Curing Time</td><td>UCS</td><td>0.937</td><td>0.879</td><td>0.352</td></tr>
</table>

Now that the correlations between the input and output parameters have been established it is required to validate the networks against unseen data. This was achieved by using a set of validation data extracted at random from the full set of input data. Figures 5.7 to 5.9 shows measured versus predicted values for the UCS, E and ε_f for Cannington paste fill. Figures 5.10 and 5.11 show similar predicted versus measured UCS graphs for international paste fills and backfills respectively.

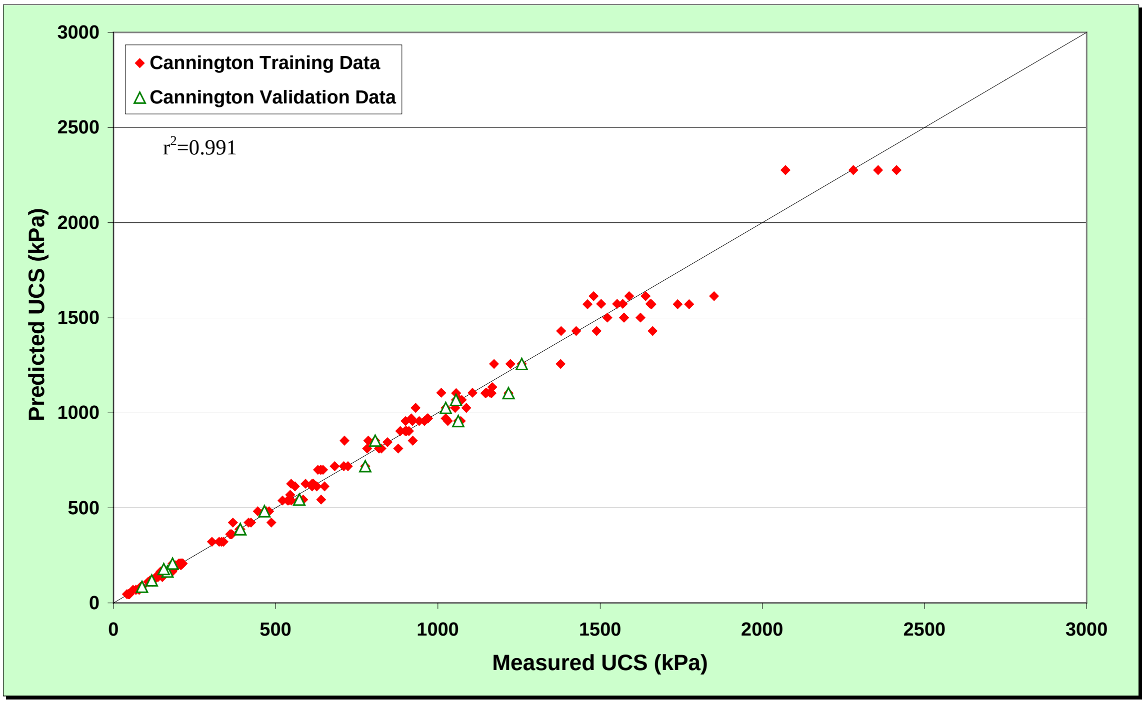

Figure 5. 8 Predicted vs. Measured Values UCS of Cannington Paste Fill

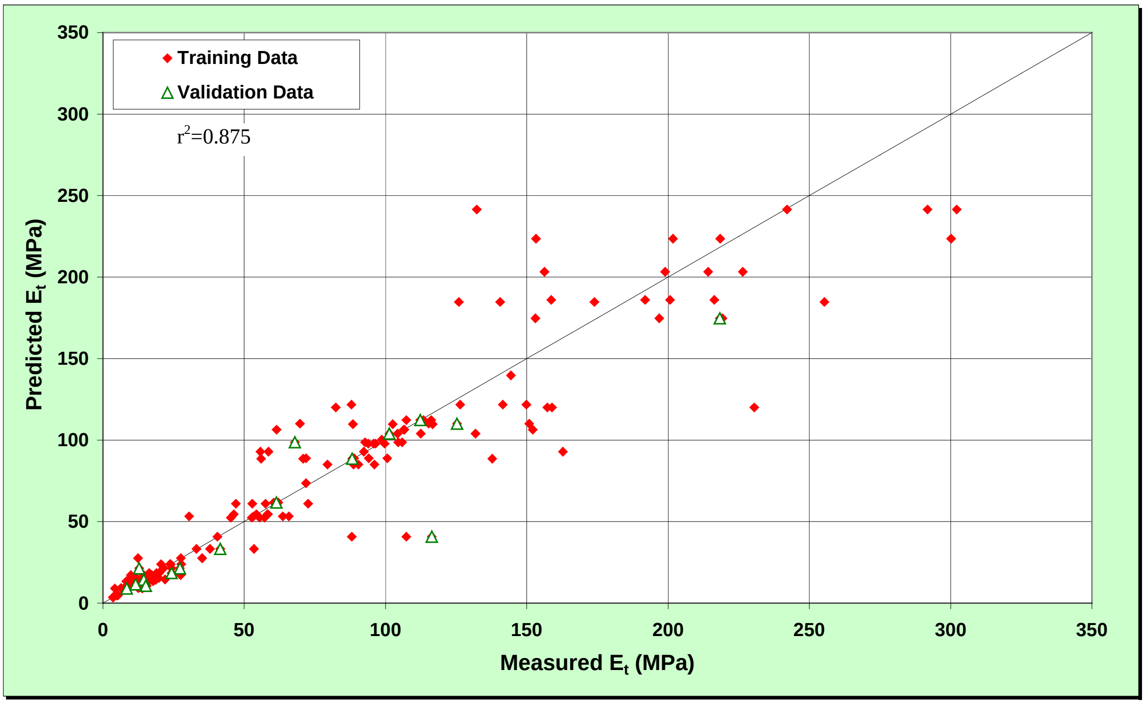

Figure 5. 9 Predicted vs. Measured Values of Young's Modulus (E) for Cannington Paste Fill

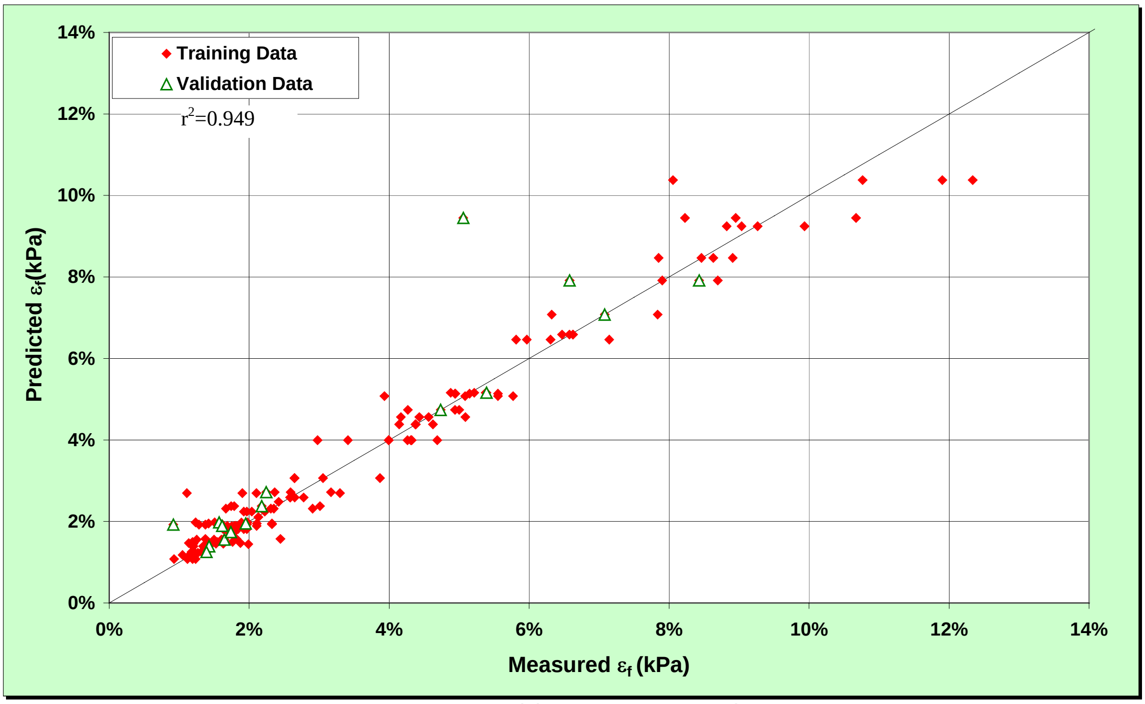

Figure 5. 10 Predicted vs. Measured Values of failure strain (ε_f) for Cannington Paste Fill

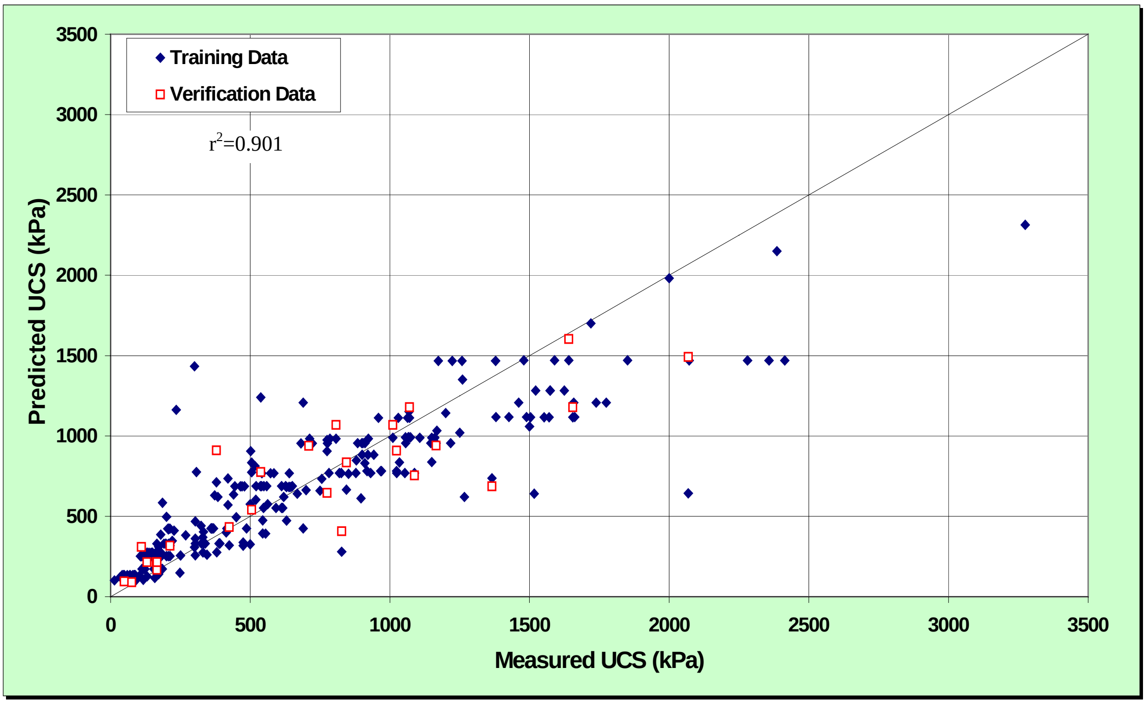

Figure 5. 11 Predicted vs. Measured Values of UCS for Paste Fill from various sources world wide

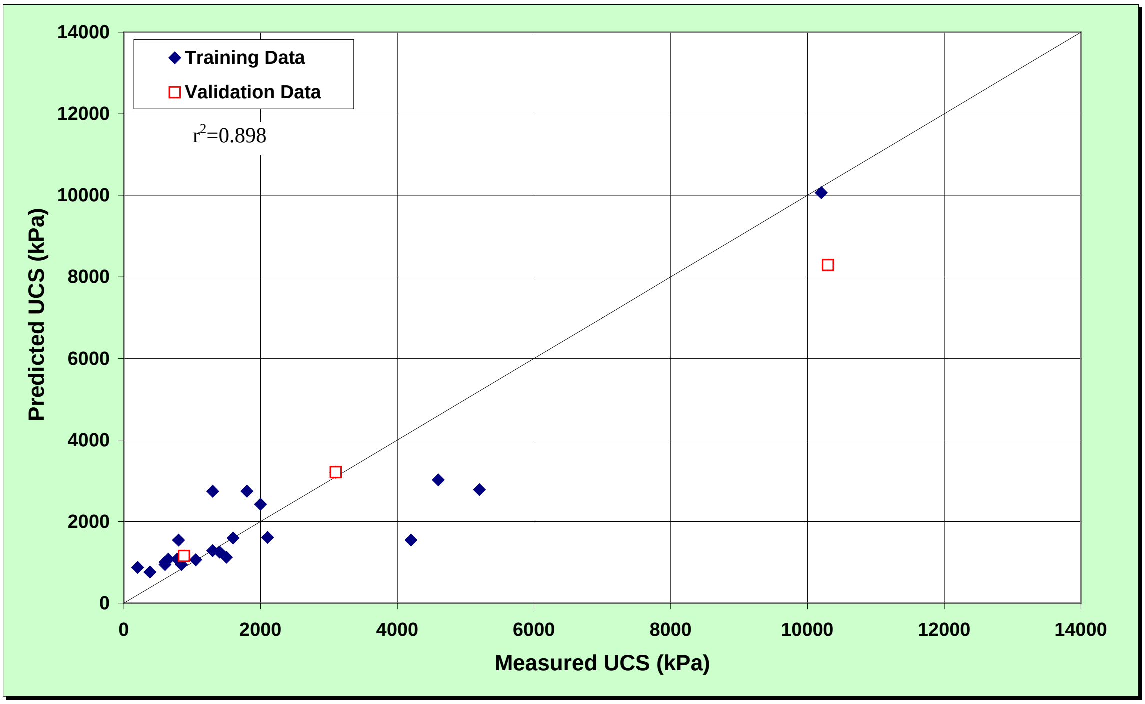

Figure 5. 12 Predicted vs. Measured Values of UCS for back fills from various sources world wide

The validation data applied to the networks shows good correlation to the predicted values, confirming the validity of the neural networks as a modelling tool for the prediction of fill strengths.

To investigate further the applicability of the ANN developed for the prediction of the output parameters for Cannington Paste fill to other backfills, predicted outputs for Cannington Fill using the ANN's developed for various backfills and paste fills from around the world were compared against their measured results. Figures 5.13 and 14 shows the results from the ANN modelling for the paste fills and various other back fills respectively. Typically, the ANN over estimates the UCS of Cannington paste fill, using the ANN's developed for alternative backfills. This is particularly true when compared to the ANN developed for paste fills worldwide. This indicates that Cannington fill is typically weaker in compression than other backfills from around the world having similar constituents. A possible contributing factor to this is the inclusion of coarse particles in the paste fill matrix (sand), which increases the strength of the fill (Luke and Rankine 2003, American Barrack Resources Inc. 1995).

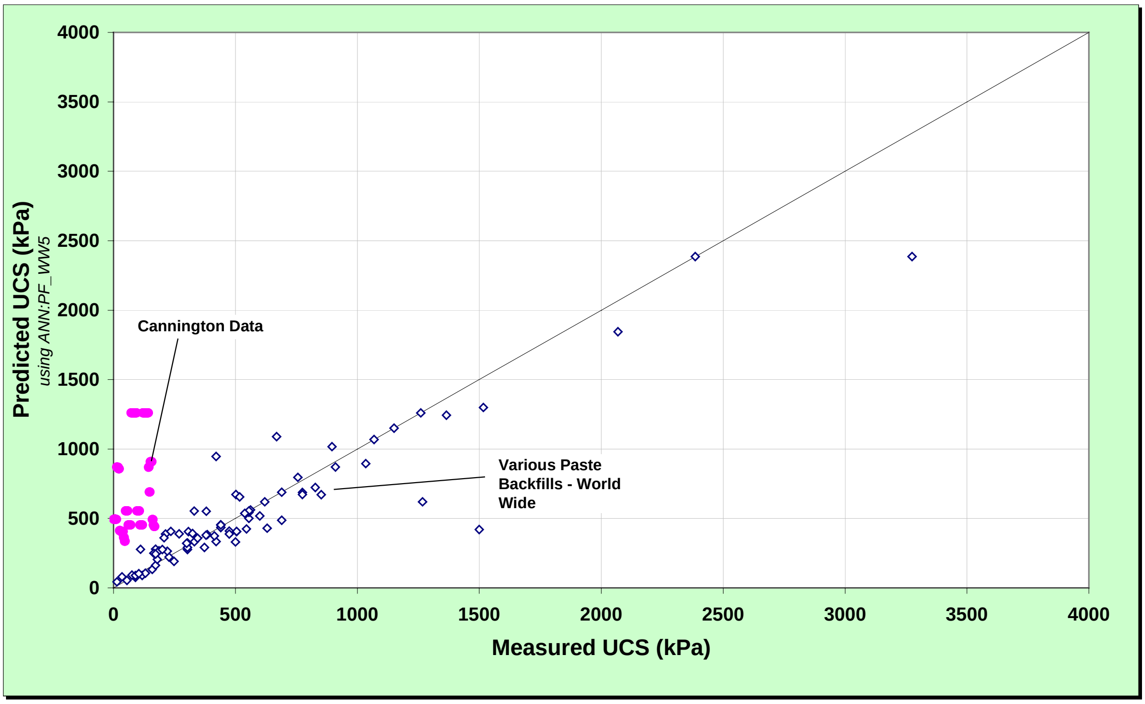

Figure 5. 13 Applicability of PFVAR_5 to Cannington Paste Fill

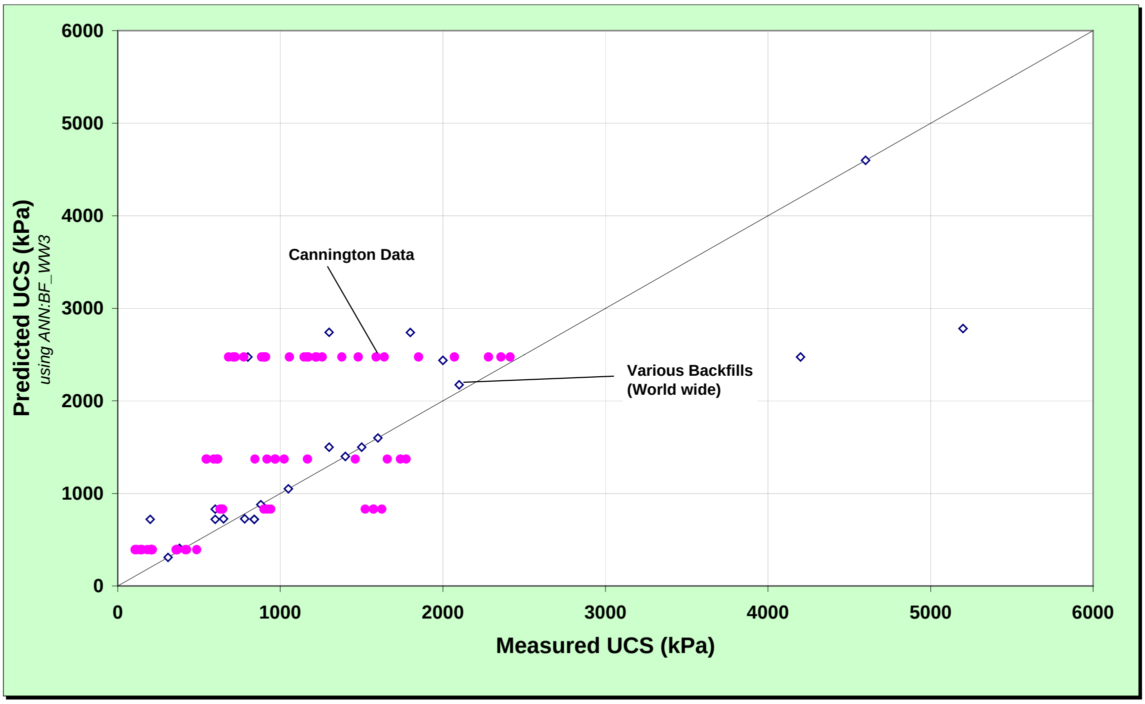

Figure 5. 14 Applicability of BFVAR_3 to Cannington Paste Fill

From Figure 5.14 it can be seen that the Cannington data is spread significantly around those strengths predicted for various backfills strengths, however again, the ANN over predicts the strengths of backfills. The long straight horizontal rows of points in Figure 5.14 show the increase in strength with the increase in the solids content. However, as the solids content was not taken into account (or was not available) as an input parameter for the ANN, the predictions made were independent of this. As the solids content increases, so does the measured strength. The ANN predictions remain constant, as no other input parameters have changed resulting in the long horizontal row of data, showing the same UCS values for all solids contents.

This indeed shows the value of a predictive tool that is specific to the site, which is able to take into account site-specific conditions. This also casts doubt over the applicability of “generic” equations used to determine fill strengths.

5.4.4 Conclusions

The principal objectives of the ANN modelling was to demonstrate the feasibility of using ANN’s to predict the strengths of fills from around the world and to identify the factors which contributed most to the development of strength in backfills masses. To achieve this three separate ANN’s were developed to investigate fill strengths on an increasingly general level. The three data sets investigated included i) Cannington paste fill ii) paste fills from around the world and iii) various forms of backfills from around the world. Each of the networks were assessed using the coefficient of determination (r^2) between the predicted and measured values for each parameter. From Table 5.5 it can be seen that r^2 for the Cannington paste fills remains consistently above 0.9 which means that more than 90% (r = 0.95) of the data can be described by the neural network developed for the application (Walpole and Myers 1993). Similar results are shown for the other two data sets. The strength of the correlations for the various backfills world wide should be treated with care as only 25 test results were used to construct the graph, and three to validate, which is small compared to the N=170 for Cannington Paste fills and N=89 for the combined paste fills from around the world (excluding Cannington data).

The second objective from the ANN modelling was to identify the contribution of each of the inputs to the development of the correlations. For Cannington paste fill, the mix proportions (%C, %S) dominated the development of any relationships, which is consistent with the data reported in Chapter 3. No single input parameter was identified as dominating the outputs for either paste fills or back fills from around the world, indicating a shared contribution from each. The low smoothing factors indicate a high degree of data smoothing has taken place and that results predicted from the neural networks will be more general.

5.5 Geotechnical Characterisation of Paste - Software Package (PASTEC)

A program (PASTEC) was developed using Microsoft Excel as an operating platform, and uses a serries of ANN's to describe the physical and geotechnical characteristics of Cannington paste fill based on basic user defined inputs, such as cement and solids content, the grain size (P80) and the cured time of the paste. An overview of the program is provided forthwith, and the full program contained on the CD provided with this dissertation.

5.5.1 Main PASTEC Program Screen

The main screen of PASTEC is shown in Figure 5.15. The user is required to identify what information regarding the paste is required and click on the associated button. Total and effective stress analysis results have been reported for paste. The total stress analysis results include the time dependent behaviour of paste for early, medium and long term strengths. The consolidation characteristics and physical properties of paste have also been incorporated into the PASTEC program.

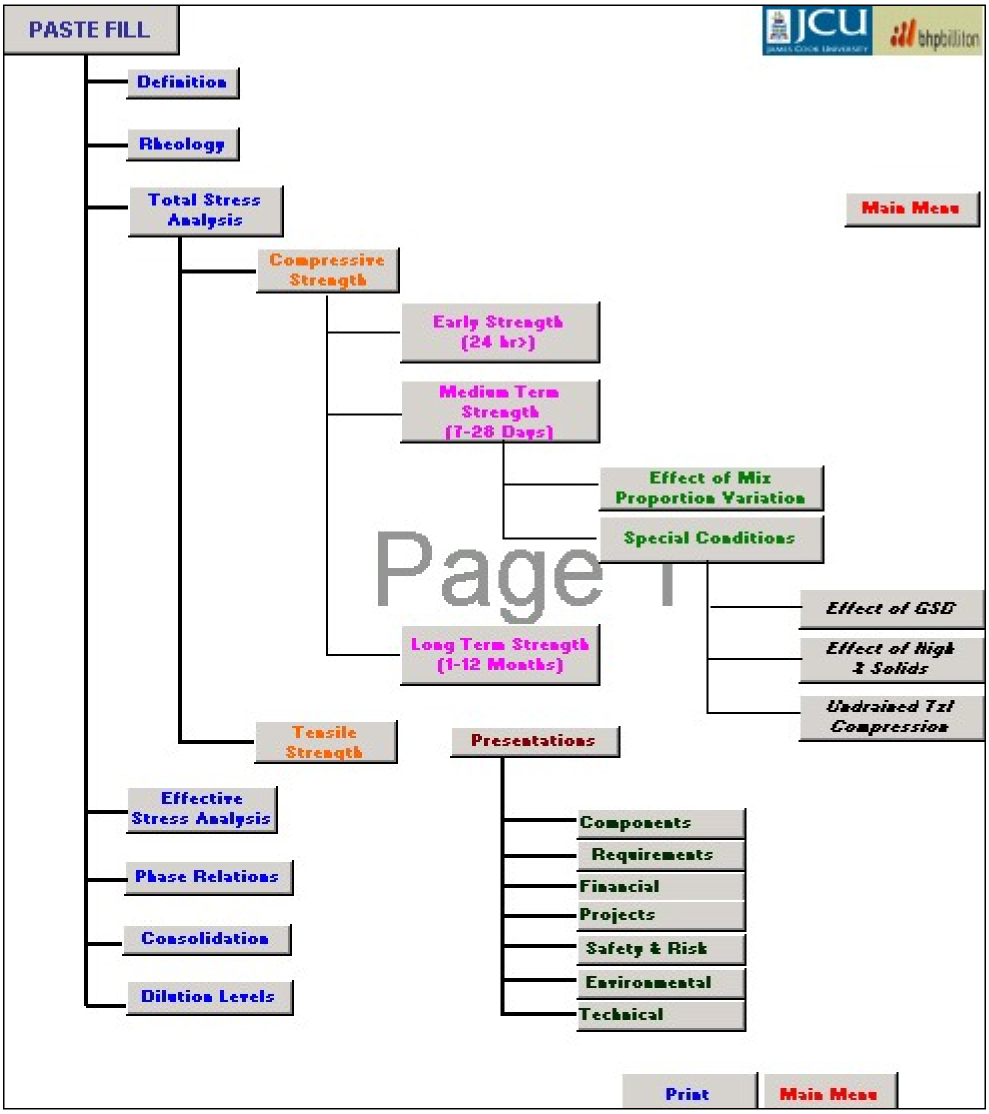

Figure 5. 15 PASTEC - Front page overview

5.5.2 User Interface Panels

Each of the user interface panels predict certain charactertics of Cannington paste fill, from basic user defined inputs such as the cement content, solids content, P80 and curing time. Figure 5.16 shows an example of the user interface panels, for the unconsolidated-undrained triaxial testing. Similar interface panels have been set up for each of the end points in the structure as shown above, but for matters of brevity and simplicity have not been included within the text, but have been included in the attached CD.

The ANN's have been embedded within Microsoft Excel and are called when the user-defined inputs have been entered.

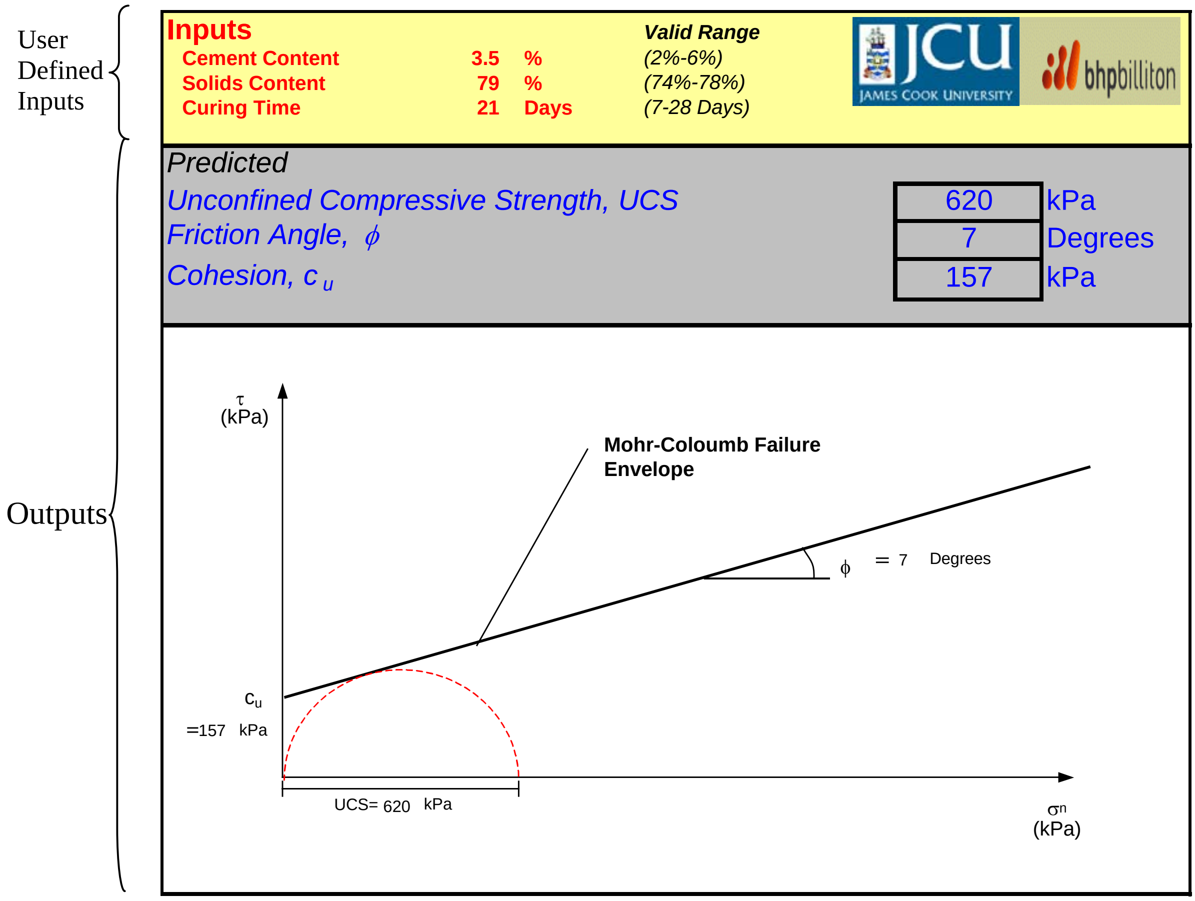

Figure 5. 16 PASTEC – User interface panel for undrained strength parameters

Similar user interface panels have been developed for each of the panels on the end of the branches shown in figure 5.12. Table 5.6 summarises the inputs, outputs and strength of relationships (r^2) between the predicted and measured results. Indeed, as such a broad spectrum of information was covered during the geotechnical investigations, that there are a reduced number of each type of tests. Correlations made with 50 data points or less have been identified (by shading) and may be investigated further with additional testing. For networks with N<30 the use of ANN's is simply a interpolation tool.

Table 5. 6 PASTEC – Overview of correlations for predictions made by ANN's for relationships relating to Cannington Paste Fill

Page	Inputs	Outputs	r^2	Comment
PASTE				
Definition	N/A	N/A	N/A	No predictions made – description only
Rheology	N/A	N/A	N/A	No predictions made – description only
Early Strength	%Solids	Yield Stress		Empirical Correlations – used to define strength vs. time vs. cement content. Limited to prediction of 79% solids at present. Further work required. Yield Stress correlation from Clayton (2000)
	% Cement, Curing Time (hrs)	Ucs, Modified Pocket Penetrometer		Empirical Correlation – derived from test work Empirical Correlation – derived from test work The correlation between the UCS and the Modified pocket penetrometer was R^2 0.76. Thus indicating that the modified pocket penetrometer may be used as an indicative measure, but should not be relied on as a Quality Control.
Mix Proportions	% Solids, Curing Time (hrs)	% Cement req'd to achieve specific design UCS strengths	r^2=0.898	Samples tested on Cannington Tailings in UCS only (N=122), also ANN can predict the Tangential Young's Modulus, E_t (kPa) and Failure Strain, ε_f (%) with correlations of R^2= 0.7176 and 0.7839 respectively. These are not used in or outputted on this sheet to the user.
Effect of High % Solids (80%-85%)	% Solids % Cement Curing Time (Days)	UCS E_t ε_f	r^2=0.9191 r^2=0.8767 r^2=0.9941	Samples tested on Cannington Tailings in UCS only (N=50). Significant variations in the two sets of samples tested to date, indicate compaction to be a key component in the achievements of higher strengths with high solids density backfills.
Effect of Grain Size Distribution	% Solids Curing Time P80	% Cement req'd to achieve specific design UCS strengths	r^2=0.9892	Samples tested on Cannington Tailings in UCS only (N=176), also ANN can predict the Tangential Young's Modulus, E_t (kPa) and Failure Strain, ε_f (%) with correlations of R^2= 0.8706 and 0.906 respectively. These are not used in or outputted on this sheet to the user.

Table 5. 6 (Cont…1)

Page	Inputs	Outputs	r^2	Comment
PASTE				
Undrained Triaxial Compression	% Solids % Cement Curing Time (Days)	UCS Friction Angle,ϕ Cohesion, c_u	r^2=0.898 r^2=0. 974 r^2=0.988	UCS strengths predicted from the net trained for mix proportion variation – based on the inputs. For determination of the friction angle and cohesion intercept N=34, (3 samples are required to make one set of results, thus $N_{samples}$=102)
Long Term Strength	% Solids % Cement Curing Time (Months)	UCS Friction Angle,ϕ Cohesion, c_u	r^2=0.952 r^2=0.949 r^2=0.914	For determination of the friction angle and cohesion intercept N=46, (3 samples are required to make one set of results, thus $N_{samples}$=138).
Tensile Strength	% Solids % Cement Curing Time (Days)	Tensile Strength, σ_t	r^2=0.900	N=52, Empirical correlations developed in body of thesis regarding tensile strength as a proportion of compressive strength also.
Effective Stress Analysis	% Solids % Cement Curing Time (Months)	UCS Effective Friction Angle,ϕ'	r^2=0.952 r^2=0.902	UCS Strength predicted from ANN developed for prediction of long term strength of paste fill. Effective friction angle interpolated between bounds. Effective Cohesion considered to be non-meaningful in all cases. Assume c'=0, to construct Mohr-Coulomb plot.

Table 5. 6 (Cont…2)

Page	Inputs	Outputs	r^2	Comment
PASTE				
Phase Relations	Medium Term (1-28 Days) % Cement %Solids Curing Time (Days)	Moisture Content Void Ratio Degree of Saturation Porosity Bulk Density Dry Density Saturated Density	r^2=0.987 r^2=0.986 r^2=0.823 r^2=0.987 R^2=0.979 R^2=0.987 R^2=0.987	N=28 for determination of medium term phase relations/ physical characteristics. R^2 correlations for the Densities and their respective Modulus values should be identical – as there is a constant numerical multiplication factor between them. (i.e. 9.81)
	Long Term (1-12 Months) % Cement %Solids Curing Time (Months)	Moisture Content Void Ratio Degree of Saturation Porosity Bulk Density Dry Density Saturated Density	r^2=0.912 r^2=0.959 r^2=0.881 r^2=0.950 r^2=0.890 r^2=0.950 r^2=0.950	N=47 for determination of medium term phase relations/ physical characteristics. R^2 correlations for the Densities and their respective Modulus values should be identical – as there is a constant numerical multiplication factor between them. (i.e. 9.81)
Consolidation	Consolidation of Curing Paste Inputs= NIL	Preliminary Test Data Showing Trends.	N/A	Preliminary Testing Data shows an increase in strength under consolidated curing conditions. The increase in the tangential young's modulus and reduction in the failure strains observed all indicates a densification of the soil matrix.
	Cured Consolidation % Cement % Solids Curing Time (Days)	Co-efficient of Consolidation, c_v Co-efficient of secondary compression, c_α	r^2=0.990 r^2=0.990	Limited to 28 Day testing results. No further test work conducted. Interpolation between very limited data (N=4) results in a high correlation co-efficient.

5.6 Conclusions

Significant points of interest which may be obtained from the ANN modelling have been summarised as follows:-

- ANN's provide an effective means of predicting fill strengths within the bounds of the input data currently available. Therefore the performance of neural networks may only be improved through the provision of additional input data.
- The performance of the neural network improved with the delineation of data into three groups, effectively trimming the data to the specific purposes. Outliers from each of the sets were trimmed also, increasing the networks performance. As with the human learning process, an input which is significantly different to the input data most commonly seen may interrupt and hinder the learning process. It may also distort the outputs if the learner attempts to incorporate the data into the analysis.
- Mix fill proportions govern the outputs from the networks developed for Cannington paste fill.
- Data was smoothed heavily for each of the networks created, indicating that the networks will provide good general solutions, but may not predict specifically for inputs.
- The developed ANN's are the most effective predictive tool for backfill strengths currently available, when compared to the myriad of empirical and semi-empirical correlations currently being used such as that by Bloss 1992.
- The development of PASTEC provides a tool for the prediction of Cannington paste fill strengths and characteristics. The correlations provide a high degree of accuracy, typically being able to predict more than 90% (r^2>0.9) of the measured results from the neural networks, developed from the input data. A centralised summary of the information to date on paste fill will provide a higher degree of confidence and reliability for the design of paste backfills and exposures.
- The development of PASTEC will allow others to have quick access to the results of this research, which constitute a significant body of work in the area of paste fills.

- The predictive ANN modelled for the various paste fills and backfills from around the world show moderately poor to very poor predictive abilities for Cannington paste fill.
- ANN developed for specific sites are more able to define and characterise the effect of each input parameter to fill strength or other modelled characteristic.
- Applicability of generic strength prediction tools should be questioned.

5.7 Summary

Neural networks consist of the brains two most significant characteristics; a parallel and distributed architecture, and the ability to learn. The heuristics of the system, or rules for the system are represented as the weights of the connections between the interconnected neurons. Data is passed through the system and correlations formed and retained. ANN's do not use conventional modelling techniques and do not provide the user with an explicit solution process. This has added to the hesitancy of engineers and other fields from embracing the new technology. Case histories were used to train neural networks to predict the strength (UCS), stiffness (E) and failure strains (ε_f) for Cannington paste fills and the UCS strength of other fills from around the world, based on simple input parameters including the cement content, curing time and P80 of the fills. The solids content was also incorporated into the networks trained for Cannington and other paste fills. The networks were shown to be able to predict well. An Excel based program, using neural networks, PASTEC, was introduced to provide a quick, easy and reliable source of the prediction of fill strengths and properties for Cannington paste fills.

Chapter 6

Numerical Modelling of Paste Backfilled Stopes

6.1 General

The static and dynamic performance requirements of backfilled stopes were defined in Section 2.3.1 and 2.3.2. The static requirements may be summarised coarsely into three primary functions. Backfill in stopes is used to:-

i. Provide stability during the mining cycle – static stability requirements.
ii. Drain freely - permeability requirements
iii. Resist dynamic forces, and prevent liquefaction – dynamic stability requirements.

The research contained within this dissertation is concerned with the first item only. Current research projects considering the dynamic stability and permeability topics are currently being undertaken by fellow colleagues at James Cook University (Kirralee Rankine- permeability and Bronwyn Van Gool - dynamic stability).

It was considered pertinent to define the characteristics that contributed significantly to the static stability of backfilled stopes. The factors which were considered to effect the static stability most were:-

- Stress development and state of the backfill mass
    - Mining Sequence (exposure in the mining sequence)
- Stope geometry
- Material characteristics of fill.

Because of the complex nature of the interaction of the various factors to the stability of the fill mass, the vexing problem arose as to how to assess the contribution of the dependent and interdependent variables presented. A number of the analytical and numerical models outlined in Chapter 2 are able to predict the stability of the fill mass for specific cases, yet the interaction of all these factors has not been understood yet. The assessment of the effect on vertical stress development of the various factors was achieved using a 3-D numerical modelling package, FLAC^{3D}.

Numerical models are used to model complex problems that cannot be solved to a sufficient degree of accuracy using other methods. Numerical models use either finite difference or finite element methods to derive a solution to a problem.

The sequential excavation and filling of the nine-stope grid arrangement required the chosen modelling package to: -

- Be stable during the non-linear response of the fill mass during failure,
- Have the ability to re-assign the characteristics of each zone during the solution process (i.e to model the mining of stopes as well as the sequential filling),
- Have a great degree of flexibility to modify the code to be specific to the mining problem and
- Have modest solution times and computer hardware requirements.

A review of commercially available numerical modeling packages was undertaken in the initial stages to identify a suitable modeling package. Table 6.1 lists the common geotechnical modeling packages. The review was limited to the packages specifically angled towards use in the geotechnical field as the constitutive models available were typically more appropriate as were the analysis tools and measured quantities (excess pore pressure for example). The analysis of the rock surrounding the stopes was undertaken using the selected numerical modeling packages by assigning suitable linear elastic properties.

Table 6. 1 Commercially available numerical modelling software for geotechnical applications

Name	Numerical Mtd.	Name	Numerical Mtd.
ABAQUS	FEM	GeoStress	FEM
AFENA	FEM	PLAXIS	FEM
BEMFEM	FEM	RHEO-STAUB	FEM
CRISP-90	FEM	SAFE	FEM
Crisp-Femsys	FEM	Sage CRISP	FEM
FE2DNL	FEM	SIGMA-W	FEM
FEADAM84	FEM	SOILSTRUCT	FEM
FEECON	FEM	TELSTA	FEM
FLAC	FDM	Upres	FEM
FLAC 3D	FDM	VERSAT-S2D	FEM
GeoFEAP	FEM	WANFE	FEM
GEOnac	FEM	ZSOIL	FEM

*FEM→Finite Element Model; FDM→Finite Difference Model

It was considered more prudent to investigate the most appropriate numerical solution method prior to investing in a specific modeling packages to ensure the compatibility of the modeling . A description of the numerical modeling techniques typically used in the analysis of geotechnical problems was taken from Brown (1987).

"Numerical models can be classified into two separate categories; differential and integral models. Differential models consider applications where the complete region of influence is modelled, integral models consider only where the boundary of the region of influence needs to be modelled. Models that use both techniques are called hybrid models."

Differential models can be further divided into two categories; continuum and discontinuum models. *Continuum models* consider applications where the physical system is modelled using a system of discrete blocks in a continuous domain, whereas *discontinuum models* represent a discontinuous domain. *Finite difference continuum models* are based on the calculation of an approximate solution to each region within the model based on the stress-strain state of adjoining regions within a given time step. In *finite element continuum models* the governing equations, which determine the deformation of all nodes within the mesh are combined to form a single set of equations to be solved. The solution to this set provides an approximate solution to the problem. The most common form of discontinuum model is the *distinct element model*. These models are based on Newton's laws of motion to determine the interactions between discrete blocks within the solution domain. Integral models approximate the deformation of the boundary."

The two most common solution processes used in geomechanics are the finite element and finite difference methods. A comparison was made to identify the applicability of each.

Both methods translate a set of differential equations into matrix equations for each element, relating forces at nodes to the corresponding displacements at the nodes. The resulting element matrices for an elastic material, are identical for each method. However the finite difference approached used by packages such as FLAC^{3D}, differs in the following respects: The "mixed discretization" scheme (Marti and Cundall, 1982) is used for accurate modelling of plastic collapse loads and plastic flow. This scheme is believed to be physically more justifiable than the "reduced integration" scheme commonly used with finite elements. The full dynamic equations of motion are used, even with modelling systems that are essentially static. This enables the numerical modelling process to follow physically unstable processes without numerical distress. The finite difference method can also be either implicit or explicit. FLAC^{3D} was the modelling package chosen to model the problem, as it was considered the best available complete modelling package, against the selection criteria. FLAC^{3D} uses an "explicit" solution scheme. This is in contrast to the more usual implicit methods. Explicit schemes can follow arbitrary non-linearity in stress-strain laws in almost the same computer time as linear laws, whereas implicit solutions can take significantly longer to solve non-linear problems. Furthermore, it is not necessary to store any matrices, which means that (a) a large number of elements may be modelled with a modest memory requirement, and (b) a large-strain simulation is hardly more time-consuming than a small-strain run, because there is no stiffness matrix to be updated. These differences are mainly in FLAC^{3D} 's favour, but there are two disadvantages:

a) Linear simulations run slower with FLAC^{3D} than with equivalent finite element programs; FLAC^{3D} is most effective when applied to non-linear or large-strain problems, or to situations in which physical instability may occur.

b) The solution time with FLAC^{3D} is determined by the ratio of the longest natural period to the shortest natural period in the system being modelled.

Certain problems are thus very inefficient to model (eg. problems that contain large disparities in elastic moduli or element sizes).

6.2 Review of FLAC^{3D}

FLAC^{3D} (**F**ast **L**agrangian **A**nalysis of **C**ontinua in **3 D**imensions) is a three-dimensional, explicit finite-difference program for engineering mechanics computation. Materials are represented by polyhedral elements within a three-dimensional grid that is adjusted by the user to fit the shape of the object to be modelled. Each element behaves according to a prescribed linear or non-linear stress-strain law in response to applied forces or boundary restraints. The material can yield and flow, and the grid can deform and move with the material that is represented. The explicit, Lagrangian calculation scheme and the mixed-discretization zoning technique used in FLAC^{3D} ensures that plastic collapse and flow are modelled very accurately. FLAC^{3D} also contains a powerful built-in programming language, FISH, which enables the user to define new variables and functions. FISH offers a unique capability to users who wish to tailor analyses to suit their specific needs. For example, FISH permits: user-prescribed property variations in the grid (e.g. non-linear increase in modulus with depth) plotting and printing of user-defined variables (i.e. custom-designed plots), implementation of special grid generators, and specification of unusual boundary conditions

6.3 Modelling Overview

This section overviews the problem and modelling requirements. The “quarter grid” problem is defined and the complete extraction sequence is explained.

6.3.1 General

The complex mine geometry was represented in an idealized nine stope grid pattern as shown in Figure 6.1 to simplify the analysis. The stopes were approximated as rectangular prisms and were systematically mined over time in the order prescribed by the numbering shown. The stopes have been designated as primary secondary and tertiary stopes. The stope used as a “base case” or “typical stope” measured 25 m x 25 m x 50 m tall. The primary analysis was performed on the base case and the results provide a reference for all future analysis.

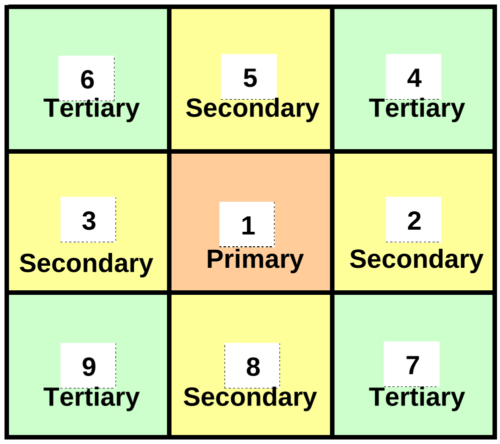

Figure 6. 1 Idealistic nine –stope grid arrangement

During the mining cycle, while the ore is being removed from a stope the confining walls become progressively "exposed". After complete extraction, the stope void is then filled with paste fill. The open stoping mining method was used at Cannington mine in preference to other mining methods because of the geometry of the ore body, desired ore extraction sequence and the surrounding rock strength. Stopes at Cannington vary in size from 20 m to 40 m wide and 25 m to 100 m tall. It should be noted that the size of any given stope is a function of the local ore body geometry, strength of surrounding rock or fill, existing stress conditions and the position during the stope mining sequence.

The problem was to develop a numerical model capable of simulating the complete mining cycle from ore extraction of the primary stope to the filling of the last tertiary stope with paste fill. The features of the model included the ability to change properties of the different zones to simulate the extraction or filling as well as the progressive curing of the fill mass within the stope. The effects of variation of the stope geometry, fill properties and exposure history were all considered important to investigate. The relative contribution of each of these factors was found using an artificial neural network, as was done in Chapter 5 (Section 5.4.3.2).

Figure 6.2 shows the steps for the development and application of the numerical model. Each of the steps outlines the major steps taken to ensure the numerical integrity of the model and rationalisation for each of the pursuing steps.

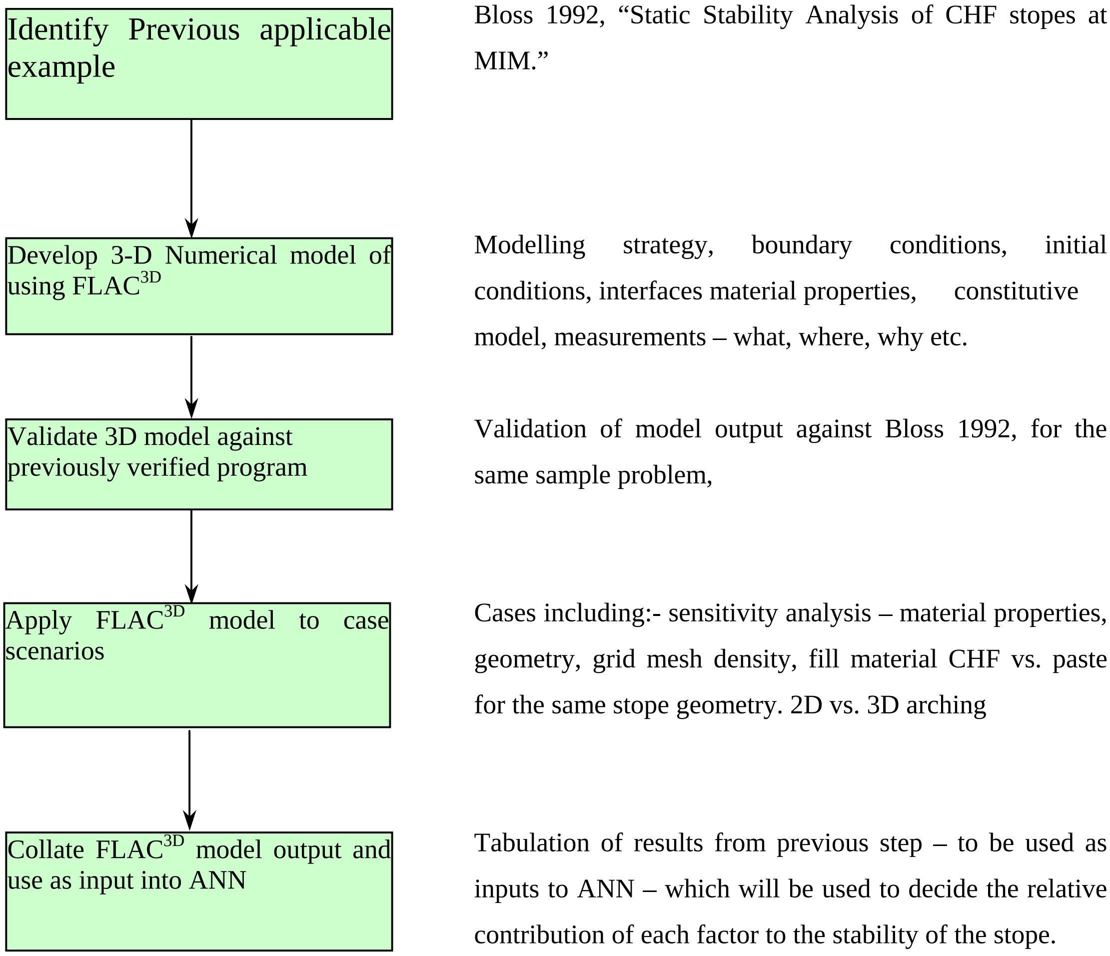

Figure 6. 2 Modelling overview

To verify the model used to assess stability at BHP Cannington mine, it was first necessary to develop a numerical model that had previously been verified by comparison with in-situ data. The modelling of the underground stability of cemented hydraulic fill (CHF) at Mount Isa Mine (Bloss 1992) was considered to be the most appropriate problem to validate the numerical model. The vertical stress profile down the centre and across the primary stope (fully confined) at mid-height, were used to compare and validate the FLAC^{3D} model against the previously calibrated TVIS model.

6.3.2 Quarter Grid Model

The geometry of the nine-stope grid (Figure 6.1) lends itself to the simplification of the problem using axes of symmetry. Figure 6.3 shows the axes of symmetry used to divide the nine-stope grid, to form the "quarter grid." This model was used for the analysis of boundary conditions; mesh fineness (convergence analysis) and a preliminary stress analysis. Note that this simplification can be made only when there is symmetry with respect to both x, y and z axis. The simplification of the problem in this manner significantly reduced the computational time for the solution process.

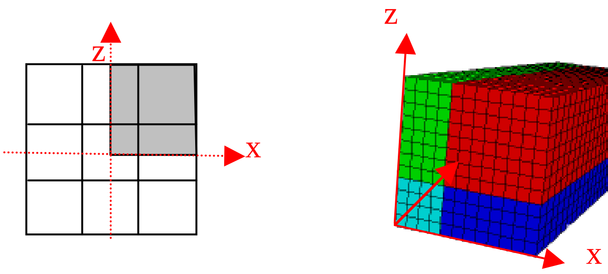

Figure 6. 3 Definition of quarter grid model

6.3.3 Complete Extraction Sequence Model

It is necessary to define a "complete mining sequence". The idealised mining sequence as numbered in Figure 6.1 has been developed over time to attempt to maintain the regional ground condition and to ensure access to the stopes being mined. It is apparent that the actual mining sequence may be very complex and far removed from the idealised sequence. Nonetheless, it is considered the most appropriate model for sequential mining and also provides the most comprehensive analysis of vertical stress profiles throughout the full mining sequence. Referring to Figure 6.2, the ideal sequence of processes is as follows:

1. Blast and excavate primary stope
2. Fill primary stope
3. Expose east wall of primary stope by the excavation of stope number 2
4. Fill stope 2
5. Expose west wall of primary stope fill mass during the excavation of stope number 3

6. Fill stope 3
7. Expose north wall of stope 2 fill mass during the excavation of stope number 4
8. Fill stope 4
9. Expose west wall of stope 4 fill mass and north wall of the primary stope fill mass during the excavation of stope number 5
10. Fill stope 5
11. Expose west wall of stope 5 fill mass and north wall of the stope 3 fill mass during the excavation of stope number 6
12. Fill stope 6
13. Expose south wall of stope 2 fill mass during the excavation of stope number 7
14. Fill stope 7
15. Expose the south wall of the primary stope and west wall of stope number 7 fill mass during the excavation of stope number 8
16. Fill stope 8
17. Expose the south wall of stope 3 fill mass and west wall of stope 8 fill masses during the excavation of stope number 9
18. Fill stope 9

6.4 Development and Verification of a FLAC^{3D} Numerical Model

This section briefly outlines the modelling strategy and model development, and the verification of the model developed.

6.4.1 Development of the FLAC^{3D} Numerical Model

The development of a three-dimensional numerical model was undertaken in accordance with Figure 6.4. The determination of material properties using laboratory tests was now considered to be included in the development of the numerical model.

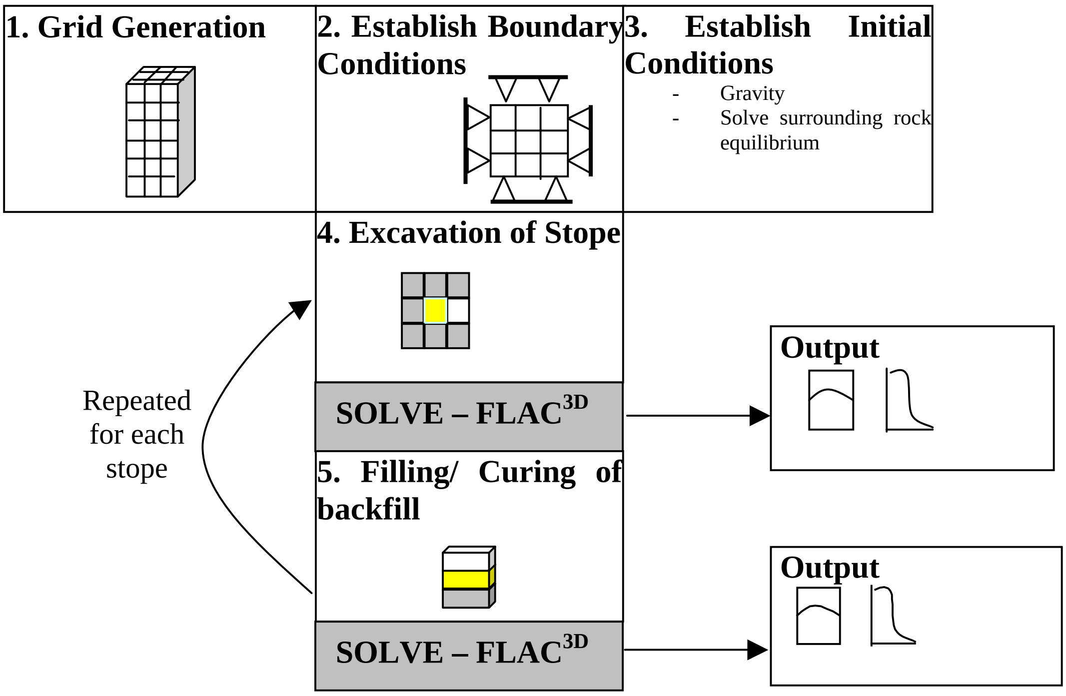

Figure 6. 4 Development of the FLAC3D numerical model for the sequential mining and backfilling of the nine-stope grid arrangement

6.4.1.1 Grid Generation

The three dimensional finite difference grid was developed in FLAC3D using the four phases shown in Figure 6.5.

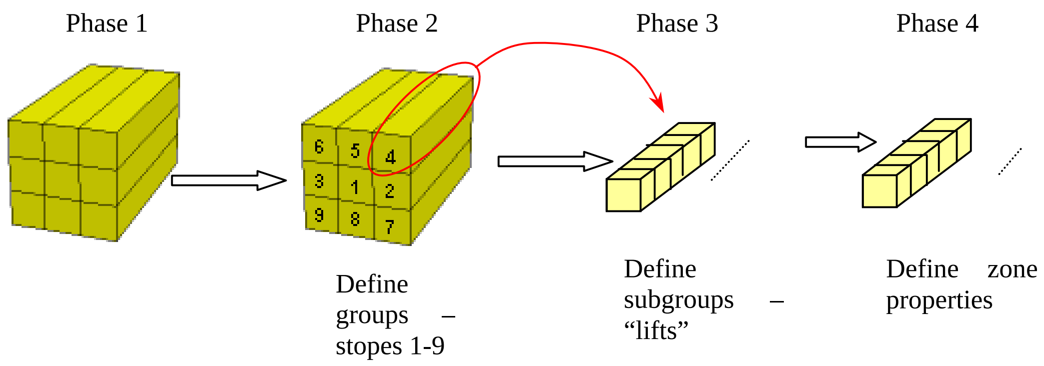

Figure 6. 5 Grid formation.

Phase 1 – Establishment of a three-dimensional grid and zones

A three-dimensional grid to model the 9 stopes was generated by using a "brick" element. A "brick" has a predefined mesh shape, which can be adjusted to match the geometry of the problem. The grid is established by defining the extent to which the grid reaches in each direction (x, y, z). When referring to Figure 6.6 the "brick" defines the plan and depth dimensions of the generic 3 x 3 stope problem. A rate of increase in the dimension in any direction (x, y, z) is then also specified. If the rate of increase was specified as 1.1 in the x and y directions and 1 in the z-direction, the grid in the x-y plan would expand at a rate of 10% for the geometry of each zone from the origin. The geometry of the zones in the z-direction would stay constant. The number of zones in each direction is then defined. The finite difference grid is then automatically generated to the specified dimensions of the brick, with the specified number of zones in each direction.

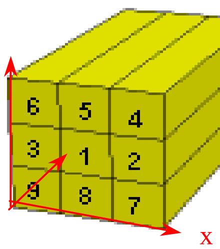

Figure 6. 6 Generic nine-stope problem

Phase 2 – Define groups

Each of the nine stopes were defined as separate groups, which allowed for the manipulation of smaller portions of the full model. This manipulation of properties of for the groups occurred during excavation and the subsequent filling of each of the stopes.

Phase 3 – Define sub-groups

To model the processes of a) filling of the stope and b) curing of the fill mass it was necessary to define sub-groups within the initial nine-groups. Each lift was defined as a sub-group. For the MIM (CHF) verification problem, there were 25 lifts (1 zone high/ lift) and for BHP Cannington, 10 lifts (1 zone high/ lift).

Phase 4 – Define zone properties

To model the sequential excavation and filling of the stopes it was necessary to have the ability to define and change the strength parameters of zones within the groups and subgroups. Initially all zones in the model were assigned the properties of rock, and solved for initial state. When the primary stope was excavated the zones in group 1 (stope 1) were assigned the properties of a void. When filling the stopes, the sub groups are sequentially activated, by assigning material properties of the curing backfill material (whether it be CHF or paste). Each lift was assumed to cure for 7 days prior to the application of the next layer. Thus, as lift 2 was activated, it was assigned properties for 7 day strength of the respective backfills and lift 1 would be assigned 14-day strength properties. This process is cycled through until the stope is full (i.e. the final lift has been assigned 7 day strength and properties). The lift properties are then increased in 7 day increments until the entire stope is fully cured. The MIM verification problem cycled strength properties through to 90 day strength in 7 day increments. BHP Cannington application properties increase to 56 day strength in 7 day increments. This process of filling/curing of the stopes is applied through stopes one to nine in the designated sequence.

6.4.1.2 Boundary Conditions

Boundary conditions for the entire nine stope arrangement were applied to the perimeter walls and the base of the model. The boundary conditions for the quarter grid consisted of fixed conditions on the outer perimeter walls and roller supports on the vertical faces created by the planes of symmetry. Roller supports were placed on these walls, because symmetrical loading restricted displacement along these walls to be in the y-direction only.

A sensitivity analysis was performed to assess the effect of roller and fixed supports around the perimeter walls, during the extraction and filling and curing of stope 1. The four separate cases, used to investigate the effect of boundary conditions were:

- a)- 9 stopes with surrounding rock with roller supports,
- b)- 9 stopes with surrounding rock with fixed supports,
- c)- 9 stopes with roller supports, and
- d)- 9 stopes with fixed supports.

Figure 6.7 show the generic layout of the cases with and without the extended surrounding rock. Rankine, K. (2001) investigated the effect of the boundary conditions when modelling the MIM problem outlined by Bloss (1992).

(a) (b)

Figure 6. 7 Generic layouts of the nine stope (a) with surrounding rocks and (b) without surrounding rocks

The vertical stress profiles for the MIM stope problem down the centre and across the stope at mid-height, for the fully confined by rock case, for the various boundary fixities are shown in Figures 4.8 and 4.9 respectively.

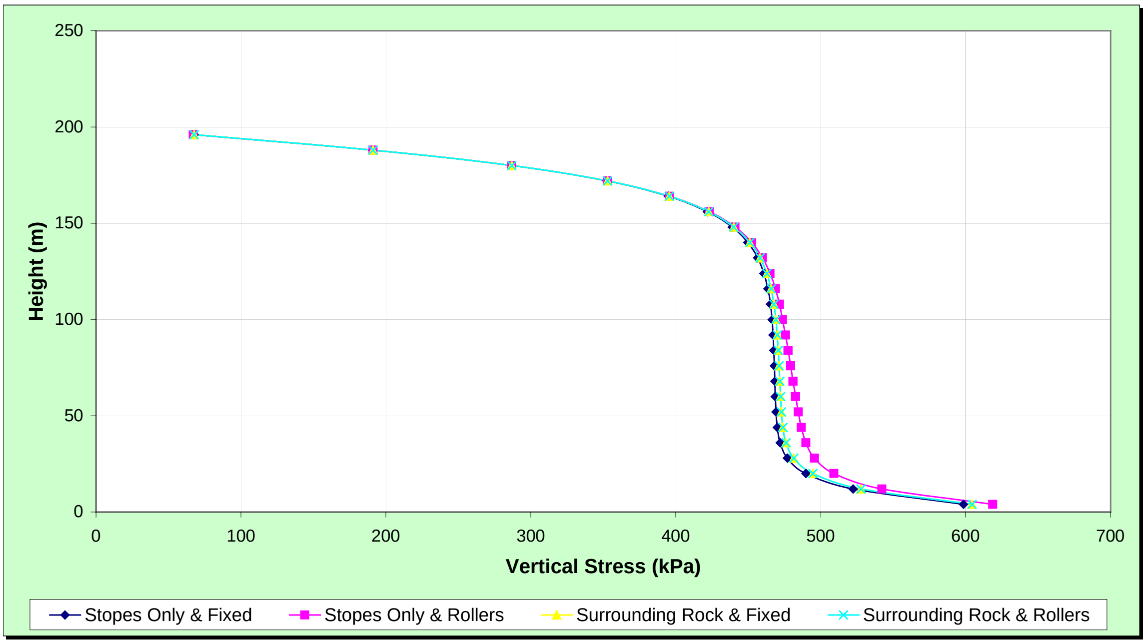

Figure 6. 8 Vertical stress distributions down the centre of stope 1 (MIM) under different boundary fixities

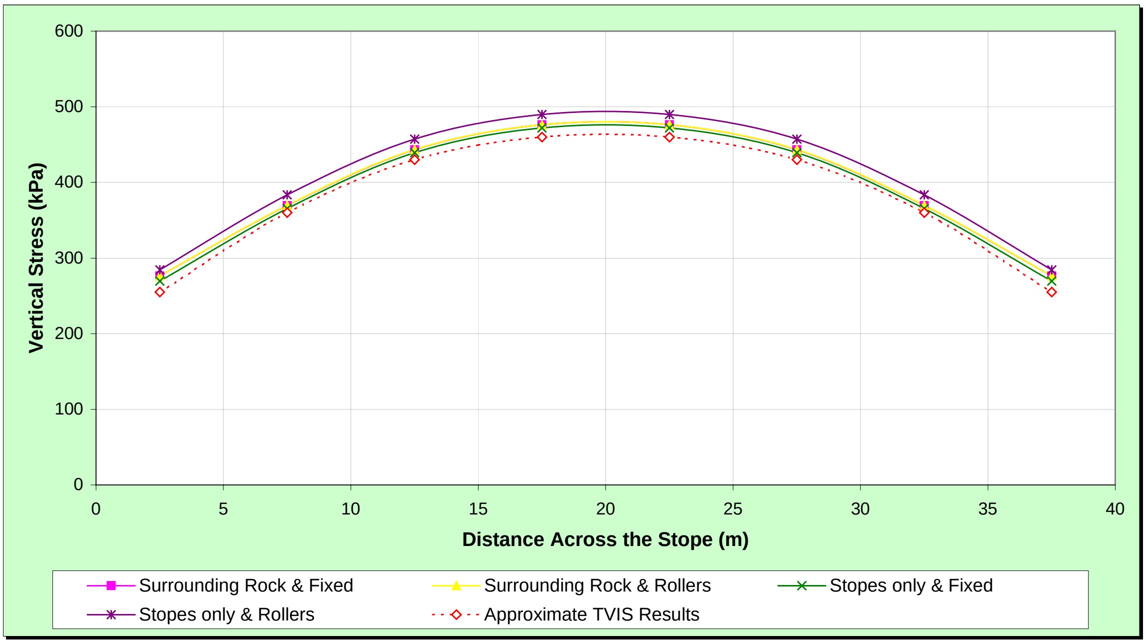

Figure 6. 9 Vertical stress profile across stope 1 (MIM - 40m from the base) under different boundary fixities

The addition of the surrounding rock width to the nine stopes was considered to be representative of an infinite medium and thought to provide the most accurate numerical solution to the stated problem. The solution times for the two boundary condition cases involving surrounding rock were very high, where as the solution times for the nine-stope grid were more reasonable. It was considered reasonable to fix the boundaries along the perimeter and base of the nine-stope grid, in both the x and y directions. The loss of accuracy, by neglecting the additional rock in the model was considered was considered minimal.

It should be noted that when using fixed boundaries, values for stresses and displacements tend to be underestimated, however, the application of a stress boundary results in an overestimation in both stresses and displacements (Itasca, 1999). Thus an approximation to the true value may be obtained by undertaking two separate analyses with the different boundary conditions and averaging the solutions, or using interface elements which are representative of the actual in situ conditions.

6.4.1.3 Initial conditions

Gravity was the only initial condition applied to the full nine stope grid, which initiates the development of internal stresses within the ore body. The stresses developed during the application of gravity to the model, provided the initial conditions for the stage of filling.

6.4.1.4 Interfaces

Interfaces may be defined as a contact surface between two distinct regions where slip occurs. In the nine-stope model interfaces can occur as either rock-fill or fill-fill. The rock mass is assumed to form a continuum (without joints) and thus no rock-rock interfaces are defined. Similarly, the continuous filling process is modelled as discrete layers of varying material properties overlaying one another. Interfaces were not appropriate between fill layers in the model.

Interface elements were not considered within the development of this model for the following reasons:-

- Simplicity. There are significant difficulties associated with the description of interface geometry and interaction using FLAC^{3D} when more than a few simple interfaces are modelled within a single model (Itasca 1997)
- Applicability of interfaces to the nine-stope grid arrangement. Interfaces can be defined on real or arbitrary, non-deformable boundaries in space. Throughout the mining sequence the stopes relax into the open voids and become distorted – which may affects the applicability of interfaces in the model. If zero the boundary conditions limit movement in the plane under consideration, interfaces elements would be applicable. This can occurs in instances such as joints, faults, bedding planes, contact planes (such as that of a foundation and a soil or an ore pass and the contained ore)
- Difficulties associated with the accurate determination of joint shear stiffness, k_s, and joint normal stiffness, k_n. The error involved with

testing here may be above the level of accuracy inherent in the numerical model itself thus compromising the integrity and accuracy of the exiting numerical model

- Boundary failure – Failure will always occur in the weakest material, which will the paste. Interfaces would enable a more accurate assessment of the mode of failure, and observation of planes of sliding or separation, but would not necessarily increase the accuracy of the point of failure. Indeed Bloss (1992) and Aubertin (2003) suggest they have very little effect on the vertical stress development within a vertical stope.

The inclusion of interfaces would be desirable in future models as it does have a potential benefits, including:-

- Accurate prediction of the deformation and failure modes
- The accurate normal and shear stress on the vertical faces of the stopes, and
- The observable reduction of stresses with the progressive curing of paste in stopes and drives.

6.4.1.5 Constitutive Models

FLAC^{3D} has ten built in material models including a “null” model, three elasticity models and six plasticity models. The Mohr-Coulomb failure criteria is the most widely recognised failure criteria applied to granular soils and is defined as:

$$\tau = c + \sigma_n \tan\theta \qquad \text{..... (6.1)}$$

where

τ = shear stress along the failure plane failure,

c = material cohesion,

σ_n = compressive normal stress acting on the failure plane at failure, and

θ = angle of internal friction for the material.

A review of the failure mode was undertaken to determine the applicability of the various failure criteria to BHP Cannington paste fill. Figure 6.10 shows the stress-strain plot for samples for each of the various paste mixes tested at 56 day in unconfined compression. Figure 6.9 gives the results of a staged unconsolidated undrained triaxial test for 6% cement and 78% solids samples in s-t space.

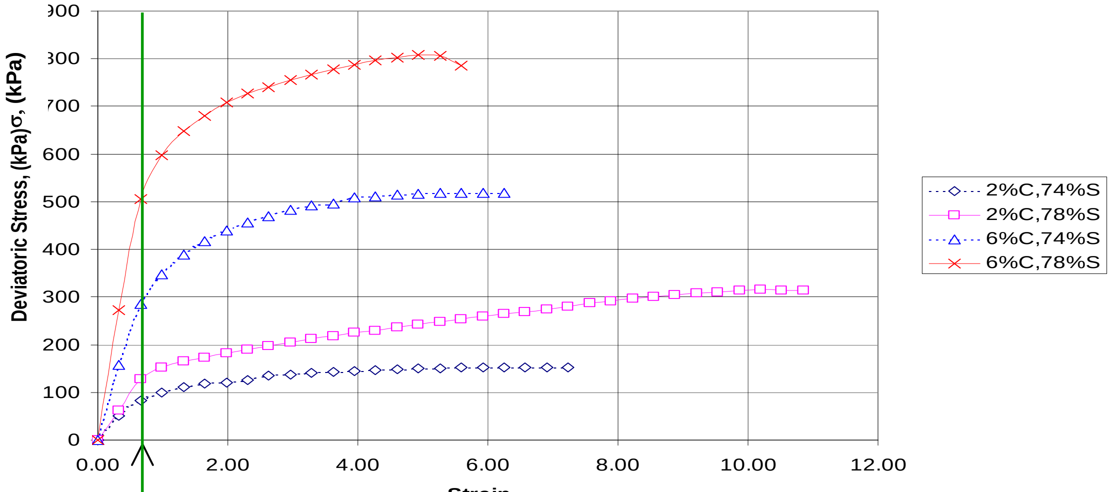

Figure 6. 10 Deviator stress versus strain plots for test specimens (56-day strength)

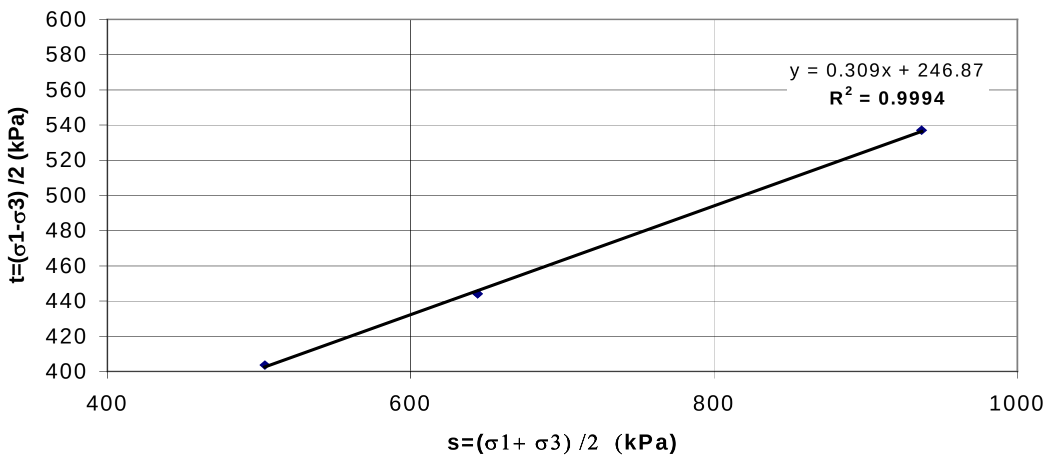

Figure 6. 11 s-t plot for 6% cement, 78% solids paste fill sample (56-day strength)

All paste fill mixes show strain-hardening characteristics and plastic strains beginning occurring at approximately 0.66%. The coefficient of correlation was typically over 0.9 for all tests performed on paste samples. These two figures are considered significant, as they justify the use of the Mohr-Coulomb failure criterion for BHP Cannington paste fill, regardless of mixture proportions.

6.4.1.6 Special Considerations

Confining Stresses

The confinement stress applied from the surrounding rock to the paste is limited to the initial conditions solved within the model, which is effectively a reaction force to the lateral force exerted by the fill prior to curing. When the stope is completely empty, the rock elastically relaxes into the void until static equilibrium is reached. Even very highly cemented backfills are soft in comparison to the surrounding rocks and contribute negligibly to the transfer of vertical stresses.

Stope wall convergence

The effect of stope wall convergence and closure strains on the stability of backfilled stopes was not considered within this analysis for two reasons: -

- The lateral strains are typically associated with high stress conditions that are more commonly found in deep mines (1 km+ underground), with narrow stopes. Such as those of the deep South African Gold Mines. Cannington Mine has a maximum depth of 640m and is not a high stress mine.
- Convergence due to elastic straining of the rocks will occur when the stope is mined out and before any backfill has been placed. Once the backfill is placed, the majority, if not all, of the lateral straining should have occurred.

The effect of high confining stresses or closure strains would be to cause the backfill material to behave in an “at rest” manner, moving the lateral earth pressure co-efficient closer to the “K_p” condition.

Effect of the stope inclination on vertical stress development

Mining stopes are rarely vertical and the effect of the inclination of the foot-wall and hanging-wall may have a significant effect on the development of vertical stresses within the stope. Aubertin (2003) and Knutsson (1981) have investigated the effect of inclination and report that stopes that are inclined at less than 30 to the vertical have vertical stresses with 10% of vertical stopes. For the purposes of this investigation, stopes were assumed to be vertical – which does in fact mimic current practice at the mine. Additional numerical modelling may be carried out as part of future research to quantify the effect of the inclination of stopes on vertical stress distribution.

6.4.1.7 Mechanics of FLAC^{3D}

The geometry of the problem defined by the grid, the constitutive behaviour and associated material properties, dictate the type and response the model will exhibit under loading or deformation, and the in-situ state is defined by the boundary and initial conditions.

With the definition of these conditions, the model in FLAC^{3D} is solved for initial equilibrium state. Alterations are then made (e.g. stopes are excavated) and the resulting response of the model is calculated by once again 'solving' the model. The model may be sequentially solved under different alterations, such as the excavation and filling of separate stopes.

FLAC^{3D} uses a cycling method to solve the algebraic equations of equilibrium. The solution is reached after a series of computational steps. The number of steps required in order to obtain a satisfactory solution (to within a certain tolerance of unbalanced forces) depends on the geometry of the system, the nature of the problem and the number of elements. The geometry or defined material properties of the system may be such that there is no convergence in the iterative cycle. In this case, it is clear that the system is unstable, and the fill mass has failed.

6.4.1.8 Monitoring of Results

Stresses are compared and collated at the centre of each lift in the primary stope. At mid-height, data from all of the grid points in the horizontal plane were collected to generate profiles of vertical stress. It should be noted that FLAC ^{3D} only stores vector quantities (eg. forces, velocities and displacements) at grid point locations, and scalar and tensor quantities (stresses, pressure, material properties) at zone centroid locations. Thus exact numerical solutions at boundaries/ interfaces etc. were restricted to a distance equal to half that of a zone width. It becomes obvious that accuracy of the numerical model will increase with the increased grading of the mesh.

6.4.1.9 Development of user interface for FLAC^{3D} stability program

Initially, the input parameters for the numerical model had to be directly programmed into FLAC^{3D} using the FISH programming language. This limits the application of the program to the solution of a specific problem. It was considered necessary to refine the program further to enable the solution of a specific, user-defined problem. A “user interface” was considered to be the most appropriate way of modifying the existing program, which prompts the user to input various paste and rock parameters prior to solving the problem. The program has been modified to enable the user to define the following parameters:

Stope Geometry:

- Width
- Depth
- Height

Paste:

- Cohesion
- Friction angle
- Tension
- Young’s modulus
- Poisson’s ratio

Rock:

- Bulk modulus
- Shear modulus

This allows superior flexibility for the required analysis, and the modelling of specific case scenarios.

6.4.2 Verification of the FLAC^{3D} Numerical Model

Using the finite element modelling package TVIS, Bloss (1992) modelled the excavation and filling of an underground stope at Mount Isa Mines. The dimensions of the stope were 40 m x 40 m x 200 m tall, and the backfill used was cemented hydraulic fill. Bloss (1992) predicted and recorded the vertical stress along the vertical centre line of the stope and the vertical stress profile across a horizontal centre line 40 m above the base of the stope using the input parameters outlined in Tables 6.2 and 6.3.

Table 6. 2 Summary of model parameters and constitutive model – Rock

Model input parameters*	Orebody/ Rock
Constitutive model:	Isotropic elastic
Bulk modulus, K, (Pa)	3.333×10^9
Shear modulus, G, (Pa)	2.5×10^9
Density, ρ, (kg/m3)	2600

Table 6. 3 Summary of input model parameters and constitutive models – backfill materials

Model input parameters	CHF*	BHP Paste Fill
Constitutive model:	Mohr-Coulomb	Mohr-Coulomb
Young's modulus, E (Pa)	5×10^8	0.1761×10^8
Poisson's ratio, ν	0.2	0.2
Cohesion, c_u, (Pa)	0.3×10^6	0.197×10^6
Friction angle, ϕ, (degrees)	34	10.3
Density, ρ, (kg/m^3)	1800	2100

* From Bloss (1992)

The large disparity in friction angles between the fill is considered to represent the likely friction angle during loading. In the case of the hydraulic fills, the fill mass is considered to be fully drained therefore the appropriate friction angle approximates ϕ'. Whereas paste fill mass, by definition retain water, and the undrained friction angle is more appropriate.

Table 6.4 summarizes information regarding the generation of a finite difference grid for the verification (MIM – CHF) and application problems (BHP-Paste). The numerical model was developed in conjunction with research undertaken by Rankine,

K. (2000). The plots and results shown forthwith to the sensitivity analysis (section 6.6) are all referenced from this research.

Table 6. 4 Finite difference grid information – MIM verification problem and BHP Cannington Application problem

Problem	Brick Size (units = m)	Rate of grid dimension increase	Number of zones	Zone Size (x, y, z)
MIM – CHF Verification Problem	x: 3 x 40 = 120	1	x:24	5m x 8m x 5m
	y: 200	1	y: 25	
	z: 3x40 = 120	1	z: 24	
BHP – Paste Application Problem	x:3x25 = 75	1	x:24	3.125m x 10m x 3.125m
	y: 50	1	y: 5	
	z: 3x25= 75	1	z: 24	

Figure 6.12 was used to investigate the reduction of vertical stress due to arching, whereas the measurements in the horizontal plane provided a profile of the vertical stress distribution in the backfill. Bloss' model was verified through in-situ stress measurements, vertical and horizontal extensometer measurements and mine survey data. It was thus concluded that verification of the FLAC ^{3D} model would be achieved if the predicted outputs matched those predicted by Bloss (1992) using TVIS. A comparison of the predicted vertical stress down the vertical centre line of the stope, and vertical stress profile in the horizontal plane 40 m above the bottom of the stope, for the FLAC^{3D} solution and TVIS (Bloss 1992) results is given in Figures 6.12 and 6.13.

Once the validation of the numerical model had been completed, the model was then applied to underground stope at BHP Cannington mine. The size of the stopes used presently at Cannington is 25 m x 25 m x 50 m tall, and the backfill used is paste fill. The material properties, found using the results from the UU triaxial and UCS tests done in the initial phase of research, were then used as the input parameters for the numerical model. It was then possible to predict the stability of the underground stopes at Cannington using paste fill.

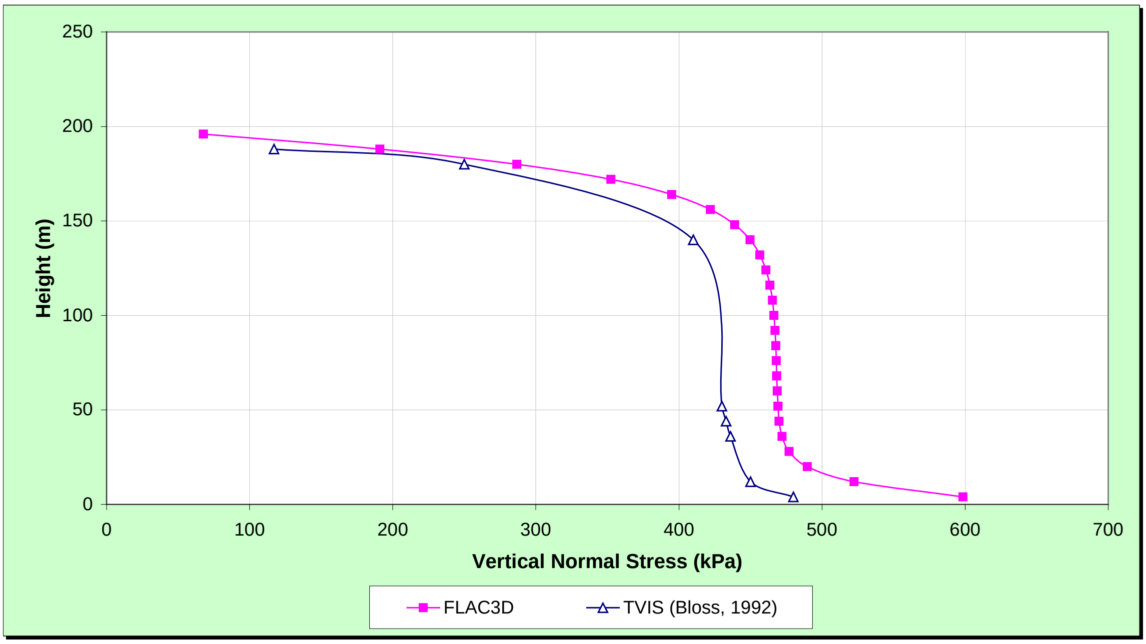

Figure 6. 12 Comparison of predicted vertical stresses for 40m x 40m x 200m stope with CHF backfill for stope 1 fully confined by rock.

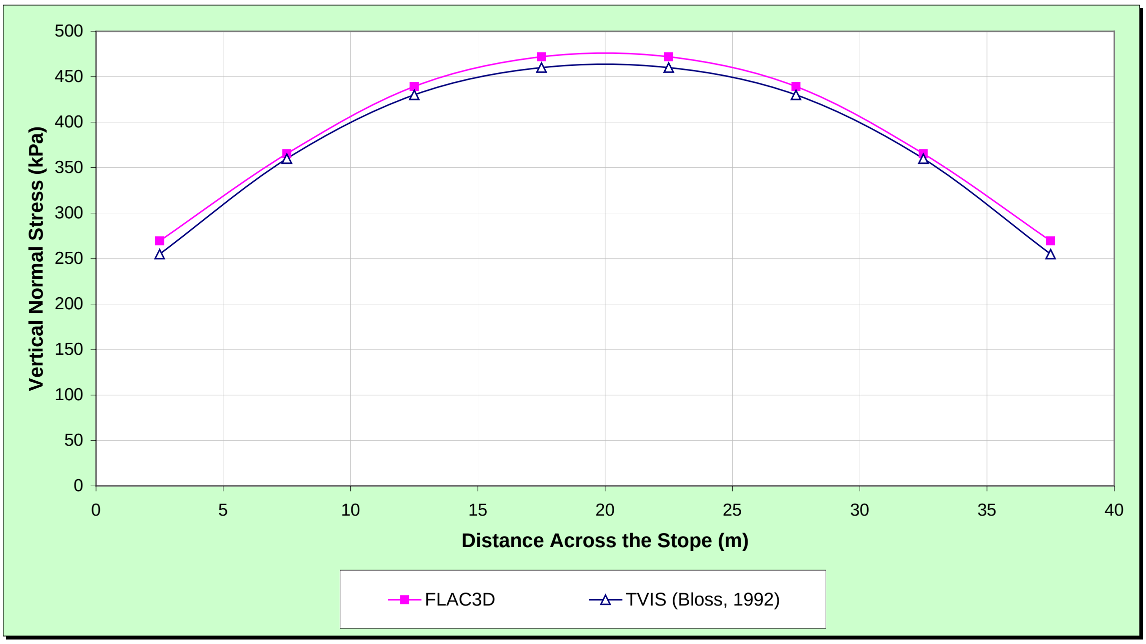

Figure 6. 13 Comparison of predicted vertical stresses profile for the 200 m high Mount Isa Mine stope at a horizontal plane at 40m above the base of the stope.

Figure 6.14 shows the calculated vertical stress values down the centre of the primary stope in a hypothetical nine-stope grid. The straight line represents the vertical stress increase with depth found by multiplying the height by unit weight (γH). These values are compared with the values for when the primary stope is: - (i) fully confined by rock and (ii) fully confined by paste.

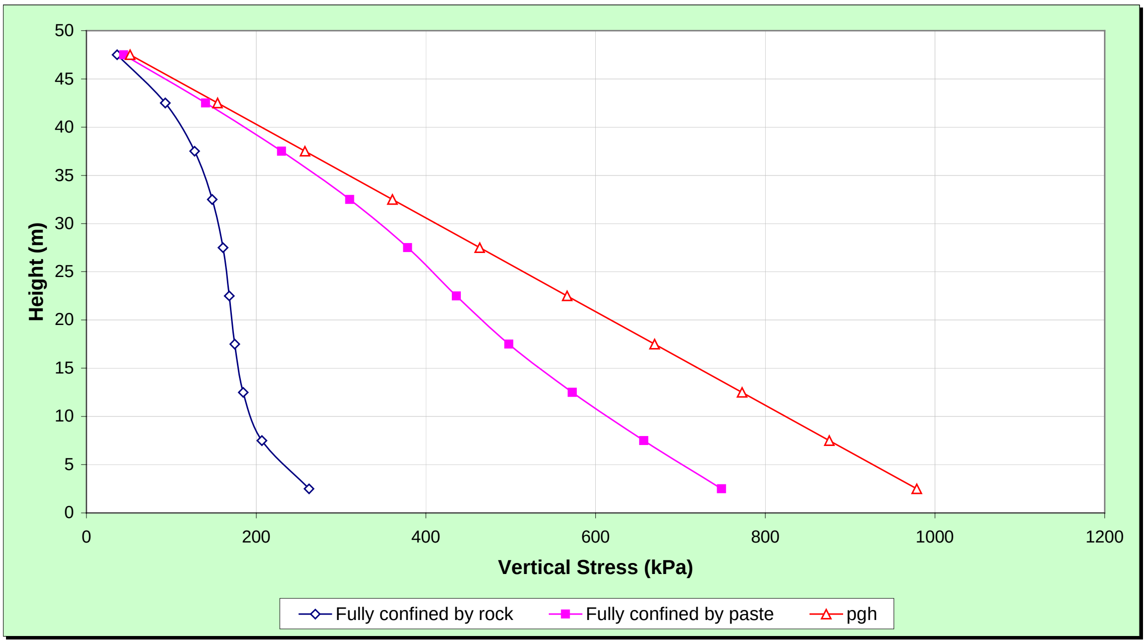

Figure 6. 14 Vertical stress profile down the centre of the primary stope under different initial conditions

Figure 6.14 shows that the confinement by rock reduces the vertical stresses substantially more than the reduction caused by the confinement by paste.

6.5 Application of the Numerical Model to the Full Mining Sequence

This section describes the application of the numerical model to the full mining sequence and the resulting changes in the stress profile in the primary stope. A comparison of two and three dimensional arching is made and the effect of support conditions considered.

6.5.1 Stress Profiling of the Primary Stope

The stress profile of the primary stope was chosen for monitoring as it is sequentially exposed on all four sides and undergoes all of the possible combinations of excavation and refilling of surrounding stopes.

The primary stope, when fully confined by rock, is able to establish a full three-dimensional arch and substantially reduce the vertical stresses to the base level.

Displacements are obviously minimised as well. The vertical stresses and displacements were recorded and used as a reference point or "datum" for the subsequent increase in stresses throughout the extraction sequence.

The surrounding rock mass contributes to arching the subsequent reduction in vertical stress in the backfill by two fundamental actions, namely 1) the ability to transfer vertical loads via shear into the stiffer and stronger ore, and 2) the confinement provided by the rock. The confinement to the backfill provided by the rock is directly related to backfill density, depth and co-efficient of lateral earth pressure. As the ore is always considered to be in a state of elastic equilibrium, the lateral earth pressure may also be calculated using Poisson's ratio and Young's Modulus. Typically, however, K_o is calculated using empirical equations. The most commonly defined relationship is defined by Jaky (1944) as:-

$$K_o = 1 - \sin\phi' \qquad \ldots(6.2)$$

where

K_o = Co-efficient of lateral earth pressure at rest

ϕ' = Effective friction angle of the geo-material

The reduction in vertical stress within the fill mass, associated with arching may be quantified by comparing the stress within a material which did not arch, such as in a fluid ($\sigma_v = \rho g h$) to one that did (such as a stope fully confined by rock). This is shown in Figure 6.15.

The vertical stresses were computed down the centre-line of the primary stope. The effects of arching are reduced at the top and bottom of the stope where the arching effect is developing and breaking down respectively, and remains constant within the middle half of the stope, where all overlying weight is transferred to the surrounding walls. This is in agreement with observations made by Bloss (1992).

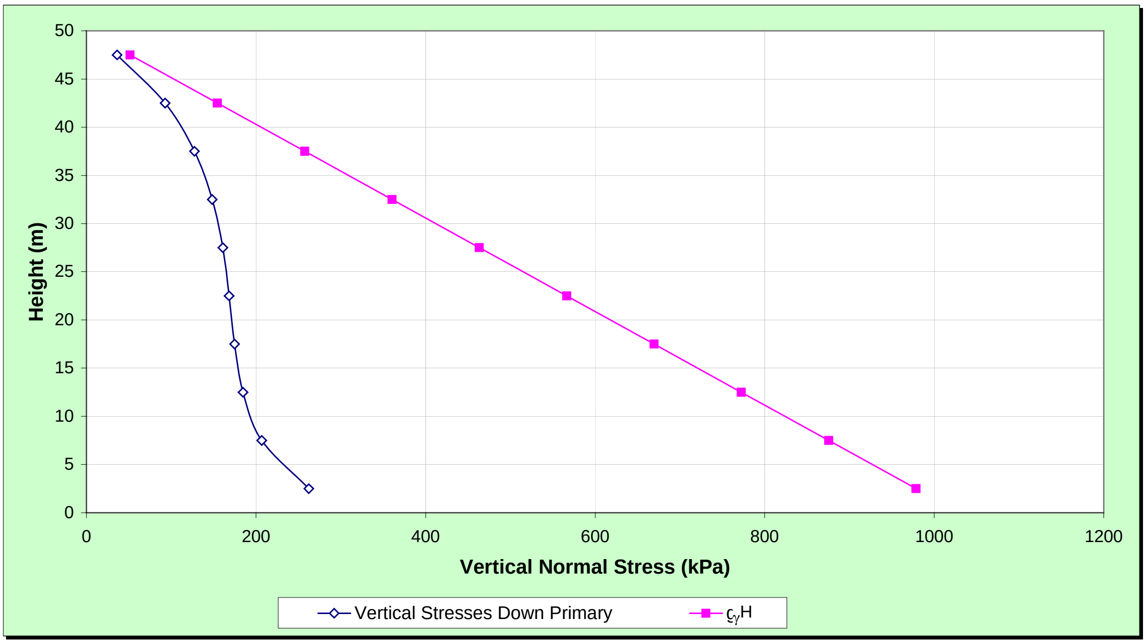

Figure 6. 15 Vertical stress distribution down the centre of stope 1, when fully confined by rock mass (arching vs. non-arching material)

As the surrounding stopes are sequentially mined and back filled with paste, the level of confinement and ability to transfer vertical loads through shear is reduced. Subsequently the level of arching reduces and the vertical stress increases. The geometry of exposures of the fill masses also significantly affects the vertical stress profiles in the fill and is in fact the most influential factor in the development of arching, as will be shown and discussed later. For example, the stress level in a stope with two opposing walls of rock and two of paste will have a significantly reduced vertical stress levels as opposed to an identical stope with two adjacent walls of rock and two adjacent walls of paste. The reason behind this is the ability of the stope to form a more effective soil arch between the two opposing rock faces. The soil arch is strongest when all four walls are rock and the arch is able to form fully in three dimensions.

6.5.1.1 Arching in Two Dimensions

The improved stability by the application of confining stresses through opposing walls, works by increasing the normal stresses acting between the particles and thus the shear strength. The vertical stresses within the stope are also reduced as a result of the transfer of vertical loads, via shear, to the walls. As distance from the confining walls increases to the center, the effect of the confinement decreases, reducing the shear stress which in turn reduces the vertical stresses that can be transferred by arching. Conversely the arching potential is greater closer to the wall as the transfer of shear stress to the walls is more effective. In the corner of a stope, the vertical loads can be transferred to either of the adjacent walls and the arching potential would be at it's highest. Therefore, if vertical stresses across the center profile of a stope were plotted, a distinct arch would exist (as shown in Figure 6.16). The lowest points being at the walls where the transfer of shear, and the effect of confinement is most effective, and the peak in the center, were they are the least effective. Likewise if the arching potential of the paste was plotted across a stope, an arch would also exist. This arch would consist of peaks at the walls, and a minimum in the center. These trends are shown in Figure 6.16.

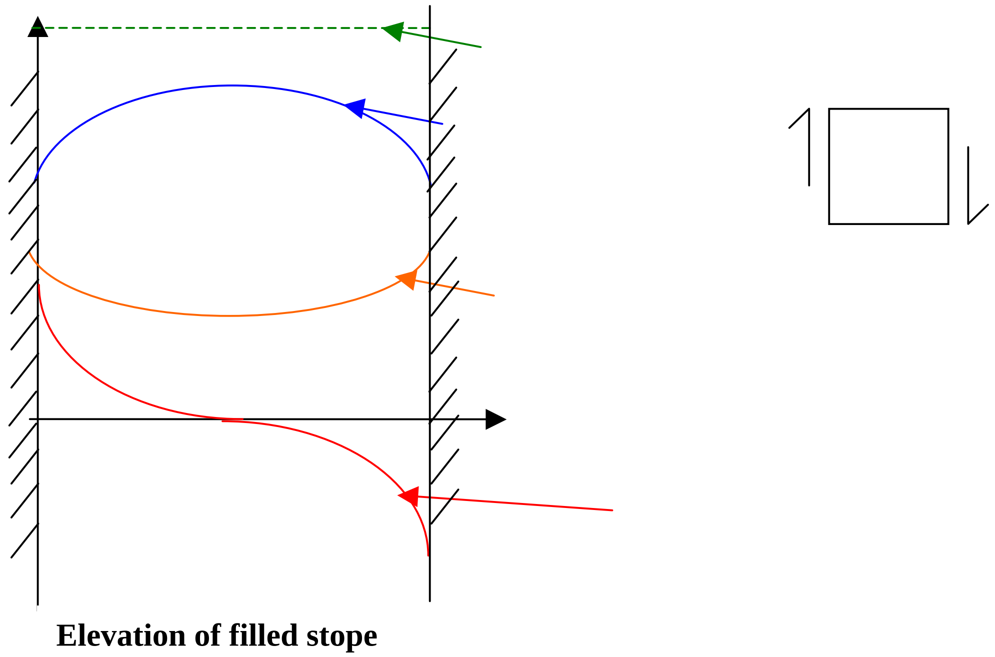

Figure 6. 16 Variation of normal and shear stress within filled stope due to arching effect (Winch, 1999)

A proposed reasoning for the trends in vertical stress distribution down a stope, as shown schematically in Figure 6.17, is presented in Table 6.5.

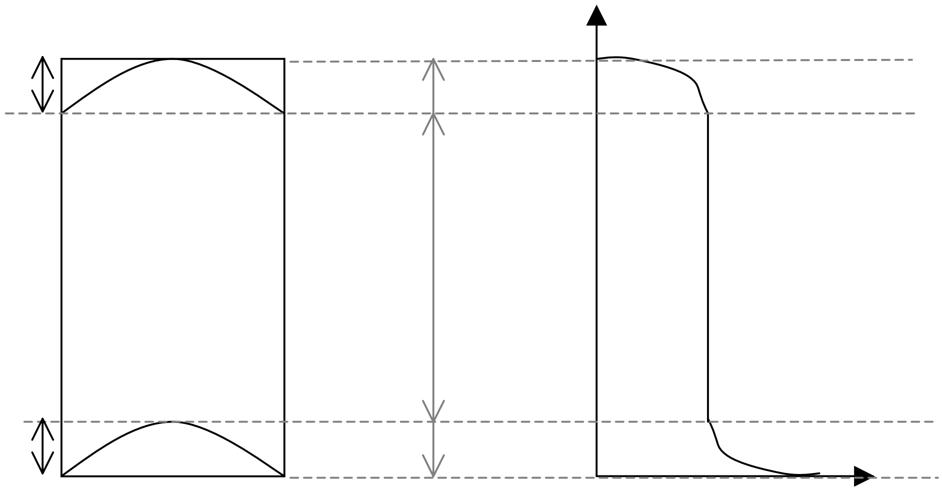

Figure 6. 17 Schematic representation of arching development down a stope

Table 6. 5 Arching regions down a stope

Region	Trend in Vertical Stress	Explanation
I	Increasing (↑) Rate of increase in σ_v slowed by development of soil arch	The confining pressures surrounding the paste are increasing with depth, thus increasing the potential for arching. Thus it can support a progressively higher amount of vertical stress with depth through shear. This reduces the vertical stress development with increasing depth and increases the variation from that of hydrostatic. Once the arch has been fully developed, transfer of shear may be achieved more effectively and additional vertical loads may be transferred directly to the confining walls (Region II)
II	Constant	For this section, the vertical stress remains at a constant value, as the additional weight of the overburden is supported by the transfer of normal loads to surrounding walls through shear.
III	Increasing (↑) Rate of increase in σ_v accelerated by breakdown of soil arch	As the bottom of the arching potential profile (Figure 6.16) reaches the bottom of the stope, the effect of the confining pressure between the paste particles is not significant enough to stop the transfer of shear to the closest path (floor of the stope) resulting in the vertical stress increasing towards the base of the stope. The vertical stress increases towards the base of the stope as the effect of confinement and the transfer of shear to the base of the stope diminish and increase respectively. Effectively the soil arch “breaks down”.

In a two-dimensional arch, there is one set of opposing rock walls, which provide the confinement necessary for the arch to develop. The other two walls will provide a lesser degree of confinement, and will subsequently provide some support to the vertical loads. Winch (1999) suggests the degree of confinement provided by paste is one quarter of that provided by rock. The effectiveness of the arch and transfer of load is substantially reduced with the lower levels of confinement.

To identify the maximum vertical stress in region II, where the arch is fully developed, it was important to avoid regions I and III in the stope where the arch was developing and breaking down respectively. Mid height of the stope was considered to be the most appropriate reference point, and the point most likely to fall outside of regions I and III. This central reference point was used to measure and quantify the arch in all of the modelling exercises.

6.5.1.2 Arching in Three Dimensions

The concept of arching described in section 6.5.1.1 can be applied to a three-dimensional analysis of stability. Figure 6.18 illustrates the form of a fully developed three-dimensional arch. It was obtained from the centre of the primary stope during the initial load case (full confinement), where primary stope is filled with paste, and all surrounding stopes were still ore.

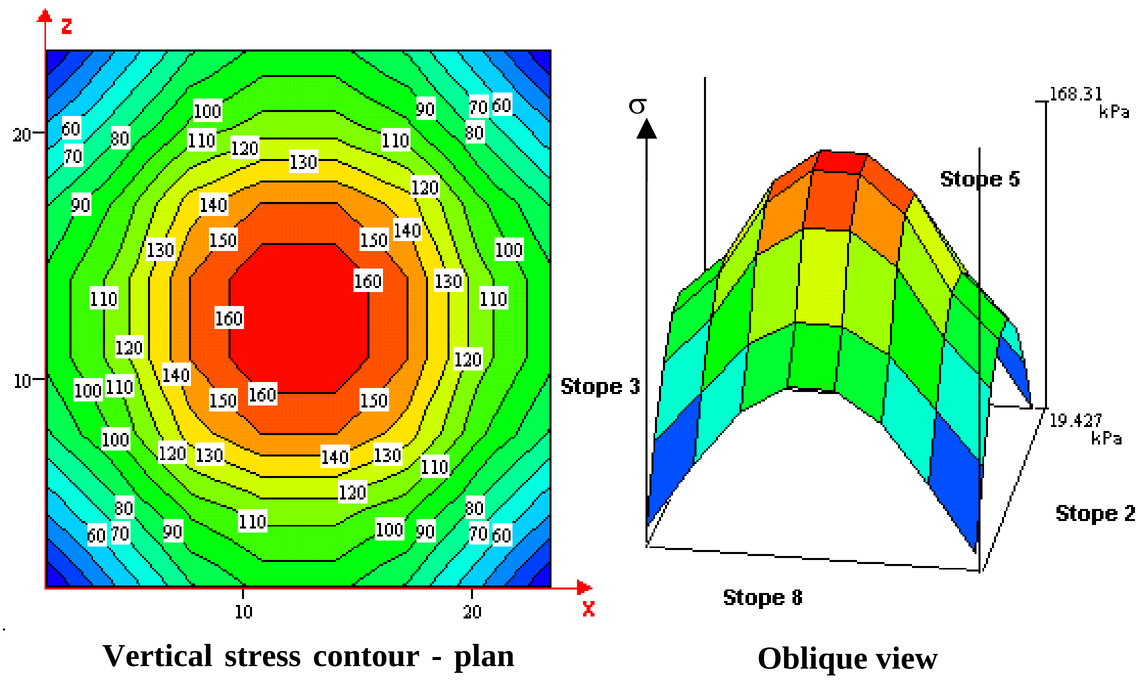

Figure 6. 18 A three-dimensional representation of the arch profile 25 m above the bottom of the primary stope, when fully confined by rock

The highest vertical stresses occur in the centre of the stope, where the transfer of vertical load through the shear is at a minimum. The shear stress and transfer of vertical load approaches a maximum towards the walls of the stope. The corners of the provide strong support to the vertical loads in both the width and depth directions resulting in the largest reduction in vertical stress.

6.5.1.3 Stability Analysis of Complete Extraction Sequence

The support offered to vertical stresses by arching through the extraction sequence may be observed by measuring the vertical stress down the center of the primary stope. Figure 6.19, indicates that arching is present throughout the entire extraction sequence, but is greatly reduced by the sequential excavation and backfilling of stopes. It is interesting to note the increase in vertical stresses associated with the removal of stope two. This is caused by the arching mechanism initially being three-dimensional (3-D rock), and then as stope two is removed the arch is redistributed to a predominantly two-dimensional arch between the two opposing rock faces, (2-D rock). The primary arch will span between the opposing rock-wall faces as they provide the strongest and stiffest support. When stope three is removed, there is again a slight increase in vertical stress resulting from the removal of the support being provided by arching in the width direction. However, the increase remains small, as the stresses are still predominantly being carried or transferred through the existing two-dimensional arch between the opposing rock walls. There is a dramatic increase in vertical stress with the removal of stope five, as it removes the support for the primary two-dimensional arch, spanning in the depth direction (between the rocks walls). Backfilling of stopes two and three does re-instate the support required for the development of an arching mechanism. However, the reduced friction and confinement between the fill-fill as opposed to fill-rock contacts results in the arching mechanism being reduced considerably. When stope eight is removed, a small degree of arching is still present, in the width direction between the opposing paste backfilled stopes (2-D paste arch).

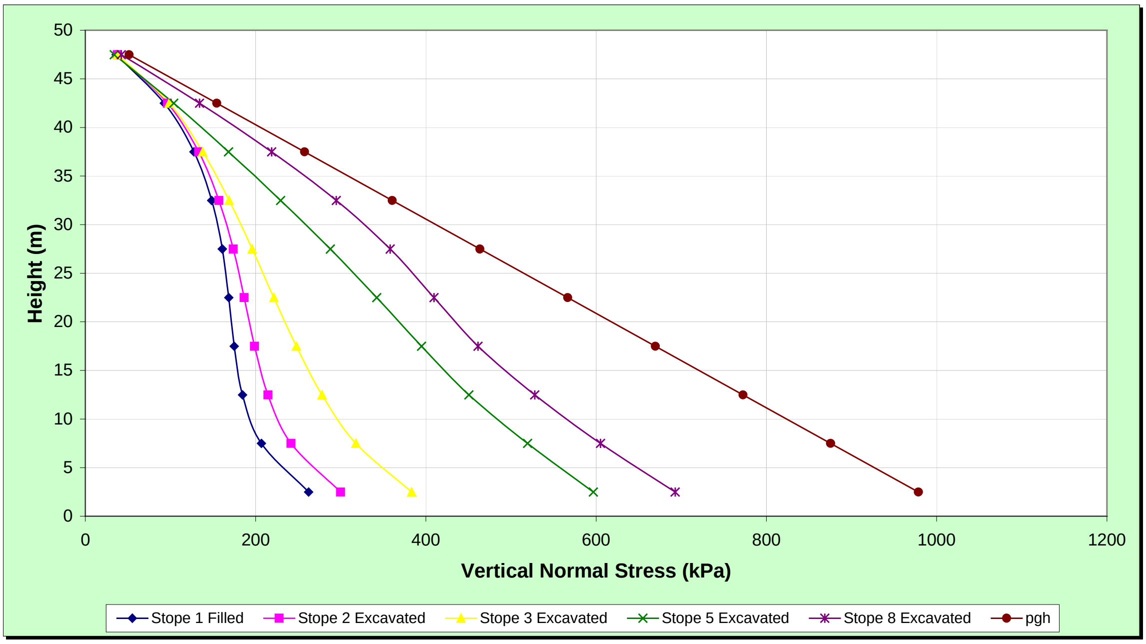

Figure 6. 19 Vertical stresses down the vertical centre of the primary stope, during the extraction sequence

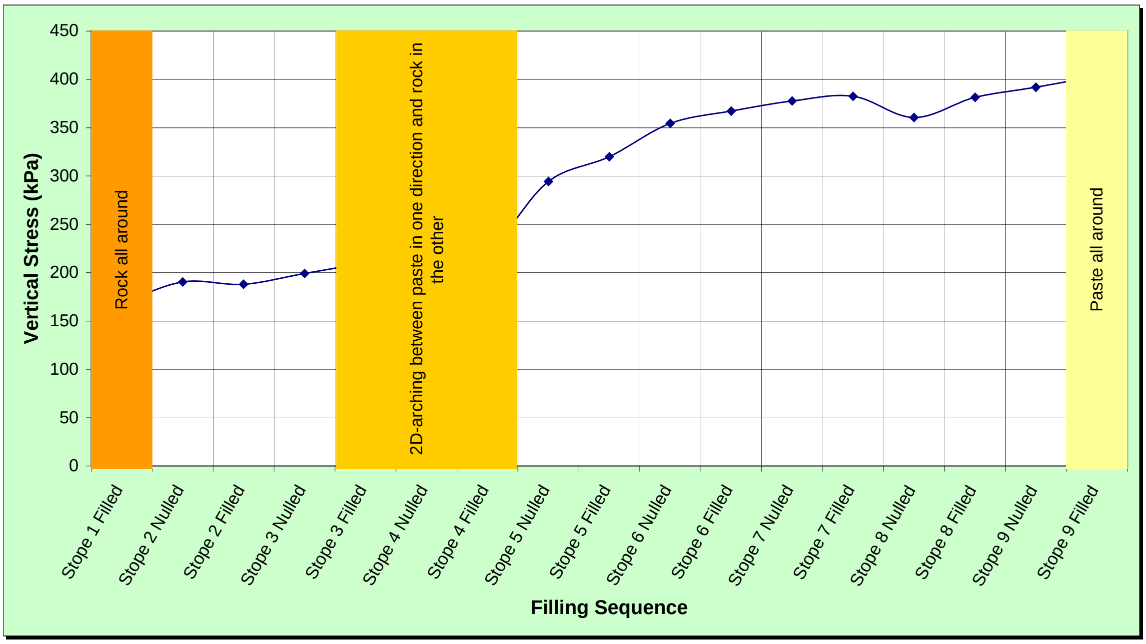

Figure 6. 20 Vertical stress at the centre and mid-height of the primary stope, during the entire extraction sequence

The calculated vertical stresses in the centre of the primary stope and confining media are shown in Figure 6.20. Vertical stresses increase with the removal of the three-dimensional arching effect by exposing stope 2. The next large increase in vertical stress occurs when stope 5 is exposed, causing the strong two-dimensional rock induced arching to be removed. From this point, the stresses increase quite rapidly until stope 8 is exposed, where further analysis showed significant displacement to have occurred, hence the reduction in vertical stress.

The shear stress profile across the mid-height of stope 1 through the ore extraction, filling and curing of stopes one to three is shown in Figure 6.21. The magnitude of the shear stress at the walls before extraction and after the backfilling indicates the degree to which confinement affects the shear stress.

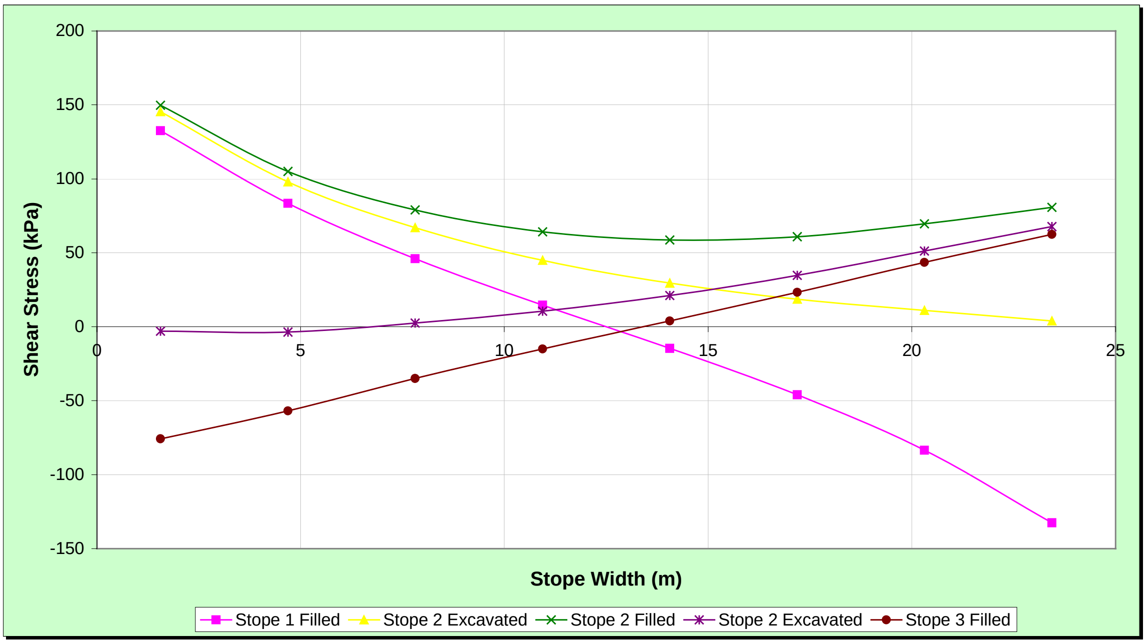

Figure 6. 21 Shear stress profile across the centre of the primary stope through the extraction, filling and curing of stopes 1 to 3.

Shear stress values, computed across the center profile of the primary stope, were used to provide an analysis in two dimensions of the shear variation during the extraction sequence. When referring to Figure 6.16 it can be seen that the shear stress profile and soil arch are closely related. An increase in shear stress, as observed near the walls, relates to a reduction in the vertical stresses (i.e. the vertical loads are being transferred through the soil mass, via increased shear stresses to the supporting walls). Figure 6.21 shows a quantitative evaluation of shear stress behavior during the mining and backfilling of stopes one to three. Table 6.6 gives a description of the behavior of the shear stress during this mining process. It should be noted that the point of zero shear stress differs between the stage where stope 1 is filled, to where stope 3 is filled. This variation results from the variation of boundary conditions from rock to paste.

Table 6. 6 Shear stress variation across the primary stope, during the extraction, filling and curing of stopes 1 to 3.

Extraction Stage	Shear Stress Plot Shape (Primary Stope)	Notes
Stope 1 Filled & Cured	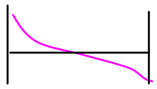	This is the expected shear plot for a fully confined stope. Both the walls from stopes 2 and 3 are applying a vertical shear on the primary stope (One value is negative due to symmetry about the centerline of the stope).
Stope 2 Excavated	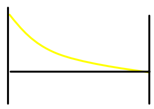	The removal of stope 2 causes a progressive decrease in shear stress across the stope, to zero at the free wall. A vertical shear stress is still applied to the primary stope, by the rock-fill boundary.
Stope 2 Filled & Cured	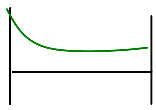	The shear stress along the fill-fill face becomes the negative of the original arrangement. This is a result of stope 2 applying a downward shear on the primary stope. (i.e. Stope 1 supports stope 2)
Stope 3 Excavated	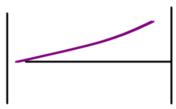	The removal of stope 3 results in a shear force of zero at the exposed wall, and a negative shear on the fill-fill wall, where the primary stope is applying an uplift on stope 2.
Stope 3 Filled & Cured	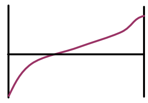	Stopes 2 and 3 are applying a negative shear (downward pull) on the primary stope. The downward pull, is significantly less than the positive shear caused by the rock mass at the first stage of the sequence, due to the reduced material friction and confinement ability.

6.5.1.4 Progressive Variation In Three-Dimensional Arching Throughout The Mining Sequence

Figures 6.22 to 6.26 show the normal vertical stress variation in the three-dimensional arch, as each of the primary supports is removed. Each of the profiles have been generated for the results recorded in a horizontal plane across the primary stope, 25 m above the base. Figure 6.22, shows the distribution of vertical stresses in the primary stope when fully confined by rock. The symmetrical nature of the three-dimensional arch is indicative of the consistency of supports. The profile can be seen to approximate that of a parabolic dome. The highest vertical stress occurring in the centre where the transfer of vertical load through shear is weakest. The lowest is in each of the corners – surrounded by two adjacent rock masses. The maximum value of vertical stress (σ_v=168 kPa) is significantly lower than the weight of the overlying fill (at this height the vertical stress would be approximately 515 kPa). The magnitude of the transfer of vertical stress through shear to the supports can be seen by the reduction of vertical stress to 19 kPa at the wall. The supporting of overlying loads by arching reduces the vertical stress by approximately 67% when fully confined by rock, of which up to 88.5% is transferred through shear to the supporting walls

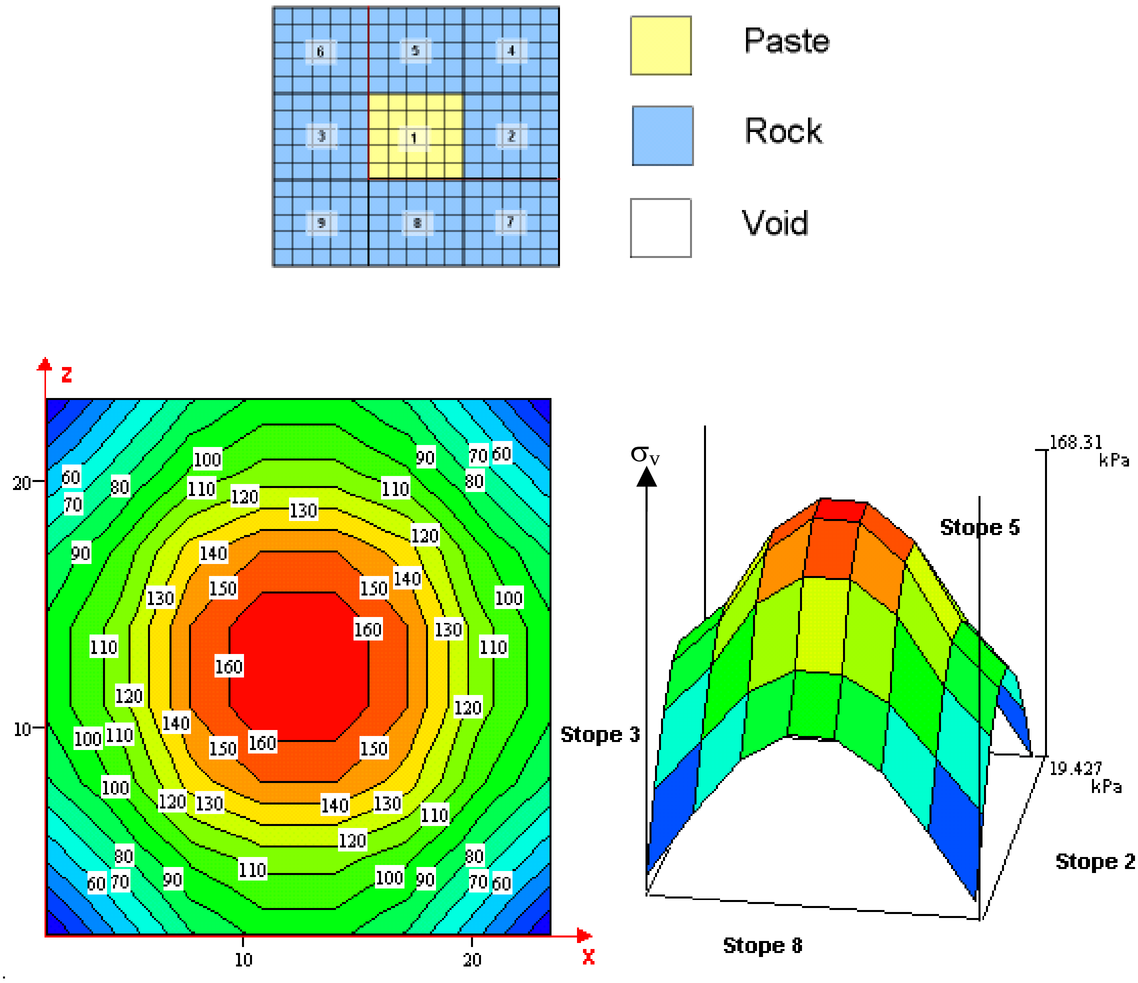

Vertical stress contour - Plan **Oblique View**

Figure 6. 22 Vertical stress plot, primary stope - fully confined by rock

The change in vertical stress distribution that results from the removal of the exposed wall support is shown in Figure 6.23. The contour plot shows an increase in vertical stress at the exposed wall. This results from the inability of the vertical loads to be transferred to any supporting structure. The result of this is the translation of the point of maximum vertical stress toward the exposed wall. The transfer of loads through a primarily two-dimensional arch is shown in the isometric view (Figure 6.23). The difference in "arch" heights at the wall faces, is indicative of increased vertical loads between the faces. The maximum vertical stress measurement of 190 kPa, is only 13% larger than the maximum measured when the paste was fully confined by rock. Similarly, the minimum vertical stress increases by 32%, from 19.4 kPa to 25.8 kPa. The arching mechanism at this stage of the extraction sequence is predominantly two-dimensional, with some partial support given by the third rock-fill contact.

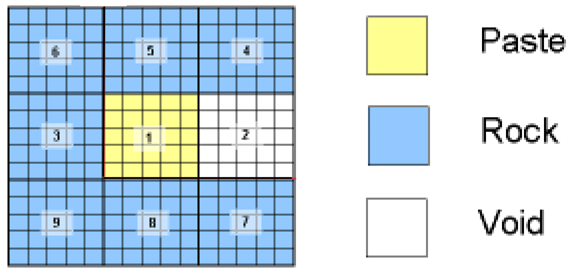

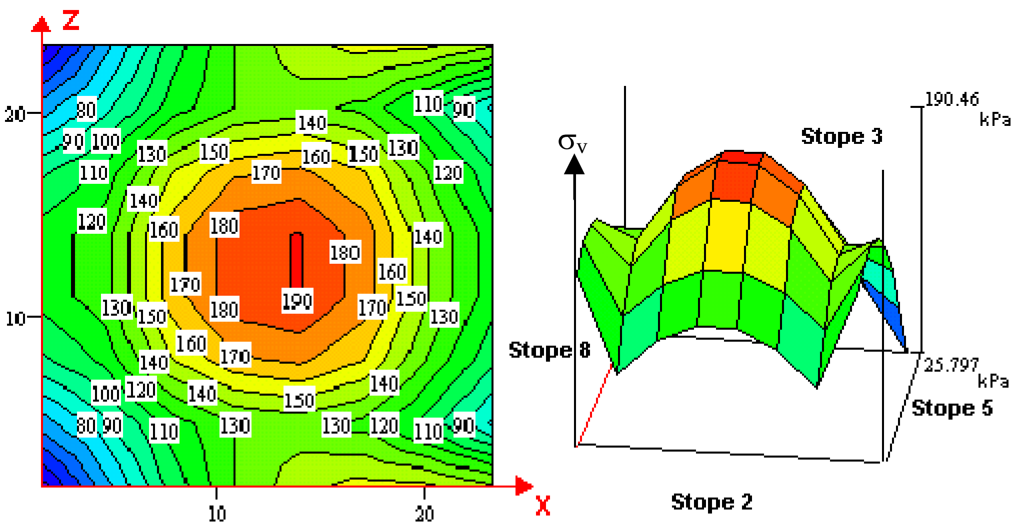

Vertical stress contour - Plan **Oblique View**

Figure 6. 23 Vertical stress plot, primary stope – one wall exposed, three rock walls

The increase in the vertical shear at the paste-rock interfaces as shown in Figure 6.23 by the "wings" on the edges of the arch, are a numerical modelling anomaly. This results because the zones at the periphery of the grid border both the paste and the surrounding rock. The properties for each zone are reported from the centre of the zone and are calculated from the values at each of the nodes. These "shared" zones then average the properties of the surrounding ore and backfill. Typically the in-situ vertical stress in the backfill mass is low, when compared to that of the rocks, simply due to the transfer of the vertical load in the fill to the rock through arching. The addition of accurate interface elements in the model would address the occurrence of the "wings", however, for reasons outlined in Section 6.4.1.3 this was not achievable for inclusion in this dissertation.

The excavation of stope 3, removes the partial support of the vertical stress in the width direction, forcing the supporting arch into two-dimensions (Figure 6.24). The fill-fill wall contact does contribute to arching, but the contribution is significantly less and therefore, for the purpose of comparison, the arching mechanism at this stage of the sequence will be considered to be two-dimensional, in the z-depth direction. The contour plot in Figure 6.24, shows the movement of the maximum vertical stress point, back to approximately the center of the primary stope. The maximum vertical stress is measured as 213.5 kPa, which is 23 % larger than the maximum when three confining walls are composed of rock-fill contact. The area of minimum vertical stress is 67 % larger than the previous excavation stage, and 75 % larger than that with all four walls confined by rock mass. It is shown that there is a 27 % increase in the maximum vertical stress measurement between having two walls confined by rock and having three rock-fill wall contacts.

The critical step in the extraction sequence occurs with the removal of stope five (Figure 6.25). At this stage, it is expected that there be a substantial increase in vertical stress as a result of the loss of two-dimensional arching. The increase between the maximum vertical stresses in the primary stope confined by one wall rock and two walls fill, and two walls rock and one wall fill, is approximately 39 %. From full rock confinement there is a 77 % increase in the maximum vertical stress, and the minimum vertical stress is increased approximately 8 fold.

The significant increase in minimum stress at the walls indicates a much lower transfer of vertical loads through shear, (i.e.- the fill-fill interface has a significant reduction in capacity for shear than the rock-fill interface). This is also shown in the oblique view, by the decrease in vertical stress values near the stope eight interface.

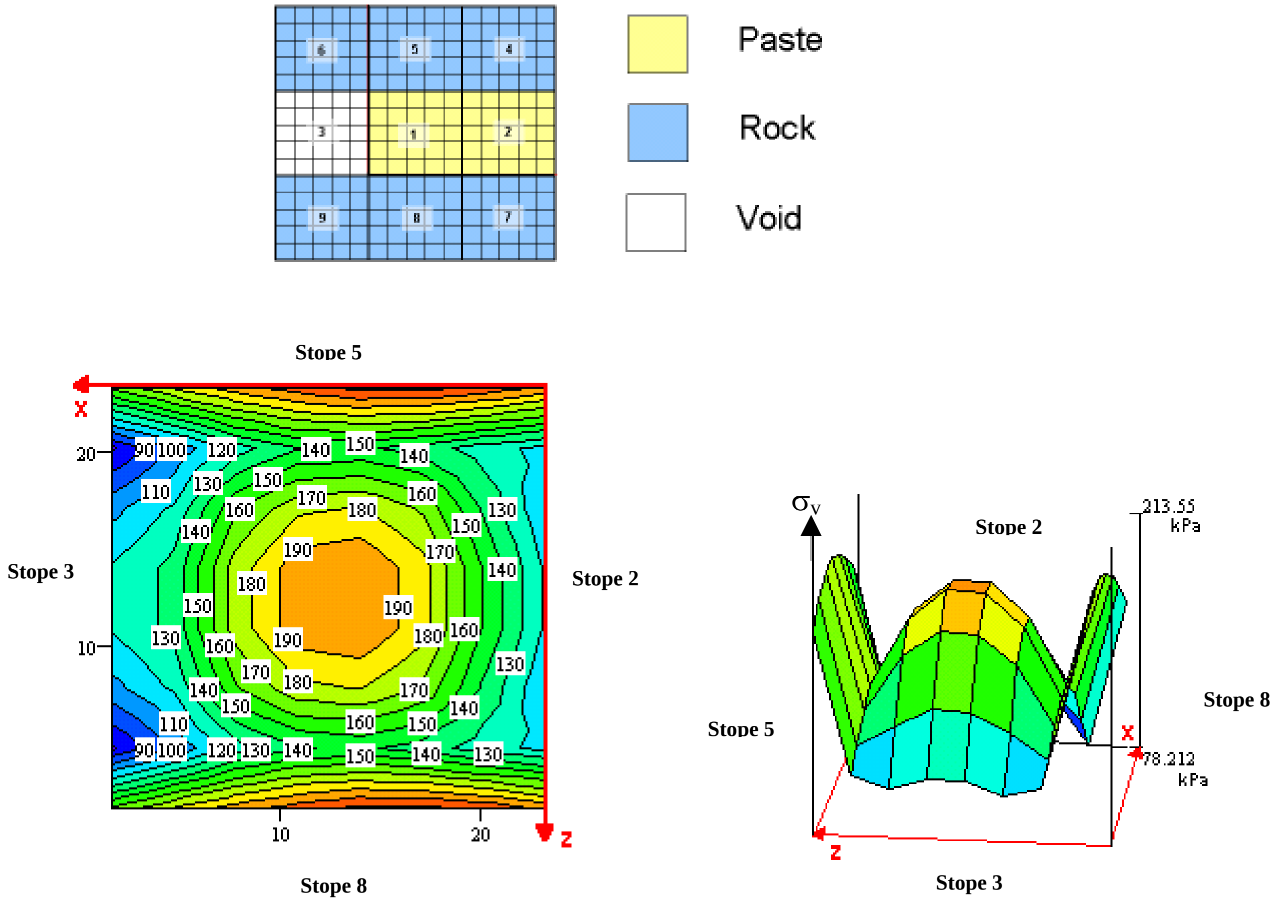

Vertical stress contour - Plan **Oblique View**

Figure 6. 24 Vertical stress plot, primary stope - stope 3 excavated

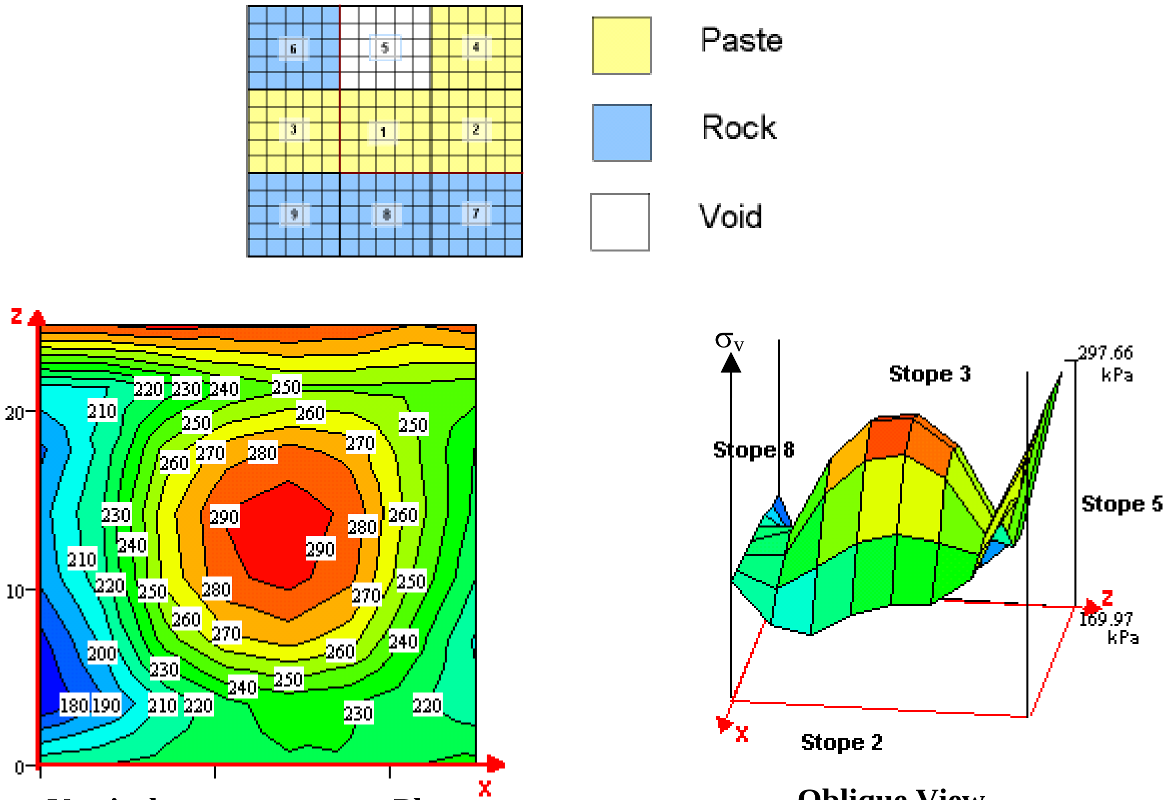

Vertical stress contour - Plan **Oblique View**

Figure 6. 25 Vertical stress plot, primary stope - stope 5 excavated

At the stage of the mining sequence when stope 8 is removed, shown in Figure 6.26, the arching mechanism is minimum, but still active to some degree. Arching is two dimensional, between two fill-fill contacts. The relatively 'flat' arch shown in the oblique view given in Figure 6.26, indicates the minimal confinement and support provided by the fill-fill wall contacts. The increase in peak vertical stress values from having one rock-fill wall contact and two fill-fill contacts to having all three walls confined by paste is about 47 %, with an increase of about 1.6 times from the maximum vertical stress computed with all four walls confined by rock. The minimum stresses are increased by a factor of about 13 from full confinement by rock, to one wall exposed, and three fill-fill walls.

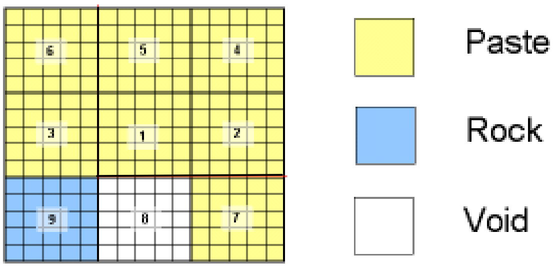

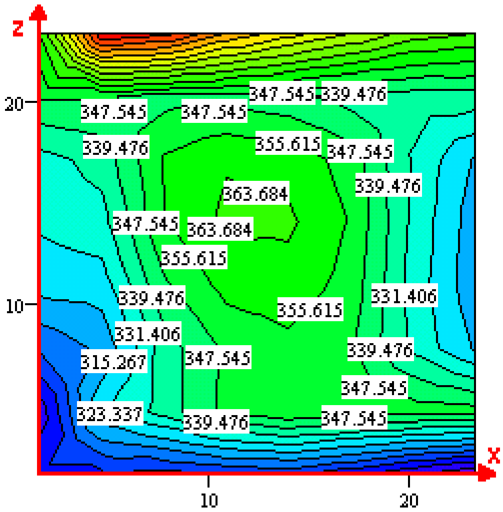

Vertical stress contour - Plan

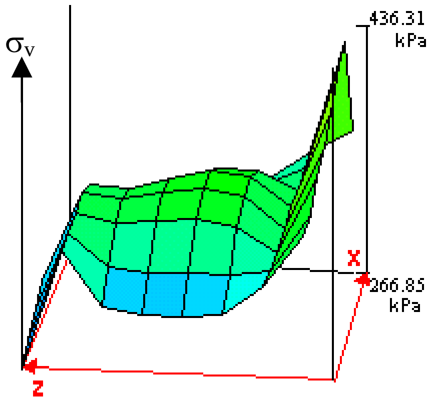

Oblique View

Figure 6. 26 Vertical stress plot, primary stope - Stope 8 excavated

By the comparison of figures 6.22 to 6.26, the following conclusions may be formed:

a)- Arching provides a significant reduction to the vertical stress in a stope

b)- Arching in the fill mass is reduced by decreased levels confinement

c)- Opposing rock-fill interfaces provide significant support to the development of a soil arch in the backfill

d)- Two-dimensional arching between rock-fill interfaces is 85% as effective as three-dimensional arching

e)- Rock-fill interfaces provide substantially greater support than fill-fill interfaces

f)- Fill has significantly less capacity to transfer vertical stress through shear stress, than rock mass

6.5.1.5 Effect of Support Conditions on Arching

Figure 6.27 shows the progressive reduction in arching support with the support conditions given in Figure 6.28 (a) to (e). The various combinations of wall support have been chosen to demonstrate the effect of arching in two and three dimensions. It is noted that not all of the exposure conditions are not practical cases, but were modeled to observe the effects on the central vertical stress profile.

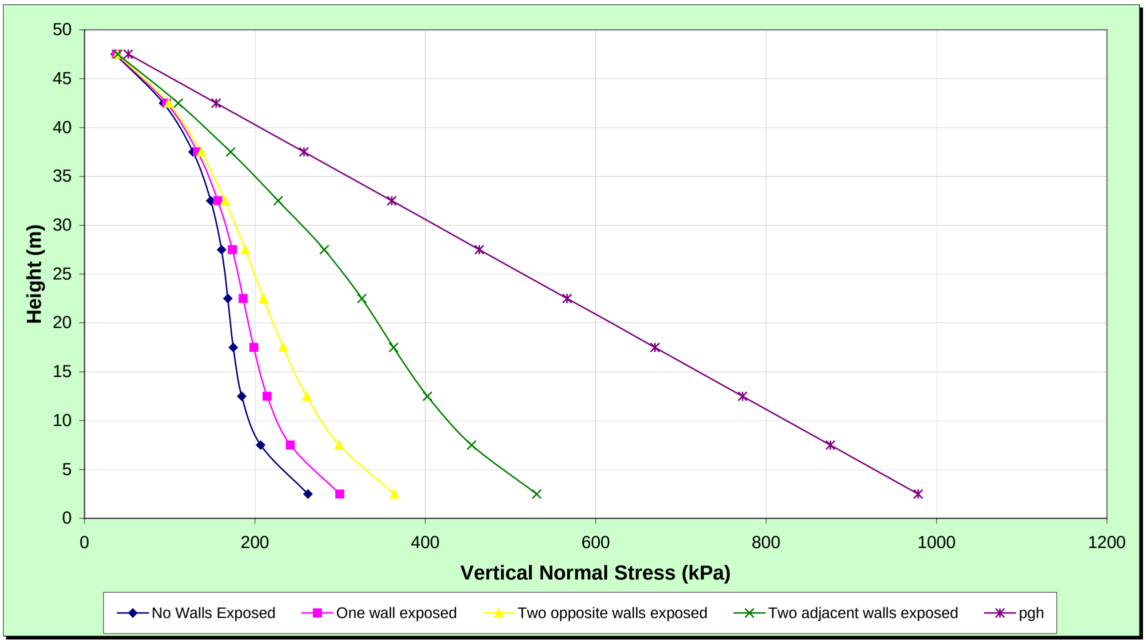

Figure 6. 27 Vertical stresses down the centre of the primary stope, under different wall exposure conditions

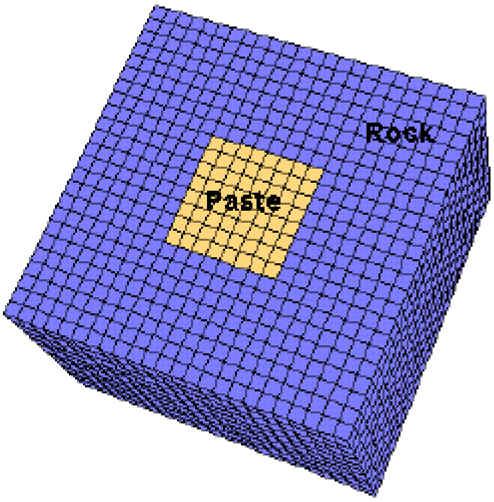

No walls exposed
(a)

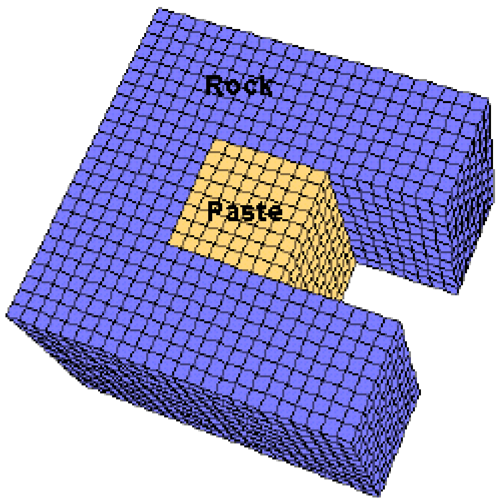

One wall exposed
(b)

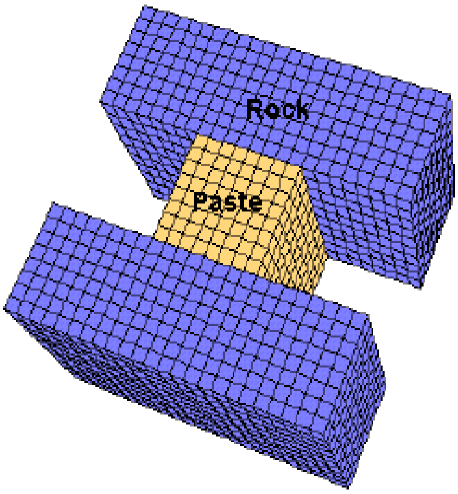

Two opposite walls exposed
(c)

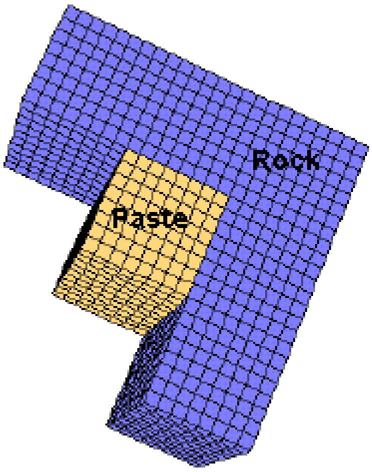

Two adjacent walls exposed
(d)

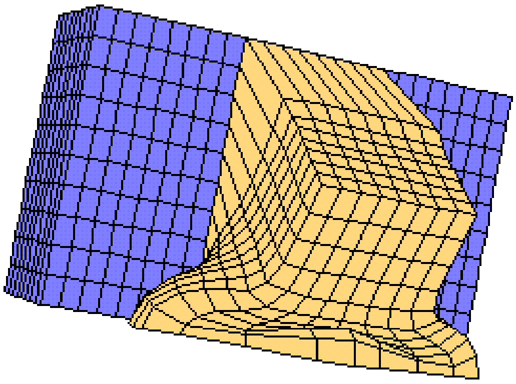

Three Walls Exposed and Failed
(e)

Figure 6. 28 Exposure combinations used to investigate the effect of 2D vs. 3D arching

As expected, the vertical stresses increase as the arching transfers from three to two-dimensional. An increase of approximately 25 %, occurs in the vertical stress at the center of the primary stope, when the arching is transferred from full three-dimensional (Figure 6.28 (a)) to two-dimensional (Figure 6.28 (c)). A diagram of these two arching mechanisms is provided in Figure 6.29. When two adjacent sides of the primary stope are exposed, the arching occurs between the supporting walls. For the confinement arrangement given in Figure 6.28 (d), the vertical stress calculations at the center of the primary are about 93 % greater those that occur when the stope is under full rock confinement.

Figure 6. 29 Graphical two and three-dimensional arch representations

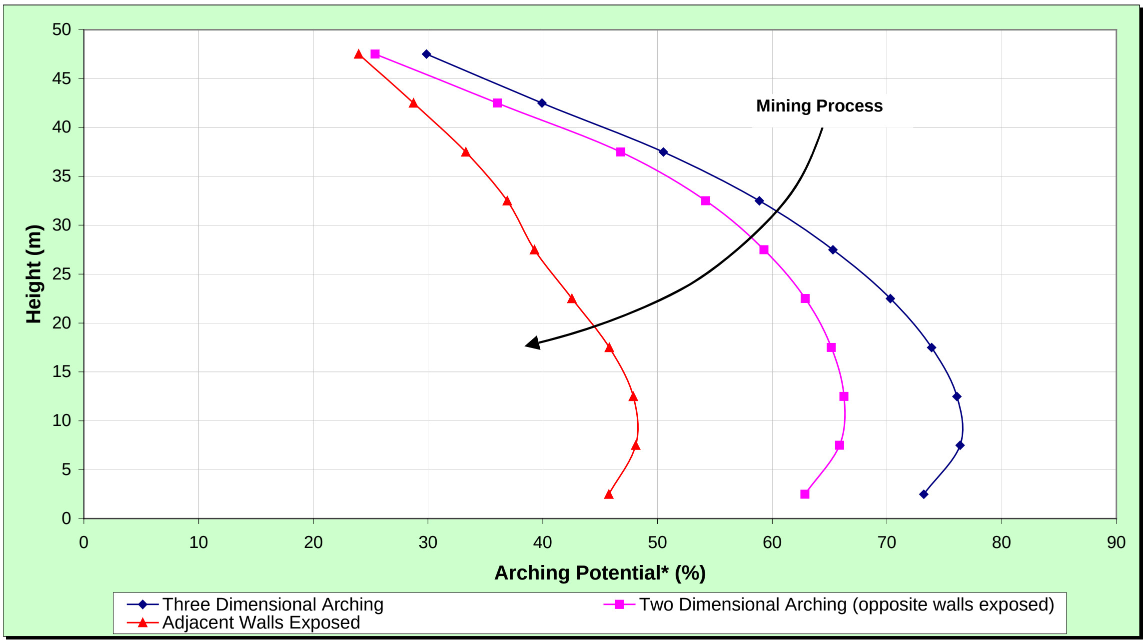

where

$$Arching\ Potential = \left(\frac{\rho hg - \sigma_v}{\rho gh}\right) x100\% \qquad \ldots(6.3)$$

Figure 6. 30 Arching potential for various wall confinement

Figure 6.30 shows that the percentage reduction in vertical stress from ρgh down the center of the primary stope caused by various degrees of wall confinement. The most obvious relation is the dramatic difference between stress reduction resulting from the removal of opposite sides, and the removal of adjacent sides.

The arching mechanism for a fully two-dimensional arch (resulting from the confinement arrangement given in Figure 6.28 (c)), is approximately 85 to 90 % as efficient as the three-dimensional arch. The arching potential of a stope with two adjacent sides exposed is only 60% of that of a stope fully confined by rock. As shown in Figure 6.30, the maximum reduction in vertical stresses, from the calculated ρgh value is approximately 73 % with three dimensional arching, 60 % with two dimensional arching, and 40 % with the arching provided from the rock confinement on two adjacent walls. This equates to a 20 % difference between having opposing walls contributing to arching, or having the arching from adjacent walls.

6.5.2 Comparison of FLAC^{3D} Numerical Model to Winch (1999) Stability Model

Winch (1999), proposed an analytical solution to predict the failure height for a backfill mass given stope geometry and backfill strength data (Refer to Chapter 2). Formulation was based on the theoretical model for the behaviour of backfill in a column proposed by Terzaghi (1943). Winch (1999) extended this concept into the third dimension, and proposed that different fill and rock provide different degrees of confinement and assistance to the development of the soil arch. This was defined in terms of an “active length” which assists in the development of the soil arch profile. Winch (1999) suggested that fill-fill wall contacts possess only one quarter of the active length of a rock-fill contact and an exposed side possesses no active length. The validation of the various wall contacts was the focus of the comparative study.

Winch’s (1999) arching potential factors were investigated numerically, by a three-dimensional analysis of the arching mechanism on a stope fully confined by paste, as compared to that fully confined by rock. The initial boundary conditions used in the analysis were applied and determined in accordance with section 6.4.1.2.

When being fully confined by paste, the stopes surrounding the primary, were filled instantaneously and assigned cured paste properties. This was done to remove any variation in arching potential caused by the sequential manner of mining. Figure 6.31 shows the vertical stress profile at mid-height for each case. The vertical stresses in the stope surrounded by paste are larger than those in the stope surrounded by rock. This is due to the increased level of confinement provided by the rock mass and greater frictional component of the rock-paste interface. The slightly upturned edges shown in Figure 6.31 (a), are a result of the transfer in vertical stress that occurs from the paste to the comparatively stronger rock mass, at the rock-fill interface. As expected these upturned edges are not present on Figure 6.31 (b), where there is no difference in material strength across the interface, and thus no increase in the "averaged" properties for the zones that occur along the perimeter of the stope. The maximum and minimum vertical stresses are denoted on the side of Figures 31 (a) and (b) respectively.

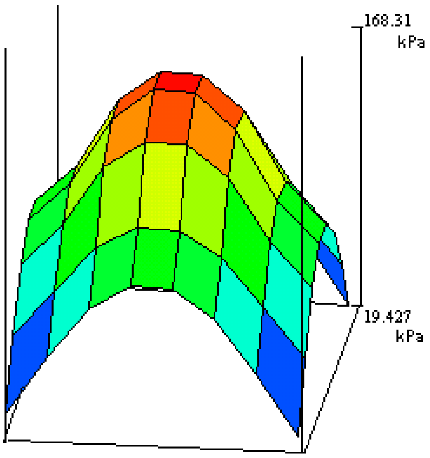

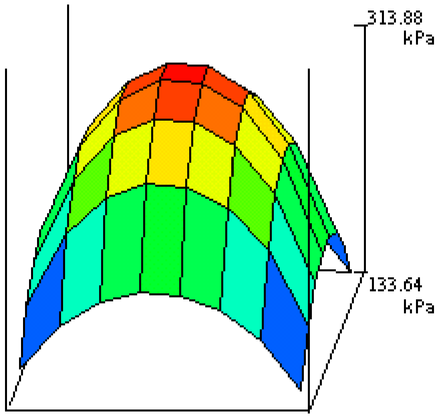

(a) **Surrounding Rock**

(b) **Surrounding Paste**

Figure 6. 31 Vertical stress profile across filled stope one, with different material confinement

Determining the reduction of verticals stress in a stope fully confined by paste and rock respectively assessed the arching potential of fill-fill and rock-fill wall contacts. The arching potential for each type of interface was calculated using equation 6.3 and is displayed in Figure 6.32. The arching potential factor down the centre of the primary stope, for fill-fill contacts ranges between approximately 9 - 52 %, while the rock-fill contacts have an arching potential of between 30 - 75 %. The proportion of arching potential provided by the fill-fill contacts when compared to rock-fill contacts is shown on Figure 6.32 as the red – dashed line. The fill-fill contacts provide between $\frac{1}{3}-\frac{2}{3}$ of the arching potential of rock-fill contacts. These results vary considerably from the currently proposed factors by Winch (1999) who suggests that fill-fill interfaces are able to transfer only one quarter of equivalent rock-fill interfaces. Which indicates that Winch's (1999) model may have been conservative in the prediction of failure.

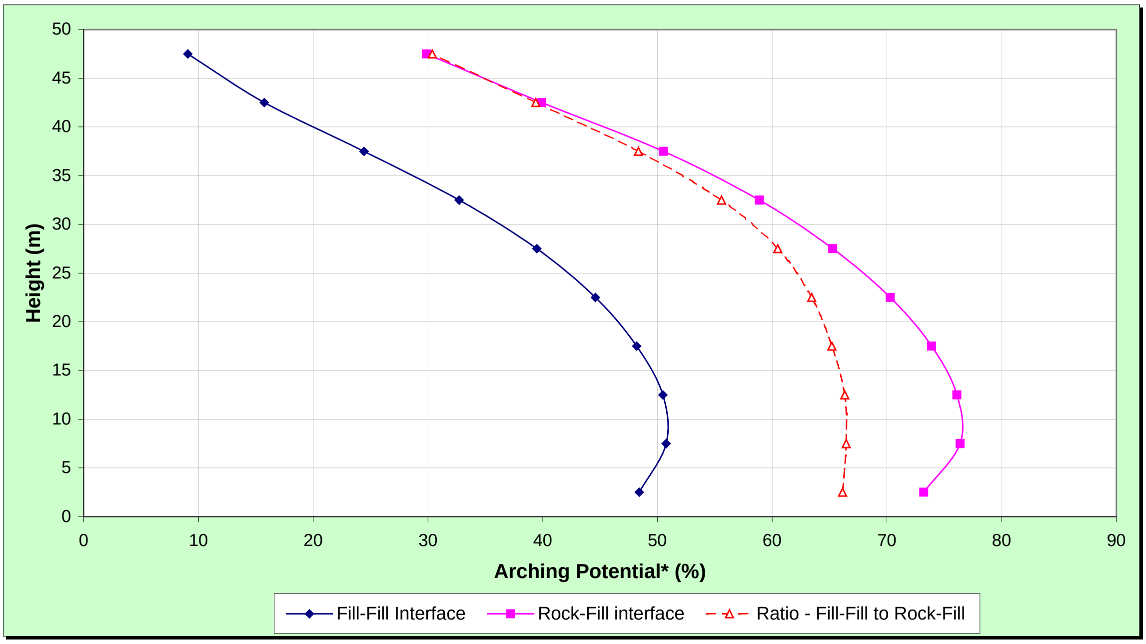

Figure 6. 32 Arching potential factors for interfaces

6.6 Sensitivity Analysis of Input Parameters

A sensitivity analysis of the model was undertaken to provide an understanding into the output from the model with the variation of the input parameters. It can be divided into two separate sections:-

1. Numerical modelling parameters
2. Physical modelling parameters

The numerical modelling parameters investigated include the grid mesh density and the boundary conditions of the model. The Mohr-Coulomb model is considered physically justifiable for Cannington paste from Figures 6.8 and 6.9. Specific constitutive models may be more appropriate for various fills, and may be developed on a case by case basis.

As part of the research, an attempt was made to develop a specific constitutive model for Cannington paste using particle image velocimetry (Singh-Samra 2001), however, the attempt was not adequately successful, with poor quality resolution limiting the accuracy and usability of results. The inclusion of a constitutive model based on the data was inappropriate and the further investigations fell outside the scope of work for this thesis, but do provide an interesting and valuable area of research for future work. Also, for the numerical modelling work done as part of the sensitivity analysis, the model by Rankine, K. (2000), was modified and improved. The result being an increase in the vertical stresses within the stopes. This is reflected in the vertical and horizontal profiles presented forthwith.

Physical modelling parameters included the stope geometry and material characteristics, but didn't include the effect of filling rate, which is significant in the early stages of stress development in a stope. This is typically of more consequence to the strength and suitability of fill barricades. This topic has been addressed and covered in Chapter 7. The faster filling rates result in less arching in a fill mass and higher levels of vertical stress. Taken to the extreme, if a stope was filled instantaneously, then the resulting pressure = ρgh. As curing occurs the arch in the fill mass develops by moving progressively through the profiles (black, blue, green and red). The degrees to which filling and curing take place are directly related to the development of vertical stress.

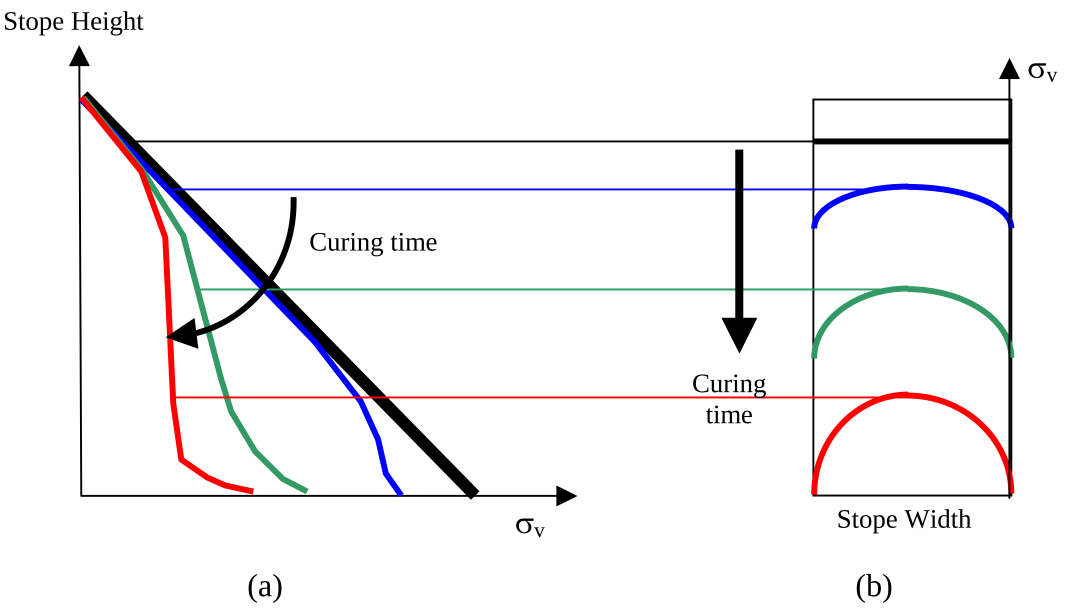

Figure 6. 33 Development of vertical arches through the curing cycle (a) down the centre of the stope and (b) across the width of a stope

The stress profiles shown in Figure 6.33 (b) are taken from the point where the horizontal lines of the same colour touch the central vertical stress profile in (a).

6.6.1 Numerical Modelling Parameters

6.6.1.1 Grid Mesh Density – Horizontal Direction

The choice of mesh coarseness typically involves a compromise between accuracy and limitations of storage capacity and execution times. Mesh grading in the horizontal directions is crucial as the number of elements in the model is equal to the square of the number of horizontal subdivisions. Thus it is necessary to assess the loss of accuracy associated with the increase in mesh coarseness. As a reference, the arch profile for the fully confined case at mid-height was used to compare the output of the numerical models with the variation of each parameter. A convergence limit was then also obtained by observing the trend in results. Figures 6.34 and 6.35 show these two plots for the variation in grid mesh density in the horizontal plane. The number of zones in the x-z direction of the plan view was set to 6, 8, 10 and 12.

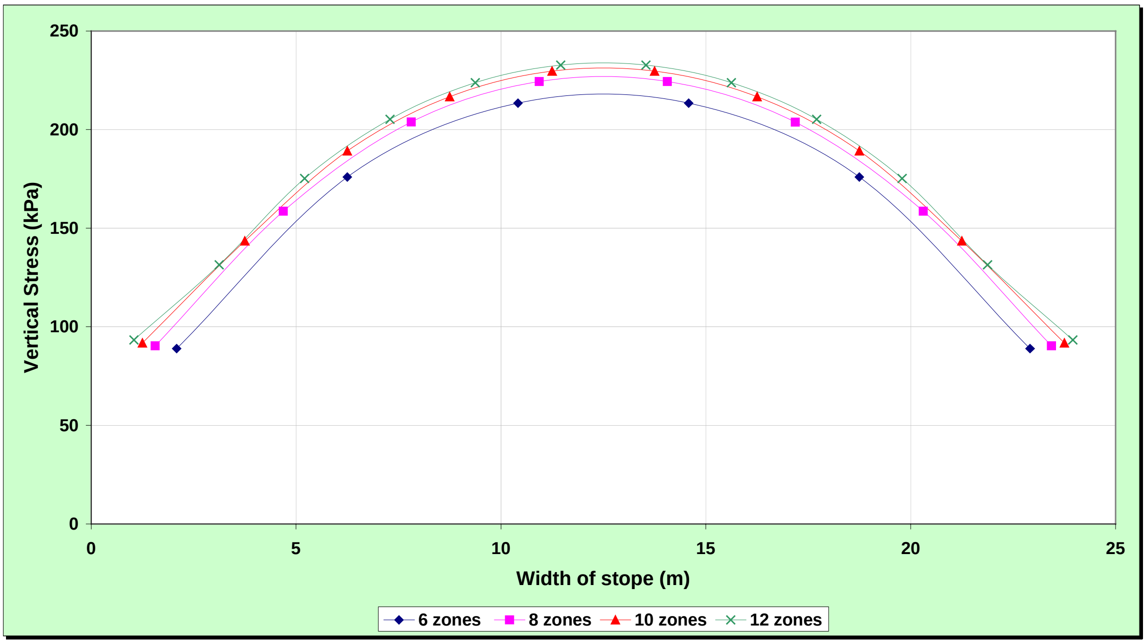

Figure 6. 34 Vertical stress profile across the centre of the stope (25 m from the base) fully confined case

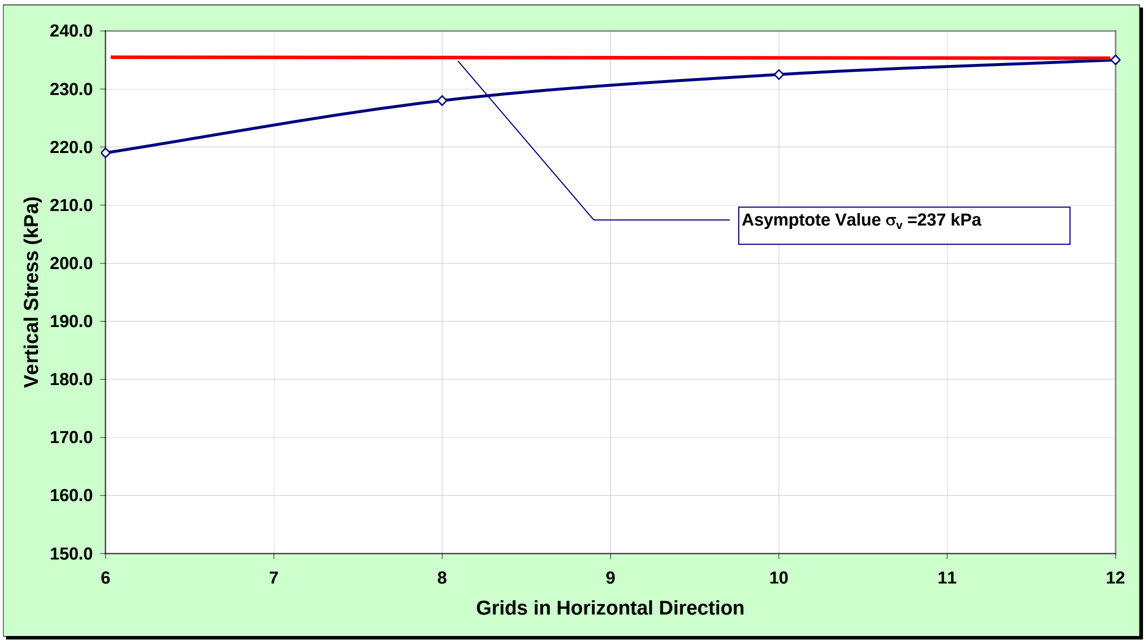

Figure 6. 35 Asymptote value for the vertical stress profile across the mid height of the stope, fully confined .

Little variation is observed in the stress profiles for the varying mesh grading. Figure 6.35 shows the convergence of the numerical solution with an increasingly fine mesh grading. The trend in figure 6.35 was extrapolated to an asymptotic values for the maximum vertical stress of 237 kPa. The relative error of each solution, when compared to σ_{vmax}=237 kPa was found, and is shown in Table 6.7. As the computational time is directly proportional to the number of zones to be solved the number of zones in the horizontal was included for comparison. By using an 8x8 grid in the horizontal plane, the computational time is more than halved (reduced by 56%) with an additional loss in accuracy of only 3.3% when compared to the 12x12 case. The loss of accuracy by using the 8x8 case was considered insignificant and an acceptable level for the reduction in solution time. It was on this basis that a 8x8 grid was used in the horizontal directions for the developed numerical model.

Table 6. 7 Error analysis data for horizontal grid mesh density sensitivity analysis

# zones across stope	# zones in horizontal plane	σ_{vmax} (kPa)	Relative Error (%)	Solution Time (hrs)
6	36	219.0	8.6	1.9
8	64	228.0	4.3	7.4
10	100	232.5	2.1	16.7
12	144	235.0	1.0	24.0

In this initial case the effect of the vertical stress profile down the centre of the stope was also investigated to investigate any variation throughout the profile (refer figure 6.36)

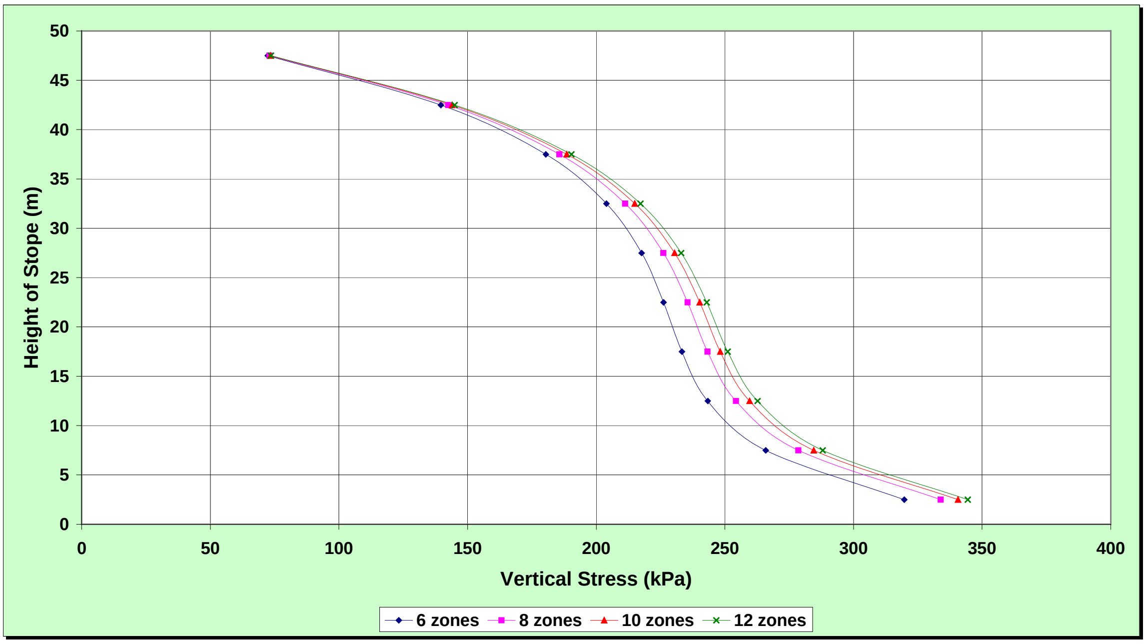

Figure 6. 36 Vertical stress profile down the centre of the stope, fully confined case

The relative error for the various horizontal grid mesh densities, shown in Table 6.7, remains reasonably constant with the increase in depth down the stope. The comparison of the vertical stress profiles across the stope at mid-height was therefore considered a justifiable basis for comparison for the sensitivity analysis.

6.6.1.2 Grid Mesh Density – Vertical Direction

The vertical grid mesh density was set to 5, 10 and 20 zones to identify the effect on the vertical stress profile at the mid-height of the stope. Figure 3.37 shows these profiles and Figure 3.38 the convergence plot.

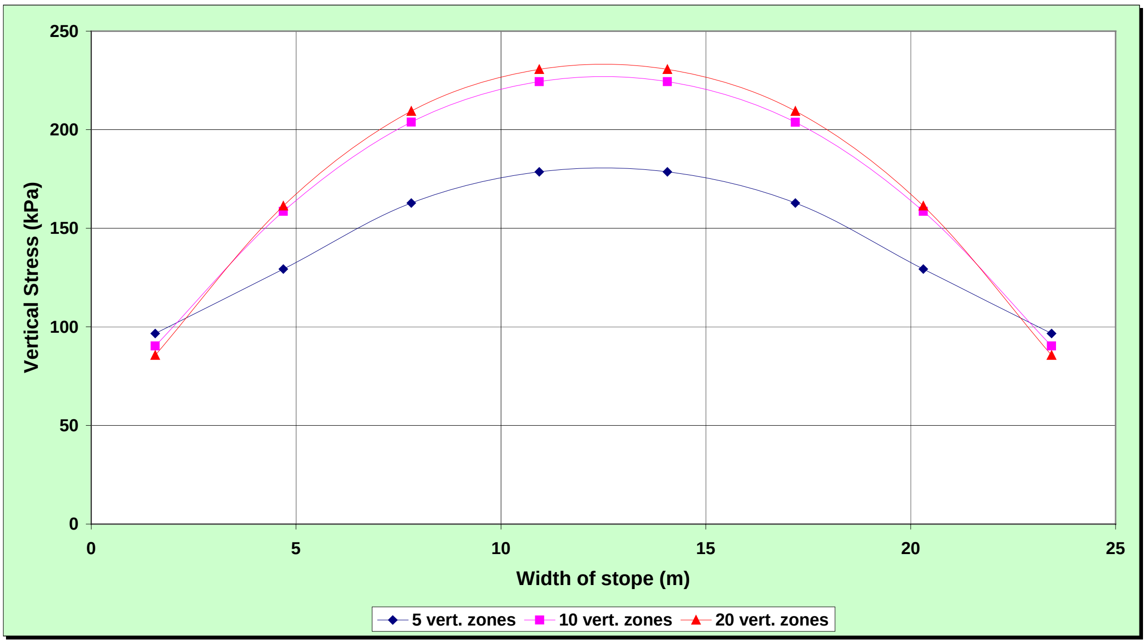

Figure 6. 37 Vertical stress profile across the centre of the stope, 25m from the base, fully confined case

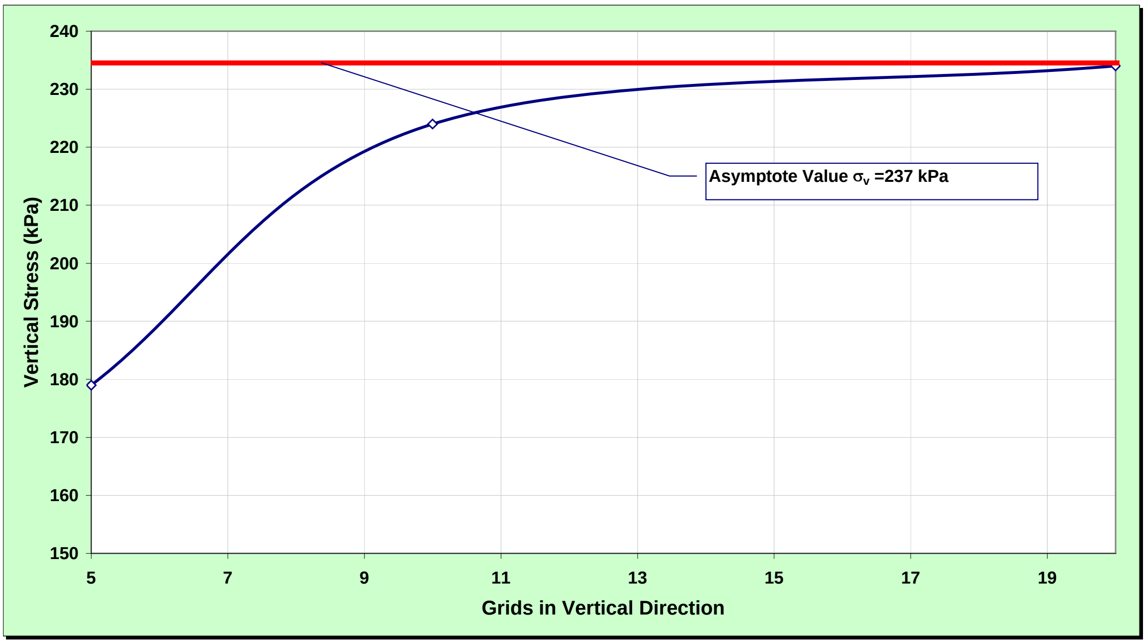

Figure 6. 38 Asymptote value for the vertical stress profile across the mid height of the stope, fully confined

The upturned edges on Figure 6.37 result from the averaging of the vertical stress values in each zone. As there are eight nodes (the corners of the rectangular zones), which measure a stress, and four of the nodes measure the increased vertical stress in the rigid supports (rock). The perimeter zones will therefore calculate higher "average" vertical stresses. As the horizontal grid mesh density reduces and the zones become coarser, the paste fill nodes calculate the vertical stress further in the fill mass, resulting averaged vertical stresses. Hence the coarser grids may return slightly higher average vertical stress values. Both plots show that using too coarse a grid may significantly reduce the accuracy of the numerical model. The numerical model with only five zones vertically showed a maximum vertical stress of 179 kPa, which is in the order of 25% lower than the asymptotic value shown on the convergence plot. In contrast to this, by increasing the number of vertical zones to ten, the error margin is reduced to 4.2%, which is considered acceptable. To provide an adequate balance between the solution time and accuracy ten vertical zones were used for the rest of the sensitivity analyses.

6.6.2 Physical Modelling Parameters

The physical modelling parameters were divided into: -

1. Material Characteristics- which included all the material properties required to define the Elastic and Mohr-Coulomb failure criteria and
2. Stope Geometry- quantified by width to height and width to depth aspect ratios.

Figure 6.39 shows the monitoring locations for the stopes studied. Table 6.8 shows the material properties studied within the sensitivity analysis. Tables 6.9 and 6.10 show the aspect ratios tested for the base to height, and width to depth analysis.

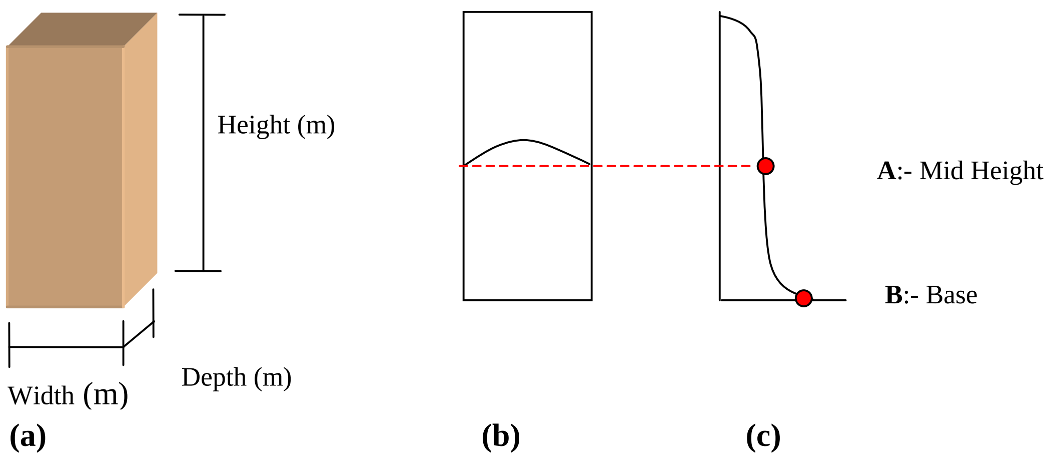

Figure 6. 39 (a) Stope naming conventions, (b) Vertical Stress profile taken across the stope at mid –height, (c) Vertical stress profile down the centre of the stope showing the two monitoring points for vertical stress

Table 6. 8 Material properties investigated in the sensitivity analysis

Material Properties	Range	Default	Units
Cohesion, c_u	100 - 1000	197	(kPa)
Density, ρ_m	1700 - 2300	2100	(kg/m^3)
Friction Angle,ϕ	0 - 30	10.3	(deg)
Young's Modulus, E	1 - 250	17.6	(MPa)
Poisson's Ratio, ν	0.15 - 0.35	0.2	
Tension, t	20 - 400	66	(kPa)
Dilation Angle, ψ	0 - 15	0	(deg)

Table 6. 9 Width to height aspect ratios investigated

(W:H)	Width to Height Aspect Ratio			
Stope Width (m)	**1:1**	**1:2**	**1:3**	**1:5**
18.75	✓	✓	✓	✓
25.00	✓	✓	✓	✓
37.50	✓	✓	✓	✓

Table 6. 10 Width to depth aspect ratios investigated

(W:D)	Width to Depth Aspect Ratio		
Stope Width (m)	**1:1**	**1:2**	**1:3**
18.75	✓	✓	✓
25.00	✓	✓	✓
37.50	✓	✓	✓

The default values were used by Rankine, K. in the preliminary analysis. To ensure that the results of this previous work were able to be correlated with the current body of research, they were used as the default values. The material properties were set to the default value, unless a sensitivity analysis was being performed it (refer to Table 6.11). The ranges of material properties and aspect ratios were defined by what could reasonably be expected to occur within practice. In each case, the vertical stress at points A and B were recorded and used in the ANN as output variables and the vertical stress profiles at mid height plotted. A summary of the data obtained from the numerical modelling, is shown in Table 6.11. Here, the first nine columns contain the input data assumed in the numerical study by FLAC^{3D}, and the last two columns are the σ_v values, computed at points A and B. This was the input data for the developed ANN. Points A and B were chosen to represent the "typical" and maximum vertical stress in the stope respectively. Failure was deemed to have occurred in the fill mass once the unconfined compressive strength was exceeded by the vertical normal stress. This is considered to be most applicable on to the paste at the base of the exposed vertical face of paste.

Table 6. 11 Modelling data summary – Material Properties

Width (m)	*Depth (m)*	*Height (m)*	*Cohesion,* c_u *(kPa)*	*Density,* ρ_m *(kg/m^3)*	*Friction Angle,* ϕ *(deg)*	*Young's Modulus, E (MPa)*	*Poisson's Ratio,* ν	*Tension, t (kPa)*	*Dilation Angle,* ψ *(deg)*	σ_{vA} (kPa)	σ_{vB} (kPa)
25	25	50	**100**	2100	10.3	17.6	0.2	66	0	240	328
25	25	50	**200**	2100	10.3	17.6	0.2	66	0	229	336
25	25	50	**500**	2100	10.3	17.6	0.2	66	0	229	336
25	25	50	**1000**	2100	10.3	17.6	0.2	66	0	229	336
25	25	50	197	**1700**	10.3	17.6	0.2	66	0	181	274
25	25	50	197	**1900**	10.3	17.6	0.2	66	0	204	305
25	25	50	197	**2100**	10.3	17.6	0.2	66	0	232	336
25	25	50	197	**2300**	10.3	17.6	0.2	66	0	250	368
25	25	50	197	2100	**0**	17.6	0.2	66	0	229	336
25	25	50	197	2100	**5**	17.6	0.2	66	0	229	336
25	25	50	197	2100	**10**	17.6	0.2	66	0	229	336
25	25	50	197	2100	**15**	17.6	0.2	66	0	229	336
25	25	50	197	2100	**20**	17.6	0.2	66	0	229	336
25	25	50	197	2100	**30**	17.6	0.2	66	0	229	336
25	25	50	197	2100	10.3	**1**	0.2	66	0	223	326
25	25	50	197	2100	10.3	**10**	0.2	66	0	228	336
25	25	50	197	2100	10.3	**50**	0.2	66	0	229	338
25	25	50	197	2100	10.3	**100**	0.2	66	0	230	339
25	25	50	197	2100	10.3	**250**	0.2	66	0	234	344
25	25	50	197	2100	10.3	17.6	**0.15**	66	0	223	330
25	25	50	197	2100	10.3	17.6	**0.20**	66	0	229	336
25	25	50	197	2100	10.3	17.6	**0.25**	66	0	236	345
25	25	50	197	2100	10.3	17.6	**0.30**	66	0	245	358
25	25	50	197	2100	10.3	17.6	**0.35**	66	0	262	379
25	25	50	197	2100	10.3	17.6	0.2	**20**	0	256	373
25	25	50	197	2100	10.3	17.6	0.2	**50**	0	235	345
25	25	50	197	2100	10.3	17.6	0.2	**100**	0	221	328
25	25	50	197	2100	10.3	17.6	0.2	**150**	0	219	326
25	25	50	197	2100	10.3	17.6	0.2	200	0	219	326
25	25	50	197	2100	10.3	17.6	0.2	400	0	219	326

***Note**: INPUT DATA – no cell shading, red- sensitivity analysis values, black – default value , OUTPUT DATA: - Shaded cells*

Table 6. 11 Modelling data summary (cont.)

Width (m)	Depth (m)	Height (m)	Cohesion, c_u (kPa)	Density, ρ_m (kg/m^3)	Friction Angle, ϕ (deg)	Young's Modulus, E (MPa)	Poisson's Ratio, ν	Tension, t (kPa)	Dilation Angle, ψ (deg)	σ_{vA} (kPa)	σ_{vB} (kPa)
25	25	50	197	2100	10.3	17.6	0.2	66	**0**	224	326
25	25	50	197	2100	10.3	17.6	0.2	66	**5**	224	326
25	25	50	197	2100	10.3	17.6	0.2	66	**10**	224	326
25	25	50	197	2100	10.3	17.6	0.2	66	**15**	224	326
18.75	18.75	**18.75**	197	2100	10.3	17.6	0.2	66	0	128.05	209
18.75	18.75	**37.50**	197	2100	10.3	17.6	0.2	66	0	138.6	228
18.75	18.75	**56.25**	197	2100	10.3	17.6	0.2	66	0	135.5	228
18.75	18.75	**93.75**	197	2100	10.3	17.6	0.2	66	0	133.1	229
25.00	25.00	**25.00**	197	2100	10.3	17.6	0.2	66	0	209	265
25.00	25.00	**50.00**	197	2100	10.3	17.6	0.2	66	0	223	294
25.00	25.00	**75.00**	197	2100	10.3	17.6	0.2	66	0	214	296
25.00	25.00	**125.00**	197	2100	10.3	17.6	0.2	66	0	213	297
37.50	37.50	**37.50**	197	2100	10.3	17.6	0.2	66	0	336.28	449
37.50	37.50	**75.00**	197	2100	10.3	17.6	0.2	66	0	367.13	497
37.50	37.50	**112.50**	197	2100	10.3	17.6	0.2	66	0	351.47	501
37.50	37.50	**187.50**	197	2100	10.3	17.6	0.2	66	0	352	502
18.75	**18.75**	50.00	197	2100	10.3	17.6	0.2	66	0	137.4	192
18.75	**37.50**	50.00	197	2100	10.3	17.6	0.2	66	0	198.3	288
18.75	**56.25**	50.00	197	2100	10.3	17.6	0.2	66	0	210	312
25.00	**25.00**	50.00	197	2100	10.3	17.6	0.2	66	0	223	326
25.00	**50.00**	50.00	197	2100	10.3	17.6	0.2	66	0	309.5	553
25.00	**75.00**	50.00	197	2100	10.3	17.6	0.2	66	0	325	570
37.50	**37.50**	50.00	197	2100	10.3	17.6	0.2	66	0	389	626
37.50	**75.00**	50.00	197	2100	10.3	17.6	0.2	66	0	446.6	701
37.50	**112.50**	50.00	197	2100	10.3	17.6	0.2	66	0	457	707

*Note: **INPUT DATA – no cell shading, red- sensitivity analysis values, black – default value , OUTPUT DATA: - Shaded cells***

6.6.2.1 Sensitivity Analysis of Material Properties

The effect of each of the material properties on the maximum vertical stresses in the stope are shown in Figures 6.40 – 6.46.

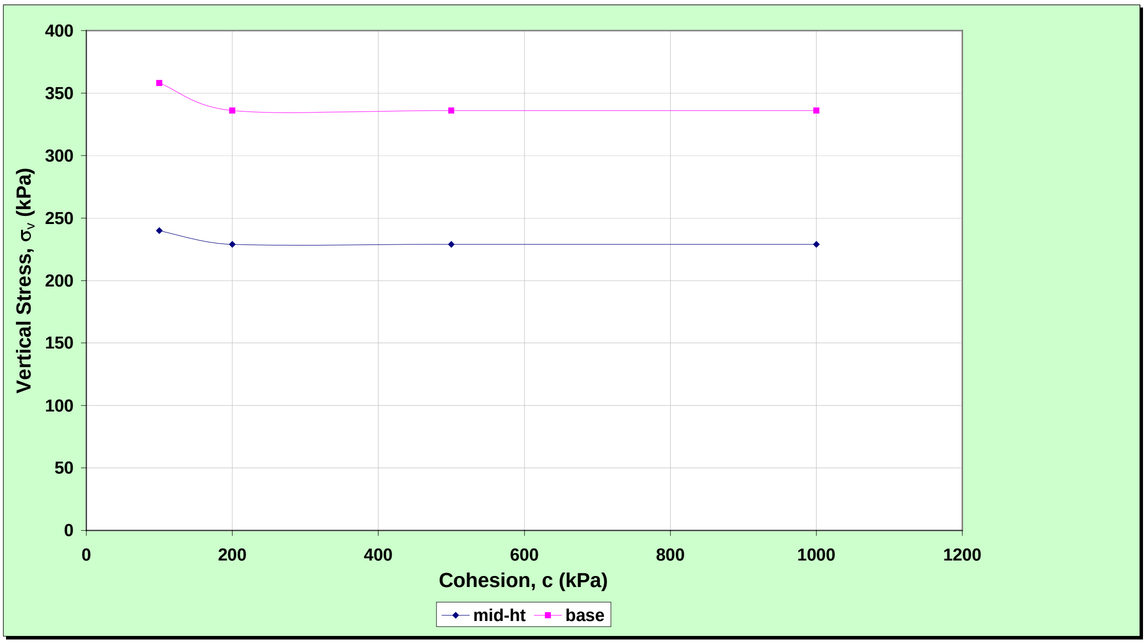

Figure 6. 40 Effect of cohesion on σ_{vmax}

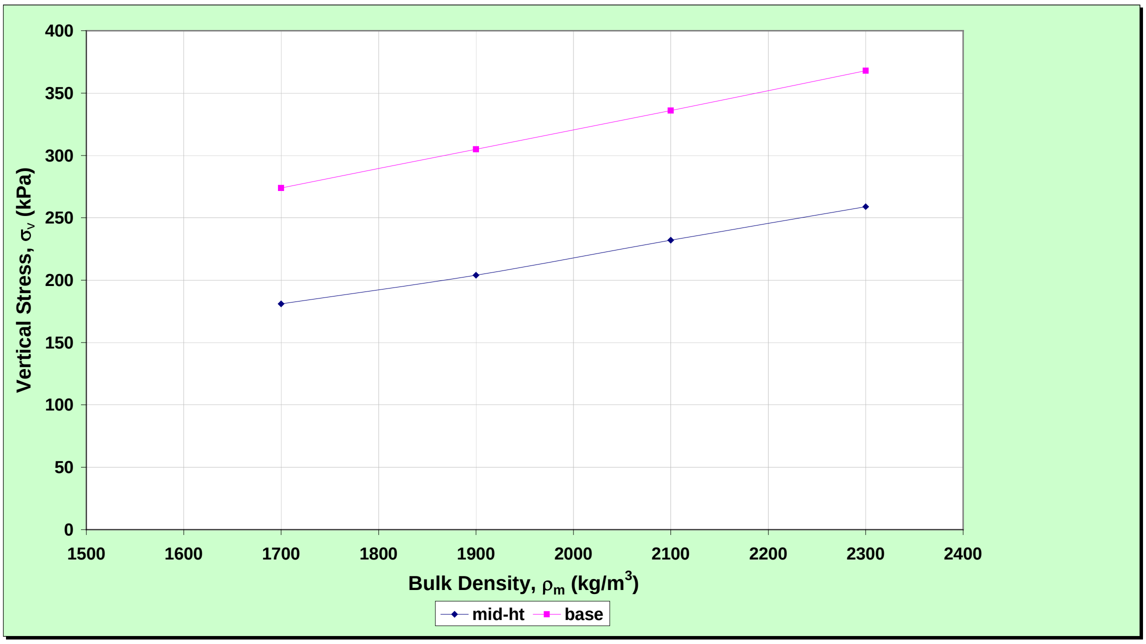

Figure 6. 41 Effect of bulk density on σ_{vmax}

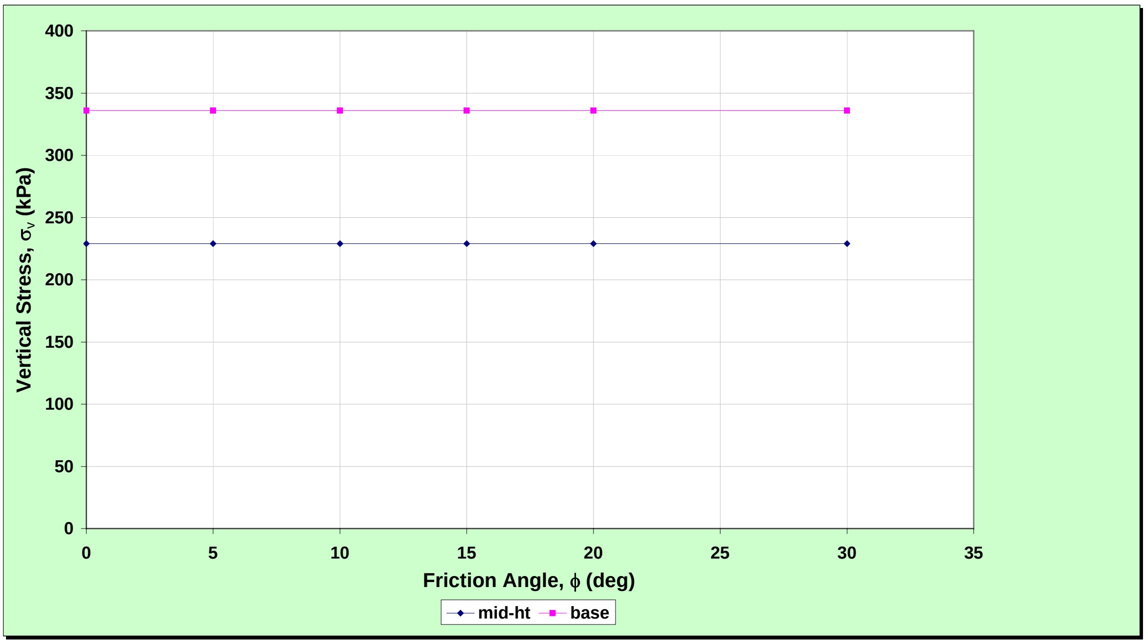

Figure 6. 42 Effect of friction angle on σ_{vmax}

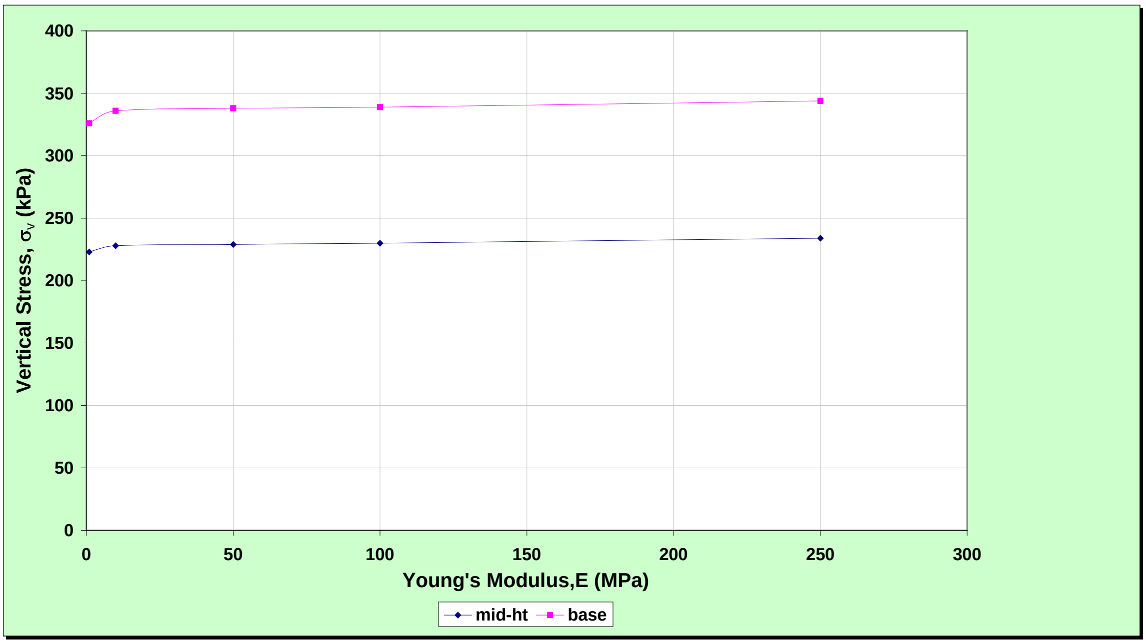

Figure 6. 43 Effect of Young's Modulus on σ_{vmax}

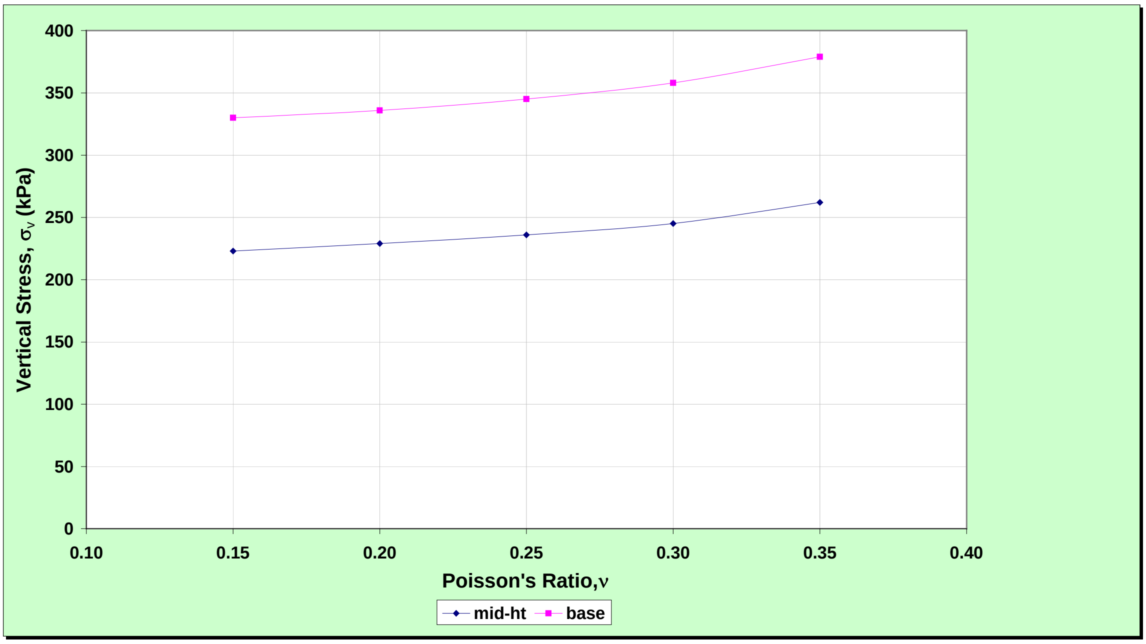

Figure 6. 44 Effect of Poisson's Ratio on σ_{vmax}

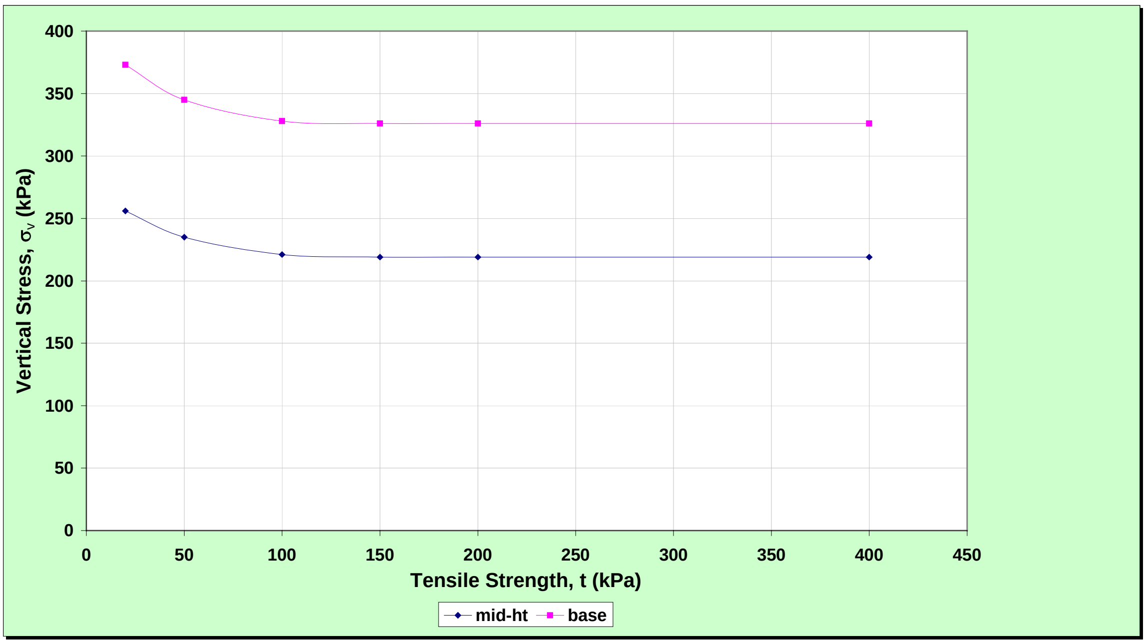

Figure 6. 45 Effect of tensile strength on σ_{vmax}

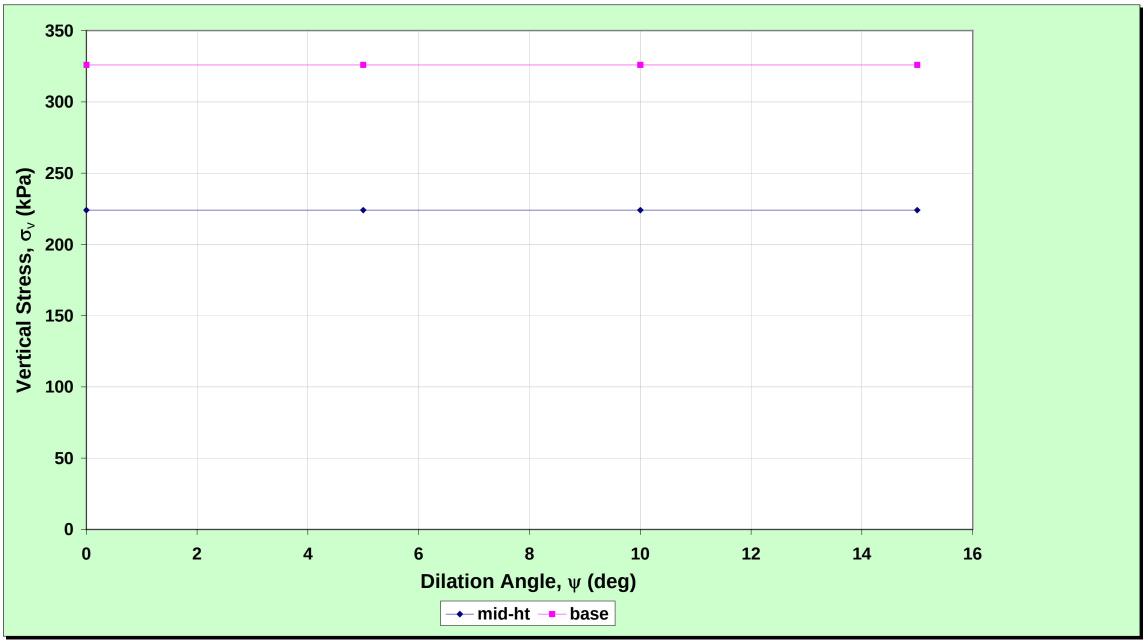

Figure 6. 46 Effect of dilation angle on σ_{vmax}

The factors which most effect the vertical stress development in the fill mass are density and Poisson's ratio. This because the development of the vertical stresses in the fill mass occur within the elastic region of soil response. Deformations are restricted by the surrounding walls and thus the effects of the plastic material properties such as cohesion, tensile strength friction angle and dilation are not observed. If the material properties are set so low as to force the material into plastic response then the material properties will have an effect on the development and distribution of vertical stress. The increase in vertical stress associated with the increase in density of the material is simply due to increased self weight and loads. The development of the soil arch will occur in the identical manner, however the magnitude of the total vertical stress will be higher. The deformation of the backfill when exposed will be governed by the material properties of the paste.

Plots of the vertical stress distribution down the centre of the stope and across the middle of the stope at mid-height, for the material property sensitivity analysis have been included in Appendix 6.2 for reference.

6.6.2.2 Sensitivity Analysis of Stope Geometry

The sensitivity of vertical stress development with stope geometry was investigated using the width to height (W:H) and width to depth (W:D) aspect ratios. The W:H ratios investigated the variation of σ_{vmax} with height and plan base dimension. The height was maintained at 50 m for the whole stope geometry analysis. The width and depth dimensions are equivalent for all stopes considered in the W:H sensitivity analysis.

Width to Height (W:H) Aspect Ratio

Stopes with a width of 18.75 m, 25 m and 37.5 m, were modelled with W:H aspect ratios of 1:1, 1:2, 1:3, 1:5. For the W:H analysis the width and depth of the base were equal in all cases. The dimensions were chosen to represent what was considered to be a reasonable range around geometry of the "typical" 25 m x 25 m x 50 m stope. The vertical stress distribution down the centre of the stope and across the mid-section were done for each of the W:H ratios identified in Table 6.9. Typical examples of this are Figures 6.47 and 6.48. Additional plots have been included in Appendix 6.2.

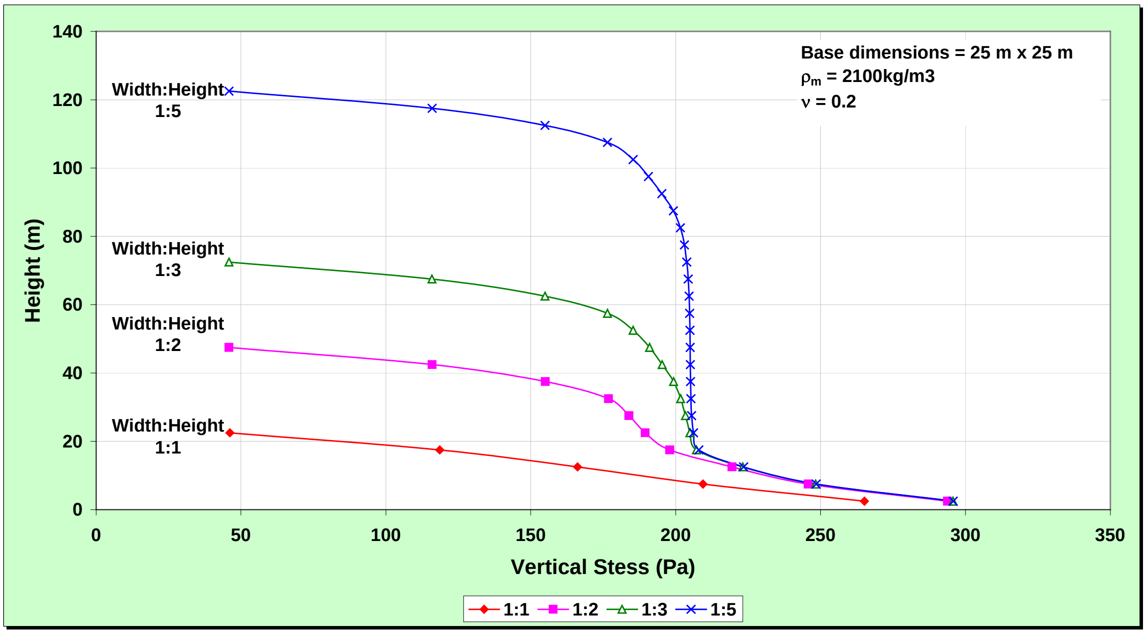

Figure 6. 47 Vertical stress profile down the centre of stopes with variable width to height ratios (base dimension = 25 m x 25 m)

To identify the general trends for the base to height aspect ratio investigated, Figure 6.48 was developed having non-dimensionalised units on both axis. As it was the maximum vertical stress that is required for the backfill design, a simple equation was derived to calculate σ_{vmax} as a function of the stope geometry.

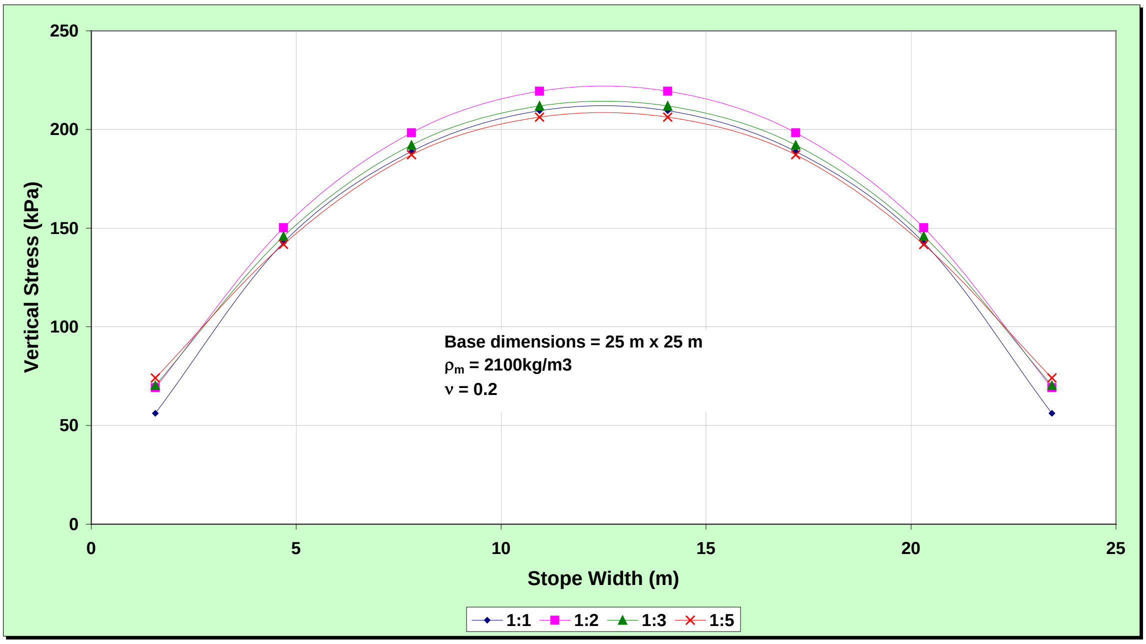

Figure 6. 48 Vertical stress profile across the mid-height of stopes with variable base to height ratios (base dimension = 25 m x 25 m)

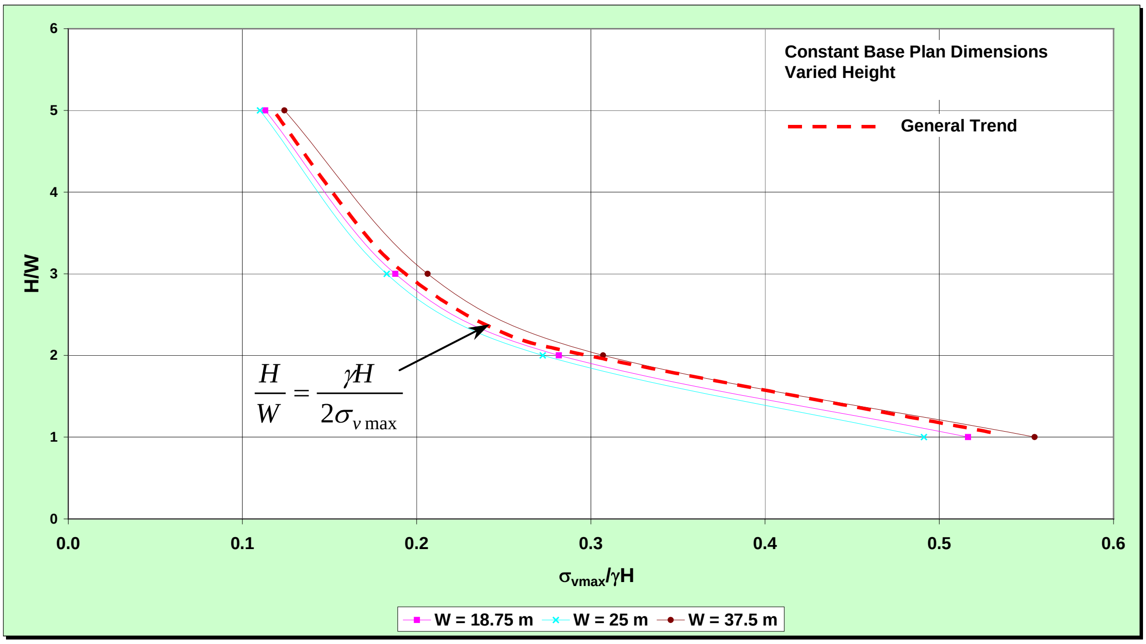

Figure 6. 49 Plot of width to height aspect ratios against $\sigma_{vmax}/\gamma H$.

The equation of the general trend for the maximum vertical stress at the base can be expressed in the form: -

$$\frac{H}{W} = \frac{\gamma H}{2\sigma_{v\max}} \quad \text{…(6.4)}$$

which can be re-arranged to determine σ_v.

$$\sigma_{v\max} = \frac{\gamma W}{2} \quad \text{…(6.5)}$$

From which the following conclusions can be made: -

- In a square base stope the development of the maximum vertical stress at the base of the stope is dependent on the base dimension of the stope only. The maximum vertical stress is equivalent to that exerted by a fill of the same density to a height of half of the base dimension, without any effects of arching.
- The point of contra-flexure on the graph occurs when the H:W aspect ratio passes approximately 2.5. Under this the stress ratio of the non-dimensional form diverges and above this it converges. This indicates that the arching mechanism requires a height of 1.25 times the base dimension to develop at the top of the stope and the same at the bottom of the stope.
- The non-dimensional stress ratio $\frac{\sigma_v}{\gamma H}$ is lower for the base values than for the mid-height values. This is due to the increased proportion of vertical stress, when compared to ρgh, transferred to the walls through shear at the base of the stope when compared to the middle of the stope.

Width to Depth (W:D) Aspect Ratio

As with the W:H aspect ratio analysis, stope widths of 18.75 m, 25 m and 37.5 m were used and W:D ratios of 1:1, 1:2 and 1:3, a constant stope height of 50 m was used throughout the analysis. Profiles such as 6.50 and 6.51 were plotted for each of the stopes investigated were plotted and have been included in Appendix 6.2. By nondimensionalising the plot, as in 6.52, the effect of the different W:D ratios can be observed. It should be noted that the results for the vertical stresses in Figure 6.52 were corrected for the variation in the B:H , or W:H in this case, prior to plotting the graph.

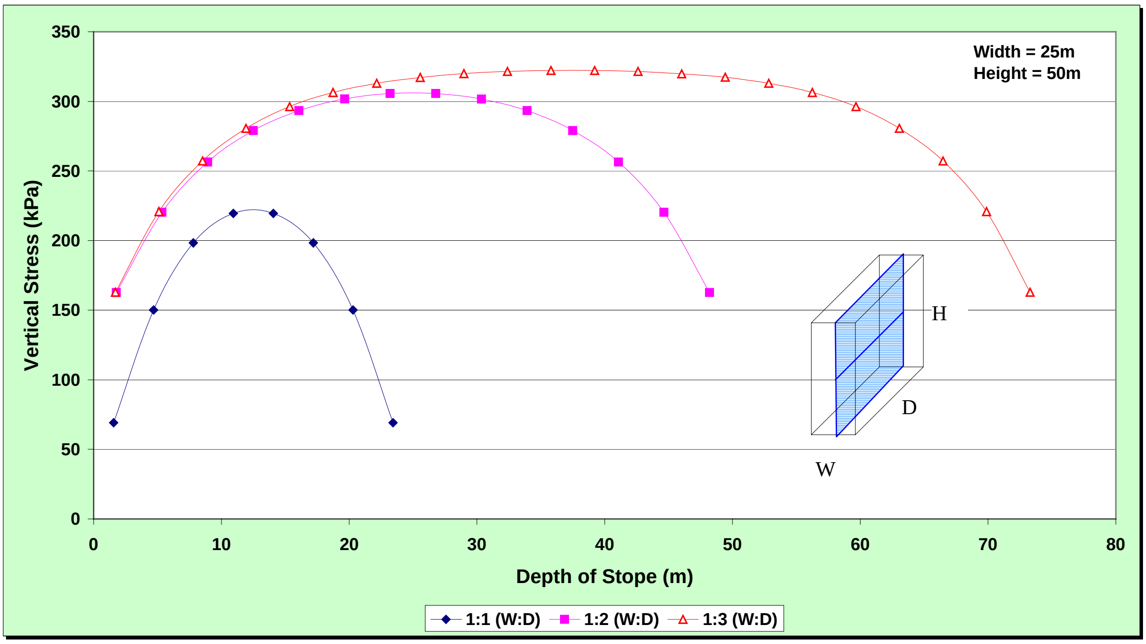

Figure 6. 50 Vertical stress profiling down the longitudinal depth of a stope (constant height=50m, constant width = 25m) at mid-height of the stope

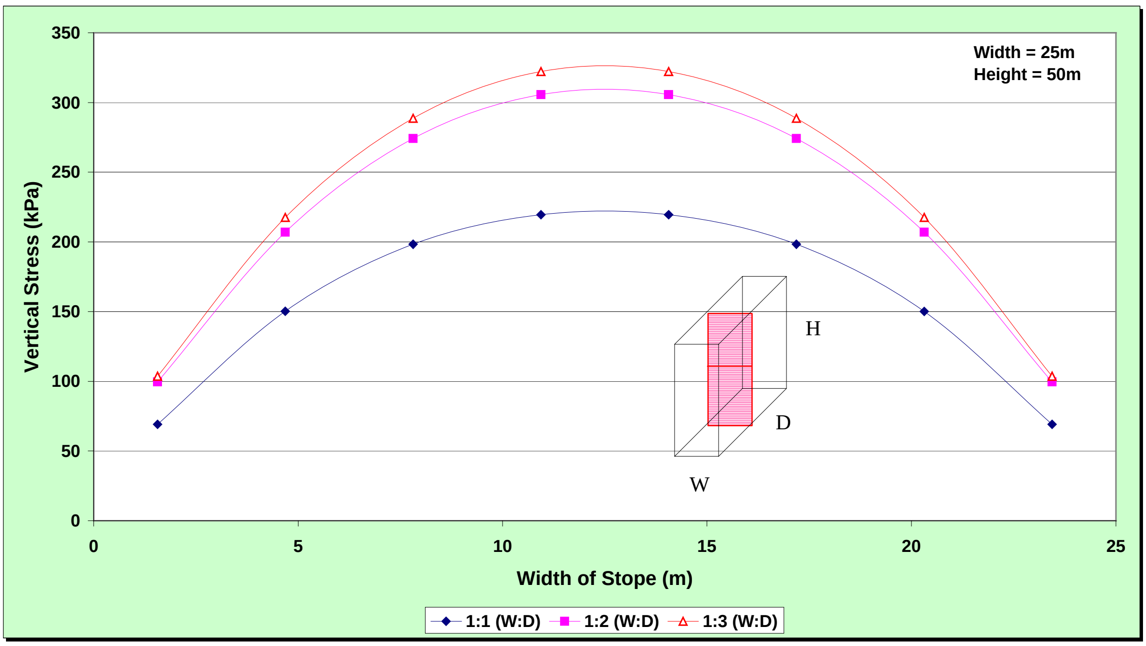

Figure 6. 51 Vertical stress profiling across the constant width of a stope with varying depth (constant height=50m, constant width = 25m) at mid-height of the stope

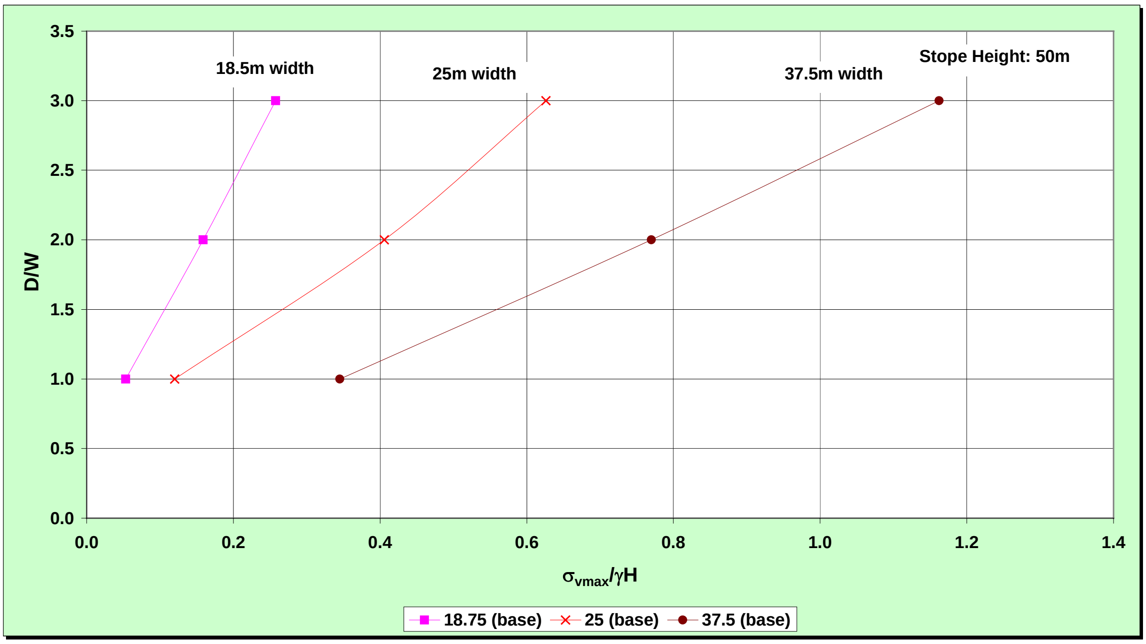

Figure 6. 52 Variation of the non-dimensional geometry parameter (D/W) with the non-dimensional stress parameter ($\sigma_{vmax}/\gamma H$)(constant height = 50m)

As the width and depth of the stope increases, so to does $\sigma_v/\gamma H$. This suggests that the soil arch is taking longer to develop in stopes with larger width/plan dimensions, and shows the increased reduction in verticals stress associated with three dimensional vs. two dimensional arching. As the W:D ratio increases the soil arch profile becomes predominantly two-dimensional. These conclusions agree well with the previous sections. It is necessary to define the change in gradient of the lines which define σ_{vmax} at the base of the stope in Figure 6.52. This was done by adding linear trendlines, (shown in Appendix 6.2) and generalising the solution, which takes the form: -

$$\frac{W}{D} = M\left(\frac{\sigma_{v\max}}{\gamma H}\right) + 0.5 \qquad \ldots(6.4)$$

where M is the gradient of the trend lines on the line on Figure 6.52.

Equation 6.4 may be rearranged to calculate the maximum vertical stress in a stope, as shown in equation 6.5.

$$\sigma_{v\max} = \frac{\gamma H}{2MW}\left(2D - W\right) \qquad \ldots(6.5)$$

The variation of M with stope base dimension is shown in Figure 6.53.

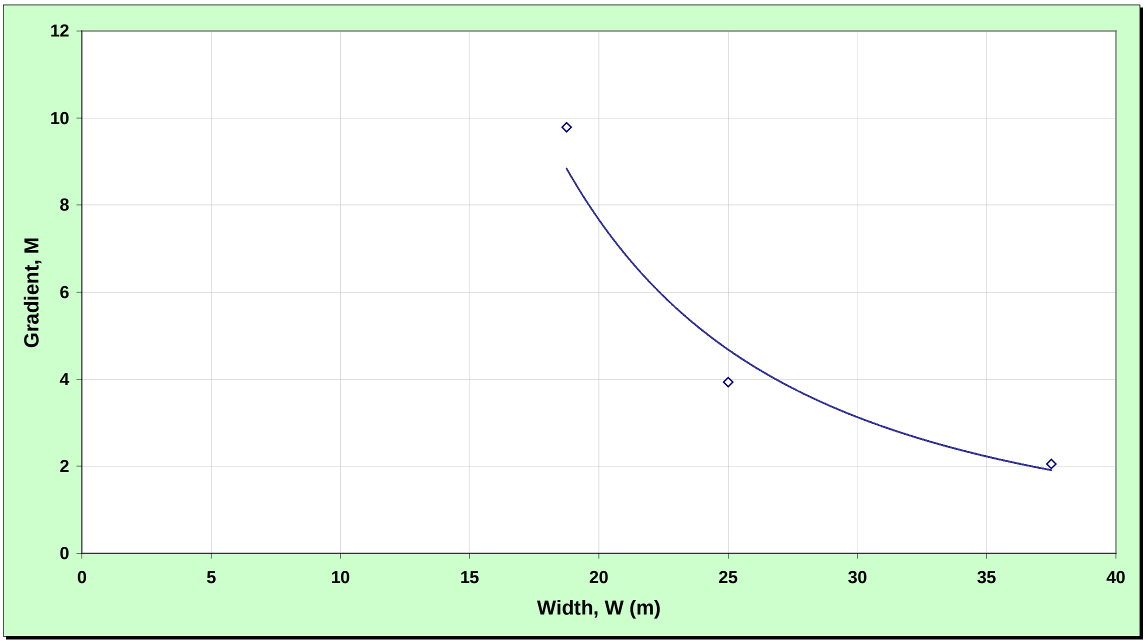

Figure 6. 53 Variation of gradient, M, with width, W (m)

From this analysis the following conclusions are drawn:-

- The gradient M, varies with the width of the stope in the form of equation 6.6:-

$$M = \frac{5764}{W^{2.2}} \qquad \ldots(6.6)$$

- The gradient asymptotes to infinity as the stope width approaches 15m, which is supported by plotting the stope width against the non-dimensionalised stress parameter $\sigma_v/\gamma H$ (refer to Appendix 6.2). As the stope width reduces towards 15 m, the maximum vertical stress in the stope reduces to minimal levels. Suggesting that a stope width of 15 m may be a critical stope width, below which all stopes are stable, regardless of stope depth or height.
- Similarly as the stope width increases to infinity, the gradient drops to an asymptotic value of approximately 1.5. Which would represent two-dimensional arching.

- The reduction of the gradient, M, with increase in stope width results from the increased distance required to develop the initial arch, as described in Section 6.5.1.1 and shown in Figure 6.17. The vertical stress in the stope therefore develops in accordance with $\sigma_v=\rho gh$, until vertical stress can be transferred through shear via the soil arch. This results in a higher $\sigma_v/\gamma H$ value and decreased gradient on the W/D vs. $\sigma_v/\gamma H$ plot.
- The vertical stress increases as the minimum width of the stope increases, this results from the longer load path for the vertical stress to the surrounding walls and the reduced effect of confinement – both of which increase the depth at which the arch may be considered to be fully developed, and hence vertical load to be transferred.
- The non-dimensional stress parameter is lower for the mid-height readings than they are for the base readings. This different is exaggerated as the W:D ratio increases. This results from the higher stresses at the base of the stope where the arching mechanism is ineffective in reducing vertical stresses.
- Vertical stresses are transferred via a 3-dimensional arch when W:D = 1, as the load paths for the transfer of σ_v to each of the surrounding walls is equidistant. As the W:D ratio increases the load is transferred via a predominantly 2-dimensional arch, between the closest two opposing walls. The tendency of the loads to be transferred by a primarily two dimensional arch is confirmed by the convergence of the vertical stress profiles in Figure 6. 50 and 6.51. The exposure and re-confinement of the stopes with backfill, forces the arch to be predominantly two dimensional through the reduction of arching potential through the fill- fill interfaces. The effect of the increase in vertical stresses in this case can be correlated closely to the change in the geometric profile, and aspect ratios. Figure 6.20, which show the progressive increase in vertical stress in the centre of the primary stope, show clearly the transfer from 3-D arching to 2-D arching. This is considered applicable to the current study of the width to depth aspect ratio.

6.7 Development of The Integrated Model Approach to Paste Back Fill Design

6.7.1 Overview

The combined use of the outputs from the numerical modelling of paste filled stopes and the geotechnical characterisation of paste fill blends will allow the cement content in the paste to be optimised. The UCS of the paste in the stope is required to be equal to or greater than the maximum vertical stress, σ_{vmax}, to ensure stability. By using σ_{vmax}, the maximum verticals stress measured at the center of the base of the stope, the approach is inherently conservative. Ideally the maximum vertical stress at the base of the face being exposed would be used as a stability criterion. Unfortunately, the exclusion of interface elements in this modeling program did not provide the opportunity to obtain accurate vertical stress values at the face of the stope[1]. The vertical stress profile across the stope becomes more uniform as the stope is sequentially surrounded by paste, rather than rock. The difference in σ_{vmax} at the center of the stope and interface therefore reduces as does the level of conservatism. In addition to this, the use of the UCS of the paste may entrain a factor of conservatism also. It is recognized that the exposed face is unconfined, however, if an element of paste at the base of the stope is considered in isolation, it is only fully unconfined on one face. The increase in strength due to confinement can be calculated using ϕ_u as outlined in Chapter 3.

Static stability of stopes requires: -

1. Prediction of σ_{vmax} based on user defined inputs such as stope geometry, fill density etc.
2. Identifying the paste fill mix that would give a UCS in excess of σ_{vmax}.

[1] Stress values for each of the zones are calculated by the averaging of the stress values at each of the eight nodes on the cubic zone. At the rock- paste interface, the stress is calculated as incorrectly, as the higher stresses in the surrounding rocks are averaged with the vertical stress in the paste filled stope, resulting in an inaccurate and elevated maximum vertical stress.

Figure 6.54 shows the general cement optimisation process and Figure 6.55 shows how this process was applied to the idealised nine-stope grid arrangement where the sequential exposure of the primary stope occurs over time.

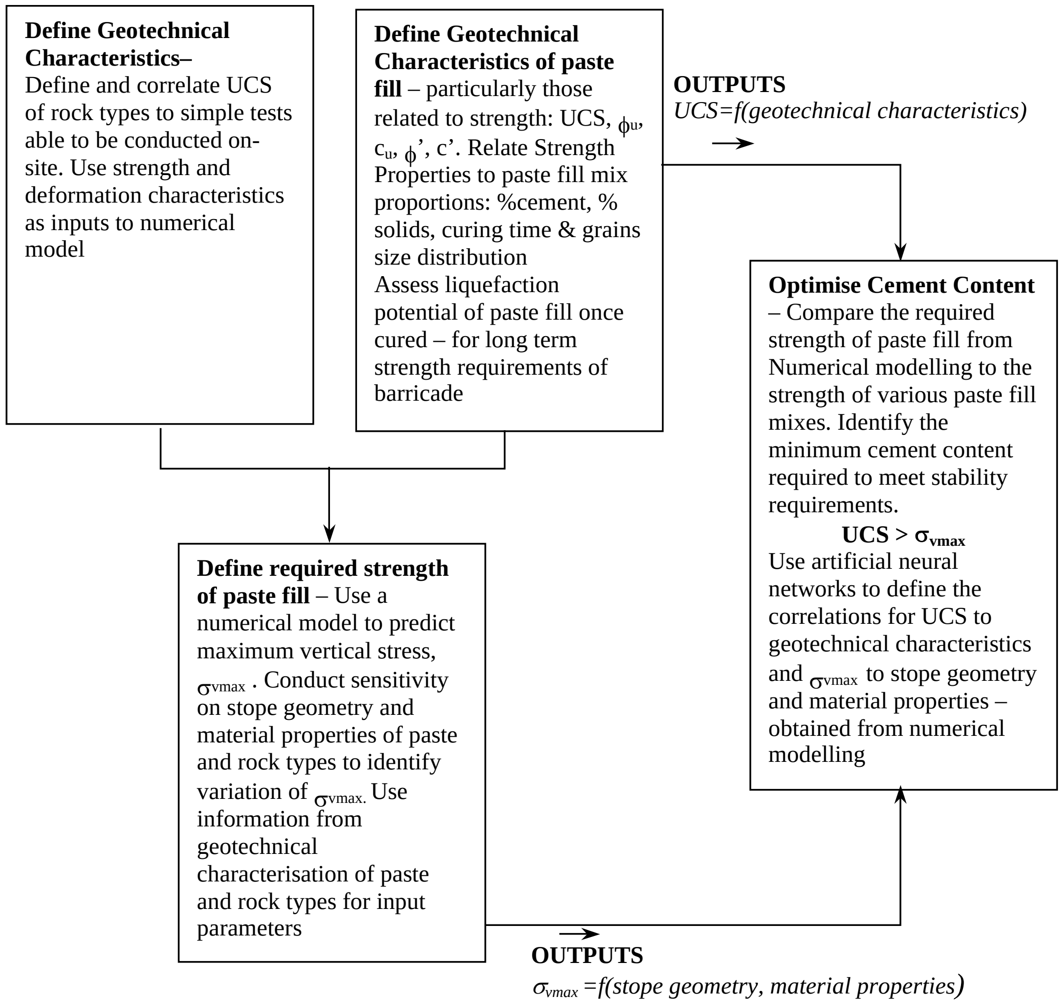

Figure 6. 54 Process flow chart for the identification of the optimum cement content for paste backfilled stopes

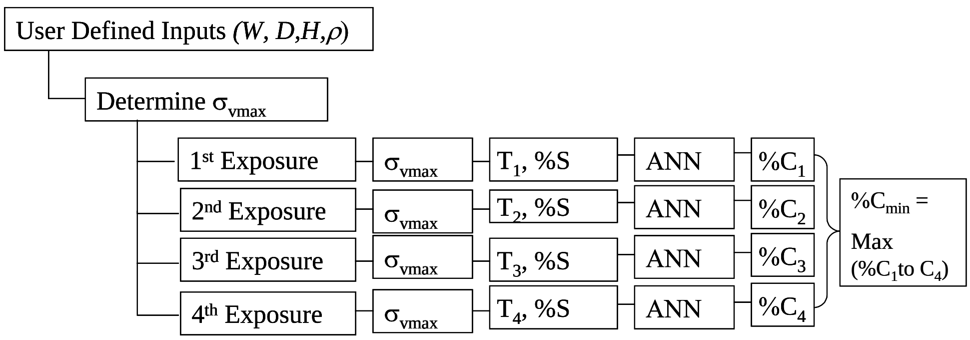

Figure 6. 55 Solution process for the integrated model, to determine the minimum cement content for any given stope

The user defined inputs of stope width (W), depth (D), height (H) and fill density (ρ) were chosen as the most important user defined input parameters for the development of σ_{vmax} from the results of the sensitivity analysis. The ANN used in the integrated model was trained on long term strength data (up to 12 months) and used to calculate the required cement content based on the defined solids content (%S) and curing time (T_n).

6.7.2 Development and Verification of the Integrated Model

All data used in the ANN modelling were assumed to have identical modelling parameters to the ANNs developed in Chapter 5, including the proportion of data used for training (85%) and validation (15%). Table 6.12 summarises the data sets used for modelling with ANN's and the parameters used for each analysis.

Table 6. 12 ANN data set delineation for the integrated model

Data Set	Description	Testing Parameters Available	ANN Type	Source
1	Paste Fills – Long term Model Name: "**PFLT**"	**Inputs:** %C, %S, Curing time, T **Outputs:** UCS	GRNN	Chapter 3
2	Maximum Vertical Stress Model Name: "**STRESS**"	**Inputs:** W, D, H, ρ **Outputs:** σ_{vmax}	GRNN	Chapter 6

Individual performances were assessed using the coefficient of correlation, r, and the coefficient of determination, r^2. The weighting for each of the input parameters found by Neuroshell 2 was used to assess the effective contribution of each of the various inputs to the designated outputs. Five models for each data set were developed for prediction, and the results reported in Tables 6.13 and 6.14. The shaded rows (PFLT5 and STRESS1) are the models with the highest predictive quality for each data set. The smoothing factor for each network was also recorded in the last column to provide an indication as to the likely generality (or specificity) of the solutions. The results show that in both cases the solutions are highly specific.

Table 6. 13 ANN modelling results for the determination of UCS of paste from user defined inputs (%C, %S, and curing time, T)

Data Set	Model Name	Input parameter Importance Most → Least			Model Output	Model Performance r	Model Performance r^2	Smoothing Factor
Long Term UCS of Cannington Paste	PFLT1	%C	T	%S	UCS	0.999	0.998	0.134
	PFLT2	T	%C	%S	UCS	0.998	0.995	0.095
	PFLT3	%C	T	%S	UCS	0.998	0.997	0.146
	PFLT4	%C	%S	T	UCS	0.999	0.997	0.154
	PFLT5	%C	T	%S	UCS	0.999	0.998	0.177

Table 6. 14 ANN modelling results for the determination of σ_{vmax} from user defined inputs (H,W,D, ρ)

Data Set	Model Name	Input parameter Importance Most → Least				Model Output	Model Performance r	Model Performance r^2	Smoothing Factor
Maximum Vertical Stress	STRESS1	H	W	ρ	D	σ_{vmax}	0.995	0.991	0.072
						σ_{vmidht}	0.999	0.998	
	STRESS2	W	H	ρ	D	σ_{vmax}	0.988	0.976	0.092
						σ_{vmidht}	0.990	0.981	
	STRESS3	W	H	ρ	D	σ_{vmax}	0.978	0.957	0.088
						σ_{vmidht}	0.977	0.955	
	STRESS4	W	H	D	ρ	σ_{vmax}	0.985	0.971	0.196
						σ_{vmidht}	0.970	0.940	
	STRESS5	H	D	W	ρ	σ_{vmax}	0.985	0.970	0.204
						σ_{vmidht}	0.968	0.937	

To predictive ability of the selected models was validated against the data extruded from the training data prior to training. Figures 6.56 and 6.57 show the results for the PFLT5 and STRESS1 networks. As shown, the predictive artificial neural networks provide a very quick and accurate method of determining the required strength of the paste, σ_{vmax}, and the strength of various paste fills based on the geotechnical characteristics.

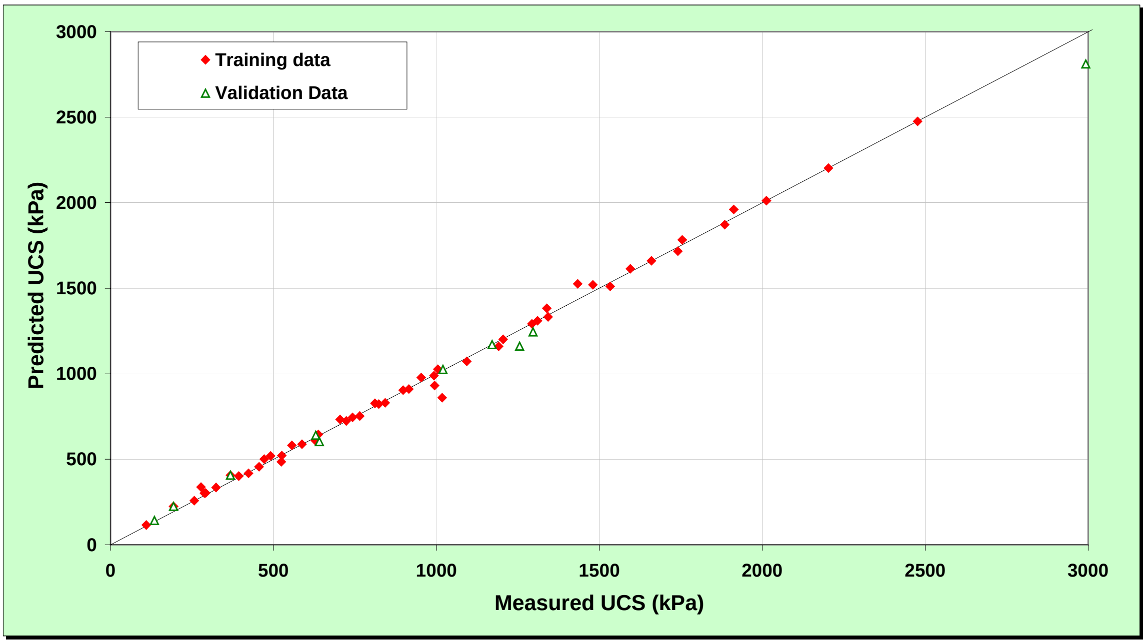

Figure 6. 56 Results for ANN modelling of the long terms strength of paste

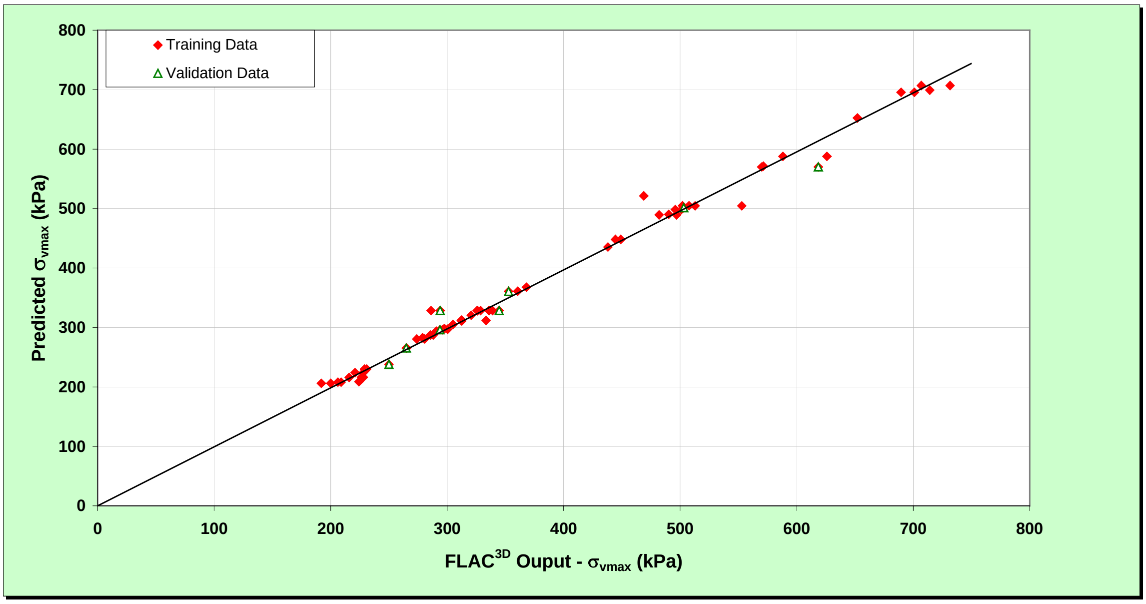

Figure 6. 57 Results for ANN modelling of the predicted maximum vertical stress at the base of stopes

These two predictive ANN's provide the basis for the resulting "integrated model". Figure 6.58 shows the user interface for the integrated model.

Inputs

Stope Width	25	m
Stope Depths	25	m
Stope Height	50	m
Fill Density	2.2	t/m^3

LEGEND

Red line	Paste Support
Black line	Rock Support
Dotted line	Exposed Side

Exposure

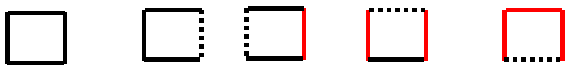

	0	1	2	3	4	(Source)
Max. Vert. Stress, σ_{vmax} (kPa)	281					FLAC^{3D} /ANN (STRESS1)
From Rankine (2000)	262	300	383	597	693	Rankine Thesis (2000)
% Cement	**2**	**2.52**	**2.63**	**2.97**	**2.49**	ANN (PFLT5)
% Solids	79	79	79	79	79	Paste Flow Model
Expected time of Exposure (Months)	0	1	3	6	12	Mine Planning Department
UCS	246	300	383	597	693	
% Cement required for UCS> σ_{vmax}		**2.5**	**2.6**	**3.0**	**2.5**	

Optimal %C =	**3.0**

Figure 6. 58 User interface for the integrated model approach to backfill design

The user is prompted for the inputs, which are used to predict σ_{vmax} using the ANN STRESS1. The modelling undertaken as part of this dissertation has considered the maximum vertical stress in the fully confined case. Rankine (2000) modelled the increase in vertical stress for a single stope throughout the full mining sequence, and the maximum vertical stresses from that analysis are defined in the second row of the analysis. The solids content of the paste is set at 79% for this example, to match the current practice at the mine. The % solids of the paste fill blend controls the rheology of the paste (refer Section 3.7.1). The % solids of the fill mix will be determined by a paste fill flow model which will determine the maximum solids density for the paste which will ensure that the paste is able to be deposited. By doing so, the solids density of the fill will be maximised, which in turn provides the basis for the determination of the required cement content. The expected exposure time for each exposure provides the time of curing available to the paste, prior to exposure. Previously, the UCS was assumed to plateau after 28 days. This is not the case, as has been shown in Chapter 3 with paste fill continuing to gain strength for periods up to one year. By defining the curing time in months, the increase in strength after 28 days is taken into account. To define the cement content required to achieve a $UCS \geq \sigma_{v\max}$ the %cement is iteratively changed until $UCS = \sigma_{v\max}$. This is done to determine the cement content required to ensure stable exposure for each progressive exposure. The minimum cement content for the fill is then the maximum of the four cement contents determined for each of the exposures.

6.7.3 Application of Integrated Model

The integrated model was applied to the "typical stope" problem (25 m x 25 m x 50 m). A cement content of 3 % is shown as the minimum cement content for the fill mix using the integrated model approach. The analytical method proposed by Winch (1999), which constitutes the currently accepted state-of-the-art, was used to determine the required cement content for the critical case (3rd exposure). The results of which are shown in Figure 6.59. A cement content of 3.3% was determined, which is an additional 10% over the integrated model. When annualised, this reduction in cement content provides a significant cost saving. For Cannington Mine, it would constitute a potential saving of \$600,000 to \$700,000/ annum.

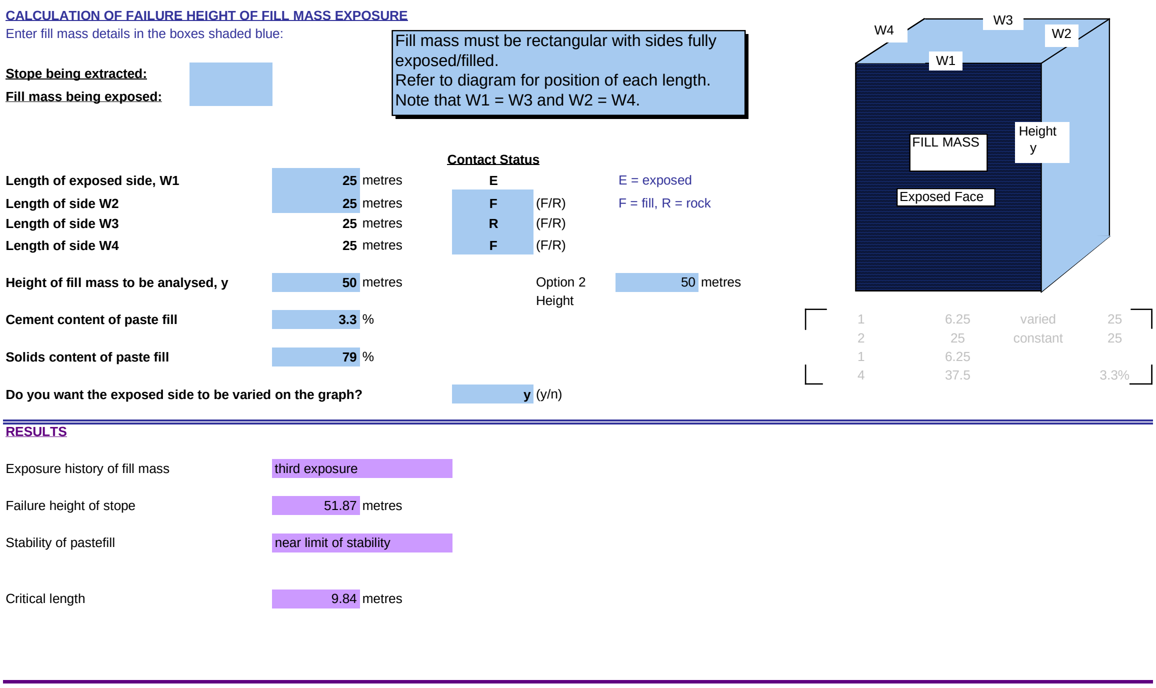

Figure 6. 59 Output from analytical solution proposed by Winch (1999) for 25m x 25m x 50m stope

To validate Winch's (1999) model a back analysis of the previously backfilled and exposed stopes at Cannington was done to find the levels of dilution. Which although not a directly comparable measure for the model, does indicate the general stability of backfilled stopes. A current average dilution level of 1.57% exists at Cannington Mine, which infers that Winch's (1999) model is predicting cement contents which do result in (very) stable stopes, during exposure. Appendix 6.3 shows a summary of dilution data and analysis.

6.7.4 Limitations of Integrated Model

- To date only enough data from numerical modelling for the fully confined case, need to incorporate the results from modelling through the full mining sequence with stopes of different aspect ratios. Can use the increase in stress through the mining sequence as identified by Rankine (2000) for a single stope (25 m x 25 m x 50 m) but not accurate, for stopes outside this
- Need to include a paste flow model to identify % solids for the model.
- Use the maximum vertical stress on the exposed face, $\sigma_{vmax\text{-}face,}$ as the failure criterion as opposed to σ_{vmax}.
- The ability of the artificial neural networks to predict is limited by the range of the input data that has been used for training. Therefore the mininum and maximum geometry of the stopes modelled using FLAC^{3D} provide the boundaries to the current predictive abilities of STRESS1 for σ_{vmax}. Similarly the predictive ability of PFLT5 is limited by the range of cement content, solids content and curing time tested.

6.8 Conclusions

Chapter 6 has described the development, validation and application of a 3-D numerical model for the sequential excavation and filling of a full nine-stope grid arrangement for paste filled stopes. The effects of the input parameters on the model were determined using sensitivity analysis for each. A integrated approach for the design of backfills was presented and the results analysed. The conclusions from this chapter have been broken into sections relating to the numerical and integrated model respectively.

Numerical Model

- FLAC^{3D} is a suitable and capable numerical modeling package for the sequential mining and backfilling of paste backfilled stopes, in the idealised nine-stope grid arrangement.
- The FLAC^{3D} model defined the profile of the soil arching mechanism in 3-dimensions and the change of the profile through the in a paste fill stopes and the change in profile throughout the mining sequence.
- Maximum vertical stresses in the paste fill mass occur through the mining sequence as the confining rock walls are sequentially replaced with paste.
- Fill-fill contacts are between 33% to 66% as effective as rock-fill interfaces for the development of arching
- There is approximately a 15% increase in maximum vertical stress measured for a two dimensional arch, compared to that of three dimensions.
- Material properties, with the exception of material density, have little affect on the development of the maximum vertical stress in a stope. The material characteristics are primarily concerned with the strength and deformation characteristics of the fill, as opposed to the development of stress within the stope.
- Arching in stopes is primarily a geometric effect with the base plan dimensions being the critical parameters
- The maximum vertical stress in stopes of a square plan dimensions may be calculated using: - $\sigma_{v\max} = \frac{\gamma W}{2}$
- The maximum vertical stress in stopes which does not have a square plan dimensions may be calculated using: - $\sigma_{v\max} = \frac{\gamma H}{2MW}(2D - W)$, where M is the gradient of the trend line on the line on the non-dimensionalised plot of W/D against $\sigma_v/\gamma H$

Integrated Model

The integrated model provides a holistic approach to backfill design. Using the long term strength gain benefits observed with paste, to determine the minimum cement content required for the stable exposure of each face of the stope. The model integrates the use of artificial neural networks for the accurate prediction of required parameters (σ_{vmax} and UCS of fill). The application of the integrated model resulted in a prediction of a cement content 10% lower than that using Winch's (1999) analytical model. This represents a significant potential cost reduction via lower cement usage in paste. The validity of Winch's (1999) model was determined by investigating the dilution levels of previously exposed stopes. The dilution levels give an indication as to the general stability of the backfilled stopes designed using Winch's (1999) model. The limitations of the integrated model were also discussed.

Recommendations for the improvement of the integrated model through numerical modelling have been presented under "Recommendations for Future Research" (refer Section 8.3).

6.9 Summary

The integrated model approach to backfill design provides the most holistic and complete approach to backfill design to date. It provides a method for the determination of the optimum cement content for each paste fill mix, depending on user defined input parameters for the stope geometry, material bulk density, curing time available to each exposure (1st to 4th) and solids density. The solids density information is expected to result from the rheological requirements for the reticulation of the paste to the stope.

Chapter 7

Numerical Modelling of Fill Barricades

Barricades form an integral part of the complete paste filling system. They are installed at the draw points of a stope to contain the paste fill. They must be designed to withstand the hydraulic pressure exerted by the paste fill before it cures sufficiently to support its own weight. The magnitude of the applied pressure on the barricade is related to the material properties of the paste, the geometry of the stope and drives, and the subsequent filling rate.

7.1 Problem Definition

Fill barricades must meet three main design criteria:-

1- Static loading
2- Dynamic loading
3- Permeability/drainage requirements

The dynamic loads on barricades, are those from seismic events or blasting related activities, and are proportional to the loads applied by the fill mass itself during the initial stages of filling. An in-situ fill barricade may be exposed to additional loads from the pressure waves created by blasting, however due to geometrical aspects of barricade position and the dynamic wave attenuation characteristics of the paste material, it is expected that this loading is significantly less than the lateral earth pressures applied while filling the stope. The permeability requirements are only required for hydraulic fills or similar which require the barricade to allow water to drain freely from the fill mass. Paste fill, by definition has very little (if any) free water and hence the barricades have no drainage requirements.

The static loading requirements of the barricades are to resist the overturning and sliding forces applied by the fill when filling the stope. Lateral earth pressure calculations may be applied to a soil, however when in the very early stages of curing the paste is in a dense slurry form, with neither solid or liquid loading characteristics. To determine an appropriate loading for design calculations, three design methodologies have been used to date: -

- Operator experience;
- Analytical solutions; with theories from both concrete and soil mechanics used to determine the required thickness for the barricades to resist the applied loading (Revell 2001, Grice 2000).
- Numerical modelling (Kuganathan 2001, Rankine 2004)

Operator experience depends on the type and location of the barricade to be installed. Ground condition and previous history of specific barricade building methods. Typically site based, this approach will not be considered any further.

Revell (2001) suggests the design lateral earth pressure for barricades should be equivalent to ten meters of uncured, overlying fill, neglecting any arching. This approach is conservative because:-

- The cementitious portion of the fill cures, providing the opportunity for loads to be transferred through the arching mechanism
- Limitations in filling rate (wmt/hr), curing time of the fill and void volume typically preclude the event of 10m of fill ever being in an uncured state behind a barricade.
- The approach assumes that the force exerted on the barricade is independent of its location within the drive. The pressure exerted on barricades decreases with the increase in distance from the draw point (Kuganathan 2001, Rankine 2004). Safety regulations prohibit working without adequate support or restraint around or under open holes.
- A common practice within the mining industry is to backfill until the level fill is just above the back of the drive and thus barricade and then suspend filling operations for a period of time to allow the fill to cure. Effectively this limits

the maximum stress to $\sigma_v = \sigma_h = \rho gh$, where h = the height of the drive. Drive heights are rarely in excess of 6m.

Grice (2001) suggests the use of a slab formula to calculate the required thickness of barricade walls. The Slab Formula uses Yield Line Theory of concrete technology, and assumes that the bulkhead has cracked in tension along diagonal line and the bulkhead-rock interface. Equation 7.1 and 7.2 may be combined to give equation 7.3, which can be used to determine the required thickness of the barricades. The process is iterative.

$$L_p = UCS\frac{t^2}{8} \quad \ldots(7.1)$$

$$w_p = \frac{24L_p}{b^2} \quad \ldots(7.2)$$

$$t = \sqrt{\frac{(w_p)(bd)}{3\ x\ UCS}} \quad \ldots(7.3)$$

where

L_p = Load required to cause plastic moment (MN)

σ_c = Uniaxial compressive strength of barricades (MPa)

t = thickness of the barricade walls (m)

b = Drive height (m)

d = Drive width (m)

w_p = Pressure required to cause plastic moment (MN/m)

The formulae were developed for a slab undergoing failure, and analysed using the yield line method. It is assumed that the reinforcement in the slab has just failed. The concrete then cracks and deforms plastically along the proposed “yield lines”, which propagate diagonally from the four corners, as shown in Figure 7.1

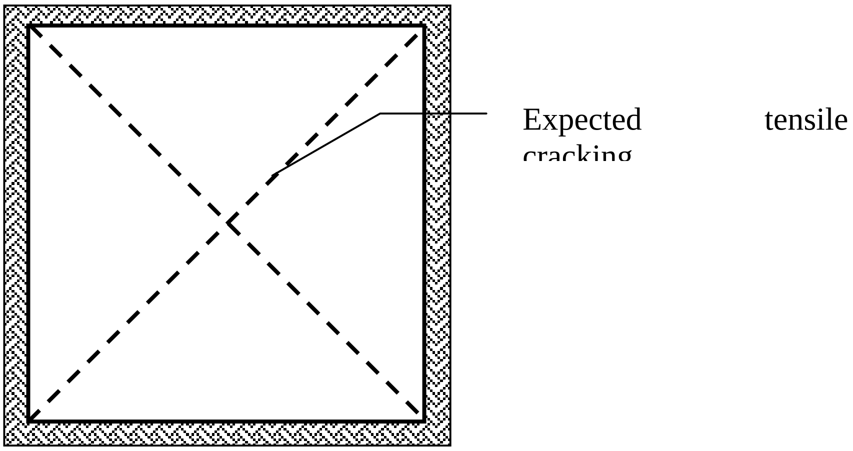

Figure 7. 1 Assumed failure pattern of fill barricades using slab formula from yield line theory

The intended application of the formula is for square openings with perimeter support. Such as in the case of barricades or square floor slabs rigidly mounted on pillars. Like many simple empirical formulae it is a gross simplification of the conditions but may be used to provide a useful insight into limits. Full-scale destructive tests carried out at Mount Isa Mines suggest that equations 7.1 – 7.3 underestimate the ultimate failure strength for masonry but overstate the loading required to cause initial cracking (Grice 2001).

The use of numerical models enable the design loads to be determined based on the defined input properties. The effects of filling rate, stope geometry, barricade geometry and location, and the variance of material properties may all be taken into account. The development of a numerical model to determine the applied loading on barricades was considered an integral and important part of the paste filling cycle.

To investigate the effect of these factors a numerical model was developed to investigate the applied stresses on a fill barricade. The outcomes of which would be used to refine filling practices and address issues with barricade design.

7.1.1 Modelling Strategy

The model was developed in FLAC^{3D} and used to investigate lateral earth pressure loadings on the barricade walls. The modelling strategy is summarised in three steps:-

1. Determine the "base case" and input parameters
2. Develop and validate the numerical model in FLAC^{3D}
3. Undertake a sensitivity analysis on important input parameters

7.1.2 Defined Input Parameters

The base case was defined as 15 m x 15 m x 50 m stope with a singular development drive located centrally along the base of one of the walls (Figure 7.2). It represents the smallest economic plan dimension for stopes at Cannington. This reduced cross-sectional area also increases the vertical height rise per hour of the paste fill and provides an indication of the maximum pressures barricades are likely to be subjected to prior to the curing of the fill. Similarly, the barricade location was considered only at the base of the stope, centrally along a side, identify the maximum stress on the barricade.

A grid mesh of 1 m spacing was used in the width and depth directions, and 0.1 m in the vertical direction, for the bottom 10 m and 1 m for the top 40 m (Figure 7.2). The fine mesh increased the solution time, however was required to maintain accuracy for hourly filling intervals. The barricade was set to be 5 m back from the vertical face of the stope in a drive with a nominal cross-sectional area of 25 m^2 (5 m x 5 m). The boundary nodes along the stope and barricade walls were fixed in all directions and the nodes along the base of the model were fixed in the vertical (z) direction only. The stope was filled in hourly intervals, and the pressures on the barricade and on the zones immediately entering the drive, were computed and recorded at each interval.

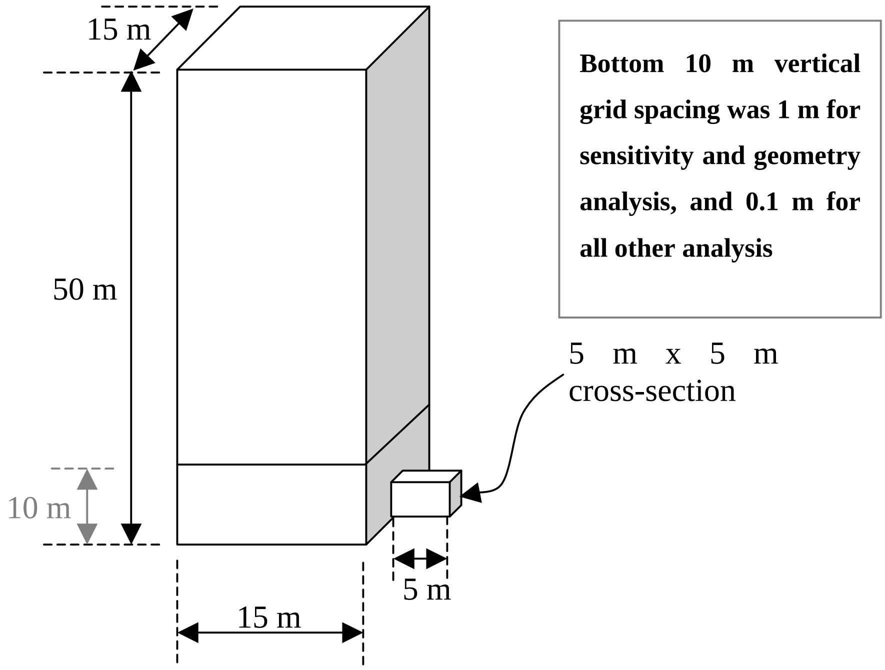

Figure 7. 2 Schematic diagram of barricade loading model, a base case.

To determine the initial material properties, test work for some of the high-density paste fill samples was used. The 80% solids content used in the testing program is thought to be the most appropriate representation of the solids density of the fill, once placed and has undergone slight consolidation.

Relationships were fitted to the laboratory test data for the time variation in Young's Modulus (E), friction angle (ϕ), and cohesion. These relationships are shown in Figures 7.3 to 7.5 and described by Equations 7.4 to 7.6.

$$c=t/(0.65+0.0016t) \quad \ldots(7.4)$$

$$E=t/(2.5E\text{-}6 + 6.25E\text{-}9\ t) \quad \ldots(7.5)$$

$$\phi_u=t/(37.5+0.097t) \quad \ldots(7.6)$$

where

c = cohesion (kPa)

E = Young's Modulus (MPa)

ϕ_u = Undrained friction angle (degrees)

t = curing time (hours)

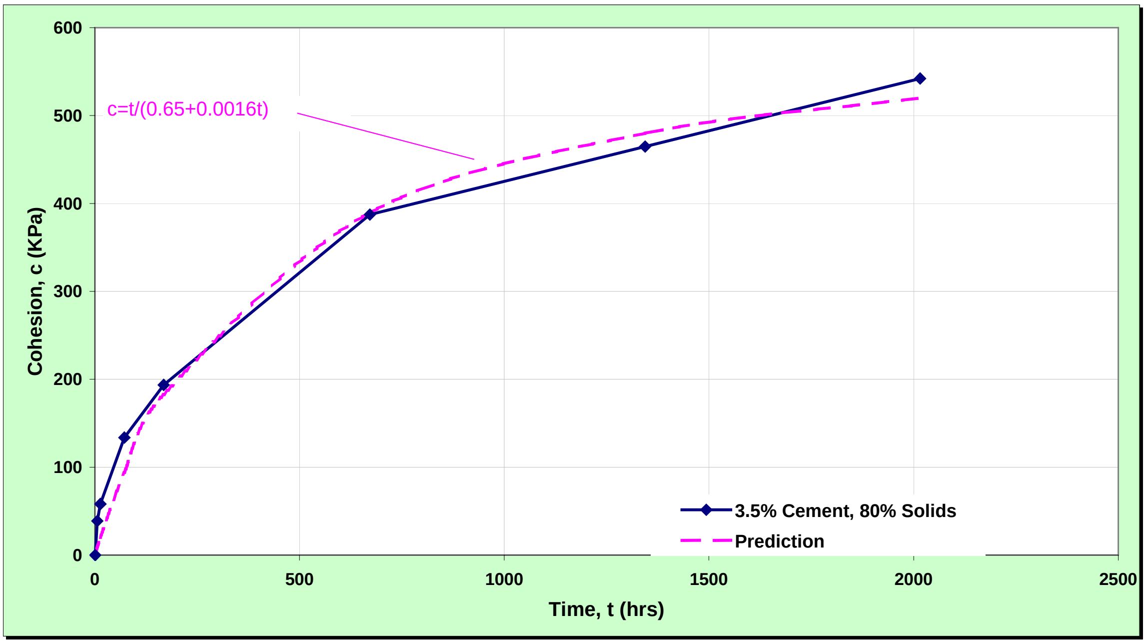

Figure 7. 3 Paste strength development relationship used for numerical model.

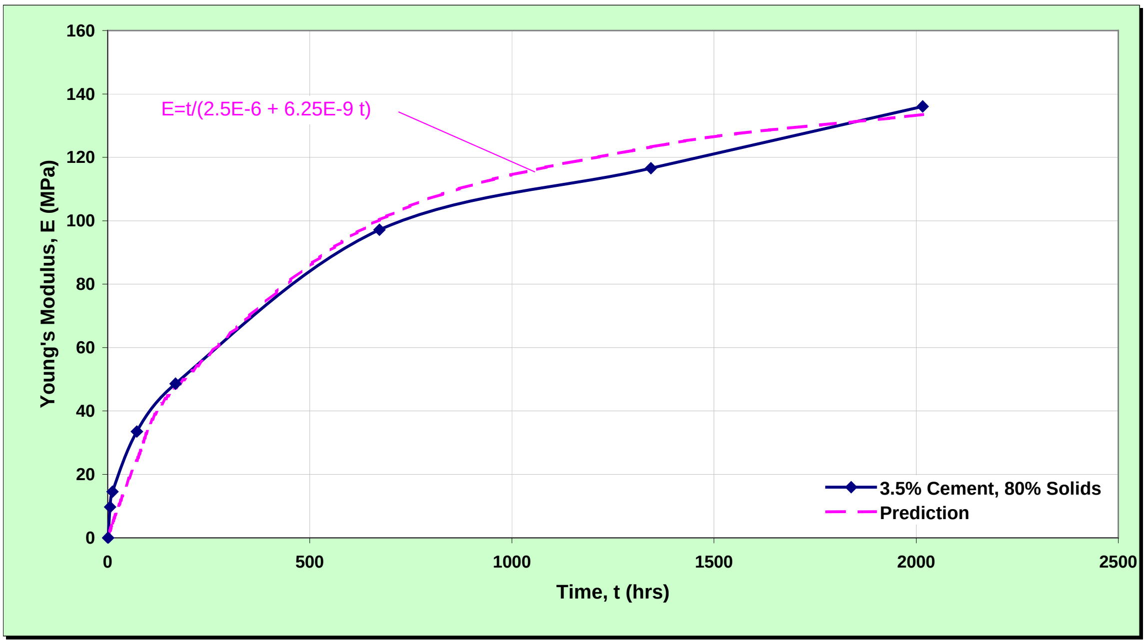

Figure 7. 4 Relationship for Young's modulus used for numerical model.

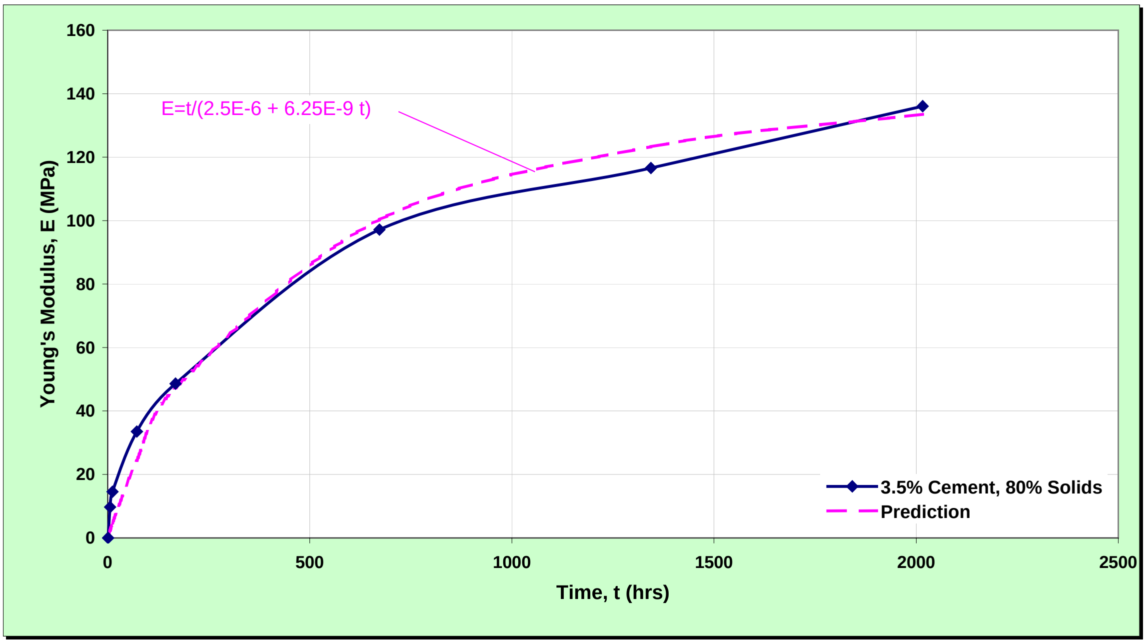

Figure 7. 5 Paste friction angle relationship used for numerical model.

Poisson's ratio (υ) for the paste was assumed to be 0.2 throughout curing, and equations 7.7 and 7.8 were used to calculate the bulk modulus (G) and shear modulus (K) respectively.

$$\text{Bulk Modulus}: K = \frac{E}{3(1-2\upsilon)} \qquad \ldots(7.7)$$

$$\text{Shear Modulus}: G = \frac{E}{2(1+\upsilon)} \qquad \ldots(7.8)$$

A paste density (ρ) of 2200 kg/m^3 and a Mohr Coulomb constitutive model was used in all simulations. The tensile strength in FLAC^{3D} defaults to the relationship whereby, $\text{tensile strength} = \frac{c}{\tan\phi}$, which is simply the x-intercept of the Mohr-Coulomb failure envelope as shown in Figure 7.6 (a) and (b).

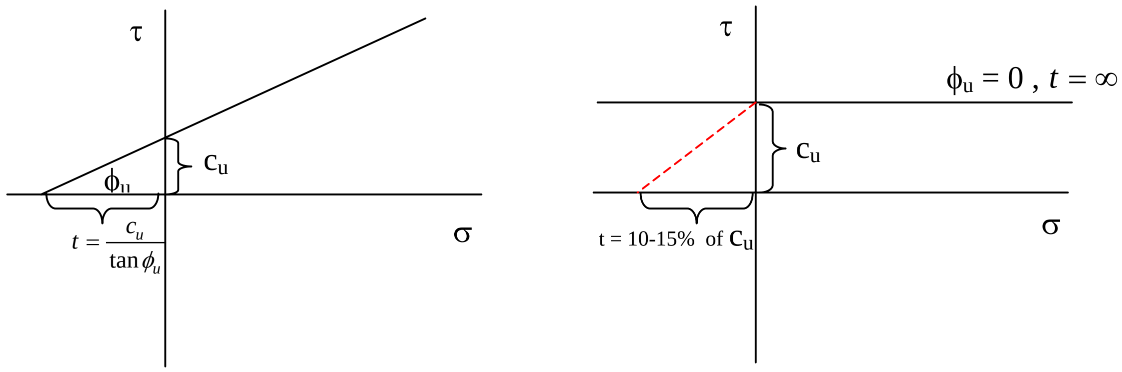

Figure 7. 6 Tensile strength determination (a) FLAC^{3D} default (b) experimental results

Subsequent to solving all the programs associated with this research it has been highlighted that this value may be too high especially when the undrained friction angles is low (ϕ_u<10). If this is taken to limit, as would be the case in a fully saturated specimen in undrained loading, the tensile strength calculated using $t = \frac{c_u}{\tan\phi_u}$ would be infinite, shown in Figure 7.6 (b). From laboratory testing, the tensile strength is typically in the vicinity of 10 – 15 % of the UCS. Modifications to the model were undertaken to determine the sensitivity of the solution to tensile strength, the results are provided in Section 7.4.

A series of simulations were undertaken to determine the sensitivity of the model to various input parameters, and to perform an analysis on filling rate and stope geometry conditions.

Table 7. 1 Modelling Summary

Run No.	**Sensitivity Analysis of**	**Filling Rate (m/hr)**	**Stope Dimensions (w x d x h)**	**Vertical Grid Spacing**	**Poisson's Ratio**	**Tensile Strength**	**Boundary Conditions***
1	Material Properties	1.0	15 m x 15 m x 50 m	1 m for entire model	0.2	c_u /tanϕ_u	roller
2							fixed
3						0.1 x UCS	
4					0.15	c_u /tanϕ_u	
5					0.25		
6	Filling Rate	0.3	15 m x 15 m x 50 m	0.1 m for base 10 m then 1 m for top section	0.2	c_u /tanϕ_u	fixed
7		0.5					
8		0.7					
9		1.0					
10		1.5					
11		2.0					
12	Stope Height	1.0	15 m x 15 m x 100 m	0.1 m for base 10 m then 1 m for top section	0.2	c_u /tanϕ_u	fixed
13		2.0					
14	Geometry	1.0	25 m x 25 m x 50 m	1 m for entire model	0.2	c_u /tanϕ_u	fixed
15			35 m x 35 m x 50 m				

* Boundary conditions for vertical stope walls.

7.2 Development of a Functional 3-Dimensional Numerical Model

A numerical model was developed in FLAC^{3D} to calculate and investigate the lateral earth pressures at barricade locations for various filling simulations. Table 7.1 summarizes the model runs and information given below.

7.2.1 Grid Generation

The stope was modelled using two rectangular prisms intersecting, as shown in Figure 7.2. The spacing of the vertical zones was dependent on the requirement for accuracy of the modelled solution. The effect of stope height and filling rate were considered two major factors influencing the pressures on barricades and were thus modelled with grid spacing of 0.1m for the bottom ten meters of the stope. Conversely the affect of the material properties and stope cross section in plan were thought to contribute less and were thus modelled with a coarser grid.

7.2.2 Initial Conditions

Initial conditions for the filling of the stope included gravitational loading only. As each lift entered the stope, the stress conditions equalized under gravity loading, thus providing the initial conditions for the next lift.

7.2.3 Boundary Conditions

The nodes along all of the vertical walls in the stope were fixed in all directions. The nodes along the floor of the stope were fixed in the vertical direction only. The effect of roller supports along the vertical walls was tested and the results collated in Section 7.4.

7.2.4 Monitoring of Results

The lateral earth pressures were computed in two vertical planes perpendicular to the drive. They were located at: - i) stope/ drive interface and ii) the other plane directly behind the barricade wall, which was recessed five meters back into the drive, as shown in Figure 7.7.

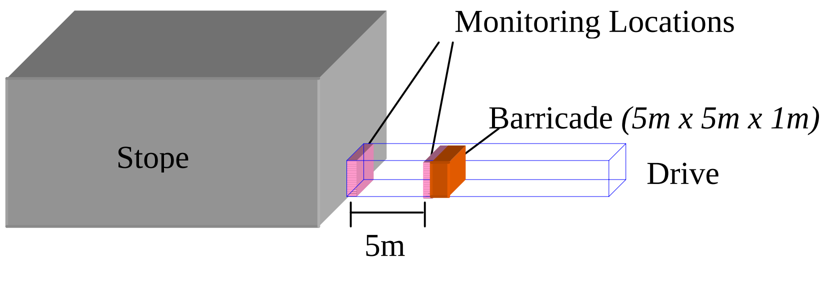

Figure 7. 7 Locations for determining lateral earth pressures.

In front elevation, the drive was divided into 25 regions of 1m grid spacings. For the models that required a higher degree of accuracy (filling rate and stope height) each of the regions were then sub-divided again into ten zones, as shown in Figure 7.8. The “average” lateral earth pressure were determined using the middle nine regions and associated zones. This minimized the edge effects resulting from the fixity of the nodes.

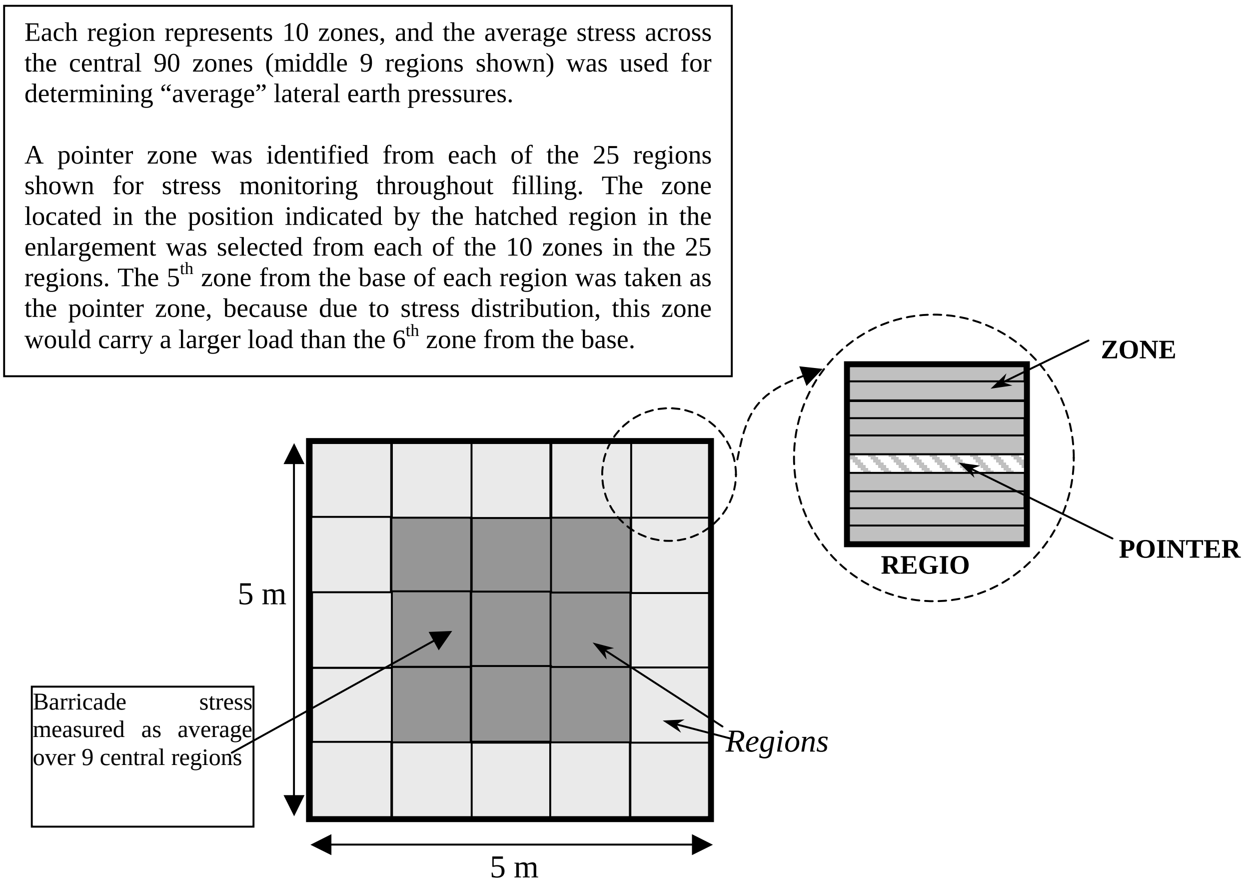

Figure 7. 8 Simplification of barricade zones

For the models with a vertical grid spacing of 0.1 m (Table 7.1), this resulted in averaging the middle 90 zones, and for the models with vertical zones at one-meter intervals, the middle 9 zones. Twenty-five pointer zones were also identified across the barricade, and individual zone stresses measured during filling.

The regions and zones shown in Figure 7.8 are three-dimensional. Each of the stress measurements was taken in the center of the zones. Resulting in the stress measurements being taken at a distance of 0.5 m from the face of the barricade and stope wall respectively. Figure 7.9 illustrates this by examining a row of zones in the drive, for the 1 m x 1 m x 1 m example, as in Run 1. The distance from the stope at which stress measurements were recorded is identical for the models simulated with zone heights of 0.1 m for the base 10 m of zones, but the height at which the readings is taken is the vertical center, therefore 0.05 m from the base of each zone.

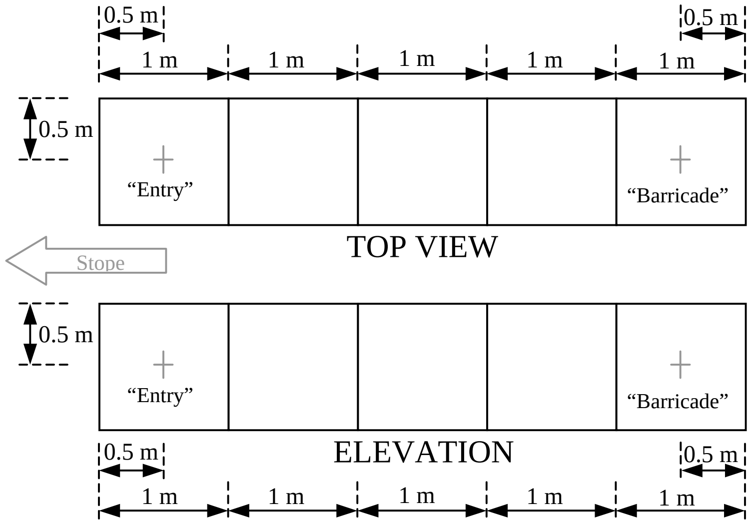

Figure 7. 9 Drive stress measurement position, when barricade is 5m from away from stope

7.3 Validation of the Numerical Model

Validation of the numerical model against in-situ measurements could not be achieved during the course of this dissertation. Previous measurements at Mount Isa Mines suggest that the maximum barricade pressures were in the vicinity of 250 – 300 kPa (Cowling 2003). It is suggested that these pressures would be applicable to hydraulic fill masses and would be excess pore pressure readings, as opposed to lateral earth pressures applied to the barricade through the backfill mass. It is suggested that a more reasonable approximation for the maximum barricade pressures for paste fill would be in the vicinity of 80 – 200 kPa depending on fill rate. The pressure relates to the height of uncured fill mass, behind the barricade, which exerts pressure. These broad guidelines were used to provide a coarse calibration to the numerical model developed and ensure it provided a reasonable approximation to actual pressures.

7.4 Modelling and Sensitivity Analysis Results

Initially, a series of problems were solved to ensure the program was functioning correctly, and to perform a sensitivity analysis on the input parameters. To reduce solution time, the mesh was increased to 1 meter node spacing in all directions.
The program was used to investigate the effect of:-

- Initial and Boundary Conditions,
- Grid Mesh Density, and
- Tensile strength (t), *(default value vs. lab test results)*
- Sensitivity of barricade pressure to filling rate
- Sensitivity of barricade pressure to stope geometry changes
- Mode of Failure

A sensitivity analysis was not performed on any other material properties as it was envisaged that the effect of material properties on stress had been covered in Chapters three and six and could be applied to the horizontal earth pressures against barricades using predefined earth pressure theory.

7.4.1 Initial and Boundary Conditions

The program was solved with roller and fixed boundary conditions, and the vertical stresses down the centre of the stope computed when the stope is fully confined. It was assumed there was no interface between the rock wall and the paste.

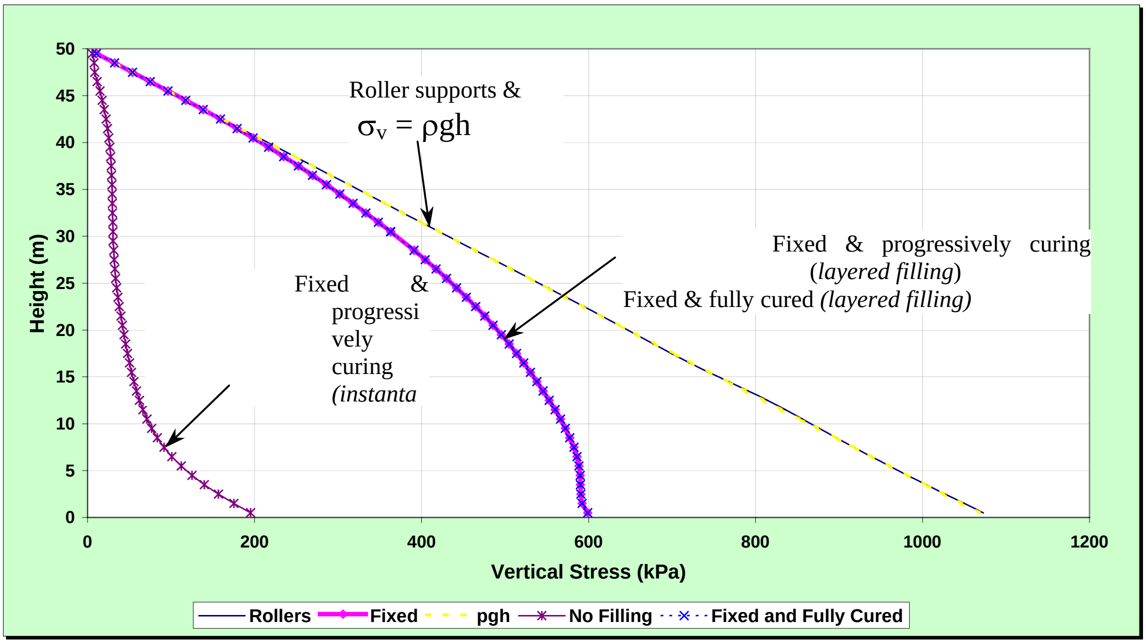

Figure 7. 10 Vertical stresses down the centre of the stope for various simulations.

Figure 7.10 plots the vertical stresses down the centre of the stope for both the roller and fixed boundary conditions. It models the point in time when the stope is filled completely, and the paste up to the height of drive is cured to full strength. As expected, the results for the roller boundary simulation maps directly onto the σ_v=ρgh line as no transfer of vertical stress to the wall is possible. The vertical stresses at the base of the stope are approximately 60 % of ρgh.

The plot also shows the effect of the curing of paste by comparing the outputs of a stope instantaneously filled with cured paste to a stope progressively filled and cured at a filling rate equivalent to a vertical height rise of 1 m/hr. Removing the filling component of the program would significantly over-predicts the arching potential[1] of the system, thus significantly under predict the vertical stress. It is thus unsuitable to simulate the stresses within a stope without incorporating the filling regime.

[1] Arching potential is defined as the difference in vertical stress from the hydraulic (ρgh) value, divided by the hydraulic value. [i.e.- $\frac{\rho gh - \sigma_v}{\rho gh}$]

In Figure 7.10, there is no reduction in vertical stresses indicated as a result of the curing of paste. This suggests that arching is independent of the stiffness of the material and highly dependent on fill rate and the associated initial stress condition. This observation would be supported by the similarity of the stress profiles for the stopes which are filled and cure progressively against those which are filled with "fully cured" paste properties. However, the reduction of lateral earth pressures *must* occur with the curing of paste, otherwise the removal of barricades, or exposure of filled stopes would always result in failure of the fill mass. This anomaly is identified as an area of future improvement to the program. As the initial stresses are critical to the design of the barricade walls it was considered pertinent to use the calculated values as those representative of the worst case for stope filling and as a basis for the calculation of barricade pressures.

7.4.2 Grid Mesh Density

The effect of the grid mesh density of the model was also investigated by plotting the lateral earth pressure on the barricade for when the vertical grid spacing was 1.0 m and 0.1 m respectively. The results are shown in Figure 7.11. The effects of the boundary conditions have been included also. The references to "Entry" and "Barricade" refer to the monitoring locations as shown in Figures 7.7 to 7.9. The more refined mesh results in a higher resolution for the problem, and converges on the actual lateral earth pressure.

As expected the stress measurements closer to the stope are significantly higher than those adjacent the barricade because of the increased level of arching. The measurements for the coarse grid mesh are slightly lower than those for the refined mesh.

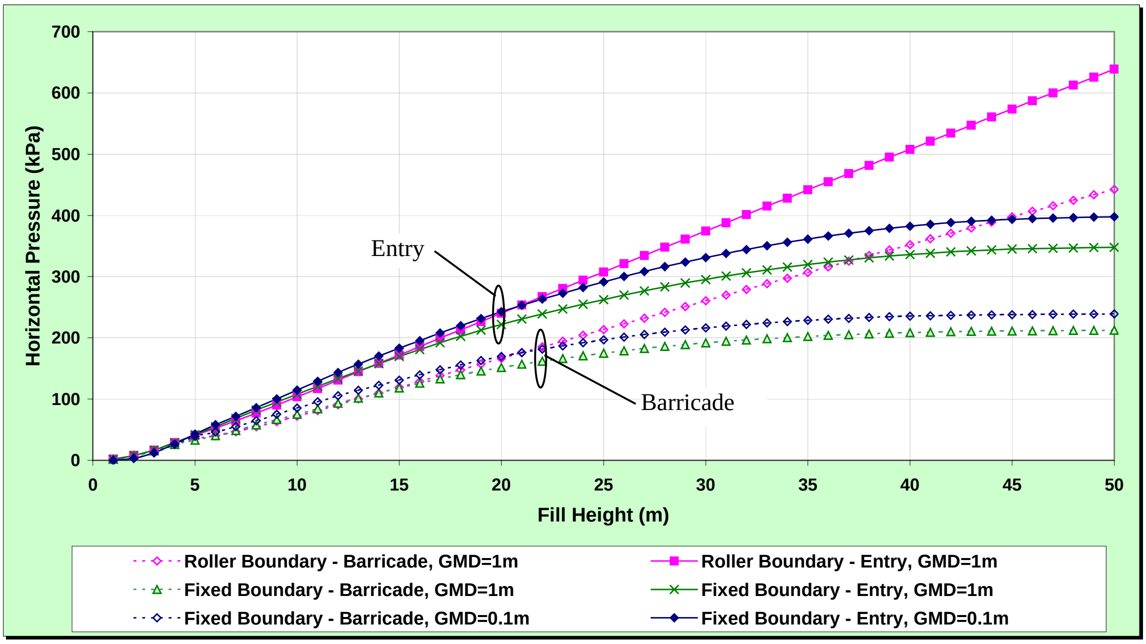

Figure 7. 11 Effect of grid mesh density on calculated lateral earth pressures

7.4.3 Tensile Strength (default value vs. laboratory test results)

FLAC[3D] defaults the tensile strength of any material to equal to $t = \frac{c_u}{\tan\phi_u}$. Laboratory testing on various rock types and paste fills suggested that tensile strength was more typically in the range of 10% of the uniaxial compressive strength. Therefore the tensile strength was taken as 10% of UCS in all computations. To quantify the effect on the output results a coarse sensitivity analysis was performed on tensile strength.

By comparing the 1 meter per hour filling solution for the default tensile input with the identical program solved with tensile strength inputted as 10 % of the UCS strength, it can be seen (refer to Figure 7.12) that there the difference is insignificant. In this instance, there are no tensile regions in the described model. It is still considered more appropriate to use t=10% UCS to ensure accuracy and applicability of the model to future investigations. (eg. Appropriate exposure time of paste behind underground fill barricades etc.)

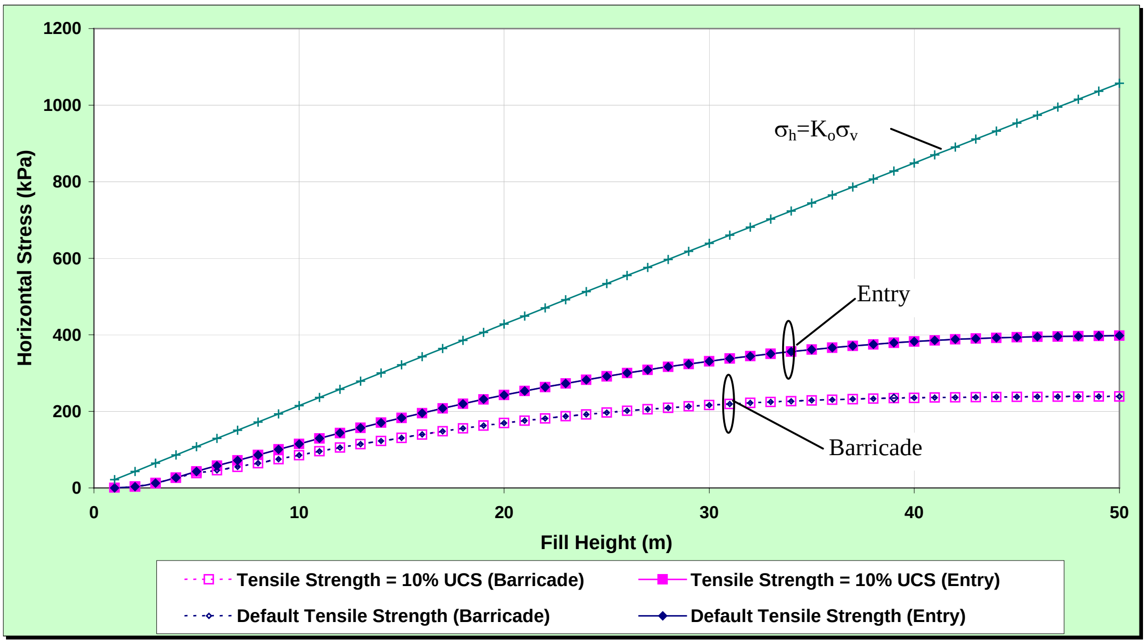

Figure 7. 12 Horizontal stress comparison for different tensile strength values.

The effect of arching in the stope can be identified by the difference between the $\sigma_h=K_o\sigma_v$ line and the lateral earth pressures line for “Entry” values. The additional reduction in the lateral loadings through arching in the drive is quantified by difference in the “Entry” and “Barricade” values. When the stope is full (H=50m), the barricade pressures are only 60% of the corresponding values of those at the entry, which matches the reduction of vertical stresses observed in a stope of equal aspect ratios.

7.4.4 Sensitivity of Barricade Pressure to Filling Rate

Filling rate (vertical meters per hour) was used to assess the effect of loading on barricades to negate the effect of fluctuations in stope geometry and filling rate.

Initially the average horizontal stresses were evaluated for the same geometrical conditions (i.e. base case = 15 m x 15 m x 50 m as in Figure 7.2). Figures 7. 13 and 7.14 show the effect of an increased filling rate on the averaged horizontal stress at the barricade and entry positions respectively.

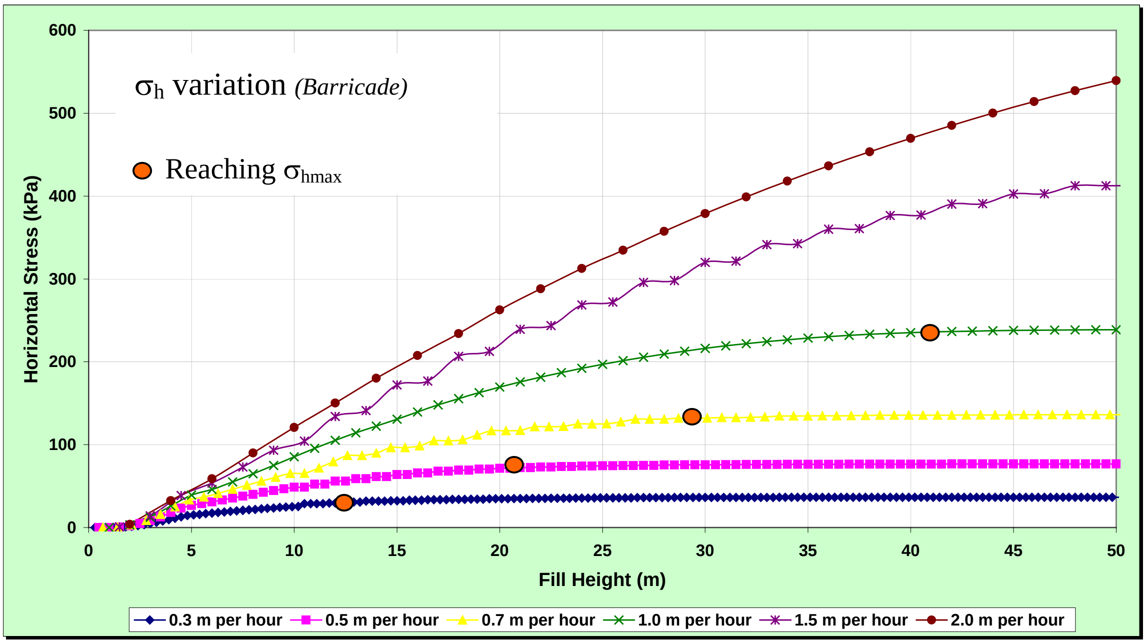

Figure 7. 13 Variation in horizontal barricade stress with paste filling rate.

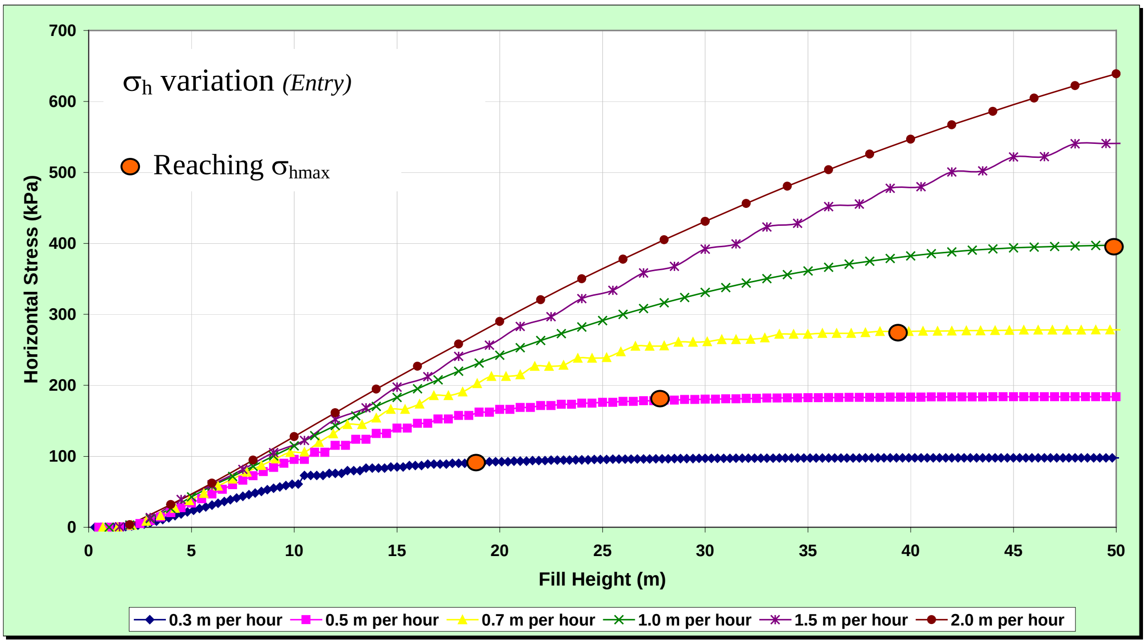

Figure 7. 14 Variation in horizontal drive entry stress with paste filling rate.

The ‘stepping’ characteristic shown in both graphs for the 1.5 m per hour filling rate results from numerical rounding of fill heights to accommodate the 1 m vertical grid spacing above the 10 m height of the stope. From these plots, it can be concluded that as the filling rates increase, so does the final horizontal stresses. The empirical industry standards suggests that filling should be capped at 10 % of the stope height per day or 0.3 m/hr, which ever is lower. These standards are shown to be very conservative from these results. For this example, this generic rule suggests filling should not exceed approximately 0.2 m per hour – this value is significantly lower than any of the fill rates investigated, and is shown to be very conservative. The second empirical industry standard often adopted within the industry with regard to filling rate, is that the stope filling rate should not exceed 10 m per day. For this simulation, this would equate to a filling rate of 0.416 m per hour, which is also shown to be excessively low, regardless of barricade position.

Barricades are not always constructed at either 0.5 m or 4.5 m from the face of the stope, as has been modeled. By analysing the variation in horizontal stresses throughout the drive, the effect of barricade location may be inferred.

As shown in both graphs (Figures 7.13 and 7.14), the average horizontal stresses plateau after a given period of filling, and this period increases with filling rate. This has been shown schematically using the orange dots on Figures 7.13 and 7.14 and the data collated in Table 7.2.

Table 7. 2 Critical fill heights used to determine σ_{hmax} for various fill rates.

Fill Rate * (vert. m/hr)	Critical fill Ht. H_c (m)		Critical Fill Time t_c (hrs))	
	Barricade	Entry	Barricade	Entry
0.3	12.5	18	42	60
0.5	21	27.5	42	55
0.7	29	38.5	41	55
1.0	41	50	41	50
1.5	*62.3*	*82.5*	*41.5*	*55.0*
2.0	*83.0*	*110.0*	*41.5*	*55.0*
		Average	***41.5***	***55.0***

* The equivalent height of overlying fill for filling rates of 1.5 m/hr and 2.0 m/hr could not be observed on Figures 7.13 or 7.14. The numbers presented are extrapolated from the trends observed for fill rates between 0.3 m/hr and 1.0 m/hr

Above this "critical fill height" of fill level, the stress doesn't increase, due to arching, and the additional fill height becomes irrelevant. The critical fill time is determined by dividing the equivalent fill height by the fill rate. The critical fill time is constant for all fill rates. The critical fill time factor, t_c, varies with barricade locations. By performing a regression analysis on the critical height data against the fill rate Figure 7.15 can be plotted.

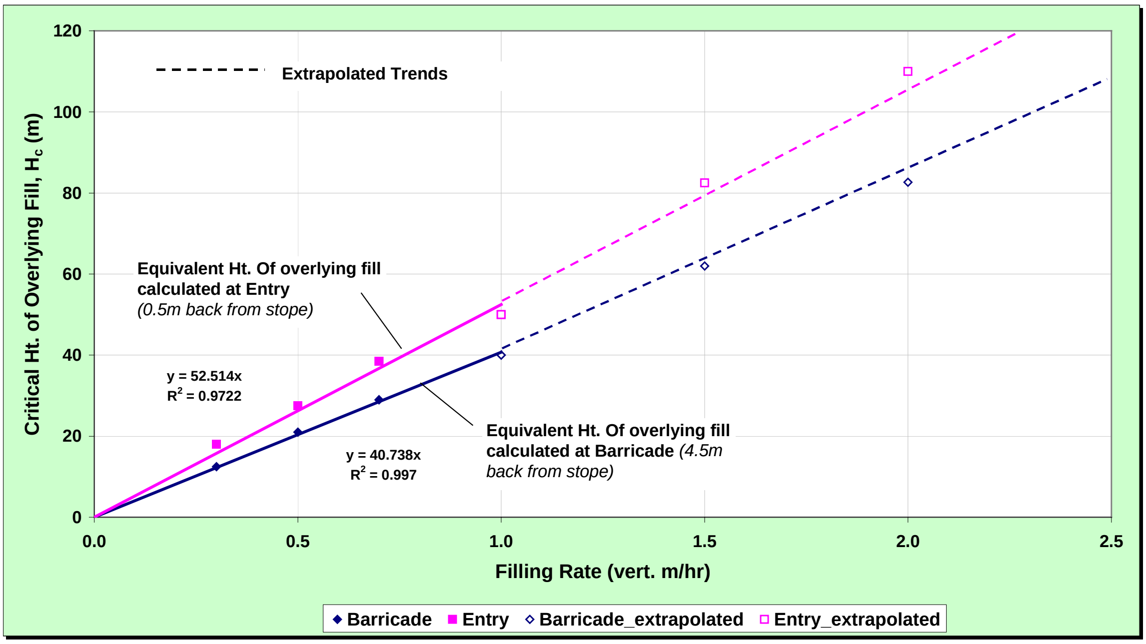

Figure 7. 15 Critical fill height as a function of filling rate

By setting the y-intercept at zero, simple linear equations to determine the critical height, H_c, can be obtained. The gradient of each line defines the critical fill time for the barricade and entry locations. The slightly different average values for t_c, from Figure 7.15 as compared to Table 7.2 is related to setting the y-intercept through zero. The difference in location of the two monitoring pointes allowed for a linear interpolation to determine the critical fill time factor, as shown in Figure 7.16.

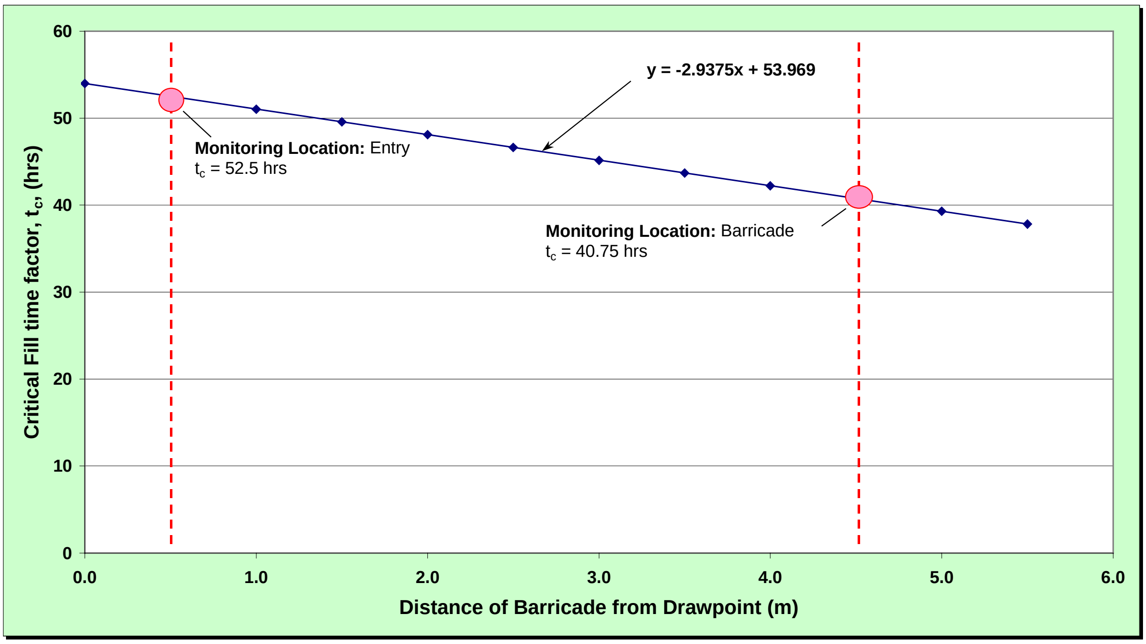

Figure 7. 16 Determination of critical fill time factor, tc as a function of barricade distance from draw point.

Equation 7.9 describes the determination of a constant critical height of fill as a function of fill filling rate and barricade location.

$$H_c = (54 - 3\bar{x})\ x\ (Filling\ Rate) \qquad \ldots(7.9)$$

Where

H_c = Critical height of overlying fill (m)

$\bar{x}$ = Distance from draw point of stope (m)

Filling Rate = Vertical height rise per hour of fill (m/hr)

This analysis gives an approximation for the maximum lateral stress on a barricade in a 15 m x 15 m x 50 m stope. The applicability of equation 7.9 to stopes of various plan dimensions is questionable. A factor to correct for geometrical considerations is required and is covered in Section 7.4.5.

To confirm that the critical fill height and time does in fact constitute the maximum lateral stress applied to the barricade, the 1 m per hour filling rate model was modified to simulate the filling and curing of both a 50 m and 100 m high stope. The resulting overlaying stress profiles in Figure 7.17, confirms this theory.

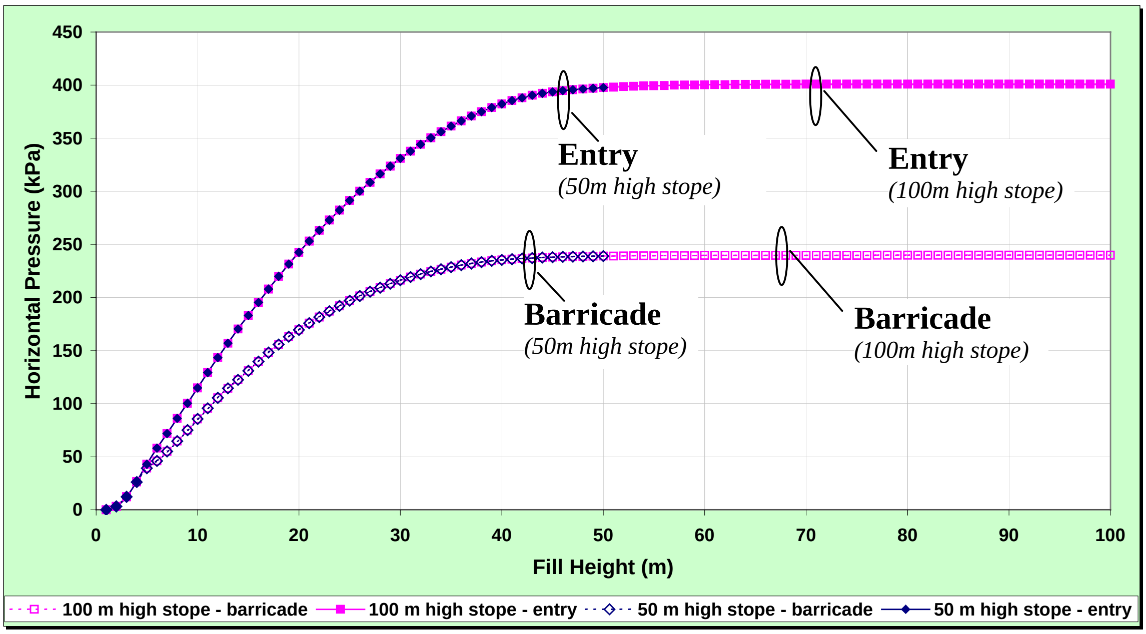

Figure 7. 17 Horizontal stress comparison between 50 m high and 100 m high stope. (filled at 1 m per hour)

To understand the development of lateral earth pressure on the barricade, Figure 7.18 was developed. It shows the variation in the average horizontal stress on the barricade against the filling rate for various fill heights. The variations in horizontal stresses on the barricade with filling rate are more pronounced with fill height, but at constant filling rate, the variation in horizontal stresses with increased tailing height reduces in magnitude. This plot provides a simple method of estimating the pressures on the barricade at a specific fill height, for any given fill rate between 0.3 and 2 m per hour.

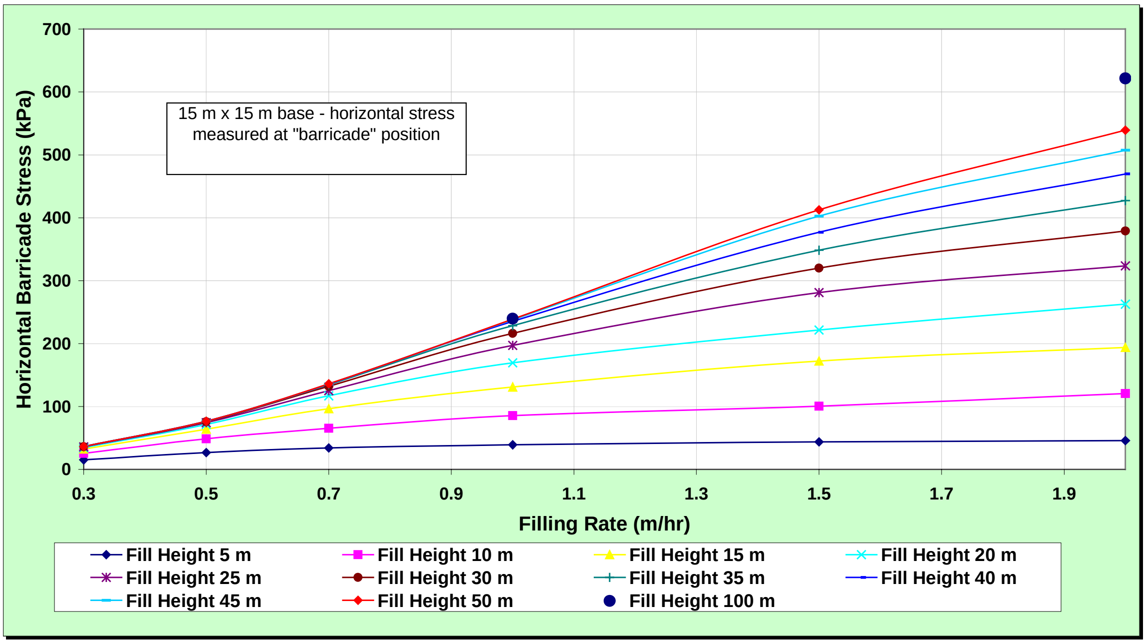

Figure 7. 18 Relationship between filling rate and horizontal barricade stress for various tailings heights.

7.4.5 Sensitivity of Barricade Pressure to Stope Geometry

A series of simulations were undertaken to investigate the influence stope geometry on the horizontal stresses applied to the barricade. Three runs were performed on stopes with square bases of 15, 25 and 35 m. The height was constant at 50 m and the filling rate was 1 m/hr. Figure 7.19 plots the average horizontal stresses at the barricade and drive entry, for each of the stopes.

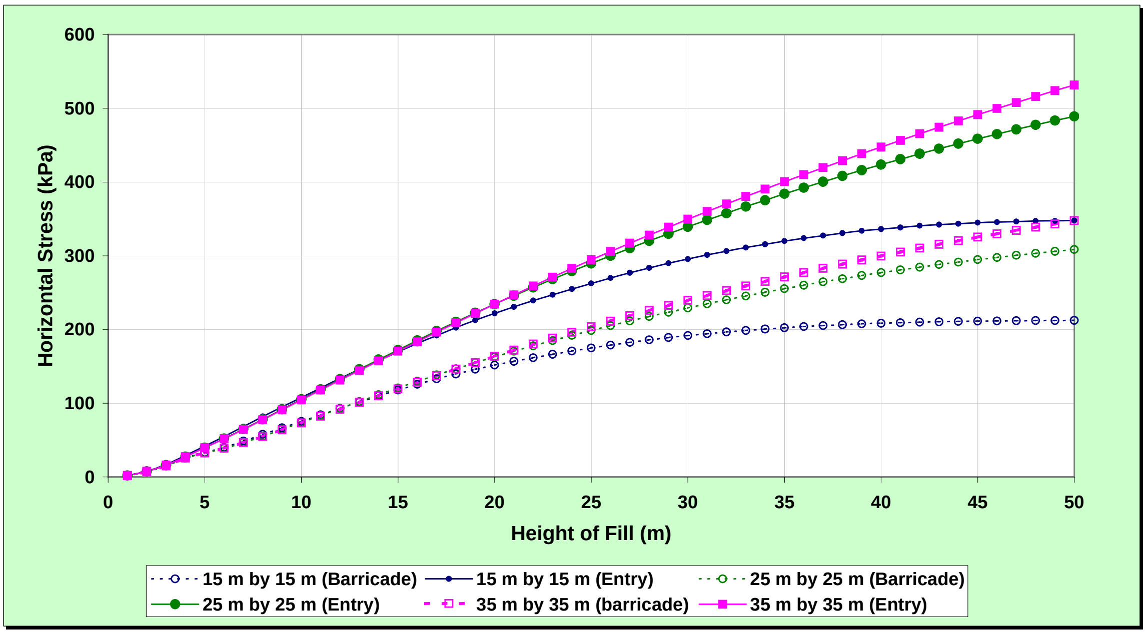

Figure 7. 19 Sensitivity of horizontal stresses to stope geometry.

This plot shows that by the time the fill has reached the 50 m level, the horizontal stresses have not converged for the stopes with a plan dimension of 25 or 35m, as they have for the 15m x 15m stope. If the simulations were undertaken for a stopes of a greater height, there would be a stage at which convergence would occur, as per Figure 7.17. The numerical model developed to study the barricades is a modification of the one used in the sensitivity analysis in Chapter 6 but focusing primarily on the very early strength of paste and so will calculate slightly different vertical and horizontal stresses values. To determine a satisfactory correction for geometry to horizontal stresses on barricades, the data from the sensitivity analysis was used. This was considered reasonable as the vertical stresses are related to the pressure on the through lateral earth pressure (K_o) theory. In the very early stages of curing, the paste typically has very low friction angles (ϕ_u<10), which results in K_o ~ 1, which further justifies the use of the stope geometry data. Table 7.3 show the data used to plot Figure 7.20. The stopes used to analyse the effect of stope geometry had a square bases of 18.75 m , 25 m and 37.5 m and base to height aspect ratios of 1,2,3 and 5.

Table 7. 3 Data used to determine effect of stope geometry on vertical stress

Base Plan Dimension B x B (m)	H/B	$\sigma_v/\gamma H$
18.75	1	0.52
	2	0.28
	3	0.19
	5	0.11
25	1	0.49
	2	0.27
	3	0.18
	5	0.11
37.5	1	0.55
	2	0.31
	3	0.21
	5	0.12

* H and B represent the height (m) of the stope and width (m) of the square base respectively. σ_v is the maximum vertical stress calculated at the base of the stope.

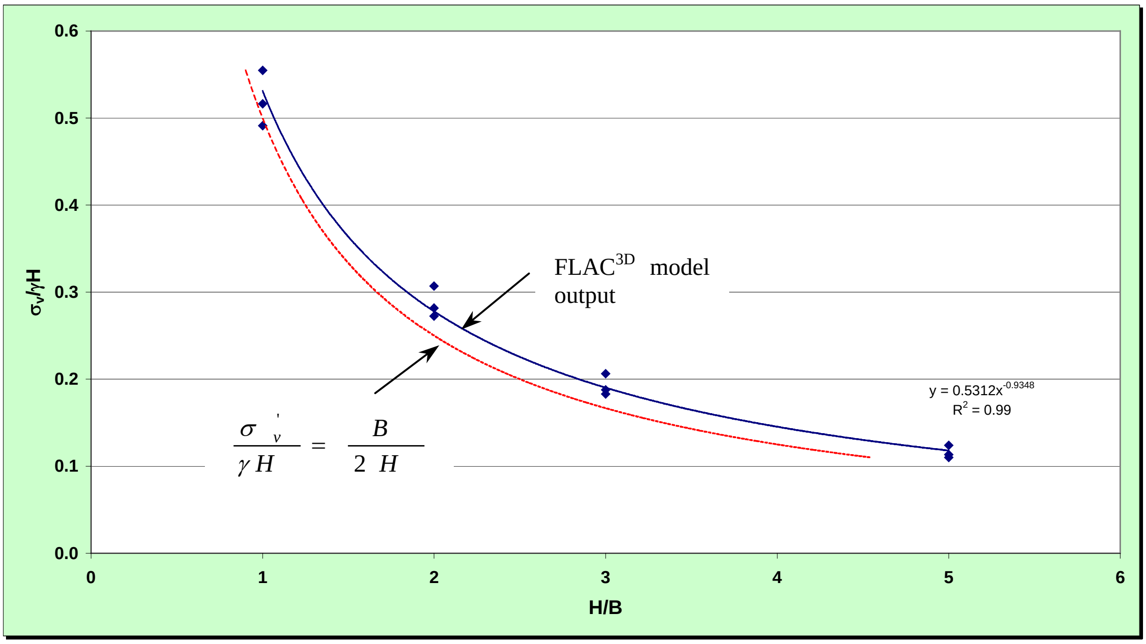

Figure 7. 20 Non – dimensional plot showing the effect of stope geometry on maximum vertical stress development in a square stope

The two profiles drawn on Figure 7.20 show the output from the FLAC^{3D} numerical model (blue), with a power-law trend line plotted through the data points and a assumed profile of $y = \frac{1}{2x}$ in red. The equation of the assumed profile was used to determine the effect of geometry on lateral earth pressures. The variation between the assumed profile and the ones obtained through FLAC^{3D} modeling shows that material properties are a secondary consideration for the arching mechanism.

From Figure 7.20

$$\frac{\sigma_{v\max}}{\gamma H} = \frac{B}{2H} \qquad \ldots(7.10)$$

therefore: -

$$\sigma_{v\max} = \frac{\gamma B}{2} \qquad \ldots(7.11)$$

and

$$\sigma_{h\max} = \frac{K_0 \gamma B}{2} \qquad \ldots(7.12)$$

Equation 7.12 suggests some interesting facts in that the maximum vertical (or horizontal) stress is dependent only on the plan width of the stope. Chapter 6 showed that the increase in vertical stress when the arching mechanism was transferred from 3-dimensions to 2-dimensions, was in the order of 15-20%. this suggests that the minimum stope plan dimension, would be the critical variable in the determination of the maximum vertical stress.

To determine the effect of geometry on the lateral earth pressures, one may simply provide the ratio of equation 7.12 for the proposed stope over the existing. Equation 7.12 reverts to the simple ratio of the plan dimensions.

$$\frac{\sigma_{h1}}{\sigma_{h2}} = \frac{B_1}{B_2} \qquad \ldots(7.13)$$

Incorporating Equation 7.13 into 7.9 the critical height of overlying fill may be obtained.

$$H_c = \frac{B_1}{B_2}\left(54 - 3\overline{x}\right) x \left(Filling\ Rate\right) \qquad \ldots(7.14)$$

Knowing that the analysis was performed for a 15 m x 15 m x 50 m stope, 7.14 may be written more specifically as:-

$$H_c = \frac{B_1}{15}(54 - 3\overline{x})\ x\ (Filling\ Rate) \qquad \ldots(7.15)$$

A more generic approach to the determination of the pressure exerted on barricades will be supported by additional numerical modeling of barricades in various locations, in stopes of various geometries.

7.4.6 Mode of Failure

A distinct pattern in stress distribution across the barricade was evident, which was consistent with the 'punching' failure mechanism reported from in-situ failures (Kuganathan, 2001, Cowling 2003, Bloss 2003). Figure 7.21, shows contours of the stress distribution computed across the barricade when the stope was full, and the stress profile fully developed. The stress intensity increases toward the base of the barricade, which is expected as a result of gravitational forces. This pattern was evident and consistent for during filling for all simulations.

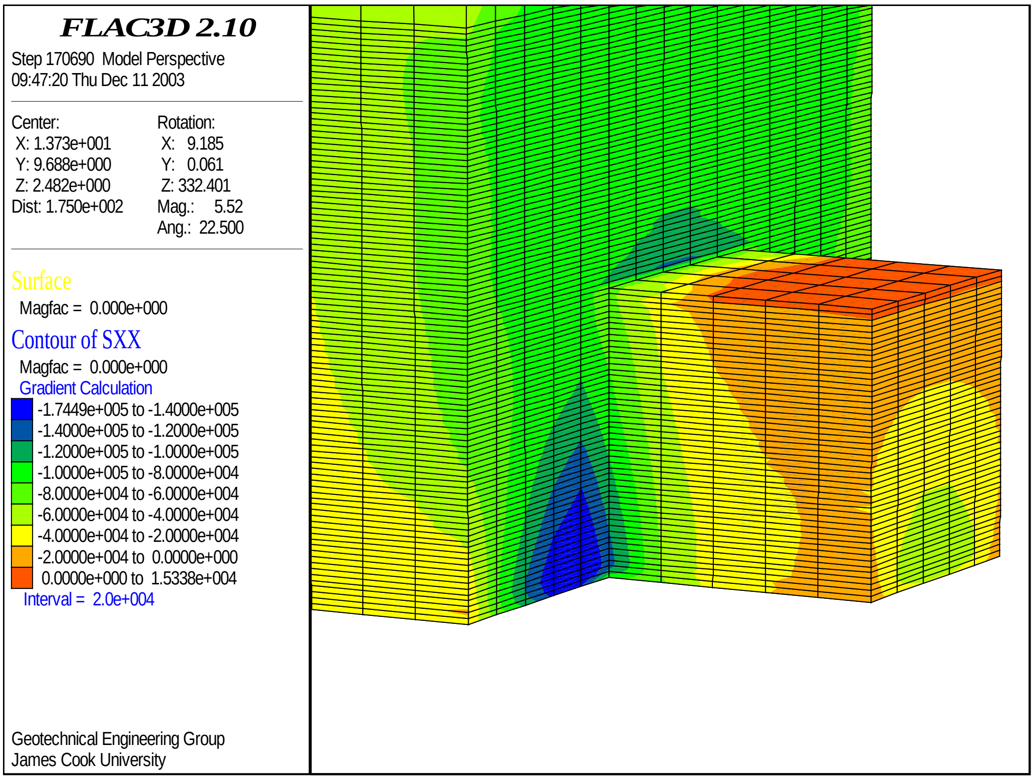

Figure 7. 21 Horizontal stress gradient across barricade for 0.3 m per hour filling program at 50 m tailings level (contours at 20 kPa intervals; the negative sign implies compression)

7.5 Conclusions

The main outcomes from numerical modeling of the barricades has been summarized as :-

- The major factors affecting the maximum lateral load on the barricade are: filling rate, barricade location and stope geometry.
  - Lateral pressures on barricades increase with an increase in filling rate/ The increase in filling rate, relates to the amount of paste which exerts pressure on the barricade wall before curing to a strength capable of supporting its own mass.
  - The position of the barricade within the drive has a significant impact on the horizontal pressures exerted on the barricade. The further from the stope entrance (draw point), the more transfer of loads through arching into the drive walls, the lower the horizontal stresses applied to the barricade.
  - As the plan dimension of the stope increases so to does the maximum vertical stress applied to the barricade.
- Arching in a fill mass is predominantly based on geometry. Material properties are a secondary consideration in the arching mechanism.
- The critical height of overlying fill, Hc, may be used to describe the maximum vertical stress applied to a barricade. Equation 7.15 which describes H_c as a function of stope geometry, filling rate and barricade location takes the form:-

$$H_c = \frac{B_1}{15}\left(54 - 3\bar{x}\right) x \left(Filling\ Rate\right)$$

- Horizontal stress profiles on the barricade replicate the failure pattern observed in-situ, with “punching” failure, which has been observed by a number of field practitioners.
- Additional investigations are required to improve the understanding of: -
  - Effect of the curing of fill on barricade pressures. Should a reduction in the applied pressure be observed?

- Effect of the curing of the fill barricades themselves (aquacrete/ shotcrete etc.) and interaction of the barricade strength requirements when related to the applied loading.
- Location of barricades: -
  - Across the base of the stope. Loading of barricades located in the corner of a stope as opposed to centrally
  - Additional setback distances from the draw point (so that a trend of the applied lateral stresses may be observed with distance)

➢ The developed numerical model suggests lateral earth pressured on barricades converge to a constant value and remain there, regardless of the effect of curing. This is not correct, and it is suggested that the convergent value is of equivalent magnitude to a peak value for design purposes, which would reduce as the paste cured.

➢ Validation: It is considered pertinent to investigate the accuracy of the modeling contained within this chapter by validating it with in-situ data.

7.6 Summary

This chapter reviews the development and application of a numerical model of paste filling against barricade walls. It reviews the effect of filling rate, stope geometry and barricade position on the development of lateral earth pressures and indicates the build up of pressure behind the walls, which indicate the likely mode of failures.

Arching in the stopes and behind the barricade walls has been shown to be a geometry effect more than a material effect. The filling rate of the stopes determines the initial stress condition in the stope, which is critical in stope barricade design. As the filling rate increases so to does the initial stress condition. The minimum plan dimension of the stope is the critical variable for the development of arching within a backfilled stope and prediction of the maximum vertical and horizontal stresses.

Final Note

Numerical modeling is not intended as an exact replication of the design problem. It is used to precisely present the numerical value of stresses and strains within the system. It is a simplification of reality, used as an intellectual means by which understanding into the behaviors of the system may be gained. As test procedures develop and the accuracy of input data increases so too will the accuracy of the modeling results – within the limitations of irregularity that occurs naturally within all geotechnical situations. The data presented in this document is provided as a tool for design, not an instruction.

Chapter 8

Summary, Conclusions and Recommendations

The chapter presents a summary of the research carried out in this dissertation, conclusions and recommendations for future research.

8.1 Summary

A review of previous research conducted into the geotechnical characteristics of paste fill and common approaches for the determination of the maximum vertical stress in stopes were presented. This review showed that current stope design procedure is largely based of the use of an analytical design method (Winch 1999, Mitchell 1981) to determine σ_{vmax}, which is used in conjunction with site based UCS testing to determine the backfill required for a specific stope. A number of analytical methods were covered in detail, as were the empirical correlations used to define the UCS of various backfills. A number of limiting assumptions are typically used with the analytical models to simplify the problem and thus make a solution possible. It is suggested that the limiting assumptions used in the analytical approach may be reduced with the use of an appropriately constructed and developed numerical model. Similarly the predictive ability required for the determination of a suitable fill mix may be improved by the use of artificial neural networks as opposed to the previously defined empirical correlations.

To achieve the improvements outlined above, a thorough geotechnical characterisation of the paste fill and surrounding ore body was conducted. The geotechnical characterisation of the paste was achieved using an extensive laboratory test program. Undrained strength parameters were determined for the paste for curing times of one hour to one year. Drained characteristics were also determined for the paste fill. The laboratory test results were then compared and the accuracy validated against in-situ paste using a series of DCP test results and UCS testing of paste fills samples taken from two different stopes. The liquefaction potential of paste fill was also addressed. The results from the geotechnical characterisation of the paste fills were used as inputs to both the artificial neural networks and the numerical models developed as part of this dissertation.

The strength and deformation characteristics of the surrounding ore body were done to provide inputs into the 3-D numerical model, which was also developed as part of this dissertation. Additional analysis was performed on the rock types to identify some indicative test methods which could be used by geotechnical engineers on site to simply and easily characterise the rocks as either ore or waste, based on the strength and deformation characteristics. They also provide inputs to the numerical model assessing the dynamic stability of backfill, another dissertation by a colleague – based on the same material.

Artificial neural networks (ANN's) were then introduced and used as a tool to characterise the paste fills with a high degree of accuracy and repeatability. The ability of the ANN's at predicting backfill strengths was tested at different levels of resolution by employing them to identify the strength of various backfill types from around the world and then specifically to other paste fills from around the world. The trained neural networks were able to predict the strength of the various types of backfills and paste fills with an r^2 value of 0.9 for each, which is significantly better than the best approximations to date (Fagerlund 1977, Swan 1985).

A 3-Dimensional numerical model was developed in FLAC^{3D} to model the sequential extraction and filling of the idealised nine-stope grid arrangement. The numerical accuracy of which was validated by comparing the results to the previously validated model presented by Bloss (1992). The vertical stress in the primary stope was measured throughout the mining cycle to identify the changes in the vertical stress profile. A sensitivity analysis of the grid mesh density and boundary conditions were done to ensure the accuracy and efficiency of the model. The variation of the maximum vertical stress with stope geometry and properties of the backfill was found for various base to height and width to depth aspect ratios. The effect of the variation of the input material properties was also determined. The output, σ_{vmax}, from each of these runs was used as inputs into another ANN that was used to predict σ_{vmax} from the user defined inputs.

The "integrated model" was proposed as a tool for the determination of the optimum cement content for each stope, from user defined inputs. The integrated model uses the user defined stope geometry to determine $\sigma_{vmax.}$ The ANN based on the long term strength of Cannington paste fills was then used to predict the required cement content to ensure stability for each exposure given the time of exposure and the solids content of the mix. Stability was assumed to occur when $UCS \geq \sigma_{v\max}$. This assumption is conservative in nature, but reasonable. The defined solids content for the paste fill mix will be defined by the paste rheology required to ensure placement of the paste, without blocking the reticulation system. The rheological characteristics of paste fall outside the scope of this thesis, but have been investigated by a number of researchers (Clayton 2002, Pullum 2003). The results showed a reduction in the cement content required for stability of paste filled stopes than current requirements by approximately 10%. The integrated model approach is considered to be state of the art and to define the most complete and holistic approach to backfill design to date.

The stress developments within the stope and the subsequent loadings on barricades are very poorly understood. Numerical modelling of the filling of a stope was conducted to identify the factors that contribute to the development of pressure on the barricades. The largest contributions to barricade pressure were made by stope geometry, filling rate and barricade location. A simple equation relating these factors was developed and presented. The knowledge of the lateral loadings on fill barricades allows for the engineering design of these barricade and the reduced potential of failures such as those which occurred at Bronzewing Mine in 2000 killing three miners (Minerals Council of Australia 2000, Grice 2001).

8.2 Conclusions

The conclusions drawn from the research are broken down into sections corresponding to the chapters of this thesis.

Geotechnical Characterisation: - *Paste Fill*

A complete geotechnical characterization of Cannington Paste fill was completed as part of this dissertation, and is discussed in detail in Chapter 3. A number of important outcomes are:-

- Paste fills share similar geotechnical characteristics and behavior as other lightly cemented soils (Saxena and Lastrico 1978, Mitchell and Katti 1981, Clough et al. 1981, Tatsuoka and Kobayashi 1983, , Kaga and Yonekura 1991,Maher and Ho 1993 and Schnaid et al. 2001).
- The undrained parameters are the most appropriate to use in the geotechnical stability analysis of paste fill. The undrained friction angle, ϕ_u, is not zero, as was previously assumed but increases with cement content, solids content and curing time. A significant increase in UCS, c_u and ϕ_u, is observed for all fill mixes after six months, which was accompanied by an increase in the air void content of the paste.
- Paste gains strength after the currently prescribed 28-day limit. Designs based on the 28-day strength may be conservative if there is additional curing time available for strength development. This strength gain in the paste was observed for the full year of testing completed.
- Laboratory testing provides a reasonable approximation to in-situ strength of paste as was verified by the comparison of the results of the in-situ and laboratory tests.
- Anecdotal evidence from the DCP testing suggests that consolidation of paste occurs with increasing depth and centrality to the stope. Preliminary test work shows that paste consolidated under surcharge show characteristics consistent with higher solids density samples. Additional anecdotal evidence supports the

"drying out" of the paste fill after a period of six months or more. The reduction in the moisture content of the paste increases the UCS.

- In-situ moisture content is required to determine the approximate in-situ strength of the paste fill. An increase in moisture content in paste results in the premature failure of samples.
- Unbound tailings have a high liquefaction potential, however, when bound by cement, or some other form of binder, the liquefaction potential is reduced significantly.

Geotechnical Characterisation: - *Cannington Deposit*

The characterisation of the different rock types into "ore and potential ore" and "waste" can be done using:-

- Density testing
- Classifications published by Deere et al. (1966).
- UCS testing. The rock types with lower UCS strengths was composed of the non-economic mineralisations (SHMU and GNES) and the ore type GH – *a very high grade brecciated ore*). Economic mineralisation types tended to have higher UCS strengths.

Correlations found during testing included:-

- Linear correlations were found for UCS and Young's Modulus (Et) values, failure strains (ε_f). The relationships took the form:-
  - UCS = 317.9ε_f – 60.86 (for 0.3% <ε_f < 0.9%)
  - UCS = 8.343E_{s50}-79.33 (for 13GPa< E_t < 36GPa), both of which are measured in Mpa.
- Point load testing; the global conversion factor of UCS=24 x $I_{s,50}$ (Bieniawski 1974) was found to be inappropriate to describe the different mineralisation types found at Cannington Mine. Individual factors were found and ranged between 9 to 35.
- The Brazilian test was used to investigate the indirect tensile strength (σ_t)of the mineralisations. Ratios of $\frac{UCS}{\sigma_t} = \frac{1}{5}\ to\ \frac{1}{17}$ were found during testing which was in reasonable agreement with previous findings by Griffith (1921).

- The average Poisson's Ratios found from testing ranged between 0.09 (AMPH) to 0.26 (GNES). The overall average for all mineralization types was $\nu = 0.16$. The results from testing correlate well with previously published data and indicate Cannington rock types, have a comparatively low Poisson's ratio.

Artificial Neural Networks

- ANN's provide an effective means of predicting fill strengths within the bounds of the input data currently available. The performance of the neural network improved with the delineation of data into three groups, effectively trimming the data to the specific purposes. Outliers from each of the sets were also trimmed, increasing the networks performance.
- Mix fill proportions govern the outputs from the networks developed for Cannington paste fill. The effective predictive tool for backfill strengths currently available, when compared to the myriad of empirical and semi-empirical correlations currently being used such as that by Bloss 1992. Cement content, solids content and curing time were the factors, which affected the strength of the paste, fill most significantly, with the grain size (P80) and also contributing to strength.
- Data was smoothed heavily for each of the networks created, indicating that the networks will provide good general solutions, but may not predict specifically for inputs.
- The development of PASTEC provides a tool for the prediction of Cannington paste fill strengths and characteristics. The correlations provide a high degree of accuracy, typically being able to predict with $r^2 > 0.9$. A centralised summary of the information to date on paste fill will provide a higher degree of confidence and reliability for the design of paste backfills and exposures.
- The predictive ANN modelled for the various paste fills and backfills from around the world show moderately poor to very poor predictive abilities when applied to Cannington paste fill. Suggesting that global predictive tools are inapplicable to Cannington fill. This finding suggests that Cannington should then derive site specific tools for the prediction of fill strength.

Numerical Modelling of paste filled stopes

- The maximum vertical stress in a stope increases with depth, centrality and reduced levels of confinement. A reduction in the confinement is associated with the sequential changing of the confining walls from rock to paste, as the mining sequence moves through the idealised nine-stope grid arrangement
- Arching potential is defined as: - $Arching\ Potential = \left(\frac{\rho hg - \sigma_v}{\rho gh}\right) x100\%$. The arching potential of paste-paste contacts ranges between $\frac{1}{3}$ *to* $\frac{2}{3}$ of the arching potential of that observed for paste-rock contacts. Winch (1999) suggested that the fill-fill contacts provided only one-quarter of the support provided by rock-fill contacts. There is an increase in maximum vertical stress of approximately 15% as the support mechanism moves from 3-D arching to 2-D arching between rocks.
- Arching is predominantly a geometrical effect. Material properties, with the exception of the bulk density and Poisson's ratio of the material, have limited effect on the development of the vertical stresses. The minimum base dimension is the critical factor in the determination of the maximum vertical stress in the stope. The maximum vertical stress in stopes of a square plan dimensions may be calculated using: - $\sigma_{v\max} = \frac{\gamma W}{2}$. In a stope which does not have a square plan dimensions, it may be calculated using: - $\sigma_{v\max} = \frac{\gamma H}{2MW}(2D - W)$, where M is the gradient of the trend line on the line on the non-dimensionalised plot of D/W against $\sigma_v/\gamma H$
- The integrated model approach to backfill design provides the most holistic and complete approach to backfill design to date. It provides a method for the determination of the optimum cement content for each paste fill mix, depending on user defined input parameters for the stope geometry, material bulk density, curing time available to each exposure (1st – 4th) and solids density. The solids density information is expected to result from the rheological requirements for the placement of paste.

Numerical Modelling of Fill Barricades

- The major factors affecting the lateral stress development behind barricades are: filling rate, barricade location and stope geometry. When combined and related to a an equivalent "critical height" of overlying fill they take the form:-

$$H_c = \frac{B_1}{B_2}\left(54 - 3\overline{x}\right) x \left(Filling\ Rate\right)$$

The "critical height," H_c, of overlying fill referrer to the height of fill above which, there is no additional increase in lateral loading on the fill barricade.

8.3 Recommendations for Future Research

While there have been considerable advancements in understanding the geotechnical characteristics and behavior of paste fill, there are many areas that are deserving of further study. The recommendations outlined have been presented under the same titles as they were presented in this dissertation

Geotechnical Characterisation: - *Paste Fill*

- A refinement of the trends for the early strength gains of paste fill
- Long term strength testing of higher solids density backfills
- Further validation of laboratory results with in-situ tests
- Further investigations into the effect of consolidation on fill masses and arching
- Determination of a minimum cement content for paste fills to restrict the onset of liquefaction through any seismic activity. Assessment of the 100 kPa limit suggested by Cough et al. (1989)
- Alternative binders and their effect on strength, geotechnical characteristics etc.
- The effect of additives used for the modification of paste fill rheology and their effect on stability. There is a trend for those who are studying the rheology not to study the effect on stability and visa-versa. This must be addressed – lest the efforts and expense of research end in a fruitless exercise.

- Investigation and development of a generic flow model for paste fill systems which may be integrated with the static stability data presented within this dissertation, which would provide for a more holistic approach to backfill design
- A standardized set of test methods, sample size, preparation, documented information etc. to be proposed and adopted, such that information from paste fill mines around the world could be used to better understand the fill properties and advance the current position
- A geotechnical database of the information from the proposed "standardized testing" to be established to provide information for research.
- Monitoring of the vertical stresses down the exposed face of the stope. This would require interface elements to be part of the model, as the value of the vertical stress is averaged from the eight nodes of each cubic zone. Thus without interface elements, the zones which are immediately adjacent to rock would have the value of σ_v distorted by the higher values in the rock or stiffer support material. By measuring the vertical stress down the face of the stope, the actual cement content required to prevent σ_v or σ_h causing failure could be determined.

Geotechnical Characterisation: - *Cannington Deposit*

- Cannington rock types vary in material characteristics significantly, and are moulded into a complex cocktail which constitutes the ore body and the structure for the mine workings. A series of tests were performed on various rock types and some defining characteristics identified. To further this, it is proposed that a database of the current information be established. The data has been incorporated into the PASTEC program outlined in Chapter 3. The data from this and any other test work should be included in the overall database. This would allow for a more tailored approach to the stability of the open stopes, using specific material characteristics, as opposed to generic material properties, which currently occurs.

Artificial Neural Networks

- Further testing for international paste fills, and various forms of fill.
- Inclusion of the moisture content of paste as an input for the ANN's.
- The accuracy of the network should be tested every six months to ensure that the input characteristics have not changed (such as the P80).
- An audit of the most appropriate neural network architecture and learning algorithm should be conducted.
- Additional investigation into the use and applicability of the cascade correlation-learning algorithm for the neural networking conducted within this dissertation.

Numerical Modelling of paste filled stopes

- Additional modelling to be carried out on various stope aspect ratios B/H and W/D. The vertical stress in the middle of the stope to be monitored and the recorded.
- Interface elements to be introduced along expected failure zones. The applicability and value of these elements is contentious, however if an accurate definition of input parameters were able to be done, the inclusion would be justified and provide an increased level of accuracy.
- Effect of closure strains on the stability of paste filled stopes.
- The potential usage of layered zones of varied cement contents to meet strength requirements for paste filled stopes.
- Modelling of the bearing capacity of paste fill. (i.e. the value of paste fill as a "working surface" for underground personnel and machinery.
- Modelling the cement content required for the "plugs" of paste which are installed when either the paste is to be exposed from underneath or, when access through the high strength cement plug is required for production requirements, (i.e the draw point through the paste fill)
- Change the default tensile strength of geo-materials in $FLAC^{3D}$ from $t=c/\tan\phi$ to a value in the range of t=1/10 of UCS, otherwise results may not be representative of what is actually occurring.

Numerical Modelling of Fill Barricades

- Effect of the curing of fill on barricade pressures. A reduction in the applied pressure be observed?
- Effect of the curing of the fill barricades themselves (aquacrete/ shotcrete etc.) and interaction of the barricade strength requirements when related to the applied loading.
- Location of barricades: -
    - Across the base of the stope. Loading of barricades located in the corner of a stope as opposed to centrally
    - Additional setback distances from the draw point (so that a trend of the applied lateral stresses may be observed with distance)
- The developed numerical model suggests lateral earth pressured on barricades converge to a constant value and remain there, regardless of the effect of curing. This is not correct, and it is suggested that the convergent value is of equivalent magnitude to a peak value for design purposes, which would reduce as the paste cured.
- Validations of the modeling accuracy of fill barricades with in-situ data.

References

1 Abu Kiefa, M.A., (1998). “General Regression Neural Networks For Driven Piles In Cohesionless Soils”, *Journal of Geotechnical and Geoenvironmental Engineering*, Vol 124, pp 1177-1185

2 Aleksander, I., & Morton, H. (1990). *An Introduction to Neural Computing*, Chapman and Hall: London.

3 American Barrick Resources Inc. (1995). “Macassa Mine Tailings-A preliminary Assessment for use as paste backfill,” *Report by The Inco Underground Paste Backfill Research Centre*

4 Anon. A. (1994). “Preparation and Transportation of Paste Backfill,” M.S. thesis, McGill University, Montreal, Quebec, Canada.

5 Aref K., and Hassani, F.P. (1988). “Strength Characteristics of paste backfill.” *Proceeding from the Conference on Applied Rock Engineering*, Newcastle-upon-Tyne, 1998, pp 4-8

6 Aref K., Hassani, F.P., and Churcher D. (1989). “A study on the liquefaction potential of paste backfill”, *Innovations in Mining Backfill technology, Proc. 4th International Symposium on Mining with Backfill*, Montreal, 2-5 October, 1989, A.A. Balkema, pp.405-415

7 Arioglu, E. (1983). “Engineering properties of cemented aggregate fill for Uludag tungsten mine of Turkey,” *3rd International Symposium on Mining with backfill*, Lulea, Sweden 3-8, (Balkema: Rotterdam)

8 Arnold, M. (1999). “Artificial Neural Networks Applied To The Prediction Of Settlements Of Shallow Foundations In Granular Soil,” M.S. (Engineering) thesis, James Cook University, Townsville, Australia

9 Arnold, M., & Sivakugan, N. (1997). “Artificial Neural Networks Applied To The Prediction Of Settlements In Sands,” *Proceedings of the Second International Symposium on Structures and Foundations in Civil Engineering*, Hong Kong

10 AS 4133.4.3 (1993). “Methods of testing rocks for engineering purposes; Rock strength tests – Determination of deformability of rock materials in uniaxial compression,” Australian Standards, Committee CE/9, Testing of Soils for Engineering Purposes (1993), 8 pp.

11 Askew, J.E., McCarthy, P.L., & Fitzgerald, D.J. (1978). "Backfill research for pillar extraction at ZC/NBHC," *12th Canadian Rock Mechanics Symposium on Mining with Backfill*, Sudbury, Canada, 85-91. (CIM:Montreal)

12 Atterberg, A. (1911). "The behaviour of Clays with Water, their Limits of Plasticity and their Degrees of Plasticity," *Kungliga Lantbruksakademiens Handlingar och Tidskrift*, Vol. 50, No. 2, pp. 132-158

13 Aubertin, M., Li, L., Arnoldi, S., Belem, T., Bussiere, B., Benzaazoua, M. & Simon, R. (2003). "Modelling arching effects in narrow backfilled stopes with FLAC", *3rd International Symposium on FLAC and FLAC3D Numerical Modelling in Geomechanics*, Ontario, Canada

14 Barrett, J.R., Stewart, J.E., Brock, J.G. (1983). "Cemented gravel fill for a small underground mine," *3rd International Symposium on Mining with backfill*, Lulea, Sweden 69-78, (Balkema: Rotterdam)

15 Barsotti, C. (1978). "The evolution of fill mining at the Ontario Division of Inco Metals", *12th Canadian Rock Mechanics Symposium on Mining with Backfill*, Sudbury, Canada, 37-41. (CIM:Montreal)

16 Been, K., Brown, E.T., Hepworth, N. (2002). "Liquefaction Potential of paste fill at Neves Corvo mine, Portugal," *Transactions of the Institute of Mining and Metalurgy (Sect. A: Mining Technology)*, 111, January-April

17 Berardi, R., and Lancellotta, R. (1994). "Predictions of settlement of footings on sand: Accuracy and Reliability," *Proceedings of Settlement '94, Geotechnical Special Publication No 40, ASCE*, A.T. Young and G.F. Felio, pp 640-651

18 Berry, P. (1981). "Geomechanical Investigations for the Design of Cemented Fill." *Symposim on the Application of Rock Mechanics to Cut and Fill Mining*, Lulea, Swede, 1980 (Ed. O.Stephansson and M.J.Jones), pp 190-192 (IMM. London)

19 Bieniawski, Z.T. (1974). "Geomechanics classification of rock masses and its application in tunneling," *Proc. Third Int. Congress on Rock Mechanics*, ISRM, Denver 1974, pp.27-32.

20 Blight, G.E. (1986). "Pressure exerted by materials stored in Silos. Part I:

Coarse materials," *Geotechnique*, 36(1):33-46

21 Bloss, M.L. (1992). "Prediction of cemented rock fill stability – design procedures and modeling techniques," PhD dissertation, The University of Queensland, Brisbane, Australia

22 Bloss, M.L. (2003), *Personal Communication*

23 Bloss, M.L., & Chen, J. (1998). "Drainage Research at Mount Isa Mines Limited 1992 – 1997," *MINEFILL '98, 6th International Symposium on Mining with Backfill*, AusIMM, Brisbane, April 1998

24 Bloss, M.L., & Greenwood, M.L., (1998). "Cemented rock fill research at Mount Isa Mines Limited 1992 – 1997," *MINEFILL '98, 6th International Symposium on Mining with Backfill*, AusIMM, Brisbane, April 1998

25 Bock, H. (1984). "Experimentation with the German Dynamic Probing Technique on the Great Barrier Reef," *4th Aust-N.Z. Conference on Geomechanics*, Perth

26 Bodon, S. B. (1998). "Paragenetic relationships and their implications for ore genesis at the Cannington Ag-Pb-Zn deposit, Mount Isa Inlier, Queensland, Australia," *Economic Geology, 93*: 1463-1488.

27 Bowles, J.E. (1995). "*Foundation Analysis and Design.*" McGraw-Hill Science/Engineering/Math; 5th edition (September 1, 1995),

28 Brackebusch, F.W. (1994). "Basics of Paste Backfill Systems," *Mining Engineering*, **46(10)** Society for Mining and Metallurgy and Exploration Inc. Littleton, USA, pp 1175 - 1178

29 Brady, A., (2001). "Point Load Strength versus Laboratory Unconfined Compressive Strength - Determination of Conversion Factor" *Mining, report for Placer Pacific Osborne Copper-Gold Project*

30 Brady, B.H.G. and Brown, E.T. (1985). "*Rock Mechanics for Underground Mining,*" George Allen & Unwin (Publishers) Ltd., London; 2nd Edition: 1993..

31 Brown, E.T. (1981). "*Rock Characterisation Testing and Monitoring, ISRM Suggested Methods*", Pergamon Press,

32 Brown, E.T. (1987). *"Analytical and Computational Methods in Engineering Rock Mechanics,"* (Allen and Unwin: UK) pp 259

33 Brown, T.A., and Heuze, F.E. (1979). "A new System for High

Temperature Triaxial Creep Testing of Rocks," *Proceedings, Twentieth U.S. Symposium on Rock Mechanics*, Austin, TX, ASCE, New York

34 Budavari, S. (1983). "Response of the Rockmass to excavations underground," *Rock Mechanics in Mining Practice*, Monographs Series Vol 5,(Ed: Budavari), South African Institute of Mining and Metallurgy: Johannesburg, pp 55 – 76

35 Casagrade, A. (1948). "Classification and Identification of Soils," *Transactions ASCE*, Vol. 113, pp 901-930

36 Casagrande, A. (1932). "Research on Atterberg Limits of Soils," *Public Roads*, Vol 13, No. 8, pp121-136

37 Clark, I.H. (1986). "The properties of hydraulic backfill," *Proceedings from the Symposium on the properties of backfill*, SAIMM and AMMSA

38 Clayton, S. (2000). "Characterisation of Mine Stope Fill "– *Progress Report, BHPBILLITON World Minerals – Cannington*, Particulate Fluids Processing Centre, Dept. Chem. Eng., University of Melbourne, Sep 2000, unpublished

39 Clayton, S. (2002), "*Paste Rheology and it's Application for Mine Stope Fill*", Ph.D dissertation, University of Melbourne, Victoria, Australia

40 Clough, G.W., Sitar N., Bachus, R.C., and Rad, N.S. (1981). "Cemented sands under static loading," *Journal of Geotechnical Engineering Division, ASCE*, 107(6), 799-817.

41 Clough, GW, Iwabuchi, J, Rad, NS and Kuppusamy, T. (1989). "Influence of Cementation on liquefaction of sands," *Journal of Geotechnical Engineering*, 115(8):1107-1117

42 Cowin, S.C. (1977). "The theory of static loads in bins," *Journal of Applied Mechanics*, 44:409-412

43 Cowling, R. (2003), *Personal Communication*

44 Cowling, R. (2003), *Personal Communication*

45 Cowling,R. (2002). Personal Communication.

46 Cubrinovski, M. & Ishihara, K. (1999). "Empirical correlation between SPT N-Value and relative density for Sandy Soils," *Soils and Foundations*, 39 (5): 61-71

47 Cubrinovski, M. & Ishihara, K. (2000). "Flow potential of Sandy solids

with different grain compositions," *Soils and Foundations*, 40 (4): 103-119

48 Cubrinovski, M. & Ishihara, K. (2001). "Correlation between penetration resistance and relative density of sandy soils," *Proceedings 15th ICSMGE*, 393-396

49 Das, B. M. (1984). *Principles of Foundation Engineering*, Brooks/Cole Engineering Division, Monterey, CA.

50 Dayhoff, J.E. (1990). *Neural Network Architectures*, Van Nostrand Reinhold: New York

51 De Souza, E. and Dirige, A.P. (2002). "Centrifuge based paste fill support design." *Proceedings of the Eleventh International Symposium on Mine Planning and Equipment Selection*, MPES 2002. Czech Republic: Technical University of Ostrava. 201-206.

52 Deere, D.U., and Miller, R.P. (1966). "Engineering classification and index properties for intact rock," *Technical Report No. AFNL-TR-65-116*, Air force Weapons Laboratory, New Mexico

53 Dirige, A.P. and De Souza, E. (2002). "Centrifuge Modelling of Mine Paste fill Sillmats,". *Proceedings of the International Conference on Physical Modelling in Geotechnics*, St. John's:Publisher. 827-832.

54 Ellis, G.W., Yao C., Zhao, R., and Penummadu, D. (1995). "Stress Modelling Of Sands Using Artificial Neural Networks," *Journal of Geotechnical Engineering*, 121 (5), 429-435

55 Fagerlund, G. (1977). "Equations for calculating the mean free distance between aggregate particles or air pores in concrete," *CBI Research 8.77, Swedish Cement and Concrete Research Institute*, Stockholm, Sweden

56 Fahlman, S.E., and Lebiere, C. (1990). "The Cascade-Correlation Learning Architecture", *Advances in Neural Information Processing Systems 3*, (ed. Touretsky, D.S., San Mateo, California, Morgan Kaufman, 524-532

57 Flood, I., & Kartman, N. (1994). "Neural networks in Civil Engineering I: Principles and Understanding," *Journal of Computing in Civil Engineering*, ASCE, 8 (2) , 131-148.

58 Foruria, V. (1984). "Engineering Properties of Coral Reefs," *Research*

Bulletin, No CS31, Dept. of Civil and Systems Engineering, James Cook University, Townsville

59 Fourie, A., (2003), "Important Material Characteristics of Thickened Tailings," *Presentation, International Seminar on Paste and Thickened Tailings*, Australian Centre for Geomechanics, Melbourne, Australia

60 Franklin, J.A. and Chandra, R. (1972). "The slake durability test," *International Journal of Rock Mechanics and Mineral Science*, 9, 325-341.

61 Franklin, J.A., and Dusseault, M.B. (1989). "*Rock Engineering*," McGraw Hill.

62 Ghabousii, J. & Joghataie, A. (1995). "Active Control Of Structures Using Neural Networks," *Journal of Engineering Mechanics*, 121 (4), 555-567

63 Goh, A.T.C. (1994). "Seismic Liquefaction Potential Assessed By Neural Networks", *Journal Geotechnical Engineering*, ASCE, 120, (9),pp. 1467-1480.

64 Goh, A.T.C. (1995). "Modeling Soil correlations using neural networks," *Geotecnique*, 45,(4),pp 709-714.

65 Goh, A.T.C. (1996). "Neural Networks Modeling Of CPT Seismic Liquefaction Data," *Journal Geotechnical Engineering*, ASCE 122(1), 70-73

66 Grice, A. (2000). "Design of Fill Barricades using Cement Yield Line Theory," *Internal memorandum to BHP Billiton*, unpublished

67 Grice, A. (2001). "Recent Minefill Developments in Australia," *Proceedings of the 7th International Symposium on Mining with Backfill*, Ed. D.Stone, ISBN:0-87335-211-4, pp 351-357

68 Grice, A. and Bloss, M.B. (2002). "BHPbilliton Cannington Mine, Paste Fill Manual," *Private Report* generated for Cannington Mine

69 Grice, A.G. (1998 a). "Stability of Hydraulic Backfill Barricades", *MINEFILL '98, 6th International Symposium on Mining with Backfill*, AusIMM, Brisbane, April 1998

70 Grice, A.G. (1998 b). "Underground Mining with Backfill," *2nd Annual Summit – Mine Tailings Disposal Systems*, Brisbane, Nov. 24-25

71 Grice, AG. (2001). *Paste Fill Manual*, BHP Billiton Internal Documentation, Cannington Mine, Queensland, Australia

72 Griffith, A.A. (1921). "The phenomena of rupture and flow in solids," *Phil. Trans. Roy. Soc*., London, A221, pp 163-198

73 Hamrin, H. (1982) "Choosing an Underground Mining Method." *In: Underground Mining Methods Handbook*, ed. by W.A. Hustrulid. New York: Soc. Mng. Engr. - AIME, 1982,Sec. 1.6, pp. 88-112.

74 Hansbo, S. (1960). "Consolidation of Clay with special reference to Influence of Vertical Sand Drains," *Proceedings No. 18, Swedish Geotechnical Institute*, 47 pp.

75 Hawkins, A.B. (1986). "Rock descriptions, Site Investigation Practice: Assessing BS 5930," *Geological Society, Engineering Geology Special Pub*

76 Hazen, A., (1911). Discussion of "Dams and Foundations" by A.C. Koeing, *Transactions, ASCE*, Vol. 73, pp. 199-203

77 Head, K.H. (1980-1996). "*Manual of Soil Laboratory Testing*," John Wiley & Sons; Vol 1-3.

78 Heuze, F.E. (1983) High Temperature Mechanical, Physical and Thermal Properties of Granite Rocks – A Review," *International Journal of Rock Mechanics and Mining Science and Geomechanics*, Vol. 20, No 1, pp. 3-10.

79 Hoek, E., and Bray, J. W. (1981). "*Rock Slope Engineering*," The Institution of Mining and Metallurgy, London, England.

80 Holtz, R.D. and Broms, B.B. (1972). "Long Term Loading Tests at Ska-Edeby," *Sweden, Proceedings of the ASCE Speciality Conference on Performance of Earth and Earth-Supported Structures*, Purdue University, Vol. I, Part 1, pp. 435-464

81 Holtz, R.D., and Kovacs W.D. (1981). *An Introduction to Geotechnical Engineering*, Prentice-Hall Inc., New Jersey.

82 Homand-Eitienne, F., and Houpert, R. (1989). "Thermally Induced Microcracking in Granites: Characterisation and Analysis," *International Journal of Rock Mechanics and Mining Science and Geomechanics*, Vol. 26, No. 2, pp. 125-134

83 http://geology.cr.usgs.gov/pub/open-file-reports/ofr-95-0831/CHAP24.PDF

84 http://ist-socrates.berkeley.edu/~eps2/wisc/sg.html

85 http://webmineral.com/data/Galena.shtml

86 http://webmineral.com/data/Sphalerite.shtml

87 http://www.geo.utexas.edu/courses/386e/mining_terms.html

88 http://www.qcl.com.au/

89 http://www.state.ar.us/agc/zinc&.htm

90 Huyhn, L. (2003). "Methods to Improve the Rheological Properties of Plant Tailings at the Cannington Mine", *Presentation – P498A Project*, Ian Wark Research Institute, University of South Australia,

91 Ingles, O.G., Neil, R.C., & Richards. (1973). "Assessment of mine fill properties are Warrego Mine, Northern Territory," *CSIRO Technical Report no*. 19, p.22, (CSIRO, Division of Applied Geomechanics: Melbourne)

92 Ishihara, K. (1993). "Liquefaction and flow failure during Earthquakes." *33rd Rankine Lecture, Geotechnique* 43 (3):351 – 415

93 Itasca, (1997). "*FLAC^{3D} Users Manuals*," Itasca Consulting Group, Thresher Square East, 708 South Third Street, Suite 310, Minneapolis, Minnesota, 55415 USA

94 Itasca, (1999). "*FLAC^{3D} v2.0 Users Manuals*," Itasca Consulting Group, Thresher Square East, 708 South Third Street, Suite 310, Minneapolis, Minnesota, 55415 USA

95 Jaeger, J.C. and Cook, N.G.W. (1969). "*Fundamentals of Rock Mechanics*," Methuen & Co. Ltd., London, 513 pp.

96 Jaky J. (1944). "The co-efficient of earth pressure at rest," *Journal of Society of Hungarian Architects and Engineers*, 355-358

97 James R.G. (1965). "Stress and Strain fields in Sand". PhD dissertation, Cambridge University, Cambridge, United Kingdom

98 Janssen, H.A. (1895). "Versuche uer Getreidedruck in Silozellen." *Zeitchrift Verein Ingenieure*, **(39):** 1045-1049

99 Jardine, R.J., Potts, D.M., Fourie, A.B., and Burland, J.B., (1984). "Studies of the influence of non-linear stress strain characteristics in soil-

structure interaction," *Geotechnique*, London, 36(3), 377-396

100 Jardine, R.J., Symes, M.J., and Burland, J.B. (1986). "The measurement of soil stiffness in the triaxial soil testing apparatus," *Geotechnique*, London, 34(3), 323-340

101 Jewell, R. (2001). "Depositional and Geotechnical Characteristics of Thickened/ Paste Tailings in the Australian Mining Industry," *Proceedings of the High Density and Paste Tailings Conference*, University of Witwatersrand, South Africa, May 10 - 11

102 Jones, H. (2000). "Designer Waste," *PASTE TECHNOLOGY 2000, An International Seminar on the Production and Disposal of Thickened/ Paste Tailings for Mine Backfill or on the Surface*, Perth, 13 – 14 April, 2000.

103 Jörgen Johansson, (2000). "Soil Liquefaction Website," University of Washington, [online] http://www.ce.washington.edu/~liquefaction/html/main.html , (Accessed 23rd March 2004)

104 Kaga, M. and Yonekura, R. (1991). "Estimation of strength of silicate-grouted sand," *Soils and Foundations*, 31(3), 43-59

105 Kelsall, P.C., Watters, R.J., and Franzone, G. (1986). "Engineering Characteristics of Fissured, Weathered Dolorite and Vesicular Basalt," *Proceedings 27th Symposium of Rock Mechanics* (Tuscaloosa, Alabama) pp77-84

106 Kim, Y.S., Tatsuoka, F., and Ochi, K. (1994). "Deformation Characteristics at small strains of sedimentary rocks by triaxial compression tests," *Geotechnique*, London, 44(3), 461-478

107 Koselka, V.A. (1983). "Consolidated Backfilling at Outokumpu Oy's Vihanti, Keretti and Vammala mines," *3rd International Symposium on Mining with backfill*, Lulea, Sweden, 151-160, (Balkema: Rotterdam)

108 Krizek, R.J., Benltayf, M.A., and Atmatzidis, D.K. (1982). "Effective stress-strain-strength behaviour of silicate-grouted sand," *Proc. Conf. On Grouting in Geotechnical Engineering*, New Orleans, Feb 10-12, ASCE, pp 331-345.

109 Kuganathan, K. (2001). "Mine backfilling, backfill drainage and

bulkhead construction: A safety first approach," Australia's Mining Monthly, February 2001, pp 58 - 64

110 Kulhawy, F. H. and Mayne, P. W. (1990). "Manual on estimating soil properties for foundation design," *Report EL-6800, Research Project 1493-6*, Electric Power Research Institute, Palo Alto, Calif., U.S.A., 1990.

111 Ladd, C.C. (1971). "Settlement Analysis for cohesive soils," *Research Report R71-2, Soils Publication 272*, Department of Civil Engineering, Massachusetts Institute of Technology, 107 pp

112 Lamos, A.W., & Clark, I.H. (1989). "The influence of material composition and sample geometry on the strength of cemented backfill," *4th International Symposium on mining with backfill, Montreal, Canada, (Eds. Hassani, Scoble & Yu), pp,* 89-94, (Balkema:Rotterdam)

113 Lamos, A.W., and Clark, I.H. (1989). "The influence of material composition and sample geometry on strength of cemented backfill," *4th International Symposium on Mining with Backfill*, Montreal, Canada, (Ed. Hassani, Scoble and Yu), pp. 89 – 94. (Balkema : Rotterdam).

114 Landriault D. A. (1995). "Paste Backfill Mix Design for Canadian underground Hard Rock Mining," *Proceedings of the 97th Annual Meeting of the CIM, Rock Mechanics and Strata Control Session*, Halifax, Nova Scotia, 14-18 May

115 Landriault, D. (2000). "What is Thickened Tailings and what is Paste," *Proceedings from PASTE TECHNOLOGY 2000, An International Seminar on the Production and Disposal of Thickened/ Paste Tailings for Mine Backfill or on the Surface, Australian Centre for Geomechanics*, Perth, April 13 – 14.

116 Landriult,D., and Lidkea, W. (1993). "Paste fill and high density slurry backfill", *Innovative Mine Design for 21st Century*, Bawden & Archibald (eds) © 1993, Balkema, Rotterdam, ISBN 905410 3256, pp. 111-117

117 Lee, D.-H., Juang, C.H., and Lei, I.-M. (1996). "High Temperature Brazilian Testing of Tensile Strength of Metamorphic Limestone," *Geotechnical Testing Journal*, GTJODJ, Vol 19, No. 2, June 1996, pp 223-226

118 Leonards, G.A. (1986). “Advanced Foundation Engineering,” *Lecture Notes*, *Purdue University*, West Lafayette, USA

119 Lewis, M.R., Arango, I., Kimball, J., Ross, T.E. (1999). “Liquefaction Resistance of Old Sand Deposits,” *XI Panamerican Conference on soil Mechanics and Geotechnical Engineering*,

120 Li, L., Aubertin, M., Simon, R., Bussiere, B., & Belem, T. (2003). “Interaction between backfill and rock mass in narrow stopes.” *Soil and Rock America* 2003, Cambridge, Rotterdam. Balkema, 1157-1164

121 Liao, S. S.,and Whitman, R.V. (1986). “Overburden Corrections Factors for Sand,” *Journal Geotechnical Engineering Division*, Vol. 112, no. 3, March, pp 373-377

122 Lidkea, W. and Landriult,D. (1993). “Tests on Paste Fill at INCO”, *Minefill ‘93*, Johannesburg, SAIMM, 1993,pp. 337-347

123 Lippman,R.P. (1987). “An introduction into computing with neural nets,” *Acoustic Speech and Signal Processing*, 4 (2),pp. 4-22

124 Luke, D. and Rankine R. (2003). “Spatial Distribution in a Paste-Rock Filled Stope,” *Proceedings from the 2003 International Seminar on Paste and Thickened Tailings*, *Australian Centre for Geomechanics*, Section 21, 22 pp. Melbourne, May 14-16, 2003

125 Lun, P.T.W. (1985). “Strength and deformation behavior of reinforced sand fill,” *CSIRO Technical Rreport no. 137*, p.143 22, (CSIRO, Division of Applied Geomechanics: Melbourne)

126 Luo, C., Schneider, T.W., White, R., Currie, J., Paranjape, M. (2003). “A simple deflection-testing method to determine Poisson's ratio for MEMS applications,” *J. Micromech. Microeng. 13* (January 2003) 129-133

127 Maher, M.H., and Ho, Y.C. (1993). “Behaviour of fibre-reinforced cemented sands under static and cyclic loads.” *Geotechnical Testing Journal*, 16(3), 330-338.

128 Manca, P.P., Massacci, G., Massidda, L., & Rossi, G. (1984). “Stabilisation of mill tailings for mining backfill with Portland cement,” *Transactions of the Institute of Mining and Metallurgy*, Sect. A93: A48-54, (Spon: London)

129 Marston, A. (1930). “The theory of external loads on closed conduits in

light of the latest experiments." Bulletin No. 96, *Iowa Engineering Experiment Station*, Ames, Iowa

130 Marti, J. and Cundall, P.A. (1982). "Mixed discretisation Procedure for Accurate Solution of Plasticity Problems," *International Journal of Numerical Methods in Geomechanics*, Vol 6, 129 - 139

131 McGuire, A.J. (1978) "Falconbridge Slag as a cementing agent in backfill", *12th Canadian Rock Mechanics Symposium on Mining with Backfill*, Sudbury, Canada, pp. 133-138. (CIM:Montreal)

132 McLintock, F.A., and Walsh, J.B. (1962). "Friction on Griffith cracks under pressure," *Proc., 4th US Nat. congress of Applied Mechanics*, pp 1015-1021

133 Mesri and Godlewski. (1977) "Time and Stress Compressibility Interrelationship," *Journal of Geotechnical Engineering Division, ASCE*, Vol. 103, No. GT5, pp 417-430

134 Mesri, G. (1973) "Coefficient of Secondary Compression," *Journal of the Soil Mechanics and Foundation Division, ASCE*, Vol. 99, No. SM1, pp. 122-137

135 Meyerhof, G. G. (1956). "Penetration Tests and Bearing Capacity of Cohesionless Soils," *Journal of the Soil Mechanics and Foundations Divisions*, American Society of Civil Engineers, Vol 82, No. SM1, pp 1-19.

136 Meyerhof, G. G. (1963). "Some Recent Research on the Bearing Capacity of Foundations," *Canadian Geotechnical Journal*, Vol 1, No. 1, pp 16-26. Available from National Research Council of Canada, Research Journals, Ottawa, ON K1A OR6, Canada.

137 Meyerhof, G.G. (1957). "Discussion on Research on determining the density of sands by penetration testing," *Proceedings of the 4th International Conference on Soil Mechanics and Foundation Engineering* , Vol 1:110

138 Minerals Council of Australia, (2000). "*Australian Minerals Industry Safety and Health, Safety Survey Report – for 1 July 1999 – 30 June 2000*", Minerals Council of Australia, 4 pp

139 Mitchell R.J., and Smith, J.D. (1979). "Mine backfill design and testing,"

Canadian Mining and Metallurgical Bulletin, (72) 801, pp 82-88

140 Mitchell, J.K. (1976). *Fundamentals of Soil Behaviour*, John Wiley & Sons, Inc., New York, 422 pp.

141 Mitchell, J.K., and Katti, R.K. (1981). "Soil improvement. State-of-the-art-report," *Proceedings of the 10th International Conference on Soil Mechanics and Foundation Engineering,* Vol 4, Balkema, Rotterdam, The Netherlands, 261-317.

142 Mitchell, R.J. and Wong, B.C. (1982). "Behaviour of cemented tailings sands", *Canadian Geotechnical Journal*, Vol. 19, no.3, pp. 289 – 295

143 Mitchell, R.J., Olsen, R.S., and Smith, J.D. (1983). "Model Studies on cemented tailings used in mine backfill," *Canadian Geotechnical Journal*, 79 (8) pp 29 – 35.

144 Mitchell,R.J. (1998). "The eleventh annual R.M. Hardy Keynote Address, 1997: Centrifugation in geoenvironmental practice and education," *Canadian Geotechnical Journal*, 35(4): pp 630-640

145 Mittal, H., and Morgenstern, N. (1975). "Parameters for the design of tailings dams," *Canadian Geotechnical Journal*, Vol. 12, pp 235-261

146 Moss, A., (unknown), Formula for predicting required UCS strength for backfill masses., unpublished, viz A. Grice 2002, personal communication

147 Nantel, J. (1998). "Recent Developments and Trends in Backfill Practices in Canada," *MINEFILL '98, 6th International Symposium on Mining with Backfill*, AusIMM, Brisbane, April 1998

148 Nantel, J., & Lecuyer, N. (1983). "Assessment of Slag backfill properties for the Noranda-Chadbourne Project," *CIM Bulletin*, 76 (849), pp. 57-60

149 NAVFAC (1982), "Soil Mechanics: Design Manual 7.1," *Department of Navy, Naval Facilities Engineering Command, USA*

150 Noranda Technology Centre, (1991). *Report to Golden Giant Mine on results of laboratory work on unclassified tailings*.

151 Ouellet, J. (1995). "Comportment contrainte-deformation d'un remblai hydraulique cimente pour le remblayage minier," *Proc. 48th Canadian Geotechnical Conference*, Vancouver, Canada

152 Ouellet, J., Bidwell, T.J., and Servant, S. (1998). "Physical and

mechanical characterisation of paste backfill by laboratory and in-situ testing," *MINEFILL 98, 6th International Symposium on Mining with Backfill*, Brisbane, (Ed: M.L. Bloss), pp 249 – 253.

153 Peck, R. B., and Bazaraa, A. S. (1969). "Discussion on Settlement of Spread Footings on Sand," *Journal of the Soil Mechanics and Foundations Division*, American Society of Civil Engineers, Vol 95, No. SM3, pp 905-909.

154 Peck, R. B., Hanson, W. E., and Thornburn, T. H. (1974). "*Foundation Engineering*," John Wiley and Sons (New York)

155 Pells, P.J.N. and Ferry, M.J., (1983). "Needless Stringency in Sample Preparation Standards for Laboratory Testing of Weak Rocks," *Proceedings of the 5th International Congress on Rock Mechanics*, (Melbourne, Australia) pp 203-208

156 Perry, R.J., & Churcher, D.L., (1990), "The application of high density paste fill at Dome Mine," *CIM Bulletin*, 83 (937), 53-58

157 Pettifer, G.S. & Fookes, P.G. (1994). "Excavatibility of Rock: The Graphical Method," *QJEG*, Vol 27, Part 2.

158 Pierce, M.E. (1997). "Laboratory and Numerical Analysis of the Strength and Deformation Behaviour of Paste Backfill," M.S. Thesis, Queens University, Ontario, Canada.

159 Pierce, ME, Bawden, WF and Paynter, J.T. (1998). "Laboratory Testing and Stability Analysis of Paste backfill at the Golden Giant Mine *MINEFILL 98, 6th International Symposium on Mining with Backfill*, Brisbane, (Ed: M.L. Bloss),pp. 159-165

160 Pollchik, J.D.; Schurr, J.N.; Johnson, E.C. (1992). "An Ultrasonic Testing Technique for Measurement of the Poisson's Ratio of Thin Adhesive Layers," *Rev. of Prog. In Quantitative Nondestructive Evaluation*, Vol. 11, pp. 1291-1298; Plenum Press, 1992.

161 Polous, H.G., and Davies E.G. (1980). "*Pile Foundation and Design*," John Wiley and Sons (New York)

162 Potvin, Y. (1988). "Empirical open stope design in Canada." Ph.D. thesis, Dept. Mining and Mineral Processing, University of British Columbia.

163 Pullum, L., (2003), "Pipeline Performance", *Proceedings from the Paste*

and Thickened Tailings Conference, Australian Centre for Geomechanics, Melbourne May, 14-16

164 Quigley, P., and McSwiney, S. (1996). “Measurement And Analysis Of Rock Mass Fractures And Their Applications In Civil Engineering**”** P*aper Presented to the Institute of Engineers, Ireland*, 13th February, 1996, pp 24

165 Rankine, K., (2004). “Numerical Modelling of Cannington fill barricades,” *BHP Billiton internal report*, unpublished.

166 Rankine, K.J. (2000). “Geotechnical Characterisation and Stability Analysis of BHP Cannington Paste Backfill,” *Undergraduate thesis*, James Cook University, Townsville, Queensland, Australia.

167 Rankine, K.J. (2003). “Permeability of backfills and barricade bricks,” PhD dissertation –research results - Unpublished, James Cook University, Townsville, Australia

168 Rankine, R.M., Rankine, K.J., Sivakugan, N., Karunasena, W., Bloss, M.L.,(2001), “Geotechnical Characterization and Stability Analysis of BHP Cannington Paste Backfill”, *XVth International Conference on Soil Mechanics and Geological Engineering*, August, 2001, Istanbul Turkey, 1241-1244

169 *Report of the Tribunal appointed to inquire into the Disaster at Aberfan on October 21st*, (1966). HMSO, London, 1967

170 Revell, M. (2001). “Design of Fill Barricades,” *Kanowna Belle Internal Report*, unpublished

171 Richards, J.C. (1966). *The Storage and Recovery of Particulate Solids*, Institution of Chemical Engineers, London

172 Robertson, P. K., and Campanella, R. G. (1983). “Interpretation of Cone Penetration Tests; Parts I and II,” *Canadian Geotechnical Journal*, Vol 20, No. 4, pp 718-745.

173 Robinsky, E.I. (1975). “Thickened Discharge - A New Approach to Tailings Disposal,” *Canadian Mining and Metallurgical Bulletin*, Vol. 68, December 1975, pp. 47-53.

174 Robinsky, E.I. (1976). “Advantages of Tailings Disposal by Thickened Discharge,” *Proceedings of the Eighth Annual Meeting of the Canadian*

Mineral Processors, Canada Centre for Mineral and Energy Technology (CANMET), Ottawa, Ontario, January 1976, pp. 290-310.

175 Robinsky, E.I. (1978). "Tailing Disposal by the Thickened Discharge Method for Improved Economy and Environmental Control," *Tailing Disposal Today - Proceedings of the 2nd International Tailings Symposium, May 1978, Denver, Colorado*, Vol. 2, pp. 75-92, 1979 by Miller Freeman Publications Inc., San Francisco, California,.

176 Roscoe K.H., Arthur J.R.F. and James R.G. (1963). The Determination of Strains in Soils by an X-ray Method. *Civil Engineering and Public Works Review*, Vol 58, pp 873-876.

177 Rosengren, K., (1994). "Updated Geotechnical Assessment for Open Pit & Underground" *Mining, report for Placer Pacific Osborne Copper-Gold Project*

178 Rumelhart, D.E., & McClelland, J.L. (1986). *Parallel Distributed Processing – Explorations in the microstructure of cognition, Vols. 1 and 2,* Massachusetts Institute of Technology Press, Cambridge, Mass

179 Rutledge, P.C. (1940). "Theories of Failure Materials Applied to the Shear Resistance of Soils," *Proceedings of Purdue Conference on Soil Mechanics and its Applications*, 191-204.

180 Saliba, D.C. (1996). "The Fundamental Properties of Backfill which Affect its Strength," Undergraduate Thesis, University of Queensland, Australia

181 Saxena, S.K., and Lastrico, R.M. (1978). "Static properties of lightly cemented sands." *Journal of Geotechnical Engineering Division, ASCE*, 104(12), 1449-1465

182 Schmertmann, J. H. (1975). "Measurement of In-Situ Strength," *Proceedings of the Conference on In-Situ Measurement of Soil Properties,* ASCE, pp 55-138.

183 Schnaid, F., Prietto, P.D.M., and Consoli N. (2001). "Characterisation of Cemented Sands in Triaxial Compression," *Journal of Geotechnical and Geo-Environmental Engineering*, Vol. 127, No. 10, October, 2001, 857 – 868.

184 Seed, H. B., Arango, I., and Chan, C. K. (1975). "Evaluation of Soil

Liquefaction Potential During Earthquakes," *Report No. EERC 75-28*, Earthquake Engineering Research Centre, College of Engineering, University of California, Berkeley, CA.

185 Seed, H.B. and Idriss, I.M. (1971). "Simplified Procedure for evaluating soil liquefaction potential," *Journal of Geotechnical Engineering Division, ASCE*, 97(9), 1249-1273

186 Seed, H.B., and De Alba, (1986). "Use of SPT and CPT tests for evaluating the liquefaction resistance of sands," *Proceeding INSITU '86, ASCE Special Conference on the Use of In Situ Testing in Geotechnical Engineering, special Publication, No. 6, ASCE*, New York, N.Y.

187 Seed, H.B., Tokimatsu, K., Harder, L.F., and Chung, R. (1985). "Influence of SPT Procedures in soil liquefaction resistance evaluations," *Journal of Geotechnical Engineering, ASCE*, 111 (12), 861-878.

188 Singh, K.H., and Hedley, D.G.F. (1981). "Review of Mining Technology in Canada", *Symposium on the Application of Rock Mechanics to Cut and Fill Mining*, Lulea, Sweden 11-24 (IMM: London)

189 Singh-Samra, H. (2001). "Investigation Of Backfill Strength Relationships And BHP Cannington Paste Fill Constitutive Behaviour," *Undergraduate Thesis*, James Cook University, Townsville, Australia

190 Sivakugan, N., Eckersley, J.D., and Li, H. (1998). "Settlements Predictions using neural networks," Australian Civil Engineering Transactions, The Institute of Engineers, Australia, CE40, pp. 49-52

191 Skempton, A.W. (1954). "The Pore Pressure Coefficients A and B," *Geotechnique*, Vol IV, pp 143-147

192 Skempton, A.W. (1986). "Standard penetration test procedures and the effects in sand of overburden pressure, relative density, particle size ageing and over consolidation." *Geotechnique*, 36 (3): 425-477

193 Smith, R. (2002). "RE3359C: Effects of Grind Size on paste rheology" *Internal Memo/ Technical Report, BHPBILLITON World Minerals*, unpublished

194 Spalngler, M.G., & Handy, R.L. (1984) *Soil Engineering*, Hardy & Row

195 Specht, D.F. (1991). "A general regression neural network", *IEEE Transaction, Neural Networks*, 2(6), pp. 568-576

196 Stark, T.D. and Olson, S.M. (1995). "Liquefaction resistance using CPT and field case histories." *Journal Geotechnical Engineering*, 121(12):856-869.

197 Stark, T.D., and Mesri, G. (1992). "Undrained shear strength of liquefied sands for stability analysis," *Journal of Geotechnical Engineering, ASCE*, 118 (11), 1727 - 1747

198 Stewart J.M., Clark, I.H., and Morris. (1986). "Assessment of Fill quality as a basis for selecting and developing optimal backfill systems for South African gold mines," *Proc. International Conference on Gold*, Vol. 1. Gold Mining Technology, Johannesburg, SAIMM

199 Stone, D.M.R. (1993). "The optimisation of Mix Designs for Rock Fill," *MINEFILL '93*, Johannesburg, SAIMM, 1993, pp 249-253

200 Swan, G. (1985). "A new approach to cemented backfill design," *The Canadian Mining and Metallurgical Bulletin*, 78 (884):53-58

201 Take, W.A., & Valsangkr, A.J. (2001). "Earth Pressures on unyielding retaining walls of narrow backfill widths" *Canadian Geotechnical Journal*, 38: 1220-1230

202 Tatsuoka F., Jardine, R. J., Lo Presti, D., Di Benedetto, H., and Kodoka, T. (1997). "Characterising the pre-deformation properties of geomaterials," *Proceedings of the 14th ICSMFE*, Vol. 1, Balkema, Rotterdam, The Netherlands, pp 809-816.

203 Tatsuoka F., Kohata, Y., Mitsumoto, K., Kim, Y., Ochi, K., and Shi, D. (1993). "Measuring small strain stiffness of soft rocks," *Proceedings of the International Symposium on Geotechnical Engineering of Hard Soils – Soft Rocks*, Vol. 1, Balkema, Rotterdam, The Netherlands, 809 - 816

204 Tatsuoka, F. and Kobayashi, A. (1983). "Triaxial strength characteristics of cement treated soft clay." *Proceedings of the 8th European Conference on Soft Soil Mechanics and Foundation Engineering*, Vol 1, Balkema, Rotterdam, The Netherlands, 421-426.

205 Tatsuoka, F. and Shibuya, S. (1992). "Deformation Characteristics of Soils and Rocks from Field and Laboratory Tests," keynote lecture for Session 1, *Proceedings the 9th Asian Regional Conferenceon SMFE, 1991*, Bangkok, Vol. 2, pp. 101–170.

206 Taylor, D.W. (1948). *Fundamentals of Soil Mechanics*, John Wiley & Sons Inc. New York, 700 pp.

207 Teh, C.I., Wong, K.S., Goh, A.T.C., and Jaritngam, S. (1997). "Prediction of pile capacities using neural networks", *Journal of Computing in Civil Engineering, ASCE*, 11(2), pp. 129-138

208 Teng, W.C. (1962). "*Foundation Design*," Prentice Hall, Englewood Cliffs, New Jersey.

209 Terzaghi, K. (1943). *Theoretical Soil Mechanics*, John Wiley and Sons, New York

210 Thomas E.G., Nantel, L.H., and Notley, K.R. (1979). *Fill technology in underground metalliferous mines*, International Academic Services Ltd., Kingston, Ont., 293 pp.

211 Thomas, E.G. (1969). "*Characteristics and Behaviour of Hydraulic Fill Material*," PhD dissertation, University of Queensland, Brisbane, Australia

212 U.S. Navy, (1971). "Soil Mechanics, Foundations and Earth Structures," *NAVFAC Design Manual DM-7*, Washington D.C.

213 Vick, S.G. (1983). *Planning, design and analysis of tailings dams*, John Wiley and Sons, New York.

214 Walpole, R.E. and Myers, R.H. (1993). *Probability and Statistics for Engineers and Scientists*, 5th Edition, MacMillan Publishing Company, New York, pp 766

215 Walters, S. and Bailey, A. (1998). "Geology and mineralisation of the Cannington Ag-Pb-Zn Deposit: an example of Broken Hill-type mineralisation in the Eastern Succession, Mount Isa Inlier, Australia." *Economic Geology*, 93: 1307-1329.

216 Walters, S.G. (1994). "Geology and Lode Characterisation - Cannington Southern Zone," *BHP Billiton Internal Report, Unpublished*

217 Weaver, W.S., & Luka, R. (1970). "Laboratory Studies of cement-stabilised mine tailings", *C.I.M., Bulletin*, 63 (701): pp. 988-1001

218 Weisner, T.J. (1982). "Pile behaviour prediction at ESOPT2," *Australian Geomechanics News*

219 Wen. B., Aydin, A., and Duzgoren-Aydin, N.S. (2002). "A comparative

study of particle size analyses by sieve-hydrometer and laser diffraction methods," *Geotechnical Testing Journal, ASTM*, 25 (4), 434-442.

220 Whitlow, R. (1990). *Basic Soil Mechanics*, 2nd Ed, Longman Scientific and Technical, Longman Group UK Ltd, 528 pp

221 Winch, C. (1999). "Geotechnical Characteristics and Stability of Paste Backfill at BHP Cannington Mine," Undergraduate Thesis, James Cook University, Townsville, Australia

222 Wissa, A. (1969). "Pore pressure measurement in saturated stiff soils," *Journal of the Soil Mechanics and Foundation Division, ASCE*, Vol. 95, No. SM4, Paper Number 6670, pp 1063 – 1073.

223 www.virtualexplorer.com.au/VEexploration/VEorebodies/Cannington/

224 Yeh, Y., Kuo, Y., & Hsu, D. (1993). "Building KBES for Diagnosing PC Pile with Artificial Neural Networks," *Journal of Computing in Civil Engineering*, ASCE, 7(1), pp. 71-93

225 Yu, T.R., & Counter, D.B. (1983). "Backfill practice and technology at Kidd Creek Mines", *CIM Bulletin*, 76 (856), pp 56-65

226 Yu, T.R., & Counter, D.B. (1988). "Use of fly ash in backfill at Kidd Creek Mines", *CIM Bulletin*, 81 (909), pp 44-50

227 Zhu, J. (1996). "Measurement Of Poisson's Ratio Of Non-Metallic Materials By Laser Holographic Interferometer," *Trends in NDE Science & Technology; Proceedings of the 14th World Conference on Non-Destructive Testing, New Delhi*, 8-13 December 1996.Vol. 3, pages 1481 - 1484

APPENDIX 2

Case Derivations from Winch (1999)

Assumptions

W_1 = side held constant

W_2 = side varied

Case 1. First Exposure - Fill mass

(i) With Exposed side constant

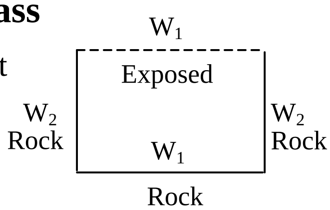

EL=W_1+2W_2

Thus:-

$\alpha = 1$

$\beta = 2$

$$W_2 > \frac{W_1\left[\left(\sigma_y - \sigma_{y0}\right)K\tan\phi + \left(c + K\sigma_{y0}\tan\phi\right)\right]}{W_1\rho g - 2\left[\left(\sigma_y - \sigma_{y0}\right)K\tan\phi + \left(c + K\sigma_{y0}\tan\phi\right)\right]}$$

(ii) With exposed side varied

EL=2W_1+W_2

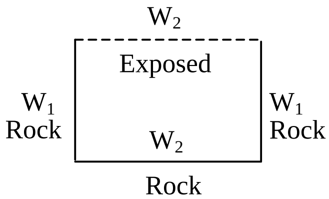

Thus:-

$\alpha = 2$

$\beta = 1$

$$W_2 > \frac{2W_1\left[\left(\sigma_y - \sigma_{y0}\right)K\tan\phi + \left(c + K\sigma_{y0}\tan\phi\right)\right]}{W_1\rho g - \left[\left(\sigma_y - \sigma_{y0}\right)K\tan\phi + \left(c + K\sigma_{y0}\tan\phi\right)\right]}$$

Case 2. Second Exposure - Fill mass

(a) Side Opposite to Fill Exposed

(i) Exposed side varied

$EL=2W_1+FW_2$

Thus:-

$\alpha = 2$

$\beta = F$

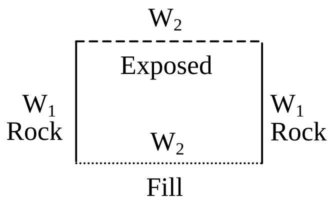

$$W_2 > \frac{2W_1\left[(\sigma_y - \sigma_{y0})K\tan\phi + (c + K\sigma_{y0}\tan\phi)\right]}{W_1\rho g - F\left[(\sigma_y - \sigma_{y0})K\tan\phi + (c + K\sigma_{y0}\tan\phi)\right]}$$

(ii) Exposed side constant

$EL=FW_1+2W_2$

Thus:-

$\alpha = F$

$\beta = 2$

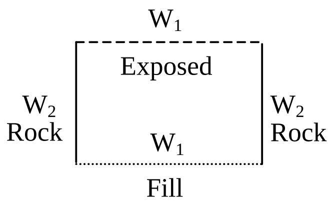

$$W_2 > \frac{FW_1\left[(\sigma_y - \sigma_{y0})K\tan\phi + (c + K\sigma_{y0}\tan\phi)\right]}{W_1\rho g - 2\left[(\sigma_y - \sigma_{y0})K\tan\phi + (c + K\sigma_{y0}\tan\phi)\right]}$$

(b) Side Adjacent to Fill Exposed

(i) Exposed side varied

$EL=(1+F)W_1+W_2$

Thus:-

$\alpha = (1+F)$

$\beta = 1$

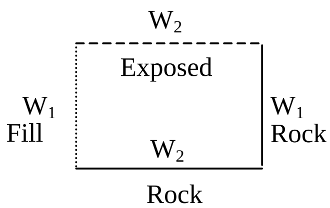

$$W_2 > \frac{(1+F)W_1\left[(\sigma_y - \sigma_{y0})K\tan\phi + (c + K\sigma_{y0}\tan\phi)\right]}{W_1\rho g - \left[(\sigma_y - \sigma_{y0})K\tan\phi + (c + K\sigma_{y0}\tan\phi)\right]}$$

(ii) Exposed side constant

EL=W_1+(1+F)W_2

Thus:-

$\alpha = 1$

$\beta = (1+F)$

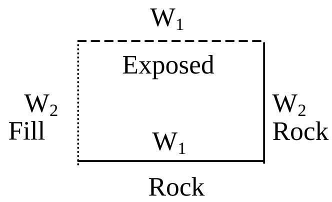

$$W_2 > \frac{W_1\left[\left(\sigma_y - \sigma_{y0}\right)K\tan\phi + \left(c + K\sigma_{y0}\tan\phi\right)\right]}{W_1\rho g - (1+F)\left[\left(\sigma_y - \sigma_{y0}\right)K\tan\phi + \left(c + K\sigma_{y0}\tan\phi\right)\right]}$$

Case 3. Third Exposure - Fill mass

(a) Fill sides adjacent

(i) Exposed side varied

EL=(1+F)W_1+FW_2

Thus:-

$\alpha = (1+F)$

$\beta = F$

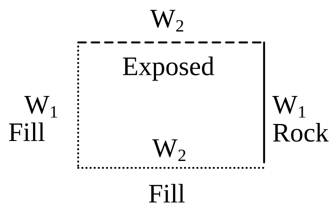

$$W_2 > \frac{(1+F)W_1\left[\left(\sigma_y - \sigma_{y0}\right)K\tan\phi + \left(c + K\sigma_{y0}\tan\phi\right)\right]}{W_1\rho g - F\left[\left(\sigma_y - \sigma_{y0}\right)K\tan\phi + \left(c + K\sigma_{y0}\tan\phi\right)\right]}$$

(ii) Exposed side constant

EL=FW_1+(1+F)W_2

Thus:-

$\alpha = 1$

$\beta = (1+F)$

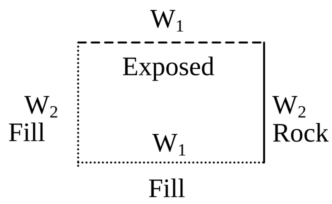

$$W_2 > \frac{1W_1\left[\left(\sigma_y - \sigma_{y0}\right)K\tan\phi + \left(c + K\sigma_{y0}\tan\phi\right)\right]}{W_1\rho g - (1+F)\left[\left(\sigma_y - \sigma_{y0}\right)K\tan\phi + \left(c + K\sigma_{y0}\tan\phi\right)\right]}$$

(c) Fill sides opposite

(iii) Exposed side varied

$EL=2FW_1+W_2$

Thus:-

$\alpha = 2F$

$\beta = 1$

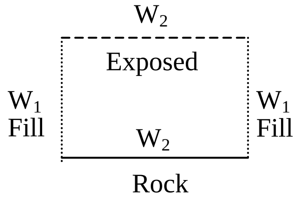

$$W_2 > \frac{2FW_1\left[\left(\sigma_y - \sigma_{y0}\right)K\tan\phi + \left(c + K\sigma_{y0}\tan\phi\right)\right]}{W_1\rho g - \left[\left(\sigma_y - \sigma_{y0}\right)K\tan\phi + \left(c + K\sigma_{y0}\tan\phi\right)\right]}$$

(iv) Exposed side constant

$EL=W_1+2F\ W_2$

Thus:-

$\alpha = 2F$

$\beta = 2F$

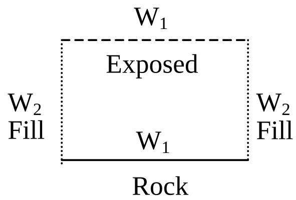

$$W_2 > \frac{2FW_1\left[\left(\sigma_y - \sigma_{y0}\right)K\tan\phi + \left(c + K\sigma_{y0}\tan\phi\right)\right]}{W_1\rho g - 1\left[\left(\sigma_y - \sigma_{y0}\right)K\tan\phi + \left(c + K\sigma_{y0}\tan\phi\right)\right]}$$

APPENDIX 3.1

Test Planning, Procedures and Program

- *Test program*
- *Testing standards used*
- *Sample preparation procedures*
    - *Tailings*
    - *Triaxial & UCS samples*
    - *Oedometer samples*
    - *Curing of samples*

The Tests performed as part of the Doctoral Research Program, are summarised in Table A3.1.1

Abbreviation	Description
UU TXL	Unconsolidated Undrained Triaxial Testing
UCS	Uniaxial Compressive Strength Testing
CD TXL	Consolidated Drained Triaxial
Tens.	Direct Tensile Testing
OD	Odometer/ Consolidation Testing
DCPT	Dynamic Cone Penetrometer Testing
PP	Physical Property Testing - includes determination of water content, saturation levels, void ratio, porosity and densities
Class	Classification Tests (GSD,SG, grain shape, Atterberg Limits)
SEM	Scanning Electron Microscope
XRF	X- Ray Fluorescence

Figure A3.1. 1 Test Planning

			Curing Time						
Test	**Mix**	**Months**			**1**	**2**	**3**	**6**	**12**
		Days	**7**	**14**	**28**	**56**	**112**	**183**	**365**
UU Txl	2%,74%		X	X	X	X			
Medium term	2%,78%		X	X	X	X			
	6%,74%		X	X	X	X			
	6%,78%		X	X	X	X			
Long term	2%,74%				X	X	X	X	X
	2%,78%				X	X	X	X	X
	6%,74%				X	X	X	X	X
	6%,78%				X	X	X	X	X
GSD Variation	2%,76%		X	X	X				
	2%,80%		X	X	X				
	6%,76%		X	X	X				
	6%,80%		X	X	X				
CD TXL	2%,74%			X	X				
	2%,78%			X	X				
	6%,74%			X	X				
	6%,78%			X	X				

Figure A3.1. 1. (cont.) Test Planning

Test	Mix		Curing Time						
		Months			1	2	3	6	12
		Days	7	14	28	56	112	183	365
Tens	2%,74%		X	X	X	X			
	2%,78%		X	X	X	X			
	6%,74%		X	X	X	X			
	6%,78%		X	X	X	X			
UCS	2%,74%		X	X	X	X			
	2%,76%		X	X	X	X			
	2%,78%		X	X	X	X			
	4%,74%		X	X	X	X			
	4%,76%		X	X	X	X			
	4%,78%		X	X	X	X			
	6%,74%		X	X	X	X			
	6%,76%		X	X	X	X			
	6%,78%		X	X	X	X			
OD	2%,74%				X				
	2%,78%				X				
	6%,74%				X				
	6%,78%				X				
In-situ Testing	*Stope: 42_61*								
DCPT	*59 XC*								
	3 holes tested	2.0 yrs							

Figure A3.1. 1. (cont. 2) Test Planning

			Curing Time						
Test	**Mix**	**Months**			**1**	**2**	**3**	**6**	**12**
		Days	**7**	**14**	**28**	**56**	**112**	**183**	**365**
In-situ Testing	*Stope: 42_61*								
UCS-cores	*59 XC*								
	4-samples tested	2.0 yrs							
	Stope: 47_73								
	77XC								
	4-samples tested	2.5yrs							
PP	*Conducted for all Tests performed*		X	X	X	X	X	X	X
Class	*Tails only - except for linear shrinkage*	N/A							
SEM	*Unbound Tails 2%,76% 6%,76%*		X	X	X				
XRF	*Unbound Tails 2%,76% 6%,76%*		X	X	X				

The Standards as Applicable to Testing of Paste Fill are Summarised in Table A3.1.2.

Standard	**Description**
AS 1289.0-2000	Methods of testing soils for engineering purposes - General requirements and list of methods
AS 1289.2.1.1-1992	Methods of testing soils for engineering purposes - Soil moisture content tests - Determination of the moisture content of a soil - Oven drying method (standard method)
AS 1289.3.1.1-1995	Methods of testing soils for engineering purposes - Soil classification tests - Determination of the liquid limit of a soil - Four point Casagrande method
AS 1289.3.1.1-1995/Amdt 1-1998	Methods of testing soils for engineering purposes - Soil classification tests - Determination of the liquid limit of a soil - Four point Casagrande method
AS 1289.3.2.1-1995	Methods of testing soils for engineering purposes - Soil classification tests - Determination of the plastic limit of a soil - Standard method
AS 1289.3.3.1-1995	Methods of testing soils for engineering purposes - Soil classification tests - Calculation of the plasticity index of a soil
AS 1289.3.3.1-1995/Amdt 1-2000	Methods of testing soils for engineering purposes - Soil classification tests - Calculation of the plasticity index of a soil
AS 1289.3.4.1-1995	Methods of testing soils for engineering purposes - Soil classification tests - Determination of the linear shrinkage of a soil - Standard method
AS 1289.3.5.1-1995	Methods of testing soils for engineering purposes - Soil classification tests - Determination of the soil particle density of a soil - Standard method
AS 1289.3.6.2-1995	Methods of testing soils for engineering purposes - Soil classification tests - Determination of the particle size distribution of a soil - Analysis by sieving in combination with hydrometer analysis (subsidiary method)
AS 1289.6.2.1-2001	Methods of testing soils for engineering purposes - Soil strength and consolidation tests - Determination of the shear strength of a soil
AS 1289.6.2.1-1997	Methods of testing soils for engineering purposes - Soil strength and consolidated tests - Determination of the shear strength of a soil - Field test using a vane
AS 1289.6.2.2-1998	Methods of testing soils for engineering purposes - Soil strength and consolidation tests - Determination of shear strength of a soil - Direct shear test using a shear box

Standard	Description
AS 1289.6.3.1-1993	Methods of testing soils for engineering purposes - Soil strength and consolidation tests - Determination of the penetration resistance of a soil - Standard penetration test (SPT)
AS 1289.6.4.1-1998	Methods of testing soils for engineering purposes - Soil strength and consolidation tests - Determination of compressive strength of a soil - Compressive strength of a specimen tested in undrained triaxial compression without measurement of pore water pressure
AS 1289.6.6.1-1998	Methods of testing soils for engineering purposes - Soil strength and consolidation tests - Determination of the one-dimensional consolidation properties of a soil - Standard method
D2936-95(2001)e1	Standard Test Method for Direct Tensile Strength of Intact Rock Core Specimens

Additional Test methods such as the Consolidated Drained Triaxial Testing were based on the procedures outlined in the soil testing manuals produced by Head (1996).

Sample Preparation Procedures

The samples for the tests were prepared as summarised below. The preparation procedure is limited to cover four sections: -

1. Tailings Preparation
2. Triaxial Sample Preparation
3. Odometer Sample Preparation
4. Curing of Samples

Preparation of Tailings for testing

The tailings provided by Cannington required significant preparation prior to use in the production of paste fill mixes. The preparation ensured homogeneity of the tailings and allowed an accurate determination of water content in fill mixes.

Cannington mine supplied two 44-gallon drums and ten 20 litre airtight containers of tailings. The average water content of the supplied tailings was between 18 and 20% for both sets of containers. Segregation of the tailings was assumed to have occurred during transportation of the tailings from Cannington to James Cook University (12 – 15 hour road trip). Figure 3.1 shows a schematic representation of the preparation of the tailings before use in the production of paste fill samples.

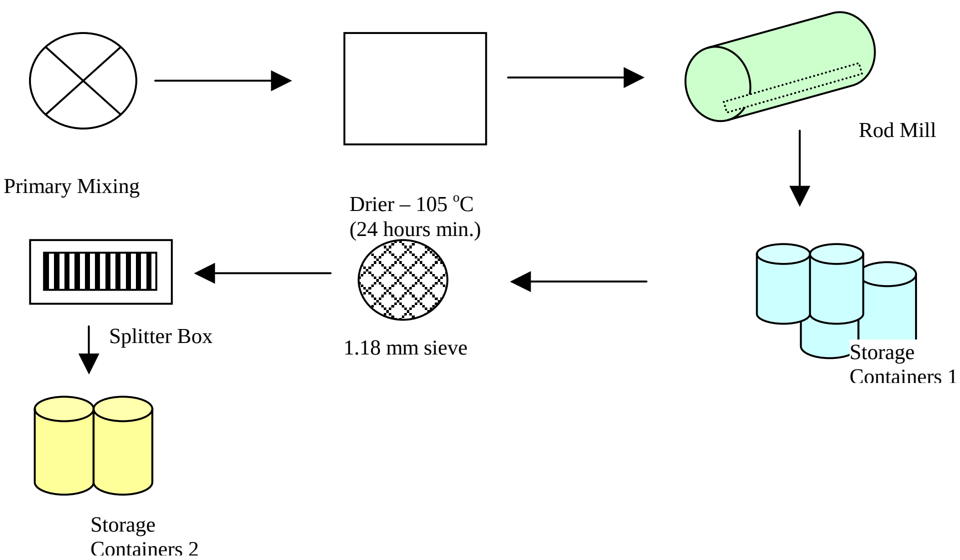

Figure A3.3. 1 Diagrammatic representation of supplied tailings preparation

The seven-step process developed for paste fill preparation can be summarised as follows:

Step 1 – Primary mixing

Tailings were removed from the drums and placed in a large concrete mixer. Primary mixing continued for one hour for each batch of tailings to ensure a homogeneous mix. Equal portions of tailings were included from each source (if more than one source), and equal portions from the top middle and lower sections of each drum were used.

Step 2 – Oven drying

After completion of the primary mixing the tailings were deposited into greased aluminium oven trays. The trays were then placed in the oven at 105° C for a period of not less than 24 hours. The chief mining metallurgist (Mr. Matthew Revell) from Cannington was consulted regarding any negative temperature effects of oven drying on the tailings. None were identified.

Step 3 – Crushing (rod mill)

The small "cakes" which formed during the drying of the tailings were placed in the rod mill to separate the tailings into individual particles. *(Note: The individual particles of the tailings were not broken down in this exercise).* The final product resembled a very fine grey powder.

Step 4 – Storage containers

Dried tailings were then stored in containers. Each of the storage containers were sealed airtight to prevent the ingress of water. A sample was taken from each of the drums to determine the water content. In each case the water content was below 0.2%.

Step 5 – Sieving (1.18mm sieve)

The tailings stored in the drums in step 4 were then sieved using a 1.18mm sieve to remove any extraneous material, which may have accumulated from the previous steps in preparation. The 1.18mm sieve was considered appropriate as previous work undertaken on the grain size distribution by Mr. Sam Clayton (personal communication, 2000) and Ms. Chrissie Winch (1999) indicated the maximum grain size of the tailings to be between 400 μm and 600 μm

Step 6 – Splitting (splitter box)

The sieved tailings were passed through a splitter box to produce two "equally representative" portions from the initial sample.

Step 7 – Storage containers 2

The split portions were placed in each of the two larger drums, which were subsequently sealed airtight. All of the samples used in laboratory testing were made from these "prepared tailings".

Preparation of Triaxial Test Samples

The triaxial test samples were made to a specified diameter of 38mm and 76 mm in length. The procedure to create and cast the samples is as follows:-

1. Sample containers were prepared by cutting PVC piping (I.D. = 38 mm) to a specified length of 100 mm. The ends were cut square and a longitudinal split was made along one side of the sample containers. All extraneous material was removed and end caps placed on the sample tubes. End caps were dust or pressure caps suitable to the 38mm ID, DWV pipe used. Each of the sample containers was then coated with a thin layer of either cooking oil or silicone spray to lubricate the surface. The sample containers were then ready for the addition of the paste
2. The mix proportions of tailings, cement and water were all weighed out and combined in the mixing bowl of a suitably small Hobart Mixer. (max.. bowl capacity of approx 5 kg)
3. The paste blend was then left to mix for a period of not less than 3 minutes, with regular checks to ensure that complete mixing had occurred (i.e. no material had coagulated in the base of the mixing bowl and was not included in the mix.
4. The paste was then poured or moulded into the containers (depending on the solids content of the sample).

5. Samples were placed in aluminium trays and 500mL of water added into the base of the tray.
6. The aluminium trays were then placed in three garbage bags, which were each individually, tied off and sealed.
7. Samples were then placed in the oven to cure at a constant temperature of 38 degrees
8. When required for testing samples were removed from the curing bags and oven.
9. Samples were extruded from the sample containers by i) removing the end caps, ii) separating the sample containers by pulling apart the longitudinal cut and forcing the samples out using either your thumb or a sample extruder
10. Samples were prepared to the right sample height by using a prefabricated steel sample-former.
11. Sample dimensions and weights required to determine the physical properties were then taken and recorded.

Consolidation Testing

Consolidation testing of different paste mixes was completed to determine the rate and magnitude of the paste's consolidation rate when restrained laterally and loaded and drained axially. Testing was completed as per Australian standards AS1289 on specimens of diameter 76 mm.

Consolidation Sample Preparation

The oedometer test samples were prepared in bulk as per the direct shear bulk samples, until Step 6, where a 76 mm diameter ring was used to prepare the samples to the correct dimensions.

Consolidation Testing Procedure

The following procedure was used to test the oedometer samples:

1. The porous plates in the consolidation cell (Fig A3.1.2) were saturated and placed in a vacuum for approximately 20 minutes to remove any trapped air within the plates. This minimizes the tendency to absorb water from the specimen, through osmosis.

2. The sample was then carefully placed in the consolidation ring. Filter paper was cut to the same size as the sample and placed on the top and bottom of the sample. Figure Fig A3.1.2 shows details of a typical oedometer consolidation cell.

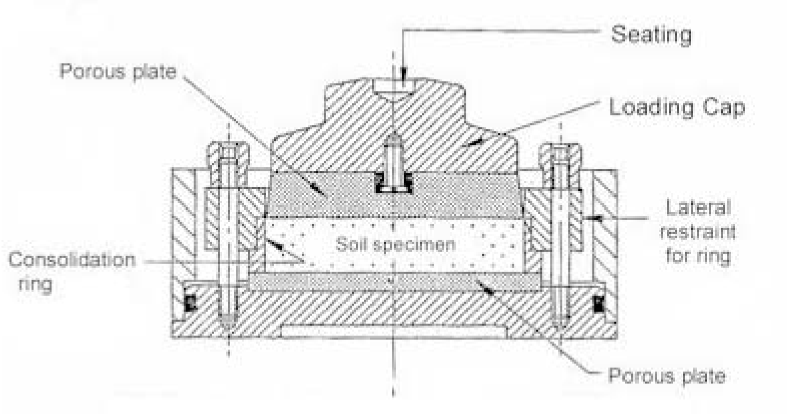

Figure A3.1. 2 Details of a typical oedometer consolidation cell (Head, 1981)

3. The consolidation cell was placed in the loading device and a seating pressure of 6.25 kPa applied. The dial gauge position was adjusted to allow for a small amount of swelling of the specimen due to the water added. The remainder of the range of travel of the dial gauge was to allow for compression.

4. Pressure was applied in increments such as to double the previous pressure. The following values, in kilopascals, were used as the test range:
   6.25, 12.5, 25, 50, 100

5. The change in thickness of the specimen was recorded before each load increment was applied and at the times of 2, 7, 15 and 30s; 1, 2, 4, 8, 16 and 32 min; 1, 2, 4, 8 and the like, hours; measured from the time of the load application.

6. After the consolidation readings were completed, the specimen was unloaded to almost zero pressure and the change in thickness recorded at time intervals specified in step five.

7. Once the specimen is fully unloaded and consolidation readings were completed, the entire sample was removed from the consolidation cell and its mass determined. The sample was then oven dried to determine the dry mass and physical properties of the specimen.

All testing results were conducted in accordance with Australian Standards AS 1289.6.2.2 – 1998.

Curing of Samples

Samples were all cured in a convection oven @ 38 degrees. To ensure the high levels of humidity required, all samples were triple bagged in garbage bags. Approximately 500mL of water was poured into the base of the innermost bag to elevate the humidity to approximately 100%. Samples were removed as required and tested, resealing the bags after the samples had been retrieved. These conditions are representative of conditions likely to be encountered underground (Bloss, personal communication 2000).

APPENDIX 3.2

Mineralogical Data

- *XRF mineralogical data*
- *XRD Analysis – JCU AAC report*

Table A3.2. 1 XRF Analysis of Cannington Tailings

Element	Concentration	Units
O	58.35	%
Na	0.179	%
Mg	1.2	%
Al	1.1	%
Si	15.9	%
P	0.0291	%
Si	1.6	%
Cl	0.111	%
K	0.35	%
Ca	4.38	%
Ti	295	ppm
V	45	ppm
Mn	1.43	%
Fe	12.6	%
Cu	160	ppm
Zn	0.566	%
Ge	25	ppm
As	0.11	%
Rb	24	ppm
Y	106	ppm
Cd	55	ppm
Sb	169	ppm
Cs	177	ppm
Ba	111	ppm
Ce	207	ppm
Pr	151	ppm
Re	150	ppm
Pb	1.67	%

XRD Analysis

Advanced Analytical Centre – James Cook University

1. PROCEDURE

Quantitative X-ray Diffraction analysis was requested for each sample.

2. METHOD

2.1 Powder X-ray Diffraction (XRD) analysis

2.1.1 Sample preparation

The samples were prepared as a smear mount: approximately 0.5 g of the sample was mixed with water and smeared onto a round glass slide (15mm diameter). This slide was then inserted into a plastic cavity mount suitable for insertion into the X-ray diffractometer.

2.1.2 Instrumentation

Data for all samples were collected with a Siemens D5000 front-loading X-ray Diffractometer. This instrument is fitted with a Copper tube (Cu Kα = 1.54178 Å), operating at 40 kV and 30 mA, and a post diffraction graphite monochromator. All samples were scanned from 1.3^o 2θ to 65^o 2θ in steps of .01^o 2θ for 2.4 secs per step.

Quantitative analysis of XRD scans

X-ray diffraction is inherently not an accurate and precise quantitative method due to factors that affect the output. These include, for the sample, particle size, orientation of the phases, variability of the chemistry and crystallinity. In addition, sample preparation, data collection settings and instrument conditions can affect the quality of the scans.

Quantification of the crystalline mineral phases was performed with the SIROQUANTTM software package. This software uses the full-profile Rietveld method of refining the profile of the calculated XRD pattern against the profile of the measured XRD pattern. The total calculated pattern is the sum of the calculated patterns of the individual patterns. Results are given as % of the total.

The limitations of XRD analysis are as follows:

a. There is a limit of detection of 1-2% on most crystalline phases.
b. Where there exist multiple phases, overlap of diffracted reflections can occur, thus rendering some ambiguity into the interpretation.
c. Some phases cannot be unambiguously identified as they are present in minor or trace amounts.

The limitation of quantification by SIROQUANTTM is as follows:

a. The method as described is standardless: it relies solely on the published crystallographic data available for each phase. Some data may not exactly describe the phases present.

Errors on the analysis are as follows:

0 -10%	+/- 1%
10 – 50%	+/- 2%
50-100%	+/- 5%

Errors quoted are absolute.

3. RESULTS

Quantitative XRD analysis for each sample is as follows:

AAC Run No		**4551-01**
Your ref		**BHP 6% 74% Top**
Quartz	SiO2	46%
Kaolinite	Al2(Si2O5)(OH)4	8%
Talc	Mg3(OH)2Si4O10	7%
Fluorite	CaF2	10%
Calcite	CaCO3	7%
Galena	PbS	0%
Magnetite	Fe3O4	15%
Gypsum	CaSO4.2H2O	7%

AAC Run No		**4551-02**
Your ref		**BHP 6% 74% Bott**
Quartz	SiO2	45%
Kaolinite	Al2(Si2O5)(OH)4	13%
Talc	Mg3(OH)2Si4O10	7%
Fluorite	CaF2	15%
Calcite	CaCO3	1%
Galena	PbS	0%
Magnetite	Fe3O4	10%
Gypsum	CaSO4.2H2O	2%
Amphibole	e.g. Ca2(Mg,Fe)5Si8O22(OH)2	6%

The change in the mineralogy of the sample indicates the chemical processes of sulphate attack can occur within the boundaries of each sample. The first set of readings were taken from the lighter coloured, powdery tailings on top of the sample, whilst the second set of samples, were taken from the unaffected base of the sample. The exact contribution of the effect of each of the separate chemical processes is not known.

APPENDIX 3.3

Physical Properties Data

- *Grain size distribution curves*
- *Specific gravity test results*
- *Atterberg test results*
- *Linear shrinkage test results*
- *Phase relations, physical property summaries and plots*

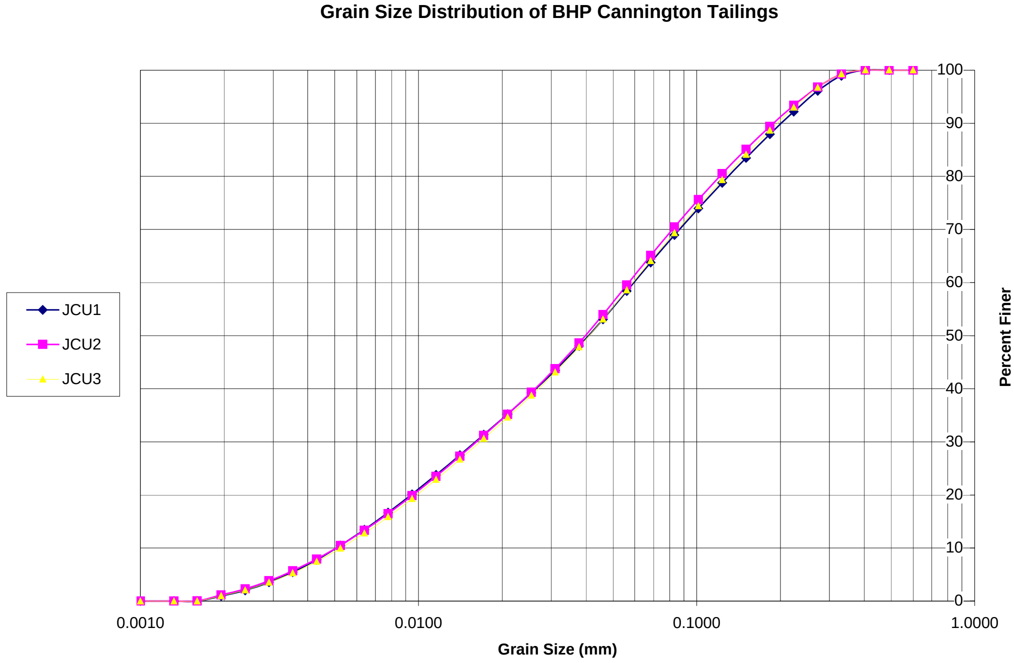

Figure A3.3. 1 GSD Curves - James Cook University (source: Malvern Mastersizer)

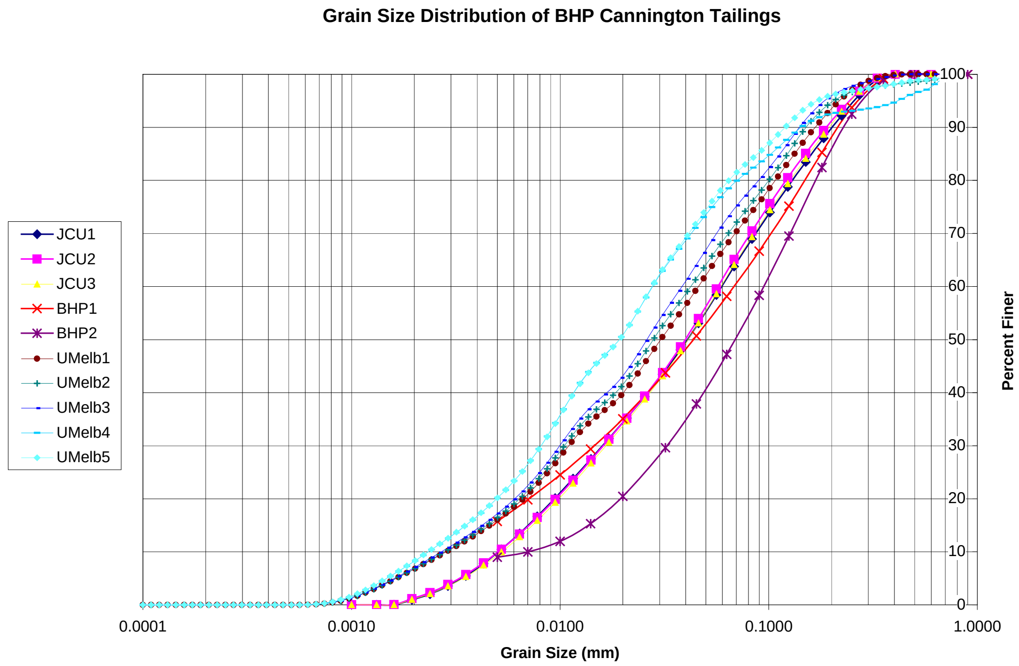

Figure A3.3. 2 GSD Curves - James Cook University, BHP Cannington and University of Melbourne (All sources: Malvern Mastersizer).

Note: Variations in plots were found/ attributed to the different models of the Malvern laser-sizer and the different "lenses" used in the laser sizing. The average of the JCU plots has been used in the body text of the thesis.

JCU ENGINEERING

PhD - Paste Backfill Engineering Properties
Characterisation of fill supplied to JCU by BHP 6/10/99

Test :- SG Test

Water Temperature 23.5^{O} C 23.5^{O} C

	Test 1	Test 2
Bottle No.	2	5
Mass of bottle (+ stopper), $\mathbf{m_1}$ (g)	146.647	142.154
Mass of bottle (+ stopper) + water , $\mathbf{m_2}$ (g)	394.348	391.663
Mass of bottle (+ stopper) + soil , $\mathbf{m_3}$ (g)	292.047	309.379
Mass of bottle (+ stopper) + soil + water , $\mathbf{m_4}$ (g)	494.263	506.658
Water Content Determination		
Container No.	B62	B51
Mass of container (g)	37.867	40.086
Mass of container + wet soil (g)	111.632	120.985
Mass of container + dry soil (g)	111.463	120.808
Water Content, **w** (%)	0.23%	0.22%
Mass of dry soil in the bottle, $\mathbf{m_s}$ (g)*	145.067	166.859
Specific Gravity, $\mathbf{G_s}$ **	3.213	3.217
Average Specific Gravity (nearest 0.01)***	**3.22**	

RESULT........ Test Result Acceptable

Figure A3.3. 3 Specific Gravity Test 1 on Cannington Tailings

JCU ENGINEERING

PhD - Paste Backfill Engineering Properties
Characterisation of fill supplied to JCU by BHP 6/10/99

Test :- SG Test

Water Temperature 24.5^{O} C 24.5^{O} C

	Test 1	**Test 2**
Bottle No.	3	4
Mass of bottle (+ stopper), $\mathbf{m_1}$ (g)	145.372	143.213
Mass of bottle (+ stopper) + water , $\mathbf{m_2}$ (g)	390.364	389.534
Mass of bottle (+ stopper) + soil , $\mathbf{m_3}$ (g)	281.955	302.123
Mass of bottle (+ stopper) + soil + water , $\mathbf{m_4}$ (g)	483.745	498.512
Water Content Determination		
Container No.	B50	B57
Mass of container (g)	39.187	40.052
Mass of container + wet soil (g)	95.525	97.805
Mass of container + dry soil (g)	95.387	97.671
Water Content, **w** (%)	0.25%	0.23%
Mass of dry soil in the bottle, $\mathbf{m_s}$ (g)*	136.248	158.541
Specific Gravity, $\mathbf{G_s}$ **	3.178	3.199
Average Specific Gravity (nearest 0.01)***	**3.19**	

RESULT…….. Test Result Acceptable

Figure A3.3. 4 Specific Gravity Test 2 on Cannington Tailings

JCU ENGINEERING

PhD - Paste Backfill Engineering Properties
Characterisation of fill supplied to JCU by BHP 6/10/99

Test :- Atterberg Limit Tests #1

Liquid Limit & Plastic Limit Determination

Test	Liquid Limit					Plastic Limit	
Tin No.	*A8*	*A38*	*A78*	*A18*	*A83*	*A102*	*A61*
Wt. Tin & wet soil (g)	40.353	56.49	50.529	37.186	64.566	24.997	21.418
Wt. Tin & dry soil (g)	37.763	50.552	45.028	33.654	55.431	24.418	21.035
Wt. Tin (g)	22.95	19.825	18.324	18.121	17.09	20.306	18.05
Moisture Content (%)	17%	19%	21%	23%	24%	14.08%	12.83%
Cone Penetration (mm)	7.85	13.50	19.30	31.00	38.40		

Linear Shrinkage Test

Mould No.	*12*
Linear Shrinkage (%)	1.73%

Summary

Liquid Limit LL (%)	**20.38%**
Plastic Limit PL (%)	**13.46%**
Plastic Index PI = LL - PL (%)	**6.93%**

Figure A3.3. 5 LL & PL Testing for Cannington Tailings (Test #1)

JCU ENGINEERING

PhD - Paste Backfill Engineering Properties
Characterisation of fill supplied to JCU by BHP 6/10/99

Test :- Atterberg Limit Tests #2

Liquid Limit & Plastic Limit Determination

Test	Liquid Limit					Plastic Limit	
Tin No.	*A103*	*A43*	*A71*	*A45*	*A64*	*A93*	*A96*
Wt. Tin & wet soil (g)	66.987	49.806	53.563	60.36	65.372	24.489	22.574
Wt. Tin & dry soil (g)	58.899	45.296	47.33	52.701	56.146	23.869	21.951
Wt. Tin (g)	17.998	22.928	17.495	19.495	17.911	19.388	17.782
Moisture Content (%)	19.77%	20.16%	20.89%	23.07%	24.13%	13.84%	14.94%
Cone Penetration (mm)	15.60	17.50	21.70	32.00	39.70		

Linear Shrinkage Test

Mould No.	*10*
Linear Shrinkage (%)	1.66%

Summary

Liquid Limit LL (%)	**20.62%**
Plastic Limit PL (%)	**14.39%**
Plastic Index PI = LL - PL (%)	**6.23%**

Figure A3.3. 6 LL & PL Testing for Cannington Tailings (Test #2)

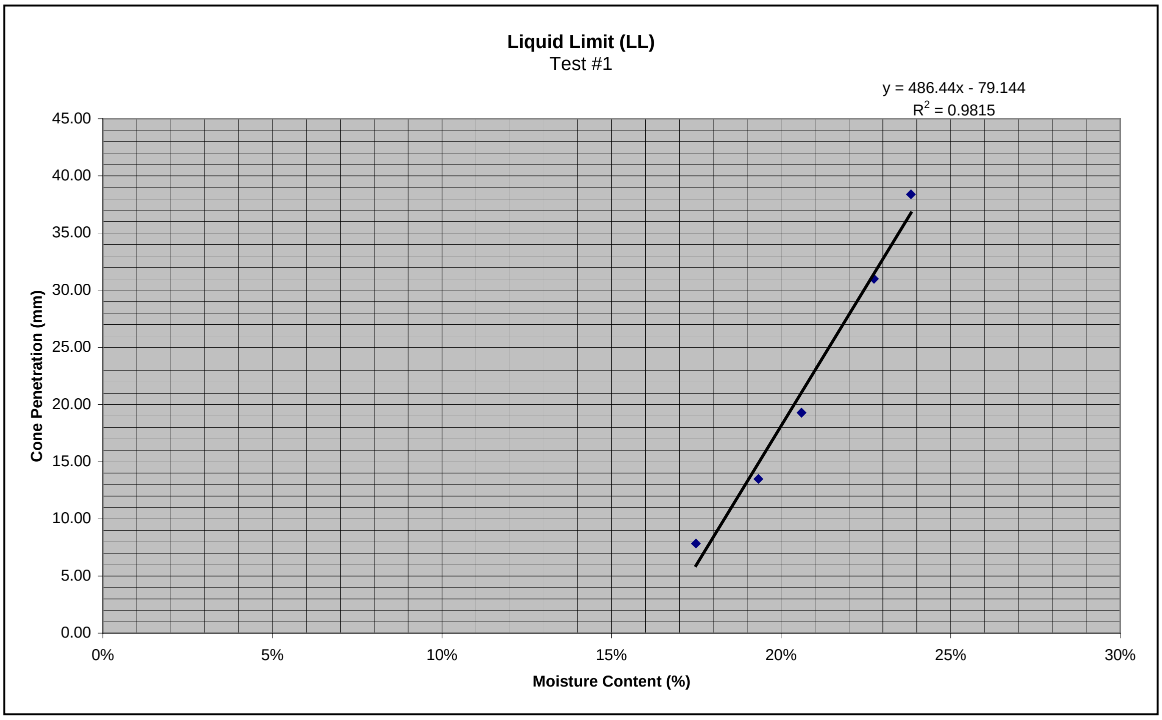

Figure A3.3. 7 Liquid Limit Plot Cannington Tailings (Test #1)

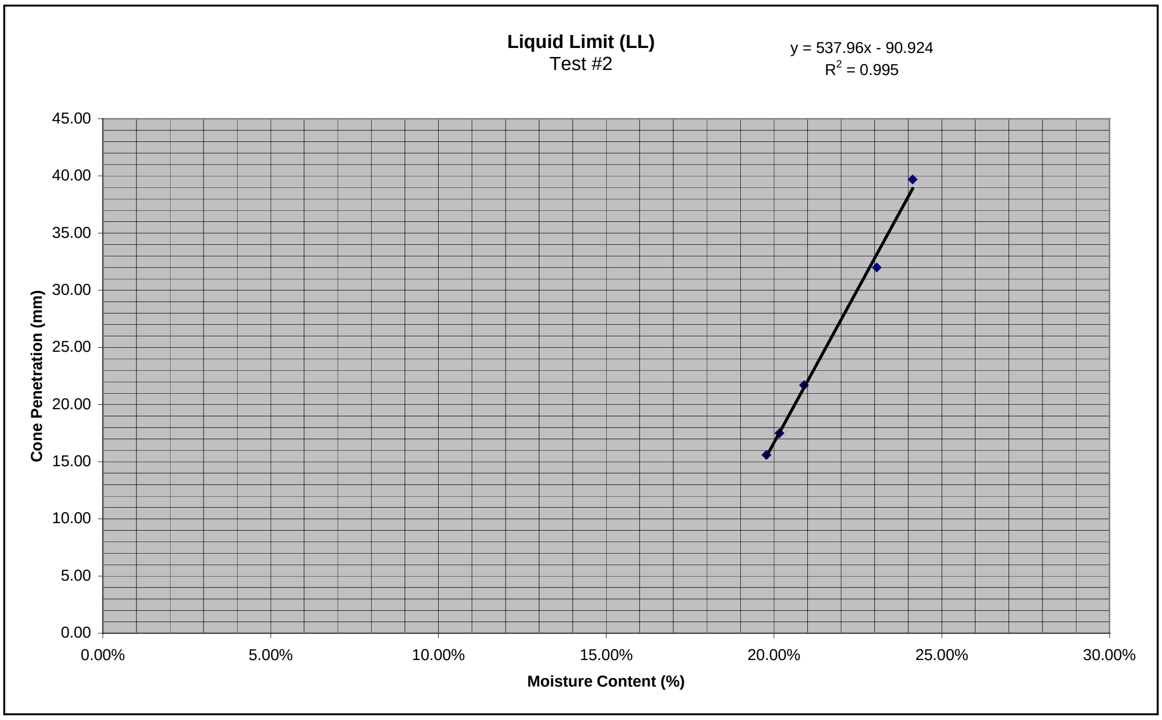

Figure A3.3. 8 Liquid Limit Plot Cannington Tailings (Test #2)

JCU ENGINEERING

PhD - Paste Backfill Engineering Properties

Characterisation of fill supplied to JCU by BHP 6/10/99

Test :- **Linear Shrinkage** **Date:-**

Water Temp = 23^{0}C

		L_x = Length of sample after x days of curing						LS_x = Linear Shrinkage after x days of curing				
Mix	Mould No.	L_0 (mm)	L_1 (mm)	L_3 (mm)	L_7 (mm)	L_{14} (mm)	L_{18} (mm)	LS_1 (mm)	LS_3 (mm)	LS_7 (mm)	LS_{14} (mm)	LS_{18} (mm)
2%,74%	14	250	244.5	243.5	243.5	243.5	243.5	2.20%	2.60%	2.60%	2.60%	2.60%
2%,78%	12	250	245.5	244	244	244	244	1.80%	2.40%	2.40%	2.40%	2.40%
4%,74%	11	250	246	245	244.5	244.5	244.5	1.60%	2.00%	2.20%	2.20%	2.20%
4%,78%	9	250	249	248	248	248	248	0.40%	0.80%	0.80%	0.80%	0.80%
6%,74%	13	250	248	247	247	247	247	0.80%	1.20%	1.20%	1.20%	1.20%
6%,78%	10	250	248.5	247.5	247	247	247	0.60%	1.00%	1.20%	1.20%	1.20%
0%,74%	7	126	126	121.5	117.5	117.5	117.5	0.00%	3.57%	6.75%	6.75%	6.75%
0%,78%	8	126	124	119.5	119.5	119	119	1.59%	5.16%	5.16%	5.56%	5.56%

****NB - Linear Shrinkage of samples ceased after 14 days***

curing @ room temp

curing @ 38 deg, 100% humidity

NOTES

* 0% 74% sample(7day) had longitudinal shrinkage also 2x1mm - dark grey in colour

* 0% 78% sample(7day) had longitudinal shrinkage also 2x0.5mm - light grey in colour

Table A3.3. 1 Linear Shrinkage Results for paste fill mixes

Table A3.3. 2 Phase Relations; Summary Table: 2% Cement, 74% Solids

					Months of Curing			
	Days of Curing				3	6	9	12
Mix Specification	**7**	**14**	**28**	**56**	**91**	**183**	**274**	**365**
Moisture Content	30.3%	30.5%	30.3%	31.6%	31.1%	32.8%	32.8%	26.8%
Void Ratio (e)	1.063	1.052	1.050	1.051	1.167	1.198	1.247	1.174
Degree of Saturation	91.0%	92.5%	92.3%	96.2%	85.1%	87.5%	84.0%	72.8%
Porosity (n)	51.5%	51.3%	51.2%	51.2%	53.8%	54.5%	55.5%	54.0%
Bulk Density (ρ_m) {t/m^3}	2.038	2.052	2.052	2.071	1.952	1.950	1.907	1.881
Dry Density (ρ_d) {t/m^3}	1.564	1.573	1.574	1.573	1.490	1.468	1.436	1.484
Sat. Density (ρ_{sat}) {t/m^3}	2.085	2.091	2.091	2.091	2.033	2.019	1.997	2.030
Bulk Modulus (γ_m) {kN/m^3}	19.99	20.13	20.13	20.32	19.15	19.13	18.71	18.46
Dry Bulk Modulus (γ_d) {kN/m^3}	15.35	15.43	15.44	15.43	14.61	14.40	14.09	14.56
Sat. Bulk Modulus (γ_{sat}) {kN/m^3}	20.45	20.51	20.52	20.51	19.95	19.80	19.59	19.91

Table A3.3. 3 Phase Relations; Summary Table: 2% Cement, 78% Solids

					Months of Curing			
	Days of Curing				3	6	9	12
Mix Specification	**7**	**14**	**28**	**56**	**91**	**183**	**274**	**365**
Moisture Content	25.7%	26.0%	28.0%	28.4%	27.2%	27.1%	26.9%	20.0%
Void Ratio (e)	0.862	0.872	0.957	0.947	0.977	0.976	0.982	0.968
Degree of Saturation	95.5%	95.1%	93.6%	95.8%	88.9%	88.9%	87.6%	66.1%
Porosity (n)	46.3%	46.6%	48.8%	48.5%	49.4%	49.4%	49.5%	49.2%
Bulk Density (ρ_m) {t/m^3}	2.180	2.172	2.113	2.132	2.076	2.077	2.066	1.968
Dry Density (ρ_d) {t/m^3}	1.733	1.724	1.652	1.662	1.632	1.633	1.628	1.640
Sat. Density (ρ_{sat}) {t/m^3}	2.201	2.195	2.145	2.152	2.131	2.132	2.129	2.136
Bulk Modulus (γ_m) {kN/m^3}	21.38	21.30	20.73	20.91	20.37	20.37	20.27	19.31
Dry Bulk Modulus (γ_d) {kN/m^3}	17.00	16.91	16.21	16.31	16.01	16.02	15.98	16.08
Sat. Bulk Modulus (γ_{sat}) {kN/m^3}	21.59	21.53	21.04	21.11	20.91	20.92	20.88	20.96

Table A3.3. 4 Phase Relations; Summary Table: 6% Cement, 74% Solids

					Months of Curing			
	Days of Curing				3	6	9	12
Mix Specification	**7**	**14**	**28**	**56**	**91**	**183**	**274**	**365**
Moisture Content	30.2%	29.9%	30.0%	32.1%	31.0%	31.8%	31.1%	6.7%
Void Ratio (e)	1.070	1.064	1.050	1.193	1.158	1.169	1.156	0.924
Degree of Saturation	90.2%	89.8%	91.2%	86.5%	85.5%	86.9%	86.0%	23.3%
Porosity (n)	51.7%	51.6%	51.2%	54.3%	53.7%	53.9%	53.6%	48.0%
Bulk Density (ρ_m) {t/m^3}	2.030	2.031	2.046	1.948	1.959	1.961	1.963	1.790
Dry Density (ρ_d) {t/m^3}	1.559	1.563	1.574	1.475	1.495	1.488	1.497	1.677
Sat. Density (ρ_{sat}) {t/m^3}	2.081	2.084	2.091	2.023	2.037	2.032	2.039	2.162
Bulk Modulus (γ_m) {kN/m^3}	19.91	19.92	20.07	19.11	19.22	19.23	19.26	17.56
Dry Bulk Modulus (γ_d) {kN/m^3}	15.30	15.34	15.44	14.47	14.67	14.60	14.69	16.45
Sat. Bulk Modulus (γ_{sat}) {kN/m^3}	20.42	20.44	20.52	19.85	19.98	19.94	20.00	21.21

Table A3.3. 5 Phase Relations; Summary Table: 6% Cement, 78% Solids

					Months of Curing			
	Days of Curing				3	6	9	12
Mix Specification	**7**	**14**	**28**	**56**	**91**	**183**	**274**	**365**
Moisture Content	25.1%	25.4%	25.6%	25.3%	26.1%	19.9%	19.9%	6.7%
Void Ratio (e)	0.862	0.876	0.866	0.864	0.940	0.920	0.856	0.924
Degree of Saturation	93.1%	92.7%	94.4%	93.6%	88.7%	69.1%	75.0%	23.3%
Porosity (n)	46.3%	46.7%	46.4%	46.3%	48.5%	47.9%	46.0%	48.0%
Bulk Density (ρ_m) {t/m^3}	2.168	2.157	2.172	2.170	2.097	2.015	2.089	1.790
Dry Density (ρ_d) {t/m^3}	1.733	1.720	1.729	1.731	1.663	1.680	1.742	1.677
Sat. Density (ρ_{sat}) {t/m^3}	2.201	2.192	2.198	2.199	2.152	2.164	2.207	2.162
Bulk Modulus (γ_m) {kN/m^3}	21.27	21.16	21.30	21.28	20.58	19.76	20.50	17.56
Dry Bulk Modulus (γ_d) {kN/m^3}	17.00	16.87	16.96	16.99	16.31	16.49	17.09	16.45
Sat. Bulk Modulus (γ_{sat}) {kN/m^3}	21.59	21.50	21.56	21.58	21.12	21.23	21.65	21.21

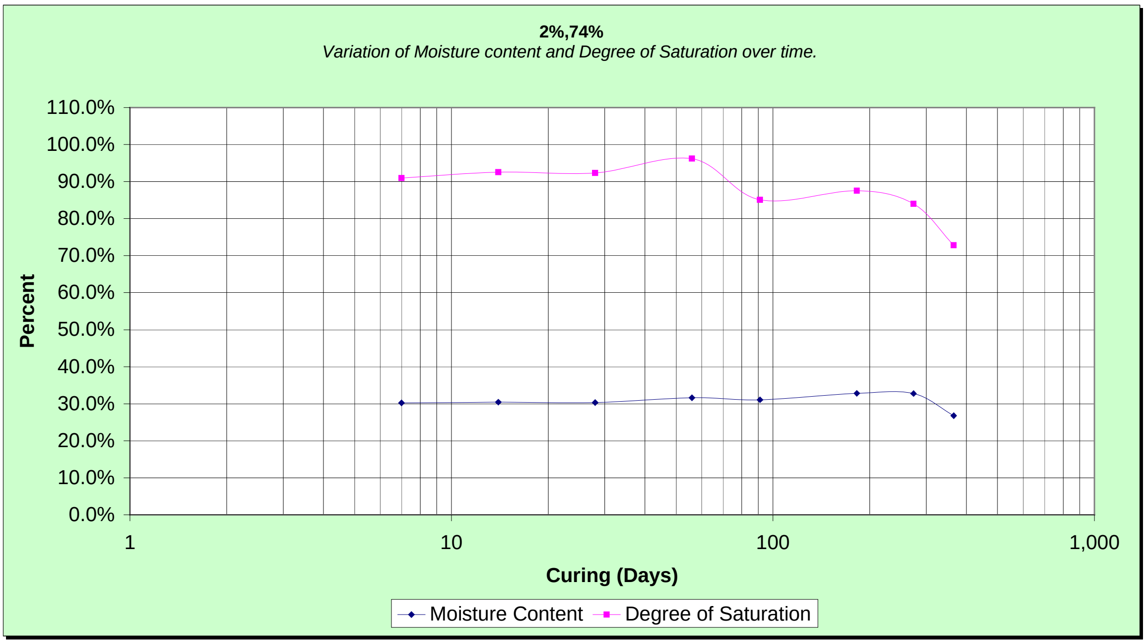

Figure A3.3. 9 Variation of Moisture Content and Degree of Saturation over Time; 2% Cement, 74% Solids

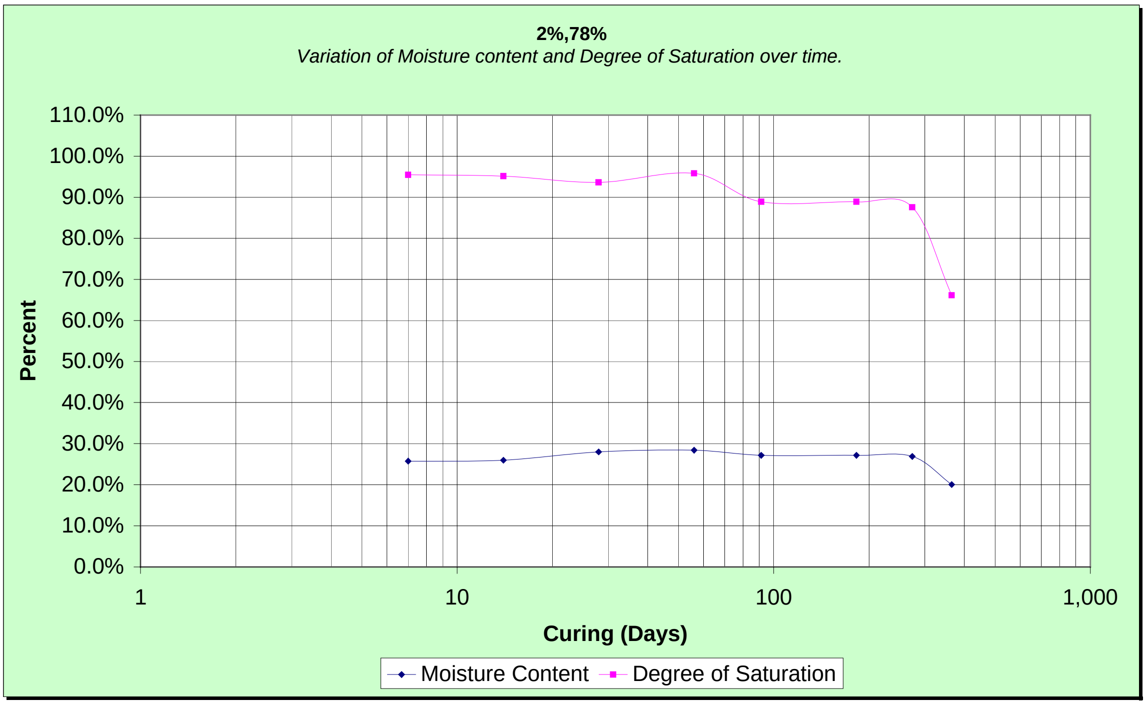

Figure A3.3. 10 Variation of Moisture Content and Degree of Saturation over Time; 2% Cement, 78% Solids

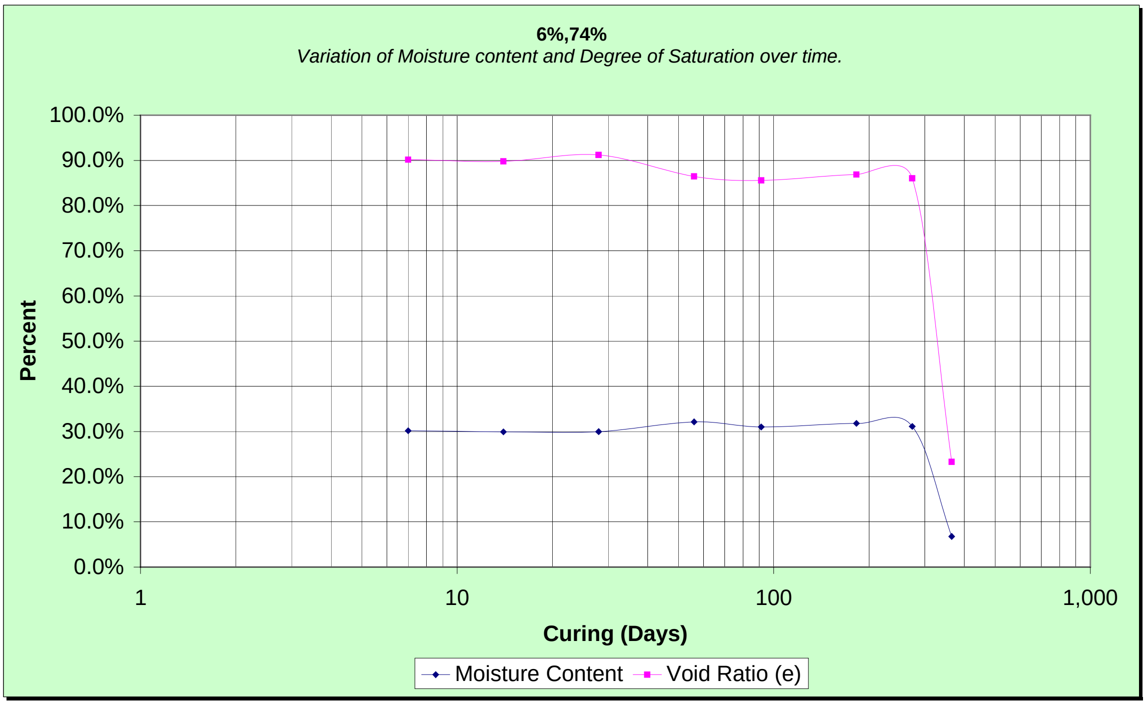

Figure A3.3. 11 Variation of Moisture Content and Degree of Saturation over Time; 6% Cement, 74% Solids

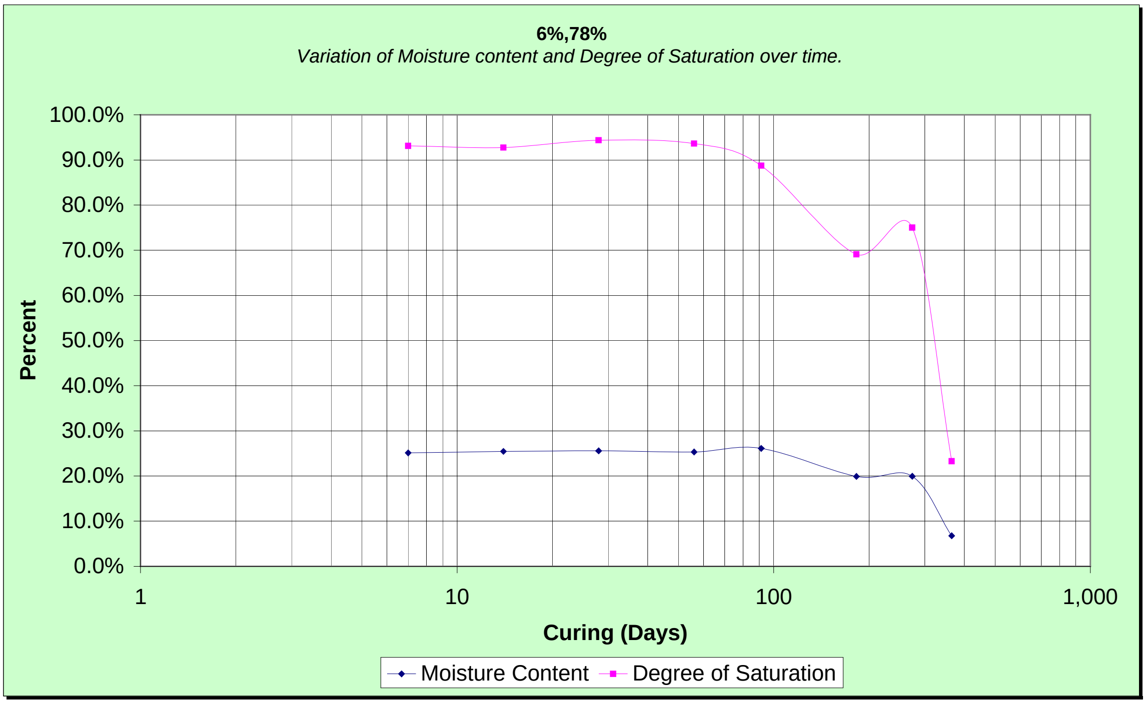

Figure A3.3. 12 Variation of Moisture Content and Degree of Saturation over Time; 6% Cement, 74% Solids

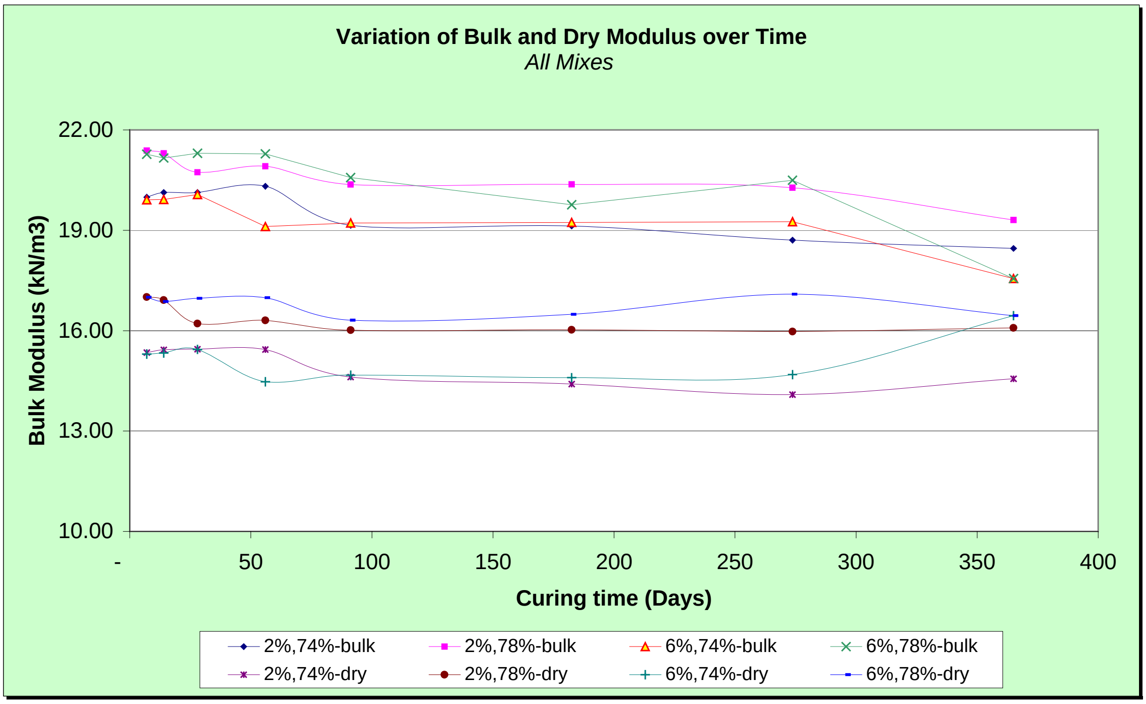

Figure A3.3. 13 Variation of the Bulk and Dry Density of Paste over Time

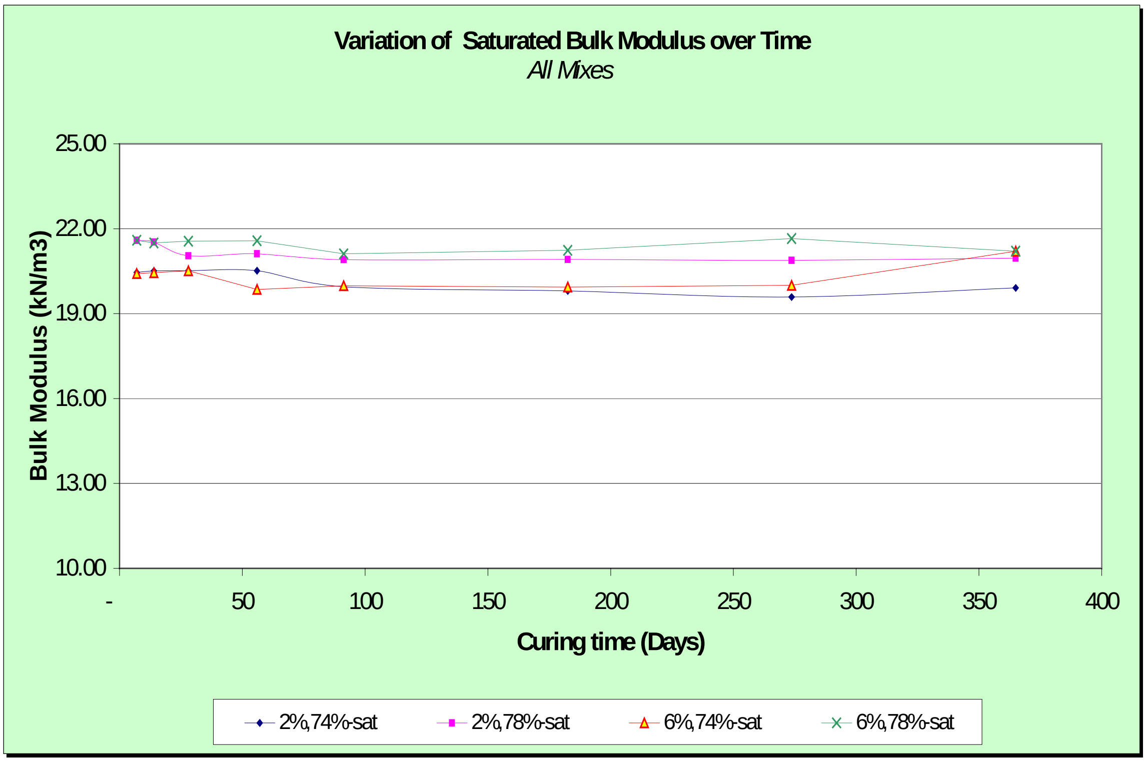

Figure A3.3. 14 Variation of the Saturated Bulk Density of Paste over Time

APPENDIX 3.4

Total Stress Analysis Data

- *Paste Rheology Data*
- *UCS Data*
  - *Mix proportion variation*
  - *Grain size distribution variation*
- *UU triaxial Data and summary plots*
  - *Physical Properties, phase relations short medium and long term samples*
  - Strength relations – plots
- *Tensile Strength Data and plots*

Table A3.4. 1 Table of Yield Stress as a Function of Pulp Density (from Clayton, 2000)

Pulp Density %w/w	Yield Stress (Pa)
70.0%	12
70.5%	14
71.0%	17
71.5%	21
72.0%	26
72.5%	31
73.0%	38
73.5%	47
74.0%	57
74.5%	69
75.0%	85
75.5%	103
76.0%	126
76.5%	154
77.0%	187
77.5%	228
78.0%	279
78.5%	340
79.0%	414
79.5%	505
80.0%	616
80.5%	751
81.0%	916

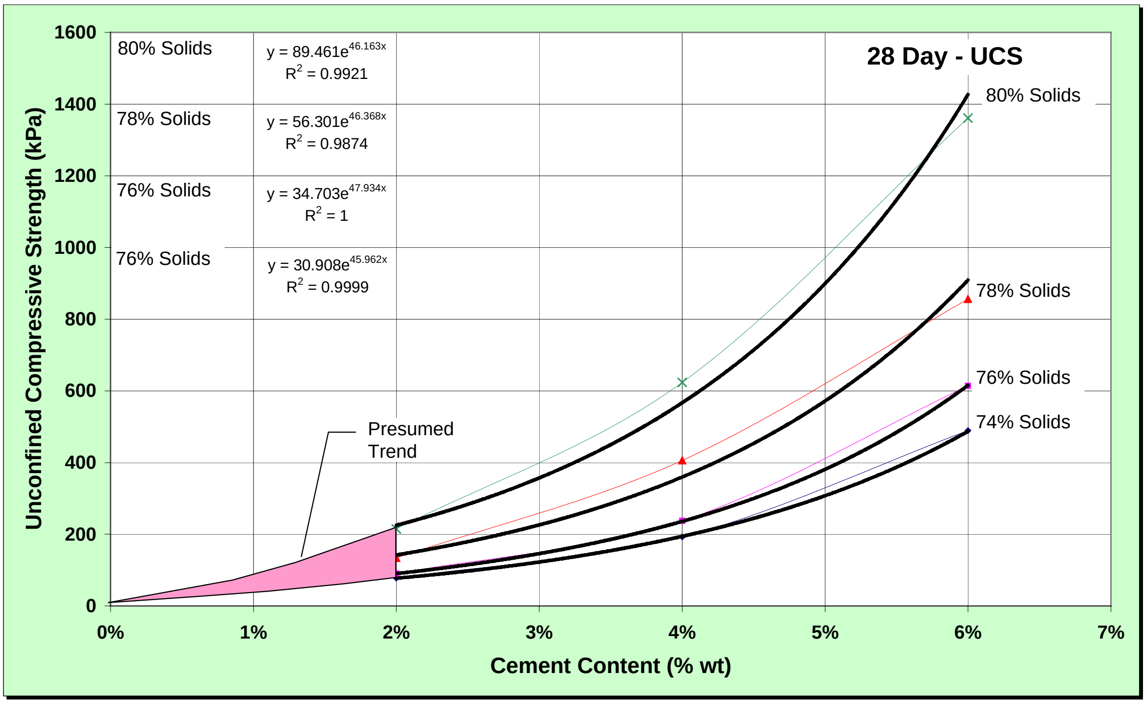

Figure A3.4. 1 Variation of Sample strength with cement content

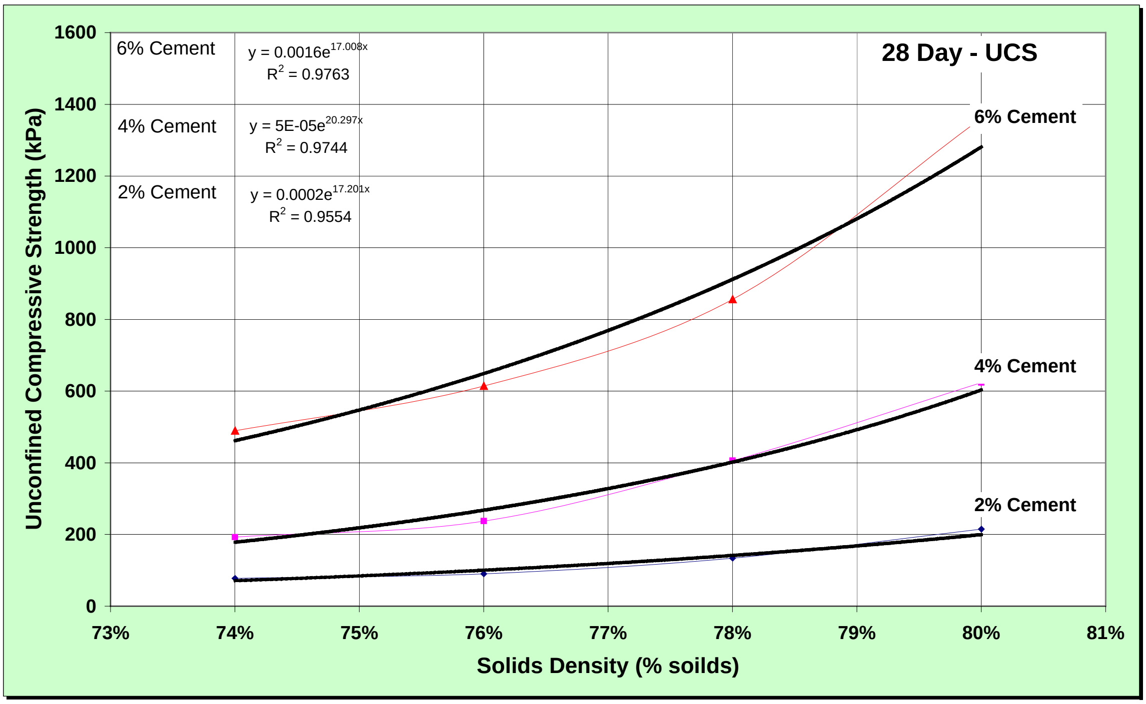

Figure A3.4. 2 Variation of Sample strength with solids content

Table A3.4. 2 Failure Strains for 28 Day UCS samples

% Cement	Solids Content			
	74%	76%	78%	80%
2%	9.6%	4.4%	3.8%	3.4%
4%	6.2%	2.0%	1.8%	1.6%
6%	1.8%	1.7%	1.6%	1.2%

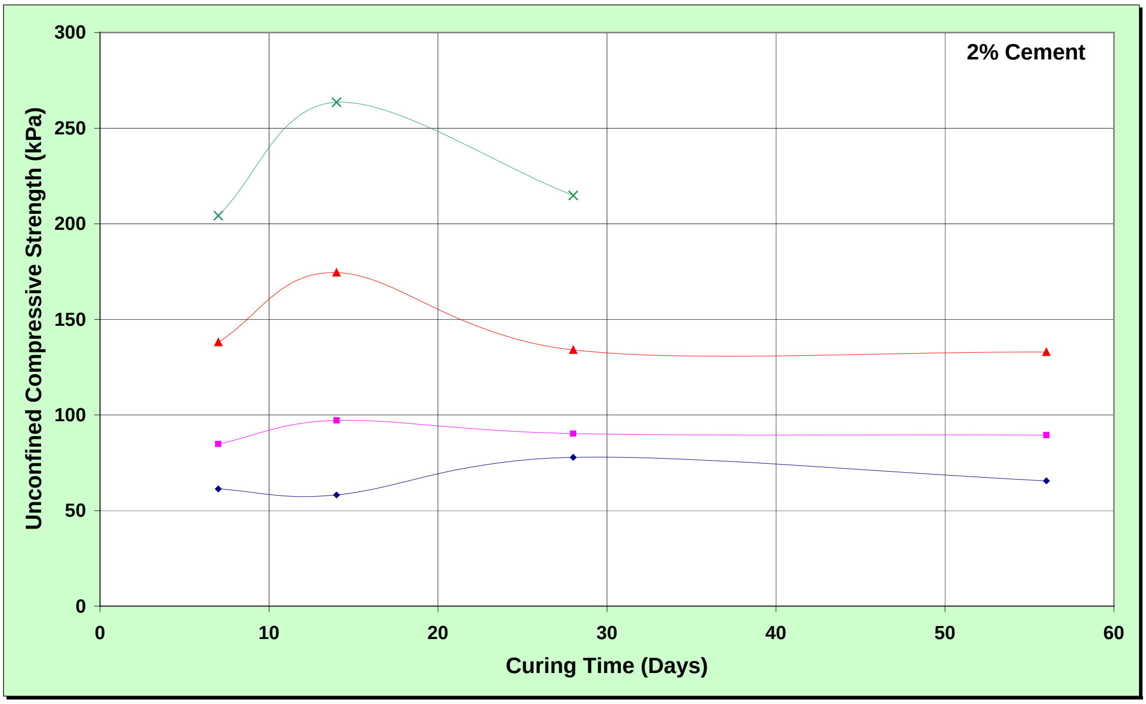

Figure A3.4. 3 Progressive strength gain of 2% cement (by dry weight) samples

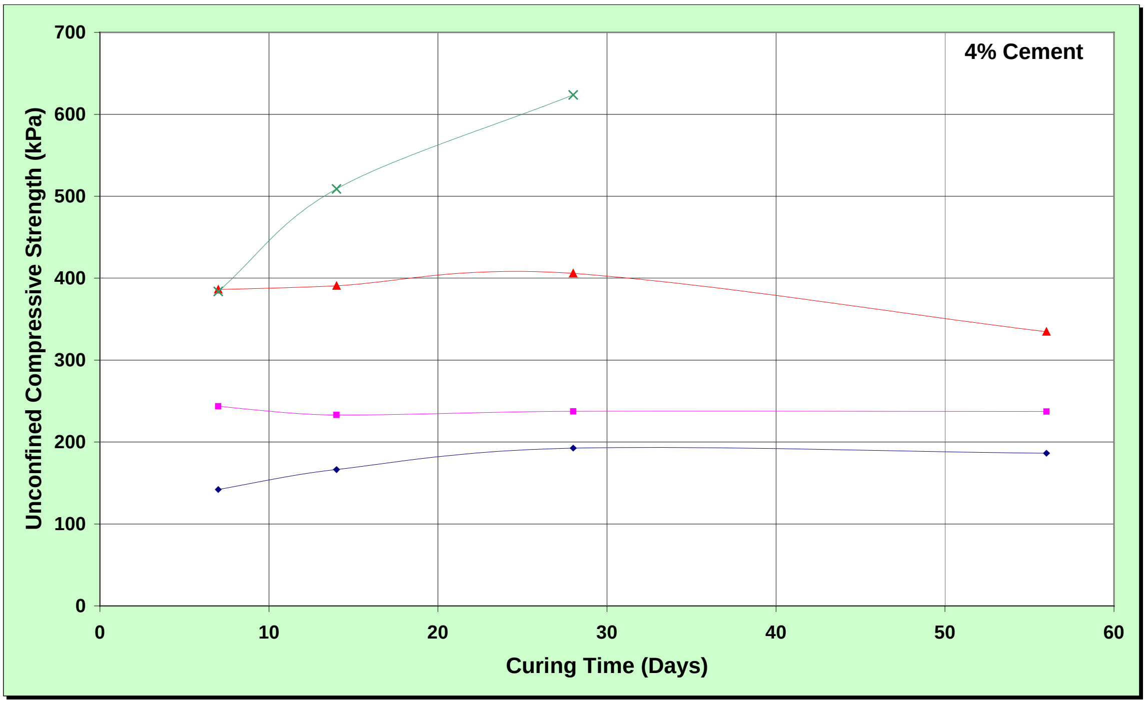

Figure A3.4. 4 Progressive strength gain of 2% cement (by dry weight) samples

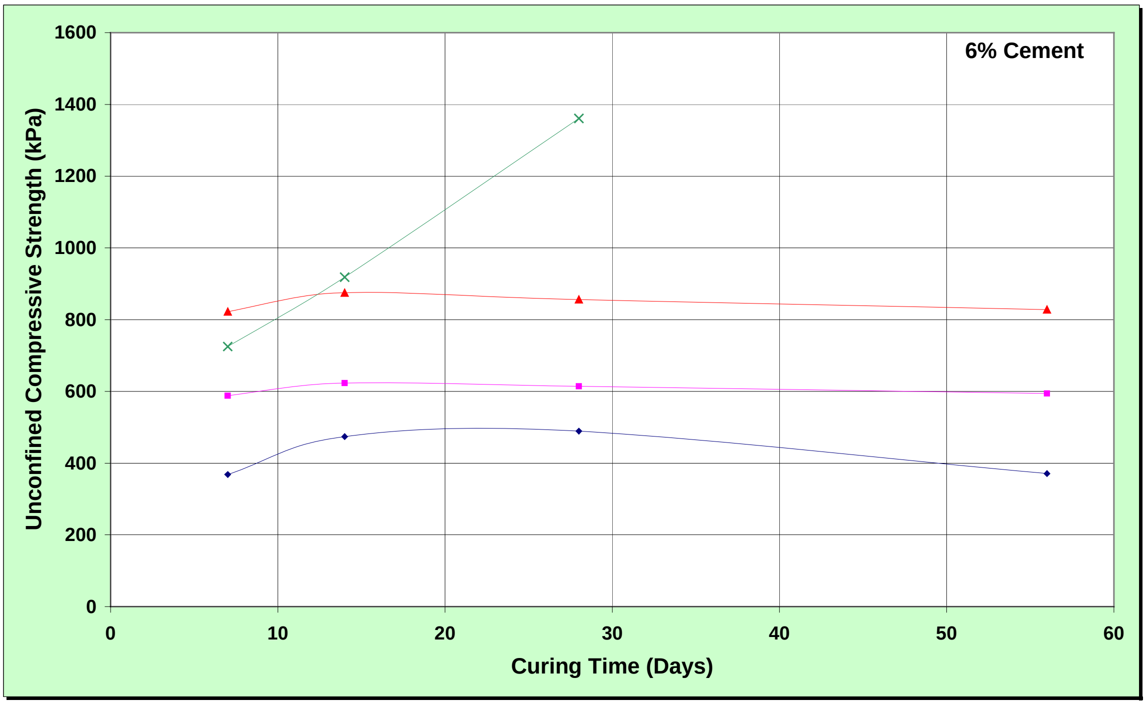

Figure A3.4. 5 Progressive strength gain of 2% cement (by dry weight) samples

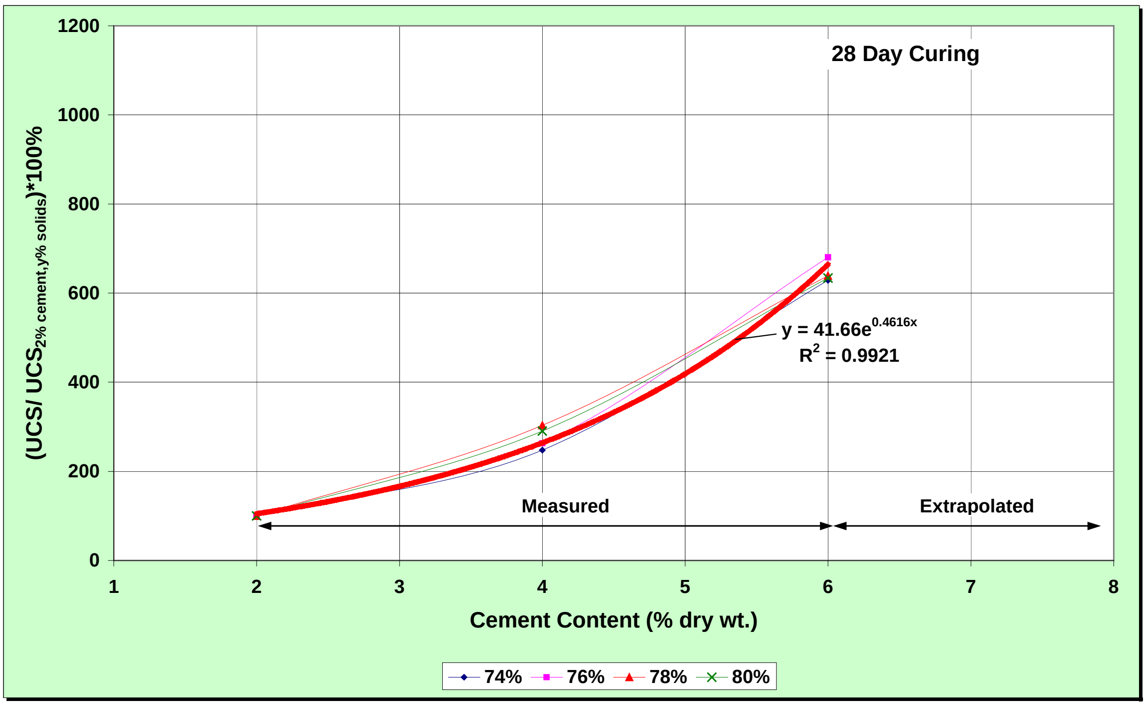

Figure A3.4. 6 UCS samples normalised to 2% cement samples

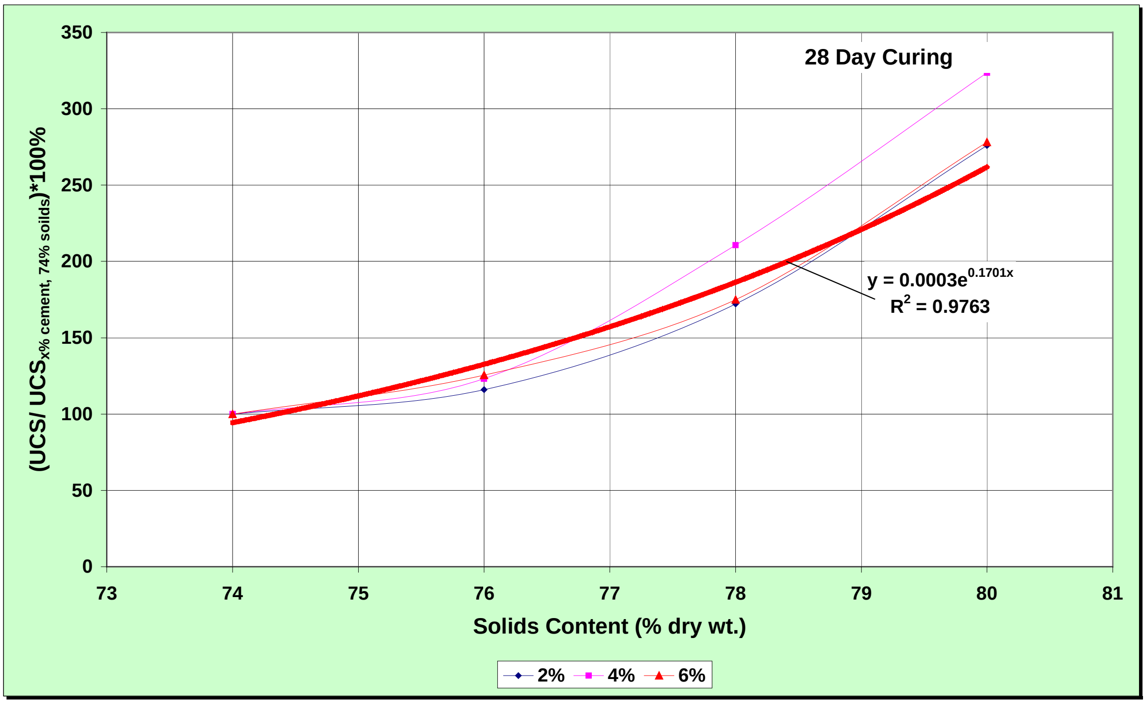

Figure A3.4. 7 UCS samples normalised to 74% solids samples

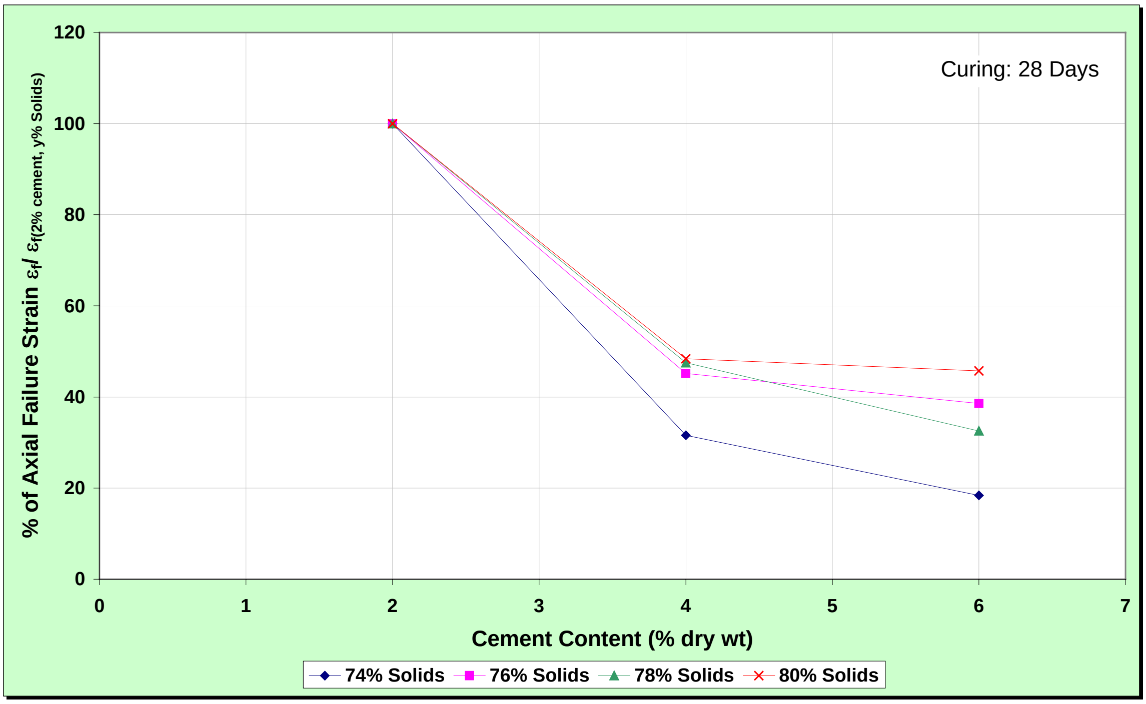

Figure A3.4. 8 UCS samples normalised to 2% cement samples

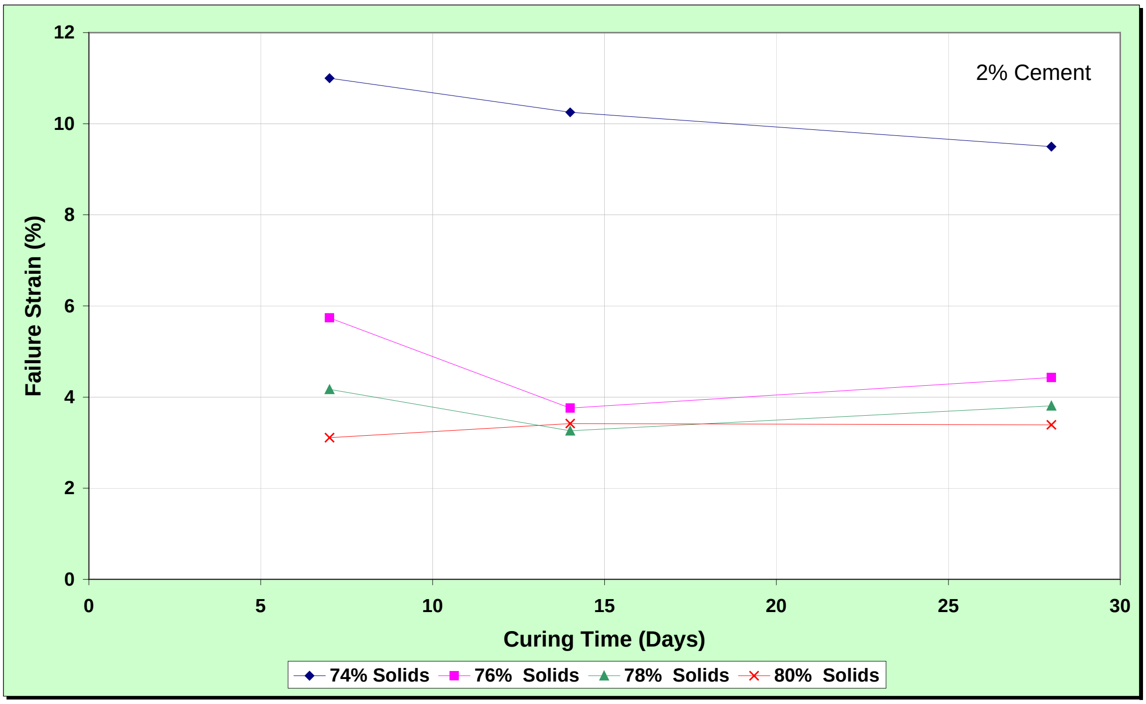

Figure A3.4. 9 Failure Strains vs. Curing Time (2% Cement)

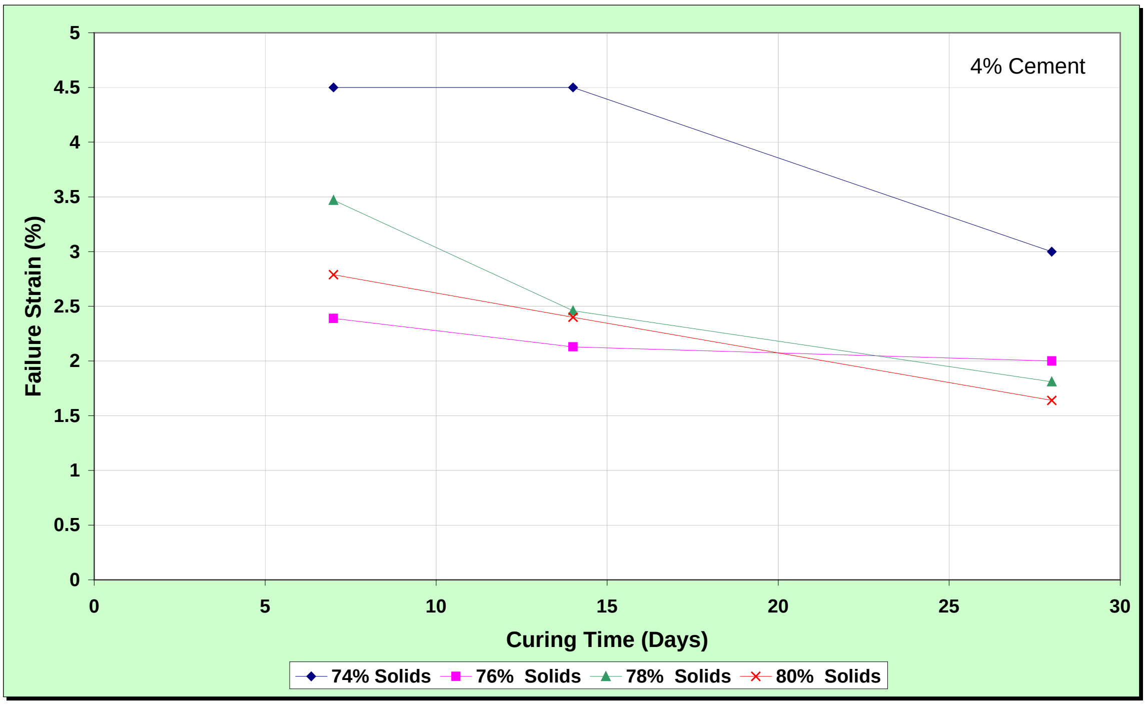

Figure A3.4. 10 Failure Strains vs. Curing Time (4% Cement)

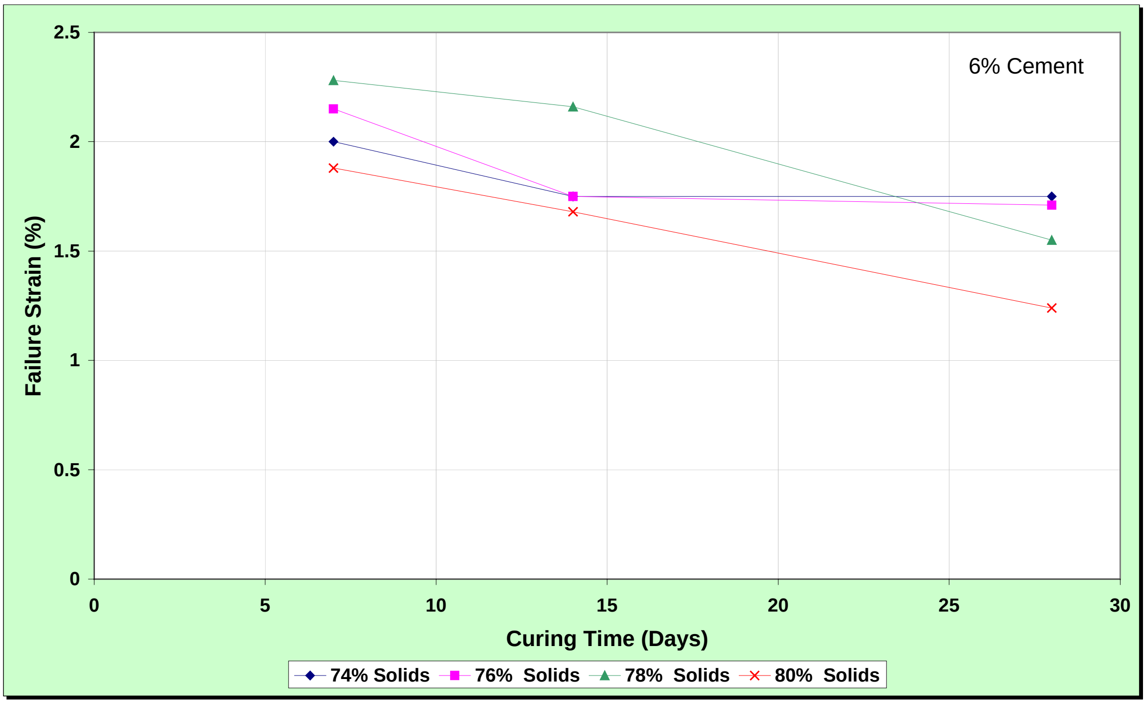

Figure A3.4. 11 Failure Strains vs. Curing Time (6% Cement)

Table A3.4. 3 Summary of Progressive UCS Strength of variations in grading of tailings grains size distribution.

Mix		Grind	7 Day Curing			14 Day Curing			28 Day Curing		
% Cement	% Solids		UCS (kPa)	E_{tmax} (kPa)	$\varepsilon_{failure}$	UCS (kPa)	E_{tmax} (kPa)	$\varepsilon_{failure}$	UCS (kPa)	E_{tmax} (kPa)	$\varepsilon_{failure}$
2%	76	Fine	69	4848	10.77%	174	12956	8.23%	201	19861	2.59%
2%	76	Med	46	3565	6.57%	118	11557	7.08%	144	27561	3.05%
2%	76	Coarse	86	8841	5.22%	117	11662	4.56%	111	15292	3.99%
Average			67	5752	7.52%	136	12059	6.62%	152	20905	3.21%
2%	80	Fine	137	9257	8.46%	390	21436	7.90%	424	52636	5.09%
2%	80	Med	162	13371	9.27%	325	16851	6.31%	362	53306	5.15%
2%	80	Coarse	166	14406	4.74%	198	17260	4.38%	209	23967	3.99%
Average			155	12345	7.49%	304	18516	6.20%	331	43303	4.74%
6%	76	Fine	612	88836	1.45%	1024	88219	1.95%	1146	196853	1.32%
6%	76	Med	537	54296	1.23%	826	126432	1.15%	899	92352	1.50%
6%	76	Coarse	465	41468	1.57%	585	88071	1.37%	722	92770	1.50%
Average			538	61533	1.42%	812	100907	1.49%	923	127325	1.44%
6%	80	Fine	1066	115270	1.80%	1489	173955	1.84%	1640	157286	2.10%
6%	80	Med	1107	106670	1.44%	1570	218403	1.12%	2281	242105	1.47%
6%	80	Coarse	807	61354	2.18%	1031	112495	1.34%	1258	112315	1.74%
Average			993	94431	1.81%	1363	168284	1.43%	1726	170569	1.77%

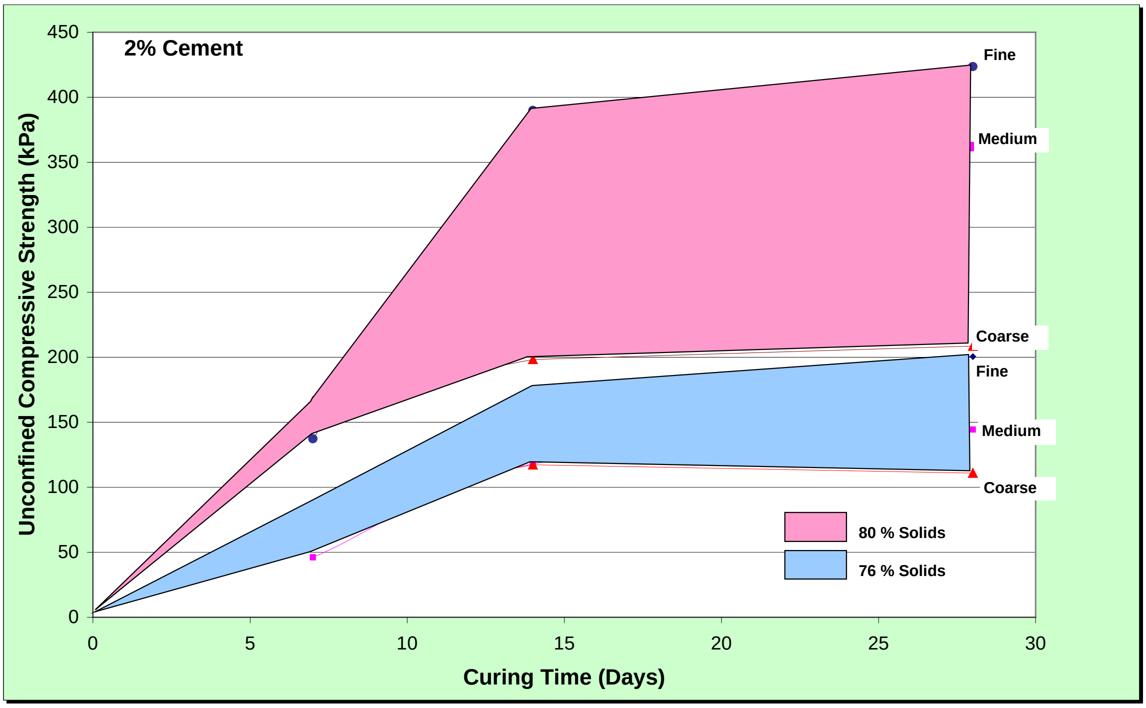

Figure A3.4. 12 Progressive strength gain of 2% cement (by dry weight) samples, with various grain size distributions

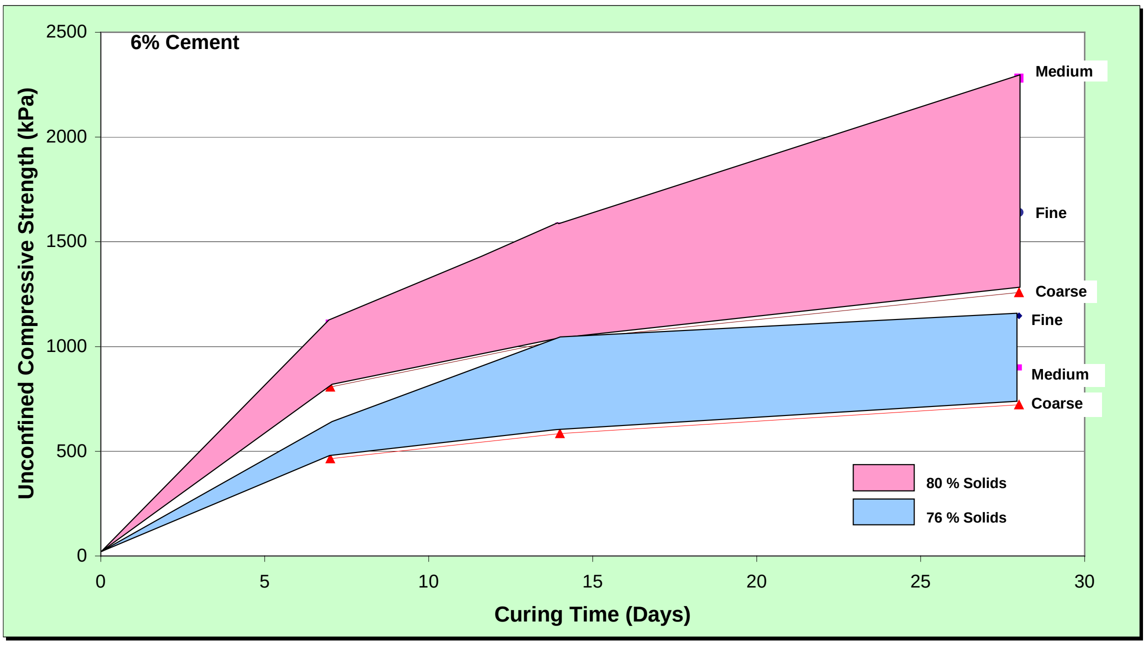

Figure A3.4. 13 Progressive strength gain of 2% cement (by dry weight) samples, with various grain size distributions

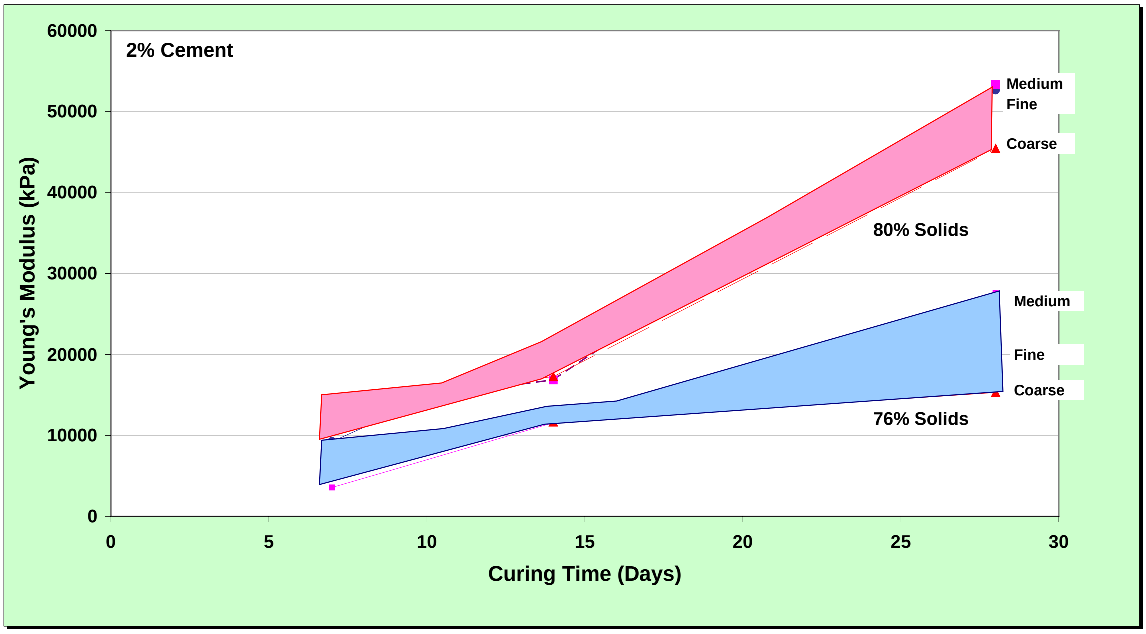

Figure A3.4. 14 Variation of the Young's Modulus for 2% cement (by dry weight) samples, with various grain size distributions

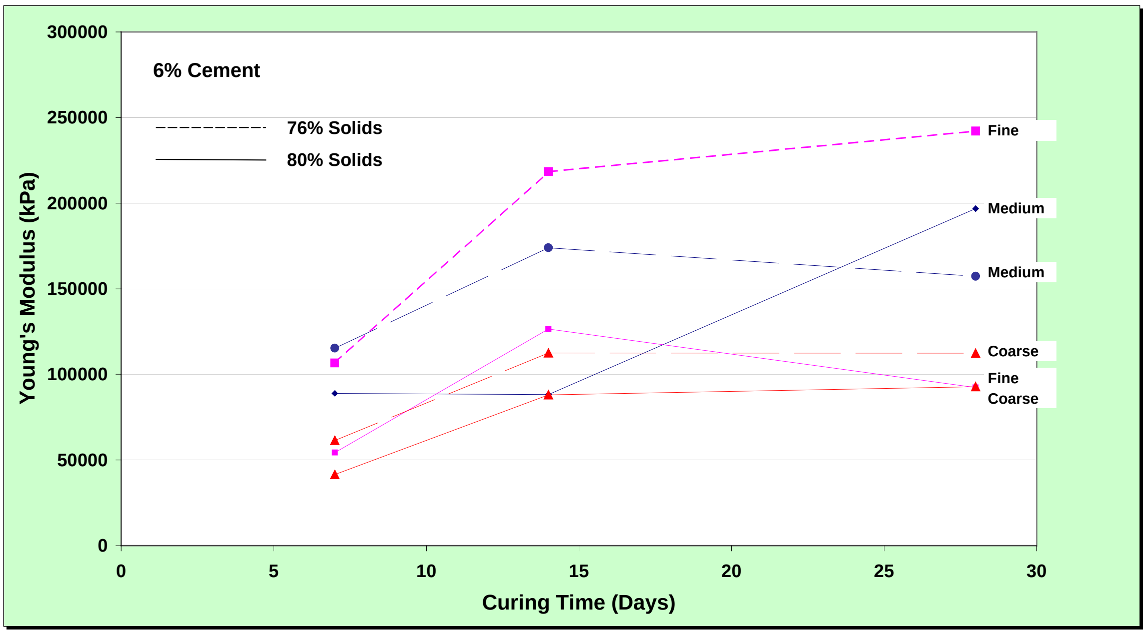

Figure A3.4. 15 Variation of the Young's Modulus for 6% cement (by dry weight) samples, with various grain size distributions

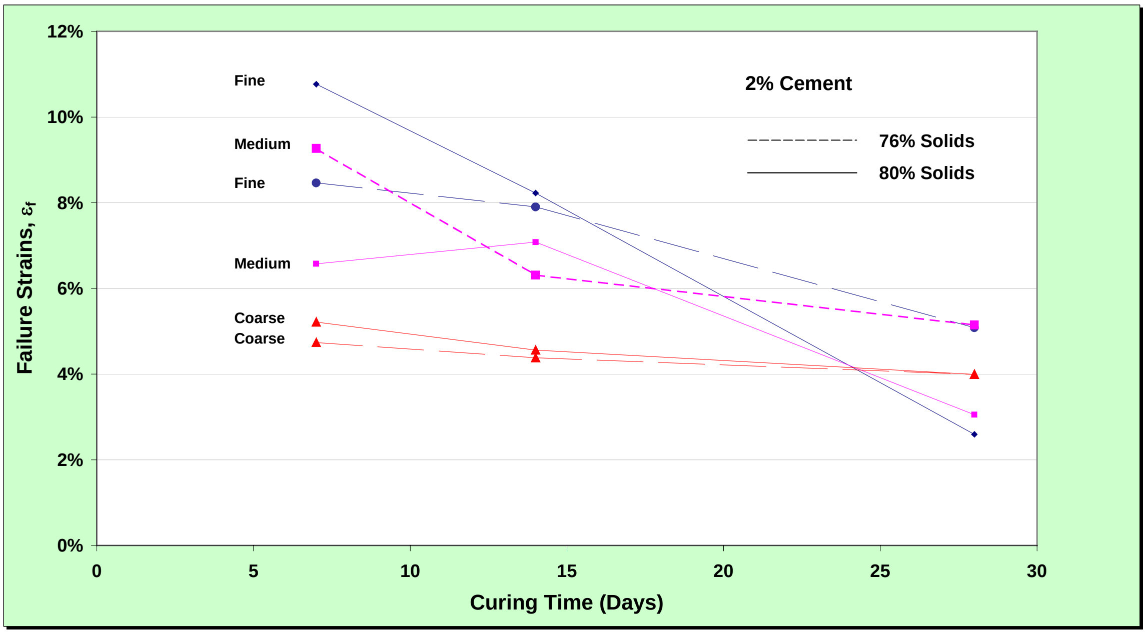

Figure A3.4. 16 Variation of the failure strains of paste sample with 2% cement (by dry weight) and various grain size distributions

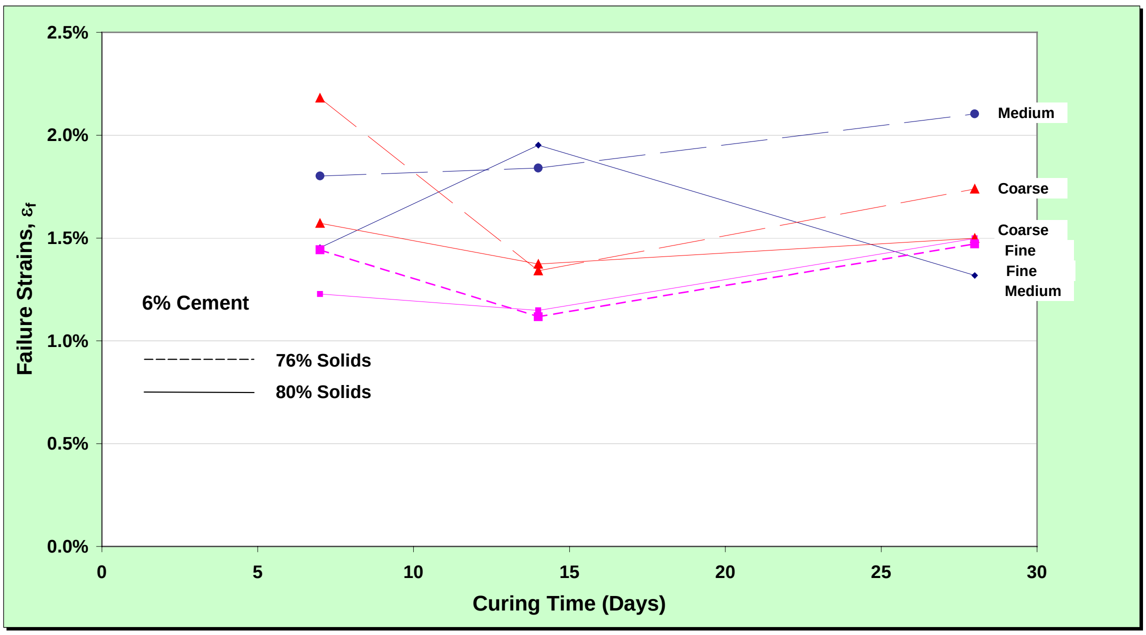

Figure A3.4. 17 Variation of the failure strains of paste sample with 6% cement (by dry weight) and various grain size distributions

Table A3.4. 4 Physical Properties – Long Term UU Triaxial Samples

Mix Specification	1 month				3 months			
Sample No.	2%,74%	2%,78%	6%,74%	6%,78%	2%,74%	2%,78%	6%,74%	6%,78%
M_t (g) =	170.4	186.0	173.8	187.1	173.4	184.4	174.0	186.3
M_s (g) =	128.6	146.8	132.4	149.0	132.3	145.0	132.8	147.7
M_w (g) =	41.8	39.1	41.4	38.1	41.1	39.4	41.2	38.6
V_t (cm^3) =	88.8	88.8	88.8	88.8	88.8	88.8	88.8	88.8
V_s (cm^3) =	39.8	45.5	41.0	46.2	41.0	44.9	41.2	45.8
V_w (cm^3) =	41.4	38.7	41.0	37.7	40.7	39.0	40.8	38.2
V_a (cm^3) =	7.6	4.6	6.8	4.9	7.1	4.9	6.9	4.8

Soil Properties

Mix Specification	1 month				3 months			
Sample No.	2%,74%	2%,78%	6%,74%	6%,78%	2%,74%	2%,78%	6%,74%	6%,78%
Moisture Content	33%	27%	31%	26%	31%	27%	31%	26%
Void ratio	1.230	0.952	1.166	0.924	1.167	0.977	1.158	0.940
Degree of Saturation	85%	89%	86%	88%	85%	89%	86%	89%
Porosity (n)	55%	49%	54%	48%	54%	49%	54%	48%
Bulk Density (ρ_m) {t/m^3}	1.918	2.094	1.957	2.106	2.0	2.1	2.0	2.1
Dry Density (ρ_d) {t/m^3}	1.447	1.653	1.490	1.677	1.5	1.6	1.5	1.7
Sat Density (ρ_{sat}) {t/m^3}	2.004	2.146	2.034	2.162	2.0	2.1	2.0	2.2
Bulk Modulus (γ_m) {kN/m^3}	18.819	20.538	19.195	20.660	19.2	20.4	19.2	20.6
Dry Bulk Modulus (γ_d) {kN/m^3}	14.200	16.216	14.619	16.452	14.6	16.0	14.7	16.3
Sat. Bulk Modulus (γ_{sat}) {kN/m^3}	19.664	21.049	19.951	21.211	19.9	20.9	20.0	21.1

Table A3.4. 5 Physical Properties – Long Term UU Triaxial Samples (cont.)

Mix Specification	**6 months**				**9 months**				**12 months**			
Sample No.	**2%,74%**	**2%,78%**	**6%,74%**	**6%,78%**	**2%,74%**	**2%,78%**	**6%,74%**	**6%,78%**	**2%,74%**	**2%,78%**	**6%,74%**	**6%,78%**
M_t (g) =	173.2	184.5	174.2	173.0	169.4	183.6	174.4	174.1	167.1	174.8	144.6	159.0
M_s (g) =	130.4	145.1	132.2	144.3	127.6	144.7	133.0	145.1	131.8	145.6	121.6	149.0
M_w (g) =	42.8	39.4	42.0	28.7	41.8	38.9	41.4	29.0	35.3	29.2	23.0	10.0
V_t (cm^3) =	88.8	88.8	88.8	85.9	88.8	88.8	88.8	83.4	88.8	88.8	80.0	88.8
V_s (cm^3) =	40.4	45.0	41.0	44.7	39.5	44.8	41.2	45.0	40.9	45.1	37.7	46.2
V_w (cm^3) =	42.4	39.0	41.6	28.4	41.4	38.5	41.0	28.7	34.9	28.9	22.8	9.9
V_a (cm^3) =	6.0	4.9	6.3	12.8	7.9	5.5	6.7	9.7	13.0	14.8	19.5	32.7

Mix Specification	**6 months**				**9 months**				**12 months**			
Sample No.	**2%,74%**	**2%,78%**	**6%,74%**	**6%,78%**	**2%,74%**	**2%,78%**	**6%,74%**	**6%,78%**	**2%,74%**	**2%,78%**	**6%,74%**	**6%,78%**
Moisture Content	33%	27%	32%	20%	33%	27%	31%	20%	27%	20%	19%	7%
Void ratio	1.198	0.976	1.169	0.920	1.247	0.982	1.156	0.856	1.174	0.968	1.122	
Degree of Saturation	88%	89%	87%	69%	84%	88%	86%	75%	73%	66%	53%	23%
Porosity (n)	55%	49%	54%	48%	55%	50%	54%	46%	54%	49%	53%	48%
Bulk Density (ρ_m) {t/m^3}	2.0	2.1	2.0	2.0	1.9	2.1	2.0	2.1	1.9	2.0	1.8	1.8
Dry Density (ρ_d) {t/m^3}	1.5	1.6	1.5	1.7	1.4	1.6	1.5	1.7	1.5	1.6	1.5	1.7
Sat Density (ρ_{sat}) {t/m^3}	2.0	2.1	2.0	2.2	2.0	2.1	2.0	2.2	2.0	2.1	2.1	2.2
Bulk Modulus (γ_m) {kN/m^3}	19.1	20.4	19.2	19.8	18.7	20.3	19.3	20.5	18.5	19.3	17.7	17.6
Dry Bulk Modulus (γ_d) {kN/m^3}	14.4	16.0	14.6	16.5	14.1	16.0	14.7	17.1	14.6	16.1	14.9	16.5
Sat. Bulk Modulus (γ_{sat}) {kN/m^3}	19.8	20.9	19.9	21.2	19.6	20.9	20.0	21.7	19.9	21.0	20.2	21.2

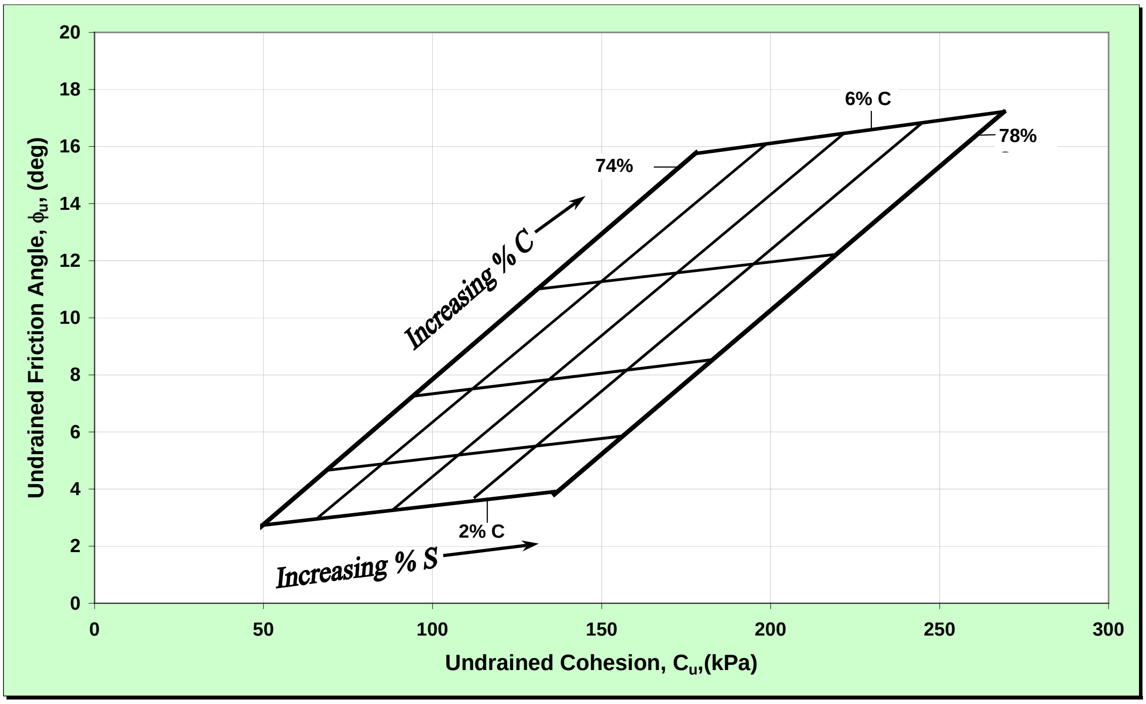

Figure A3.4. 18 Undrained friction angle vs. undrained cohesion intercept (7-56 days curing)

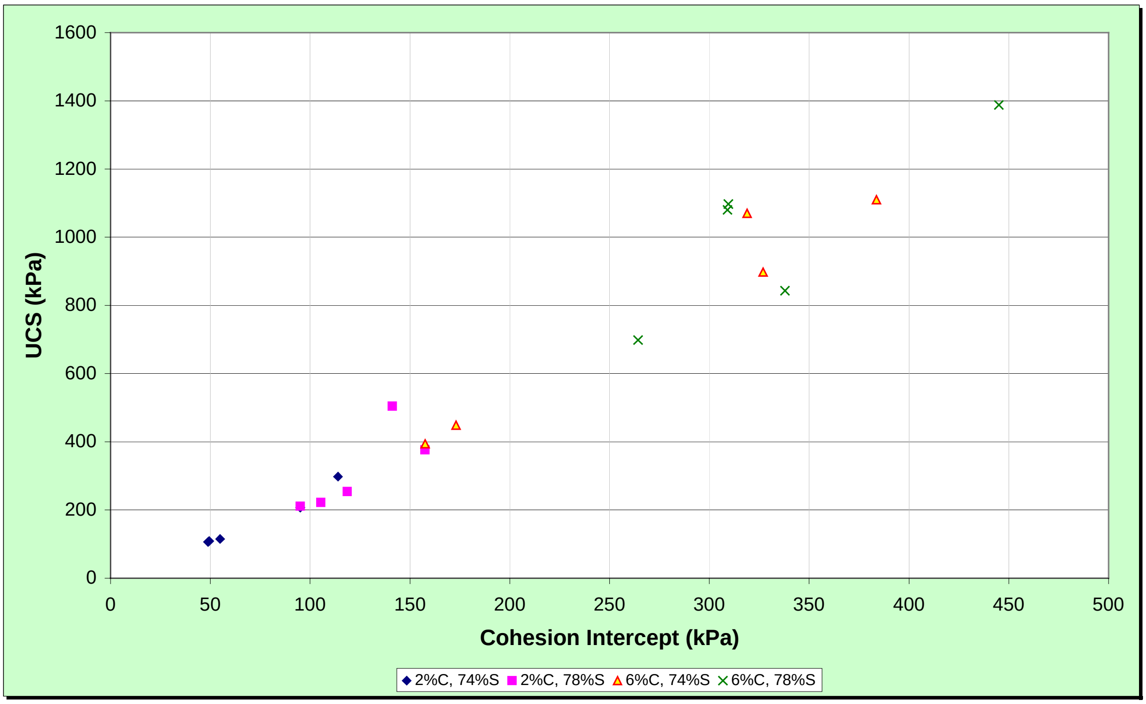

Figure A3.4. 19 UCS vs. Cohesion intercept (various mixes)

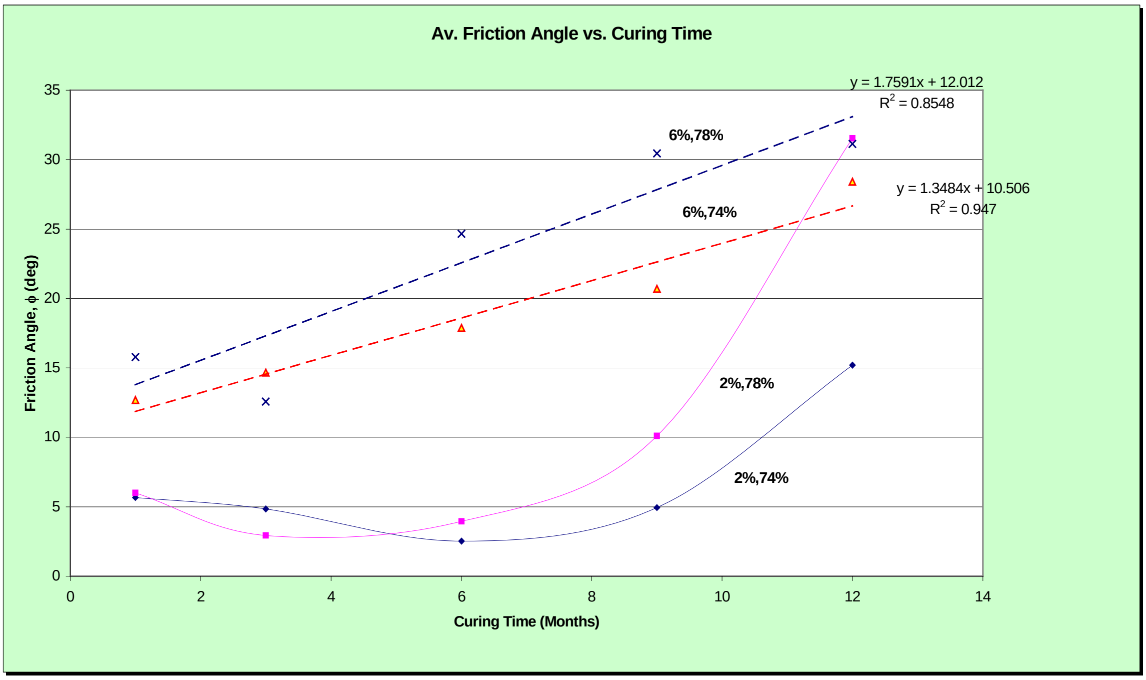

Figure A3.4. 20 Progressive friction angle development

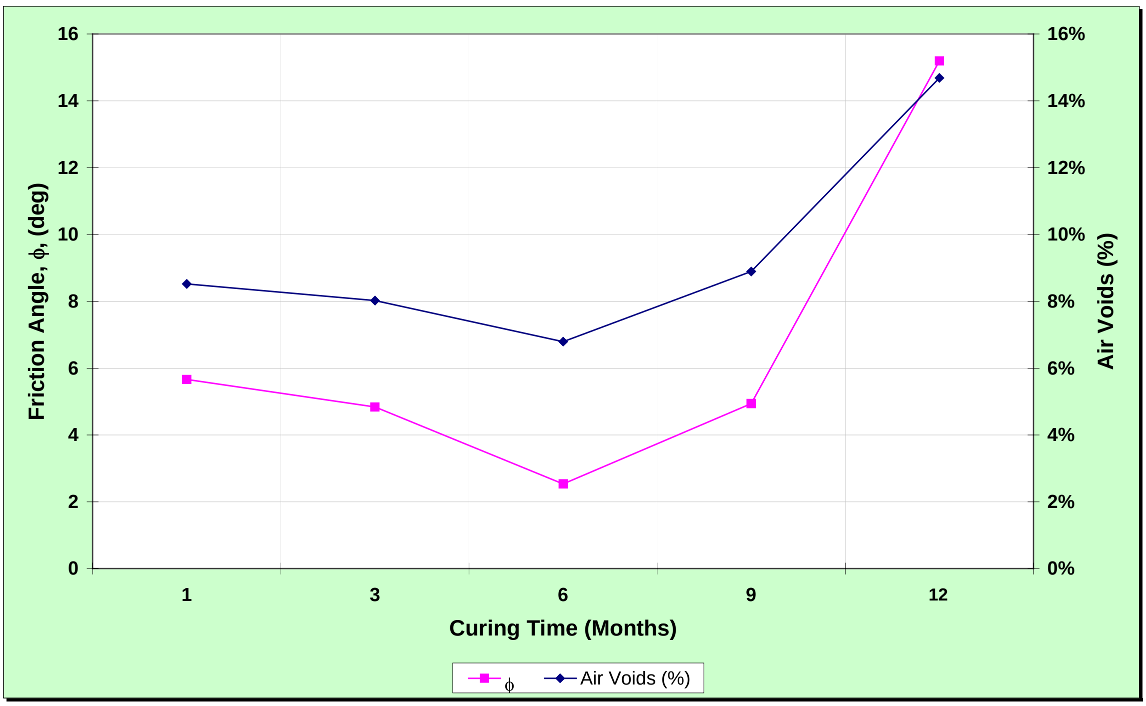

Figure A3.4. 21 Relationship between Friction angle, curing time and air volume (2%, 74% samples)

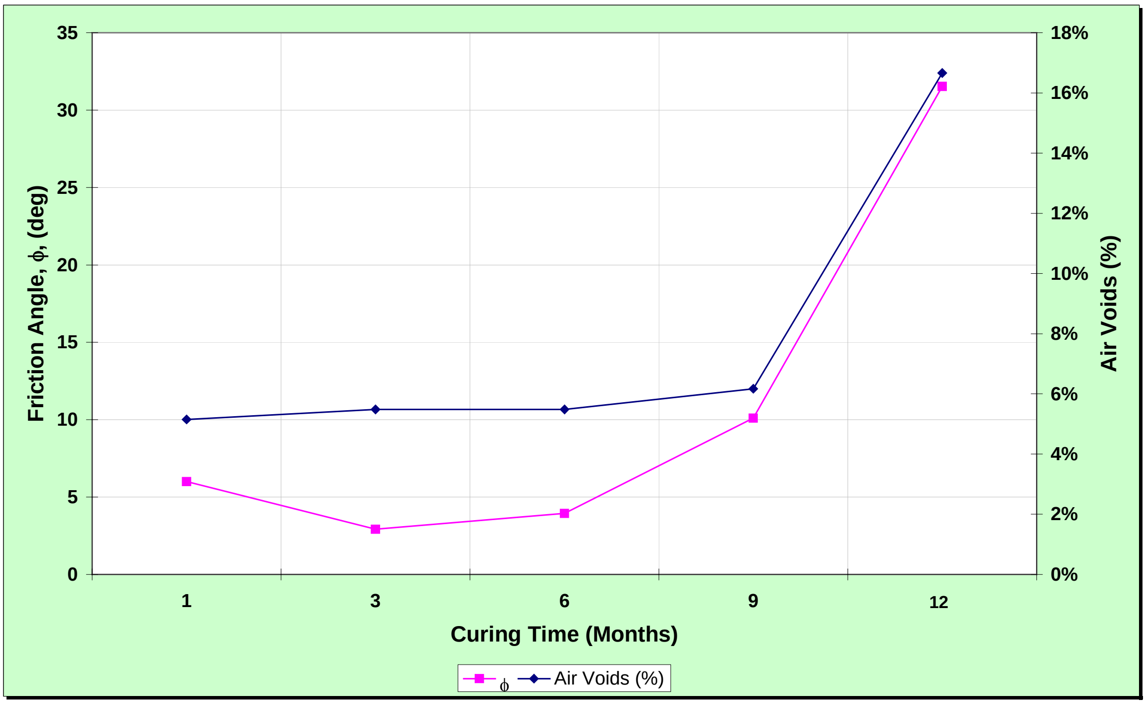

Figure A3.4. 22 Relationship between Friction angle, curing time and air volume (2%, 78% samples)

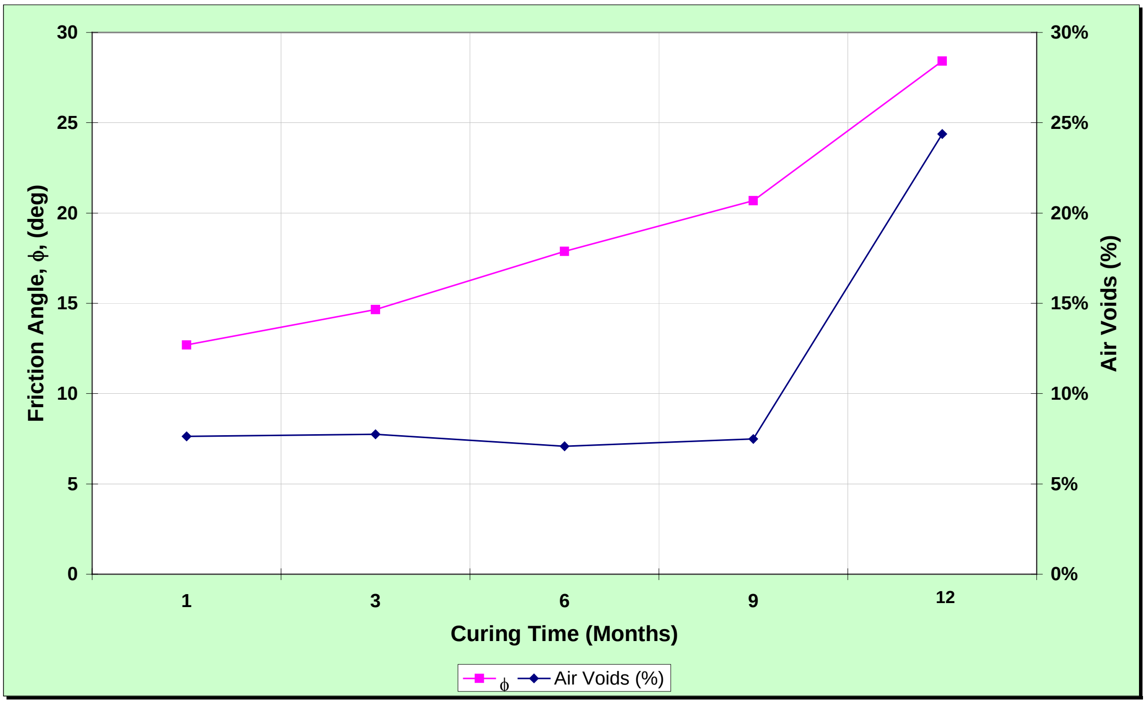

Figure A3.4. 23 Relationship between Friction angle, curing time and air volume (6%, 74% samples)

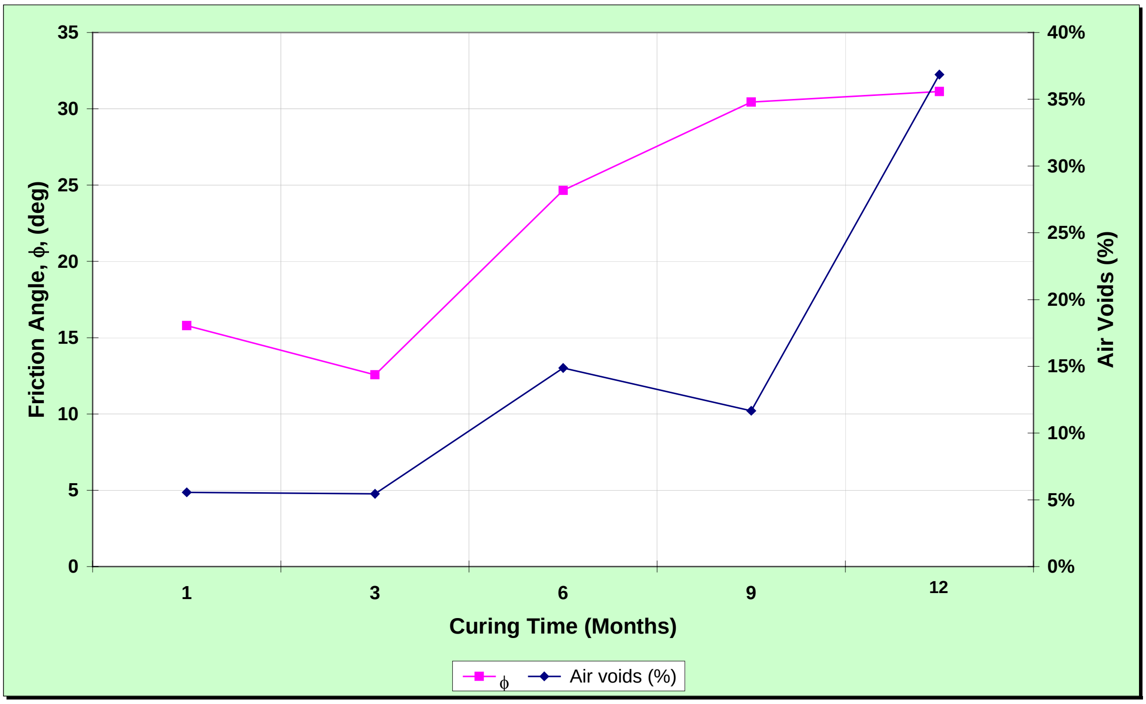

Figure A3.4. 24 Relationship between Friction angle, curing time and air volume (6%, 78% samples)

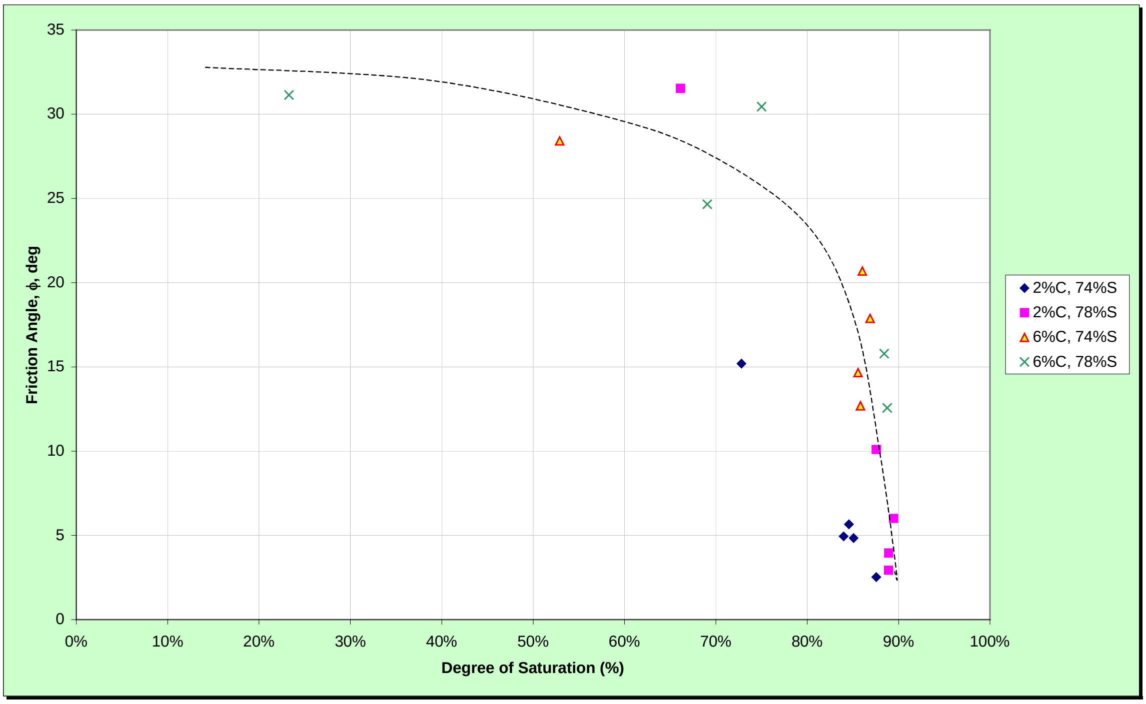

Figure A3.4. 25 Relationship between Friction angle and degree of saturation (6%, 78% samples)

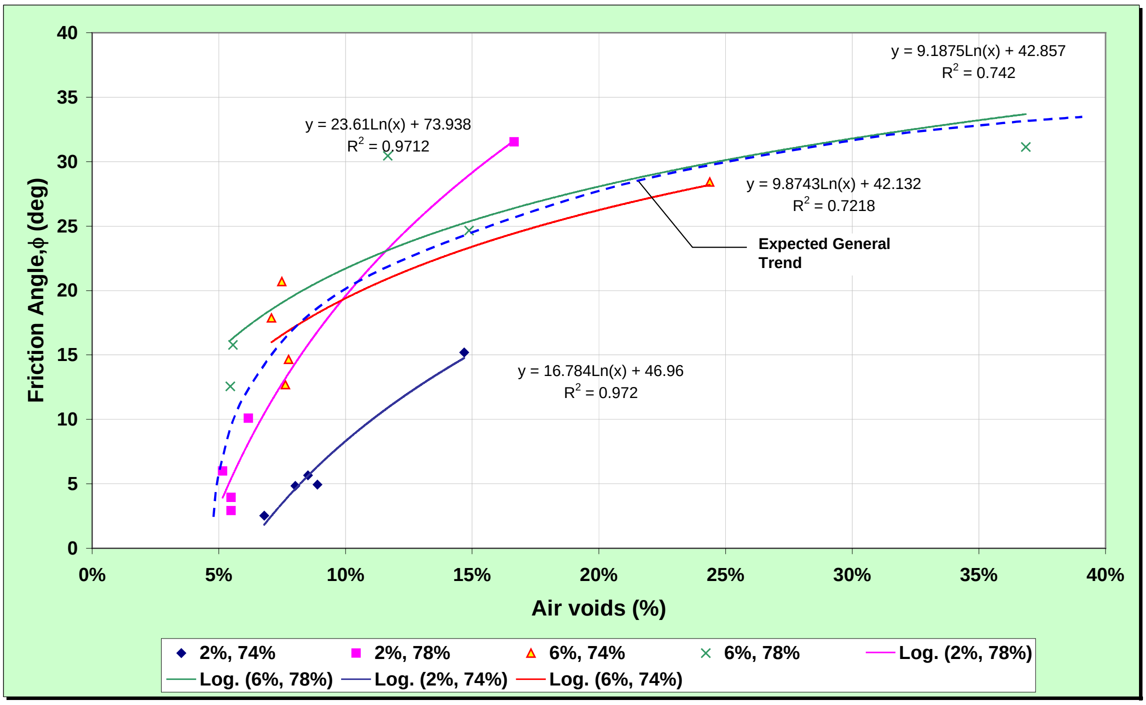

Figure A3.4. 26 Relationship between friction angle and Air voids (%)

Early Strength

Mix	Cure Time (hrs)	Vane No.	H (mm)	D (mm)	Spring No.	Sample No.	Degrees of Rotation	Torque	Cu.
3%, 79%	3	1	25.5	12.5	1	1	20	0.168	23.07
	3	1	25.5	12.5	1	2	22	0.185	25.38
	3	1	25.5	12.5	1	3	20	0.168	23.07
Av.	3.00						20.667	0.174	23.84
3%, 79%	6	1	25.5	12.5	1	1	28	0.235	32.30
	6	1	25.5	12.5	1	2	22	0.185	25.38
	6	1	25.5	12.5	1	3	35	0.294	40.38
Av.	6.00						28.333	0.238	32.69
3%, 79%	10.25	1	25.5	12.5	1	1	34.5	0.290	39.80
	10.25	1	25.5	12.5	1	2	27	0.227	31.15
	10.25	1	25.5	12.5	1	3	29	0.244	33.46
Av.	10.25						30.167	0.253	34.80
3%, 79%	24	1	25.5	12.5	1	1	49	0.412	56.53
	24	1	25.5	12.5	1	2	59	0.496	68.06
	24	1	25.5	12.5	1	3	49	0.412	56.53
Av.	24.00						52.333	0.440	60.37
3%, 79%	96	2	19	12.5	4	1	62	2.3374	411.08
	96	2	19	12.5	4	2	59	2.2243	391.19
	96	2	19	12.5	4	3	52	1.9604	344.78
Av.	96.00						57.667	2.174	382.35

Where

Shear Vane	H (mm)	D (mm)	Description
1	25.5	12.5	Largest
2	19	12.5	Medium

Table A3.4. 6 Early Strength Gains, Paste Fill, (3.5% C, 79% solids) - Using mechanical shear vane

Pocket Penotrometer

Mix	Cure Time	Sample No.	PP Rdg	UCS (kPa)	UCS corrected for foot
3%, 79%	3	1	0.8	78.4532	3.138128
	3	2	0.85	83.35653	3.334261
	3	3	1	98.0665	3.92266
Av.	3.00		0.883	86.625	3.465
3%, 79%	6	1	0.8	78.4532	3.138128
	6	2	1.2	117.6798	4.707192
	6	3	1.25	122.5831	4.903325
	6	4	1.15	112.7765	4.511059
Av.	6.00		1.100	107.873	4.315
3%, 79%	10.25	1	1.9	186.3264	7.453054
	10.25	2	1.7	166.7131	6.668522
	10.25	3	1.5	147.0998	5.88399
	10.25	4	1.6	156.9064	6.276256
	10.25	5	1.55	152.0031	6.080123
Av.	10.25		1.650	161.810	6.472
3%, 79%	24	1	2	196.133	7.84532
	24	2	2.45	240.2629	9.610517
	24	3	2	196.133	7.84532
	24	4	2	196.133	7.84532
Av.	24.00		2.113	207.165	8.287
3%, 79%	96	1	0.85	83.35653	
	96	2	0.75	73.54988	
	96	3	0.65	63.74323	
	96	4	0.5	49.03325	
Av.	96.00		0.688	67.421	

Table A3.4. 7 Early Strength Gains, Paste Fill, (3.5% C, 79% solids) – using pocket penetrometer – with Adaptor Foot.

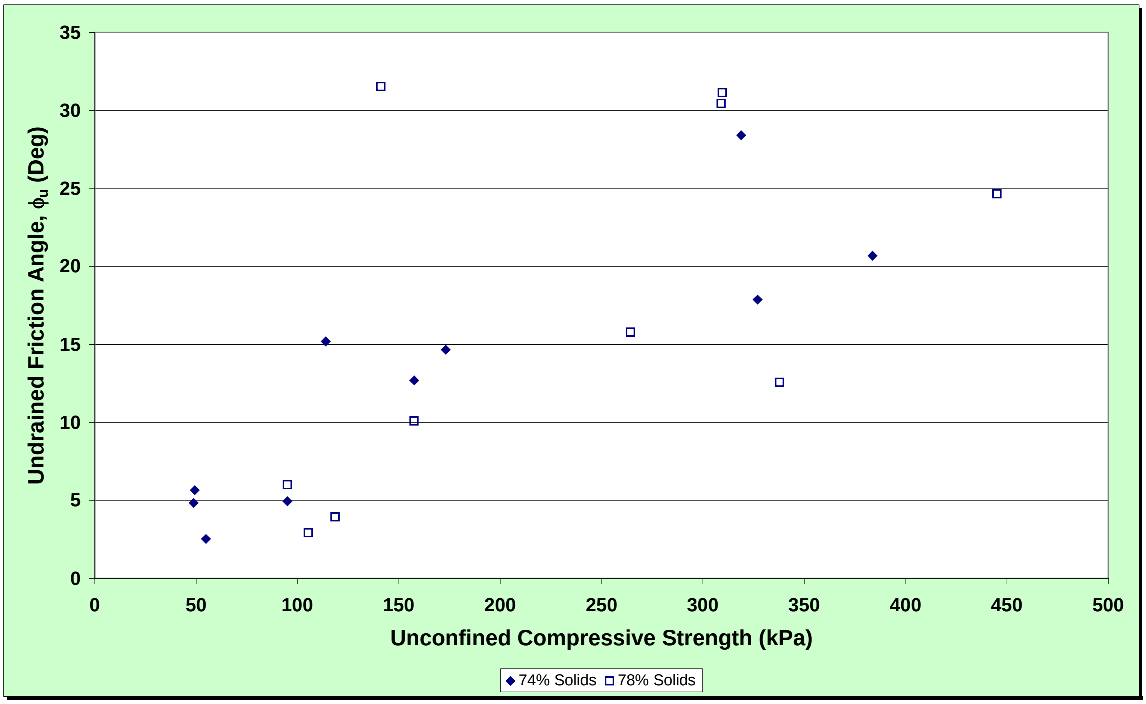

Figure A3.4. 27 Undrained friction angle vs. Unconfined Compressive Strength (UU Txl – long term samples (1-12 months).

Table A3.4. 8 Calculation of the Ratio of Tensile Strength to UCS

Calculated UCS

	Curing Time - (Days)			
Mix	7	14	28	56
2%, 74%	104.9	118.6	96.5	129.9
2%, 78%	309.0	308.1	367.6	327.5
6%, 74%	357.5	419.5	435.7	458.2
6%, 78%	697.5	666.8	682.5	727.0

Measured Tensile Strength

	Curing Time - (Days)			
Mix	7	14	28	56
2%, 74%	37.8	35.0	39.7	45.1
2%, 78%	50.6	50.5	56.3	56.5
6%, 74%	66.1	77.3	68.7	65.3
6%, 78%	79.3	109.9	102.4	113.1

Ratio Tensile Strength/ UCS

	Curing Time - (Days)				
Mix	7	14	28	56	Av.
2%, 74%	0.36	0.30	0.41	0.35	0.35
2%, 78%	0.16	0.16	0.15	0.17	0.16
6%, 74%	0.18	0.18	0.16	0.14	0.17
6%, 78%	0.11	0.16	0.15	0.16	0.15

APPENDIX 3.5

Effective Stress Analysis Data

- *Summary Data*
- *Es vs. q plots – All mixes, 14 & 28 day curing*
- *Quick reference guide to obtain c' from mix proportions*
- *s-t plot for CD triaxial testing*
- *Direct shear plots for the densest and loosest possible states for Cannington tailings*

Consolidated Drained Triaxial Testing

Table A3.5. 1 CD Txl Test Data Summary (14 Day Curing)

% Cement	% Solids	Curing Time (days)	Test	Initial Mean Effective Stress, p_i (kN/m^2)	σ_{1f}' (kPa)	ε_f	q_f (σ_1-σ_3) (kPa)	E_o (kN/m^2)	E_s (kN/m^2)	$E_{s\ (0.1)}$ (kN/m^2)	Comment
2	74	14	UCS (1)	0	43	13.16%	43	2499	1046	2502	
2	74	14	UCS (2)	0	41	15.13%	41	3519	1820	3522	
2	74	14	CD-TXL	100	634	21.61%	534	3906	3898	407	
2	74	14	CD-TXL	200	1101	19.05%	901	6961	6857	4688	
2	74	14	CD-TXL	500	1700	18.05%	1200	9030	8581	8798	
2	78	14	UCS (1)	0	172	6.25%	172	26248	26248	26251	
2	78	14	UCS (2)	0	185	8.22%	185	15175	12581	15178	
2	78	14	CD-TXL	100	447	14.42%	347	6240	5322	3086	
2	78	14	CD-TXL	200							Invalid data
2	78	14	CD-TXL	500	1840	19.05%	1340	10780	10780	10784	
6	74	14	UCS (1)	0	640	0.99%	640	134066	134067	134069	
6	74	14	UCS (2)	0	607	0.99%	607	127656	127656	127659	
6	74	14	CD-TXL	100	723	11.03%	623	13479	11380	6722	
6	74	14	CD-TXL	200	1339	16.04%	1139	9999	9405	5281	
6	74	14	CD-TXL	500	1888	21.59%	1388	10520	10520	10524	Premature Failure of sample
6	78	14	UCS (1)	0	1276	0.99%	1276	296377	296377	296380	
6	78	14	UCS (2)	0	1345	0.99%	1345	193164	164327	145726	
6	78	14	CD-TXL	100	1463	8.02%	1363	23176	17425	23179	
6	78	14	CD-TXL	200	2061	12.03%	1861	22921	22127	16763	
6	78	14	CD-TXL	500	2250	17.13%	1750	20384	17274	20388	Premature Failure of sample

Table A3.5. 2 CD Txl Test Data Summary (28 Day Curing)

% Cement	% Solids	Curing Time (days)	Test	Initial Mean Effective Stress, p_i (kN/m^2)	σ_{1f}' (kPa)	ε_f	q_f (σ_1-σ_3) (kPa)	E_o (kN/m^2)	E_s (kN/m^2)	$E_{s\,(0.1)}$ (kN/m^2)	Comment
2	74	28	UCS (1)	0	84	11.51%			84	12698	12382
2	74	28	UCS (2)	0	78	7.57%			78	10221	6894
2	74	28	CD-TXL	100	640	19.05%			540	13225	4944
2	74	28	CD-TXL	200	422	19.05%			222	1815	1815
2	74	28	CD-TXL	500	1755	23.23%			1255	8240	8158
2	78	28	UCS (1)	0	219	3.62%			219	40527	40527
2	78	28	UCS (2)	0	213	1.97%			213	42858	42858
2	78	28	CD-TXL	132	772	17.04%			672	9781	7837
2	78	28	CD-TXL	200	795	18.05%			595	5311	5311
2	78	28	CD-TXL	500	1835	20.05%			1335	9764	8354
6	74	28	UCS (1)	0	701	1.32%			701	155339	155339
6	74	28	UCS (2)	0	716	2.30%			716	93270	92748
6	74	28	CD-TXL	100	748	18.13%			648	10738	4109
6	74	28	CD-TXL	200	1324	10.03%			1124	14303	14303
6	74	28	CD-TXL	500	1873	21.06%			1373	10738	10738
6	78	28	UCS (1)	0	1345	0.99%			1345	262283	262283
6	78	28	UCS (2)	0	1319	0.99%			1319	262866	262866
6	78	28	CD-TXL	100	1490	11.03%			1390	26429	22986
6	78	28	CD-TXL	200							
6	78	28	CD-TXL	500	2295	13.03%			1795	18704	17159

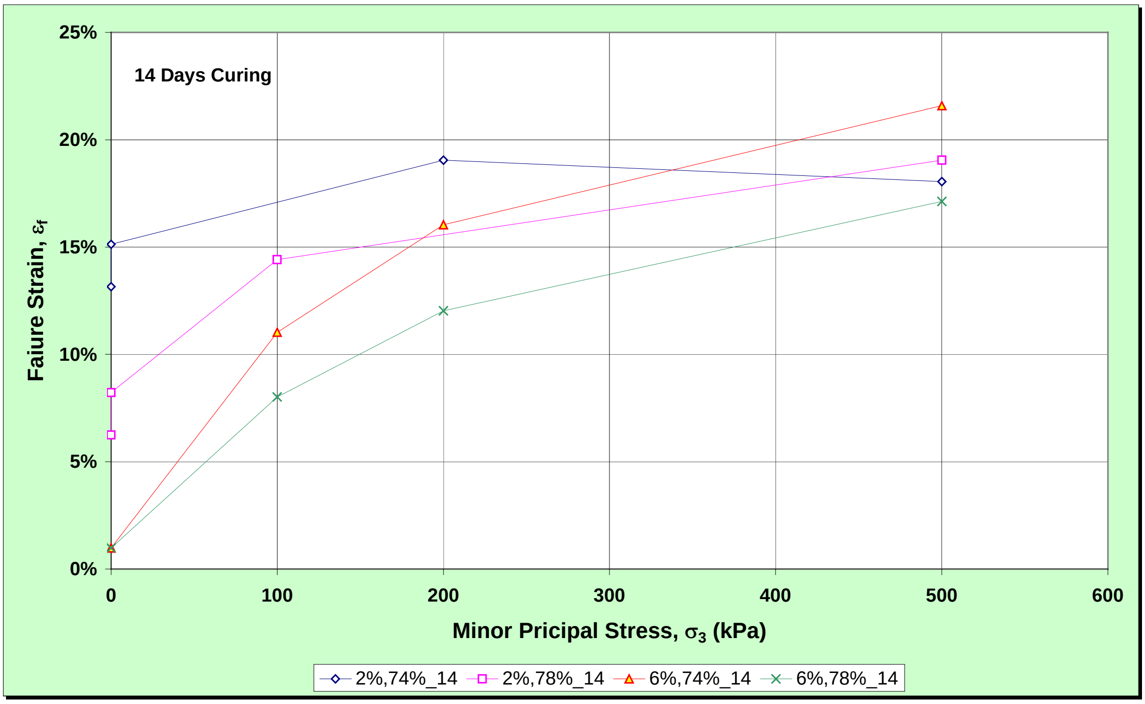

Figure A3.5. 1 Failure Strain vs. minor principal Stress, 14 Days Curing, All paste mixes

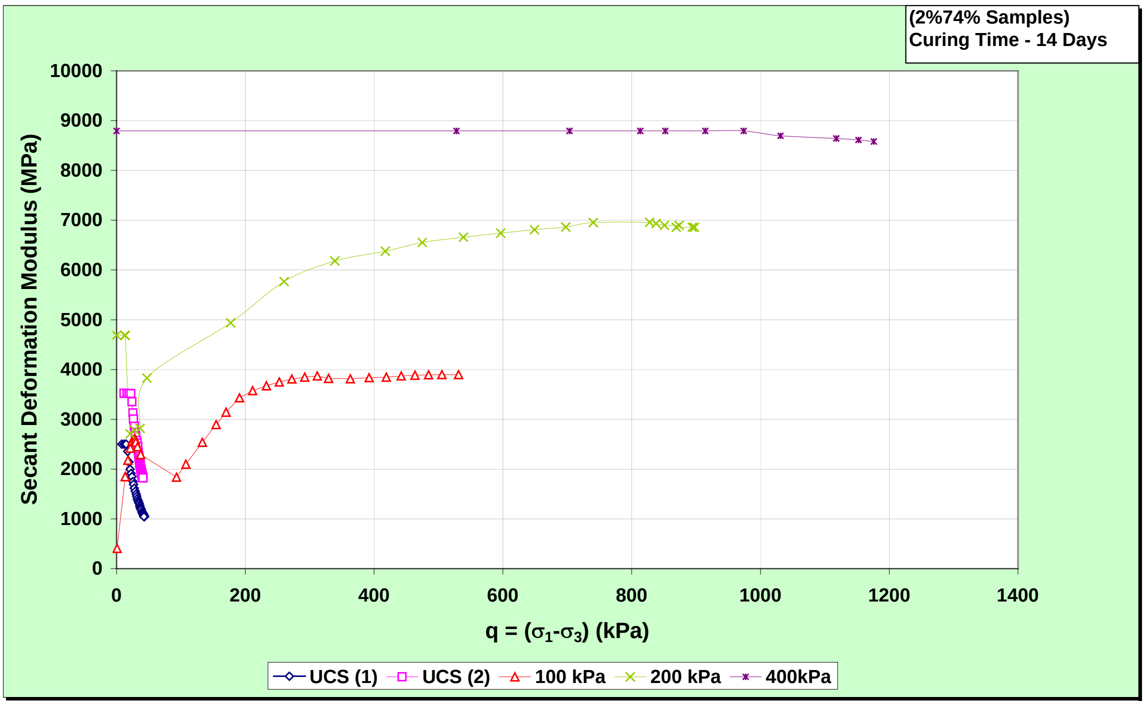

Figure A3.5. 2 Secant deformation modulus (Es) vs deviator stress (CD triaxial test, 2%,74%, 14 days curing)

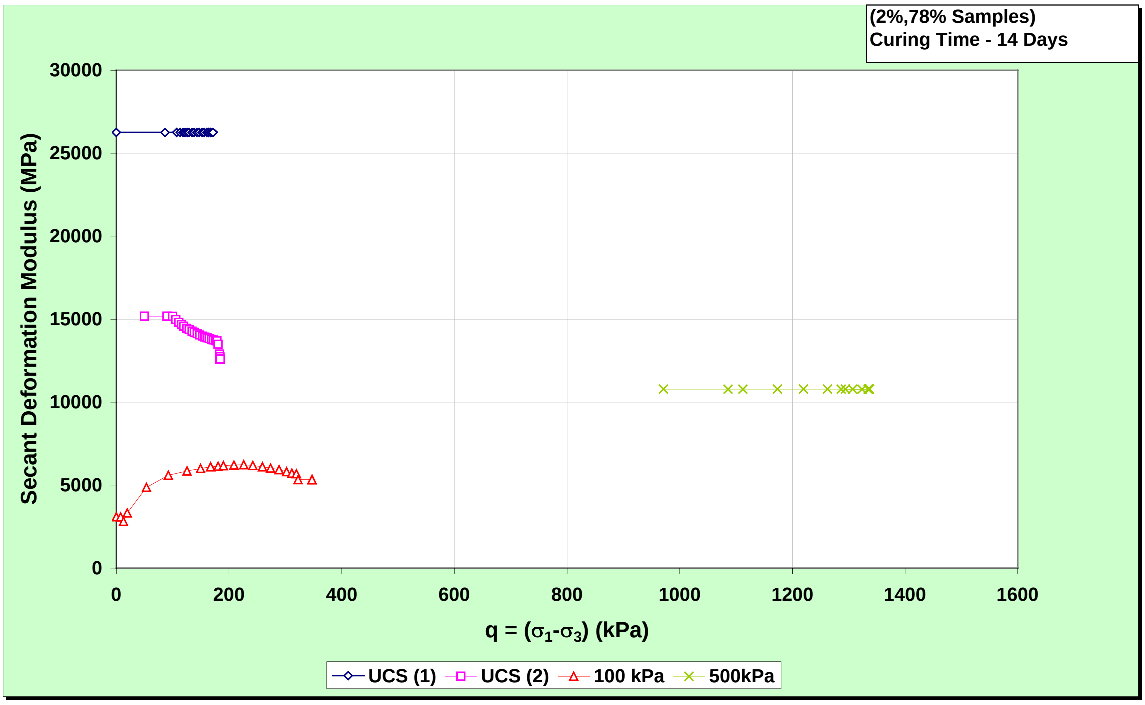

Figure A3.5. 3 Secant deformation modulus (Es) vs deviator stress (CD triaxial test, 2%,78%, 14 days curing)

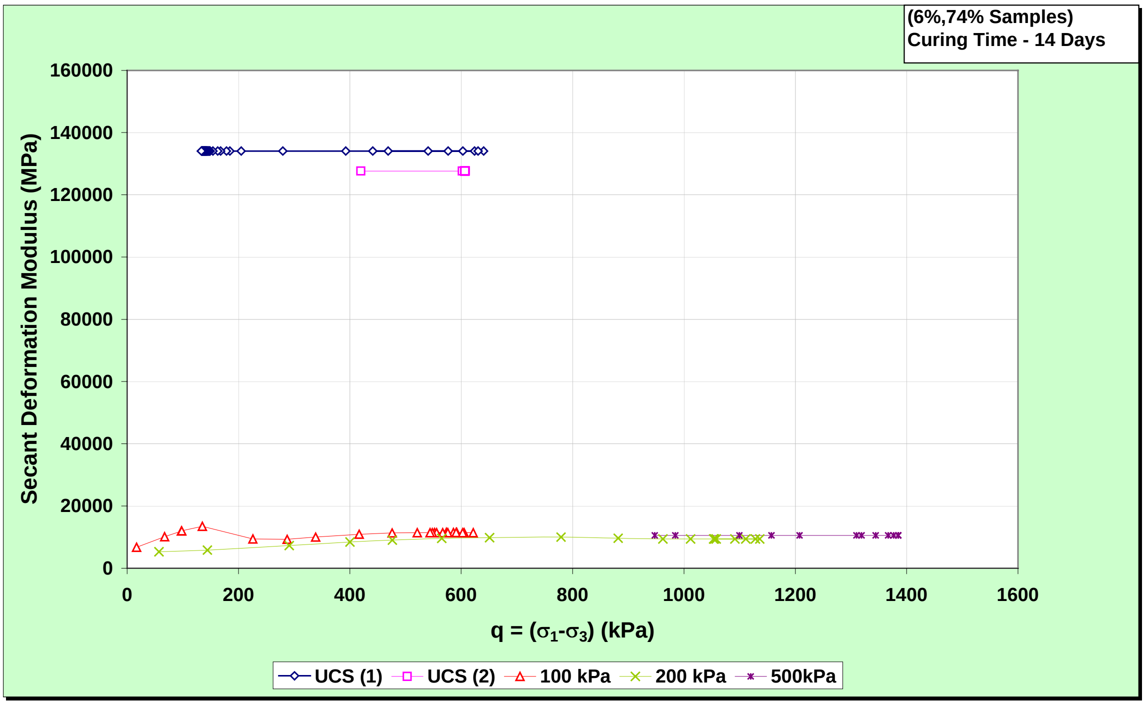

Figure A3.5. 4 Secant deformation modulus (Es) vs deviator stress (CD triaxial test, 6%, 74%, 14 days curing)

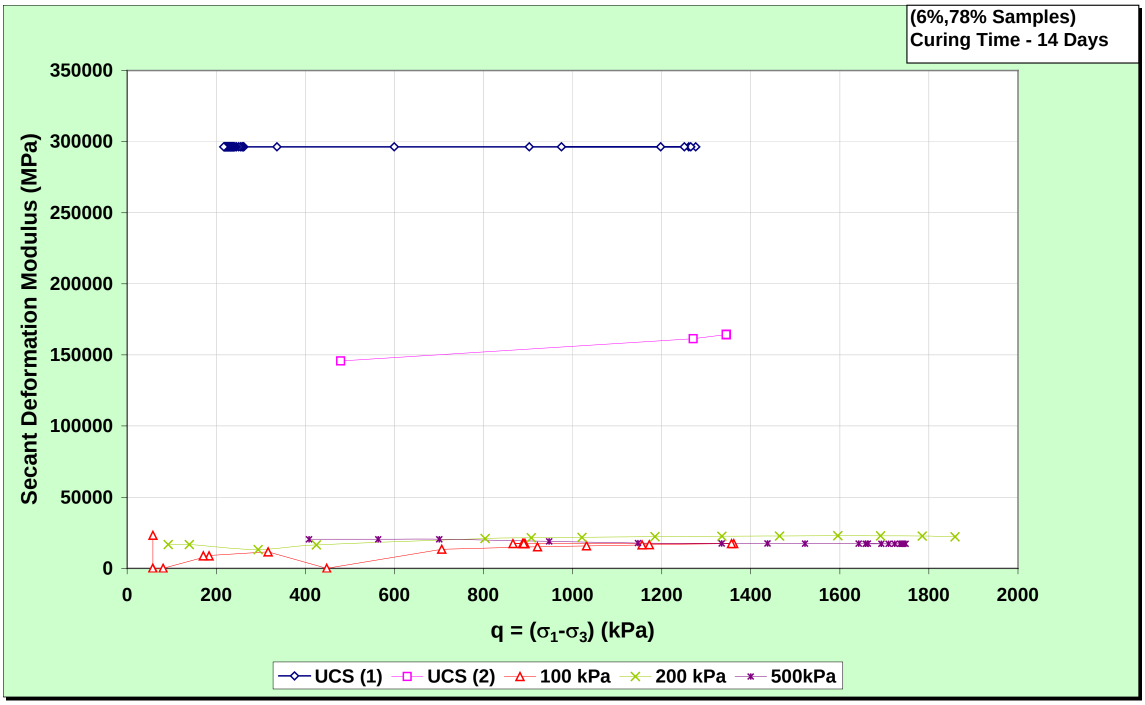

Figure A3.5. 5 Secant deformation modulus (Es) vs deviator stress (CD triaxial test, 6%, 78%, 14 days curing)

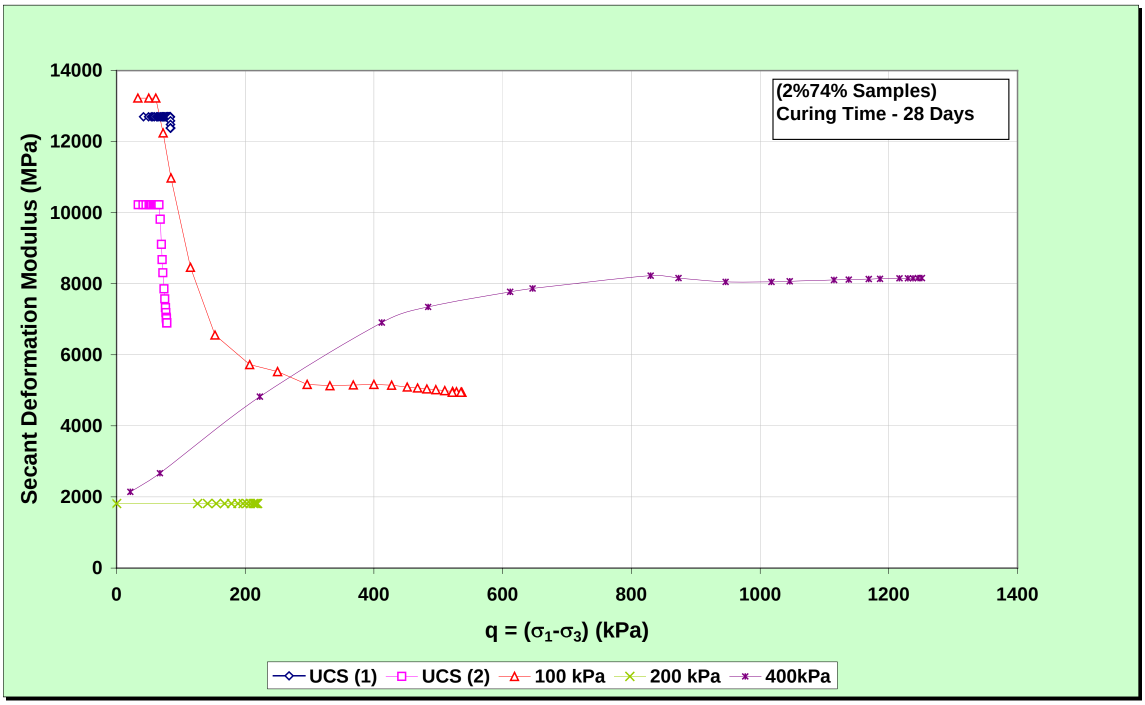

Figure A3.5. 6 Secant deformation modulus (Es) vs deviator stress (CD triaxial test, 2%, 74%, 28 days curing)

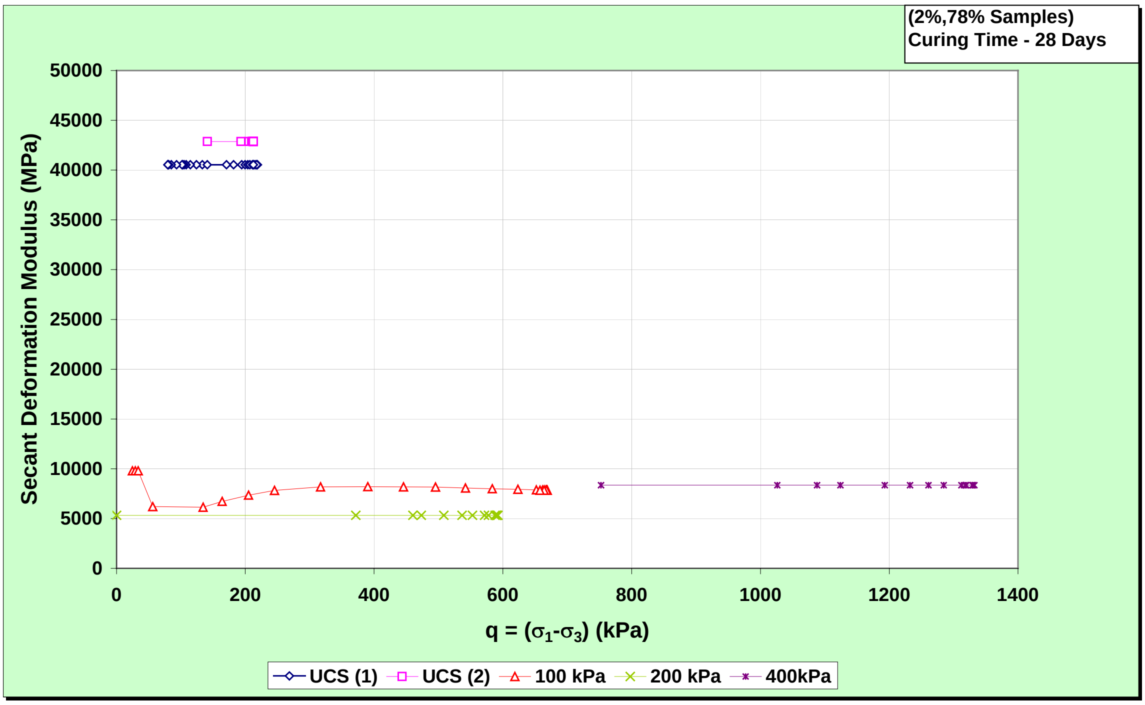

Figure A3.5. 7 Secant deformation modulus (Es) vs deviator stress (CD triaxial test, 2%, 78%, 28 days curing)

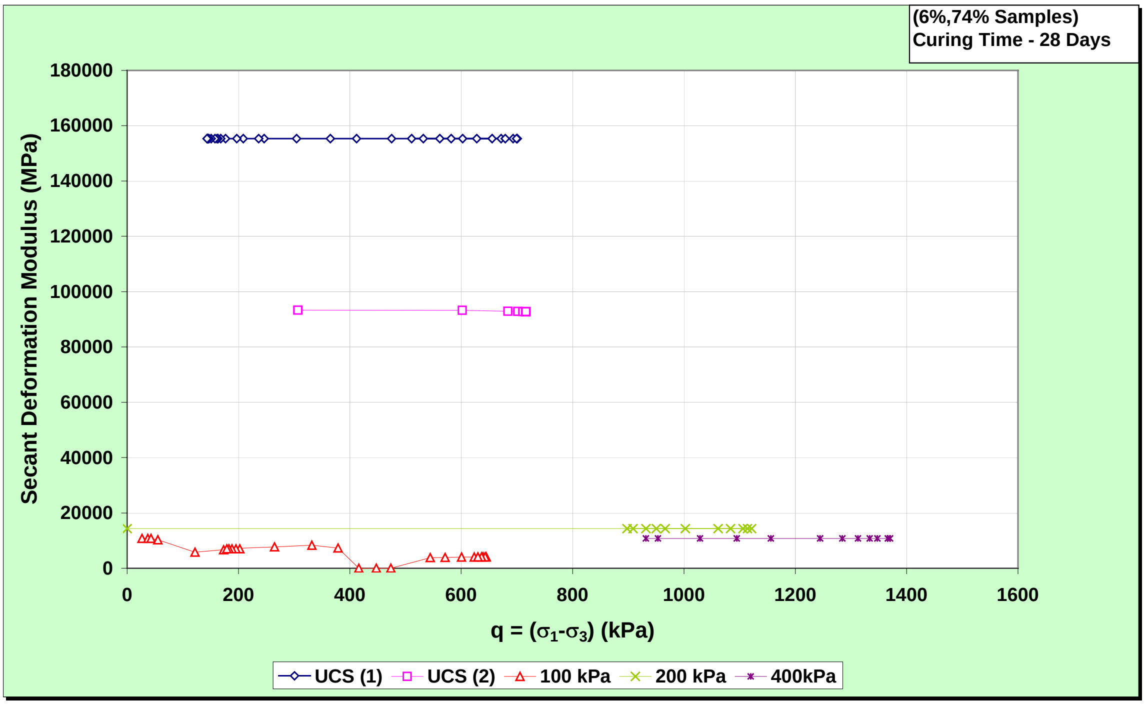

Figure A3.5. 8 Secant deformation modulus (Es) vs deviator stress (CD triaxial test, 6%, 74%, 28 days curing)

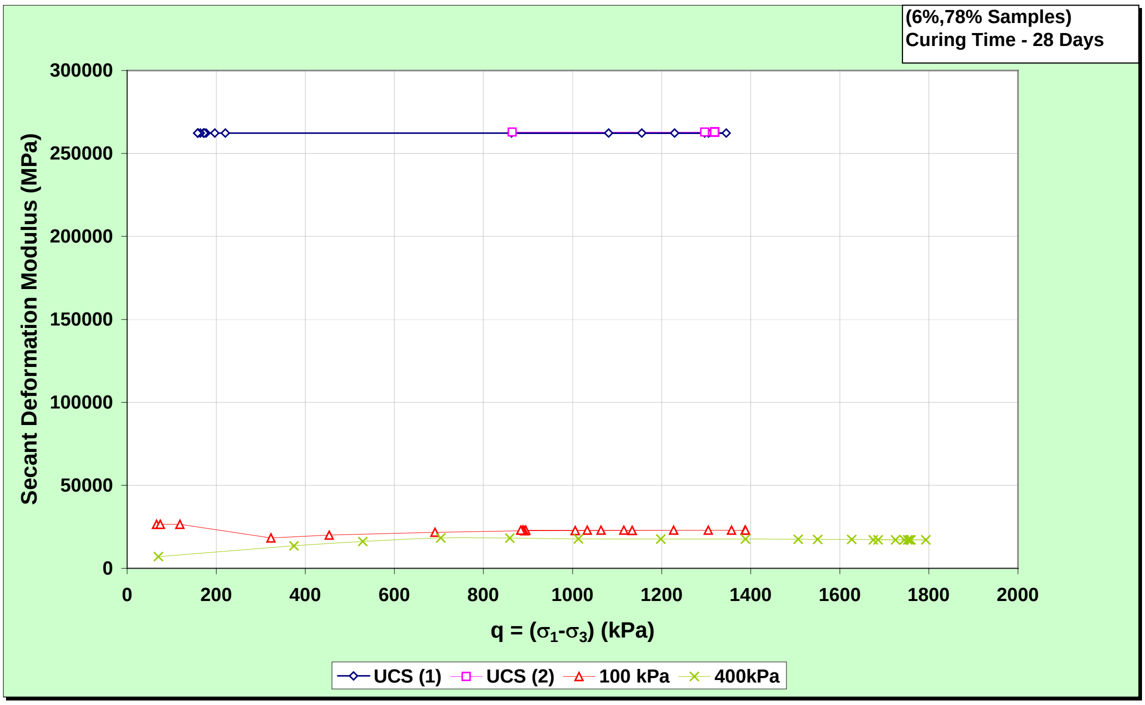

Figure A3.5. 9 Secant deformation modulus (Es) vs deviator stress (CD triaxial test, 6%, 78%, 28 days curing)

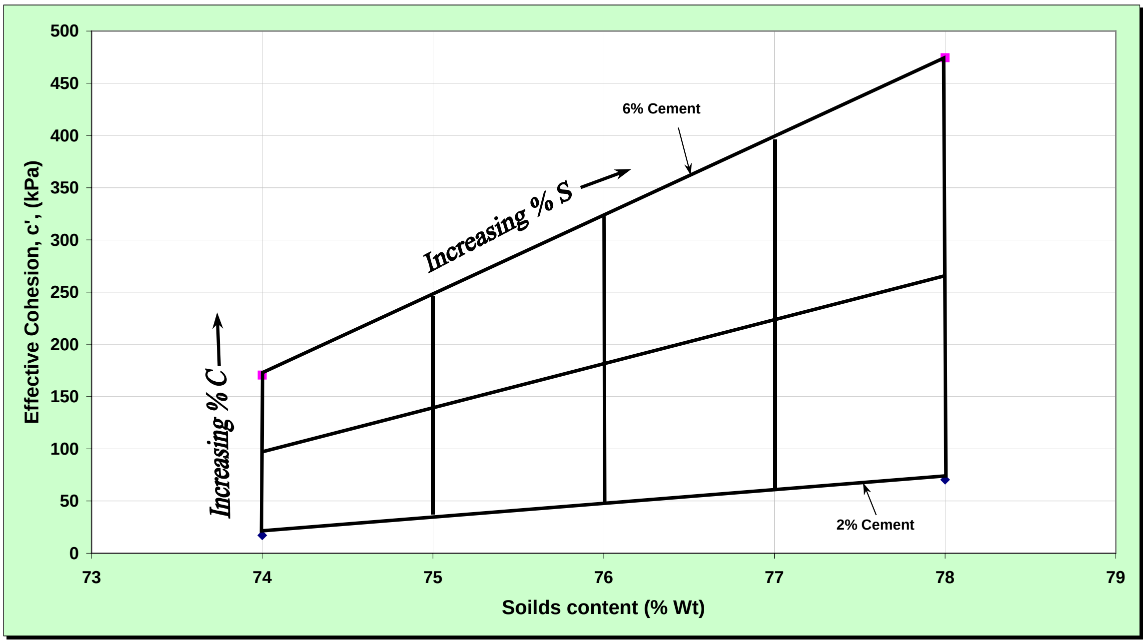

Figure A3.5. 10 Quick reference guide for the determination of effective cohesion based on mix proportions (28 day curing).

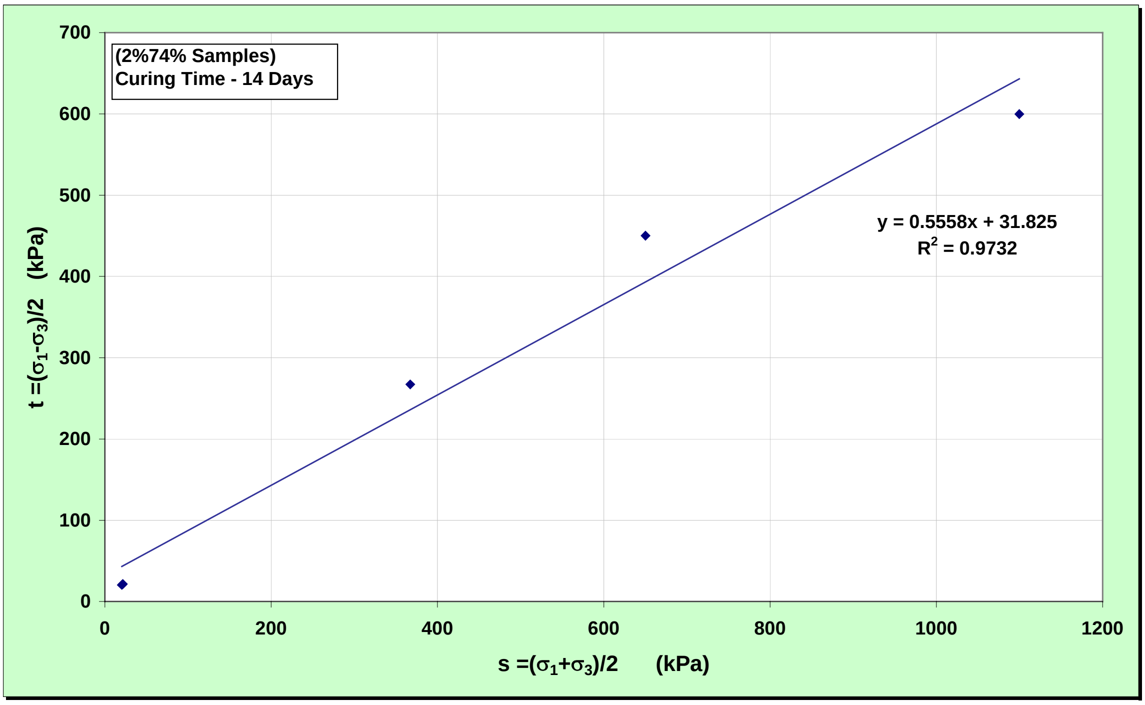

Figure A3.5. 11 s-t plot for CD triaxial testing, 2%,74%, 14 days curing

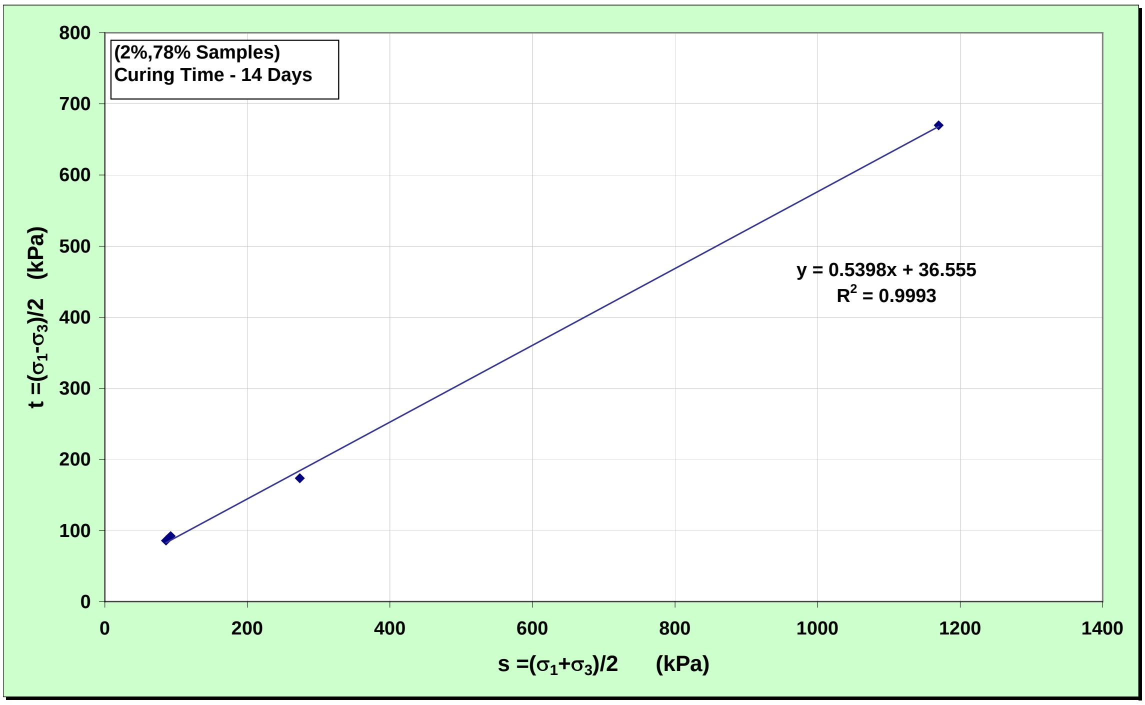

Figure A3.5. 12 s-t plot for CD triaxial testing, 2%, 78%, 14 days curing

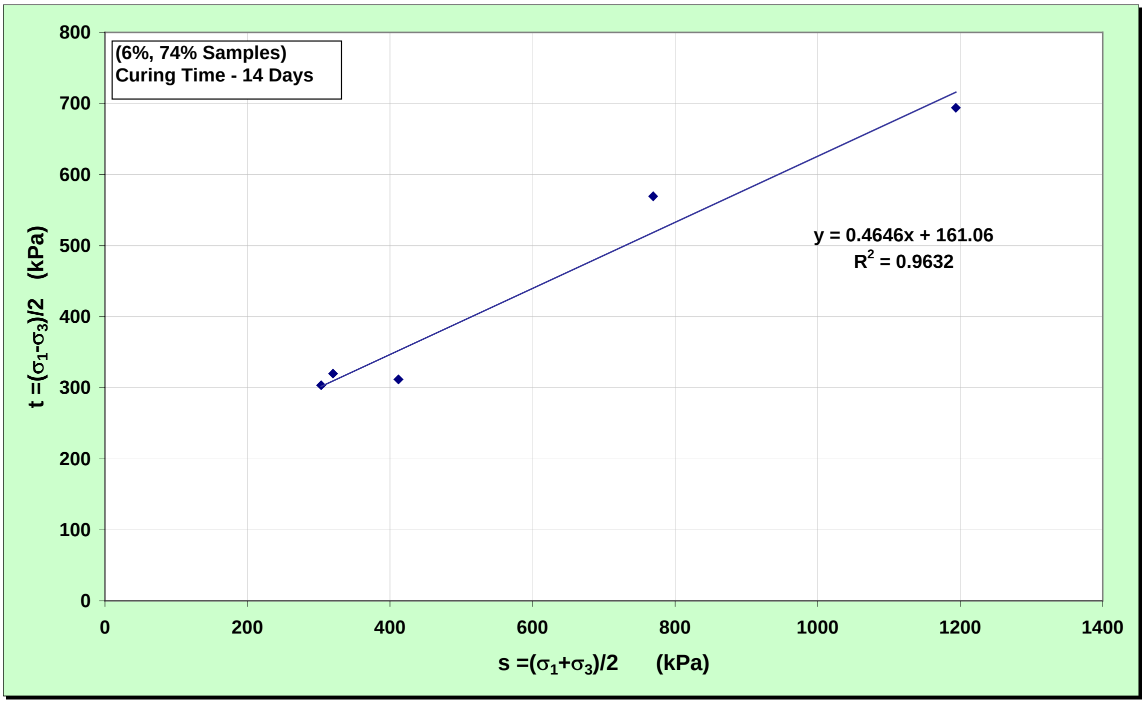

Figure A3.5. 13 s-t plot for CD triaxial testing, 6%, 74%, 14 days curing

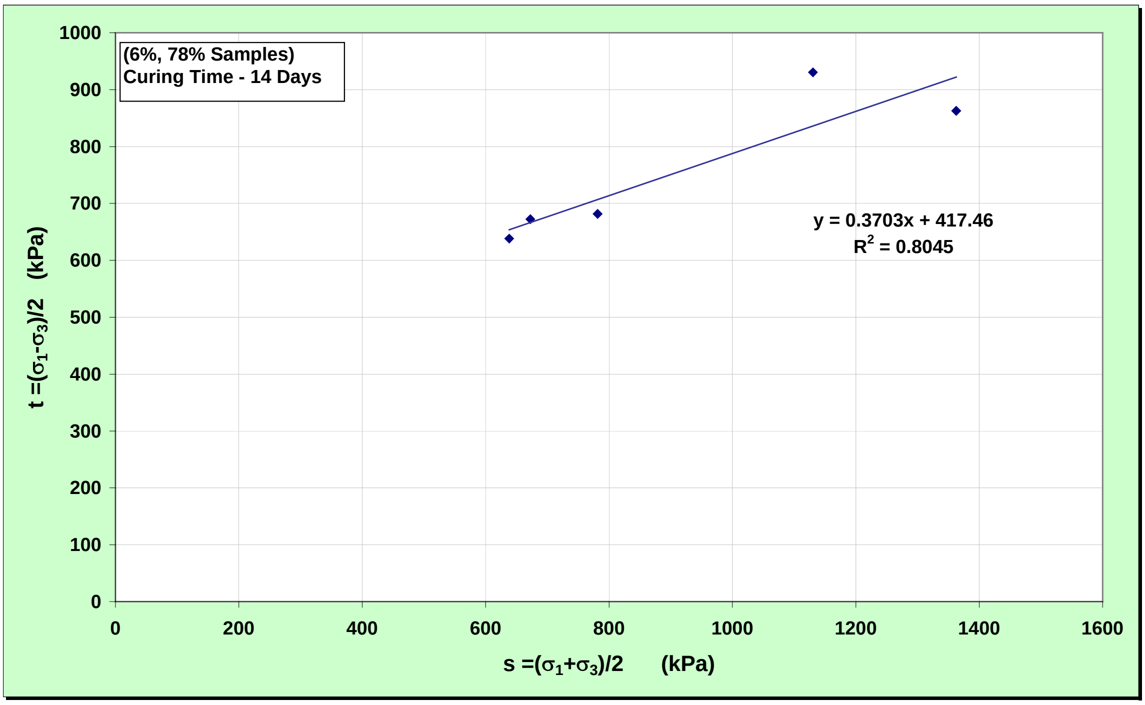

Figure A3.5. 14 s-t plot for CD triaxial testing, 6%, 78%, 14 days curing

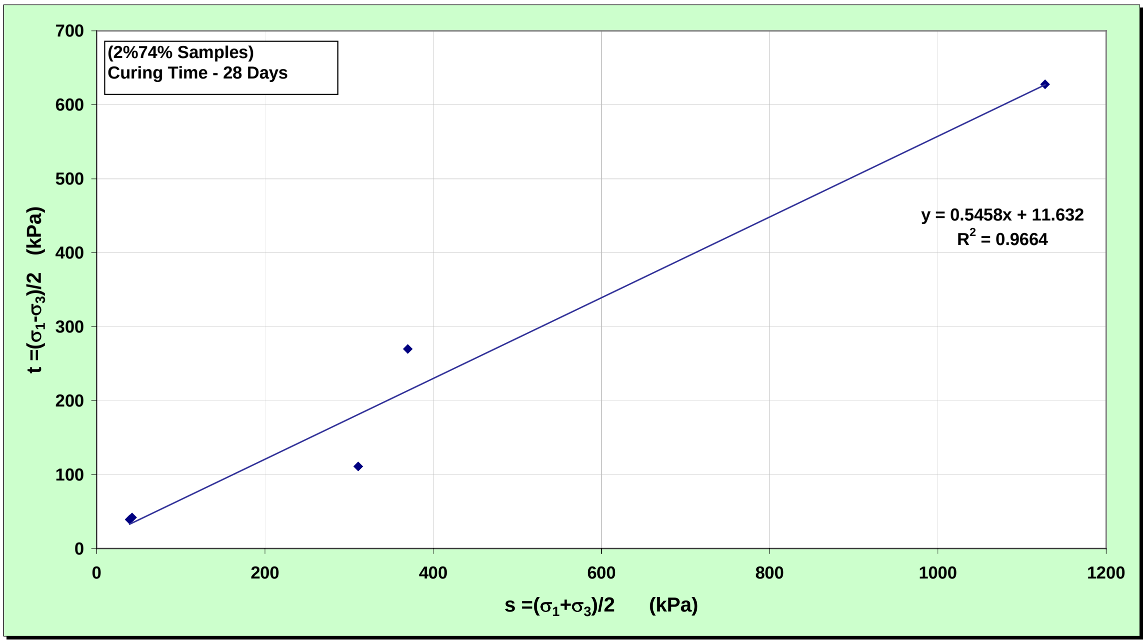

Figure A3.5. 15 s-t plot for CD triaxial testing, 2%, 74%, 28 days curing

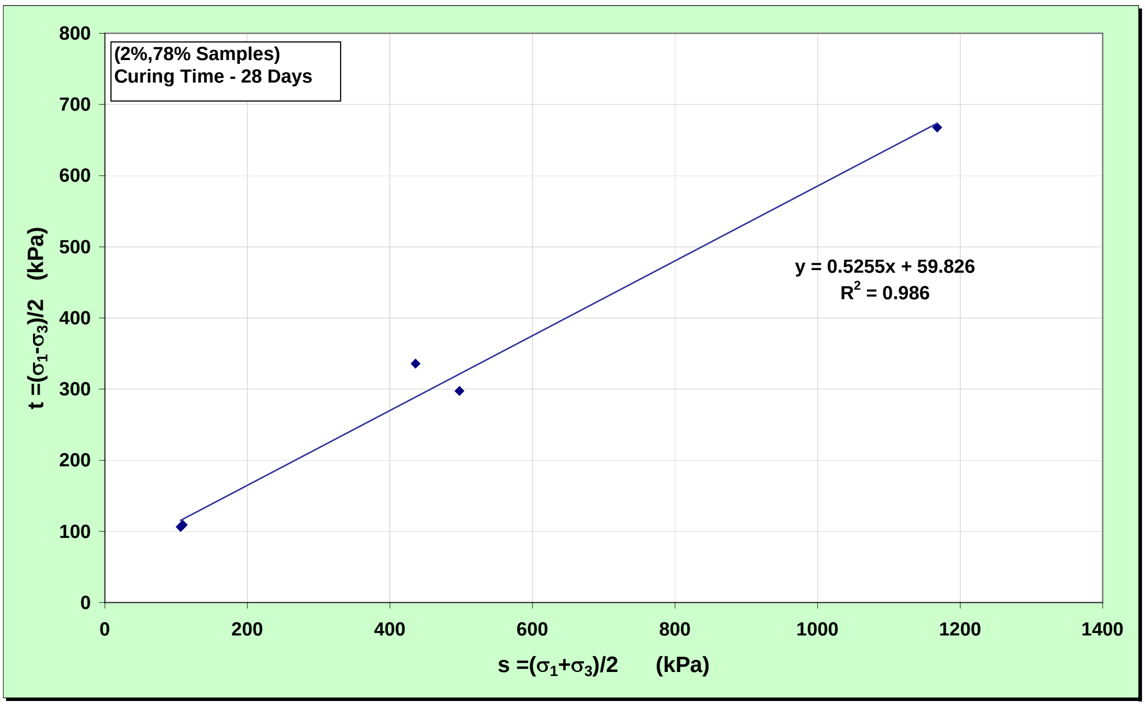

Figure A3.5. 16 s-t plot for CD triaxial testing, 2%, 78%, 28 days curing

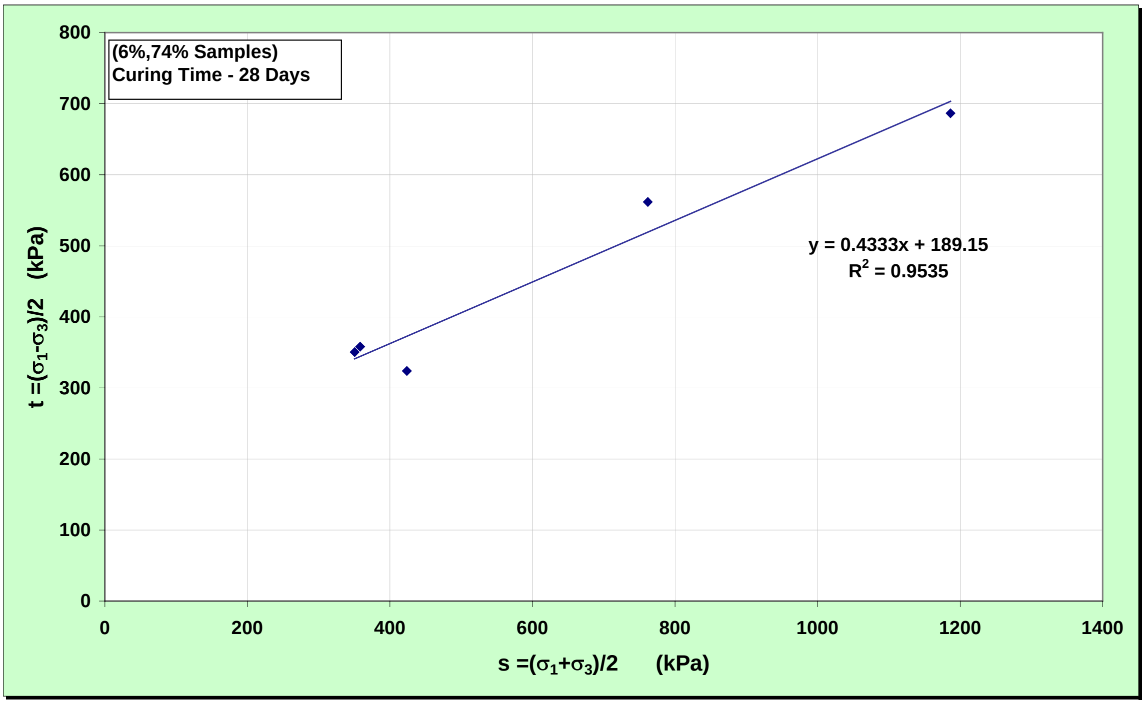

Figure A3.5. 17 s-t plot for CD triaxial testing, 6%, 74%, 28 days curing

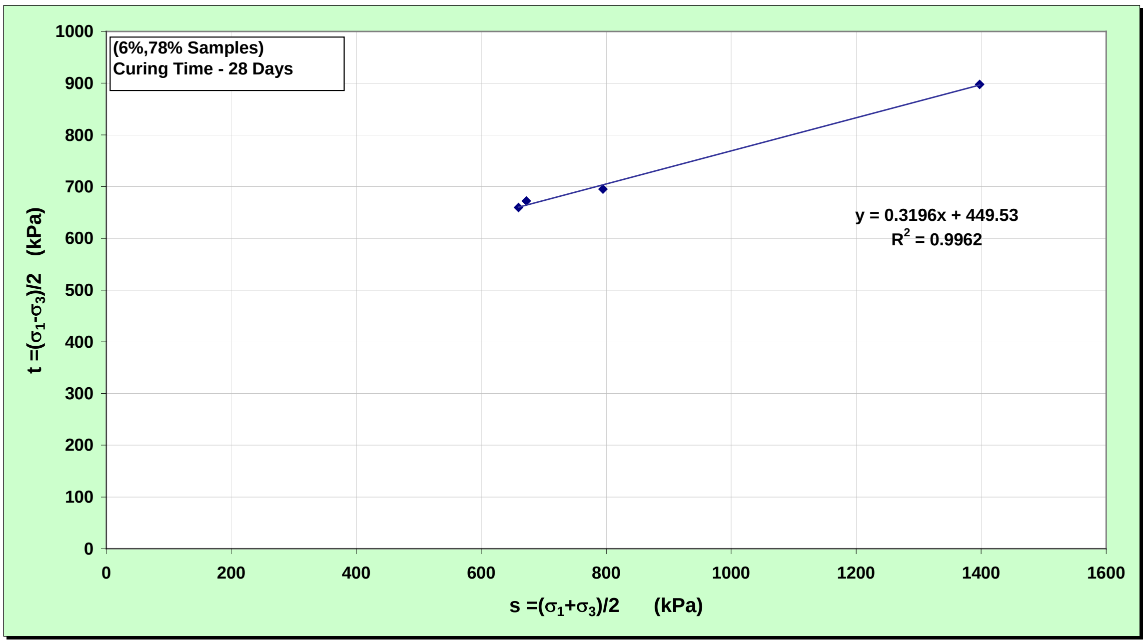

Figure A3.5. 18 s-t plot for CD triaxial testing, 6%, 78%, 28 days curing

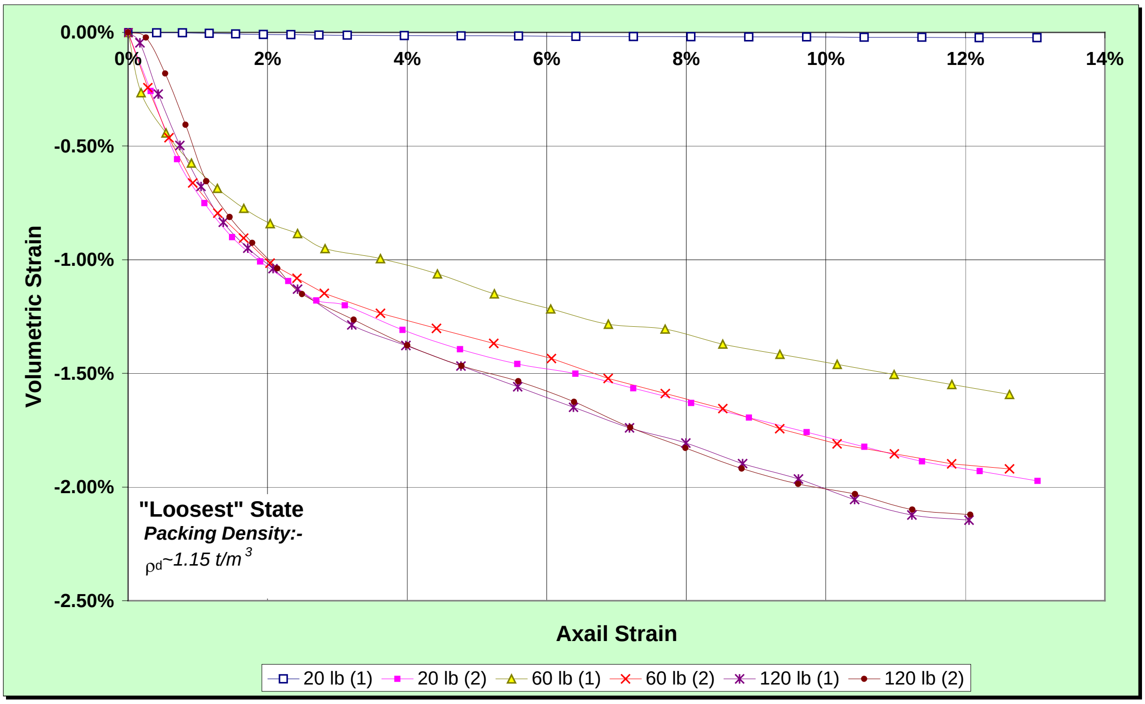

Figure A3.5. 19 Volumetric Strain vs. Axial Strain, tailings – Loosest State

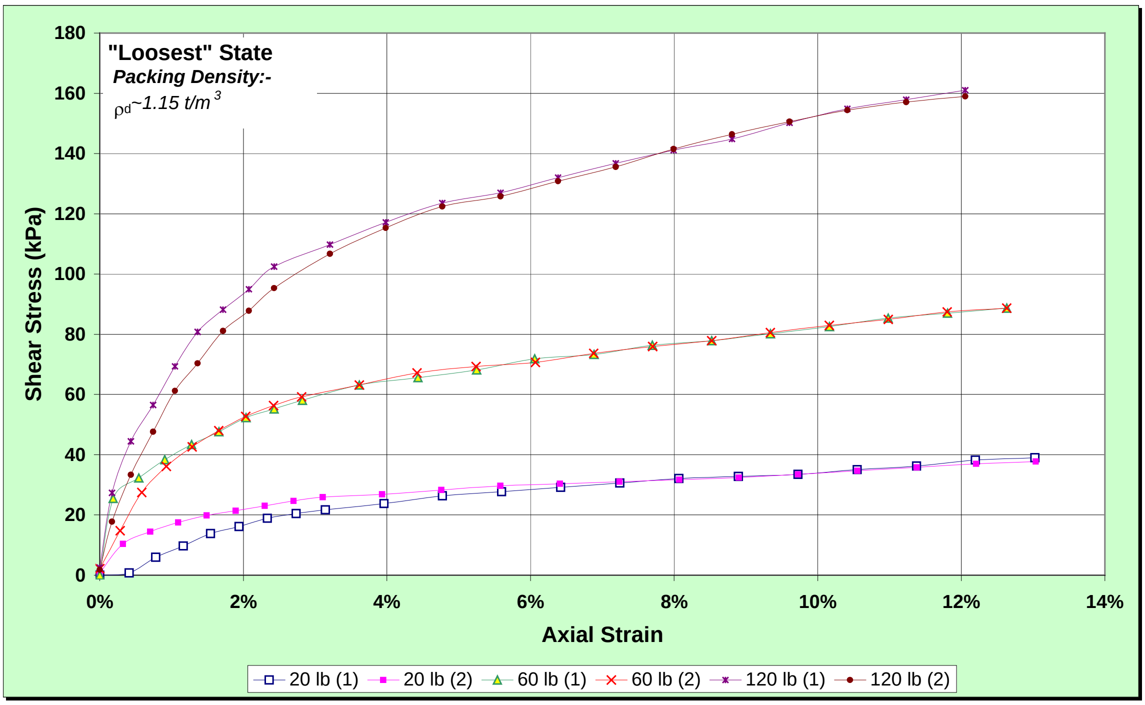

Figure A3.5. 20 Shear Stress vs. Axial Strain, tailings – Loosest State

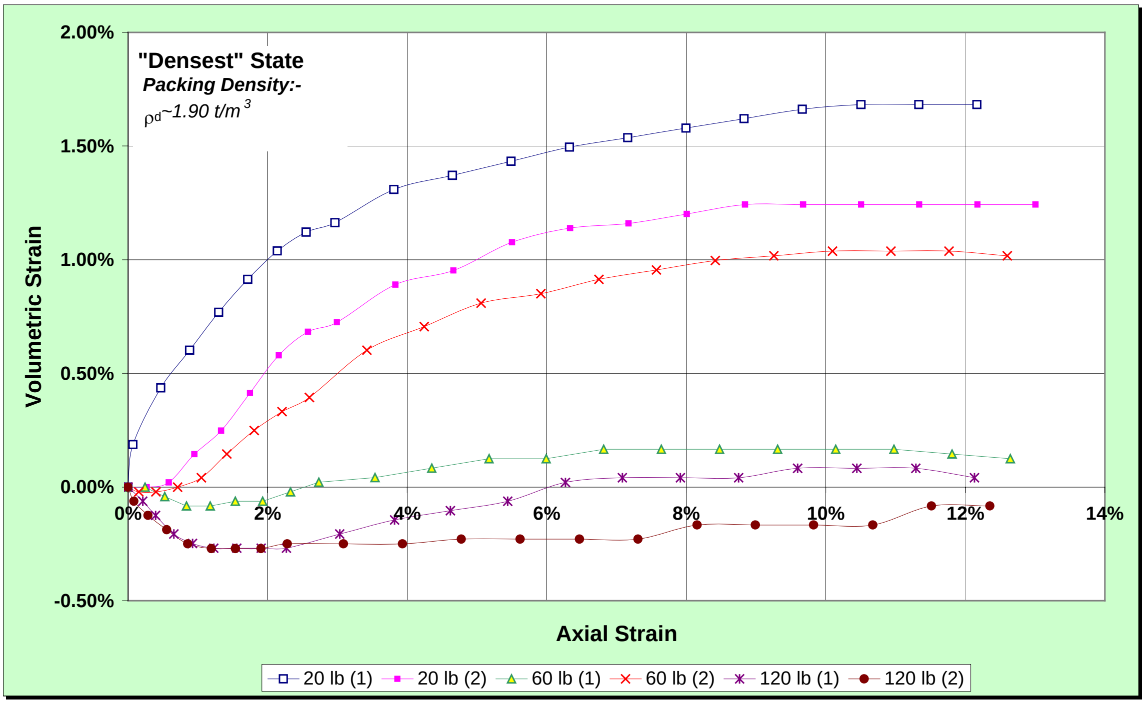

Figure A3.5. 21 Volumetric Strain vs. Axial Strain, Tailings – Densest State

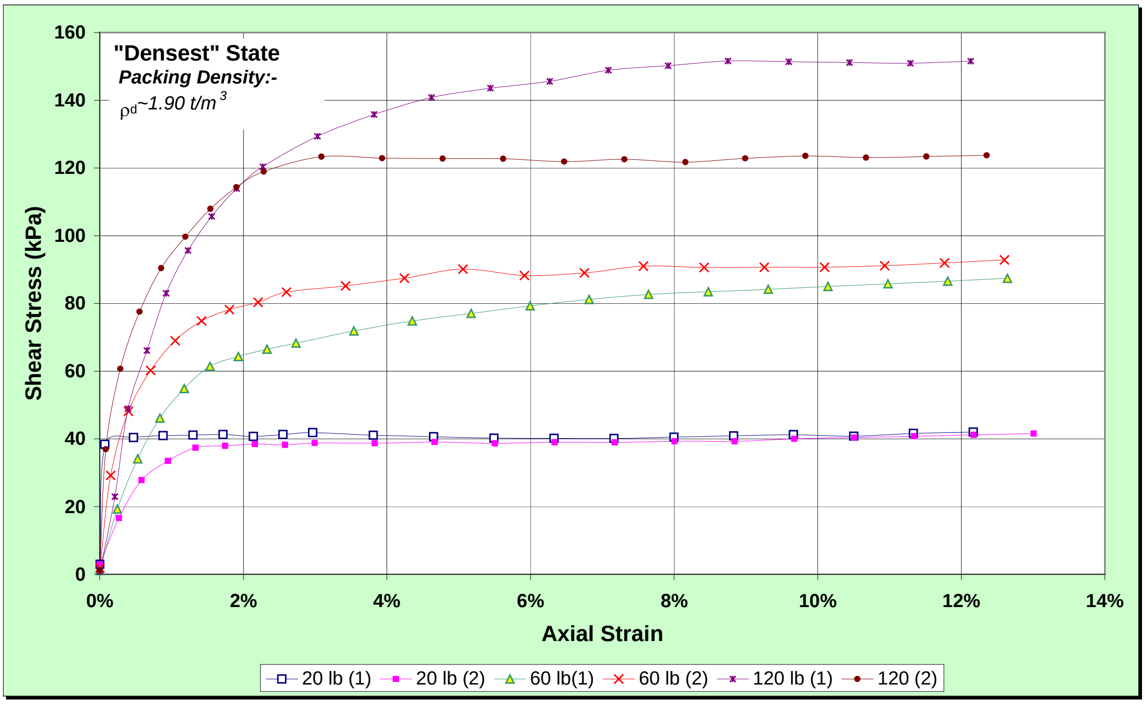

Figure A3.5. 22 Shear Stress vs. Axial Strain, tailings – Densest State

APPENDIX 3.6

Consolidation Testing Results

- *Oedometer test results*
- *Summary plots of UCS tests under confined curing*

Oedometer Testing Results

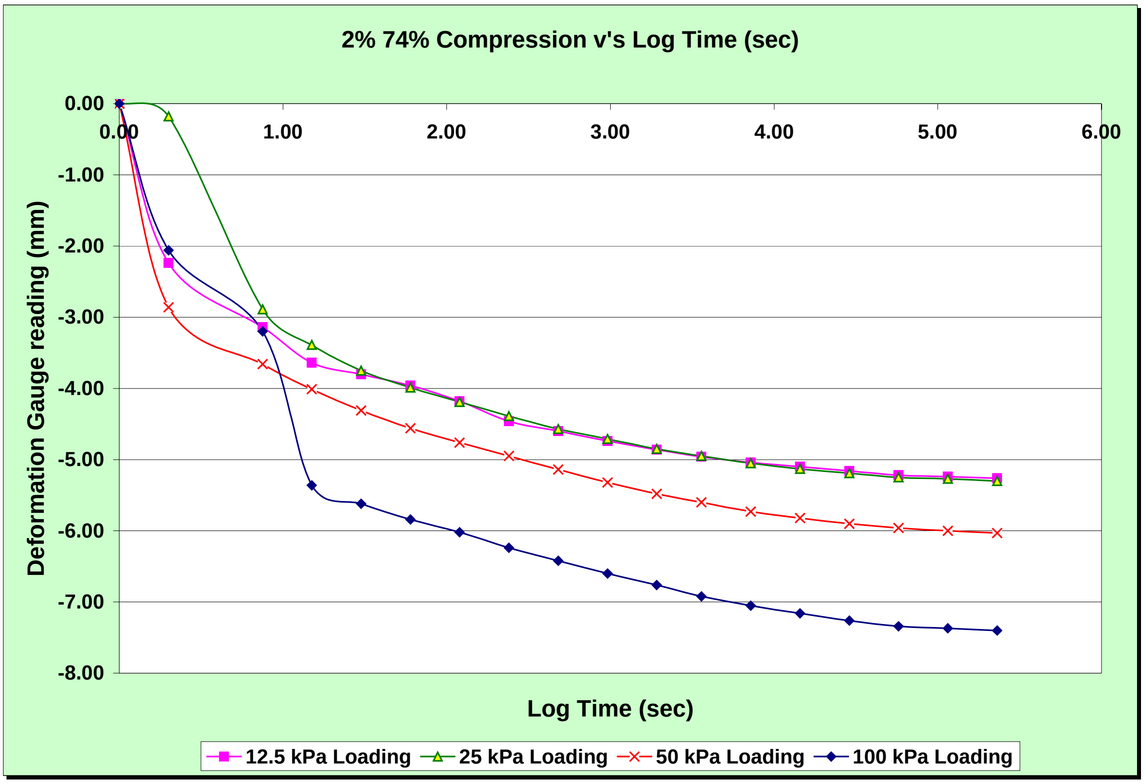

Figure A3.6. 1Displacement vs log time, 2% cement, 74% solids paste, 28 days curing

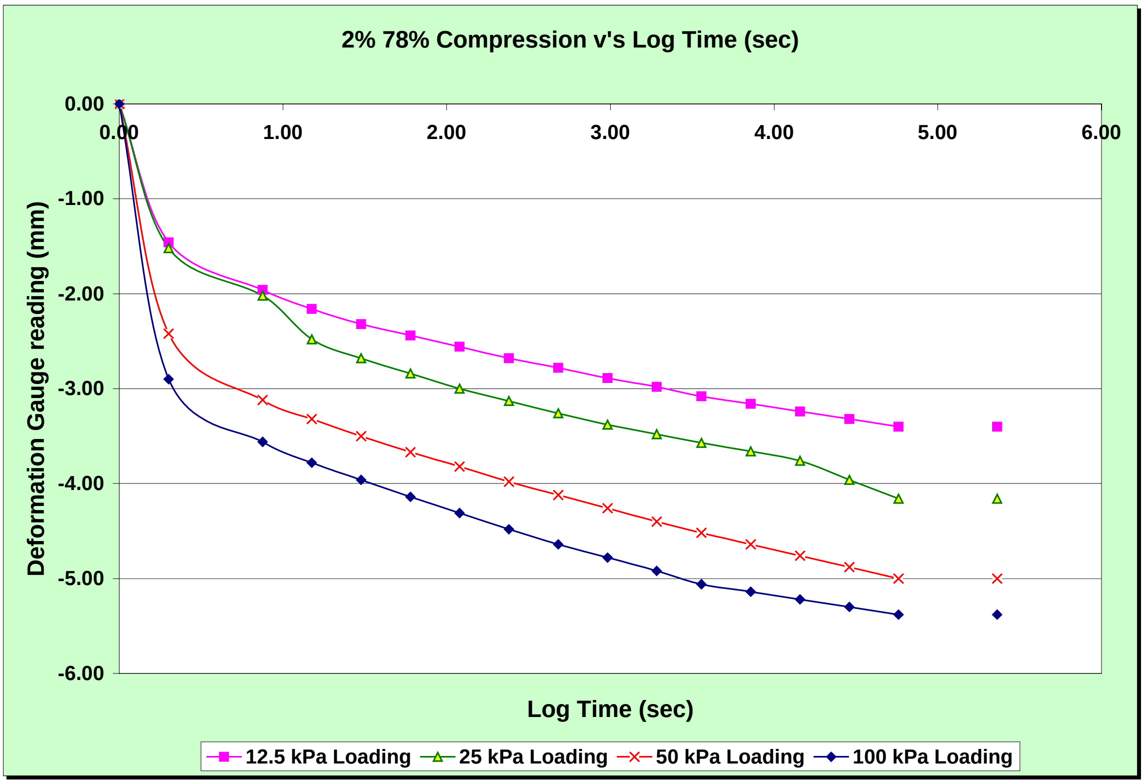

Figure A3.6. 2Displacement vs log time, 2% cement, 78% solids paste, 28 days curing

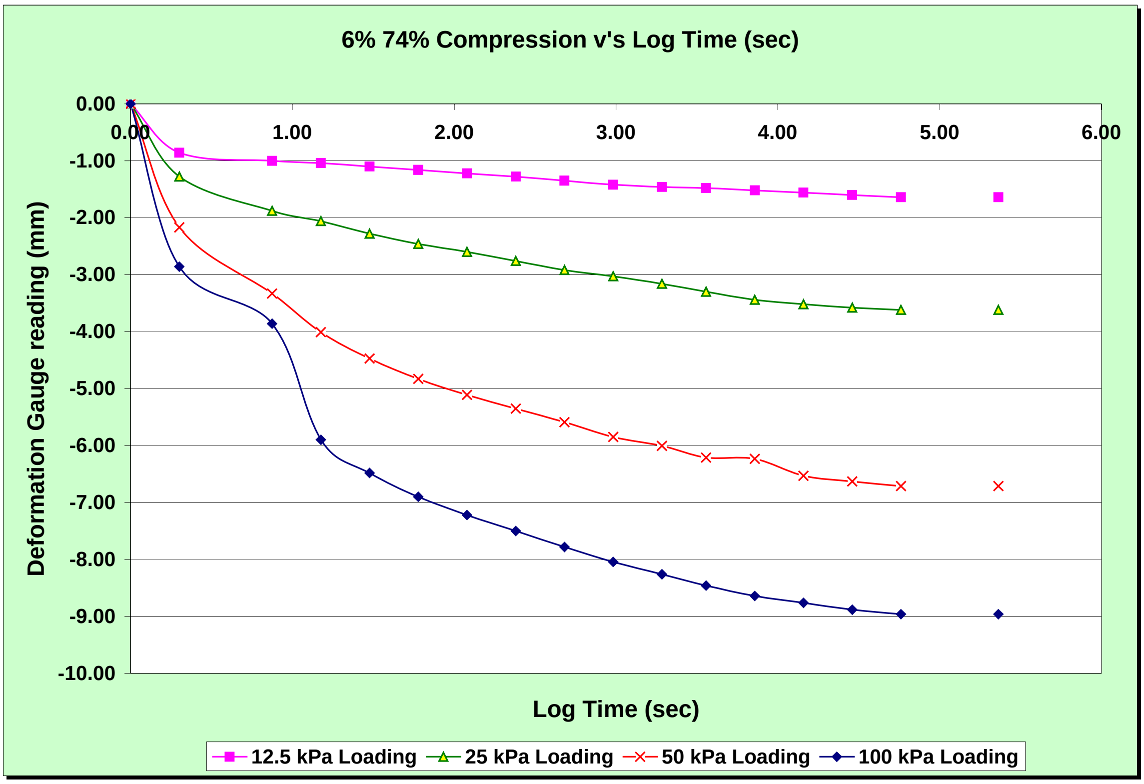

Figure A3.6. 3Displacement vs log time, 6% cement, 74% solids paste, 28 days curing

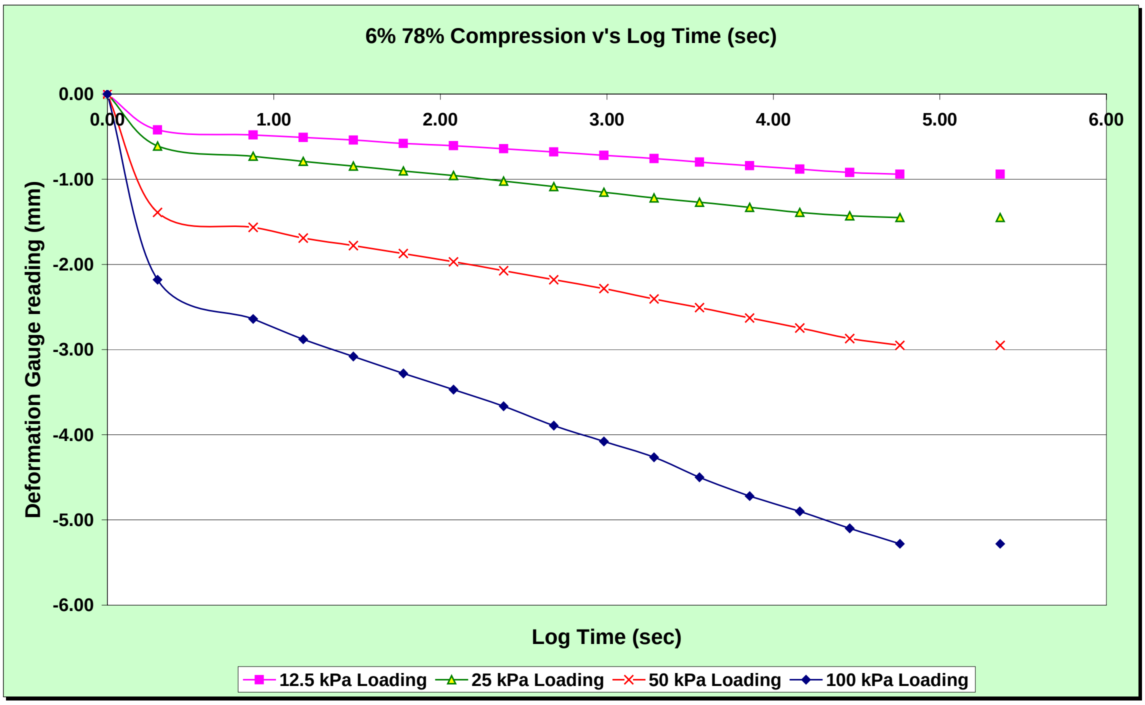

Figure A3.6. 4Displacement vs log time, 6% cement, 78% solids paste, 28 days curing

Preliminary "Consolidated Curing" Test Results

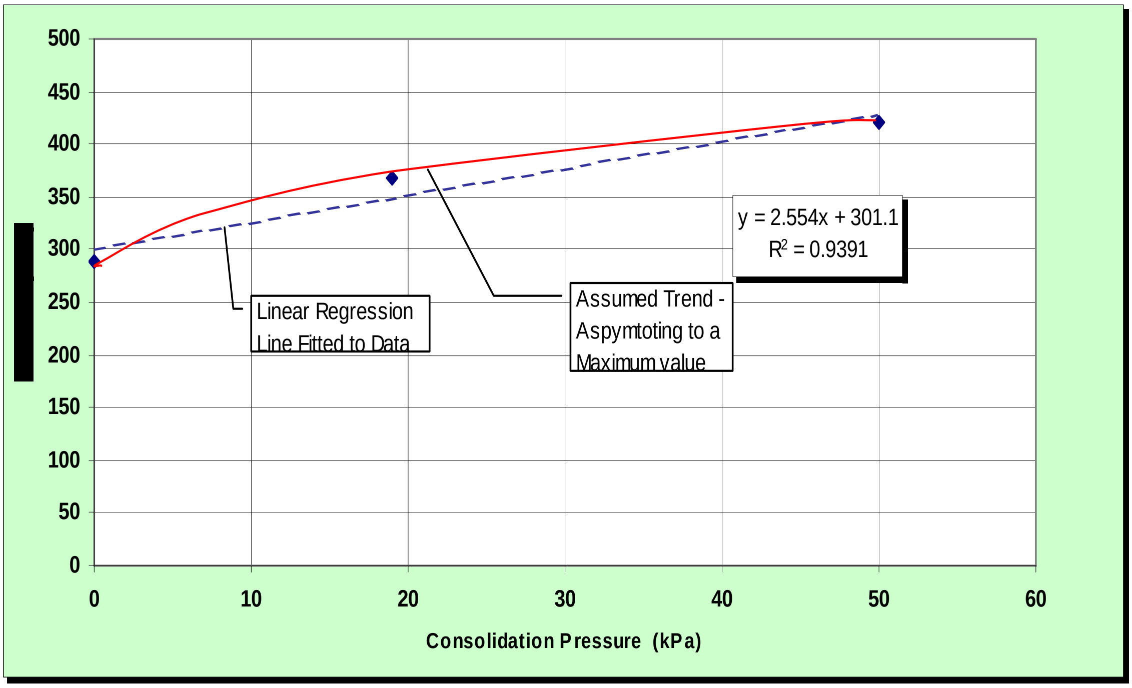

Figure A3.6. 5 Increase in UCS associated with increase in the consolidation pressure during curing

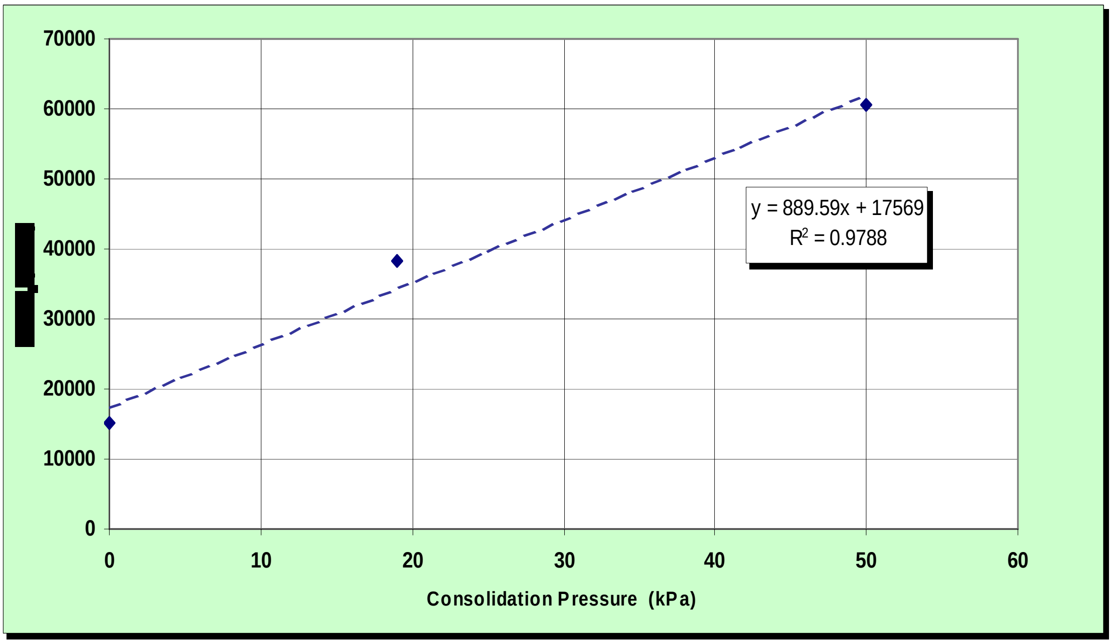

Figure A3.6. 6 Increase in tangential Young's Modulus, E_t associated with increase in the consolidation pressure during curing

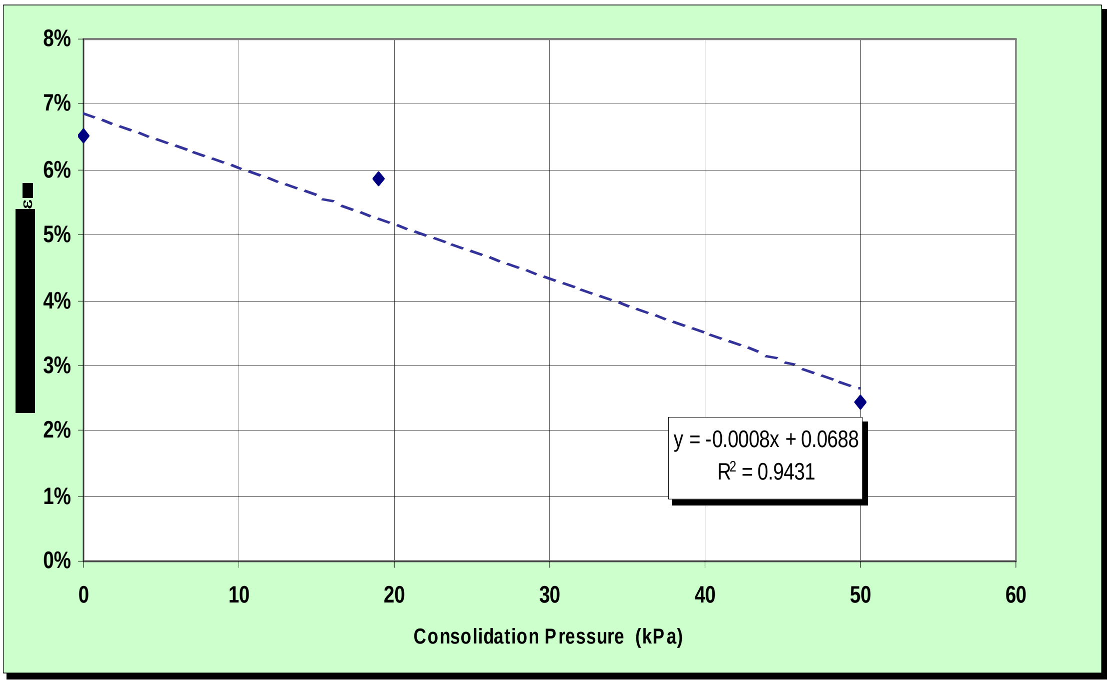

Figure A3.6. 7 Decrease in Failure Strain, ε_f associated with increase in the consolidation pressure during curing

APPENDIX 3.7

In-situ Testing Results

- *DCP testing*
  - *Raw data and plots*
  - *SPT – N Plots*
- *Empirical Correlations*
- *In-situ core testing results*

Table A3.7. 1DCPT Data, Hole #1

D (m)	# Blows	D (m)	# Blows	D (m)	# Blows	D (m)	# Blows	D (m)	# Blows
0.10	0	5.10	17	10.10	26	15.10	31	20.10	21
0.20	0	5.20	16	10.20	24	15.20	30	20.20	23
0.30	0	5.30	17	10.30	26	15.30	26	20.30	26
0.40	0	5.40	18	10.40	25	15.40	29	20.40	22
0.50	0	5.50	17	10.50	22	15.50	26	20.50	25
0.60	0	5.60	20	10.60	22	15.60	19	20.60	24
0.70	0	5.70	18	10.70	21	15.70	12	20.70	23
0.80	0	5.80	18	10.80	19	15.80	12	20.80	26
0.90	0	5.90	18	10.90	18	15.90	13	20.90	24
1.00	0	6.00	18	11.00	18	16.00	13	21.00	24
1.10	0	6.10	22	11.10	22	16.10	14	21.10	24
1.20	0	6.20	20	11.20	21	16.20	13	21.20	21
1.30	0	6.30	16	11.30	20	16.30	14	21.30	23
1.40	0	6.40	17	11.40	18	16.40	16	21.40	21
1.50	0	6.50	17	11.50	22	16.50	16	21.50	21
1.60	0	6.60	19	11.60	21	16.60	17	21.60	22
1.70	0	6.70	18	11.70	20	16.70	15	21.70	22
1.80	0	6.80	19	11.80	20	16.80	13	21.80	21
1.90	0	6.90	19	11.90	21	16.90	14	21.90	24
2.00	2	7.00	18	12.00	22	17.00	16	22.00	23
2.10	4	7.10	20	12.10	20	17.10	15	22.10	18
2.20	4	7.20	18	12.20	20	17.20	16	22.20	21
2.30	4	7.30	20	12.30	21	17.30	14	22.30	22
2.40	6	7.40	20	12.40	22	17.40	16	22.40	21
2.50	8	7.50	18	12.50	23	17.50	16	22.50	22
2.60	12	7.60	20	12.60	23	17.60	16	22.60	20
2.70	16	7.70	19	12.70	22	17.70	16	22.70	23
2.80	17	7.80	19	12.80	23	17.80	17	22.80	57
2.90	17	7.90	20	12.90	20	17.90	17	22.90	127
3.00	18	8.00	22	13.00	20	18.00	18	23.00	
3.10	18	8.10	23	13.10	20	18.10	17	23.10	
3.20	17	8.20	23	13.20	19	18.20	17	23.20	
3.30	16	8.30	21	13.30	17	18.30	18	23.30	
3.40	17	8.40	20	13.40	20	18.40	13	23.40	
3.50	17	8.50	21	13.50	19	18.50	10	23.50	
3.60	17	8.60	22	13.60	20	18.60	15	23.60	
3.70	16	8.70	22	13.70	21	18.70	20	23.70	
3.80	17	8.80	24	13.80	19	18.80	21	23.80	
3.90	17	8.90	22	13.90	20	18.90	20	23.90	
4.00	16	9.00	23	14.00	19	19.00	21	24.00	
4.10	18	9.10	25	14.10	21	19.10	39	24.10	
4.20	16	9.20	22	14.20	21	19.20	32	24.20	
4.30	15	9.30	23	14.30	21	19.30	21	24.30	
4.40	16	9.40	22	14.40	25	19.40	21	24.40	
4.50	16	9.50	26	14.50	26	19.50	23	24.50	
4.60	10	9.60	26	14.60	30	19.60	24	24.60	
4.70	19	9.70	27	14.70	34	19.70	23	24.70	
4.80	19	9.80	27	14.80	27	19.80	21	24.80	
4.90	11	9.90	29	14.90	27	19.90	24	24.90	
5.00	12	10.00	28	15.00	28	20.00	25	25.00	

Note: The shaded cells at the beginning of the testing represent the fraction/ depth of paste which had been prepared for testing. The shaded area at the end of the tables represents the bedrock, and the end of the test.

Table A3.7. 2 DCPT Data, Hole #3

D (m)	# Blows	D (m)	# Blows	D (m)	# Blows	D (m)	# Blows	D (m)	# Blows
0.10		5.10	16	10.10	21	15.10	31	20.10	22
0.20		5.20	17	10.20	18	15.20	31	20.20	24
0.30		5.30	17	10.30	18	15.30	34	20.30	24
0.40		5.40	17	10.40	18	15.40	35	20.40	25
0.50		5.50	17	10.50	21	15.50	31	20.50	27
0.60		5.60	18	10.60	20	15.60	23	20.60	26
0.70		5.70	17	10.70	19	15.70	17	20.70	28
0.80		5.80	17	10.80	21	15.80	19	20.80	27
0.90		5.90	17	10.90	25	15.90	20	20.90	28
1.00		6.00	17	11.00	24	16.00	20	21.00	30
1.10		6.10	18	11.10	22	16.10	18	21.10	24
1.20		6.20	19	11.20	23	16.20	17	21.20	26
1.30		6.30	19	11.30	24	16.30	18	21.30	25
1.40		6.40	17	11.40	21	16.40	19	21.40	22
1.50		6.50	18	11.50	18	16.50	20	21.50	27
1.60	3.00	6.60	18	11.60	22	16.60	21	21.60	23
1.70	6.00	6.70	20	11.70	24	16.70	19	21.70	23
1.80	6.00	6.80	21	11.80	24	16.80	19	21.80	23
1.90	12.00	6.90	21	11.90	22	16.90	19	21.90	23
2.00	12	7.00	21	12.00	25	17.00	22	22.00	27
2.10	11	7.10	21	12.10	21	17.10	18	22.10	19
2.20	13	7.20	22	12.20	22	17.20	22	22.20	30
2.30	14	7.30	19	12.30	22	17.30	22	22.30	28
2.40	15	7.40	21	12.40	24	17.40	22	22.40	27
2.50	16	7.50	24	12.50	25	17.50	21	22.50	27
2.60	15	7.60	20	12.60	23	17.60	25	22.60	29
2.70	21	7.70	20	12.70	27	17.70	22	22.70	26
2.80	19	7.80	19	12.80	26	17.80	22	22.80	25
2.90	15	7.90	20	12.90	22	17.90	24	22.90	25
3.00	17	8.00	19	13.00	24	18.00	23	23.00	31
3.10	16	8.10	18	13.10	22	18.10	22	23.10	100
3.20	17	8.20	21	13.20	23	18.20	22	23.20	
3.30	16	8.30	19	13.30	23	18.30	20	23.30	
3.40	17	8.40	17	13.40	22	18.40	22	23.40	
3.50	20	8.50	20	13.50	23	18.50	23	23.50	
3.60	17	8.60	20	13.60	23	18.60	27	23.60	
3.70	15	8.70	21	13.70	26	18.70	25	23.70	
3.80	17	8.80	26	13.80	24	18.80	21	23.80	
3.90	20	8.90	25	13.90	24	18.90	24	23.90	
4.00	21	9.00	23	14.00	25	19.00	27	24.00	
4.10	22	9.10	24	14.10	18	19.10	24	24.10	
4.20	24	9.20	25	14.20	25	19.20	26	24.20	
4.30	21	9.30	21	14.30	24	19.30	18	24.30	
4.40	22	9.40	23	14.40	24	19.40	22	24.40	
4.50	20	9.50	22	14.50	26	19.50	24	24.50	
4.60	21	9.60	25	14.60	29	19.60	23	24.60	
4.70	24	9.70	26	14.70	31	19.70	22	24.70	
4.80	24	9.80	26	14.80	28	19.80	21	24.80	
4.90	18	9.90	27	14.90	35	19.90	22	24.90	
5.00	15	10.00	27	15.00	32	20.00	23	25.00	

Table A3.7. 3 DCPT Data, Hole #5

D (m)	# Blows	D (m)	# Blows	D (m)	# Blows	D (m)	# Blows	D (m)	# Blows
0.10		5.10	13	10.10	27	15.10	43	20.10	28
0.20		5.20	14	10.20	31	15.20	40	20.20	28
0.30		5.30	13	10.30	30	15.30	39	20.30	26
0.40		5.40	14	10.40	24	15.40	38	20.40	29
0.50		5.50	16	10.50	20	15.50	26	20.50	28
0.60		5.60	14	10.60	18	15.60	22	20.60	24
0.70		5.70	17	10.70	20	15.70	22	20.70	28
0.80		5.80	17	10.80	20	15.80	19	20.80	28
0.90		5.90	19	10.90	22	15.90	20	20.90	30
1.00		6.00	17	11.00	26	16.00	22	21.00	32
1.10		6.10	14	11.10	23	16.10	19	21.10	29
1.20		6.20	15	11.20	24	16.20	20	21.20	29
1.30		6.30	14	11.30	19	16.30	21	21.30	30
1.40		6.40	17	11.40	15	16.40	22	21.40	30
1.50		6.50	16	11.50	21	16.50	23	21.50	30
1.60	3	6.60	18	11.60	25	16.60	21	21.60	27
1.70	6	6.70	21	11.70	25	16.70	22	21.70	30
1.80	22	6.80	22	11.80	23	16.80	22	21.80	22
1.90	12	6.90	95	11.90	26	16.90	24	21.90	29
2.00	12	7.00	24	12.00	27	17.00	22	22.00	24
2.10	9	7.10	21	12.10	26	17.10	21	22.10	30
2.20	10	7.20	23	12.20	26	17.20	21	22.20	26
2.30	11	7.30	22	12.30	25	17.30	21	22.30	26
2.40	11	7.40	18	12.40	22	17.40	19	22.40	28
2.50	11	7.50	17	12.50	23	17.50	19	22.50	29
2.60	11	7.60	17	12.60	24	17.60	19	22.60	30
2.70	11	7.70	21	12.70	25	17.70	22	22.70	29
2.80	15	7.80	21	12.80	23	17.80	22	22.80	27
2.90	13	7.90	20	12.90	26	17.90	21	22.90	30
3.00	16	8.00	22	13.00	23	18.00	22	23.00	43
3.10	15	8.10	20	13.10	24	18.10	35	23.10	100
3.20	15	8.20	19	13.20	24	18.20	54	23.20	
3.30	11	8.30	19	13.30	23	18.30	25	23.30	
3.40	13	8.40	16	13.40	23	18.40	23	23.40	
3.50	14	8.50	17	13.50	21	18.50	17	23.50	
3.60	20	8.60	18	13.60	24	18.60	23	23.60	
3.70	18	8.70	18	13.70	24	18.70	28	23.70	
3.80	14	8.80	19	13.80	23	18.80	23	23.80	
3.90	16	8.90	18	13.90	25	18.90	22	23.90	
4.00	21	9.00	18	14.00	26	19.00	28	24.00	
4.10	16	9.10	18	14.10	24	19.10	25	24.10	
4.20	20	9.20	19	14.20	27	19.20	25	24.20	
4.30	23	9.30	19	14.30	36	19.30	24	24.30	
4.40	44	9.40	19	14.40	45	19.40	35	24.40	
4.50	15	9.50	21	14.50	48	19.50	29	24.50	
4.60	15	9.60	22	14.60	42	19.60	25	24.60	
4.70	14	9.70	20	14.70	44	19.70	27	24.70	
4.80	14	9.80	21	14.80	38	19.80	52	24.80	
4.90	13	9.90	28	14.90	41	19.90	38	24.90	
5.00	15	10.00	28	15.00	35	20.00	28	25.00	

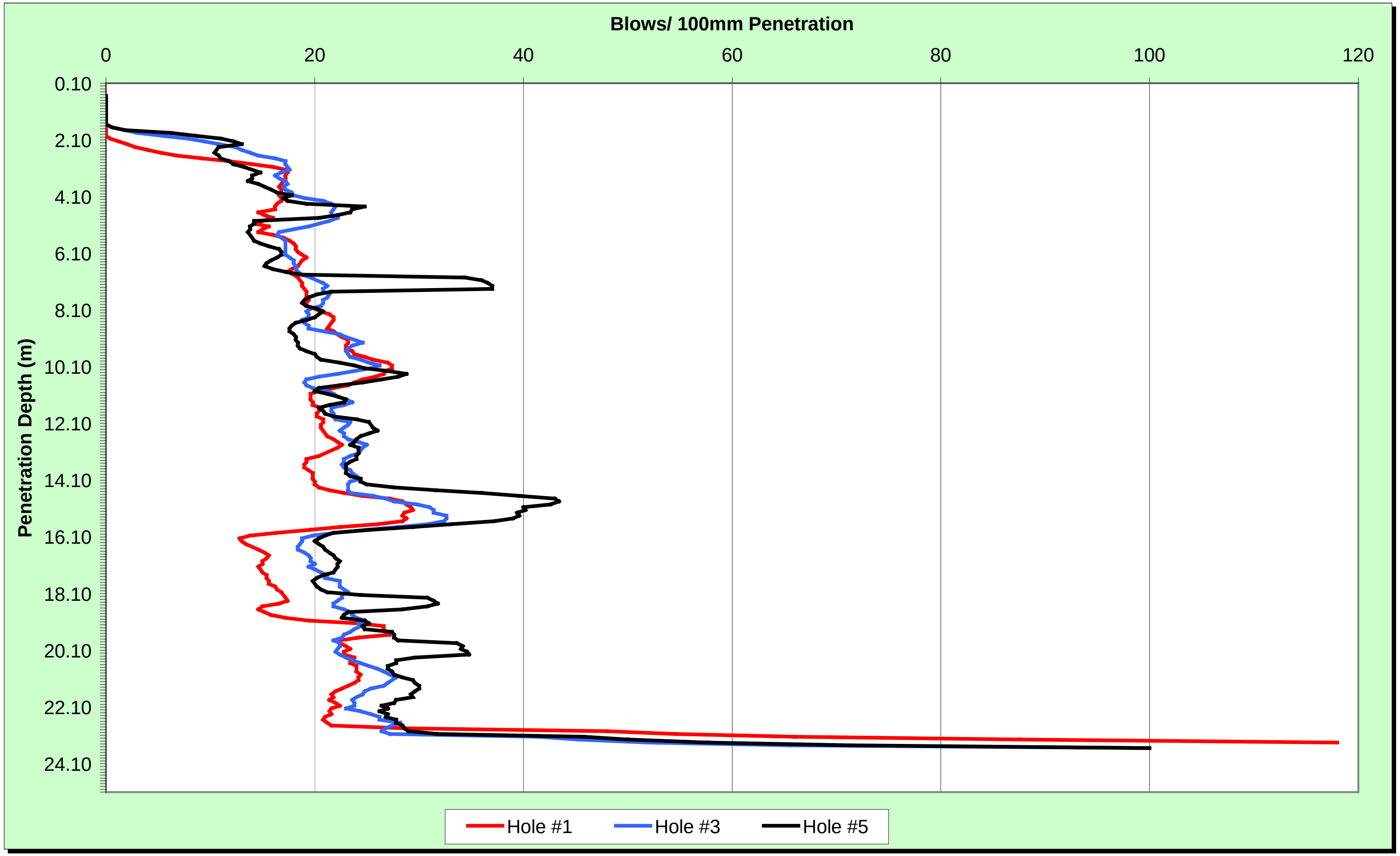

Figure A3.7. 1DCPT Data (5point moving average)

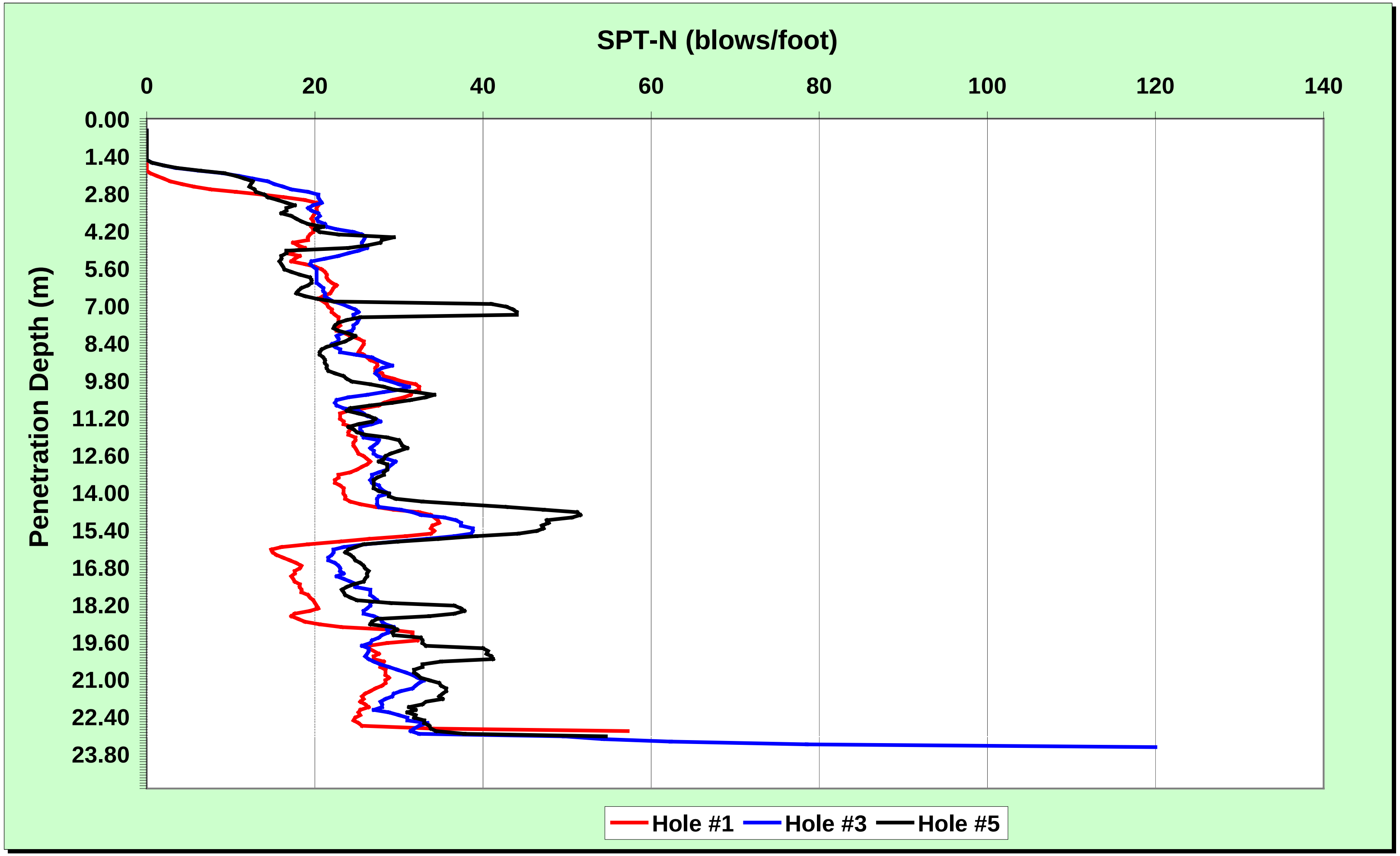

Figure A3.7. 2Equivalent SPT-N (5 point moving average)

Table A3.7. 4 Empirical correlations between soil properties and penetration test results (from www.cee.princeton.edu/~radu/papers/const/node16.html#SECTION00052200000000000000)

Property	Reference	Basic relation	Remarks
Low strain shear modulus (G_0)	Ohsaki and Iwasaki (1973)	$G_0 = a(N_{SPT})^b$	Japanese practice
	Ohta and Goto (1978)	$G_0 = f(N_{SPT}$, depth, age, soil type)	correl. with sh. wave velocity
	Bellotti et al (1986)	$G_0 = 400\, p_a \cdot \exp\{1.39 D_r\} \left(\frac{\sigma'}{p_a}\right)^{0.43}$	Ticino sand (fine)
	Baldi et al (1989)	chart: $\frac{G_0}{q_c} - \frac{q_c}{\sqrt{\sigma'_{v0}}}$	Ticino sand
Relative density (D_r)	Marcuson and Bieganousky (1977)	$D_r = f(N_{SPT}, \sigma'_{v0}, OCR, C_u)$	coarse sands
	Tokimatsu and Yoshimi (1983)	$D_r = 21\sqrt{\frac{N_{72}}{\sigma'_{v0}/p_a+0.7} + \frac{F}{1.7}}$	Japanese standards
	Kulhawy and Mayne (1990)	$\frac{(N_1)_{60}}{D_r^2} = 60 + 25 \log D_{50}$ $D_r = f($test cond., aging, $(N_1)_{60}, OCR)$	NC sands
	Meyerhof (1957)	$D_r = 21\sqrt{N_{78}/(\frac{\sigma'}{p_a} + 0.7)}$	Japanese stnd.
	Holts and Gibbs (1979)	$D_r = f(N_{SPT}, \sigma'_{v0})$	
	Skempton (1986)	$D_r \approx \sqrt{(N_1)_{60}/C}$; with $C = 65$ (coarse); 60 (medium); 55 (fine); and 40 (NC fills)	
	Baldi et al (1982)	chart: $D_r = f(q_c, \sigma'_{h0})$	uncem., unag. quartz sands
	Jamiolkowski et al (1985)	$D_r = 68[\log \frac{q_c/K_1}{p_a} - 1]$	calibration chamber studies
	Kulhawy and Mayne (1990)	$D_r = f(q_c, Q_c, OCR)$	
	Huntsman et al (1986)	chart: $f_s - \sigma'_{h0} - D_r$	calibration chamber
Phase tr. angle ($\bar{\phi}$)	Koerner (1970)	$\phi = f(D_r$, gr. size, fabric)	single mineral soil
State parameter (ψ)	Been et al (1987)	$\psi = f(q_c, p'$, soil type)	various sands
	ibid.	$\psi = f(q_c, p', \lambda_{ss})$	

Table A3.7. 4 (cont)

Property	Reference	Basic relation	Remarks
Friction	Schmertmann (1975)	$\tan^{-1}\left[\frac{N_{SPT}}{12.2+20.3\frac{\sigma'_{v0}}{p_a}}\right]^{0.34}$	depth > 1m
angle at	Parry (1977)	chart: $\phi = f(N_{SPT}/\sigma'_{v0})$	
failure	NAVFAC (1982)	chart: $\phi = f(D_r)$	fine sands
(ϕ)	Parry (1977)	chart: $\phi = f(D_r)$	
	Robertson and Campanella (1983)	$\tan^{-1}\left[0.1+0.38\log\frac{q_c}{\sigma'_{v0}}\right]$	
	Kulhawy and Maine (1990)	$\phi = 17.6 + 11.0\log\frac{q_c}{p_a}$	$SD = 2.8°$; $R^2 = 0.64$
	Olsen and Farr (1986)	chart: $\phi = f(q_n, f_s/\sigma'_{v0})$ chart: $\phi = f(q_n, \text{soil type})$	clean sands sand ... clay
	Jefferies and Been (1987)	$\phi = 32(1-1.67\psi)$	$SD \approx 2°$
	Been and Jefferies (1985)	$\phi - \bar{\phi} = f(\psi)$ (and $\bar{\phi} \approx 30° \ldots 32°$)	
Soil classification and OCR	Schmertmann (1978) Douglas and Olsen (1981) Robertson and Campanella (1983)	various charts showing the soil type as a function of q_c/p_a and F_r	mech. CPT electric friction CPT
	Olsen and Farr (1986)	soil type $= f(q_n, \frac{f_s}{\sigma'_{v0}})$	electric CPT
	Senneset and Janbu (1985)	soil type $= f(B_q, \frac{q_T}{p_a})$	various correl.
	Jones and Rust (1982)	soil type $= f(u, q_T, \sigma'_{v0})$	with
	Robertson (1990)	soil type $= f(q_T, F_r, \sigma'_{v0})$	results
	Jefferies and Davies (1991)	chart: soil type $= f(q_T, B_q, F_r, \sigma'_{v0})$	of CPTU

Table A3.7. 4 (cont)

Reference	Basic relation	Remarks
Robertson et al (1982)	chart: $\frac{q_c(\text{bars})}{N_{60}}$ vs. D_{50}	various sands
Seed and De Alba (1986)	chart: $\frac{q_c(\text{tsf})}{N_{60}}$ vs. D_{50}	$D_{50} \leq 1\text{mm}$
Kulhawy and Mayne (1990)	$\frac{q_c/p_a}{N_{60}} = 5.44 D_{50}$ (mm)	$SD = 1.03$; $R^2 = 0.7$
ibid.	$\frac{q_c/p_a}{N_{60}} = 4.25 - \frac{F}{41.3}$	$SD = 0.86$; $R^2 = 0.41$
Jefferies and Davies (1993)	chart: $\frac{q_c(\text{MPa})}{N_{60}}$ vs. D_{50}	$0.01\text{mm} \leq D_{50} \leq 10\text{mm}$
ibid.	$\frac{q_c(\text{MPa})}{N_{60}} = f(q_T, \sigma'_{v0}, B_q)$	five sites
Stark and Olson (1995)	chart: $\frac{q_c(\text{MPa})}{N_{60}}$ vs. D_{50}	based on liquefaction potential relationships

In-situ UCS Core Testing Results

Table A3.7. 5 In-situ UCS Core Summary

			Mix				
Sample No.	**Stope No.**	**Source Location**	**% Cement**	**% Solids**	**Date of Filling**	**Curing time (yrs)**	**Comments**
IS.4773.1	47_73	77XC- 475	8%	77%	Jan-00	2.5	Soaked for 10 days
IS.4773.2	47_73	77XC- 475	8%	77%	Jan-00	2.5	Short sample 58mm length, 38 mm dia.
IS.4773.3	47_73	77XC- 475	8%	77%	Jan-00	2.5	Good sample - Tested as per the state of insitu sample
IS.4773.4	47_73	77XC- 475	8%	77%	Jan-00	2.5	Soaked for 3.5 hrs before testing
IS.4261.1	42_61	59XC-400	3.5%	76%	Nov-00	2.0	*160mm slump ~76%solids
IS.4261.2	42_61	59XC-400	3.5%	76%	Nov-00	2.0	
IS.4261.3	42_61	59XC-400	3.5%	76%	Nov-00	2.0	
IS.4261.4	42_61	59XC-400	3.5%	76%	Nov-00	2.0	

Table A3.7. 6 In-situ UCS Core Testing Summary

Sample No.	UCS (kPa)	E_{tmax} (kPa)	ε_f	Moisture Content	Void ratio	Degree of Saturation	Porosity (n)	Bulk Density (ρ_m) {t/m^3}	Dry Density (ρ_d) {t/m^3}	Saturated Density (ρ_{sat}) {t/m^3}
IS.4773.1	874	135667.5	1.20%	32.23%	1.04	99%	0.51	2.09	1.58	2.09
IS.4773.2	1311	156290.9	2.66%	26.94%	1.01	86%	0.50	2.04	1.61	2.12
IS.4773.3	2262	491772.5	0.95%	15.35%	1.02	48%	0.50	1.84	1.60	2.11
IS.4773.4	1374	227773.5	0.84%	25.80%	0.85	98%	0.46	2.23	1.77	2.24
IS.4261.1	478	41201.33	1.65%	5.50%	0.90	20%	0.47	1.79	1.70	2.18
IS.4261.2	244	20187.02	2.08%	24.05%	0.99	78%	0.50	2.02	1.63	2.13
IS.4261.3	250	49142.55	0.94%	24.48%	1.03	76%	0.51	1.98	1.59	2.10
IS.4261.4	337	49303.53	1.16%	10.58%	0.91	37%	0.48	1.87	1.69	2.17

APPENDIX 4.1

Mineralogy

- *Galena*
- *Sphalerite*

Galena Mineral Data

General Information

Chemical Formula:	PbS
Composition:	Molecular Weight = 239.27 gm Lead 86.60 % Pb Sulfur 13.40 % S ______ 100.00 %
Empirical Formula:	PbS
Environment:	Lead sulfide ore veins, and disseminated in igneous and sedimentary rocks.
Locality:	Joplin district of Missouri, Kansas, and Oklahoma and other world wide occurrences. Link to MinDat.org Location Data.
Name Origin:	The Roman naturalist, Pliny, used the name galena to describe lead ore.
Synonym:	Blue Lead Lead Glance Lead Sulfide

Galena Image

Images:

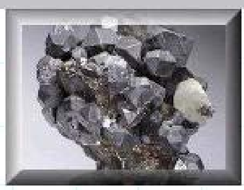

Specimen of Galena on pyrrhotite. The crystals of galena reach to 1.5 cm across. All are cubic with octahedral modifications. Dal'Negorsk, Russia. 6 x 4 cm. Photo by John Veevaert

Crystallography

Cell Dimensions:	a = 5.936, Z = 4; V = 209.16 Den(Calc)= 7.60
Crystal System:	**Isometric - Hexoctahedral** H-M Symbol (4/m -3 2/m) Space Group: Fm3m
X Ray Diffraction:	By Intensity(I/I_o): 2.969(1) 3.429(0.84) 2.099(0.57)

Forms:

Mouse
Dbl Clk - Start-Stop Rotation
RMB - Cycle Display Modes
Drag1 - Manipulate Crystal
Drag2 - Resize
Keyboard
S - Stereo
I - Indicies
<space> - Start-Stop Rotation
F - Fit to Screen
Help on Above

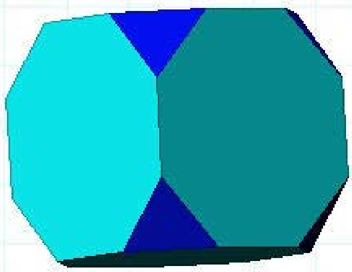

Forms: [1 0 0] [1 1 1]

Large Pop-Up

Warning: this large pop-up is very compute intensive and may not work well with some computers.

Figure A4.1.1 Galena Data Sheet (http://webmineral.com/data/Galena.shtml)

Physical Properties	
Cleavage:	[001] Perfect, [010] Perfect, [100] Perfect
Color:	light lead gray or dark lead gray.
Density:	7.2 - 7.6, Average = 7.4
Diaphaniety:	Opaque
Fracture:	Brittle - Generally displayed by glasses and most non-metallic minerals.
Habits:	Euhedral Crystals - Occurs as well-formed crystals showing good external form., Massive - Granular - Common texture observed in granite and other igneous rock., Massive - Uniformly in distinguishable crystals forming large m
Hardness:	2.5 - Finger Nail
Luminescence:	None.
Luster:	Metallic
Streak:	grayish black
Classification	
Dana Class:	**2.8.1.1** (2)Sulfides - Including Selenides and Tellurides (2.8)where Am Bn Xp, with (m+n):p=1:1 (2.8.1)Galena Group (Isometric: Fm3m) 2.8.1.1 Galena PbS Fm3m 4/m -3 2/m 2.8.1.2 Clausthalite PbSe Fm3m 4/m -3 2/m 2.8.1.3 Altaite PbTe Fm3m 4/m -3 2/m 2.8.1.4 Alabandite MnS Fm3m 4/m -3 2/m 2.8.1.5 Oldhamite (Ca,Mg,Fe,Mn)S Fm3m 4/m -3 2/m 2.8.1.6 Niningerite (Mg,Fe,Mn)S Fm3m 4/m -3 2/m 2.8.1.7 Borovskite Pd3SbTe4 Fm3m 4/m -3 2/m 2.8.1.8 Crerarite (Pt,Pb)Bi3(S,Se)4-x(x~0.7) Fm3m 4/m -3 2/m
Strunz Class:	**II/C.15-40** II - Sulfides and sulphosalts II/C - Sulfides with metal: sulfur, selenium and tellurium = 1:1 II/C.15 - STRUNZ II/C.15-40 - Sulfides and sulphosalts [Sulfides with metal: sulfur, selenium and tellurium = 1:1 {Galenite group}] II/C.15-10 Niningerite (Mg,Fe,Mn)S Fm3m 4/m -3 2/m II/C.15-20 Oldhamite (Ca,Mg,Fe,Mn)S Fm3m 4/m -3 2/m II/C.15-30 Alabandite MnS Fm3m 4/m -3 2/m II/C.15-40 Galena PbS Fm3m 4/m -3 2/m II/C.15-50 Clausthalite PbSe Fm3m 4/m -3 2/m II/C.15-60 Altaite PbTe Fm3m 4/m -3 2/m II/C.15-70 Crerarite (Pt,Pb)Bi3(S,Se)4-x(x~0.7) Fm3m 4/m -3 2/m
Other Information	
References:	NAME(Duda&Rejl90) PHYS. PROP.(Enc. of Minerals,2nd ed.,1990)

Figure A4.1.1 (cont) Galena Data Sheet (http://webmineral.com/data/Galena.shtml)

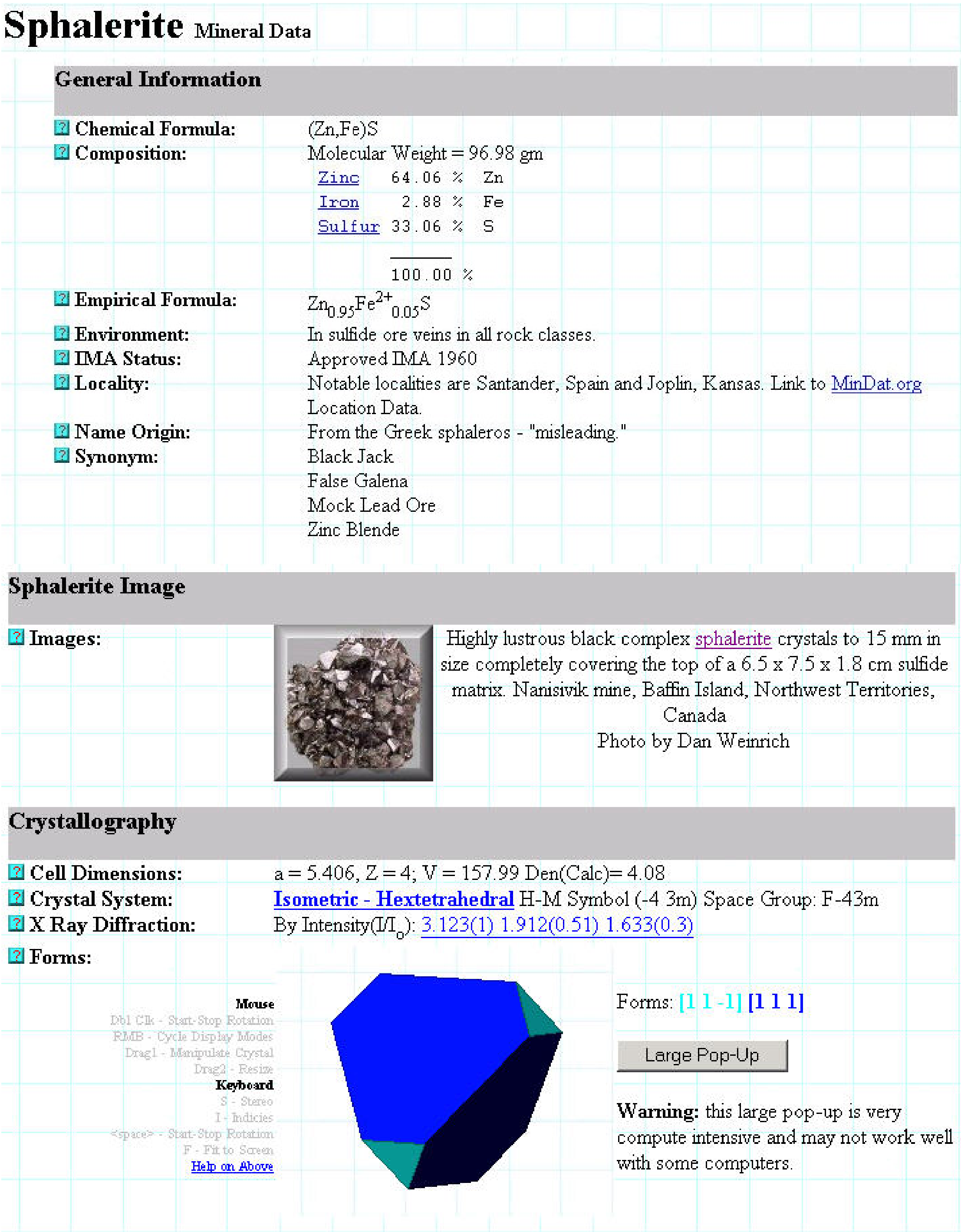

Sphalerite Mineral Data

General Information

Chemical Formula:	(Zn,Fe)S
Composition:	Molecular Weight = 96.98 gm
	Zinc 64.06 % Zn
	Iron 2.88 % Fe
	Sulfur 33.06 % S
	100.00 %
Empirical Formula:	$Zn_{0.95}Fe^{2+}_{0.05}S$
Environment:	In sulfide ore veins in all rock classes.
IMA Status:	Approved IMA 1960
Locality:	Notable localities are Santander, Spain and Joplin, Kansas. Link to MinDat.org Location Data.
Name Origin:	From the Greek sphaleros - "misleading."
Synonym:	Black Jack False Galena Mock Lead Ore Zinc Blende

Sphalerite Image

Images:

Highly lustrous black complex sphalerite crystals to 15 mm in size completely covering the top of a 6.5 x 7.5 x 1.8 cm sulfide matrix. Nanisivik mine, Baffin Island, Northwest Territories, Canada

Photo by Dan Weinrich

Crystallography

Cell Dimensions:	a = 5.406, Z = 4; V = 157.99 Den(Calc)= 4.08
Crystal System:	Isometric - Hextetrahedral H-M Symbol (-4 3m) Space Group: F-43m
X Ray Diffraction:	By Intensity(I/I_o): 3.123(1) 1.912(0.51) 1.633(0.3)

Forms:

Mouse
Dbl Clk - Start-Stop Rotation
RMB - Cycle Display Modes
Drag1 - Manipulate Crystal
Drag2 - Resize
Keyboard
S - Stereo
I - Indicies
<space> - Start-Stop Rotation
F - Fit to Screen
Help on Above

Forms: [1 1 -1] [1 1 1]

Large Pop-Up

Warning: this large pop-up is very compute intensive and may not work well with some computers.

Figure A4.1.2 Sphalerite Data Sheet (http://webmineral.com/data/Sphalerite.shtml)

Physical Properties

Cleavage:	[110] Perfect, [110] Perfect, [110] Perfect
Color:	brown, yellow, red, green, or black.
Density:	3.9 - 4.2, Average = 4.05
Diaphaniety:	Translucent to transparent
Fracture:	Uneven - Flat surfaces (not cleavage) fractured in an uneven pattern.
Habits:	Euhedral Crystals - Occurs as well-formed crystals showing good external form., Granular - Generally occurs as anhedral to subhedral crystals in matrix., Colloform - Forming from a ge l or colloidal mass.
Hardness:	3.5-4 - Copper Penny-Fluorite
Luminescence:	Fluorescent and triboluminescent.
Luster:	Resinous - Greasy
Streak:	brownish white

Optical Properties

Optical Data:	Isotropic, n=2.37-2.43.

Optical Properties

Optical Data:	Isotropic, n=2.37-2.43.

Classification

Dana Class:	**2.8.2.1** (2)Sulfides - Including Selenides and Tellurides (2.8)where Am Bn Xp, with (m+n):p=1:1 (2.8.2)Sphalerite Group (Isometric: F4¯3m) 2.8.2.1 Sphalerite (Zn,Fe)S F-43m -4 3m 2.8.2.2 Stilleite ZnSe F-43m -4 3m 2.8.2.3 Metacinnabar HgS F-43m -4 3m 2.8.2.4 Tiemannite HgSe F-43m -4 3m 2.8.2.5 Coloradoite HgTe F-43m -4 3m 2.8.2.6 Hawleyite CdS F-43m -4 3m
Strunz Class:	**II/C.01-10** II - Sulfides and sulphosalts II/C - Sulfides with metal: sulfur, selenium and tellurium = 1:1 II/C.01 - STRUNZ II/C.01-10 - Sulfides and sulphosalts [Sulfides with metal: sulfur, selenium and tellurium = 1:1 {Sphalerite group and related compounds (with II/C.01-10 Sphalerite (Zn,Fe)S F-43m -4 3m II/C.01-20 Hawleyite CdS F-43m -4 3m II/C.01-30 Metacinnabar HgS F-43m -4 3m II/C.01-40 Stilleite ZnSe F-43m -4 3m II/C.01-50 Tiemannite HgSe F-43m -4 3m II/C.01-60 Coloradoite HgTe F-43m -4 3m II/C.01-70 Polhemusite (Zn,Hg)S P4/n 4/m

Other Information

References:	NAME(Duda&Rejl90) PHYS. PROP.(Enc. of Minerals,2nd ed.,1990) OPTIC PROP.(Ford32)

Figure A4.2. 2 (cont) Sphalerite Data Sheet (http://webmineral.com/data/Sphalerite.shtml)

APPENDIX 4.2

Sample Preparation and Testing Methodologies

- *Summary – Test Methods*
- *Indirect Tensile Strength Testing*
- *Poisson's Ratio Testing*
- *Uniaxial Compressive Strength Testing*
- *Point Load Strength Testing*

Table A4.2.1 Summary of test procedures

Standard	Description
AS 4133.0-1993	Methods of testing rocks for engineering purposes - General requirements and list of methods
AS 4133.2.1.2-1993	Methods of testing rocks for engineering purposes - Rock porosity and density tests - Determination of rock porosity and dry density - Saturation and buoyancy techniques
AS 4133.4.1-1993	Methods of testing rocks for engineering purposes - Rock strength tests - Determination of point load strength index
AS 4133.4.1-1993/Amdt 1-1994	Methods of testing rocks for engineering purposes - Rock strength tests - Determination of point load strength index
AS 4133.4.2-1993	Methods of testing rocks for engineering purposes - Rock strength tests - Determination of uniaxial compressive strength
AS 4133.4.3-1993	Methods of testing rocks for engineering purposes - Rock strength tests - Determination of deformability of rock materials in uniaxial compression
AS 4133.5-2002	Methods of testing rocks for engineering purposes - Sampling of rock core

Brazilian Indirect Tensile Strength

In a Brazilian indirect tensile strength test, a core with aspect ratio of 2 was placed horizontally, and subjected to a line load as shown in Fig. A4.2.1 (a). The load was increased until the core splits down the vertical diameter. The loads were applied through a 500 kN Avery loading machine shown in Fig. A4.2.1 (b).

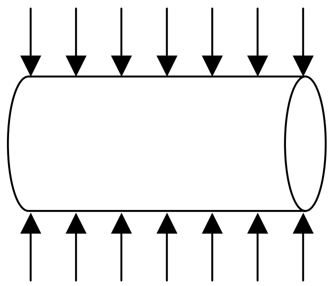

(a) (b)

Figure A4.2.1 Brazilian Indirect tensile Strength Test (a) Schematic Diagram (b) Loading Machine

The Brazilian indirect tensile strength is given by $P/(\pi dL)$, where P, d, and L are the applied load, core diameter and the length of the core respectively.

Poisson's Ratio Test

Poisson's ratios of the rock cores were determined at approximately 40-60% of the uniaxial compressive strengths. The uniaxial compressive strengths were estimated prior to testing using the Brazilian indirect tensile strength values. A number of the preliminary tests on the rock cores revealed irregular patterns of lateral deformations possibly due to micro fissures and heterogeneity. To overcome this and obtain more representative results, four dial gauges were used to measure the lateral deformations in perpendicular directions (i.e., at 0°, 90°, 180°, and 270°), at mid-height of the cores, as shown in Figure A4.2.2. (The Australian Standards only require two dial gauges to be used). The average value of the lateral expansion, as read from these four dial gauges, was used in computing Poisson's ratio.

At the completion of the measurements of lateral deformations, the cores were unloaded for the subsequent uniaxial compression tests.

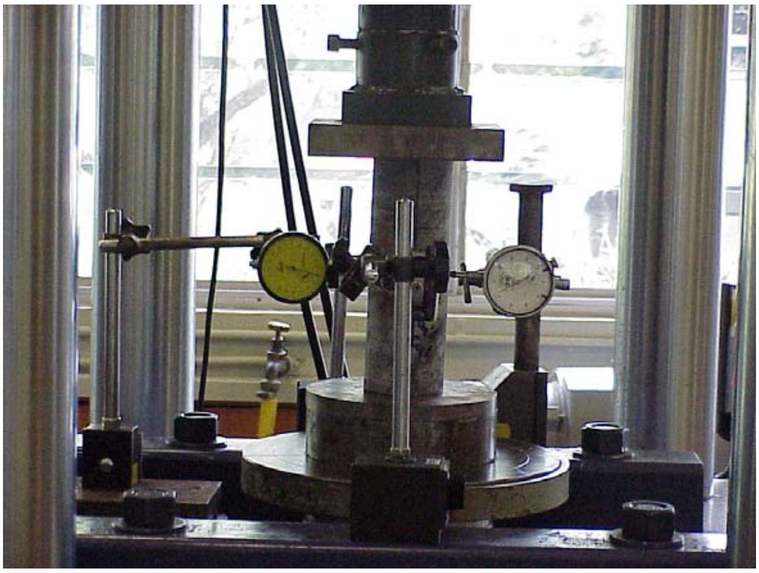

Figure A4.2.2 Poisson's Ratio Test Setup

Uniaxial Compression Test

The uniaxial compression tests were carried out on the fully automated MTS machine shown in Figure A4.2.3. The loads were applied at the strain rate of 0.5 mm/min. The tests were carried out on the cores that were used for Poisson's ratio determination. Generally, the failure occurred at less than 1% axial strain.

Figure A4.2.3 MTS Machine Setup

Point Load Strength Testing

AS 4133.4.1-1993: Methods of testing rocks for engineering purposes - Rock strength tests - Determination of point load strength index

This Standard sets out the method for determining the strength of rock specimens in the field using portable equipment. Specimens in the form of either rock core (the diametral and axial tests) or irregular lumps (the irregular lump test) are broken by application of a concentrated load using a pair of conical platens. A point load strength index, Is(50), is obtained and may be used to classify rocks by strength.

The testing machine (Model 6000 – Point Load Tester) consisted of a loading frame, which could measure the force required to break the sample. Rock specimens in the form of either core, cut blocks, or irregular lumps can all be broken through the application of a concentrated load through a pair of spherically truncated, conical platens. In this report, irregular lump specimens will be used. Figure A4.2.4 shows the Point Load Testing Apparatus.

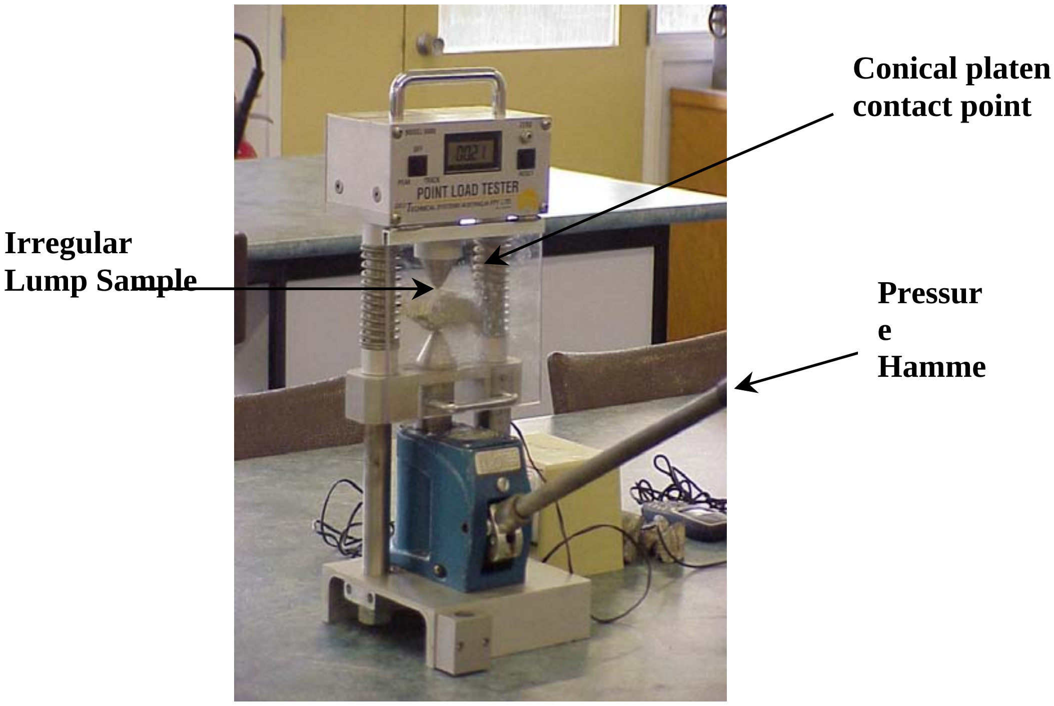

Figure A4.2.4 Point Load Tester Setup

Because the rock specimens were irregular lump in shape, certain testing requirements needed to be applied. These were:

- L>0.5D
- 0.3W<D<W

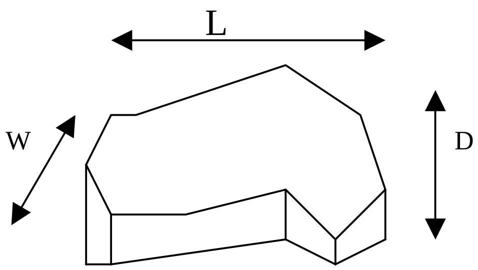

Figure A4.2.5 Irregular Lump Rock

The load was applied to the core samples by pumping the hydraulic lever arm at the front of the apparatus. Samples were loaded with even strokes over a twelve to fifteen second period to obtain a uniform loading distribution, and also because the peak load recorder sampled three times per second. The point load strength indices (I_{s50}), standardised for a 50mm diameter specimen.

APPENDIX 4.3

Physical Properties

Figure A4.3. 1 Physical Properties - UCS Samples

					Dimensions (mm)										
					Diameter, ϕ				Height, H						
No.	Rock Type	Hole	Sample Interval	Sample Number	ϕ_1	ϕ_2	ϕ_3	Avg	H_1	H_2	H_3	Avg	*Volume* *(cm^3)*	*Mass* *(g)*	Bulk Density (Kg/m^3)
1	SHMU	CAD339	187.2 - 187.4	GM58344	47.52	47.48	47.49	47.50	141	142	143	141.83	251.30	712.00	2.83
2	SHMU	CAD033	106.7 - 106.9	GM58346	50.42	50.32	50.54	50.43	149	149	149	149.00	297.58	837.00	2.81
3	SHMU	CAD564a	46.1 - 46.4	GM58348	63.35	63.32	63.38	63.35	185	186	186	185.67	585.22	1618.00	2.76
4	SHMU	CAD562	95.9 - 96.2	GM58350	63.25	63.30	63.20	63.25	192	192	191	191.67	602.22	1665.00	2.76
	SHMU	CAD494	149.0 - 149.2	GM58352	47.56	47.62	47.51	47.56	143	144	144	143.50	254.97	699.00	2.74
6	AMPH	CAD346	68.3 - 68.5	GM58354	62.95	62.86	62.85	62.89	194	193	193	193.17	599.98	1820.00	3.03
7	AMPH	CAD562	322.2 - 322.4	GM58358	60.82	60.78	60.79	60.80	176	176	177	176.33	511.90	1413.00	2.76
8	AMPH	CAD494	291.0 - 291.2	GM58360	47.37	47.55	47.54	47.49	143	143	143	143.00	253.26	777.00	3.07
9	AMPH	CAD387	254.1 - 254.3	GM58362	61.02	61.03	61.02	61.02	184	185	184	184.33	539.12	1661.00	3.08
10	PEGM	CAD033	261.1 - 261.3	GM58366	50.65	50.59	50.61	50.62	151	151	151	151.00	303.85	792.00	2.61
11	PEGM	CAD503	257.0 - 257.2	GM58368	47.36	47.39	47.40	47.38	139	140	139	139.33	245.69	648.00	2.64
12	PEGM	CAD299	248.4 - 248.6	GM58370	47.30	47.33	47.31	47.31	142	143	143	142.67	250.83	659.00	2.63
13	PEGM	CAD387	248.9 - 249.1	GM58372	61.38	61.31	61.38	61.36	184	184	182	183.33	542.07	1399.00	2.58
14	GNES	CAD530	96.7 - 96.9	GM58374	61.05	61.05	61.03	61.04	183	182	184	183.00	535.57	1436.00	2.68
15	GNES	CAD373	116.0 - 116.2	GM58376	63.15	63.33	63.32	63.27	181	182	181	181.33	570.06	1495.00	2.62
16	GNES	CAD531	163.6 - 164.0	GM58378	60.98	61.12	61.13	61.08	183	184	184	183.67	538.11	1437.00	2.67
17	GNES	CAD495	152.5 - 152.7	GM58380	61.04	60.94	60.86	60.95	184	183	184	183.67	535.82	1414.00	2.64
18	GNES	CAD519	138.1 - 138.3	GM58382	60.80	60.93	60.94	60.89	188	187	186	187.00	544.53	1436.00	2.64
19	Burnham	CAD562	263.5 - 263.7	GM58384	63.43	63.37	63.39	63.40	193	192	192	192.33	607.12	2593.00	4.27
20	Burnham	CAD564a	246.5 - 246.7	GM58386	63.21	63.19	63.18	63.19	190	190	189	189.67	594.87	2542.00	4.27
21	Burnham	CAD563	217.0 - 217.2	GM58388	63.40	63.51	63.41	63.44	191	192	191	191.33	604.79	2777.00	4.59

Figure A4.3. 1 Physical Properties - UCS Samples (cont'd)

					Dimensions (mm)										
					Diameter, ϕ				Height, H						
No.	Rock Type	Hole	Sample Interval	Sample Number	ϕ_1	ϕ_2	ϕ_3	Avg	H_1	H_2	H_3	Avg	*Volume (cm^3)*	*Mass (g)*	Bulk Density (Kg/m^3)
22	Broadlands	CAD562	212.4 - 212.6	GM58394	63.54	63.52	63.53	63.53	191	192	193	192.00	608.62	2072.00	3.40
23	Broadlands	CAD563	190.2 - 190.5	GM58396	63.37	63.41	63.46	63.41	190	190	189	189.67	599.02	2185.00	3.65
24	Broadlands	CAD566	87.1 - 87.3	GM58398	**Sample not provided**										
25	Broadlands	CAD564a	203.7 - 203.9	GM58400	63.33	63.30	63.40	63.34	190	190	190	190.00	598.75	2111.00	3.53
26	Glenholm	CAD386	287.5 - 287.8	GM58404	61.10	61.09	61.10	61.10	183	184	185	184.00	539.44	2176.00	4.03
27	Glenholm	CAD564a	120.4 - 120.6	GM58406	63.48	63.43	63.43	63.45	195	195	196	195.33	617.57	2341.00	3.79
28	Glenholm	CAD562	204.4 - 204.7	GM58408	63.53	63.36	63.36	63.42	193	193	192	192.67	608.56	2366.00	3.89
29	Glenholm	CAD563	61.6 - 61.8	GM58410	63.30	63.30	63.39	63.33	188	188	188	188.00	592.20	2075.00	3.50
30	QZGA/IT	CAD386	284.2 - 284.6	GM58414	61.11	61.10	61.07	61.09	184	183	184	183.67	538.40	1614.00	3.00
31	QZGA/IT	CAD387	75.2 - 75.5	GM58416	61.03	61.24	61.07	61.11	183	183	182	182.67	535.82	1575.00	2.94
32	QZGA/IT	CAD562	227.5 - 227.7	GM58418	63.48	63.44	63.46	63.46	192	193	194	193.00	610.45	1849.00	3.03
33	QZGA/IT	CAD564a	71.4 - 71.6	GM58422	63.55	63.49	63.47	63.50	192	192	193	192.33	609.17	1691.00	2.78
34	QZHD	CAD386	288.7 - 289.0	GM58424	61.38	61.09	61.08	61.18	183	183	184	183.17	538.52	1886.00	3.50
35	QZHD	CAD387	163.8 - 164.0	GM58426	60.86	60.88	60.91	60.88	186	186	187	186.17	541.99	1849.00	3.41
36	QZHD	CAD562	219.7 - 219.9	GM58428	63.60	63.50	63.53	63.54	190	190	189	189.67	601.48	1883.00	3.13
37	QZHD	CAD564a	137.1 - 137.3	GM58430	63.41	63.30	63.40	63.37	193	191	192	192.00	605.56	1934.00	3.19
38	QZHD	CAD563	113.0 - 113.2	GM58432	63.30	63.25	63.40	63.32	191	190	190	190.33	599.30	1968.00	3.28
39	HDMT	CAD387	160.5 - 160.7	GM58434	61.90	60.88	60.96	61.25	182	182	183	182.33	537.18	2113.00	3.93
40	HDMT	CAD386	208.8 - 209.1	GM58436	60.74	60.87	60.82	60.81	187	187	186	186.67	542.13	2291.00	4.23
41	HDMT	CAD563	211.4 - 211.6	GM58438	63.38	63.37	63.33	63.36	189	188	189	188.67	594.86	2636.00	4.43
42	PXAM	CAD387	164.6 - 164.8	GM58444	60.91	60.82	60.88	60.87	186	185	185	185.33	539.32	1963.00	3.64
43	PXAM	CAD562	82.8 - 83.0	GM58446	63.11	63.20	63.21	63.17	193	192	191	192.00	601.81	2291.00	3.81
44	PXAM	CAD563	32.8 - 33.0	GM58448	63.28	63.26	63.22	63.25	188	188	189	188.33	591.81	2254.00	3.81

Figure A4.3. 2 Physical Properties - Poisson's Ratio Testing

					Dimensions (mm)										
					Diameter, ϕ				Height, H						
No.	Rock Type	Hole	Sample Interval	Sample Number	ϕ_1	ϕ_2	ϕ_3	Avg	H_1	H_2	H_3	Avg	*Volume* (cm^3)	*Mass (g)*	Bulk Density (Kg/m^3)
1	SHMU	CAD339	187.2 - 187.4	GM58344	47.52	47.48	47.49	47.50	141	142	143	141.83	251.30	712.00	2.83
2	SHMU	CAD033	106.7 - 106.9	GM58346	50.42	50.32	50.54	50.43	149	149	149	149.00	297.58	837.00	2.81
3	SHMU	CAD564a	46.1 - 46.4	GM58348	63.35	63.32	63.38	63.35	185	186	186	185.67	585.22	1618.00	2.76
4	SHMU	CAD562	95.9 - 96.2	GM58350	63.25	63.30	63.20	63.25	192	192	191	191.67	602.22	1665.00	2.76
5	SHMU	CAD494	149.0 - 149.2	GM58352	47.56	47.62	47.51	47.56	143	144	144	143.50	254.97	699.00	2.74
Rock Type	***SHMU***								***Note: Next 3 No.s***			ρ_{av}	ρ_{min}	ρ_{max}	***2.78***
6	AMPH	CAD346	68.3 - 68.5	GM58354	62.95	62.86	62.85	62.89	194	193	193	193.17	599.98	1820.00	3.03
7	AMPH	CAD562	322.2 - 322.4	GM58358	60.82	60.78	60.79	60.80	176	176	177	176.33	511.90	1413.00	2.76
8	AMPH	CAD494	291.0 - 291.2	GM58360	47.37	47.55	47.54	47.49	143	143	143	143.00	253.26	777.00	3.07
9	AMPH	CAD387	254.1 - 254.3	GM58362	61.02	61.03	61.02	61.02	184	185	184	184.33	539.12	1661.00	3.08
Rock Type	***AMPH***								***Note: Next 3 No.s***			ρ_{av}	ρ_{min}	ρ_{max}	***2.99***
10	PEGM	CAD033	261.1 - 261.3	GM58366	50.65	50.59	50.61	50.62	151	151	151	151.00	303.85	792.00	2.61
11	PEGM	CAD503	257.0 - 257.2	GM58368	47.36	47.39	47.40	47.38	139	140	139	139.33	245.69	648.00	2.64
12	PEGM	CAD299	248.4 - 248.6	GM58370	47.30	47.33	47.31	47.31	142	143	143	142.67	250.83	659.00	2.63
13	PEGM	CAD387	248.9 - 249.1	GM58372	61.38	61.31	61.38	61.36	184	184	182	183.33	542.07	1399.00	2.58
Rock Type	***PEGM***								***Note: Next 3 No.s***			ρ_{av}	ρ_{min}	ρ_{max}	***2.61***
14	GNES	CAD530	96.7 - 96.9	GM58374	61.05	61.05	61.03	61.04	183	182	184	183.00	535.57	1436.00	2.68
15	GNES	CAD373	116.0 - 116.2	GM58376	63.15	63.33	63.32	63.27	181	182	181	181.33	570.06	1495.00	2.62
16	GNES	CAD531	163.6 - 164.0	GM58378	60.98	61.12	61.13	61.08	183	184	184	183.67	538.11	1437.00	2.67
17	GNES	CAD495	152.5 - 152.7	GM58380	61.04	60.94	60.86	60.95	184	183	184	183.67	535.82	1414.00	2.64
18	GNES	CAD519	138.1 - 138.3	GM58382	60.80	60.93	60.94	60.89	188	187	186	187.00	544.53	1436.00	2.64
Rock Type	***GNES***								***Note: Next 3 No.s***			ρ_{av}	ρ_{min}	ρ_{max}	***2.65***
19	Burnham	CAD562	263.5 - 263.7	GM58384	63.43	63.37	63.39	63.40	193	192	192	192.33	607.12	2593.00	4.27
20	Burnham	CAD564a	246.5 - 246.7	GM58386	63.21	63.19	63.18	63.19	190	190	189	189.67	594.87	2542.00	4.27
21	Burnham	CAD563	217.0 - 217.2	GM58388	63.40	63.51	63.41	63.44	191	192	191	191.33	604.79	2777.00	4.59
Rock Type	***Burnham***								***Note: Next 3 No.s***			ρ_{av}	ρ_{min}	ρ_{max}	***4.38***

Figure A4.3. 2 Physical Properties - Poisson's Ratio Testing (cont'd)

					Dimensions (mm)										
					Diameter, ϕ				Height, H						
No.	Rock Type	Hole	Sample Interval	Sample Number	ϕ_1	ϕ_2	ϕ_3	Avg	H_1	H_2	H_3	Avg	*Volume* *(cm^3)*	*Mass* *(g)*	Bulk Density (Kg/m^3)
22	Broadlands	CAD562	212.4 - 212.6	GM58394	63.54	63.52	63.53	63.53	191	192	193	192.00	608.62	2072.00	3.40
23	Broadlands	CAD563	190.2 - 190.5	GM58396	63.37	63.41	63.46	63.41	190	190	189	189.67	599.02	2185.00	3.65
24	Broadlands	CAD566	87.1 - 87.3	GM58398	**Sample Not Provided**										
25	Broadlands	CAD564a	203.7 - 203.9	GM58400	63.33	63.30	63.40	63.34	190	190	190	190.00	598.75	2111.00	3.53
Rock Type	***Broadlands***								***Note: Next 3 No.s***			ρ_{av}	ρ_{min}	ρ_{max}	***3.53***
26	Glenholm	CAD386	287.5 - 287.8	GM58404	61.10	61.09	61.10	61.10	183	184	185	184.00	539.44	2176.00	4.03
27	Glenholm	CAD564a	120.4 - 120.6	GM58406	63.48	63.43	63.43	63.45	195	195	196	195.33	617.57	2341.00	3.79
28	Glenholm	CAD562	204.4 - 204.7	GM58408	63.53	63.36	63.36	63.42	193	193	192	192.67	608.56	2366.00	3.89
29	Glenholm	CAD563	61.6 - 61.8	GM58410	63.30	63.30	63.39	63.33	188	188	188	188.00	592.20	2075.00	3.50
Rock Type	***Glenholm***								***Note: Next 3 No.s***			ρ_{av}	ρ_{min}	ρ_{max}	***3.80***
30	QZGA/IT	CAD386	284.2 - 284.6	GM58414	61.11	61.10	61.07	61.09	184	183	184	183.67	538.40	1614.00	3.00
31	QZGA/IT	CAD387	75.2 - 75.5	GM58416	61.03	61.24	61.07	61.11	183	183	182	182.67	535.82	1575.00	2.94
32	QZGA/IT	CAD562	227.5 - 227.7	GM58418	63.48	63.44	63.46	63.46	192	193	194	193.00	610.45	1849.00	3.03
33	QZGA/IT	CAD564a	71.4 - 71.6	GM58422	63.55	63.49	63.47	63.50	192	192	193	192.33	609.17	1691.00	2.78
Rock Type	***QZGA/IT***								***Note: Next 3 No.s***			ρ_{av}	ρ_{min}	ρ_{max}	***2.94***
34	QZHD	CAD386	288.7 - 289.0	GM58424	61.38	61.09	61.08	61.18	183	183	184	183.17	538.52	1886.00	3.50
35	QZHD	CAD387	163.8 - 164.0	GM58426	60.86	60.88	60.91	60.88	186	186	187	186.17	541.99	1849.00	3.41
36	QZHD	CAD562	219.7 - 219.9	GM58428	63.60	63.50	63.53	63.54	190	190	189	189.67	601.48	1883.00	3.13
37	QZHD	CAD564a	137.1 - 137.3	GM58430	63.41	63.30	63.40	63.37	193	191	192	192.00	605.56	1934.00	3.19
38	QZHD	CAD563	113.0 - 113.2	GM58432	63.30	63.25	63.40	63.32	191	190	190	190.33	599.30	1968.00	3.28
Rock Type	***QZHD***								***Note: Next 3 No.s***			ρ_{av}	ρ_{min}	ρ_{max}	***3.30***
39	HDMT	CAD387	160.5 - 160.7	GM58434	61.90	60.88	60.96	61.25	182	182	183	182.33	537.18	2113.00	3.93
40	HDMT	CAD386	208.8 - 209.1	GM58436	60.74	60.87	60.82	60.81	187	187	186	186.67	542.13	2291.00	4.23
41	HDMT	CAD563	211.4 - 211.6	GM58438	63.38	63.37	63.33	63.36	189	188	189	188.67	594.86	2636.00	4.43
Rock Type	***HDMT***								***Note: Next 3 No.s***			ρ_{av}	ρ_{min}	ρ_{max}	***4.20***
42	PXAM	CAD387	164.6 - 164.8	GM58444	60.91	60.82	60.88	60.87	186	185	185	185.33	539.32	1963.00	3.64
43	PXAM	CAD562	82.8 - 83.0	GM58446	63.11	63.20	63.21	63.17	193	192	191	192.00	601.81	2291.00	3.81
44	PXAM	CAD563	32.8 - 33.0	GM58448	63.28	63.26	63.22	63.25	188	188	189	188.33	591.81	2254.00	3.81
Rock Type	***PXAM***								***Note: Next 3 No.s***			ρ_{av}	ρ_{min}	ρ_{max}	***3.75***

Figure A4.3. 3 Physical Properties - Indirect Tensile Testing

					Dimensions (mm)										
					Diameter, ϕ				Height, H						
No.	Rock Type	Hole	Sample Interval	Sample Number	ϕ_1	ϕ_2	ϕ_3	Avg	H_1	H_2	H_3	Avg	*Volume (cm^3)*	*Mass (g)*	Bulk Density (Kg/m^3)
1	SHMU	CAD339	187.4 - 187.6	GM58345	47.66	47.56	47.61	47.61	96.44	96.56	96.54	96.51	171.82	485.00	2.82
2A	SHMU	CAD033	106.9 - 107.2	GM58347	50.44	50.56	50.46	50.49	96.57	96.70	96.69	96.65	193.49	550.00	2.84
2B	SHMU	CAD033	106.9 - 107.2	GM58347	50.50	50.78	56.70	52.66	100.92	100.96	101.16	101.01	220.00	566.00	2.57
3	SHMU	CAD564a	46.4 - 46.7	GM58349	63.53	63.40	63.40	63.44	127.09	127.14	127.46	127.23	402.21	1104.00	2.74
4	SHMU	CAD562	96.2 - 96.5	GM58351	63.31	63.24	63.28	63.28	127.76	127.79	127.83	127.79	401.87	1112.00	2.77
5A	SHMU	CAD494	149.2 - 149.5	GM58353	47.53	47.40	47.50	47.48	97.01	96.97	97.03	97.00	171.73	476.00	2.77
5B	SHMU	CAD494	149.2 - 149.5	GM58353	47.53	47.70	47.42	47.55	89.92	89.92	89.86	89.90	159.64	443.00	2.77
6	AMPH	CAD346	68.5 - 68.7	GM58355	63.90	62.99	62.99	63.29	124.72	124.90	124.99	124.87	392.88	1179.00	3.00
7	AMPH	CAD562	322.4 - 322.7	GM58359	60.84	60.89	60.74	60.82	121.19	121.16	121.20	121.18	352.11	968.00	2.75
8	AMPH	CAD494	291.2 - 291.4	GM58361	47.39	47.42	47.39	47.40	96.83	96.84	96.91	96.86	170.92	515.00	3.01
9	AMPH	CAD387	254.3 - 254.5	GM58363	61.04	61.14	61.16	61.11	125.99	126.01	125.85	125.95	369.45	1110.00	3.00
10A	PEGM	CAD033	261.3 - 261.5	GM58367	50.67	50.66	50.64	50.66	97.32	97.44	97.38	97.38	196.26	505.00	2.57
10B	PEGM	CAD033	261.3 - 261.5	GM58367	50.67	50.86	50.99	50.84	96.34	96.44	96.40	96.39	195.68	505.00	2.58
11A	PEGM	CAD503	257.2 - 257.4	GM58369	47.99	47.48	47.39	47.62	91.82	91.80	91.81	91.81	163.52	428.00	2.62
11B	PEGM	CAD503	257.2 - 257.4	GM58369	47.47	47.99	47.55	47.67	96.81	96.73	96.69	96.74	172.66	440.00	2.55
12A	PEGM	CAD299	248.6 - 248.8	GM58371	47.35	47.32	47.32	47.33	94.02	93.89	93.92	93.94	165.28	426.00	2.58
12B	PEGM	CAD299	248.6 - 248.8	GM58371	47.35	47.30	47.40	47.35	90.12	90.14	90.16	90.14	158.73	410.00	2.58
13	PEGM	CAD387	249.1 - 249.4	GM58373	61.30	61.14	61.25	61.23	123.16	123.16	123.21	123.18	362.70	941.00	2.59
14	GNES	CAD530	99.8 - 100.0	GM58375	60.60	60.95	60.93	60.83	126.73	126.16	126.89	126.59	367.87	970.00	2.64
15	GNES	CAD373	115.6 - 115.8	GM58377	63.26	63.14	63.18	63.19	125.57	125.40	125.50	125.49	393.59	1035.00	2.63
16	GNES	CAD531	164.0 - 164.4	GM58379	60.93	60.94	60.90	60.92	124.61	124.30	124.30	124.40	362.65	978.00	2.70
17	GNES	CAD495	154.3 - 154.5	GM58381	60.93	60.77	60.76	60.82	120.33	120.18	120.10	120.20	349.22	932.00	2.67
18	GNES	CAD519	138.3 - 138.5	GM58383	60.87	60.88	60.88	60.88	57.47	57.77	57.76	57.67	167.85	439.00	2.62
19	Burnham	CAD562	263.7 - 263.9	GM58385	63.45	63.46	63.45	63.45	129.70	130.16	129.81	129.89	410.75	1748.00	4.26
20	Burnham	CAD564a	246.7 - 246.9	GM58387	63.15	63.18	63.16	63.16	122.48	122.22	122.30	122.33	383.32	1676.00	4.37
21	Burnham	CAD563	215.3 - 215.5	GM58389	63.34	63.49	63.36	63.40	127.49	127.42	127.45	127.45	402.32	1887.00	4.69

Figure A4.3. 3 Physical Properties - Indirect Tensile Testing (cont'd)

					Dimensions (mm)										
					Diameter, ϕ				Height, H						
No.	Rock Type	Hole	Sample Interval	Sample Number	ϕ_1	ϕ_2	ϕ_3	Avg	H_1	H_2	H_3	Avg	Volume (cm^3)	Mass (g)	Bulk Density (Kg/m^3)
22	Broadlands	CAD562	212.6 - 212.8	GM58395	63.59	63.59	63.58	63.59	215.97	126.05	125.29	155.77	494.66	1258.00	2.54
23A	Broadlands	CAD563	190.5 - 190.8	GM58397	63.41	63.36	63.43	63.40	124.95	124.96	125.38	125.10	394.92	1696.00	4.29
23B	Broadlands	CAD563	190.5 - 190.8	GM58397	63.36	63.37	63.42	63.38	124.34	124.77	125.97	125.03	394.50	1560.00	3.95
24	Broadlands	CAD566	87.3 - 87.5	GM58399	Sample Not Provided										
25	Broadlands	CAD564a	203.9 - 204.1	GM58401	63.30	63.42	63.36	63.36	127.31	127.35	127.47	127.38	401.62	1446.00	3.60
26	Glenholm	CAD386	287.8 - 288.1	GM58405	61.16	61.24	61.09	61.16	123.12	123.14	123.71	123.32	362.34	1448.00	4.00
27	Glenholm	CAD564a	120.8 - 121.0	GM58407	63.50	63.46	63.47	63.48	128.90	128.92	128.23	128.68	407.23	1540.00	3.78
28	Glenholm	CAD562	204.7 - 204.9	GM58409	63.47	63.47	63.47	63.47	129.56	129.56	129.34	129.49	409.69	1396.00	3.41
29	Glenholm	CAD563	61.9 - 62.1	GM58411	63.27	63.38	63.30	63.32	124.72	124.45	124.26	124.48	391.93	1639.00	4.18
30	QZGA/IT	CAD386	284.6 - 285.0	GM58415	61.05	61.10	61.50	61.22	123.05	122.43	125.06	123.51	363.53	1029.00	2.83
31	QZGA/IT	CAD387	75.5 - 75.9	GM58417	61.09	61.05	61.11	61.08	125.10	122.90	124.97	124.32	364.32	1119.00	3.07
32	QZGA/IT	CAD562	227.7 - 227.9	GM58419	63.48	63.50	63.44	63.47	127.96	127.86	127.98	127.93	404.81	1195.00	2.95
33	QZGA/IT	CAD564a	71.6 - 71.8	GM58423	63.49	63.44	63.42	63.45	128.03	128.04	128.14	128.07	404.95	1153.00	2.85
34	QZHD	CAD386	289.0 - 289.3	GM58425	61.11	61.20	61.22	61.18	126.13	125.84	126.28	126.08	370.61	1307.00	3.53
35	QZHD	CAD387	164.0 - 164.2	GM58427	60.82	60.89	60.85	60.85	123.44	213.47	213.43	183.45	533.54	1194.00	2.24
36	QZHD	CAD562	219.9 - 220.1	GM58429	63.50	63.63	63.57	63.57	125.56	125.90	125.80	125.75	399.09	1139.00	2.85
37	QZHD	CAD564a	137.3 - 137.5	GM58431	63.44	63.57	63.64	63.55	126.26	126.05	216.22	156.18	495.38	1274.00	2.57
38	QZHD	CAD563	113.2 - 113.4	GM58433	63.42	63.44	63.45	63.44	127.40	127.38	127.24	127.34	402.47	1277.00	3.17
39	HDMT	CAD387	160.7 - 161.0	GM58435	60.81	60.97	60.95	60.91	121.43	121.34	121.56	121.44	353.87	1357.00	3.83
40	HDMT	CAD386	209.1 - 209.3	GM58437	60.40	60.72	60.77	60.63	120.46	120.44	120.48	120.46	347.78	1411.00	4.06
41	HDMT	CAD563	211.6 - 211.8	GM58439	63.32	63.26	63.32	63.30	124.23	124.47	124.51	124.40	391.50	1681.00	4.29
42	PXAM	CAD387	163.2 - 163.4	GM58445	60.96	60.93	60.91	60.93	126.73	126.92	126.98	126.88	370.00	1353.00	3.66
43	PXAM	CAD562	83.0 - 83.2	GM58447	63.35	63.29	63.20	63.28	122.60	122.97	122.12	122.56	385.46	1442.00	3.74
44	PXAM	CAD563	33.9 - 34.1	GM58449	63.21	63.31	63.23	63.25	128.82	128.82	128.67	128.77	404.60	1463.00	3.62

APPENDIX 4.4

Uniaxial Compressive Strength Testing

- *UCS Plots*

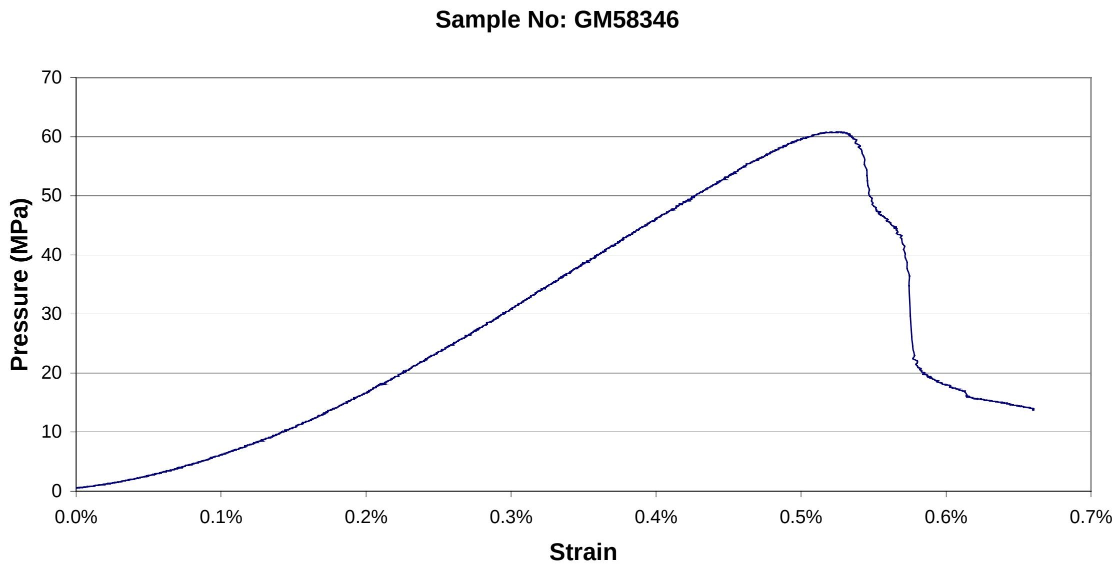

Figure A4.4. 1 Stress Strain Curve for Sample GM58346

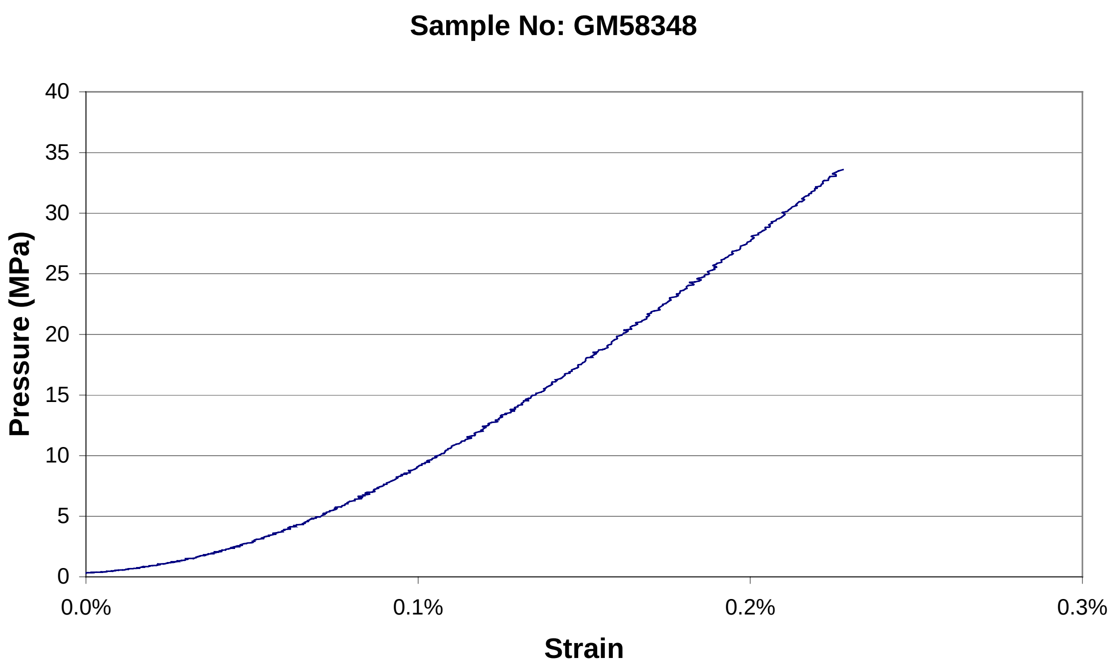

Figure A4.4. 2 Stress Strain Curve for Sample GM58348

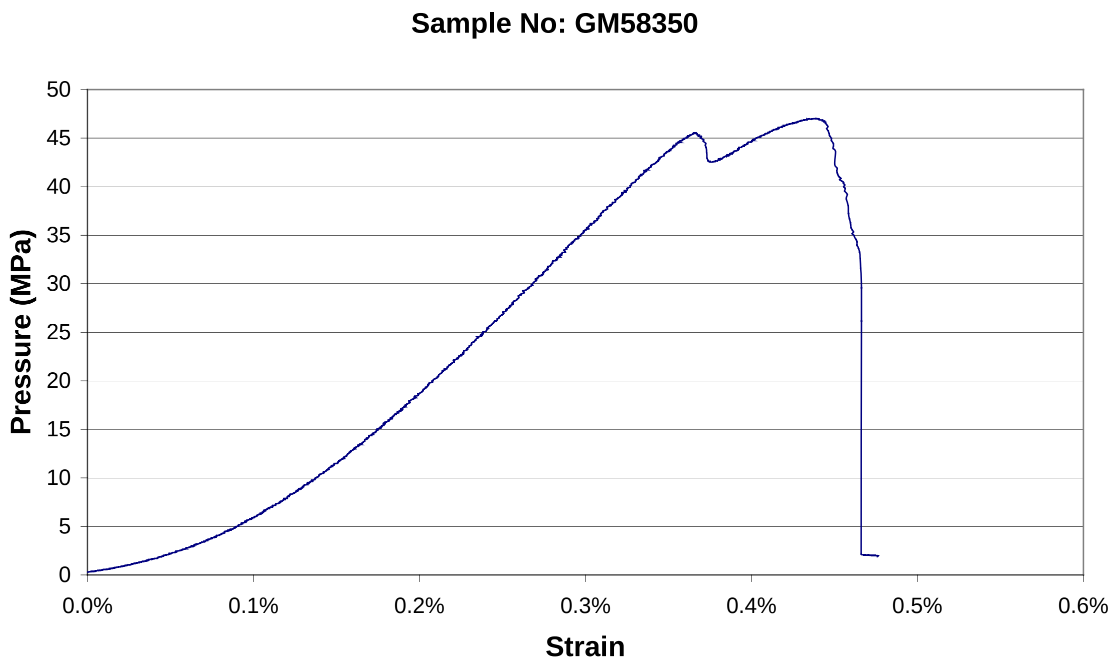

Figure A4.4. 3 Stress Strain Curve for Sample GM58350

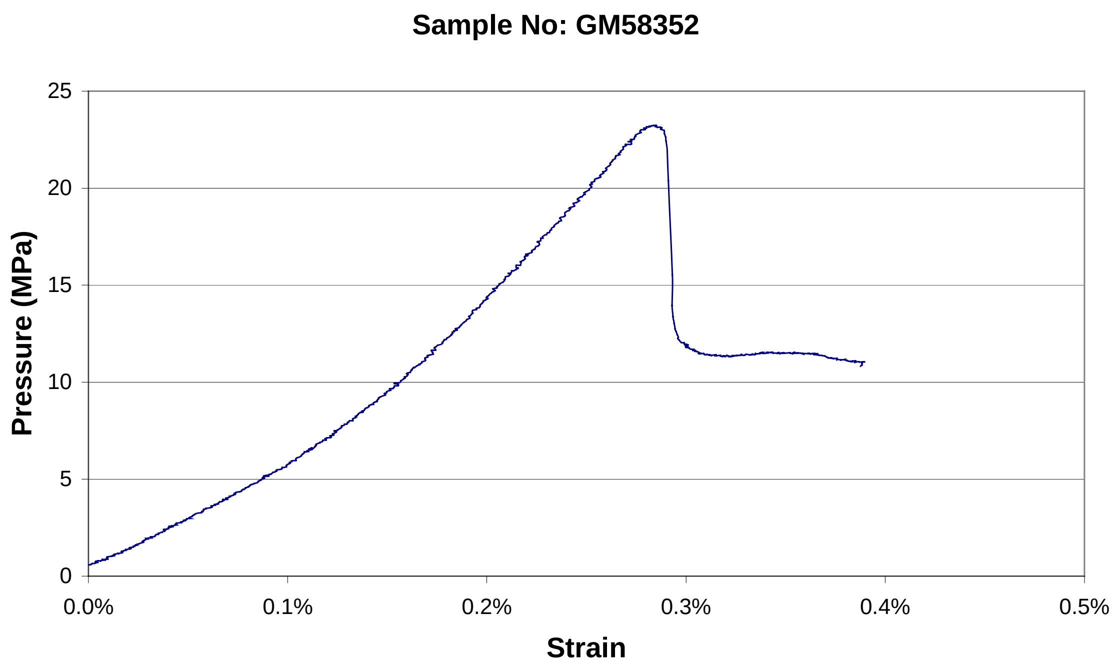

Figure A4.4. 4 Stress Strain Curve for Sample GM58352

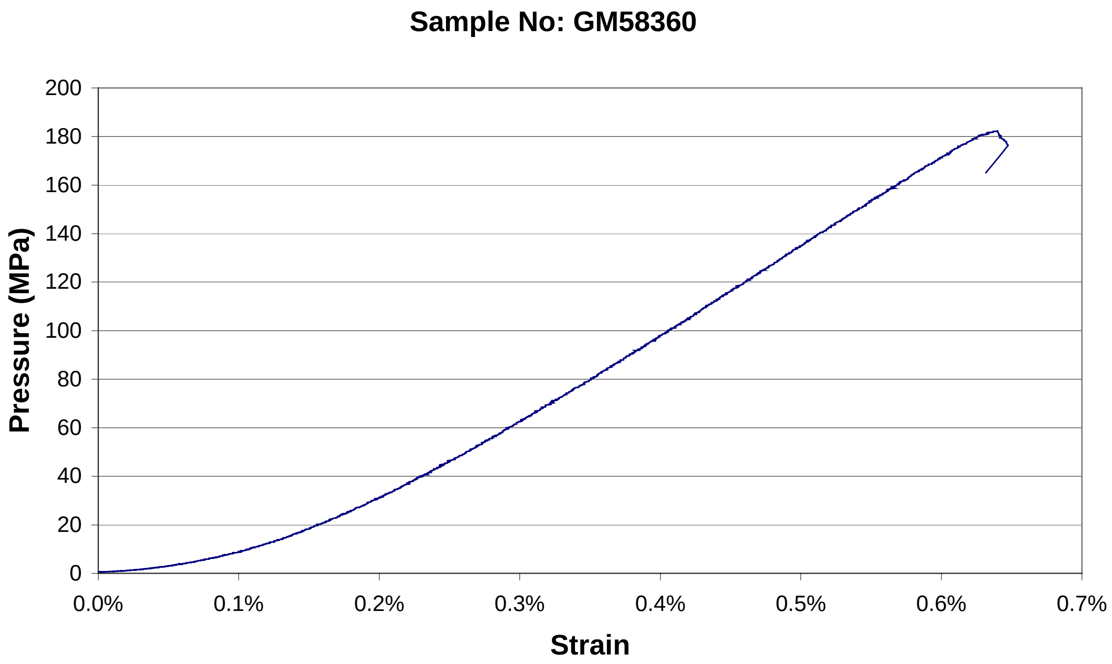

Figure A4.4. 5 Stress Strain Curve for Sample GM58360

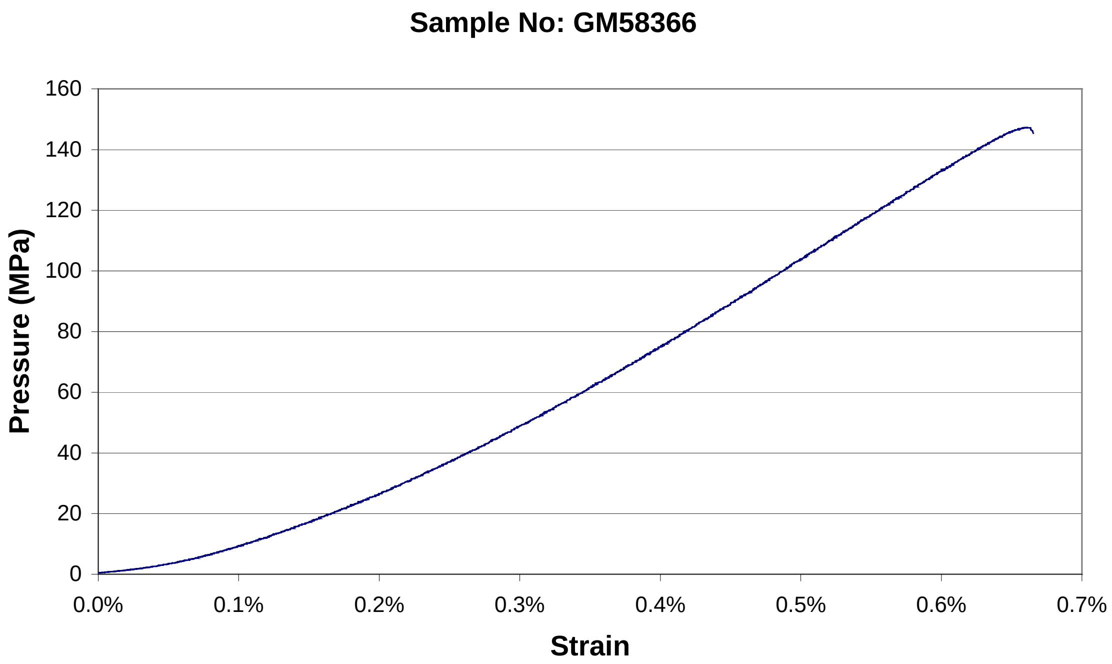

Figure A4.4. 6 Stress Strain Curve for Sample GM58366

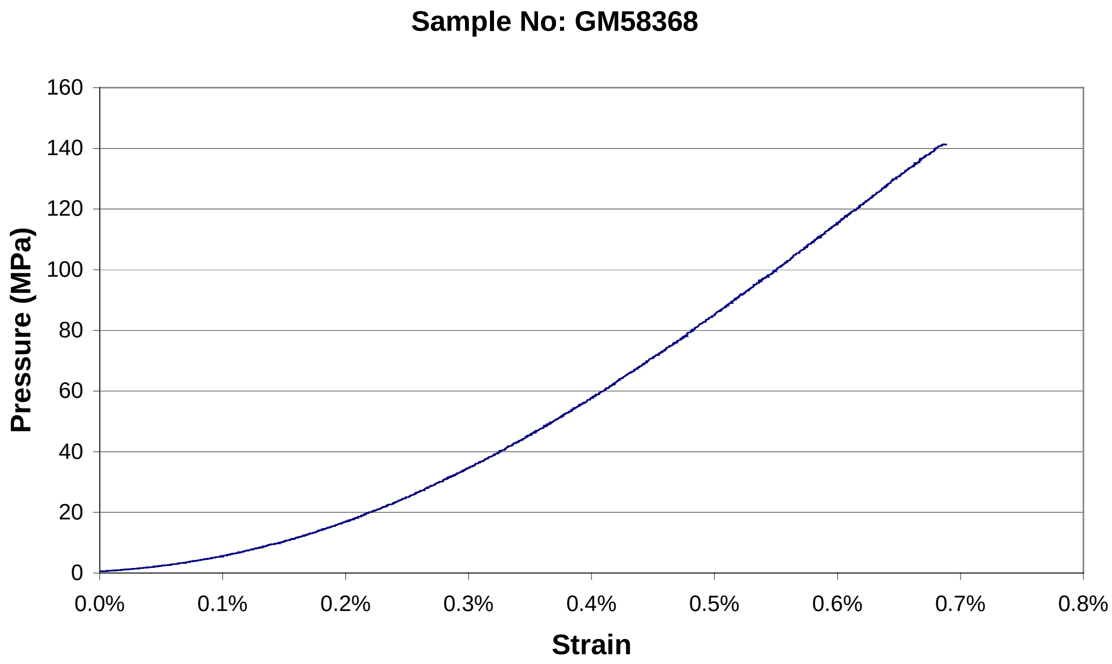

Figure A4.4. 7 Stress Strain Curve for Sample GM58368

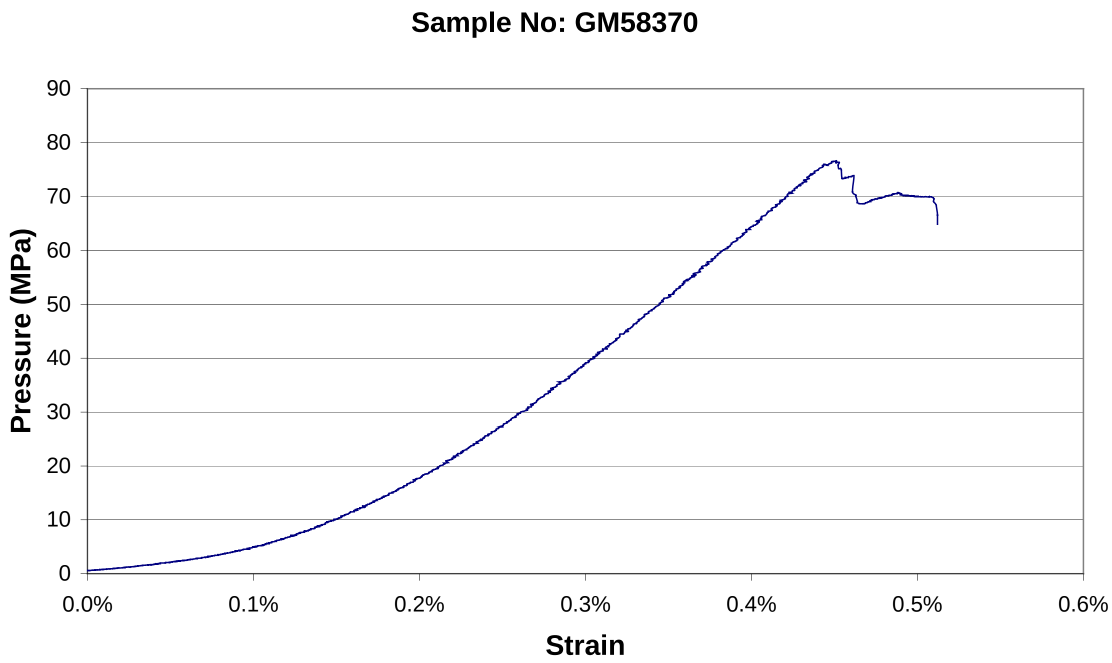

Figure A4.4. 8 Stress Strain Curve for Sample GM58370

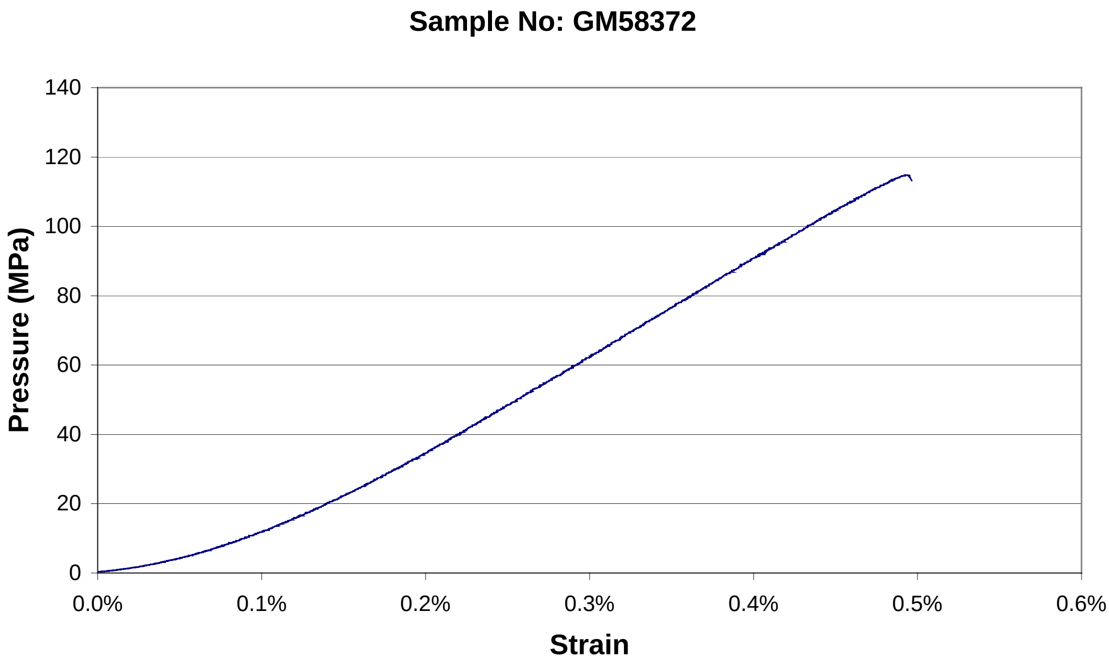

Figure A4.4. 9 Stress Strain Curve for Sample GM58372

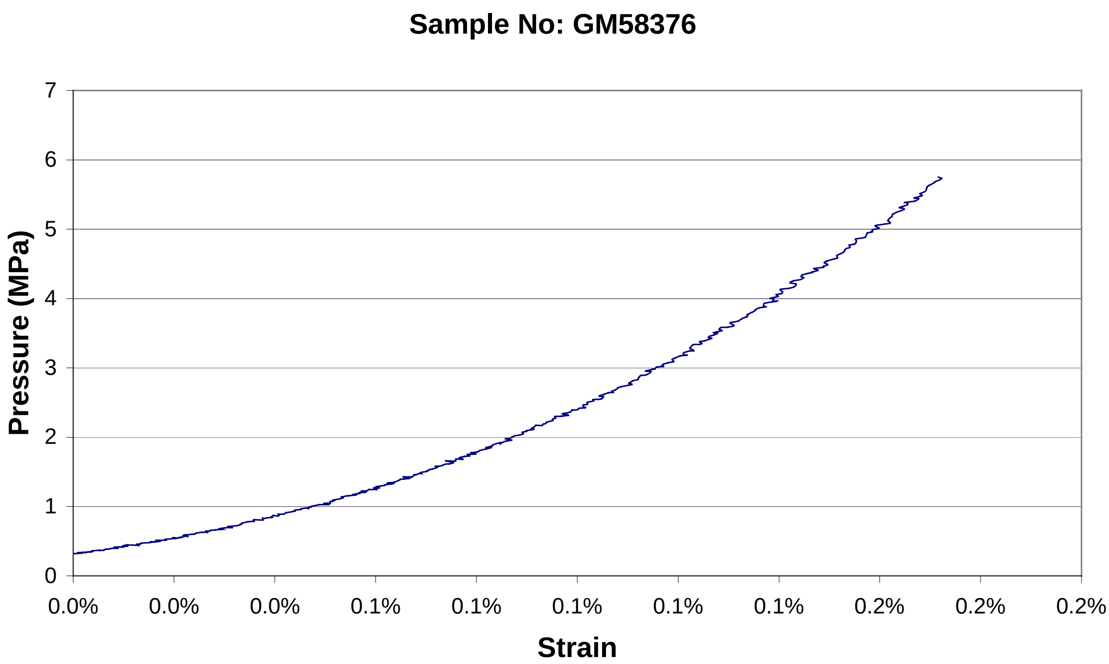

Figure A4.4. 10 Stress Strain Curve for Sample GM58376

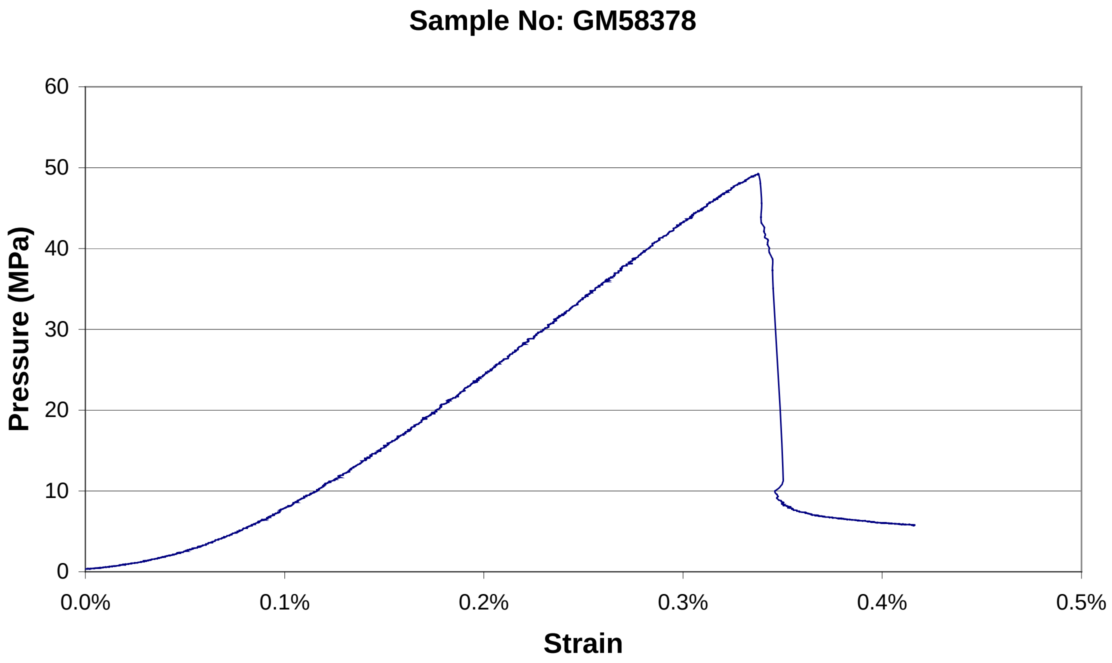

Figure A4.4. 11 Stress Strain Curve for Sample GM58378

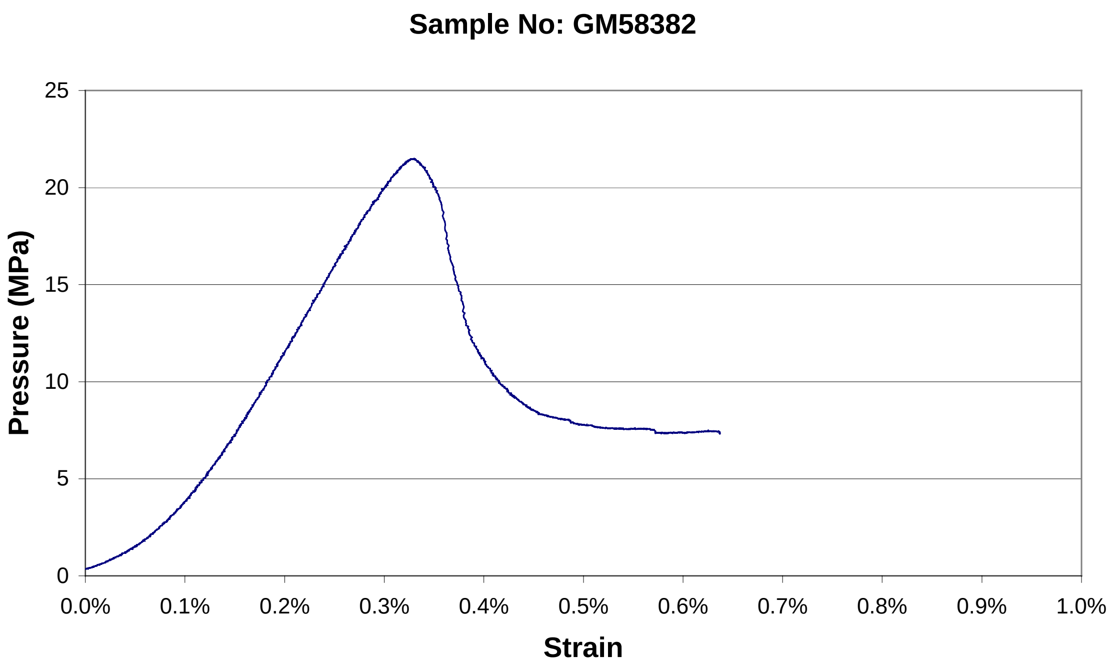

Figure A4.4. 12 Stress Strain Curve for Sample GM58382

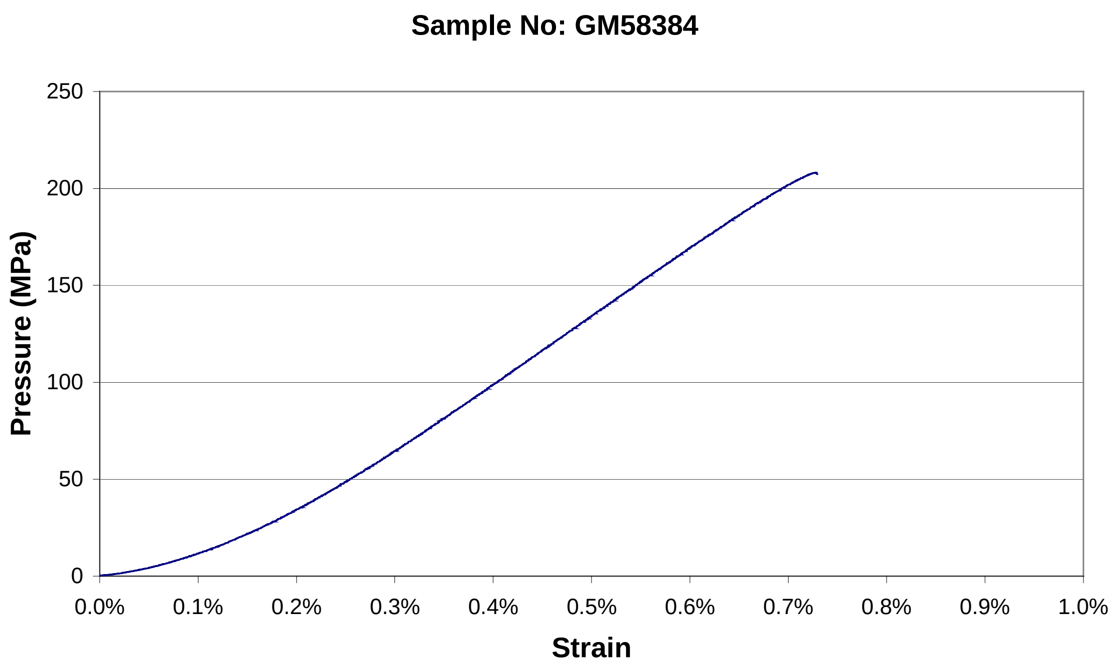

Figure A4.4. 13 Stress Strain Curve for Sample GM58384

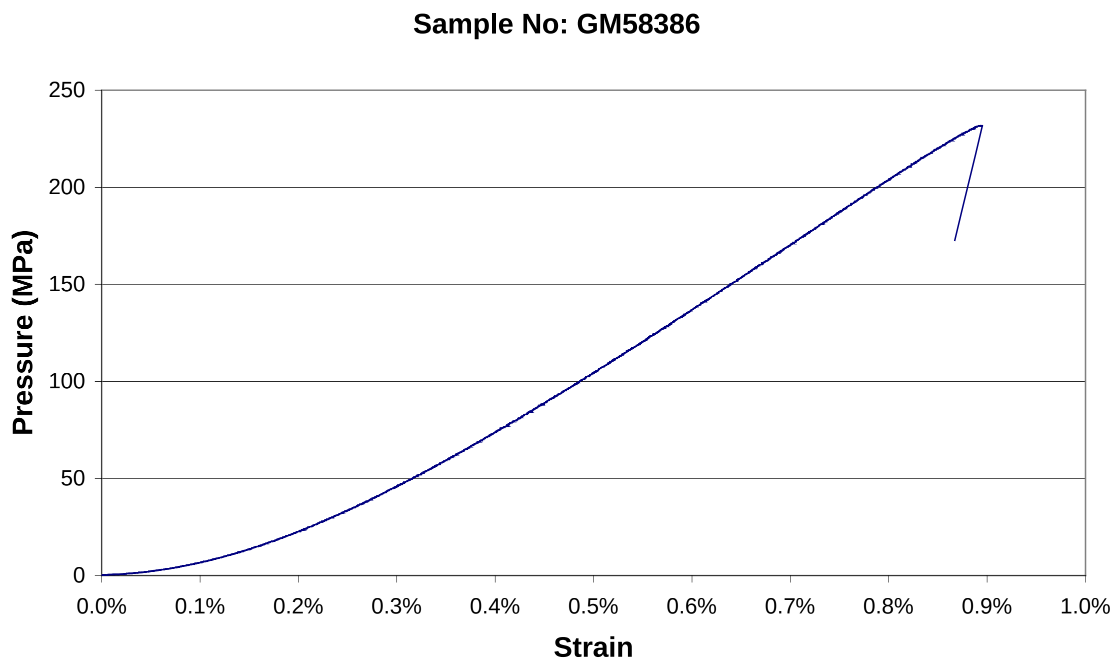

Figure A4.4. 14 Stress Strain Curve for Sample GM58386

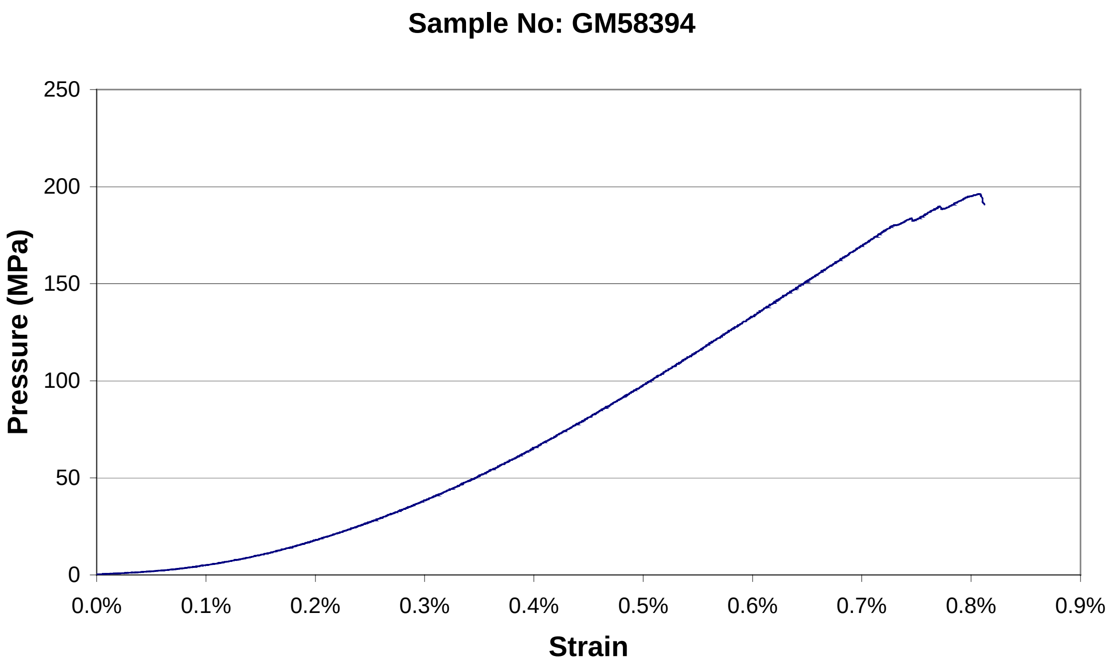

Figure A4.4. 15 Stress Strain Curve for Sample GM58394

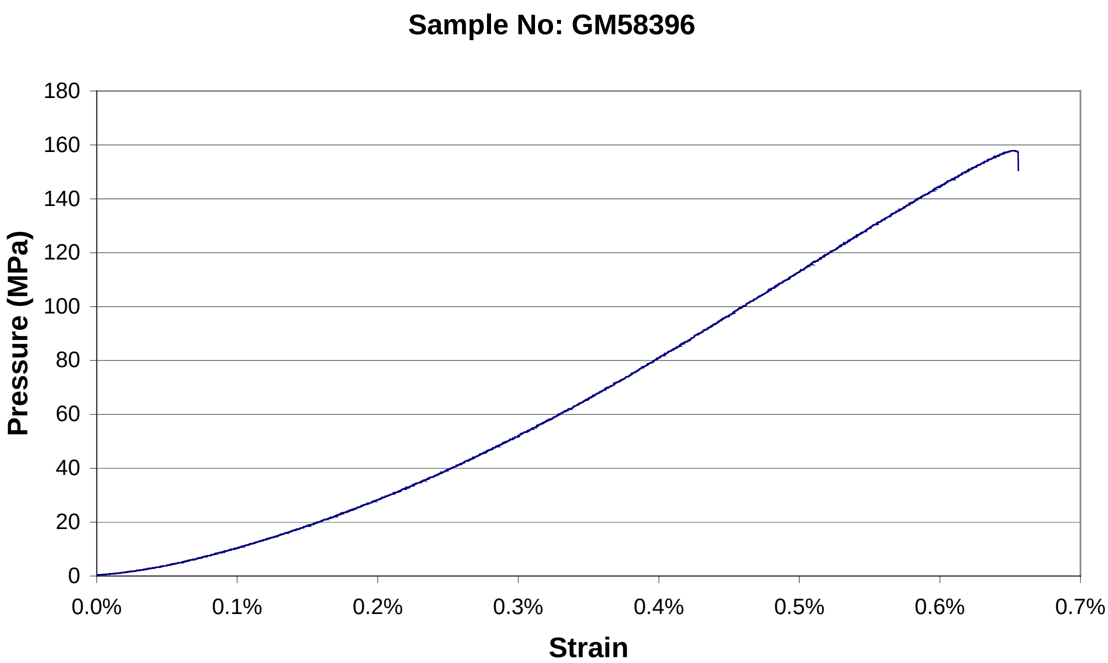

Figure A4.4. 16 Stress Strain Curve for Sample GM58396

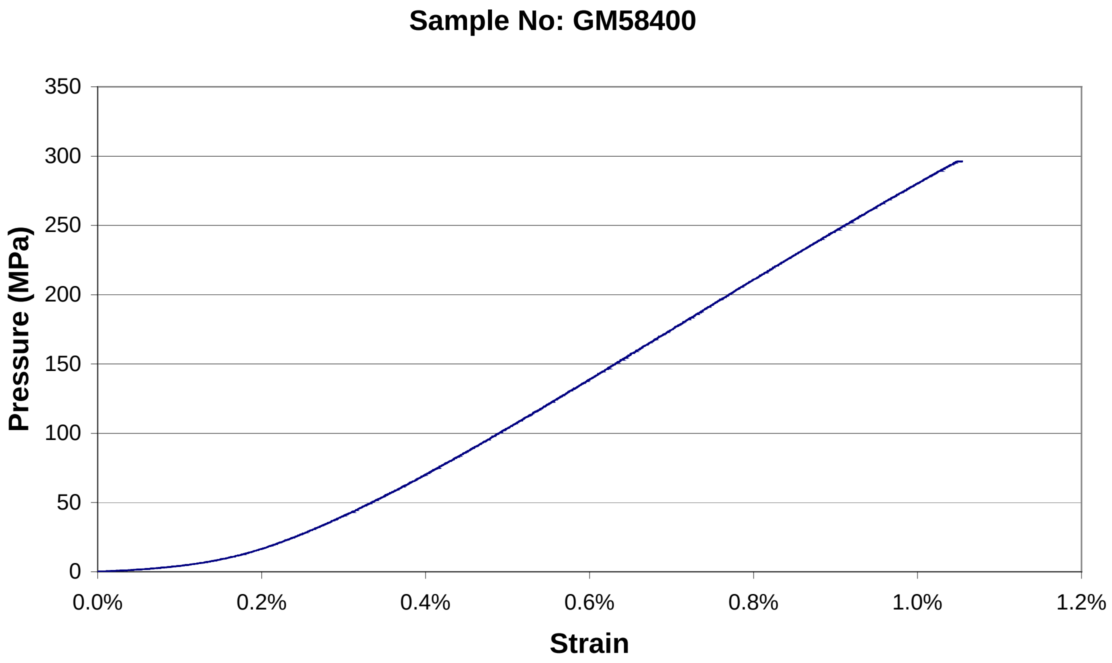

Figure A4.4. 17 Stress Strain Curve for Sample GM58400

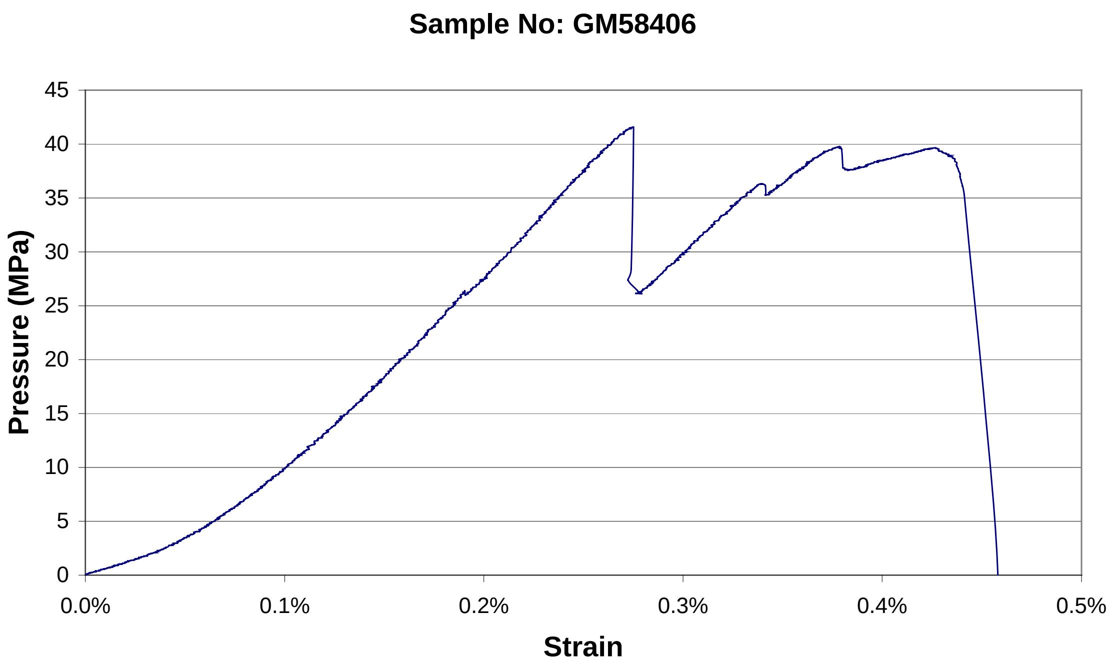

Figure A4.4. 18 Stress Strain Curve for Sample GM58406

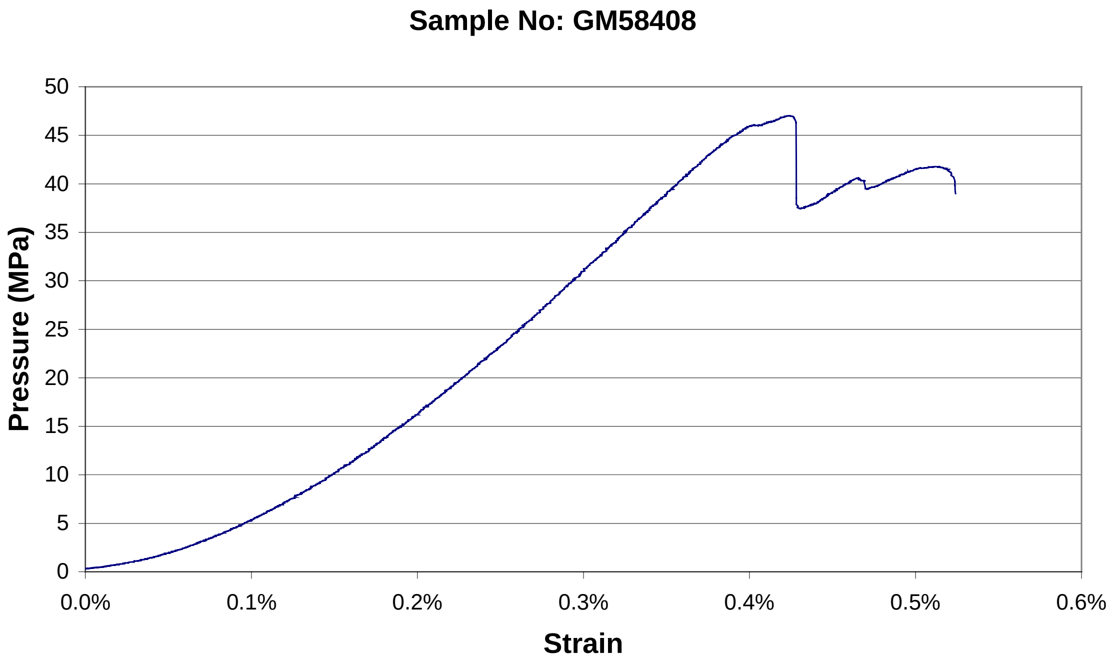

Figure A4.4. 19 Stress Strain Curve for Sample GM58408

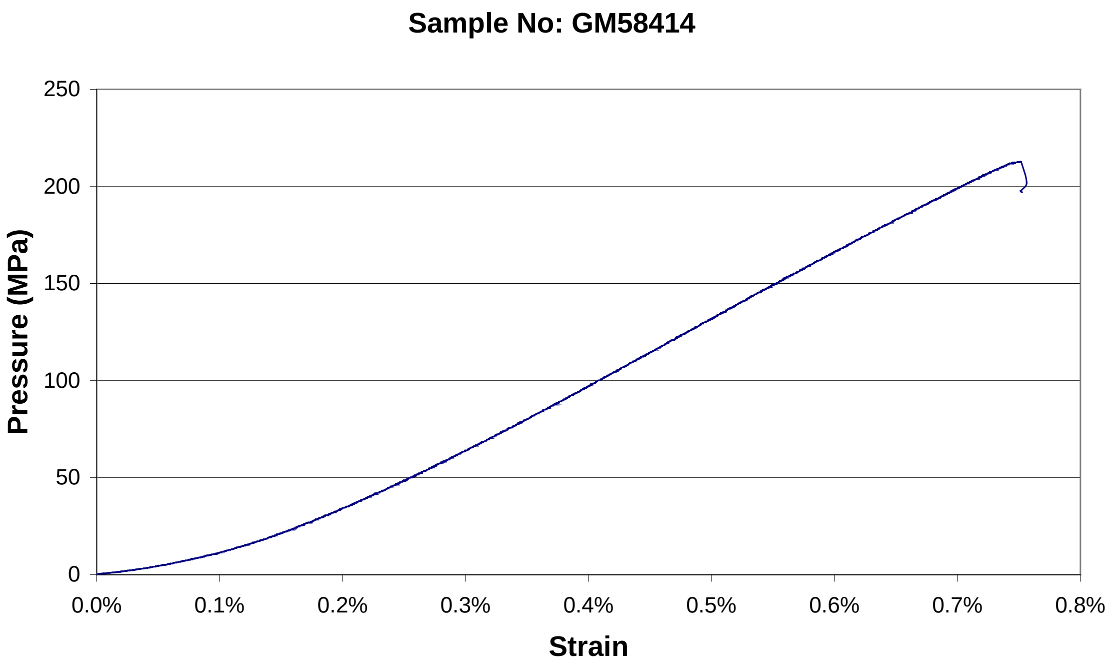

Figure A4.4. 20 Stress Strain Curve for Sample GM58414

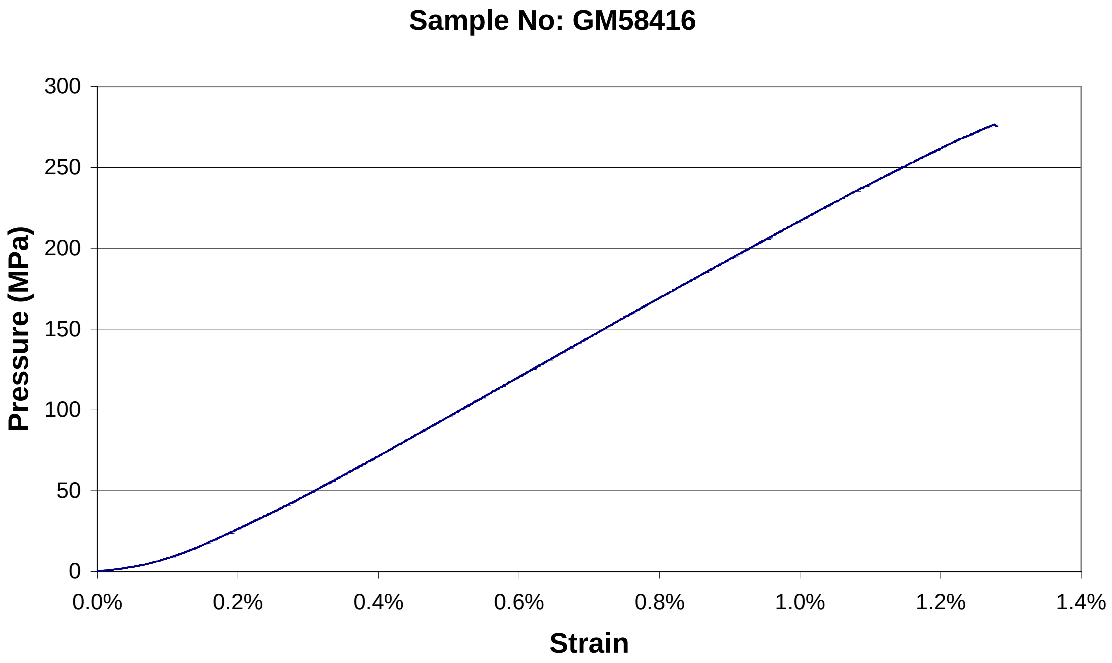

Figure A4.4. 21 Stress Strain Curve for Sample GM58416

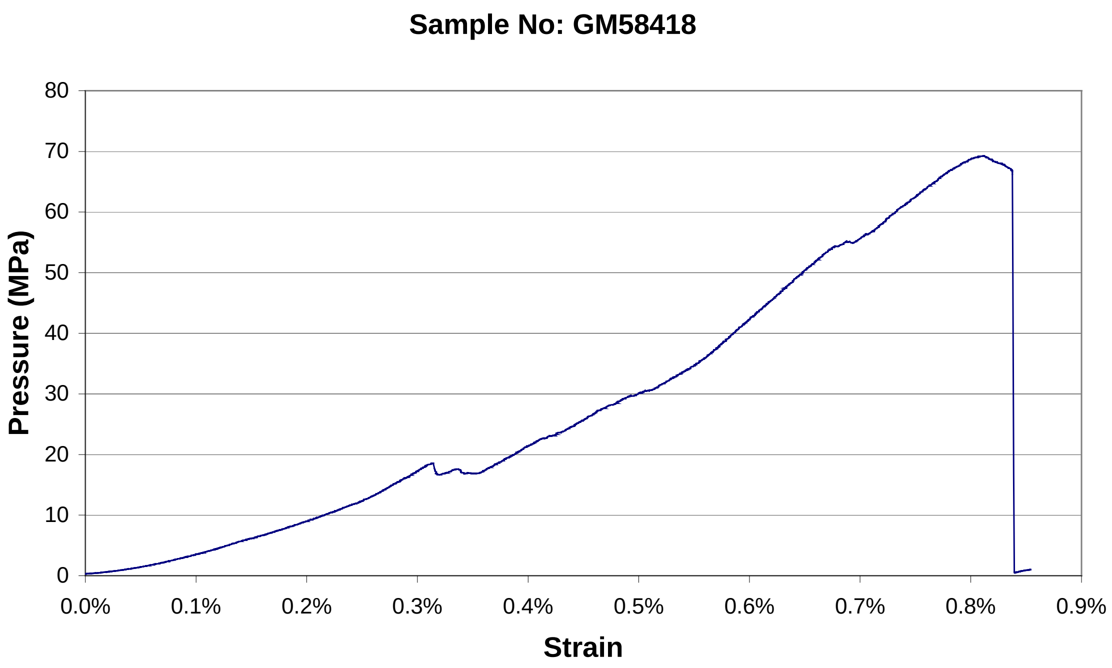

Figure A4.4. 22 Stress Strain Curve for Sample GM58418

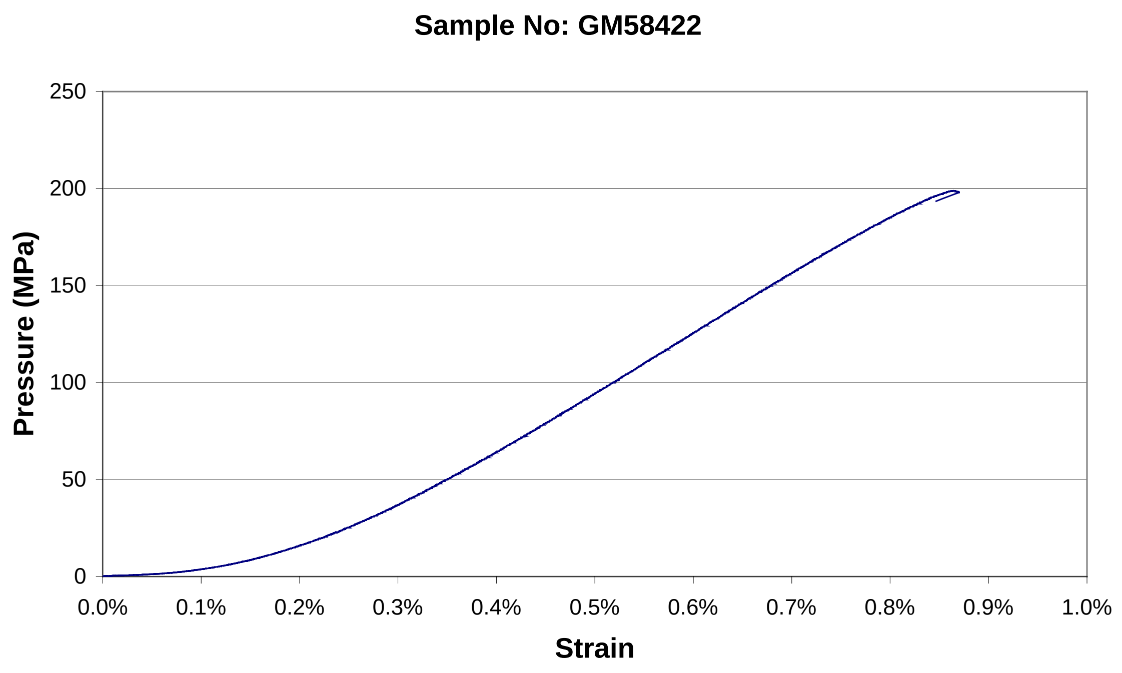

Figure A4.4. 23 Stress Strain Curve for Sample GM58422

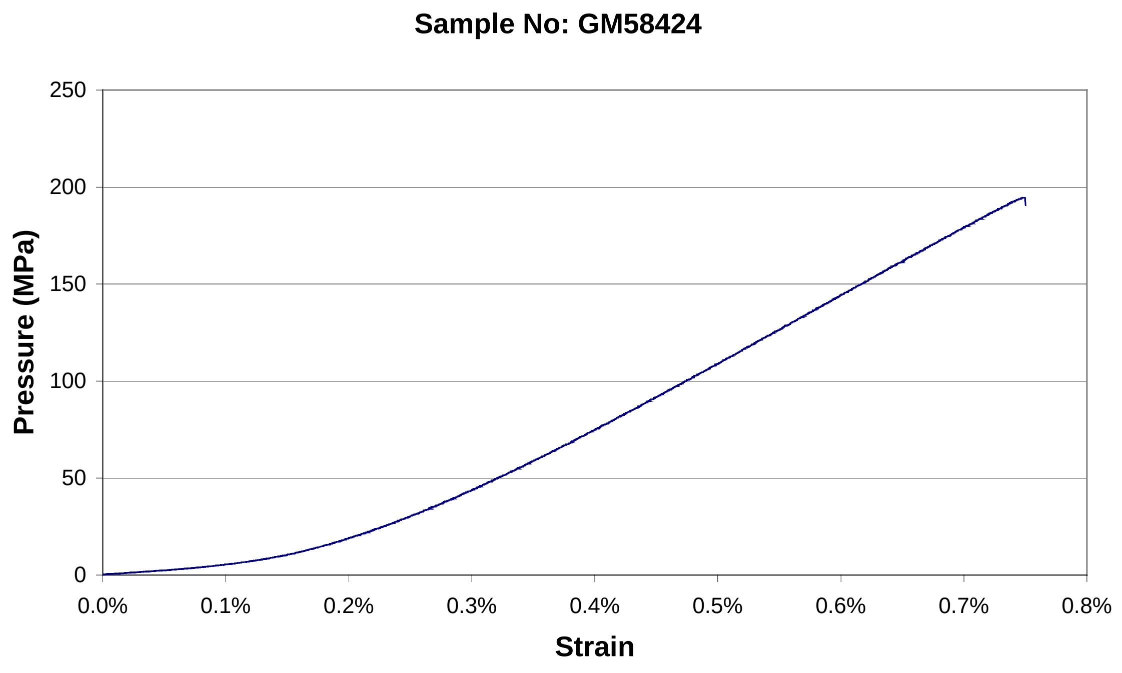

Figure A4.4. 24 Stress Strain Curve for Sample GM58424

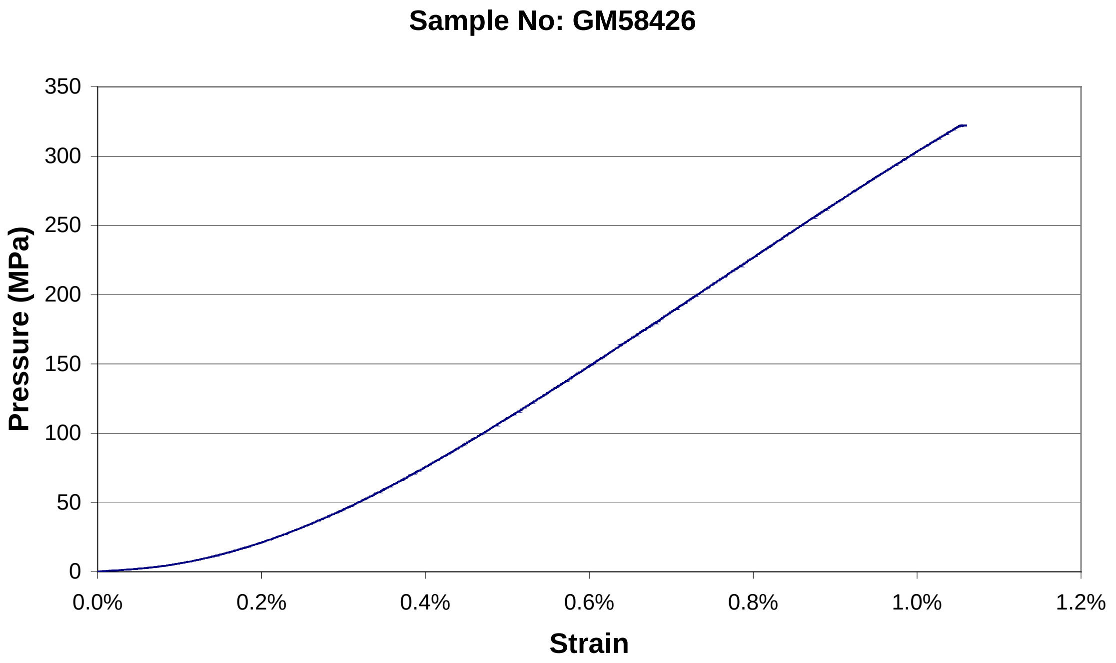

Figure A4.4. 25 Stress Strain Curve for Sample GM58426

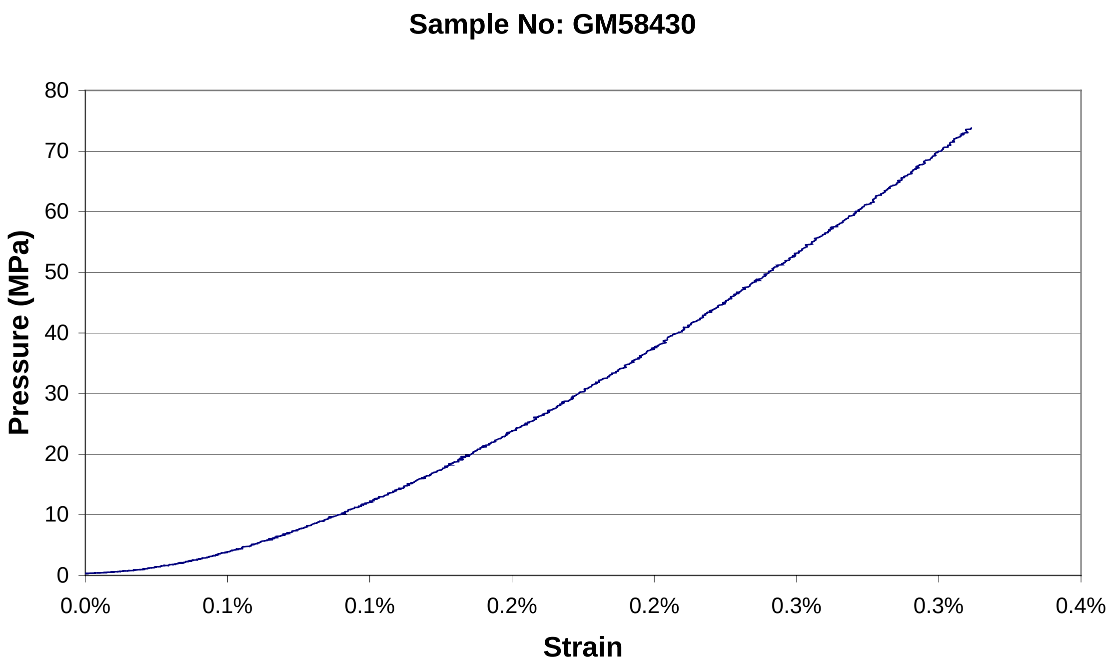

Figure A4.4. 26 Stress Strain Curve for Sample GM58430

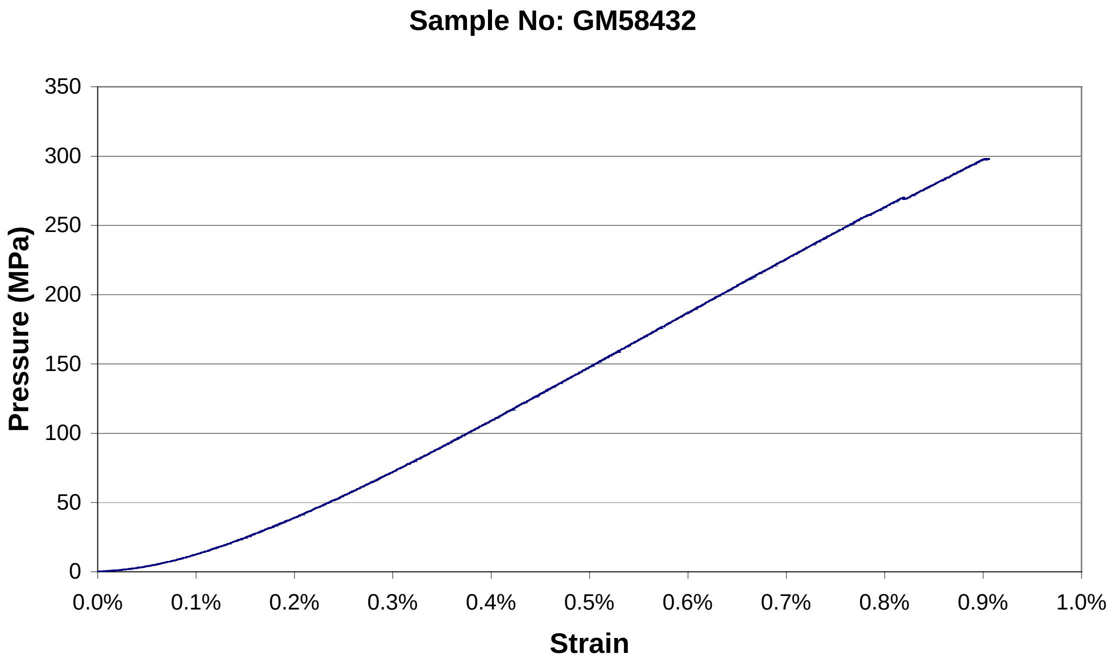

Figure A4.4. 27 Stress Strain Curve for Sample GM58432

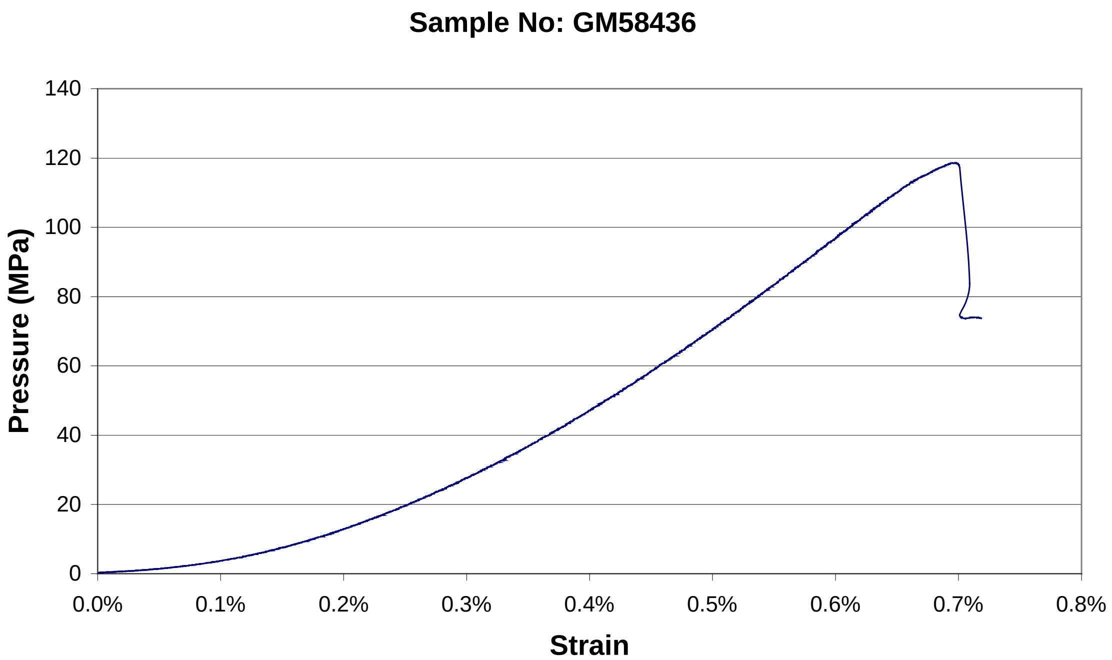

Figure A4.4. 28 Stress Strain Curve for Sample GM58436

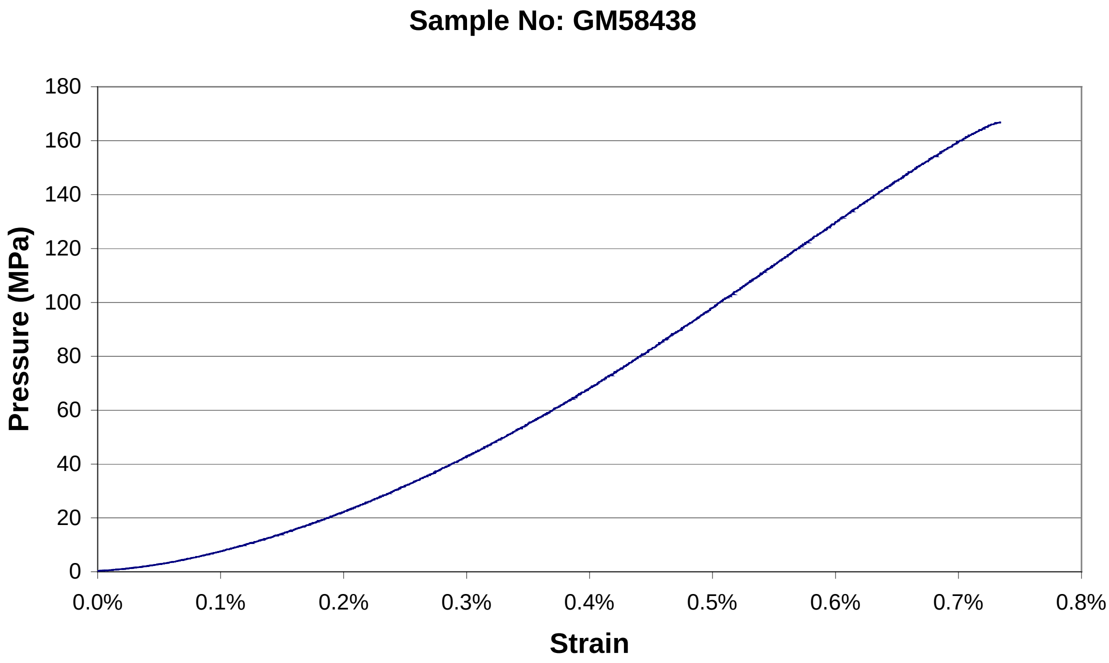

Figure A4.4. 29 Stress Strain Curve for Sample GM58438

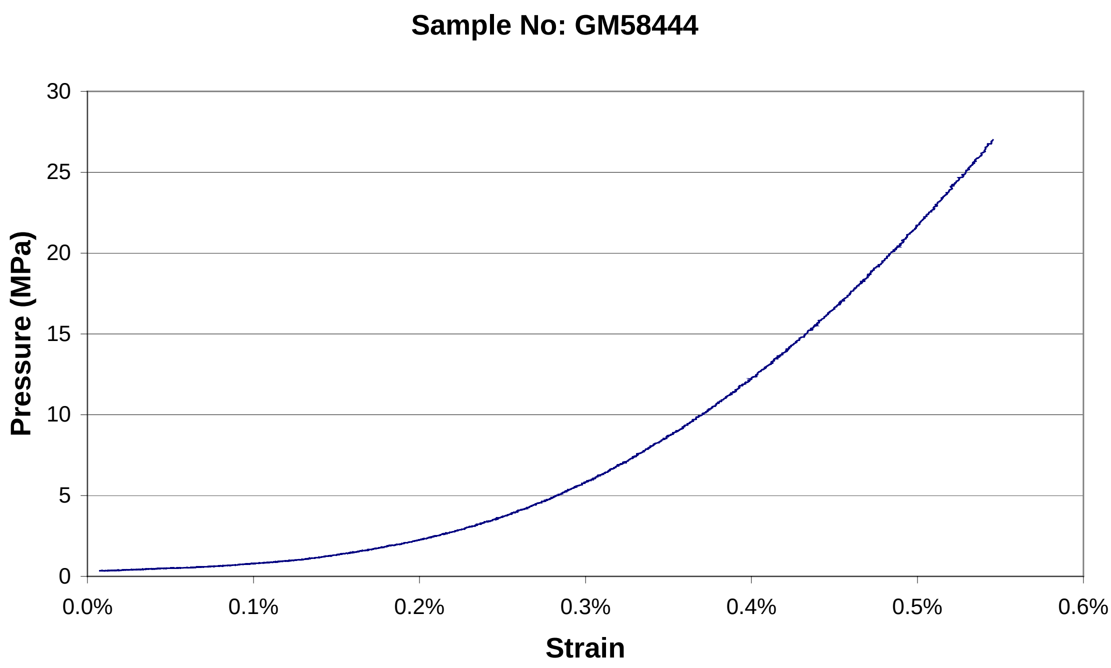

Figure A4.4. 30 Stress Strain Curve for Sample GM58444

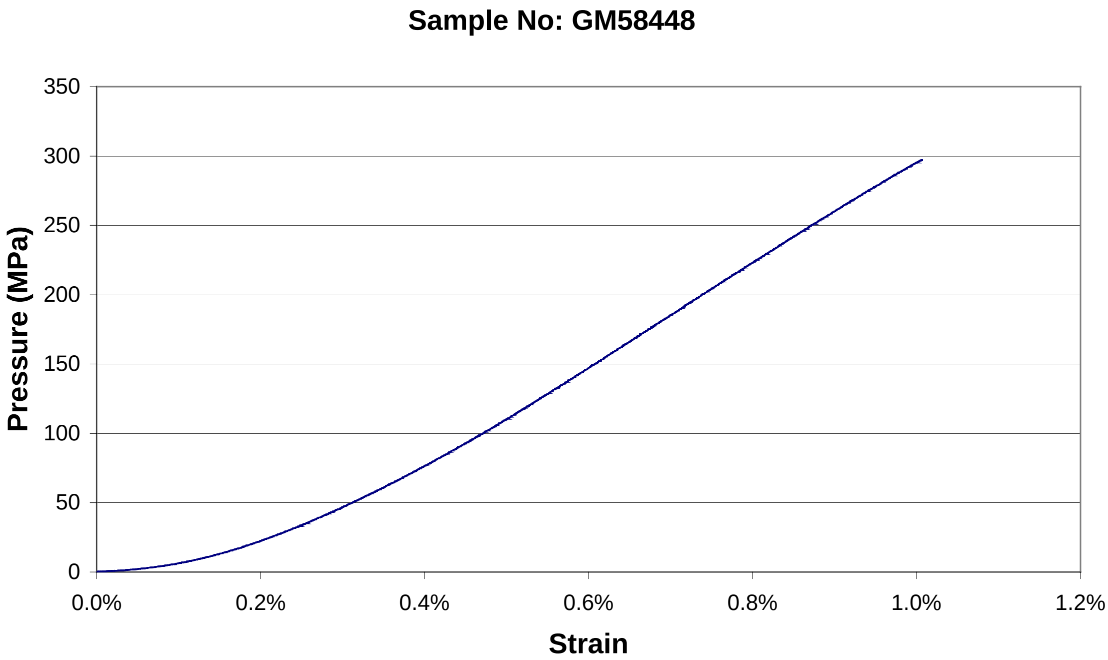

Figure A4.4. 31 Stress Strain Curve for Sample GM58448

Figure A4.4. 32 Samples after uniaxial testing

APPENDIX 4.5

Point Load Strength Testing

- *Summary of Test Results*
- *Test Data – Calculation of areas of Irregular Lumps*
- *Regression Analysis – I_{s50} vs. UCS*

No.	Rock Type	Hole	Sample Interval	Sample Number	Test Type (A)xial (D)iametral (I)rregular Lump	Minimum X-sect. Area b/n loading pnts (A) (mm^2)	D_e	P (kN)	Is (Mpa)	Is_{50}	Interpreted Rock Strength*
1	SHMU	CAD339	187.4 - 187.6	GM58345	I	815	32.213	4.170	4.019	3.297	VH
2A	SHMU	CAD033	106.9 - 107.2	GM58347	I	800	31.915	5.06	4.968	4.059	VH
2B	SHMU	CAD033	106.9 - 107.2	GM58347	I	921	34.244	6.8	5.799	4.891	VH
3	SHMU	CAD564a	46.4 - 46.7	GM58349	I	1335	41.228	12.4	7.295	6.689	VH
4	SHMU	CAD562	96.2 - 96.5	GM58351	I	1304	40.747	7.98	4.806	4.383	VH
5A	SHMU	CAD494	149.2 - 149.5	GM58353	I	752	30.943	4.85	5.065	4.082	VH
5B	SHMU	CAD494	149.2 - 149.5	GM58353	I	793	31.775	3.75	3.714	3.029	VH
	SHMU			Note next 3 cells	*Is50 (min)*	*Is50 (max)*	*Is50 (av)*	***3.029***	***6.689***	***4.347***	***VH***
6	AMPH	CAD346	68.5 - 68.7	GM58355	I	1270	40.212	7.38	4.564	4.138	VH
7	AMPH	CAD562	322.4 - 322.7	GM58359	I	1648	45.807	10.92	5.204	5.003	VH
8	AMPH	CAD494	291.2 - 291.4	GM58361	I	740	30.695	5.83	6.188	4.968	VH
9	AMPH	CAD387	254.3 - 254.5	GM58363	I	1012	35.896	14.58	11.315	9.748	VH
	AMPH			Note next 3 cells	*Is50 (min)*	*Is50 (max)*	*Is50 (av)*	***4.138***	***9.748***	***5.964***	***VH***
10A	PEGM	CAD033	261.3 - 261.5	GM58367	I	1297	40.637	1.89	1.144	1.043	H
10B	PEGM	CAD033	261.3 - 261.5	GM58367	I	876	33.397	2.86	2.564	2.138	H
11A	PEGM	CAD503	257.2 - 257.4	GM58369	I	815	32.213	6.06	5.840	4.792	VH
11B	PEGM	CAD503	257.2 - 257.4	GM58369	I	650	28.768	6.79	8.204	6.398	VH
12A	PEGM	CAD299	248.6 - 248.8	GM58371	I	565	26.821	5.66	7.868	5.945	VH
12B	PEGM	CAD299	248.6 - 248.8	GM58371	I	695	29.747	3.51	3.967	3.140	VH
13	PEGM	CAD387	249.1 - 249.4	GM58373	I	1520	43.992	13.46	6.955	6.566	VH
	PEGM			Note next 3 cells	*Is50 (min)*	*Is50 (max)*	*Is50 (av)*	***1.043***	***6.566***	***4.289***	***VH***

Table A4.5. 1 Point Load Strength Testing Results

No.	Rock Type	Hole	Sample Interval	Sample Number	Test Type (A)xial (D)iametral (I)rregular Lump	Minimum X-sect. Area b/n loading pnts (A) (mm^2)	D_e	P (kN)	Is (Mpa)	Is_{50}	Interpreted Rock Strength*
14	GNES	CAD530	99.8 - 100.0	GM58375	I	1600	45.135	5.1	2.503	2.391	H
15	GNES	CAD373	115.6 - 115.8	GM58377	I	890	33.663	3.9	3.442	2.880	H
16	GNES	CAD531	164.0 - 164.4	GM58379	I	1138	38.065	6.14	4.238	3.748	VH
17	GNES	CAD495	154.3 - 154.5	GM58381	I	1040	36.389	6.28	4.743	4.111	VH
18	GNES	CAD519	138.3 - 138.5	GM58383	I	1050	36.564	0.76	0.568	0.494	M
	GNES			Note next 3 cells	*Is50 (min)*	*Is50 (max)*	*Is50 (av)*	***0.494***	***4.111***	***2.725***	***VH***
19	Burnham	CAD562	263.7 - 263.9	GM58385	I	1807	47.966	16.33	7.098	6.966	VH
20	Burnham	CAD564a	246.7 - 246.9	GM58387	I	1020	36.038	13.72	10.564	9.117	VH
21	Burnham	CAD563	215.3 - 215.5	GM58389	I	1270	40.212	1.98	1.224	1.110	H
	Burnham			Note next 3 cells	*Is50 (min)*	*Is50 (max)*	*Is50 (av)*	***1.110***	***9.117***	***5.731***	***H***
22	Broadlands	CAD562	212.6 - 212.8	GM58395	I	778	31.473	16.03	16.182433	13.140	EH
23A	Broadlands	CAD563	190.5 - 190.8	GM58397	I	1039	36.372	17.12	12.941306	11.215	EH
23B	Broadlands	CAD563	190.5 - 190.8	GM58397	I	1510	43.847	5.58	2.9023323	2.736	H
24	Broadlands	CAD566	87.3 - 87.5	GM58399	I						*NO SAMPLE*
25	Broadlands	CAD564a	203.9 - 204.1	GM58401	I	964	35.034	6.91	5.6297731	4.797	VH
	Broadlands			Note next 3 cells	*Is50 (min)*	*Is50 (max)*	*Is50 (av)*	***2.736***	***13.140***	***7.972***	***H***
26	Glenholm	CAD386	287.8 - 288.1	GM58405	I	1300	40.684	7.27	4.392	4.003	VH
27	Glenholm	CAD564a	120.8 - 121.0	GM58407	I	625	28.209	6.71	8.432	6.517	VH
28	Glenholm	CAD562	204.7 - 204.9	GM58409	I	1245	39.814	9.92	6.258	5.648	VH
29	Glenholm	CAD563	61.9 - 62.1	GM58411	I	855	32.994	4.25	3.904	3.238	VH
	Glenholm			Note next 3 cells	*Is50 (min)*	*Is50 (max)*	*Is50 (av)*	***3.238***	***6.517***	***4.852***	***VH***

Table A4.5. 1 (cont. (1))Point Load Strength Testing Results

No.	Rock Type	Hole	Sample Interval	Sample Number	Test Type (A)xial (D)iametral (I)rregular Lump	Minimum X-sect. Area b/n loading pnts (A) (mm^2)	D_e	P (kN)	Is (Mpa)	Is_{50}	Interpreted Rock Strength*
30	QZGA/IT	CAD386	284.6 - 285.0	GM58415	I	1087	37.202	11.34	8.194	7.173	VH
31	QZGA/IT	CAD387	75.5 - 75.9	GM58417	I	1020	36.038	5.75	4.427	3.821	VH
32	QZGA/IT	CAD562	227.7 - 227.9	GM58419	I	880	33.473	7.98	7.122	5.945	VH
33	QZGA/IT	CAD564a	71.6 - 71.8	GM58423	I	1175	38.679	8.24	5.508	4.907	VH
	QZGA/IT			Note next 3 cells	*Is50 (min)*	*Is50 (max)*	*Is50 (av)*	***3.821***	***7.173***	***5.462***	***VH***
34	QZHD	CAD386	289.0 - 289.3	GM58425	I	1150	38.265	11.4	7.786	6.903	VH
35	QZHD	CAD387	164.0 - 164.2	GM58427	I	1633	45.598	18.1	8.705	8.352	VH
36	QZHD	CAD562	219.9 - 220.1	GM58429	I	1722	46.824	7.24	3.302	3.206	VH
37	QZHD	CAD564a	137.3 - 137.5	GM58431	I	1480	43.410	20.58	10.921	10.248	EH
38	QZHD	CAD563	113.2 - 113.4	GM58433	I	875	33.378	18.06	16.211	13.515	EH
	QZHD			Note next 3 cells	*Is50 (min)*	*Is50 (max)*	*Is50 (av)*	***3.206***	***13.515***	***8.445***	***VH***
39	HDMT	CAD387	160.7 - 161.0	GM58435	I	1232	39.606	14.84	9.460	8.519	VH
40	HDMT	CAD386	209.1 - 209.3	GM58437	I	731	30.508	9.96	10.701	8.568	VH
41	HDMT	CAD563	211.6 - 211.8	GM58439	I	1044	36.459	3.74	2.814	2.441	H
	HDMT			Note next 3 cells	*Is50 (min)*	*Is50 (max)*	*Is50 (av)*	***2.441***	***8.568***	***6.509***	***VH***
42	PXAM	CAD387	163.2 - 163.4	GM58445	I	310	19.867	16.33	41.373	27.311	EH
43	PXAM	CAD562	83.0 - 83.2	GM58447	I	1346	41.398	24.44	14.261	13.099	EH
44	PXAM	CAD563	33.9 - 34.1	GM58449	I	2026	50.790	16.41	6.361	6.407	VH
	PXAM			Note next 3 cells	*Is50 (min)*	*Is50 (max)*	*Is50 (av)*	***6.407***	***27.311***	***15.606***	***EH***

* From Table A8 of Australian Standard 1726-1993

Table A4.5. 1 (cont. (2))Point Load Strength Testing Results

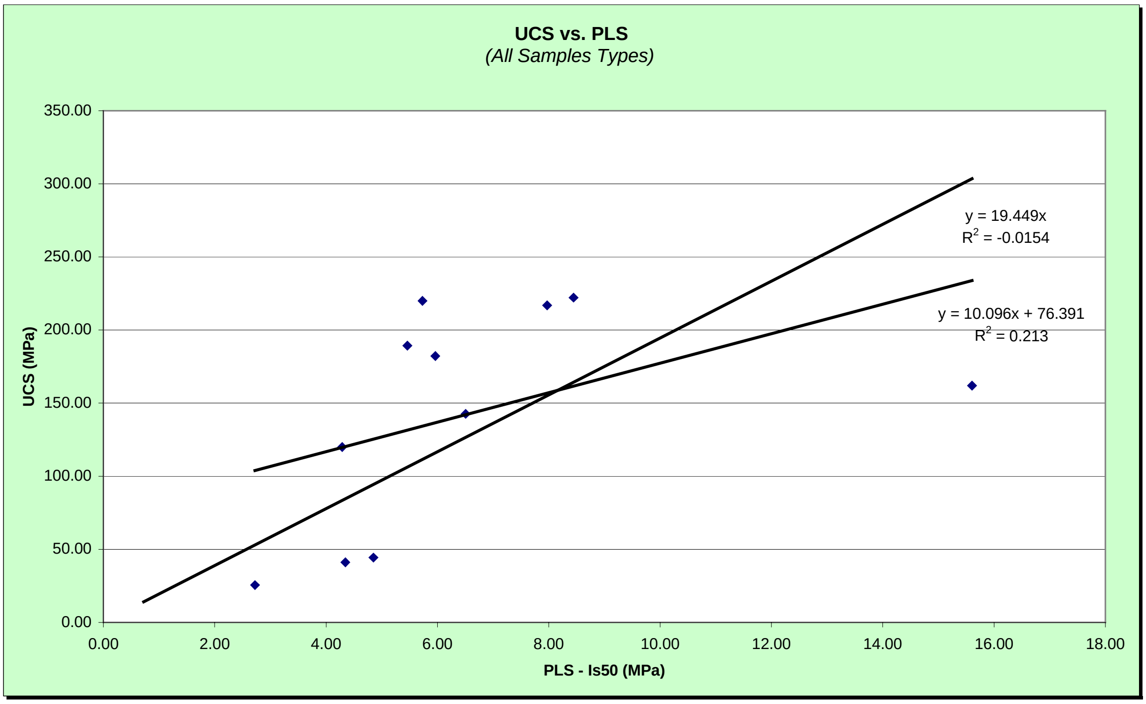

Figure A4.5. 1 Regression Analysis for relating Point Load Strength to the uniaxial compressive strength (using all sample types).

From the above graph, the two line represent the initial analysis, where a linear relationship was described. (10.096x+76.391). As can be seen the correlation co-efficient is low – indicating a poor correlation. A simplified relation factor was determined by setting the intercept to zero. Which is considered reasonable. The analysis was carried out again and the conversion factor of 19.449 found (as a global) conversion factor. – (Albeit having a very poor correlation to the actual data). As can be seen from the above data, one data set is to the extreme right of the plot and significantly and adversely affects the results. The data set was identified as the PXAM rock type. It was considered pertinent to re-do the analysis excluding the PXAM rock type. The results are as shown in Figure A4.5.2. The average conversion factor of 19.45 calculated above is different to the average of 22.30, which is reported in the text, (Table 4.11). This because the average in the text is purely a numerical average of the conversion factors, where as the 19.45, which results from the linear regression analysis, fixing the intercept at zero.

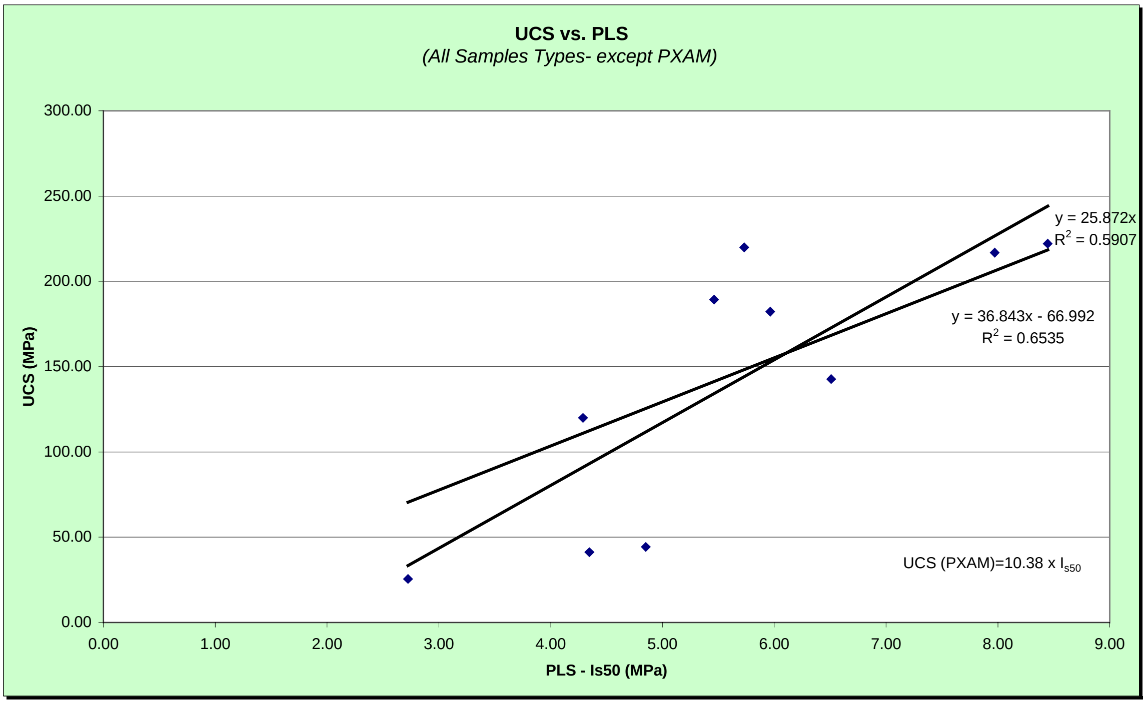

Figure A4.5. 2 Regression Analysis for relating Point Load Strength to the uniaxial compressive strength (excluding PXAM rock type).

The correlation co-efficient is significantly higher. The simple conversion factor between I_{s50} and UCS increased to 25.9 with a correlation co-efficient of 0.59.

Both analysis, results in low correlation co-efficient, thus it was concluded that calculation of conversion factors or the individual rock types was more appropriate.

APPENDIX 4.6

Indirect Tensile Testing

- *Sample Properties*
- *Indirect Tensile Strength Testing Results*
- *Digital Photographs – Tested Cores*

Table A4.6. 1 Dimensions, Masses, and Bulk Densities of the Rock Cores tested using the Brazilian indirect tensile strength test

Rock Type	Hole	Sample Interval	Sample Number	ϕ Av. (mm)	Ht.av. (mm)	Vol. (cm^3)	Mass (g)	Bulk Density (Kg/m^3)	Aspect Ratio (H/ϕ)
SHMU	CAD339	187.4 - 187.6	GM58345	47.61	96.51	171.82	485.00	2.82	2.03
SHMU	CAD033	106.9 - 107.2	GM58347	50.49	96.65	193.49	550.00	2.84	1.91
SHMU	CAD033	106.9 - 107.2	GM58347	52.66	101.01	220.00	566.00	2.57	1.92
SHMU	CAD564a	46.4 - 46.7	GM58349	63.44	127.23	402.21	1104.00	2.74	2.01
SHMU	CAD562	96.2 - 96.5	GM58351	63.28	127.79	401.87	1112.00	2.77	2.02
SHMU	CAD494	149.2 - 149.5	GM58353	47.48	97.00	171.73	476.00	2.77	2.04
SHMU	CAD494	149.2 - 149.5	GM58353	47.55	89.90	159.64	443.00	2.77	1.89
AMPH	CAD346	68.5 - 68.7	GM58355	63.29	124.87	392.88	1179.00	3.00	1.97
AMPH	CAD562	322.4 - 322.7	GM58359	60.82	121.18	352.11	968.00	2.75	1.99
AMPH	CAD494	291.2 - 291.4	GM58361	47.40	96.86	170.92	515.00	3.01	2.04
AMPH	CAD387	254.3 - 254.5	GM58363	61.11	125.95	369.45	1110.00	3.00	2.06
PEGM	CAD033	261.3 - 261.5	GM58367	50.66	97.38	196.26	505.00	2.57	1.92
PEGM	CAD033	261.3 - 261.5	GM58367	50.84	96.39	195.68	505.00	2.58	1.90
PEGM	CAD503	257.2 - 257.4	GM58369	47.62	91.81	163.52	428.00	2.62	1.93
PEGM	CAD503	257.2 - 257.4	GM58369	47.67	96.74	172.66	440.00	2.55	2.03
PEGM	CAD299	248.6 - 248.8	GM58371	47.33	93.94	165.28	426.00	2.58	1.98
PEGM	CAD299	248.6 - 248.8	GM58371	47.35	90.14	158.73	410.00	2.58	1.90
PEGM	CAD387	249.1 - 249.4	GM58373	61.23	123.18	362.70	941.00	2.59	2.01
GNES	CAD530	99.8 - 100.0	GM58375	60.83	126.59	367.87	970.00	2.64	2.08
GNES	CAD373	115.6 - 115.8	GM58377	63.19	125.49	393.59	1035.00	2.63	1.99
GNES	CAD531	164.0 - 164.4	GM58379	60.92	124.40	362.65	978.00	2.70	2.04
GNES	CAD495	154.3 - 154.5	GM58381	60.82	120.20	349.22	932.00	2.67	1.98
GNES	CAD519	138.3 - 138.5	GM58383	60.88	57.67	167.85	439.00	2.62	0.95
Burnham	CAD562	263.7 - 263.9	GM58385	63.45	129.89	410.75	1748.00	4.26	2.05
Burnham	CAD564a	246.7 - 246.9	GM58387	63.16	122.33	383.32	1676.00	4.37	1.94
Burnham	CAD563	215.3 - 215.5	GM58389	63.40	127.45	402.32	1887.00	4.69	2.01
Broadlands	CAD562	212.6 - 212.8	GM58395	63.59	155.77	494.66	1258.00	2.54	2.45
Broadlands	CAD563	190.5 - 190.8	GM58397	63.40	125.10	394.92	1696.00	4.29	1.97
Broadlands	CAD563	190.5 - 190.8	GM58397	63.38	125.03	394.50	1560.00	3.95	1.97
Broadlands	CAD564a	203.9 - 204.1	GM58401	63.36	127.38	401.62	1446.00	3.60	2.01
Glenholm	CAD386	287.8 - 288.1	GM58405	61.16	123.32	362.34	1448.00	4.00	2.02
Glenholm	CAD564a	120.8 - 121.0	GM58407	63.48	128.68	407.23	1540.00	3.78	2.03
Glenholm	CAD562	204.7 - 204.9	GM58409	63.47	129.49	409.69	1396.00	3.41	2.04
Glenholm	CAD563	61.9 - 62.1	GM58411	63.32	124.48	391.93	1639.00	4.18	1.97
QZGA/IT	CAD386	284.6 - 285.0	GM58415	61.22	123.51	363.53	1029.00	2.83	2.02
QZGA/IT	CAD387	75.5 - 75.9	GM58417	61.08	124.32	364.32	1119.00	3.07	2.04
QZGA/IT	CAD562	227.7 - 227.9	GM58419	63.47	127.93	404.81	1195.00	2.95	2.02
QZGA/IT	CAD564a	71.6 - 71.8	GM58423	63.45	128.07	404.95	1153.00	2.85	2.02
QZHD	CAD386	289.0 - 289.3	GM58425	61.18	126.08	370.61	1307.00	3.53	2.06
QZHD	CAD387	164.0 - 164.2	GM58427	60.85	183.45	533.54	1194.00	2.24	3.01
QZHD	CAD562	219.9 - 220.1	GM58429	63.57	125.75	399.09	1139.00	2.85	1.98
QZHD	CAD564a	137.3 - 137.5	GM58431	63.55	156.18	495.38	1274.00	2.57	2.46
QZHD	CAD563	113.2 - 113.4	GM58433	63.44	127.34	402.47	1277.00	3.17	2.01
HDMT	CAD387	160.7 - 161.0	GM58435	60.91	121.44	353.87	1357.00	3.83	1.99
HDMT	CAD386	209.1 - 209.3	GM58437	60.63	120.46	347.78	1411.00	4.06	1.99
HDMT	CAD563	211.6 - 211.8	GM58439	63.30	124.40	391.50	1681.00	4.29	1.97
PXAM	CAD387	163.2 - 163.4	GM58445	60.93	126.88	370.00	1353.00	3.66	2.08
PXAM	CAD562	83.0 - 83.2	GM58447	63.28	122.56	385.46	1442.00	3.74	1.94
PXAM	CAD563	33.9 - 34.1	GM58449	63.25	128.77	404.60	1463.00	3.62	2.04

On six different cores (GM58347, GM58353, GM58367, GM58369, GM58371, and GM58397), where the samples were longer than necessary, we were able to cut extra cores and do additional Brazilian indirect tensile strength tests.

Table A4.6. 2 Indirect Tensile Test Results

Rock Type	Hole	Sample Interval	Sample Number	ϕ_{av} (mm)	Ht.$_{av}$ (mm)	Loading Rate (kN/ min)	Ultimate Load (kN)	Indirect Tensile Strength (Mpa)	Predicted Compresive Strength, σ_c, (Mpa) Lower Bound (~10*σt)	Lower Bound (~15*σt)
SHMU	CAD339	187.4 - 187.6	GM58345	47.61	96.51	100.00	54.00	7.48	74.81	112.22
SHMU	CAD033	106.9 - 107.2	GM58347	50.49	96.65	50.00	82.50	10.76	107.63	161.45
SHMU	CAD033	106.9 - 107.2	GM58347	52.66	101.01	50.00	69.50	8.32	83.18	124.77
SHMU	CAD564a	46.4 - 46.7	GM58349	63.44	127.23	50.00	94.25	7.43	74.33	111.50
SHMU	CAD562	96.2 - 96.5	GM58351	63.28	127.79	50.00	103.50	8.15	81.48	122.22
SHMU	CAD494	149.2 - 149.5	GM58353	47.48	97.00	50.00	68.00	9.40	94.00	141.00
SHMU	CAD494	149.2 - 149.5	GM58353	47.55	89.90	50.00	61.50	9.16	91.59	137.38
SHMU						***Average***	***76.18***	***8.67***	***86.72***	***130.08***
AMPH	CAD346	68.5 - 68.7	GM58355	63.29	124.87	50.00	240.00	19.33	193.32	289.98
AMPH	CAD562	322.4 - 322.7	GM58359	60.82	121.18	50.00	74.00	6.39	63.91	95.87
AMPH	CAD494	291.2 - 291.4	GM58361	47.40	96.86	50.00	148.00	20.52	205.22	307.83
AMPH	CAD387	254.3 - 254.5	GM58363	61.11	125.95	100.00	160.00	13.23	132.33	198.50
AMPH						***Average***	***155.50***	***14.87***	***148.70***	***223.04***
PEGM	CAD033	261.3 - 261.5	GM58367	50.66	97.38	50.00	81.00	10.45	104.53	156.80
PEGM	CAD033	261.3 - 261.5	GM58367	50.84	96.39	50.00	86.00	11.17	111.72	167.58
PEGM	CAD503	257.2 - 257.4	GM58369	47.62	91.81	50.00	172.50	25.12	251.18	376.77
PEGM	CAD503	257.2 - 257.4	GM58369	47.67	96.74	50.00	95.50	13.18	131.83	197.75
PEGM	CAD299	248.6 - 248.8	GM58371	47.33	93.94	50.00	77.50	11.10	110.96	166.44
PEGM	CAD299	248.6 - 248.8	GM58371	47.35	90.14	50.00	62.50	9.32	93.22	139.83
PEGM	CAD387	249.1 - 249.4	GM58373	61.23	123.18	50.00	120.00	10.13	101.29	151.94
PEGM						***Average***	***99.29***	***12.92***	***129.25***	***193.87***
GNES	CAD530	99.8 - 100.0	GM58375	60.83	126.59	50.00	63.00	5.21	52.09	78.13
GNES	CAD373	115.6 - 115.8	GM58377	63.19	125.49	50.00	47.50	3.81	38.13	57.20
GNES	CAD531	164.0 - 164.4	GM58379	60.92	124.40	50.00	81.50	6.85	68.46	102.69
GNES	CAD495	154.3 - 154.5	GM58381	60.82	120.20	50.00	74.00	6.44	64.44	96.66
GNES	CAD519	138.3 - 138.5	GM58383	60.88	57.67	50.00	5.00	0.91	9.07	13.60
GNES						***Average***	***66.50***	***5.58***	***55.78***	***83.67***

Table A4.6. 2 Indirect Tensile Test Results… cont(1)

Rock Type	Hole	Sample Interval	Sample Number	ϕ_{av} (mm)	Ht.$_{av}$ (mm)	Loading Rate (kN/ min)	Ultimate Load (kN)	Indirect Tensile Strength (Mpa)	Predicted Compresive Strength, σ_c, (Mpa) Lower Bound (~10*σt)	Predicted Compresive Strength, σ_c, (Mpa) Lower Bound (~15*σt)
Burnham	CAD562	263.7 - 263.9	GM58385	63.45	129.89	100.00	205.00	15.83	158.34	237.52
Burnham	CAD564a	246.7 - 246.9	GM58387	63.16	122.33	100.00	248.00	20.43	204.33	306.49
Burnham	CAD563	215.3 - 215.5	GM58389	63.40	127.45	100.00	157.00	12.37	123.70	185.55
Burnham						***Average***	***203.33***	***16.21***	***162.12***	***243.18***
Broadlands	CAD562	212.6 - 212.8	GM58395	63.59	155.77	100.00	211.00	13.56	135.62	203.42
Broadlands	CAD563	190.5 - 190.8	GM58397	63.40	125.10	100.00	108.50	8.71	87.09	130.64
Broadlands	CAD563	190.5 - 190.8	GM58397	63.38	125.03	100.00	187.00	15.02	150.23	225.34
Broadlands	CAD564a	203.9 - 204.1	GM58401	63.36	127.38	100.00	193.50	15.26	152.64	228.95
Broadlands						***Average***	***175.00***	***13.14***	***131.39***	***197.09***
Glenholm	CAD386	287.8 - 288.1	GM58405	61.16	123.32	100.00	92.00	7.76	77.65	116.47
Glenholm	CAD564a	120.8 - 121.0	GM58407	63.48	128.68	100.00	143.50	11.18	111.84	167.76
Glenholm	CAD562	204.7 - 204.9	GM58409	63.47	129.49	100.00	126.00	9.76	97.60	146.40
Glenholm	CAD563	61.9 - 62.1	GM58411	63.32	124.48	100.00	87.00	7.03	70.27	105.41
Glenholm						***Average***	***112.13***	***8.93***	***89.34***	***134.01***
QZGA/IT	CAD386	284.6 - 285.0	GM58415	61.22	123.51	100.00	227.00	19.11	191.13	286.69
QZGA/IT	CAD387	75.5 - 75.9	GM58417	61.08	124.32	100.00	90.00	7.54	75.45	113.17
QZGA/IT	CAD562	227.7 - 227.9	GM58419	63.47	127.93	100.00	203.00	15.91	159.15	238.72
QZGA/IT	CAD564a	71.6 - 71.8	GM58423	63.45	128.07	100.00	110.00	8.62	86.18	129.27
QZGA/IT						***Average***	***157.50***	***12.80***	***127.98***	***191.96***
QZHD	CAD386	289.0 - 289.3	GM58425	61.18	126.08	100.00	137.00	11.31	113.07	169.61
QZHD	CAD387	164.0 - 164.2	GM58427	60.85	183.45	100.00	276.00	15.74	157.40	236.09
QZHD	CAD562	219.9 - 220.1	GM58429	63.57	125.75	100.00	201.50	16.05	160.47	240.71
QZHD	CAD564a	137.3 - 137.5	GM58431	63.55	156.18	100.00	219.50	14.08	140.79	211.19
QZHD	CAD563	113.2 - 113.4	GM58433	63.44	127.34	100.00	204.00	16.08	160.77	241.16
QZHD						***Average***	***207.60***	***14.65***	***146.50***	***219.75***

Table A4.6. 2 Indirect Tensile Test Results… cont(2)

Rock Type	Hole	Sample Interval	Sample Number	ϕ_{av} (mm)	$Ht._{av}$ (mm)	Loading Rate (kN/ min)	Ultimate Load (kN)	Indirect Tensile Strength (Mpa)	Predicted Compressive Strength, σc, (Mpa) Lower Bound (~10*σt)	Predicted Compressive Strength, σc, (Mpa) Lower Bound (~15*σt)
HDMT	CAD387	160.7 - 161.0	GM58435	60.91	121.44	100.00	161.00	13.86	138.56	207.84
HDMT	CAD386	209.1 - 209.3	GM58437	60.63	120.46	100.00	181.50	15.82	158.21	237.31
HDMT	CAD563	211.6 - 211.8	GM58439	63.30	124.40	100.00	200.00	16.17	161.69	242.53
HDMT						***Average***	***180.83***	***15.28***	***152.82***	***229.23***
PXAM	CAD387	163.2 - 163.4	GM58445	60.93	126.88	100.00	245.00	20.17	201.74	302.62
PXAM	CAD562	83.0 - 83.2	GM58447	63.28	122.56	100.00	225.00	18.47	184.69	277.03
PXAM	CAD563	33.9 - 34.1	GM58449	63.25	128.77	100.00	368.00	28.76	287.64	431.46
PXAM						***Average***	***279.33***	***22.47***	***224.69***	***337.04***

Figure A4.6. 1 Cores GM58345 to GM58367 after Indirect Tensile Testing

Figure A4.6. 2 Cores GM58369 to GM58387 after Indirect Tensile Testing

Figure A4.6. 3 Cores GM58389 to GM58417 after Indirect Tensile Testing

Figure A4.6. 4 Cores GM58419 to GM58449 after Indirect Tensile Testing

APPENDIX 4.7

Poisson's Ratio Testing

- *Typical Poisson's Ratio values*
- *Test Data*

Figure A4.7. 1 Static elastic parameters for various rock types from laboratory tests on intact rock specimens* (from Franklin, J.A., and Dusseault, M.B., 1989)

	Young's Modulus, E (GPa)	**Poisson's Ratio, *v***
Crystalline limestones	60 (17-100)	0.25 (0.06-0.50)
Porous limestones	45 (10-100)	0.24 (0.15-0.29)
Chalk	2 (0.1-12)	0.10 (0.05-0.15)
Salt	26 (5-44)	0.26 (0.06-0.73)
Sandstones	18 (1-100)	0.15 (0.02-0.51)
Quartzite	62 (11-119)	0.18 (0.10-0.40)
Slates and high-durability shales	40 (12-96)	0.22 (0.02-0.38)
Low-durability shales	5 (2-30)	
Coal	3 (1-30)	0.42 (0.17-0.49)
Coarse-grained igneous rocks	56 (8-125)	0.20 (0.05-0.39)
Fine-grained igneous rocks	62 (7-117)	0.22 (0.07-0.38)
Schists	40 (5-98)	0.15 (0.01-0.40)

Typical values (mode of between 10 and 30 reported test results) are given together with ranges of reported values in parentheses.

The aforementioned values should only be used as a rough guide , given the large variation in rocks and testing methods used.

Table A4.7. 1 Sample Properties - Poisson's Ratio Testing

					Sample Dimensions											
					Diameter, ϕ, (mm)				Height, H, (mm)							
No.	Rock Type	Hole	Sample Interval	Sample Number	ϕ_1	ϕ_2	ϕ_3	Avg	H_1	H_2	H_3	Avg	*Volume* *(cm^3)*	*Mass* *(g)*	Bulk Density (Kg/m^3)	Aspect Ratio (H/ϕ)
1	SHMU	CAD339	187.2 - 187.4	GM58344	47.52	47.48	47.49	47.50	141	142	143	141.83	251.30	712.00	2.83	2.99
2	SHMU	CAD033	106.7 - 106.9	GM58346	50.42	50.32	50.54	50.43	149	149	149	149.00	297.58	837.00	2.81	2.95
3	SHMU	CAD564a	46.1 - 46.4	GM58348	63.35	63.32	63.38	63.35	185	186	186	185.67	585.22	1618.00	2.76	2.93
4	SHMU	CAD562	95.9 - 96.2	GM58350	63.25	63.30	63.20	63.25	192	192	191	191.67	602.22	1665.00	2.76	3.03
	SHMU	CAD494	149.0 - 149.2	GM58352	47.56	47.62	47.51	47.56	143	144	144	143.50	254.97	699.00	2.74	3.02
6	AMPH	CAD346	68.3 - 68.5	GM58354	62.95	62.86	62.85	62.89	194	193	193	193.17	599.98	1820.00	3.03	3.07
7	AMPH	CAD562	322.2 - 322.4	GM58358	60.82	60.78	60.79	60.80	176	176	177	176.33	511.90	1413.00	2.76	2.90
8	AMPH	CAD494	291.0 - 291.2	GM58360	47.37	47.55	47.54	47.49	143	143	143	143.00	253.26	777.00	3.07	3.01
9	AMPH	CAD387	254.1 - 254.3	GM58362	61.02	61.03	61.02	61.02	184	185	184	184.33	539.12	1661.00	3.08	3.02
10	PEGM	CAD033	261.1 - 261.3	GM58366	50.65	50.59	50.61	50.62	151	151	151	151.00	303.85	792.00	2.61	2.98
11	PEGM	CAD503	257.0 - 257.2	GM58368	47.36	47.39	47.40	47.38	139	140	139	139.33	245.69	648.00	2.64	2.94
12	PEGM	CAD299	248.4 - 248.6	GM58370	47.30	47.33	47.31	47.31	142	143	143	142.67	250.83	659.00	2.63	3.02
13	PEGM	CAD387	248.9 - 249.1	GM58372	61.38	61.31	61.38	61.36	184	184	182	183.33	542.07	1399.00	2.58	2.99
14	GNES	CAD530	96.7 - 96.9	GM58374	61.05	61.05	61.03	61.04	183	182	184	183.00	535.57	1436.00	2.68	3.00
15	GNES	CAD373	116.0 - 116.2	GM58376	63.15	63.33	63.32	63.27	181	182	181	181.33	570.06	1495.00	2.62	2.87
16	GNES	CAD531	163.6 - 164.0	GM58378	60.98	61.12	61.13	61.08	183	184	184	183.67	538.11	1437.00	2.67	3.01
17	GNES	CAD495	152.5 - 152.7	GM58380	61.04	60.94	60.86	60.95	184	183	184	183.67	535.82	1414.00	2.64	3.01
18	GNES	CAD519	138.1 - 138.3	GM58382	60.80	60.93	60.94	60.89	188	187	186	187.00	544.53	1436.00	2.64	3.07
19	Burnham	CAD562	263.5 - 263.7	GM58384	63.43	63.37	63.39	63.40	193	192	192	192.33	607.12	2593.00	4.27	3.03
20	Burnham	CAD564a	246.5 - 246.7	GM58386	63.21	63.19	63.18	63.19	190	190	189	189.67	594.87	2542.00	4.27	3.00
21	Burnham	CAD563	217.0 - 217.2	GM58388	63.40	63.51	63.41	63.44	191	192	191	191.33	604.79	2777.00	4.59	3.02
22	Broadlands	CAD562	212.4 - 212.6	GM58394	63.54	63.52	63.53	63.53	191	192	193	192.00	608.62	2072.00	3.40	3.02
23	Broadlands	CAD563	190.2 - 190.5	GM58396	63.37	63.41	63.46	63.41	190	190	189	189.67	599.02	2185.00	3.65	2.99
24	Broadlands	CAD566	87.1 - 87.3	GM58398	SAMPLE NOT RECEIVED ON DELIVERY											
25	Broadlands	CAD564a	203.7 - 203.9	GM58400	63.33	63.30	63.40	63.34	190	190	190	190.00	598.75	2111.00	3.53	3.00
26	Glenholm	CAD386	287.5 - 287.8	GM58404	61.10	61.09	61.10	61.10	183	184	185	184.00	539.44	2176.00	4.03	3.01
27	Glenholm	CAD564a	120.4 - 120.6	GM58406	63.48	63.43	63.43	63.45	195	195	196	195.33	617.57	2341.00	3.79	3.08
28	Glenholm	CAD562	204.4 - 204.7	GM58408	63.53	63.36	63.36	63.42	193	193	192	192.67	608.56	2366.00	3.89	3.04
29	Glenholm	CAD563	61.6 - 61.8	GM58410	63.30	63.30	63.39	63.33	188	188	188	188.00	592.20	2075.00	3.50	2.97

Table A4.7. 1 Sample Properties - Poisson's Ratio Testing (cont. 1)

					Sample Dimensions											
					Diameter, ϕ, (mm)				Height, H, (mm)							
No.	Rock Type	Hole	Sample Interval	Sample Number	ϕ_1	ϕ_2	ϕ_3	Avg	H_1	H_2	H_3	Avg	*Volume* *(cm^3)*	*Mass* *(g)*	Bulk Density (Kg/m^3)	Aspect Ratio (H/ϕ)
30	QZGA/IT	CAD386	284.2 - 284.6	GM58414	61.11	61.10	61.07	61.09	184	183	184	183.67	538.40	1614.00	3.00	3.01
31	QZGA/IT	CAD387	75.2 - 75.5	GM58416	61.03	61.24	61.07	61.11	183	183	182	182.67	535.82	1575.00	2.94	2.99
32	QZGA/IT	CAD562	227.5 - 227.7	GM58418	63.48	63.44	63.46	63.46	192	193	194	193.00	610.45	1849.00	3.03	3.04
33	QZGA/IT	CAD564a	71.4 - 71.6	GM58422	63.55	63.49	63.47	63.50	192	192	193	192.33	609.17	1691.00	2.78	3.03
34	QZHD	CAD386	288.7 - 289.0	GM58424	61.38	61.09	61.08	61.18	183	183	184	183.17	538.52	1886.00	3.50	2.99
35	QZHD	CAD387	163.8 - 164.0	GM58426	60.86	60.88	60.91	60.88	186	186	187	186.17	541.99	1849.00	3.41	3.06
36	QZHD	CAD562	219.7 - 219.9	GM58428	63.60	63.50	63.53	63.54	190	190	189	189.67	601.48	1883.00	3.13	2.98
37	QZHD	CAD564a	137.1 - 137.3	GM58430	63.41	63.30	63.40	63.37	193	191	192	192.00	605.56	1934.00	3.19	3.03
38	QZHD	CAD563	113.0 - 113.2	GM58432	63.30	63.25	63.40	63.32	191	190	190	190.33	599.30	1968.00	3.28	3.01
39	HDMT	CAD387	160.5 - 160.7	GM58434	61.90	60.88	60.96	61.25	182	182	183	182.33	537.18	2113.00	3.93	2.98
40	HDMT	CAD386	208.8 - 209.1	GM58436	60.74	60.87	60.82	60.81	187	187	186	186.67	542.13	2291.00	4.23	3.07
41	HDMT	CAD563	211.4 - 211.6	GM58438	63.38	63.37	63.33	63.36	189	188	189	188.67	594.86	2636.00	4.43	2.98
42	PXAM	CAD387	164.6 - 164.8	GM58444	60.91	60.82	60.88	60.87	186	185	185	185.33	539.32	1963.00	3.64	3.04
43	PXAM	CAD562	82.8 - 83.0	GM58446	63.11	63.20	63.21	63.17	193	192	191	192.00	601.81	2291.00	3.81	3.04
44	PXAM	CAD563	32.8 - 33.0	GM58448	63.28	63.26	63.22	63.25	188	188	189	188.33	591.81	2254.00	3.81	2.98

Table A4.7. 2 Poisson's Ratio Testing Results

No.	Rock Type	Sample Number	f_{av}	H_{av}	Δl (mm)	Δd_{1-3} (mm)	Δd_{2-4} (mm)	ε_a	$\varepsilon_{d\,(1-3)}$	$\varepsilon_{d\,(2-4)}$	ν_{av}	Comments
1	SHMU	GM58344	47.50	141.83	0.853	0.116	0.002	0.006	0.002	0.000	0.207	
2	SHMU	GM58346	50.43	149.00	0.295	0.002	0.020	0.002	0.000	0.000	0.110	
3	SHMU	GM58348	63.35	185.67	0.137	0.002	0.010	0.001	0.000	0.000	0.128	
4	SHMU	GM58350	63.25	191.67	0.297	0.002	0.006	0.002	0.000	0.000	0.041	
5	SHMU	GM58352	47.56	143.50	0.347	0.006	0.014	0.002	0.000	0.000	0.087	
Rock Type:-	***SHMU***				***Average Poisson's Ratio, n (av).***						***0.115***	
6	AMPH	GM58354	62.89	193.17	0.485	0.004	0.020	0.003	0.000	0.000	0.076	
7	AMPH	GM58358	60.80	176.33	0.000	0.000	0.000	0.000	0.000	0.000	#DIV/0!	Sample failed below 100kN - No Results Obtained
8	AMPH	GM58360	47.49	143.00	0.300	0.004	0.006	0.002	0.000	0.000	0.050	
9	AMPH	GM58362	61.02	184.33	0.441	0.006	0.040	0.002	0.000	0.001	0.158	
Rock Type:-	***AMPH***				***Average Poisson's Ratio, n (av).***						***0.095***	
10	PEGM	GM58366	50.62	151.00	0.484	0.066	0.052	0.003	0.001	0.001	0.364	
11	PEGM	GM58368	47.38	139.33	0.292	0.004	0.048	0.002	0.000	0.001	0.262	Cracking visible in sample
12	PEGM	GM58370	47.31	142.67	0.294	0.006	0.012	0.002	0.000	0.000	0.092	
13	PEGM	GM58372	61.36	183.33	0.437	0.006	0.038	0.002	0.000	0.001	0.150	
Rock Type:-	***PEGM***				***Average Poisson's Ratio, n (av).***						***0.217***	
14	GNES	GM58374	61.04	183.00	0.000	0.000	0.000	0.000	0.000	0.000	#DIV/0!	Sample failed - No Results Obtained
15	GNES	GM58376	63.27	181.33	0.528	0.048	0.052	0.003	0.001	0.001	0.271	
16	GNES	GM58378	61.08	183.67	0.330	0.042	0.034	0.002	0.001	0.001	0.346	
17	GNES	GM58380	60.95	183.67	0.551	0.035	0.020	0.003	0.001	0.000	0.150	
18	GNES	GM58382	60.89	187.00	0.603	0.036	0.024	0.003	0.001	0.000	0.153	
Rock Type:-	***GNES***				***Average Poisson's Ratio, n (av).***						***0.230***	
19	Burnham	GM58384	63.40	192.33	0.617	0.098	0.020	0.003	0.002	0.000	0.290	
20	Burnham	GM58386	63.19	189.67	0.377	0.000	0.026	0.002	0.000	0.000	0.103	
21	Burnham	GM58388	63.44	191.33	0.432	0.035	0.036	0.002	0.001	0.001	0.248	
Rock Type:-	***Burnham***				***Average Poisson's Ratio, n (av).***						***0.214***	

Table A4.7. 2 Poisson's Ratio Testing Results (cont.)

No.	Rock Type	Sample Number	f_{av}	H_{av}	Δl (mm)	Δd_{1-3} (mm)	Δd_{2-4} (mm)	ε_a	$\varepsilon_{d\,(1-3)}$	$\varepsilon_{d\,(2-4)}$	ν_{av}	Comments
22	Broadlands	GM58394	63.53	192.00	0.510	0.070	0.002	0.003	0.001	0.000	0.213	
23	Broadlands	GM58396	63.41	189.67	0.510	0.049	0.012	0.003	0.001	0.000	0.179	
24	Broadlands	GM58398	0.00	0.00	0.000	0.000	0.000	#DIV/0!	#DIV/0!	#DIV/0!	#DIV/0!	Sample failed - No Results Obtained
25	Broadlands	GM58400	63.34	190.00	0.423	0.016	0.014	0.002	0.000	0.000	0.106	
Rock Type:-	***Broadlands***				***Average Poisson's Ratio, n (av).***						***0.166***	
26	Glenholm	GM58404	61.10	184.00	0.363	0.011	0.004	0.002	0.000	0.000	0.062	
27	Glenholm	GM58406	63.45	195.33	0.535	0.008	0.010	0.003	0.000	0.000	0.052	
28	Glenholm	GM58408	63.42	192.67	0.516	0.020	0.022	0.003	0.000	0.000	0.124	
29	Glenholm	GM58410	63.33	188.00	0.407	0.028	0.024	0.002	0.000	0.000	0.190	
Rock Type:-	***Glenholm***				***Average Poisson's Ratio, n (av).***						***0.107***	
30	QZGA/IT	GM58414	61.09	183.67	0.418	0.018	0.040	0.002	0.000	0.001	0.209	
31	QZGA/IT	GM58416	61.11	182.67	0.445	0.009	0.010	0.002	0.000	0.000	0.064	
32	QZGA/IT	GM58418	63.46	193.00	0.408	0.010	0.026	0.002	0.000	0.000	0.134	
33	QZGA/IT	GM58422	63.50	192.33	0.523	0.046	0.048	0.003	0.001	0.001	0.272	
Rock Type:-	***QZGA/IT***				***Average Poisson's Ratio, n (av).***						***0.170***	
34	QZHD	GM58424	61.18	183.17	0.000	0.000	0.000	0.000	0.000	0.000	#DIV/0!	Sample failed below max. applied load.
35	QZHD	GM58426	60.88	186.17	0.387	0.004	0.020	0.002	0.000	0.000	0.095	
36	QZHD	GM58428	63.54	189.67	0.474	0.034	0.022	0.002	0.001	0.000	0.176	Sample broke during Poisson's ratio testing
37	QZHD	GM58430	63.37	192.00	0.413	0.015	0.004	0.002	0.000	0.000	0.070	
38	QZHD	GM58432	63.32	190.33	0.535	0.018	0.050	0.003	0.000	0.001	0.191	
Rock Type:-	***QZHD***				***Average Poisson's Ratio, n (av).***						***0.133***	
39	HDMT	GM58434	61.25	182.33	0.401	0.010	0.018	0.002	0.000	0.000	0.104	
40	HDMT	GM58436	60.81	186.67	0.445	0.036	0.016	0.002	0.001	0.000	0.179	
41	HDMT	GM58438	63.36	188.67	0.483	0.028	0.008	0.003	0.000	0.000	0.111	
Rock Type:-	***HDMT***				***Average Poisson's Ratio, n (av).***						***0.131***	
42	PXAM	GM58444	60.87	185.33	0.399	0.020	0.028	0.002	0.000	0.000	0.183	
43	PXAM	GM58446	63.17	192.00	0.570	0.020	0.002	0.003	0.000	0.000	0.059	
44	PXAM	GM58448	63.25	188.33	0.601	0.058	0.050	0.003	0.001	0.001	0.268	
Rock Type:-	***PXAM***				***Average Poisson's Ratio, n (av).***						***0.170***	

APPENDIX 6.1

FLAC^{3D} code for Numerical Model

- *Excerpts from Numerical Code*

STOPE.dat

```
def inputparameters
coh_case= in (' Input Cohesion of Paste (Pa): ')
pastecoh=coh_case
;
fric_case= in (' Input Friction Angle of Paste (Degrees): ')
pastefric=fric_case
;
tens_case= in (' Input Tension of Paste (Pa): ')
pastetens=tens_case
;
Youngs_case= in (' Input Youngs Modulus of Paste (Pa): ')
pasteymod=bulk_case
;
pois_case= in (' Input Poissons Ratio of Paste : ')
pastepratio=pois_case
;
bulk_case= in (' Input Bulk Modulus of Rock (kg/m3): ')
rockbmod=bulk_case
;
she_case= in (' Input Shear Modulus of Rock (pa) : ')
rocksmod=she_case
;
end
inputparameters
;
call rocksolve.dat
```

ROCKSOLVE.dat

```
; Define all constants
def mod_parameters
width=25 ; width
depth=25 ; depth
height=50 ; height
midwidth=width/2
middepth=depth/2
heightsize=10 ; number of zones in height
widthsize=8 ; number of zones in width
depthsize=8 ; number of zones in depth
```

```
totwzones=3*widthsize ; total number of zones across width of model
totdzones=3*depthsize ; total number of zones across depth of model
end
mod_parameters
;
define mod_setup
dis_2=0.001
dis_1=-0.001
negwidth=-1*width
negdepth=-1*depth
outreach_x=2*width
outreach_z=2*depth
pwidth=width+dis_1
nwidth=width+dis_2
pdepth=depth+dis_1
ndepth=depth+dis_2
xbound_1=outreach_x+dis_1
xbound_2=outreach_x+dis_2
negxbound_1=-1*width+dis_1
negxbound_2=-1*width+dis_2
zbound_1=outreach_z+dis_1
zbound_2=outreach_z+dis_2
negzbound_1=-1*depth+dis_1
negzbound_2=-1*depth+dis_2
middepth=depth/2
end
mod_setup
;
; --- Specify Rock Grid ---
gen zone brick size totwzones heightsize totdzones rat 1 1 1  p0 negwidth 0 negdepth p1 outreach_x 0
negdepth p2 negwidth height negdepth &
p3 negwidth 0 outreach_z
;
; --- Assign Groups ---
group stope1 range x 0 width y 0 height z 0 depth
group stope2 range x width outreach_x y 0 height z 0 depth
group stope3 range x negwidth 0 y 0 height z 0 depth
group stope4 range x width outreach_x y 0 height z depth outreach_z
group stope5 range x 0 width y 0 height z depth outreach_z
group stope6 range x negwidth 0 y 0 height z depth outreach_z
```

```
group stope7 range x width outreach_x y 0 height z negdepth 0
group stope8 range x 0 width y 0 height z negdepth 0
group stope9 range x negwidth 0 y 0 height z negdepth 0
;
; --- Assign Range Names of Stopes ---
range name=stope1 group stope1
range name=stope2 group stope2
range name=stope3 group stope3
range name=stope4 group stope4
range name=stope5 group stope5
range name=stope6 group stope6
range name=stope7 group stope7
range name=stope8 group stope8
range name=stope9 group stope9
;
; --- Assign models to stopes ---
model elastic
;
; --- Assign Properties ---
prop bulk rockbmod shear rocksmod dens 2600
;
;--- Initial conditions ---
set grav 0 -9.81 0
;
; Boundary Conditions
fix x y z range z zbound_1 zbound_2
fix x y z range z negzbound_1 negzbound_2
fix x y z range x xbound_1 xbound_2
fix x y z range x negxbound_1 negxbound_2
fix y range y dis_1 dis_2
;
solve
;

save rockcond.sav
call nullstope1.dat
save stope1nulled.sav
call fillingstope1.dat
save stope1filled.sav
;
```

```
call nullstope2.dat
save stope2nulled.sav
call fillingstope2.dat
save stope2filled.sav
;
call nullstope3.dat
save stope3nulled.sav
call fillingstope3.dat
save stope3filled.sav
;
call nullstope4.dat
save stope4nulled.sav
call fillingstope4.dat
save stope4filled.sav
;
call nullstope5.dat
save stope5nulled.sav
call fillingstope5.dat
save stope5filled.sav
;
call nullstope6.dat
save stope6nulled.sav
call fillingstope6.dat
save stope6filled.sav
;
call nullstope7.dat
save stope7nulled.sav
call fillingstope7.dat
save stope7filled.sav
;
call nullstope8.dat
save stope8nulled.sav
call fillingstope8.dat
save stope8filled.sav
;
call nullstope9.dat
save stope9nulled.sav
call fillingstope9.dat
save stope9filled.sav
;
```

THEBRICK1.dat

```
define step1
command
model mohr range group lift1
prop bulk pastebmod7 shear pastesmod7 dens 2100 coh pastecoh fric pastefric tens pastetens range group lift1
model null range group lift2
model null range group lift3
model null range group lift4
model null range group lift5
model null range group lift6
model null range group lift7
model null range group lift8
model null range group lift9
model null range group lift10
end_command
end
;
define step2
command
model mohr range lift1
prop bulk pastebmod14 shear pastesmod14 coh pastecoh fric pastefric tens pastetens range lift1
model mohr range lift2
prop bulk pastebmod7 shear pastesmod7 dens 2100 coh pastecoh fric pastefric tens pastetens range lift2
model null range group lift3
model null range group lift4
model null range group lift5
model null range group lift6
model null range group lift7
model null range group lift8
model null range group lift9
model null range group lift10
end_command
end
;
define step3
command
model mohr range lift1
prop bulk pastebmod21 shear pastesmod21 coh pastecoh fric pastefric tens pastetens range lift1
model mohr range lift2
```

```
prop bulk pastebmod14 shear pastesmod14 coh pastecoh fric pastefric tens pastetens range lift2
model mohr range lift3
prop bulk pastebmod7 shear pastesmod7 dens 2100 coh pastecoh fric pastefric tens pastetens range lift3
model null range group lift4
model null range group lift5
model null range group lift6
model null range group lift7
model null range group lift8
model null range group lift9
model null range group lift10
end_command
end
;
define step4
command
model mohr range lift1
prop bulk pastebmod28 shear pastesmod28 coh pastecoh fric pastefric tens pastetens range lift1
model mohr range lift2
prop bulk pastebmod21 shear pastesmod21 coh pastecoh fric pastefric tens pastetens range lift2
model mohr range lift3
prop bulk pastebmod14 shear pastesmod14 coh pastecoh fric pastefric tens pastetens range lift3
model mohr range lift4
prop bulk pastebmod7 shear pastesmod7 dens 2100 coh pastecoh fric pastefric tens pastetens range lift4
model null range group lift5
model null range group lift6
model null range group lift7
model null range group lift8
model null range group lift9
model null range group lift10
end_command
end
;
define step5
command
model mohr range lift1
prop bulk pastebmod35 shear pastesmod35 coh pastecoh fric pastefric tens pastetens range lift1
model mohr range lift2
prop bulk pastebmod28 shear pastesmod28 coh pastecoh fric pastefric tens pastetens range lift2
model mohr range lift3
prop bulk pastebmod21 shear pastesmod21 coh pastecoh fric pastefric tens pastetens range lift3
```

```
model mohr range lift4
prop bulk pastebmod14 shear pastesmod14 coh pastecoh fric pastefric tens pastetens range lift4
model mohr range lift5
prop bulk pastebmod7 shear pastesmod7 dens 2100 coh pastecoh fric pastefric tens pastetens range lift5
model null range group lift6
model null range group lift7
model null range group lift8
model null range group lift9
model null range group lift10
end_command
end
;
define step6
command
model mohr range lift1
prop bulk pastebmod42 shear pastesmod42 coh pastecoh fric pastefric tens pastetens range lift1
model mohr range lift2
prop bulk pastebmod35 shear pastesmod35 coh pastecoh fric pastefric tens pastetens range lift2
model mohr range lift3
prop bulk pastebmod28 shear pastesmod28 coh pastecoh fric pastefric tens pastetens range lift3
model mohr range lift4
prop bulk pastebmod21 shear pastesmod21 coh pastecoh fric pastefric tens pastetens range lift4
model mohr range lift5
prop bulk pastebmod14 shear pastesmod14 coh pastecoh fric pastefric tens pastetens range lift5
model mohr range lift6
prop bulk pastebmod7 shear pastesmod7 dens 2100 coh pastecoh fric pastefric tens pastetens range lift6
model null range group lift7
model null range group lift8
model null range group lift9
model null range group lift10
end_command
end
;
define step7
command
model mohr range lift1
prop bulk pastebmod49 shear pastesmod49 coh pastecoh fric pastefric tens pastetens range lift1
model mohr range lift2
prop bulk pastebmod42 shear pastesmod42 coh pastecoh fric pastefric tens pastetens range lift2
model mohr range lift3
```

```
prop bulk pastebmod35 shear pastesmod35 coh pastecoh fric pastefric tens pastetens range lift3
model mohr range lift4
prop bulk pastebmod28 shear pastesmod28 coh pastecoh fric pastefric tens pastetens range lift4
model mohr range lift5
prop bulk pastebmod21 shear pastesmod28 coh pastecoh fric pastefric tens pastetens range lift5
model mohr range lift6
prop bulk pastebmod14 shear pastesmod14 coh pastecoh fric pastefric tens pastetens range lift6
model mohr range lift7
prop bulk pastebmod7 shear pastesmod7 dens 2100 coh pastecoh fric pastefric tens pastetens range lift7
model null range group lift8
model null range group lift9
model null range group lift10
end_command
end
;
define step8
command
model mohr range lift1
prop bulk pastebmod56 shear pastesmod56 coh pastecoh fric pastefric tens pastetens range lift1
model mohr range lift2
prop bulk pastebmod49 shear pastesmod49 coh pastecoh fric pastefric tens pastetens range lift2
model mohr range lift3
prop bulk pastebmod42 shear pastesmod42 coh pastecoh fric pastefric tens pastetens range lift3
model mohr range lift4
prop bulk pastebmod35 shear pastesmod35 coh pastecoh fric pastefric tens pastetens range lift4
model mohr range lift5
prop bulk pastebmod28 shear pastesmod28 coh pastecoh fric pastefric tens pastetens range lift5
model mohr range lift6
prop bulk pastebmod21 shear pastesmod21 coh pastecoh fric pastefric tens pastetens range lift6
model mohr range lift7
prop bulk pastebmod14 shear pastesmod14 coh pastecoh fric pastefric tens pastetens range lift7
model mohr range lift8
prop bulk pastebmod7 shear pastesmod7 dens 2100 coh pastecoh fric pastefric tens pastetens range lift8
model null range group lift9
model null range group lift10
end_command
end
;
define step9
command
```

```
model mohr range lift1
prop bulk pastebmod63 shear pastesmod63 coh pastecoh fric pastefric tens pastetens range lift1
model mohr range lift2
prop bulk pastebmod56 shear pastesmod56 coh pastecoh fric pastefric tens pastetens range lift2
model mohr range lift3
prop bulk pastebmod49 shear pastesmod49 coh pastecoh fric pastefric tens pastetens range lift3
model mohr range lift4
prop bulk pastebmod42 shear pastesmod42 coh pastecoh fric pastefric tens pastetens range lift4
model mohr range lift5
prop bulk pastebmod35 shear pastesmod35 coh pastecoh fric pastefric tens pastetens range lift5
model mohr range lift6
prop bulk pastebmod28 shear pastesmod28 coh pastecoh fric pastefric tens pastetens range lift6
model mohr range lift7
prop bulk pastebmod21 shear pastesmod21 coh pastecoh fric pastefric tens pastetens range lift7
model mohr range lift8
prop bulk pastebmod14 shear pastesmod14 coh pastecoh fric pastefric tens pastetens range lift8
model mohr range lift9
prop bulk pastebmod7 shear pastesmod7 dens 2100 coh pastecoh fric pastefric tens pastetens range lift9
model null range group lift10
end_command
end
;
define step10
command
model mohr range lift1
prop bulk pastebmod70 shear pastesmod70 coh pastecoh fric pastefric tens pastetens range lift1
model mohr range lift2
prop bulk pastebmod63 shear pastesmod63 coh pastecoh fric pastefric tens pastetens range lift2
model mohr range lift3
prop bulk pastebmod56 shear pastesmod56 coh pastecoh fric pastefric tens pastetens range lift3
model mohr range lift4
prop bulk pastebmod49 shear pastesmod49 coh pastecoh fric pastefric tens pastetens range lift4
model mohr range lift5
prop bulk pastebmod42 shear pastesmod42 coh pastecoh fric pastefric tens pastetens range lift5
model mohr range lift6
prop bulk pastebmod35 shear pastesmod35 coh pastecoh fric pastefric tens pastetens range lift6
model mohr range lift7
prop bulk pastebmod28 shear pastesmod28 coh pastecoh fric pastefric tens pastetens range lift7
model mohr range lift8
prop bulk pastebmod21 shear pastesmod21 coh pastecoh fric pastefric tens pastetens range lift8
```

```
model mohr range lift9
prop bulk pastebmod14 shear pastesmod14 coh pastecoh fric pastefric tens pastetens range lift9
model mohr range lift10
prop bulk pastebmod7 shear pastesmod7 dens 2100 coh pastecoh fric pastefric tens pastetens range lift10
end_command
end
```

NULLSTOPE1.dat

```
model null range group stope1
;
;--- Initial conditions ---
set grav 0 -9.81 0
;
; Boundary Conditions
fix x y z range z zbound_1 zbound_2
fix x y z range z negzbound_1 negzbound_2
fix x y z range x xbound_1 xbound_2
fix x y z range x negxbound_1 negxbound_2
fix y range y dis_1 dis_2
;
;
solve
;
;---Assign Names to Lift Zones---
Define Ranges
dely=height/heightsize
previousht=0
r=1
loop r(1,heightsize)
liftnumber=r
nextht=r*dely
numlift='lift'+string(liftnumber)
command
group numlift range x 0 width y previousht nextht z 0 depth
end_command
previousht=nextht
endloop
end
```

```
Ranges
;
;---Define Young's Modulus Ratios for Curing Time---
Define define_mods
pastesmod7=2.9422*pasteymod/(2*(1+pastepratio))
pastebmod7=2.9422*pasteymod/(3*(1-2*pastepratio))
;
pastesmod14=1.0497*pasteymod/(2*(1+pastepratio))
pastebmod14=1.0497*pasteymod/(3*(1-2*pastepratio))
;
pastesmod21=1.1922*pasteymod/(2*(1+pastepratio))
pastebmod21=1.1922*pasteymod/(3*(1-2*pastepratio))
;
pastesmod28=1.3348*pasteymod/(2*(1+pastepratio))
pastebmod28=1.3348*pasteymod/(3*(1-2*pastepratio))
;
pastesmod35=1.2511*pasteymod/(2*(1+pastepratio))
pastebmod35=1.2511*pasteymod/(3*(1-2*pastepratio))
;
pastesmod42=1.1674*pasteymod/(2*(1+pastepratio))
pastebmod42=1.1674*pasteymod/(3*(1-2*pastepratio))
;
pastesmod49=1.0837*pasteymod/(2*(1+pastepratio))
pastebmod49=1.0837*pasteymod/(3*(1-2*pastepratio))
;
pastesmod56=1*pasteymod/(2*(1+pastepratio))
pastebmod56=1*pasteymod/(3*(1-2*pastepratio))
;
pastesmod63=1*pasteymod/(2*(1+pastepratio))
pastebmod63=1*pasteymod/(3*(1-2*pastepratio))
;
pastesmod70=1*pasteymod/(2*(1+pastepratio))
pastebmod70=1*pasteymod/(3*(1-2*pastepratio))
;
pastesmod77=1*pasteymod/(2*(1+pastepratio))
pastebmod77=1*pasteymod/(3*(1-2*pastepratio))
;
pastesmod84=1*pasteymod/(2*(1+pastepratio))
pastebmod84=1*pasteymod/(3*(1-2*pastepratio))
;
```

```
pastesmod90=1*pasteymod/(2*(1+pastepratio))
pastebmod90=1*pasteymod/(3*(1-2*pastepratio))
;
pastesmodfull=pasteymod/(2*(1+pastepratio))
pastebmodfull=pasteymod/(3*(1-2*pastepratio))
;
end
define_mods
;
Define namesforlifts
command
;---Assign Range Names to Lift Groups---
range name lift1 group lift1
range name lift2 group lift2
range name lift3 group lift3
range name lift4 group lift4
range name lift5 group lift5
range name lift6 group lift6
range name lift7 group lift7
range name lift8 group lift8
range name lift9 group lift9
range name lift10 group lift10
end_command
end
namesforlifts
```

FILLINGSTOPE1.dat

```
Define Sequentialfilling
heightbound=height+0.01
pwidth=width+dis_1
nwidth=width+dis_2
pdepth=depth+dis_1
ndepth=depth+dis_2
previouscuredht=0
;
command
call thebrick1
call thebrick2
```

```
;
end_command
;
loop p(1,23)
liftnum=p
dely=height/heightsize
currentht=p*dely
previouscuredht=(p-2)*dely
curedht=(p-1)*dely
curedhtbound_1=curedht+dis_1
curedhtbound_2=curedht+dis_2
countht=p*dely
if countht<200
actualht=countht
else
actualht=200
end_if
;
caseof liftnum
;
case 1
command
step1
;---Boundary Conditions---
fix x y z range z zbound_1 zbound_2
fix x y z range z negzbound_1 negzbound_2
fix x y z range x xbound_1 xbound_2
fix x y z range x negxbound_1 negxbound_2
fix y range y dis_1 dis_2
;---Initial Conditions---
set grav 0 -9.81 0
solve
end_command
;
case 2
command
step2
;---Boundary Conditions---
fix x y z range z zbound_1 zbound_2
fix x y z range z negzbound_1 negzbound_2
```

```
fix x y z range x xbound_1 xbound_2
fix x y z range x negxbound_1 negxbound_2
fix y range y dis_1 dis_2
;---Initial Conditions---
set grav 0 -9.81 0
solve
end_command
;
case 3
command
step3
;---Boundary Conditions---
fix x y z range z zbound_1 zbound_2
fix x y z range z negzbound_1 negzbound_2
fix x y z range x xbound_1 xbound_2
fix x y z range x negxbound_1 negxbound_2
fix y range y dis_1 dis_2
;---Initial Conditions---
set grav 0 -9.81 0
solve
end_command
;
case 4
command
step4
;---Boundary Conditions---
fix x y z range z zbound_1 zbound_2
fix x y z range z negzbound_1 negzbound_2
fix x y z range x xbound_1 xbound_2
fix x y z range x negxbound_1 negxbound_2
fix y range y dis_1 dis_2
;---Initial Conditions---
set grav 0 -9.81 0
solve
end_command
;
case 5
command
step5
;---Boundary Conditions---
```

```
fix x y z range z zbound_1 zbound_2
fix x y z range z negzbound_1 negzbound_2
fix x y z range x xbound_1 xbound_2
fix x y z range x negxbound_1 negxbound_2
fix y range y dis_1 dis_2
;---Initial Conditions---
set grav 0 -9.81 0
solve
end_command
;
case 6
command
step6
;---Boundary Conditions---
fix x y z range z zbound_1 zbound_2
fix x y z range z negzbound_1 negzbound_2
fix x y z range x xbound_1 xbound_2
fix x y z range x negxbound_1 negxbound_2
fix y range y dis_1 dis_2
;---Initial Conditions---
set grav 0 -9.81 0
solve
end_command
;
case 7
command
step7
;---Boundary Conditions---
fix x y z range z zbound_1 zbound_2
fix x y z range z negzbound_1 negzbound_2
fix x y z range x xbound_1 xbound_2
fix x y z range x negxbound_1 negxbound_2
fix y range y dis_1 dis_2
;---Initial Conditions---
set grav 0 -9.81 0
solve
end_command
;
case 8
command
```

```
step8
;---Boundary Conditions---
fix x y z range z zbound_1 zbound_2
fix x y z range z negzbound_1 negzbound_2
fix x y z range x xbound_1 xbound_2
fix x y z range x negxbound_1 negxbound_2
fix y range y dis_1 dis_2
;---Initial Conditions---
set grav 0 -9.81 0
solve
end_command
;
case 9
command
step9
;---Boundary Conditions---
fix x y z range z zbound_1 zbound_2
fix x y z range z negzbound_1 negzbound_2
fix x y z range x xbound_1 xbound_2
fix x y z range x negxbound_1 negxbound_2
fix y range y dis_1 dis_2
;---Initial Conditions---
set grav 0 -9.81 0
solve
end_command
;
case 10
command
step10
;---Boundary Conditions---
fix x y z range z zbound_1 zbound_2
fix x y z range z negzbound_1 negzbound_2
fix x y z range x xbound_1 xbound_2
fix x y z range x negxbound_1 negxbound_2
fix y range y dis_1 dis_2
;---Initial Conditions---
set grav 0 -9.81 0
solve
end_command
;
```

```
case 11
command
step11
;---Boundary Conditions---
fix x y z range z zbound_1 zbound_2
fix x y z range z negzbound_1 negzbound_2
fix x y z range x xbound_1 xbound_2
fix x y z range x negxbound_1 negxbound_2
fix y range y dis_1 dis_2
;---Initial Conditions---
set grav 0 -9.81 0
solve
end_command
;
case 12
command
step12
;---Boundary Conditions---
fix x y z range z zbound_1 zbound_2
fix x y z range z negzbound_1 negzbound_2
fix x y z range x xbound_1 xbound_2
fix x y z range x negxbound_1 negxbound_2
fix y range y dis_1 dis_2
;---Initial Conditions---
set grav 0 -9.81 0
solve
end_command
;
case 13
command
step13
;---Boundary Conditions---
fix x y z range z zbound_1 zbound_2
fix x y z range z negzbound_1 negzbound_2
fix x y z range x xbound_1 xbound_2
fix x y z range x negxbound_1 negxbound_2
fix y range y dis_1 dis_2
;---Initial Conditions---
set grav 0 -9.81 0
solve
```

```
end_command
;
case 14
command
step14
;---Boundary Conditions---
fix x y z range z zbound_1 zbound_2
fix x y z range z negzbound_1 negzbound_2
fix x y z range x xbound_1 xbound_2
fix x y z range x negxbound_1 negxbound_2
fix y range y dis_1 dis_2
;---Initial Conditions---
set grav 0 -9.81 0
solve
end_command
;
case 15
command
step15
;---Boundary Conditions---
fix x y z range z zbound_1 zbound_2
fix x y z range z negzbound_1 negzbound_2
fix x y z range x xbound_1 xbound_2
fix x y z range x negxbound_1 negxbound_2
fix y range y dis_1 dis_2
;---Initial Conditions---
set grav 0 -9.81 0
solve
end_command
;
case 16
command
step16
;---Boundary Conditions---
fix x y z range z zbound_1 zbound_2
fix x y z range z negzbound_1 negzbound_2
fix x y z range x xbound_1 xbound_2
fix x y z range x negxbound_1 negxbound_2
fix y range y dis_1 dis_2
;---Initial Conditions---
```

```
set grav 0 -9.81 0
solve
end_command
;
case 17
command
step17
;---Boundary Conditions---
fix x y z range z zbound_1 zbound_2
fix x y z range z negzbound_1 negzbound_2
fix x y z range x xbound_1 xbound_2
fix x y z range x negxbound_1 negxbound_2
fix y range y dis_1 dis_2
;---Initial Conditions---
set grav 0 -9.81 0
solve
end_command
;
case 18
command
step18
;---Boundary Conditions---
fix x y z range z zbound_1 zbound_2
fix x y z range z negzbound_1 negzbound_2
fix x y z range x xbound_1 xbound_2
fix x y z range x negxbound_1 negxbound_2
fix y range y dis_1 dis_2
;---Initial Conditions---
set grav 0 -9.81 0
solve
end_command
;
case 19
command
step19
;---Boundary Conditions---
fix x y z range z zbound_1 zbound_2
fix x y z range z negzbound_1 negzbound_2
fix x y z range x xbound_1 xbound_2
fix x y z range x negxbound_1 negxbound_2
```

```
fix y range y dis_1 dis_2
;---Initial Conditions---
set grav 0 -9.81 0
solve
end_command
;
case 20
command
step20
;---Boundary Conditions---
fix x y z range z zbound_1 zbound_2
fix x y z range z negzbound_1 negzbound_2
fix x y z range x xbound_1 xbound_2
fix x y z range x negxbound_1 negxbound_2
fix y range y dis_1 dis_2
;---Initial Conditions---
set grav 0 -9.81 0
solve
end_command
;
case 21
command
step21
;---Boundary Conditions---
fix x y z range z zbound_1 zbound_2
fix x y z range z negzbound_1 negzbound_2
fix x y z range x xbound_1 xbound_2
fix x y z range x negxbound_1 negxbound_2
fix y range y dis_1 dis_2
;---Initial Conditions---
set grav 0 -9.81 0
solve
end_command
;
case 22
command
step22
;---Boundary Conditions---
fix x y z range z zbound_1 zbound_2
fix x y z range z negzbound_1 negzbound_2
```

```
fix x y z range x xbound_1 xbound_2
fix x y z range x negxbound_1 negxbound_2
fix y range y dis_1 dis_2
;---Initial Conditions---
set grav 0 -9.81 0
solve
end_command
;
case 23
command
step23
;---Boundary Conditions---
fix y range y dis_1 dis_2
fix x y z range z zbound_1 zbound_2
fix x y z range z negzbound_1 negzbound_2
fix x y z range x xbound_1 xbound_2
fix x y z range x negxbound_1 negxbound_2
fix y range y dis_1 dis_2
;---Initial Conditions---
set grav 0 -9.81 0
solve
end_command
;
end_case
;
end_loop
end
Sequentialfilling
save stope1filledcann.sav
```

SHEARPROFILE.dat

```
Define Sequentialfilling
heightbound=height+0.01
pwidth=width+dis_1
nwidth=width+dis_2
pdepth=depth+dis_1
ndepth=depth+dis_2
previouscuredht=0
;
command
call thebrick1
call thebrick2
;
end_command
```

```
;
loop p(1,23)
liftnum=p
dely=height/heightsize
currentht=p*dely
previouscuredht=(p-2)*dely
curedht=(p-1)*dely
curedhtbound_1=curedht+dis_1
curedhtbound_2=curedht+dis_2
countht=p*dely
if countht<200
actualht=countht
else
actualht=200
end_if
;
caseof liftnum
;
case 1
command
step1
;---Boundary Conditions---
fix x y z range z zbound_1 zbound_2
fix x y z range z negzbound_1 negzbound_2
fix x y z range x xbound_1 xbound_2
fix x y z range x negxbound_1 negxbound_2
fix y range y dis_1 dis_2
;---Initial Conditions---
set grav 0 -9.81 0
solve
end_command
;
case 2
command
step2
;---Boundary Conditions---
fix x y z range z zbound_1 zbound_2
fix x y z range z negzbound_1 negzbound_2
fix x y z range x xbound_1 xbound_2
fix x y z range x negxbound_1 negxbound_2
fix y range y dis_1 dis_2
;---Initial Conditions---
set grav 0 -9.81 0
solve
end_command
;
case 3
command
step3
;---Boundary Conditions---
fix x y z range z zbound_1 zbound_2
fix x y z range z negzbound_1 negzbound_2
fix x y z range x xbound_1 xbound_2
fix x y z range x negxbound_1 negxbound_2
fix y range y dis_1 dis_2
;---Initial Conditions---
set grav 0 -9.81 0
solve
end_command
;
```

```
case 4
command
step4
;---Boundary Conditions---
fix x y z range z zbound_1 zbound_2
fix x y z range z negzbound_1 negzbound_2
fix x y z range x xbound_1 xbound_2
fix x y z range x negxbound_1 negxbound_2
fix y range y dis_1 dis_2
;---Initial Conditions---
set grav 0 -9.81 0
solve
end_command
;
case 5
command
step5
;---Boundary Conditions---
fix x y z range z zbound_1 zbound_2
fix x y z range z negzbound_1 negzbound_2
fix x y z range x xbound_1 xbound_2
fix x y z range x negxbound_1 negxbound_2
fix y range y dis_1 dis_2
;---Initial Conditions---
set grav 0 -9.81 0
solve
end_command
;
case 6
command
step6
;---Boundary Conditions---
fix x y z range z zbound_1 zbound_2
fix x y z range z negzbound_1 negzbound_2
fix x y z range x xbound_1 xbound_2
fix x y z range x negxbound_1 negxbound_2
fix y range y dis_1 dis_2
;---Initial Conditions---
set grav 0 -9.81 0
solve
end_command
;
case 7
command
step7
;---Boundary Conditions---
fix x y z range z zbound_1 zbound_2
fix x y z range z negzbound_1 negzbound_2
fix x y z range x xbound_1 xbound_2
fix x y z range x negxbound_1 negxbound_2
fix y range y dis_1 dis_2
;---Initial Conditions---
set grav 0 -9.81 0
solve
end_command
;
case 8
command
step8
;---Boundary Conditions---
```

```
fix x y z range z zbound_1 zbound_2
fix x y z range z negzbound_1 negzbound_2
fix x y z range x xbound_1 xbound_2
fix x y z range x negxbound_1 negxbound_2
fix y range y dis_1 dis_2
;---Initial Conditions---
set grav 0 -9.81 0
solve
end_command
;
case 9
command
step9
;---Boundary Conditions---
fix x y z range z zbound_1 zbound_2
fix x y z range z negzbound_1 negzbound_2
fix x y z range x xbound_1 xbound_2
fix x y z range x negxbound_1 negxbound_2
fix y range y dis_1 dis_2
;---Initial Conditions---
set grav 0 -9.81 0
solve
end_command
;
case 10
command
step10
;---Boundary Conditions---
fix x y z range z zbound_1 zbound_2
fix x y z range z negzbound_1 negzbound_2
fix x y z range x xbound_1 xbound_2
fix x y z range x negxbound_1 negxbound_2
fix y range y dis_1 dis_2
;---Initial Conditions---
set grav 0 -9.81 0
solve
end_command
;
case 11
command
step11
;---Boundary Conditions---
fix x y z range z zbound_1 zbound_2
fix x y z range z negzbound_1 negzbound_2
fix x y z range x xbound_1 xbound_2
fix x y z range x negxbound_1 negxbound_2
fix y range y dis_1 dis_2
;---Initial Conditions---
set grav 0 -9.81 0
solve
end_command
;
case 12
command
step12
;---Boundary Conditions---
fix x y z range z zbound_1 zbound_2
fix x y z range z negzbound_1 negzbound_2
fix x y z range x xbound_1 xbound_2
fix x y z range x negxbound_1 negxbound_2
```

```
fix y range y dis_1 dis_2
;---Initial Conditions---
set grav 0 -9.81 0
solve
end_command
;
case 13
command
step13
;---Boundary Conditions---
fix x y z range z zbound_1 zbound_2
fix x y z range z negzbound_1 negzbound_2
fix x y z range x xbound_1 xbound_2
fix x y z range x negxbound_1 negxbound_2
fix y range y dis_1 dis_2
;---Initial Conditions---
set grav 0 -9.81 0
solve
end_command
;
case 14
command
step14
;---Boundary Conditions---
fix x y z range z zbound_1 zbound_2
fix x y z range z negzbound_1 negzbound_2
fix x y z range x xbound_1 xbound_2
fix x y z range x negxbound_1 negxbound_2
fix y range y dis_1 dis_2
;---Initial Conditions---
set grav 0 -9.81 0
solve
end_command
;
case 15
command
step15
;---Boundary Conditions---
fix x y z range z zbound_1 zbound_2
fix x y z range z negzbound_1 negzbound_2
fix x y z range x xbound_1 xbound_2
fix x y z range x negxbound_1 negxbound_2
fix y range y dis_1 dis_2
;---Initial Conditions---
set grav 0 -9.81 0
solve
end_command
;
case 16
command
step16
;---Boundary Conditions---
fix x y z range z zbound_1 zbound_2
fix x y z range z negzbound_1 negzbound_2
fix x y z range x xbound_1 xbound_2
fix x y z range x negxbound_1 negxbound_2
fix y range y dis_1 dis_2
;---Initial Conditions---
set grav 0 -9.81 0
solve
```

```
end_command
;
case 17
command
step17
;---Boundary Conditions---
fix x y z range z zbound_1 zbound_2
fix x y z range z negzbound_1 negzbound_2
fix x y z range x xbound_1 xbound_2
fix x y z range x negxbound_1 negxbound_2
fix y range y dis_1 dis_2
;---Initial Conditions---
set grav 0 -9.81 0
solve
end_command
;
case 18
command
step18
;---Boundary Conditions---
fix x y z range z zbound_1 zbound_2
fix x y z range z negzbound_1 negzbound_2
fix x y z range x xbound_1 xbound_2
fix x y z range x negxbound_1 negxbound_2
fix y range y dis_1 dis_2
;---Initial Conditions---
set grav 0 -9.81 0
solve
end_command
;
case 19
command
step19
;---Boundary Conditions---
fix x y z range z zbound_1 zbound_2
fix x y z range z negzbound_1 negzbound_2
fix x y z range x xbound_1 xbound_2
fix x y z range x negxbound_1 negxbound_2
fix y range y dis_1 dis_2
;---Initial Conditions---
set grav 0 -9.81 0
solve
end_command
;
case 20
command
step20
;---Boundary Conditions---
fix x y z range z zbound_1 zbound_2
fix x y z range z negzbound_1 negzbound_2
fix x y z range x xbound_1 xbound_2
fix x y z range x negxbound_1 negxbound_2
fix y range y dis_1 dis_2
;---Initial Conditions---
set grav 0 -9.81 0
solve
end_command
;
case 21
command
```

```
step21
;---Boundary Conditions---
fix x y z range z zbound_1 zbound_2
fix x y z range z negzbound_1 negzbound_2
fix x y z range x xbound_1 xbound_2
fix x y z range x negxbound_1 negxbound_2
fix y range y dis_1 dis_2
;---Initial Conditions---
set grav 0 -9.81 0
solve
end_command
;
case 22
command
step22
;---Boundary Conditions---
fix x y z range z zbound_1 zbound_2
fix x y z range z negzbound_1 negzbound_2
fix x y z range x xbound_1 xbound_2
fix x y z range x negxbound_1 negxbound_2
fix y range y dis_1 dis_2
;---Initial Conditions---
set grav 0 -9.81 0
solve
end_command
;
case 23
command
step23
;---Boundary Conditions---
fix y range y dis_1 dis_2
fix x y z range z zbound_1 zbound_2
fix x y z range z negzbound_1 negzbound_2
fix x y z range x xbound_1 xbound_2
fix x y z range x negxbound_1 negxbound_2
fix y range y dis_1 dis_2
;---Initial Conditions---
set grav 0 -9.81 0
solve
end_command
;
end_case
;
end_loop
end
Sequentialfilling
save stope1filledcann.sav
```

Note: This is only an except of the code that was available at the end of the PhD studies. It may not be the final FLAC3D program and does not constitute the full program. The inclusion in the thesis is done to provide a starting point/ reference point for any additional programming.

APPENDIX 6.2

Sensitivity Analysis Results

- *W:H Aspect Ratio Sensitivity Analysis Profiles*
  - *W= 18.75 m, 25 m, 37.5 m*
- *W:D Aspect Ratio Sensitivity Analysis Profiles*
  - *W= 18.75 m, 25 m, 37.5 m*

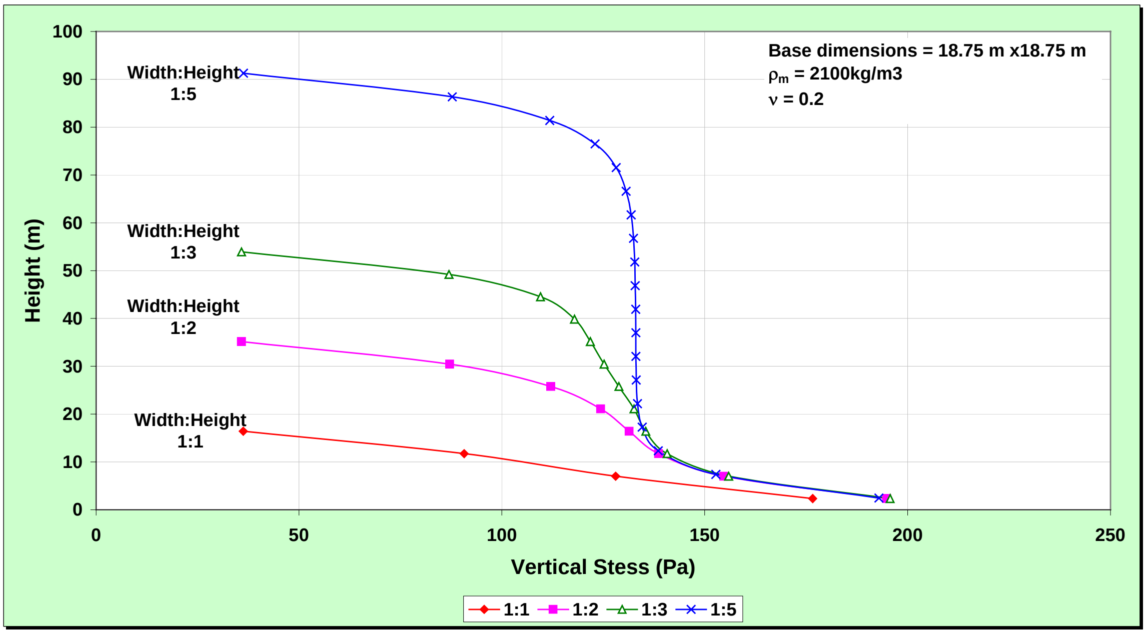

Figure A6.2.1 Effect of various W:H aspect ratios on the central vertical stress profile (W = 18.75m)

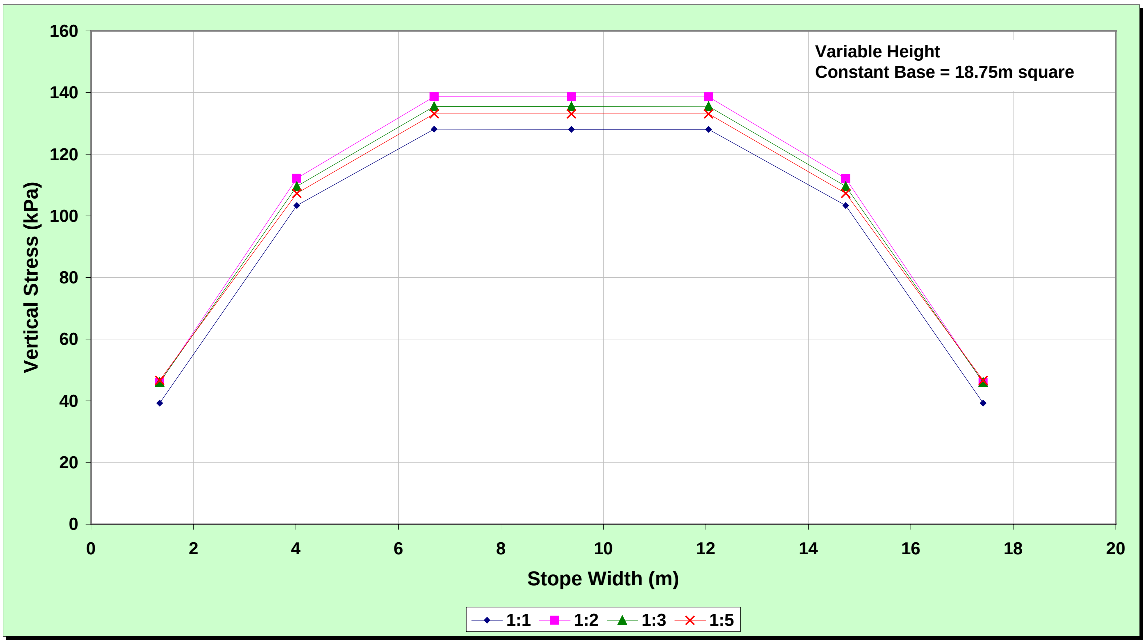

Figure A6.2.2 Vertical Stress profile across the centre of the stope for various W:H aspect ratios (W = 18.75m)

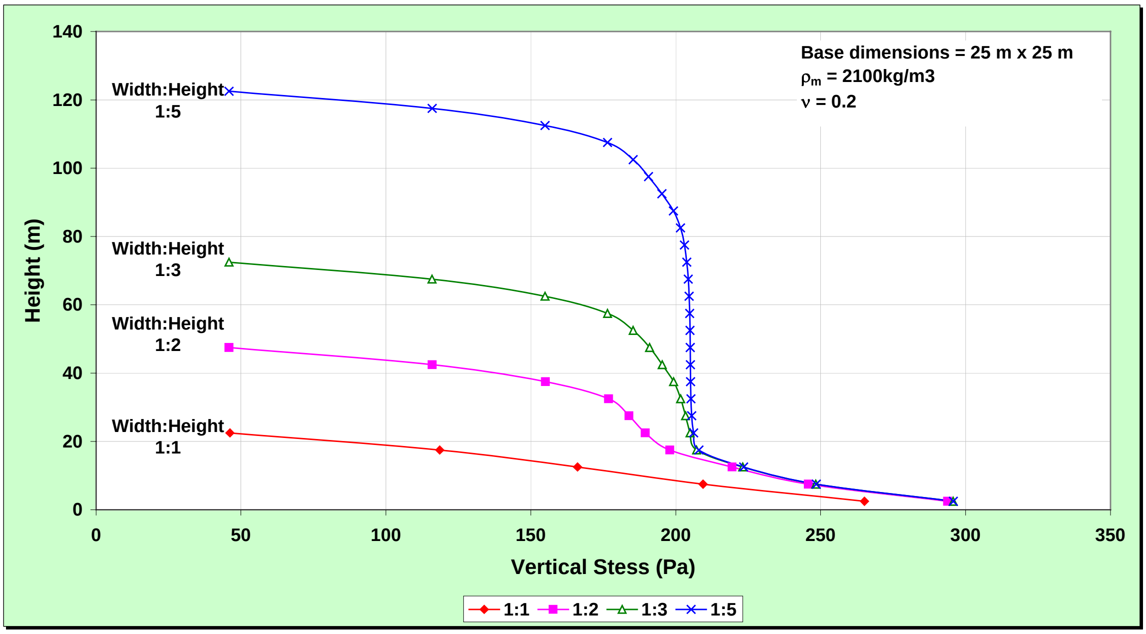

Figure A6.2.3 Effect of various W:H aspect ratios on the central vertical stress profile (W = 25 m)

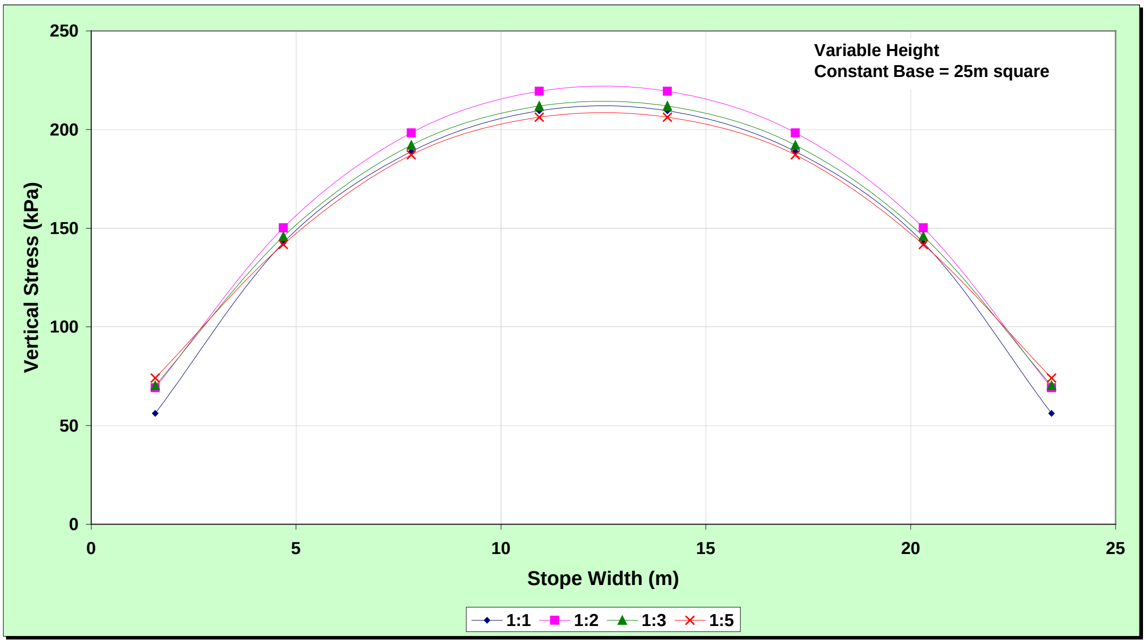

Figure A6.2.4 Vertical Stress profile across the centre of the stope for various W:H aspect ratios (W = 25 m)

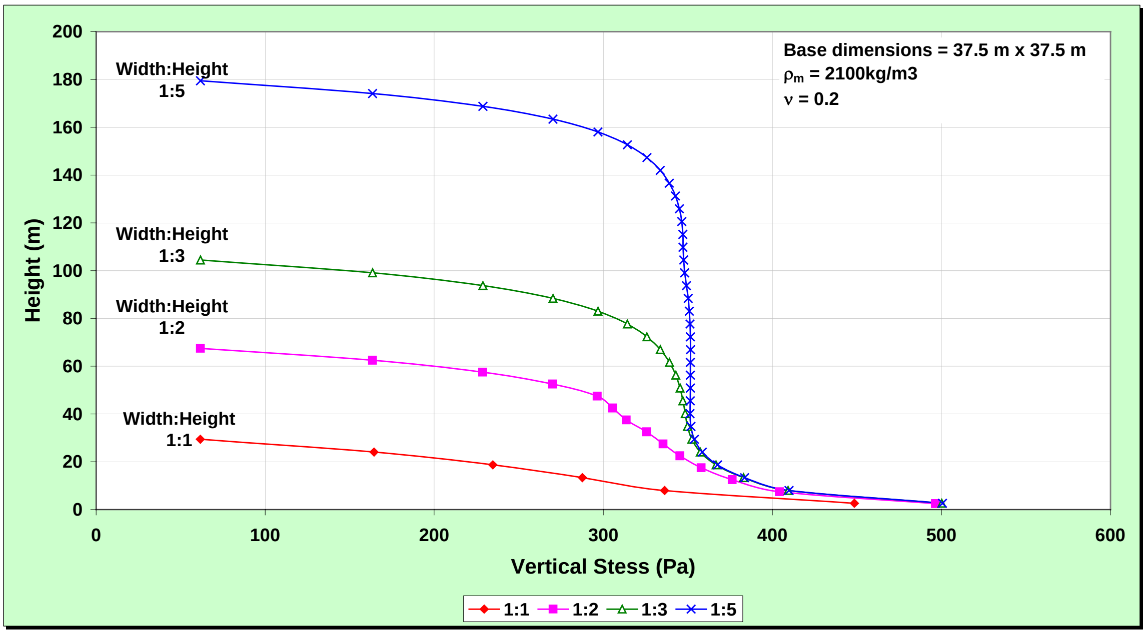

Figure A6.2.5 Effect of various W:H aspect ratios on the central vertical stress profile (W = 37.5 m)

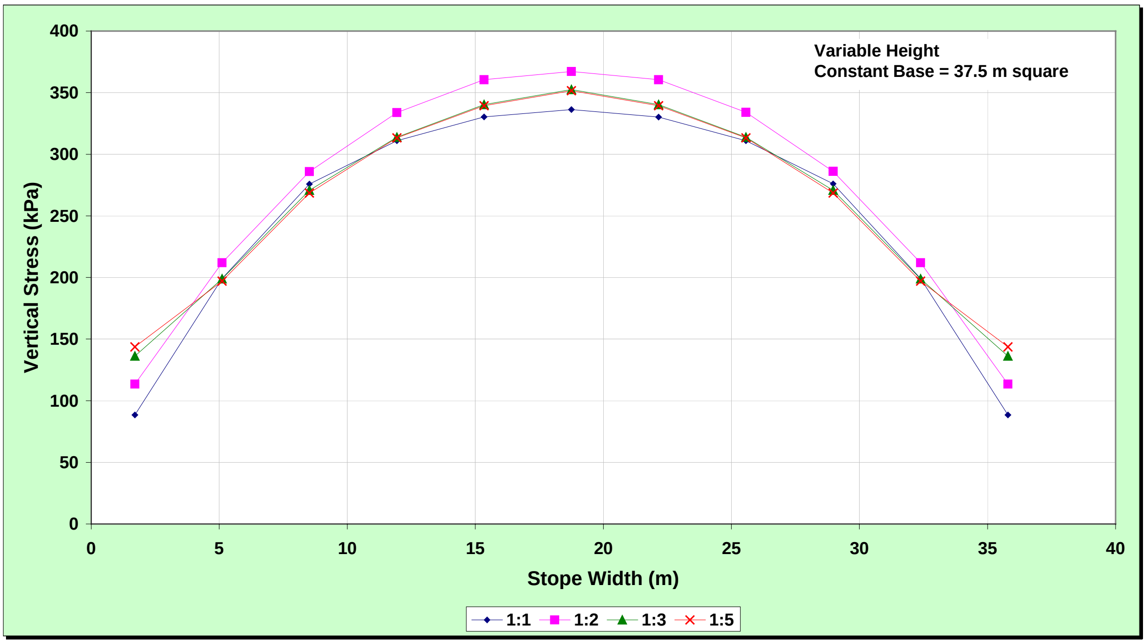

Figure A6.2.6 Vertical Stress profile across the centre of the stope for various W:H aspect ratios (W = 37.5 m)

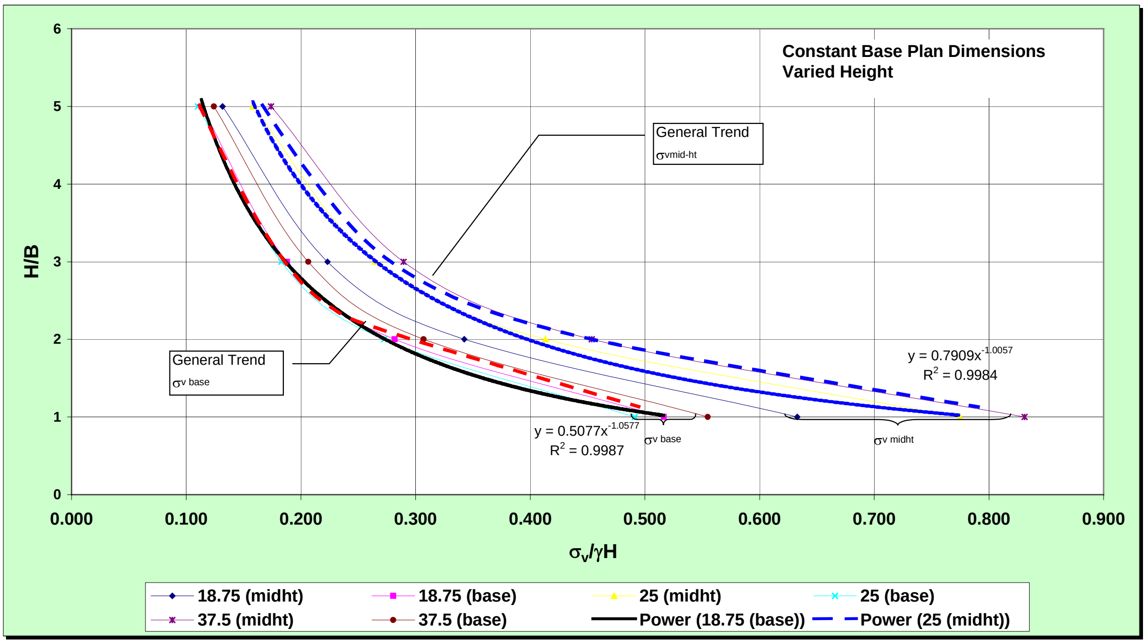

Figure A6.2.7 Plot of width to height aspect ratios against $\sigma_v/\gamma H$ at the base and mid-height of the stope.

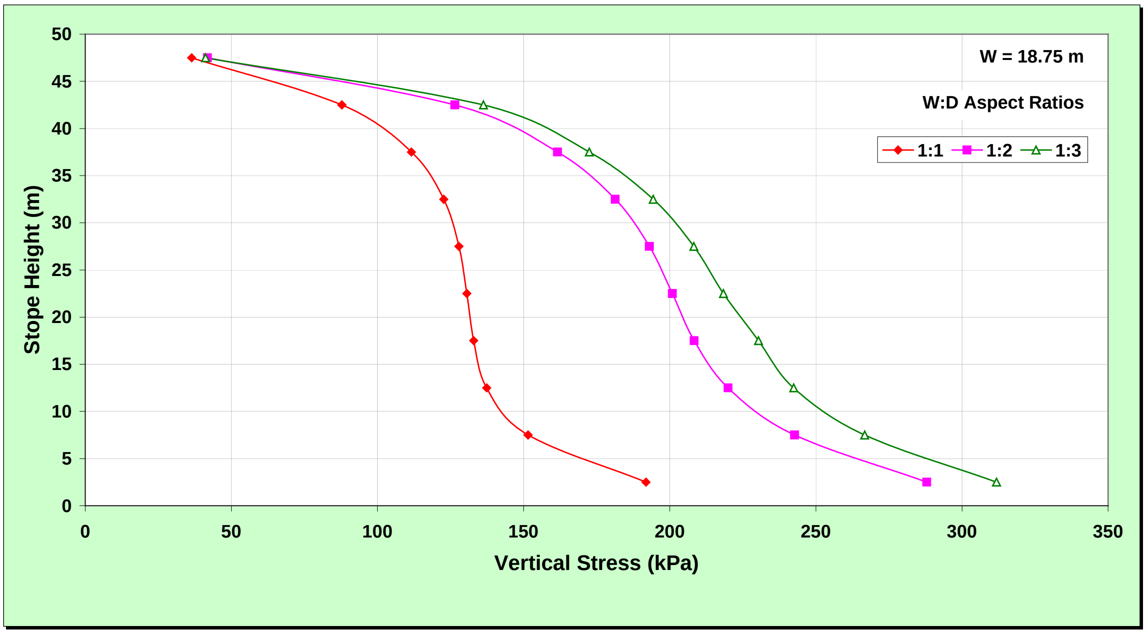

Figure A6.2.8 Central vertical stress profiling for a stope (constant height=50m, constant width = 18.75 m)

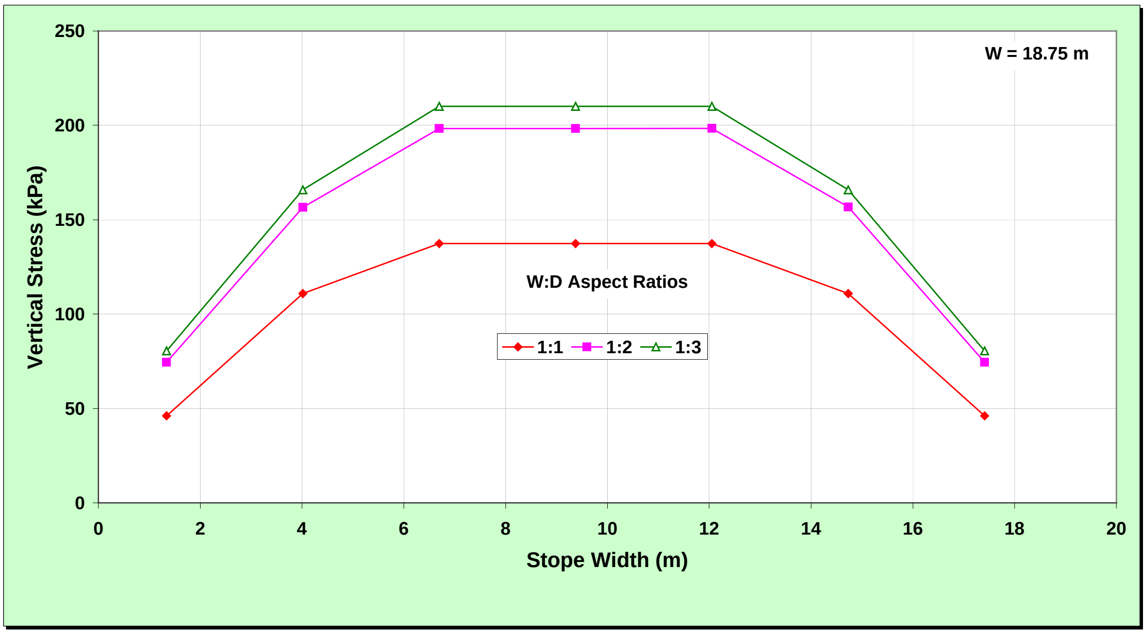

Figure A6.2.9 Vertical stress profiling across the constant width of a stope with varying depth (constant height=50m, constant width = 18.75m)

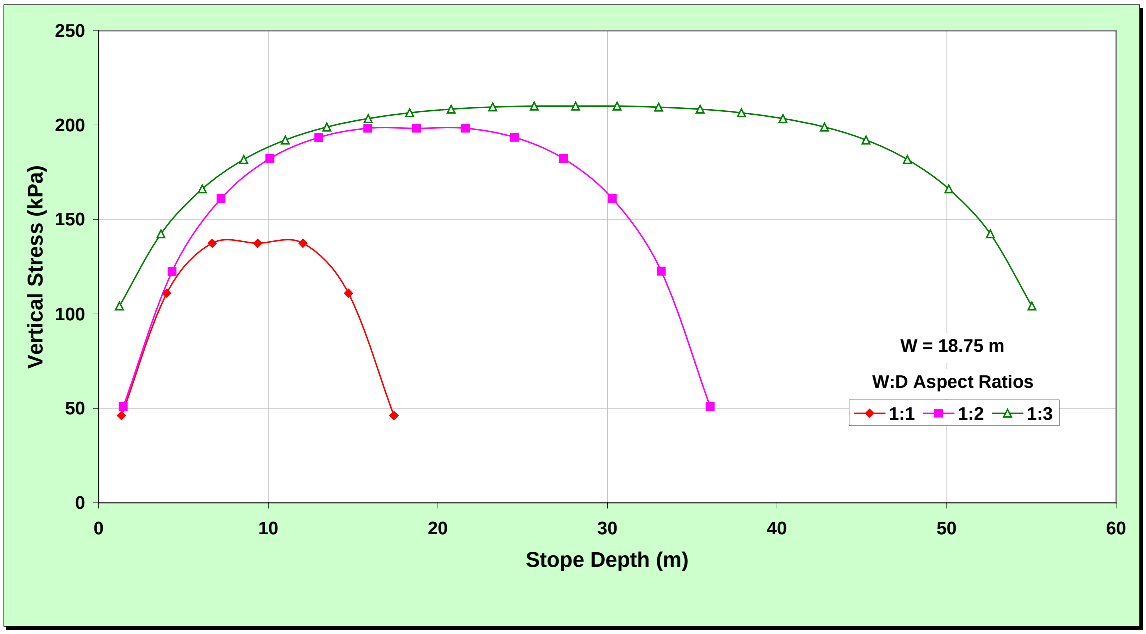

Figure A6.2.10 Vertical stress profiling down the longitudinal depth of a stope (constant height=50m, constant width = 18.75 m)

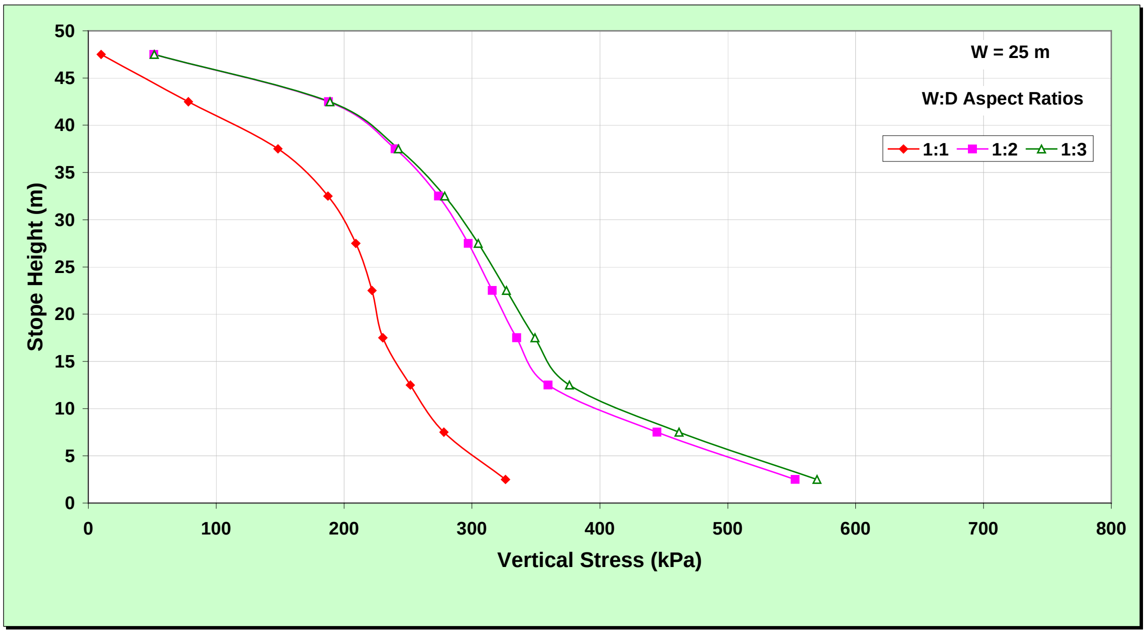

Figure A6.2.11 Central vertical stress profiling for a stope (constant height=50m, constant width = 25 m)

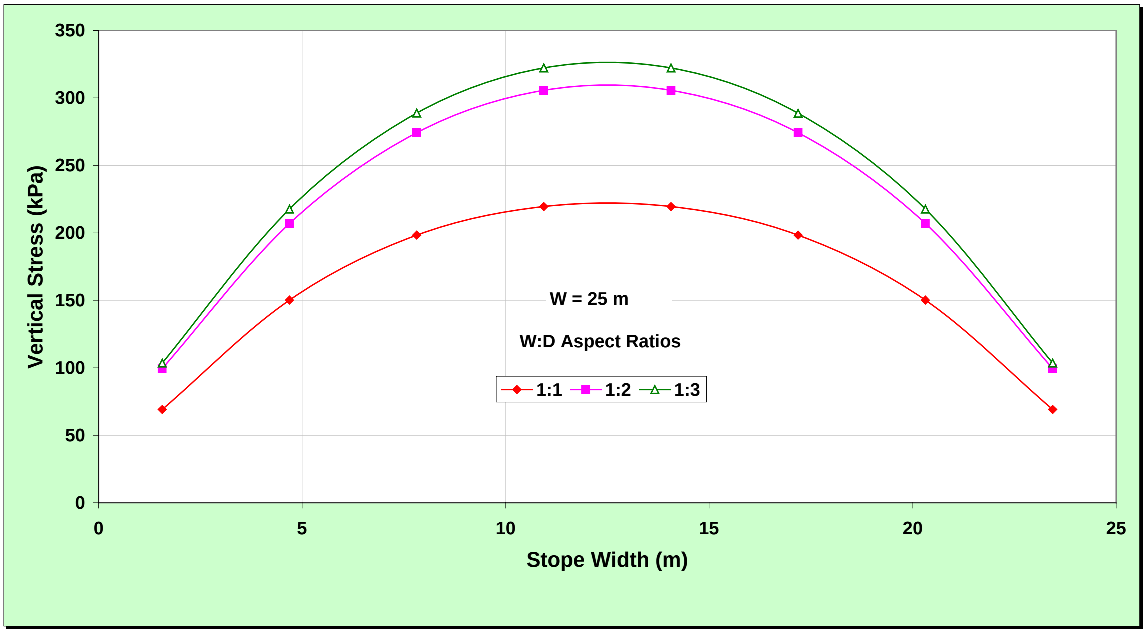

Figure A6.2.12 Vertical stress profiling across the constant width of a stope with varying depth (constant height=50m, constant width = 25m)

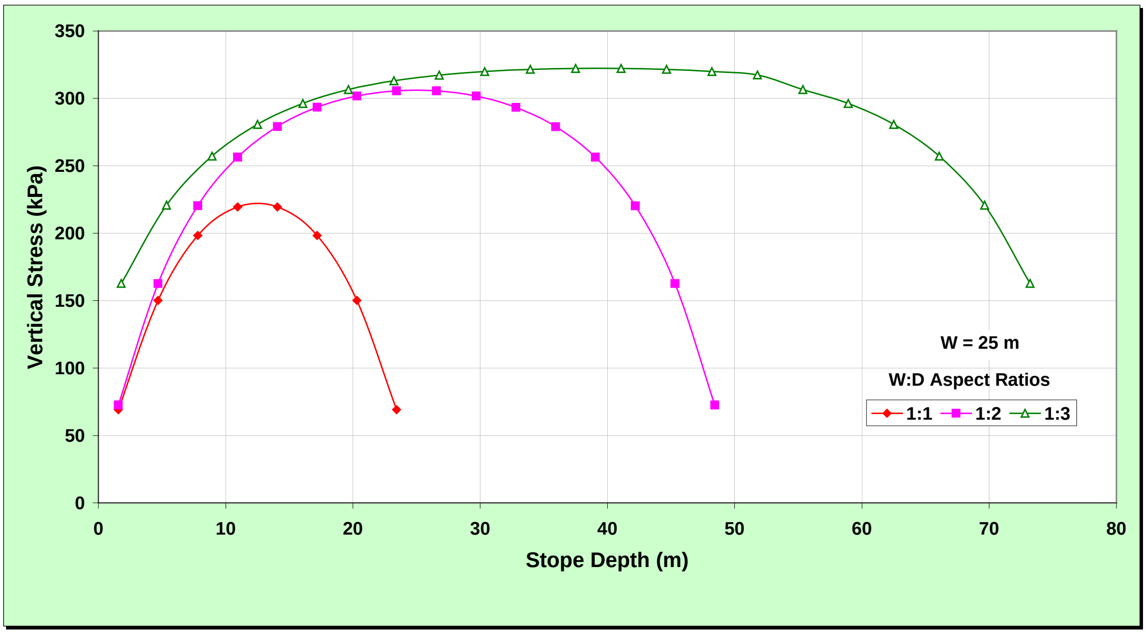

Figure A6.2.13 Vertical stress profiling down the longitudinal depth of a stope (constant height=50m, constant width = 25m)

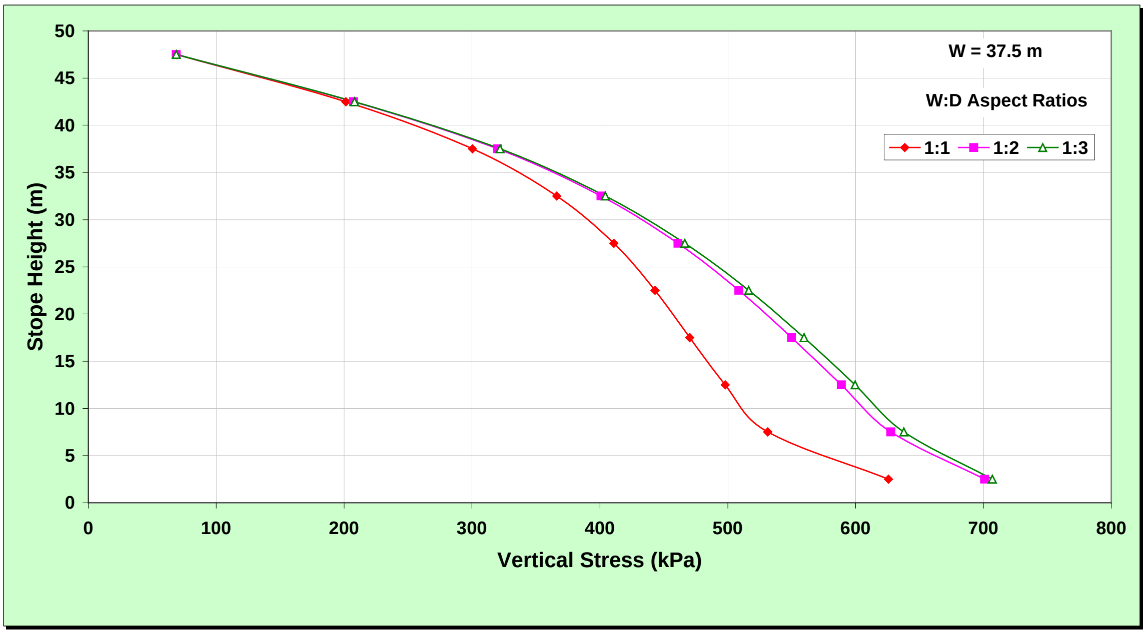

Figure A6.2.14 Central vertical stress profiling for a stope (constant height=50m, constant width = 37.5 m)

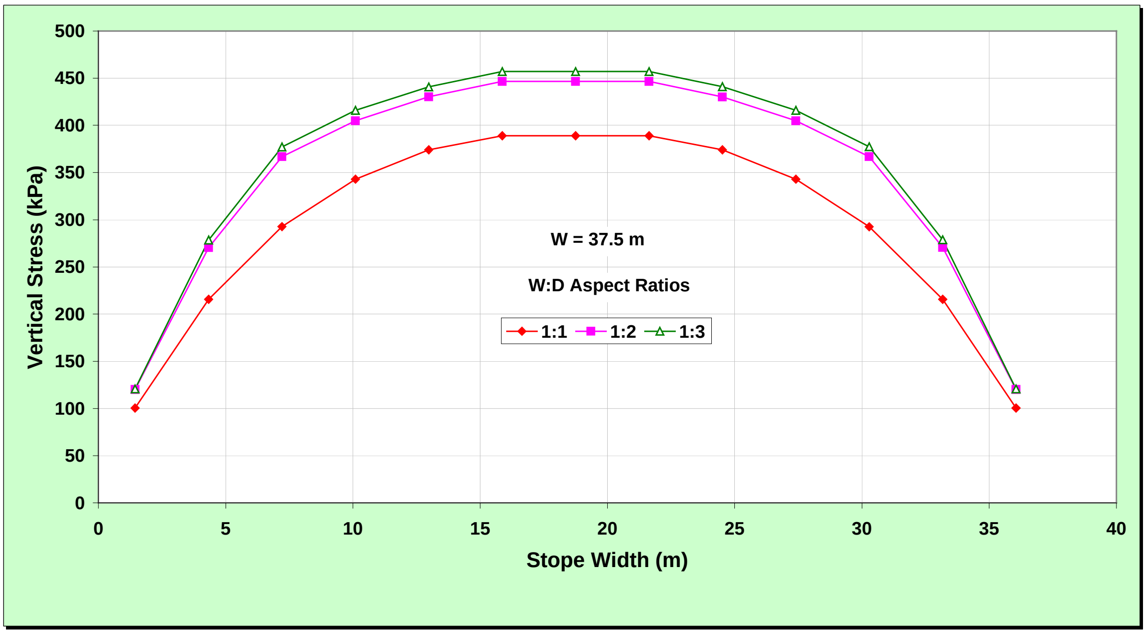

Figure A6.2.15 Vertical stress profiling across the constant width of a stope with varying depth (constant height=50m, constant width = 37.5 m)

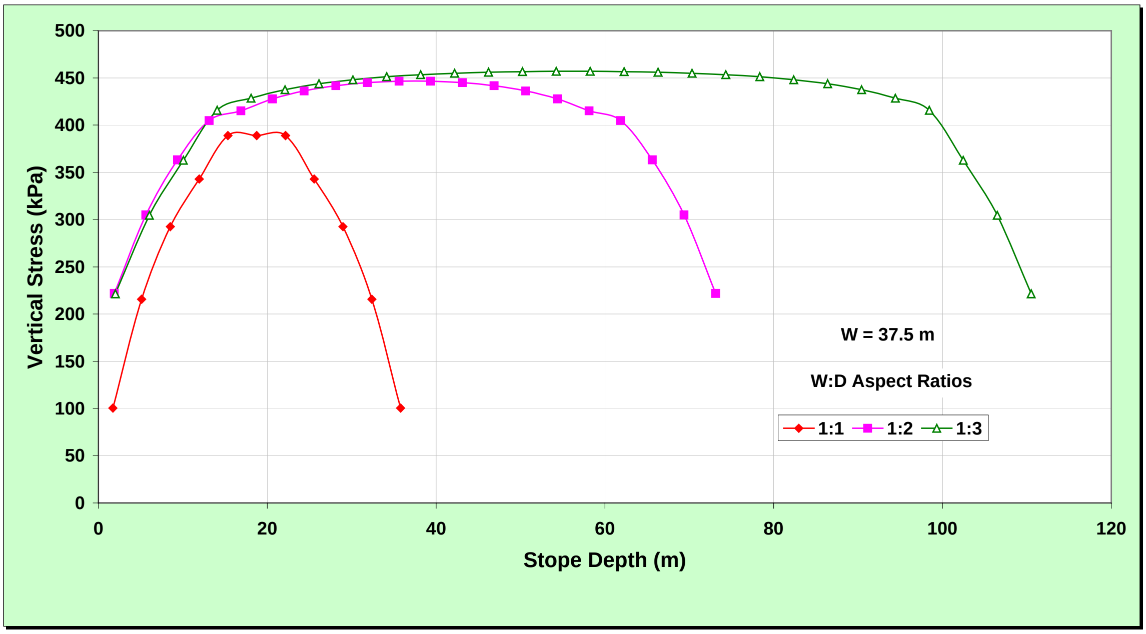

Figure A6.2.16 Vertical stress profiling down the longitudinal depth of a stope (constant height=50m, constant width = 37.5 m)

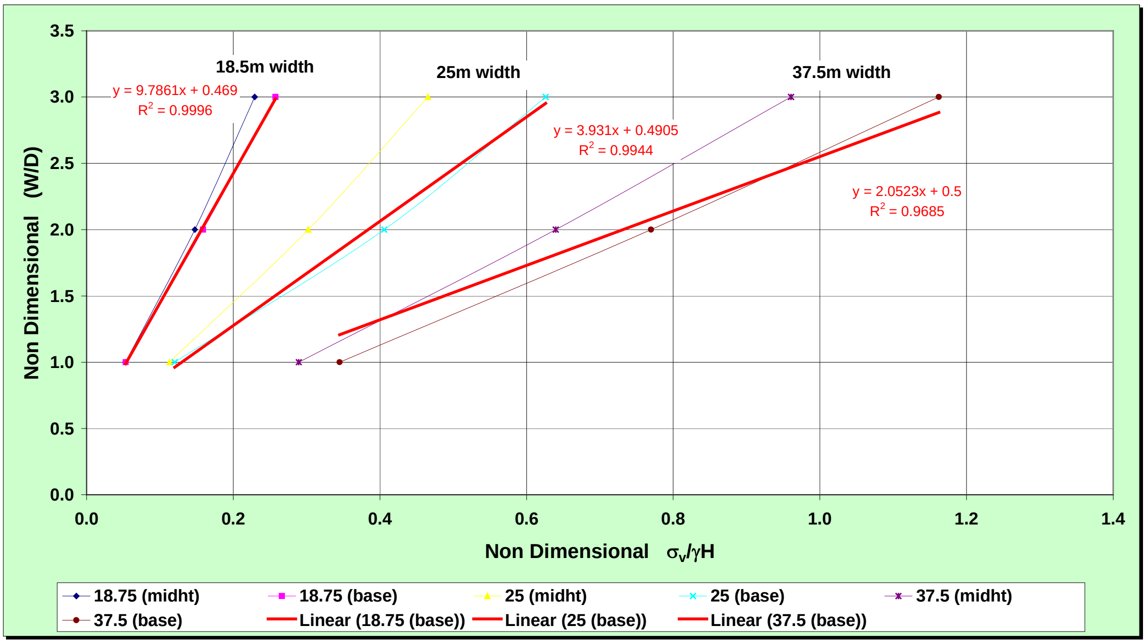

Figure A6.2.17 Non-dimensionalised plot showing the variation of the non-dimensional geometry parameter with the non-dimensional stress parameter (constant height = 50m), with linear trend lines applied.

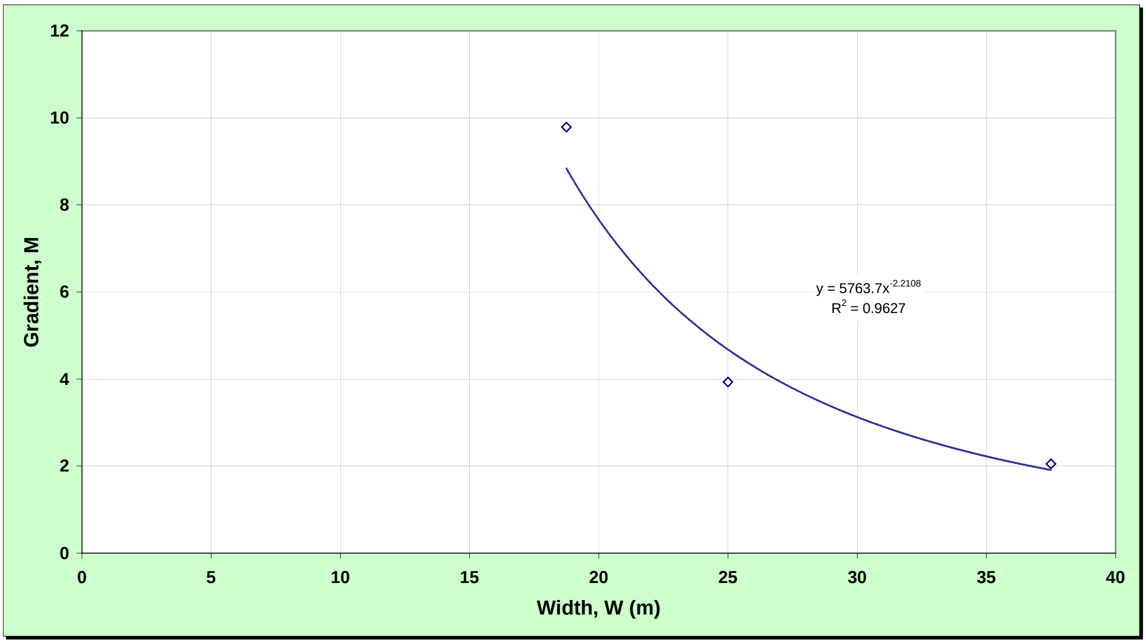

Figure A6.2.18 Variation of gradient, M, with width, W (m)

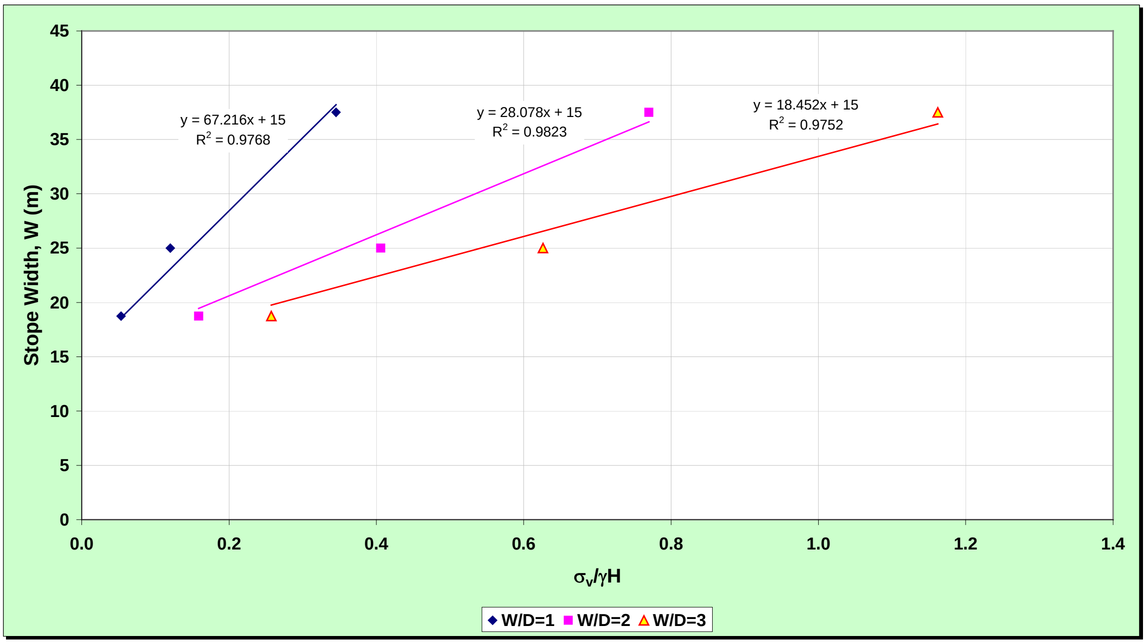

Figure A6.2.19 Variation of non-dimensionalised stress parameter with stope width for W/D aspect ratios from 1:1 to 1:3

APPENDIX 6.3

Back Analysis Data – Dilution Levels

Table A6.3.1 Back-analysis data for the determination of dilution levels of fill

BHP Projects

Paste Backfill analysis

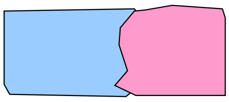

PASTE **ORE**

Assumtions

Stope 1 - PASTE, Stope 2 -ORE

Area between Stope 1&2 = amount of dilution of ore

First Round Analysis decided on the follc

Dilution Level

<2% NO

>2% OR <0.15% YES

Second Round Analysis includes stopes

Dilution Level

<2%

Density (t/m^3) Rocks

3.8 Hanging Wall Lead

3.2 Glen-holme Breccia

3.6 Footwall Lead

3.5 Kewell -Glenholme Brecia

		Volumes			Density		Mass (Tonnes)		% Dilution	Analysis Required	
Paste fill Stope	Exposed By Stope	Vol Paste Stope (m^3)	Vol Stope 2 (m^3)	Vol Intersection (m^3)	Ore (t/m^3)	Paste (t/m^3)	Stope 2 (tonnes)	Failed Paste (int.)-Tonnes	=(Tonnes PATSE)/ (Tonnes ORE)	1st Round	2nd Round
3590HL	3789HL	10464	40280	286.9	3.8	2.2	153064	631.18	0.41%		x
3590HL	3788HL	10464	21726	881.3	3.8	2.2	82559	1938.86	2.35%	x	
3789HL	3785HL	40280	27628	183.7	3.8	2.2	104986	404.14	0.38%		x
3789HL	3788HL	40280	21726	1364.2	3.8	2.2	82559	3001.24	3.64%	x	
3789HL	3791HG	40280	21427	130	3.2	2.2	68566	286	0.42%		x
4081HL	4082HL	17925	29030	479.3	3.8	2.2	110314	1054.46	0.96%		x
3594HL	3596HL	24000	32010	946.9	3.8	2.2	121638	2083.18	1.71%		x
4077HL	4276HL	50085	25676		3.8	2.2	97569	0			
4077HL	4080HL	50085	16522	225.1	3.8	2.2	62784	495.22	0.79%		x
4077HL	4079HL	50085			3.8	2.2	0	0			
4274HL	4272HL	55834	20995	323.3	3.8	2.2	79781	711.26	0.89%		x
4274HL	4276HL	55834	25676		3.8	2.2	97569	0			
4082HL	4080HL	29030	16522	1534.1	3.8	2.2	62784	3375.02	5.38%	x	
4082HL	4079HL	29030	0		3.8	2.2	0	0			
3785HL	3788HL	27628	21726		3.8	2.2	82559	0			
3598HL	3596HL	14858	32010	677	3.8	2.2	121638	1489.4	1.22%		x
3598HL	32A0HL	14858	14325	413.5	3.8	2.2	54435	909.7	1.67%		x
4261HL	4762HL	56160	24893	2124.9	3.8	2.2	94593	4674.78	4.94%	x	
4261HL	4760HL	56160	22494	210.5	3.8	2.2	85477	463.1	0.54%		x
4261HL	4763HL	56160	57206	286.8	3.8	2.2	217383	630.96	0.29%		x
4272HL	4271HL	20995	41562		3.8	2.2	157936	0			
4762HL	4760HL	24893	22494	520.6	3.8	2.2	85477	1145.32	1.34%		x
32A3HL	32A0HL	7523	14325		3.8	2.2	54435	0			
45e49HL	42e47HL	40796	29016	1737.4	3.8	2.2	110261	3822.28	3.47%	x	
4592GBE	4789HG	53320	23400	28.6	3.2	2.2	74880	62.92	0.08%	x	
4592GBE	4594HG	53320	21875		3.2	2.2	70000	0			
4592GBE	4289HG	53320	34879	223.8	3.2	2.2	111613	492.36	0.44%		x
4592GBE	4290HG	53320	34974.8		3.2	2.2	111919	0			
4596GB	4594HG	12165	21875	43.9	3.2	2.2	70000	96.58	0.14%	x	
4586GB	4789HG	37045	23400	0	3.2	2.2	74880	0			
4586GB	4784HG	37045	13487.6	609.4	3.2	2.2	43160	1340.68	3.11%	x	
4586GB	4284HG	37045	9944.3		3.2	2.2	31822	0			
4586GB	4290HG	37045	34974.8		3.2	2.2	111919	0			

Table A6.3.1 (cont'd)

		Volumes			Density		Mass (Tonnes)		% Dilution	Analysis Required	
Paste fill Stope	Exposed By Stope	Vol Paste Stope (m^3)	Vol Stope 2 (m^3)	Vol Intersection (m^3)	Ore (t/m^3)	Paste (t/m^3)	Stope 2 (tonnes)	Failed Paste (int.)-Tonnes	=(Tonnes PATSE)/(Tonnes ORE)	1st Round	2nd Round
4783GB	4583HG	16496	13866	41.6	3.2	2.2	44371	91.52	0.21%		x
4783GB	4784HG	16496	13487.6	32.8	3.2	2.2	43160	72.16	0.17%		x
4783GB	4780HG	16496	13732	1.1	3.2	2.2	43942	2.42	0.01%	x	
4777HG	4778HG	19429	30435	653.1	3.2	2.2	97392	1436.82	1.48%		x
4777HG	4775HG	19429	22705.7	106.9	3.2	2.2	72658	235.18	0.32%		x
4777HG	4780HG	19429	13732	60.4	3.2	2.2	43942	132.88	0.30%		x
4092HG	4289HG	51284	34879	864	3.2	2.2	111613	1900.8	1.70%		x
4092HG	4290HG	51284	34974.8		3.2	2.2	111919	0			
4092HG	4094HG	51284	0		3.2	2.2	0	0			
4086HG	4284HG	14498	9944.3	0.1	3.2	2.2	31822	0.22	0.00%	x	
4086HG	4290HG	14498	34974.8		3.2	2.2	111919	0			
4086HG	4084HG	14498	12015.6	463.6	3.2	2.2	38450	1019.92	2.65%	x	
4086HG	3790HG	14498	14045	335.8	3.2	2.2	44944	738.76	1.64%		x
4098HG	4096HG	15768	8995	315	3.2	2.2	28784	693	2.41%	x	
4098HG	4097HG	15768	10650	87.4	3.2	2.2	34080	192.28	0.56%		x
4778HG	4780HG	30435	13732	414.1	3.2	2.2	43942	911.02	2.07%	x	
4778HG	4580HG	30435	19046	578.8	3.2	2.2	60947	1273.36	2.09%	x	
4778HG	4278HG	30435	14737	0	3.2	2.2	47158	0			
4773HG	4775HG	12030	22705.7	567.7	3.2	2.2	72658	1248.94	1.72%		x
4780HG	4580HG	13732	19046		3.2	2.2	60947	0			
4583HG	4283HG	13866	24501	403.6	3.2	2.2	78403	887.92	1.13%		x
4583HG	4784HG	13866	13487.6	80.6	3.2	2.2	43160	177.32	0.41%		x
4583HG	4284HG	13866	9944.3		3.2	2.2	31822	0			
4583HG	4580HG	13866	19046	42.6	3.2	2.2	60947	93.72	0.15%	x	
4096HG	4094HG	8995	0		3.2	2.2	0	0			
4096HG	4097HG	8995	10650	141.5	3.2	2.2	34080	311.3	0.91%		x
4283HG	4284HG	24501	9944.3	526	3.2	2.2	31822	1157.2	3.64%	x	
4283HG	4280HG	24501	26326	1658.5	3.2	2.2	84243	3648.7	4.33%	x	
4580HG	4280HG	19046	26326	265.8	3.2	2.2	84243	584.76	0.69%		x
4289HG	4290HG	34879	34974.8		3.2	2.2	111919	0			
4094HG	4095HG	0	0		3.2	2.2	0	0			
3790HG	3791HG	14045	21472		3.2	2.2	68710	0			
4280HG	4278HG	26326	14737	1085.1	3.2	2.2	47158	2387.22	5.06%	x	
4097HG	4095HG	10650	0		3.2	2.2	0	0			
5574HG	5369HG	11691	22039	616.8	3.2	2.2	70525	1356.96	1.92%	x	
5574HG	5371HG	11691	13640.4	12.1	3.2	2.2	43649	26.62	0.06%	x	
5574HG	5368HG	11691	10234.6	65.5	3.2	2.2	32751	144.1	0.44%		x
5369HG	5370HG	22039			3.2	2.2	0	0			
5369HG	5367HG	22039	20900.8	1171.5	3.2	2.2	66883	2577.3	3.85%	x	
5375HG	5371HG	14006	13640.4	389.7	3.2	2.2	43649	857.34	1.96%	x	
5375HG	5377HG	14006			3.2	2.2	0	0			
5769KG	57d71KG	13954	14745.7	0	3.5	2.2	51610	0			
5769KG	57d69KG	13954	13954	244.2	3.5	2.2	48839	537.24	1.10%		x
5772KG	5774KG	13343	11691.2	210.9	3.5	2.2	40919	463.98	1.13%		x
5772KG	57d71KG	13343	14745.7	371	3.5	2.2	51610	816.2	1.58%		x
5774KG	55c75KG	11691	10115.8	23.6	3.5	2.2	35405	51.92	0.15%	x	
57e71KG	57d71KG	14405	14745.7	674.7	3.5	2.2	51610	1484.34	2.88%	x	
57d69KG	57d71KG	12731	14745.7	863.9	3.5	2.2	51610	1900.58	3.68%	x	

ound through using Surpac

Average	***1.57%***
Maximum	***5.38%***
Minimum	***0.000691%***